Imperial College
London

Optimization of Continuous Flow Polymerase Chain Reaction with Microfluidic Reactors

Submitted for the Degree of Doctor or Philosophy

By

Yasemin Koç

January 2008

Department of Chemistry
Imperial College London

BIBL. LONDON UNIV.

This work is dedicated to the deceased
Madame de Pompadour.

Abstract

The ultimate goal of this thesis was to demonstrate reproducible continuous flow PCR within a microfluidic device and achieve higher amplification efficiencies when compared to conventional thermal cyclers. The realization of successful continuous flow PCR of *Bacillus globigii* on microfluidic devices was established in four steps.

The first part of this thesis is concerned with optimizing and assessing the robustness of the *Bacillus globigii* PCR system on the macroscale before transferral to a microfluidic format. The most important results relate to variations in PCR component concentrations and variations of temperature cycling conditions, and are presented in Chapter 2.

The second part of this thesis presents the fabrication of microfluidic devices and includes an optimisation study relating to etching of microfluidic channels in planar glass substrates. This study quantifies the influence of different etchant solutions on the topology of channel surfaces. These data are presented in Chapter 3.

In the case of continuous-flow PCR, the times associated with sample heating and cooling depend (in principle) only on the speed with which sample may be moved between the localised temperature zones. In such a situation, thermal inertia is reduced to a minimum because only the sample thermal mass needs to be considered. This fact can be used to improve product yields. However, determination and control of temperature on the microscale is difficult. When performing PCR, the ability to accurately control system temperatures is especially important. Accordingly, the third part of this thesis focuses on the introduction of a method to directly measure fluidic temperatures within microchannel environments that utilises fluorescence lifetime imaging. These experiments are detailed in Chapter 4.

Another concern when performing continuous-flow PCR on the microscale is a loss in efficiency. Although this problem can usually be traced to inhibitory materials used in microdevice fabrication (e.g. residual chromium from chrome masks in glass chip fabrication or thermocouples), the most predominant problem encountered is the adsorption of PCR components onto the microchannel facilitated by increased surface-to-volume ratios. To address this issue, a variety of surface treatments are

applied to microchannel surfaces with the aim of improving the efficiency of the reaction. These studies are presented in Chapter 5.

Finally, the introduction of superhydrophobic coatings on microchannel surfaces is introduced in Chapter 6.

Table of Contents

1 Introduction 1
1.1 History of Microfluidics 2
1.1.1 Early Analytical Devices – Chromatography on the Microscale 3
1.2 Miniaturised Total Analysis Systems 5
1.3 Physical Characteristics of Fluid Flow 6
1.3.1 Reynolds Number 6
1.3.2 Diffusion 8
1.3.3 Surface-to-Volume Ratio 9
1.4 Literature Review 10
1.4.1 Molecular Separations 10
1.4.2 Cell Analysis 14
1.4.2.1 Cell Handling 14
1.4.2.2 Cell Culture 16
1.4.3 Clinical Diagnostics 19
1.4.4 Immunoassays 21
1.4.5 Small Volume Detection 25
1.5 The Polymerase Chain Reaction 32
1.6 Polymerase Chain Reaction on the Microscale 40
1.6.1 Microfluidic Thermocyclers 41
1.6.2 Problems with Microfluidic PCR Instrumentation 47
2 Polymerase Chain Reaction on the Macroscale 68
2.1 Bacillus Globigii - PCR System 69
2.2 Experimental Methods 72
2.2.1 Instrumentation 73
2.2.1.1 Thermal Cycler 73
2.2.1.2 Chip-Based Gel-Electrophoresis Instrument 76
2.3 Results 80
2.3.1 Optimization of Thermal Cycling Conditions 80
2.3.1.1 Temperature and Time 80
2.3.1.1.1 Hot-Start Phase 81
2.3.1.1.1.1 Conventional PCR System 81
2.3.1.1.1.2 Real-Time PCR System 83
2.3.1.1.2 Denaturation 85
2.3.1.1.2.1 Conventional PCR System 85

2.3.1.1.2.2 Real-Time PCR System 87
2.3.1.1.3 Annealing and Extension 90
2.3.1.1.3.1 Conventional PCR System 90
2.3.1.1.3.2 Real-Time PCR System 92
2.3.1.2 Assessment of Optimum Number of Cycles 95
2.3.1.2.1 Conventional PCR System 95
2.3.1.2.2 Real-Time PCR System 96
2.3.1.3 Temperature Ramp Rate Variation 98
2.3.1.3.1 Conventional PCR System 98
2.3.1.3.2 Real-Time PCR System 98
2.3.2 Optimization of PCR Components and Additives 100
2.3.2.1 Primer Optimization 100
2.3.2.1.1 Conventional PCR System 100
2.3.2.1.2 Real-Time PCR System 102
2.3.2.2 Taq Polymerase Optimization 104
2.3.2.2.1 Conventional PCR System 104
2.3.2.2.2 Real-Time PCR System 105
2.3.2.3 Magnesium Chloride Concentration 106
2.3.2.3.1 Conventional PCR System 106
2.3.2.3.2 Real-Time PCR System 107
2.3.2.4 Target Concentration Optimization 109
2.3.2.4.1 Real-Time PCR System 109
2.3.2.5 PCR Additives 111
2.3.2.5.1 BSA Optimization 111
2.3.2.5.1.1 Conventional PCR System 111
2.3.2.5.1.2 Real-Time PCR System 112
2.3.2.5.2 PVP Optimization 114
2.3.2.5.2.1 Conventional PCR System 114
2.3.2.5.2.2 Real-Time PCR System 115
2.4 Discussion 116
3 Chip Fabrication 120
3.1 Microchip Fabrication Process 122
3.2 Design Patterning 126
3.3 Etching 127
3.3.1 Etchant Solutions 128
3.4 Bonding 133
4 Fluorescence Lifetime Imaging in Microfluidic Systems 140

4.1 Temperature Measurements in Microfluidic Channels 141
4.2 Unimolecular Photophysics 144
4.2.1 Fluorescence 145
4.2.2 Single Photon and Multi Photon Excitation 146
4.2.3 The Fluorescence Lifetime 147
4.3 Methods for Measuring Fluorescence Lifetimes 149
4.3.1 Wide-Field Techniques 149
4.3.2 Time-Correlated-Single-Photon-Counting (TCSPC) 150
4.3.3 Molecular Dyes for FLIM 151
4.4 Experimental Methods 152
4.4.1 Wide-Field Imaging System 152
4.4.2 TCSPC - Imaging Techniques 153
4.4.3 Temperature Measurements 155
4.4.3.1 Temperature Calibration with Aqueous Rhodamine B 156
4.4.3.2 Imaging Fluidic Temperature in Microchannels 157
4.4.3.3 Imaging Fluidic Temperature Gradients in Microchannels 158
4.4.3.4 Mapping of Fluidic Temperatures in Three Dimensions 159
4.4.3.5 Imaging Microfluidic Temperature Variations Using Chip II 159
4.4.3.6 Imaging Microfluidic Temperature Variations Using Chip III 160
4.5 Results 160
4.5.1 System Calibration 160
4.5.2 Wide-Field Imaging Techniques 162
4.5.2.1 Imaging Fluidic Temperature in Microchannels 162
4.5.2.2 Imaging Microfluidic Temperature Gradients 163
4.5.2.3 3D-Mapping of Channel Temperature 166
4.5.3 TCSPC – Techniques 168
4.5.3.1 Imaging Microfluidic Temperature Gradients on Chip II 168
4.5.3.2 Imaging Microfluidic Temperature Gradients Under Reversed Flow (CHIPII) 170
4.5.3.3 Imaging Microfluidic Temperature Gradients whilst Varying Volume Flowrates 171
4.5.3.4 Imaging Microfluidic Temperature Gradients (chip III) 173
4.6 Discussion 175
5 PCR on the Microscale 179
5.1 Surfaces on the Microscale 180
5.1.1 Experimental Methods 182
5.1.1.1 Continuous-Flow PCR within Untreated Glass Microchannels .. 182

5.1.1.1.1 Interaction between PCR Components and a Cold Microfluidic Device 184
5.1.1.1.2 Assessment of Enzyme Adsorption in Hot Microfluidic Devices 191
5.1.1.2 Functionalization of Microfluidic Channel Surfaces 192
5.1.1.2.1 Water Contact Angle Measurements of Functionalized Surfaces 192
5.1.1.2.2 Water Flow Profile Measurements in Functionalized Channels 195
5.1.1.2.2.1 Surface Treatment with Dichlorodimethlysilane (silane I) 197
5.1.1.2.2.2 Surface Treatment with Silane I and PEG 197
5.1.1.2.2.3 Surface Treatment with Silane I and BSA 197
5.1.1.2.2.4 Surface Treatment with Silane I and PVP 197
5.1.1.2.2.5 Surface Treatment with Teflon 198
5.1.1.2.2.6 Surface Treatment with Silane II 198
5.1.2 Protein Adsorption Assessment and CF PCR Results 198
5.1.2.1 Protein Adsorption Assessment Studies on Coated Microchannels 199
5.1.2.1.1 Protein Adsorption Assessment on Microchannels Coated with Silane I 199
5.1.2.1.2 Protein Adsorption Assessment on Microchannels Coated with Silane I and PEG 201
5.1.2.1.3 Protein Adsorption Assessment on Microchannels Coated with Silane I and BSA 202
5.1.2.1.4 Protein Adsorption Assessment on Microchannels Coated with Silane I and PVP 204
5.1.2.2 CF PCR on Coated Microchannels 205
5.1.2.2.1 CF PCR on Silane I Coated Microchannels 206
5.1.2.2.2 CF PCR on Silane I and BSA Coated Microchannels 209
5.1.2.2.3 CF PCR on Teflon I Coated Microchannels 211
5.1.2.2.4 CF PCR on Silane II Coated Microchannels 212
5.1.3 Discussion 215
6 Development of Superhydrophobic Microfluidic Channels 222
6.1 Background Theory 223
6.2 Experimental Methods 225
6.2.1 Generation of Bulk Superhydrophobic Surfaces 225

6.2.1.1 Surface Preparation 225
6.2.1.1.1 Superhydrophobic Surfaces on Glass 226
6.2.1.1.2 Superhydrophobic Surfaces on Copper 228
6.2.1.1.3 Assessment of Water Contact Angles on Bulk Surfaces 229
6.2.1.2 Surface Adsorption Experiments on Bulk Surfaces 231
6.2.2 Generation of Superhydrophobic Surfaces in Microchannels 232
6.2.2.1 Surface Preparation 232
6.2.2.2 Assessment of Water Flow Profiles in Treated Microchannels .. 235
6.2.2.3 Surface Adsorption Experiments in Microchannels 236
6.3 Results 237
6.3.1 Protein Adsorption Assessment of Bulk 237
6.3.1.1 Protein Adsorption Assessment of Bulk Surfaces Under Static Conditions 237
6.3.1.2 Protein Adsorption Assessment of Bulk Surfaces Under Dynamic Conditions 238
6.3.2 Protein Adsorption Assessment in Surface Treated Microchannels 240
6.4 Discussion 242
7 Discussion 246
8 Appendix 250
8.1 Chapter 1: Appendix A 251
8.2 Chapter 4:AppendixB 258
8.2.1 Modelling 258
8.2.1.1 Background 258
8.2.1.1.1 Pre-Processing 258
8.2.1.1.2 Solving 259
8.2.1.1.3 Post-Processing 259
8.2.1.2 Process of Modeling 261
8.2.1.3 Results 262

TEXT BOUND INTO

THE SPINE

List of Figures

Figure 1.1 Annual microfluidics publications across all journals. Data created through a Web of Science search incorporating the keywords "microchannel", "microfluidics" and "lab on a chip". 3

Figure 1.2 Photograph of an LC chip containing column and detector electrodes. [3] 4

Figure 1.3 Schematic of the individual components of a generic analytical procedure 5

Figure 1.4 The principle of Osborne Reynolds' experiment (a) laminar flow and (b) turbulent flow [35]. 7

Figure 1.5 Schematic layout of the subdivision of the separation channel [69]. 12

Figure 1.6 The microfluidic assembly has a bonded two-layer glass body and two interface boards. Both boards, anode and cathode contain buffer solution. All 16 lanes taper off for the scanning region, where they are parallel and have a total width of 3.2 mm [71]. 13

Figure 1.8 Schematic view of a device for particle sorting with transducers as emitters of ultrasound waves. 15

Figure 1.9 a) A design of a high speed bubble-jet cell sorter b) A 20 μm microsphere entering the detection window and being pushed toward outlet 2 by the bubble jet on the opposite side [86]. 16

Figure 1.10 (A) PDMS microfluidic biochip used for in vitro liver cell culturing. (B) Hepatoma-derived cell line. (C) and (D) cultivated cells in microfluidic biochip [103]. 18

Figure 1.11 Photomicrograph (magnification 40X) showing cancer cells flowed through PDMS channel with flow rate of 4 μl/min a) and 20 μl/min b) [108]. 19

Figure 1.12 Schematic illustration showing the bead 10 X 10 array chip which is packaged into a fluid cell. The pyramidal pits extend through the entire thickness of the wafer, thereby creating square openings (~100 μm X ~100 μm) on the remote side of the chip. These openings both provide optical access to the bead element and serve as a drain for the reaction/analysis chambers. The package assembly is suitable for both fluorometric and colorimetric analysis [111]. 20

Figure 1.13 Schematic of an enzyme analysis chip. The channels terminate at reservoirs containing the indicated solutions. The channels are 9 μm deep and 35 μm wide [34]. 22

Figure 1.15 Schemes for the delivery and attachment of two different IgGs using a μFN. A) followed by an immunoassay for the attached proteins after removal of the μFN. B) Recognition fluorescent signals when bound to each partner. C) Red channel

compromises chicken Immunoglobulin and the green channel compromises mouse immunoglobulin [118]. 24

Figure 1.16 Microfluidic device that detects ant-HIV-1 antibodies. The HIV antigen is patterned onto a polystyrene surface as a strip, and a slab of PDMS with microchannels is placed orthogonally to the stripe [120]. 25

Figure 1.17 Schematic of the laser- excited confocal-fluorescence scanner and a capillary array electrophoresis chip [24]. 27

Figure 1.18 Mask design used to photolithographically pattern the 12-channel CAE chips. A) injection channels, B) separation channels, C) optical alignment channels, D) detection region, 1) Injection waste reservoirs, 2) ground reservoirs, 3) injection reservoirs, 4) high voltage anode reservoir [24]. 28

Figure 1.19 Schematic diagram of the microchip ESI-MS interface. The voltage for ESI was sequentially applied to one well of each channel containing buffer and a platinum electrode. The second well of each channel contained sample and was connected to a syringe pump to provide a flow rate of 100-200 nl/min. The exit ports of the microchip were aligned sequentially with the orifice of the MS using a 3D stage [154]. 29

Figure 1.20 Device layout and concept. a) Photograph of an integrated device with embedded sensors (right dotted area), PCR microfluidic channel with integrated valves (left dotted area) and metal resistive heaters and sensors (features above and below PCR channel). b) 3D rendering of device centred on sensors (top and bottom squares) and excitation metal electrode. Adjacent features include gold traces for electrical connections, inlet of sensor channel, and an integrated valve controlling the interface to the PCR channel. The gold traces are connected to the respective gold electrode and field-effect sensors by buried conductive traces in silicon (not shown). Conceptual schematic of sensor cross section illustrating the physical changes caused by binding of (c) positively charged polyelectrolyte followed by d) negatively charged product DNA in the PCR mix. The mobile positive charge carriers in the sensor redistribute depending on the polarity of surface charge, affecting the depth of the charge depletion region in the process. This subsequent change in depletion capacitance is monitored by applying an AC voltage to the metal electrode and measuring the resulting current through the doped sensor region in silicon [160]..... 31

Figure 1.21 Schematic of the PCR amplification process. During the first step of the polymerase chain reaction the double strand DNA template becomes two single strands. This step is performed between 94 °C and 96 °C to provide the energy necessary to break the hydrogen bonds between the two strands. The temperature is then

lowered for the annealing step: the primers specifically bind to the DNA template. At this stage, the temperature is primer-dependant and usually varies between 50 °C and 65 °C. Finally the temperature is raised for the extension phase where the template is replicated by the polymerase enzyme. Interestingly, at the end of the 1st cycle, the product obtained is specific only at one end, as the replication lasts as long as the temperature allows it. It is only at the end of the 2nd cycle that a truly specific product is produced. Two types of replication occur at the same time: semi-specific products (e.g. from cycle 2) lead to linear replication, whereas truly specific products lead to exponential replication (see end of 3rd cycle)..... 35

Figure 1.22 The exponential amplification of DNA fragment in PCR..... 36

Figure 1.23 Saiki *et al.* [200] presented first PCR by using a chamber and a water bath. Wilding *et al.* [201] performed the first PCR in a chamber. Woolley *et al.* [202] demonstrated the first chamber PCR with integrated separation and online detection. Kopp *et al* [203] presented the first continuous-flow PCR. Belanger *et al.*[204] introduced the first PCR on the fastest commercial thermal cycler. Ohashi *et al.* [205] presented droplet based- PCR..... 40

Figure 1.24 Schematic of the integrated PCR – capillary electrophoresis microdevice. (A) Laser excitation source, detection and PCR-CE chip. (B) PCR chamber (C) Cross section of junction between PCR and CE [202]..... 42

Figure 1.25 Set-up for infrared-mediated thermocycling. (A) Single-microchamber configuration. (B) Dual-microchamber configuration where one chamber acts solely for temperature sensing while the other is used for PCR [207]. 44

Figure 1.26 Rayleigh-Bénard cell schematic. Due to the difference in temperature, a convective flow develops in the cell, with an upward flux in the centre and downward fluxes at the sides. As the sample moves up and down in the cell, thermal cycling is accomplished and DNA amplified [227]..... 45

Figure 1.27 A continuous flow PCR device with two inlets and one outlet. The sample is pumped through different temperature zones for denaturation, annealing and extension [203] . 46

Figure 1.28 Schematic of integrated device. The only electronic component not fabricated on the silicon device is the excitation source [217]..... 48

Figure 2.1 Step 1: Target and Scorpion stem sequence are denatured. Step 2: Scorpion primer anneals to target. Step 3: Scorpion primer extends and produces double stranded DNA. Step 4: double-stranded DNA produced in step 3 is denatured. This results in a single-stranded target molecule with the Scorpion primer attached. Step 5: The mixture cools down and the Scorpion probe sequence binds to its target in an intramolecular manner..... 71

Figure 2.2 The optical system allows the measurement of fluorescence in four channels at the same time. High intensity LEDs and optical filters are optimized for spectral separation. 16 independently programmable reaction sites can simultaneously perform 16 different cycling protocols in one system [7]. 74

Figure 2.3 A plot of fluorescence versus cycle number produces a sigmoidal shaped curve called the growth curve with baseline, log-linear and plateau regions. 75

Figure 2.4 (a) The Agilent 2100 Bioanalyzer, (c) the electrophoresis chip which is placed into the detection receptacle (b). 76

Figure 2.5 An electropherogram for a standard DNA ladder. The concentrations and sizes of the individual base pairs are preset in the assay..... 77

Figure 2.6 An electropherogram of an amplified DNA sample (middle peak) bracketed by the lower marker (left peak) and the upper marker (right peak). The lower marker and upper marker are internal standards used to align the ladder data with data from the sample wells. 78

Figure 2.7 Normalised absorption and emission spectra of FAM and SYBR Green. 79

Figure 2.8 a) Electropherogram of product amplified using a conventional PCR system..... 80

Figure 2.9 Variation of peak area as a function of time during the hot start phase. Five replicates were used to define each data point with hot a start temperature at 95°C.

82

Figure 2.10 Variation of peak area as a function of temperature during the hot start phase. Five replicates were used to define each data point with a hot start duration of 30s. 82

Figure 2.11 Variation of C_t value as a function of time during the hot start phase. Five replicates were used to define each data point with the hot start temperature set to 95°C. 83

Figure 2.12 Variation of peak area as a function of time during the hot start phase. Five replicates were used to define each data point with a hot start temperature of 95°C.

84

Figure 2.13 Variation of C_t value as a function of temperature during the hot start phase. Five replicates were used to define each data point with a hot start duration of 30s. 84

Figure 2.14 Variation of peak area as a function of temperature during the hot start phase. Five replicates were used to define each data point with hot start times of 20s. 85

Figure 2.15 Variation of peak area as a function of time during the denaturation phase. Five replicates were used to define each data point with a denaturation temperature of 95°C. 86

Figure 2.16 Variation of peak area as a function of temperature during the dentauration phase. Five replicates were used to define each data point with a denaturation time of 5s.

87

Figure 2.17 Variation of C_t value as a function of time during the denaturation phase. Five replicates were used to define each data point with a denaturation temperature of 95°C. 88

Figure 2.18 Variation of peak area as a function of temperature during the denaturation phase. Five replicates were used to define each data point with a denaturation temperature of 95°C. 88

Figure 2.19 Variation of C_t values as a function of temperature during the denaturation phase. Five replicates were used to define each data point with a denaturation time of 1s. 89

Figure 2.20 Variation of product peak area as a function of temperature during the denaturation phase. Five replicates were used to define each data point with a denaturation time of 1s. 89

Figure 2.21 Variation of peak area as a function of time during the annealing and extension phase. Five replicates were used to define each data point with an annealing and extension temperature of 65°C. 91

Figure 2.22 Variation of peak area as a function of temperature during the annealing and extension phase. Five replicates were used to define each data point with an annealing and extension time of 10s. 91

Figure 2.23 Variation of C_t value as a function of time during the annealing and extension phase. Five replicates were used to define each data point with an annealing and extension temperature of 65°C. 92

Figure 2.24 Variation of product peak area as a function of time during the annealing and extension phase. Five replicates were used to define each data point with an annealing and extension temperature of 65°C. 93

Figure 2.25 Variation of C_t value as a function of temperature during the annealing and extension phase. Five replicates were used to define each data point with an annealing and extension time of 5s. 93

Figure 2.26 Variation of sample peak area as a function of temperature during the annealing and extension phase. Five replicates were used to define each data point with an annealing and extension time of 5s. 94

Figure 2.27 Variation of peak area as a function of cycle number. Five replicates were used to define each data point with defined protocol conditions as presented in Table 2.5. 96

Figure 2.28 Variation of C_t as a function of cycle number. Five replicates were used to define each data point with defined protocol conditions as presented in Table 2.6. 97

Figure 2.29 Variation of peak area as a function of cycle number. Five replicates were used to define each data point with defined protocol conditions as presented in Table 2.6. 97

Figure 2.30 Variation of peak areas as a function of ramp rates. Five replicates were used to define each data point with protocol conditions as presented in Table 2.5. 98
Figure 2.31 Variation of C_t as a function of ramp rate. Five replicates were used to define each data point with defined protocol conditions as presented in Table 2.6. 99
Figure 2.32 Variation of peak areas as a function of ramp rate. Five replicates were used to define each data point with defined protocol conditions as presented in Table 2.6. 99
Figure 2.33 Variation of peak area as a function of primer concentration. Five replicates were used to define each data point. 101
Figure 2.34 a) Electropherogram of product amplified using primer concentrations of 0.5 µM. b) Electropherogram of PCR product and bi-products using primer concentrations of 0.8 µM. 101
Figure 2.35 Variation of C_t value as a function of primer ratio. Five replicates were used to define each data point. 102
Figure 2.36 Variation of C_t value as a function of primer concentration. Five replicates were used to define each data point. 103
Figure 2.37 Variation of peak areas as a function of primer concentration. Five replicates were used to define each data point. 103
Figure 2.38 Variation of peak area as a function of enzyme concentration. Five replicates were used to define each data point. 105
Figure 2.39 Variation of C_t value as a function of enzyme concentration. Five replicates were used to define each data point. 106
Figure 2.40 Variation of peak area as a function of magnesium chloride concentration. Five replicates were used to define each data point. 107
Figure 2.41 Variation of C_t value as a function of magnesium chloride concentration. Five replicates were used to define each data point. 108
Figure 2.42 Variation of peak area as a function of magnesium chloride concentration. Five replicates were used to define each data point. 108
Figure 2.43 Variation of C_t as a function of $\log_{10}$ target concentrations. Five replicates were used to define each data point. 110
Figure 2.44 Variation of peak area as a function of BSA concentration. Five replicates were used to define each data point. 112
Figure 2.45 Variation of C_t value as a function of BSA concentration. Five replicates were used to define each data point. 113
Figure 2.46 Variation of peak area as a function of BSA concentration. Five replicates were used to define each data point. 113
Figure 2.47 Variation of peak area as a function of PVP concentration. Five replicates were used to define each data point. 114

Figure 2.48 Variation of C_t value as a function of PVP concentration. Five replicates were used to define each data point. 115
Figure 2.49 Variation of peak area as a function of PVP concentration. Five replicates were used to define each data point. 116
Figure 3.1 Chip fabrication consists of three main parts: patterning, etching and closure. The flow diagram presents the chronology of this process..... 123
Figure 3.2 The individual steps in microchip fabrication 124
Figure 3.3 Example of an AutoCAD design with dimensions in µm [34]. 126
Figure 3.4 Schematic of isotropically and anisotropically etched channels in cross section. For calculations of the etch depth of a channel, ω is the total channel width, W is the design width and d is the etch depth of the channel..... 128
Figure 3.5 Images of two parallel channels no impurities in (a) (187 µm wide and 62.5 µm deep) and showing impurities in (b) (218 µm wide and 77.8 µm deep)..... 129
Figure 3.6 (a) The Dektak profilometer (b) image of the scanning tip. The top tip is the tip which scans the surface, (c) A depth profile of five parallel channels. 130
Figure 3.7 (a) Depth variation across whole width of a microfluidic channel. (b) Depth variation when impurities are present on the channel surface. 131
Figure 3.8 a) Depth variation across whole width of a microfluidic channel. b) Depth variation when impurities are not present on the channel surface. 132
Figure 3.9 Images of channels etched with a 20 % HF solution. a) microphotograph of channels b) 2D image of channels c) 3D image of channels made with the interferometer microscope. 132
Figure 3.10 Images of channels etched with a 5 % HF solution. a) microphotograph of channels b) 2D image of channels c) 3D image of channels made with the interferometer microscope. 133
Figure 3.11 Temperature cycle used for the thermal bonding of glass wafers in the fabrication of microfluidic devices. 135
Figure 4.1 (a) An integrated microfluidic device [2] consisting of silicon (doped with boron), silicon oxide, titanium oxide, p-xylylene and glass layers. The heater and sensor elements are embedded beneath a plastic coating immediately below the reaction area. (b) An integrated microfluidic device [3] consisting of silicon, glass, titanium, platinum and gold layers with etched heating and RTD elements..... 142
Figure 4.2 Fluorescence intensity as a function of temperature for a 0.1mM Rhodamine B solution in carbonate buffer. 144
Figure 4.3 Jablonski diagram outlining possible photophysical transitions. Blue represents single photon excitation, red represents multiphoton excitation, grey represents internal conversion, green represents radiative fluorescence emission, dotted grey

represents non-radiative relaxation, brown represents phosphorescence, black represents intersystem crossing and dashed black presents energy transfer to another molecule. 146

Figure 4.4 Single photon excitation (SPE) compared with multiple photon excitation (MPE) of a fluorescein solution [13]. For SPE fluorescein is excited across the entirety of the optical path, whereas for MPE fluorescein is excited in a small volume close to the focal point of the laser beam. 147

Figure 4.5 Illustration of how the fluorescence decay is recorded on a plot with intensity (I) versus time (t) in (a) and with log intensity versus time (t) in (b). Fluorescence information is acquired at varying time points, t_n, on the fluorescence decay and fitted for fluorescence lifetimes. Here the fluorescence lifetime can be extracted from the slope of the curve. 149

Figure 4.6 a) Schematic of a time-gated fluorescence system with b) three different gate delay positions in respect to the excitation pulse and c) transition from gated images to FLIM images [19]. The green and red curve represent different fluorescent dyes with different fluorescence lifetime decays. 150

Figure 4.7 TCSPC measurement principle[21] . A histogram of arrival times of individual photon events is built up which represents the fluorescence decay of the sample. 151

Figure 4.8 Pulsed infrared illumination is coupled into the TriM-Scope. This illumination is focused into the sample, where two-photon absorption occurs in a thin optical section only. The fluorescence emission is then imaged onto a gated optical intensifier relayed to a CCD camera High Rate Image intensifier. Solid black lines indicate triggering connections. 153

Figure 4.9 A supercontinuum source (435-1150 nm) is coupled to a prism-based spectrometer, producing a central wavelength of 550 nm. The resulting fluorescence signal is de-scanned by the scanning mirrors, spectrally separated using a dichroic mirror, imaged through a pinhole and finally detected by a photomultiplier tube. Here back reflection to the laser is disabled by the components between laser and beam expander. The Photonic Crystal Fibre enables all wavelengths to travel at the same speed. 155

Figure 4.10 The microfluidic devices used for temperature measurements. 156

Figure 4.11 TCSPC set-up used to assess the fluorescence lifetime of aqueous Rhodamine B. The flow cell connected to microscope set-up and water bath with Teflon tubing are shown. 157

Figure 4.12 The microfluidic chip mounted on the microchannel heater using heat-conductive paste. Rhodamine B is motivated through the microfluidic chip, while excitation and detection of fluorescence is carried out from below. 158
Figure 4.13 Schematic of chip (I) arrangement for temperature measurements. Data are recorded from two scans along the temperature gradient denoted *profile 1* and *profile 2.* 159
Figure 4.14 Schematic of measurement regions within CHIPII. 160
Figure 4.15 Calibration data of 10^{-4} M Rhodamine B in water measured in flow cell. With increasing temperature a decrease in Lifetime is observed. (a) presents calibration for TCSPC set-up and (b) presents calibration for the wide-field set-up. 161
Figure 4.16 Fluorescence lifetime imaging of a Rhodamine B solution in a microchannel. (a) fluorescence lifetime image measured at 66°C (b) fluorescence lifetime image measured at 93°C, (c) variation of fluorescence lifetimes (green and blue lines) and time-integrated intensities (green and blue dashed lines) across the microchannel width. The fluorescence lifetime is approximately constant over the width of the microchannel, whilst the fluorescence intensity shows a much less uniform behaviour. 163
Figure 4.17 Variation of fluorescence lifetime as a function of lateral position across the microfluidic device. Violet data points represent measurements along profile 1, while green data points represent measurements along profile 2. 164
Figure 4.18 Uncalibrated time-integrated intensity data as a function of lateral position across the microfluidic device. Violet data points represent measurements along profile 1, while green data points represent measurements along profile 2. 165
Figure 4.19 Fluidic temperature profiles calculated using fluorescence lifetime data. Violet data points represent measurements along profile 1, while green data points represent measurements along profile 2. 165
Figure 4.20 3D mapping of fluidic temperatures. False-color rendered 3D-image of fluorescence lifetime variations of a methanolic solution of Rhodamine B within a 130x40x100 µm microchannel segment and at a flow rate of 10 µL/min. Channel boundaries are indicated with white dotted lines. The upper surface of the microchannel is held at 73°C. 166
Figure 4.21 Variation of temperature as a function of distance away from the upper microchannel surface at volumetric flow rates of 0.1 (black line) and 10 µl/min (red line). 167

Figure 4.22 Variation of temperature as a function of distance across the microchannel at half the channel depth and at volumetric flow rates of 0.1 (black line) and 10 (red line) µL/min. 167
Figure 4.23 Variation of fluorescence lifetime as a function of distance along profile 1 (violet) and profile 2 (green). 169
Figure 4.24 Variation of temperature as a function of distance across the device along profile 1 (violet) and profile 2 (green). 169
Figure 4.25 Variation of fluorescence lifetime as a function of distance (along profile 1 (violet) and profile 2 (green)) with forward flow (filled squares) and reversed flow (empty squares). 170
Figure 4.26 Variation of temperature as a function of distance (along profile 1 (violet) and profile 2 (green)) with flow forward (filled squares) and reversed flow (empty squares).. 171
Figure 4.27 Variation of fluorescence lifetime as a function of distance across the device with volumetric flow rates of 1 µl/min (black), 3 µl/min (green) and 10 µl/min (red)..... 172
Figure 4.28 Variation of temperature as a function of distance across the device at flow rates of 1 µl/min (black), 3 µl/min (green) and 10 µl/min (red)..... 172
Figure 4.29 Variation of temperature as a function of distance across the device with flow rates of 1 µl/min (black), 3 µl/min (red) and 10 µl/min (green)..... 173
Figure 4.30 Fluorescence lifetime determination as a function of distance along profile 1 (violet), profile 2 (orange) and profile 3 (green) on CHIP III. 174
Figure 4.31 Temperature variation as a function of distance along profile 1 (brown), profile 2 (purple) and profile 3 (green) on CHIP III. 174
Figure 5.1 (a) In this case charges are the same which results in repulsion. (b) In this case charges are opposite which results in attraction..... 180
Figure 5.2 Hydrolysis of Si-OH groups with Silane in order to create Si-O-Si groups which reduce the adsorption of components on the surface. 182
Figure 5.3 Variation of fluorescence intensity as a function of number of cycles. Black data points represent the reference and grey data points represent the sample. 183
Figure 5.4 Electropherograms resulting from the analysis of both sample and reference. (a) exhibits two unique product peaks for the reference. (b) exhibits no product for the sample. 184
Figure 5.5 Variation of fluorescence intensity as a function of the number of thermal cycles. Five replicates were performed to generate each curve. The black curve represents the reference, the red curve represents the sample with excess of enzyme, the yellow curve represents the sample with excess of DNA, the green curve represents the sample with excess of magnesium chloride and the blue curve represents the sample with excess of primers. 185

Figure 5.6 Electropherograms resulting from the analysis of reference and samples with an excess of DNA, magnesium chloride, primers and enzyme. (a) exhibits two unique peaks for the reference sample. (b) exhibits no peaks for the sample with excess of DNA. (c) exhibits no peaks for the sample with excess of magnesium chloride. (d) exhibits no peaks for sample with excess of primers. (e) exhibits two unique peaks for the sample with excess of enzyme..... 186

Figure 5.7 Variation of Ct as a function of number of samples. The black curve represents the reference, the yellow curve represents sample with 1X enzyme, the blue curve represents sample with 2X enzyme and the red curve represents sample with 4X enzyme. 188

Figure 5.8 Electropherograms resulting from the analysis of reference and samples with an excess of 1X enzyme, 2X enzyme and 3X enzyme. (a) exhibits three product peaks for the reference sample. (b) exhibits two product peaks for the sample with 1X excess of enzyme. (c) exhibits three product peaks for the sample with 2X excess of enzyme. (d) exhibits three product peaks for sample with 4X excess of enzyme. 189

Figure 5.9 Variation of fluorescence intensity as a function of the number of cycles. The black curve represents the reference and the red curve represents the sample..... 191

Figure 5.10 Electropherograms resulting from the analysis of reference and the sample. (a) exhibits three unique peaks for the reference, (b) exhibits no product peaks for the sample. 192

Figure 5.11 A liquid droplet resting on a solid surface. The contact angle θ is defined as the angle between the liquid-vapor and solid-liquid interface of a solid-liquid-vapor system. γ_{SV} is the solid-vapor surface tension, γ_{SL} is the solid-liquid surface tension and γ_{LV} is liquid-vapor surface tension. 193

Figure 5.12 Drop Shape Analysis (DSA 10 MK2 Krüss) for contact angle measurements. A syringe dispenses a 2µl droplet of water on a sample surface and the contact angle is measured. 194

Figure 5.13 Water droplets (2µl) on microscope slides with different surface coatings. Each droplet is ejected on a sample surface and the contact angle is measured with the Drop Shape Analysis System. (a) A droplet on an untreated glass surface. (b) A droplet on a silane I surface. (c) A droplet on a silane II surface. (d) A droplet on a silane I+PEG surface. (e) A droplet on a silane I+BSA surface. (f) A water droplet on a silane I+PVP surface and (g) A droplet on a Teflon surface. 195

Figure 5.14 Assessment of the contact angle θ of a liquid in a vertical tube. In case (a) the contact angle is less than 90° with the liquid adhering to the walls. In case (b) the contact angle is greater than 90° with the liquid repelled from the walls..... 196

Figure 5.15 Fluorescence intensity as a function of the number of cycles. Black curve represents the reference and red curve represents the sample..... 200
Figure 5.16 Electropherograms resulting from the analysis of reference and sample, (a) exhibits three product peaks for reference, (b) exhibits two product peaks for the sample.200
Figure 5.17 Electropherograms resulting from the analysis of reference and sample. (a) one product peak for reference sample.(b) no product peak for the sample..... 202
Figure 5.18 Fluorescence intensity as a function of the number of cycles. Black curve represents the reference and red curve represents the sample..... 203
Figure 5.19 Electropherograms resulting from the analysis of reference and sample. (a) exhibits three product peaks for the reference.(b) exhibits two product peaks for the sample. 203
Figure 5.20 Fluorescence intensity as a function of the number of cycles. Black curve represents the reference and red curve represents the sample..... 205
Figure 5.21 Electropherograms resulting from the analysis of reference and the sample. (a) exhibits three product peaks for reference sample.(b) exhibits no product peak for the sample. 205
Figure 5.22 Fluorescence intensity as a function of the number of cycles. The black curve represents the reference and the red curve represents the sample..... 207
Figure 5.23 Electropherograms resulting from the analysis of reference and the sample. (a) exhibits three product peaks for reference sample, (b) exhibits no product peak for the sample. 207
Figure 5.24 Electropherograms resulting from the analysis of reference and sample. (a) exhibits one product peak for the reference, (b) exhibits one unique product peak for the sample. 208
Figure 5.25 Photograph of mirochannel coated with silane I before and after PCR. (a) shows channel with coating, (b) shows channel with adsorption after PCR..... 209
Figure 5.26 Fluorescence intensity as a function of the number of cycles. Black curve represents the reference and red curve represents the sample..... 210
Figure 5.27 Electropherograms resulting from the analysis of reference and sample. (a) exhibits three product peaks for the reference (b) exhibits no product peaks for the sample. 210
Figure 5.28 Electropherograms resulting from the analysis of reference and sample. (a) exhibits one product peak for reference. (b) exhibits one product peak for the sample. 211
Figure 5.29 Electropherograms resulting from the analysis of reference and sample. (a) exhibits one product peak for the reference. (b) exhibits one unique sample peak for the sample. 213

Figure 5.30 Electropherograms resulting from the analysis of reference and sample. (a) exhibits two product peaks for reference.(b) exhibits two product peaks for the sample. .. 214
Figure 6.1 (a) A water droplet spreads on a solid smooth surface. (b) A water droplet does not spread on a solid surface due to its roughness. 223
Figure 6.2 (a) Wenzel model for a water droplet on a rough surface. (b) Cassie-Baxter model for a water droplet on a rough surface. Here water is only in contact with the tips of the surface. 225
Figure 6.3 Electron micrographs of the larger scale sol-gel material taken with a reflection electron microscope (JEOL,GSM) with an acceleration voltage of 20kV. 227
Figure 6.4 Electron micrographs of the smaller scale sol-gel material taken with a REM (same conditions as Figure 6.3). 227
Figure 6.5 Copper slides in slide holder soaked in 36 mM ammonia solution at 4°C. 229
Figure 6.6 Electron micrographs of copper oxide nano-needles taken with a REM (JEOL,GSM) with an acceleration voltage of 20kV. 229
Figure 6.7 2 µl water droplets on treated surfaces: (a) glass with a hydrocarbon terminated surface shows a contact angle of 112° (b) glass with a fluorocarbon terminated surface shows a contact angle of 117° (c) sol-gel with a hydrocarbon terminated surface shows a contact angle of 145° (d) sol-gel with a fluorocarbonated surface shows a contact angle of 145° (e) copper with hydrocarbon terminated surface shows a contact angle of 165° (f) copper with a fluorocarboanted surface shows a contact angle of 165°. 230
Figure 6.8 Flow cell chamber 1500 µm wide and 500 µm deep. (a) the opened flow cell and exposed sol-gel surface, (b) the flow cell assembly during use. 232
Figure 6.9 Photograph of the sputtering system at Nottingham Trent University. Glass microscope slides are coated with both titanium and copper films..... 233
Figure 6.10 Images of glass substrates sputtered with Zinc. (a)-(c) present different oxidization stages of Zinc with (c) being the completely oxidized state, visible when glass substrate becomes transparent. 234
Figure 6.11 (a) Microfluidic device containing six parallel zinc oxide channels: with two untreated channels, two hydrocarbon terminated surface channels and two fluorocarbon terminated surface channels. (b) Microfludic device containing six parallel copper oxide channels: two untreated channels, two hydrocarbon terminated surface channels and two fluorocarbon terminated surface channels. 235
Figure 6.12 Water flow profiles in CuO and ZnO channels. (a) presents water in an untreated CuO channel with a contact angle of 90°, (b) presents water in a hydrocarbon terminated CuO channel with a contact angle of 120°, (c) presents water in a fluorocarbon terminated CuO channel with a contact angle of 150°, (d) presents

water in an untreated ZnO channel with a contact angle of 90°, (e) presents water in a hydrocarbon terminated ZnO channel with a contact angle of 90°, (f) presents water in a fluorocarbon terminated ZnO channel with contact angle of 90 °. 236

Figure 6.13 Albumin adsorption onto micro-scale and nano-scale surfaces which are hydrocarbon or fluorocarbon terminated, under static conditions..... 238

Figure 6.14 Albumin adsorption onto micro-scale and nano-scale surfaces which are hydrocarbon or fluorocarbon terminated under dynamic conditions..... 239

Figure 6.15 Electropherograms resulting from the analysis of product after CF-PCR in untreated glass channels, untreated zinc oxide channels, hydrocarbon terminated zinc oxide channels, fluorocarbon terminated zinc oxide channels and untreated copper oxide channels. 241

Figure 8.1 a) 3-D schematic of microfluidic channel. b) mesh plot of cover glass, microfluidic channel and bottom glass. 260

Figure 8.2 Velocity plot of fluid in microfluidic channel. The two outer lines represent the channel walls of a microfludic channel, while the arrows represent the flow of a fluid in the microchannel. The colour of the arrows represents the speed with which the fluid moves through the channels with higher velocities in the centre of the channel and slower velocities at the edges of the channel. 261

Figure 8.3 Variation of temperature as a function of distance across the device with volumetric flow rates of 1 µl/min (black), 3 µl/min (green) and 10 µl/min (red) for simulation. 263

Figure 8.4 Variation of temperature as a function of distance across the device with volumetric flow rates of 1 µl/min (black), 3 µl/min (green) and 10 µl/min (red) for fluorescence experiment. 263

Figure 8.5 False colour images of temperature distribution within a microfluidic channel. The image on the left shows the temperature distribution from 95 to 65 °C and the image on the right side showed the temperature distribution from 65 to 95 °C..... 264

Publications

Miniaturized nucleic acid analysis; P.-A., Auroux, Y. Koc, A. deMello, A. Manz, P.J. Day, Lab on a chip, 2004. **4**: p. 534-546.

Quantitative 3D Mapping of Fluidic Temperatures within Microchannel Networks Using Fluorescence Lifetime Imaging; Benninger, R., Y. Koc, O.Hofmann, J. R.-Isidro, M.A.A.Neil, P.M.W. French, A. deMello, Analytical Chemistry, 2006. **78** (7): p. 2272-2278.

Nano-scale Superhydrophobicity: Suppression of Protein Adsorption and Promotion of Flow-Induced Detachment; Y. Koc, A.J. de Mello, G. McHale, M.I. Newton, P. Roach, N.J.Shirtcliffe; (in the process of submission)

Acknowledgements

This PhD would not have been possible without all my friends and colleagues turning into magic fairies who would never refuse to help.

However, the two people who guided me through this challenging period of my life are my father, Ali Kemal Koc and my supervisor Andrew deMello. Their aspirations, inspirations and believe in my success gave me the strength to achieve my PhD.

My family and my friends also formed an important support during this period. Nina Kaun, my best friend with who in 1996 I had embarked on the study of Chemistry in Vienna where we prepared for all "exams" in and outside university together. She has always been my rock and I want to thank her for that! Markus Fischer, Marko Susnik, Michael Schnürch, Christian Einzinger, David Sebinger and Petra Gruber my closest friends and colleagues made my studies in Vienna to an unforgettable experience.

Dimitri Iossifidis, my first and closest friend at Imperial College who transformed into my soul mate in the lab as well as outside the lab.

Sepp Bruderman, "the sun", who made every day a positive day, Patrick Jäger, who with the words " I am your biggest fan" never failed to believe in me, Ayşe Ataş who always trusted in me and my stars.

Sylvie Borrel, the person in my life who showed me that the most important thing in life is "to experience the down in order to appreciate the up", made me enjoy and appreciate my PhD.

My very precious lab mates Monpichar Sri Sa-Art and Andrea Laine who helped me to overcome all obstacles during my PhD I could not solve on my own.

Oliver Hofmann and Nicole Pamme, my friends and colleagues who supported me unconditionally in professional and personal matters.

Nick Woolley who constantly pushed me to stay positive and who did a wonderful job helping me with my references. Thanks Nick!

Professor Andreas Manz who encouraged and motivated me to investigate all possible angles within the project of my PhD.

The members of the Manz group who introduced me to the world of microfluidics. Many thanks to Torsten Vilkner, Dirk Janasek and Gareth Jenkins who taught me how to produce my first microfluidic devices.

The members of the deMello group who now form the world of microfluidics at Imperial College. Many thanks to Richard Winkle, Siva Krishnadasan and Chris Cullen who would NEVER refuse to help even if the problem would be too simple to mention.

Rob Wootton, whose valuable input made this PhD a successful PhD.

Steve Atkins and Simon Turner who helped to build and realize my whole set-up.

Richard Benninger, Tom Robbins and James McGinty, at the Photonics Department at Imperial College, who dedicated hours and hours in laser labs, so that we could introduce the novel approach of direct temperature measurements in microchannels.

Neil Shirtcliffe and Paul Roach, at Nottingham Trent University, who spend days and days on creating superhydrophobic materials so that we could introduce these on microfluidic devices.

Valluri Prashant, at the Chemical Engineering Department at Imperial College, who helped with the simulation work.

Special thanks also to Catherine Mills, at Smiths Detection, who always made time to help, support and encourage me during my PhD project.

For financial support, thanks go to Smiths Detection.

List of Abbreviations

µ-FN	-	Micro Fluidic Network
µ- FACS	-	Micro Fluorescence-Activated Cell Sorter
µ- TAS	-	Micro-Total-Analysis-System
3D	-	3 Dimensional
BOE	-	Buffered Oxide Etch
BSA	-	Bovine Serum Albumin
CAD	-	Computer Aided Design
CAE	-	Capillary Array Electrophoresis
CCD	-	Charged-Coupled Device
CFD	-	Computational Fluid Dynamics
CF-PCR	-	Continuous Flow Polymerase Chain Reaction
COC	-	Cyclic Olefin Copolymer
DEP	-	Dielectrophoresis
DMF	-	Dimethylformamide
DMSO	-	Dimethlysulfoxide
DNA	-	Deoxyribonucleic Acid
dNTP	-	Deoxynucleotide Trisphosphate
ECV	-	Effective Culture Volume
EFPI	-	Extrinsic Fabry-Perot Interferometry
ESI-MS	-	Electrospray Ionization Mass Spectrometer
FAM	-	Carboxyfluorescein
FIA	-	Flow Injection Analysis
FLIM	-	Fluorescence Lifetime Imaging
FRET	-	Fluorescent Resonant Energy Transfer
HAS	-	Human Serum Albumin
HEG	-	Hexethylene Glycol

HF	-	Hydrogen Fluoride
HPLC	-	High Pressure Liquid Chromatography
HSV	-	Hue-Saturation-Value
IRF	-	Instrument Response Function
ITO	-	Indium Tin Oxide
LED	-	Light Emitting Diode
LC	-	Liquid chromatography
MATCI	-	Miniature Analytical Cycling Instrument
MEMS	-	Micro-Electro-Mechanical Systems
MFC	-	Micro Fabricated Chamber
MIP	-	Molecularly Imprinted Polymer
MR	-	Methylred
NMR	-	Nuclear Magnetic Resonance
OLED	-	Organic Light Emitting Diode
PBS	-	Phosphate Buffer Saline
PC	-	Polycarbonate
PCR	-	Polymerase Chain Reaction
PDMS	-	Polydimethylsiloxane
PEG	-	Polyethyleneglycol
PEEK	-	Polyethyleneketones
PID	-	Proportional, Integral and Derivative
PMMA	-	Polymethylmethacrylate
PMT	-	Photomultiplier
PVP	-	Polyvinylpyrolidone
PTFE	-	Polytetrafluoroethylene
RAP	-	Resonant Acoustic Profiling
RIE	-	Reactive Ion Etching

RNA	-	Robonucleic Acid
RTD	-	Resistance Temperature Detector
STD	-	Sexually Transmitted Disease
SWCNT	-	Single Walled Carbon Nanotube
TCSPC	-	Time Correlated Single Photon Counting
TLC	-	Thermochromic Liquid Crystal
UV	-	Ultra Violet

1

Introduction

In this chapter, an overview of the origins and development of microfluidic technology in the chemical and biological sciences is provided. The process of DNA amplification and the rationale for performing the polymerase chain reaction in microfluidic systems is also discussed. In addition, a theoretical treatment of basic scaling laws and their influence on chemical and biological processes is provided.

1.1 History of Microfluidics

Microfluidic devices are miniaturized systems for performing chemical and biochemical analyses. They contain internal structures, such as fluid channels, that have dimensions most conveniently measured in microns. Their application can be analytical (e.g. in molecular separation and detection), or preparative (fluid handling) or synthetic. Miniaturized analysis systems show significant advantages when compared to their macroscale counterparts. Small reaction volumes and high heat and mass transfer rates allow for precise adjustment of process conditions, short response times, and controllable residence times. These in turn result in greater process control and higher yields and selectivity (for synthetic applications), and improved efficiency and resolution (in separation applications). Over the last decade, there has been a rapid growth of both academic and commercial interest in the field of microfluidics. Initial microfluidic publications first appeared in the literature in 1989 [1] and since then have undergone a period of exponential growth which is illustrated in Figure 1.1.

In the early years most research was focused on the fabrication of functional microfluidic components such as micropumps, and microvalves. In the mid 1990's flow behaviour on the microscale was intensely investigated, new materials and fabrication methods were introduced, novel detection methods were developed and synthesis and analysis were performed within integrated systems [2-4]. By 1998 the microfluidic community had grown drastically and research applications had diversified immensely [5-7] . In the last ten years the microfluidic community has refined most of these approaches and introduced new application areas and core technologies which will be discussed in detail in later sections.

Commercial applications of microfluidic technology have also increased dramatically over the past decade in almost all areas of the physical and biological sciences. These include drug discovery, high-throughput screening, chemical synthesis, genomics, proteomics, cell analysis, forensics, analytical chemistry and environmental analysis. Appendix A provides a comprehensive and up to date snapshot of microfluidic companies operating in the chemical and biological sciences.

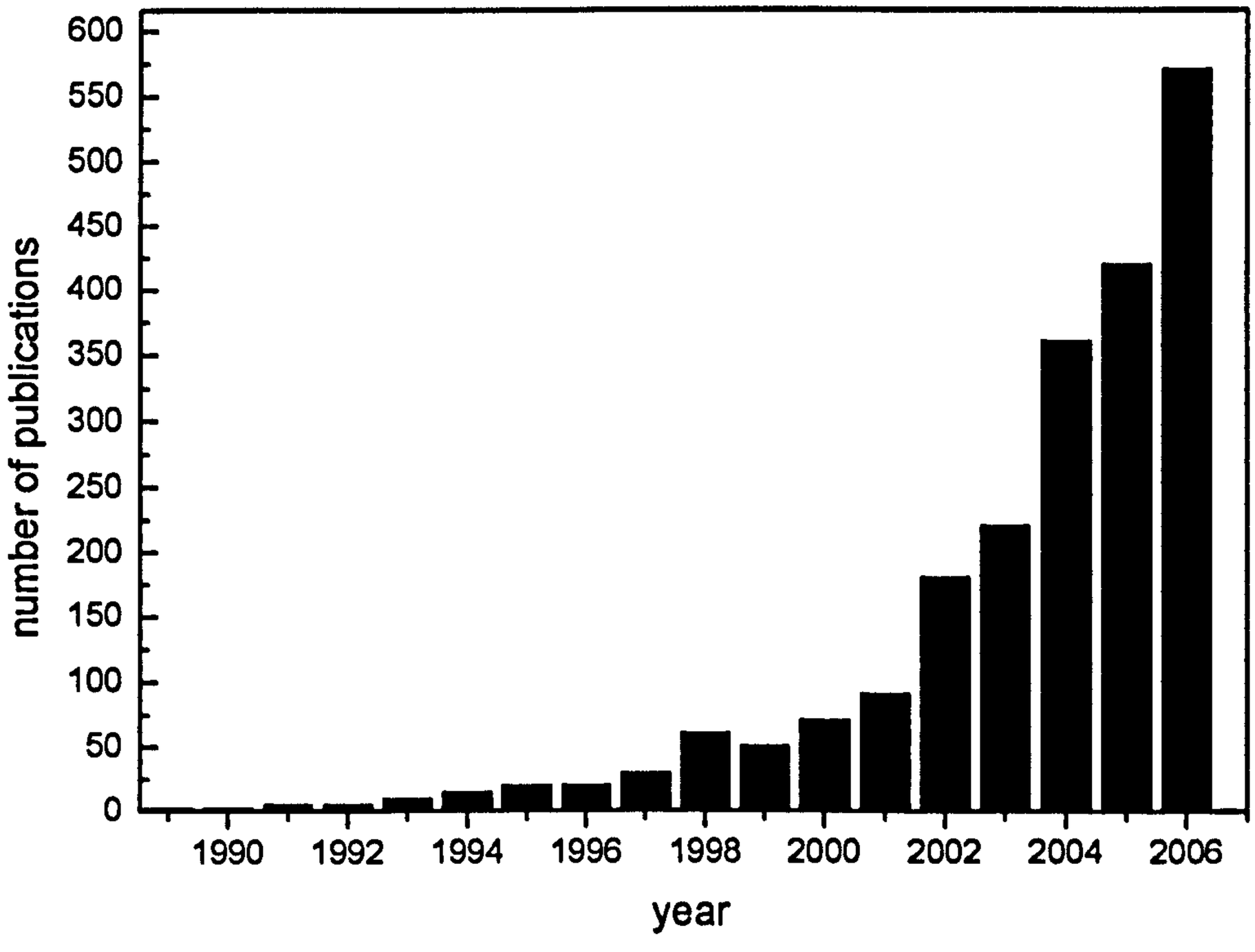


Figure 1.1 **Annual microfluidics publications across all journals. Data created through a Web of Science search incorporating the keywords "microchannel", "microfluidics" and "lab on a chip".**

1.1.1 Early Analytical Devices – Chromatography on the Microscale

Early demonstrations of the efficacy of microfluidic systems in the chemical and biological sciences were predominantly applied to analytical techniques such as chromatography and electrophoresis. The first miniaturized analytical device was introduced by Terry et al. [8] in 1979. A gas chromatograph was fabricated on a silicon wafer and contained all necessary components to perform a separation of organic volatiles. The chromatography system consisted of a sample injection valve and a 1.5 m long capillary column. A thermal conductivity detector was separately fabricated and mechanically interfaced with the wafer containing the separation column. To test the operational performance of the system a mixture of nitrogen, pentane and hexane vapours were analysed. The mixture was injected at the

column inlet and swept through by an inert carrier gas. The column was coated with a liquid stationary phase, with the migration rate of each component being controlled by the carrier gas velocity and the degree to which the vapour interacts with the stationary phase. The separation of these three components was performed rapidly with nitrogen appearing after 2.6 s, pentene after 3.3 s and hexane after 4.6 s. Thus the miniature capillary column enabled separation in less than 10 s, whilst a comparable separation in a conventional column typically required several minutes. In 1990 a miniaturized open-tubular liquid chromatograph on a silicon wafer was presented by Manz et al. [9]. This 5 x 5 mm silicon chip consisted of an open tubular column 6 µm wide, 2 µm deep and 15 cm long and a conductometric detector which was connected to an off-chip pressure system. In conventional packed-bed chromatography the analysis time is limited by the separation efficiency and the applied pressure. In theory these obstacles may be overcome by using open tubular columns [10] as these work under low pressure drops and result in short analysis times. In this set-up the liquid chromatograph (LC) chip (Figure 1.2) was operated by a conventional high performance liquid chromatography (HPLC) pump. The sample was injected by pressure-pulse-driven stopped flow injection [11] and detection was performed via conductometry by positioning two platinum electrodes symmetrically on the microchannel surface and measuring the conductance of the mobile phase. It should be noted that within this study, chip parameters influencing the separation efficiency were compared and discussed but no actual separation results were reported.

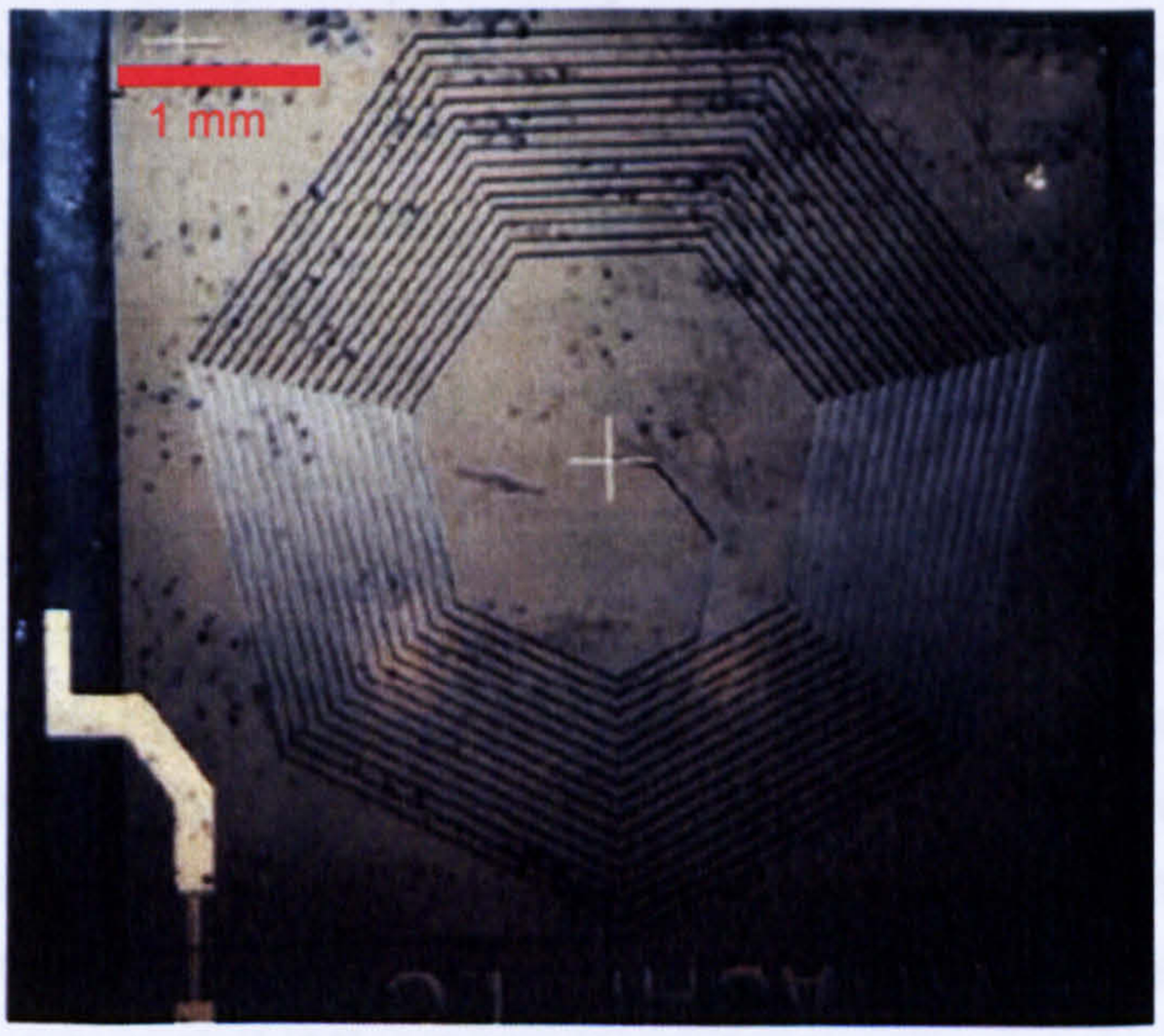


Figure 1.2 **Photograph of an LC chip containing column and detector electrodes. [3]**

1.2 Miniaturised Total Analysis Systems

In general an analytical procedure can be broken down into two basic concepts. Firstly the analytical principle on which the measurement is based and secondly the analytical method which optimises the conditions for the chosen analytical principle. In simple terms the analytical procedure encompasses all considerations from analyte to analytical result. Figure 1.3 presents a schematic of a generic analytical process.

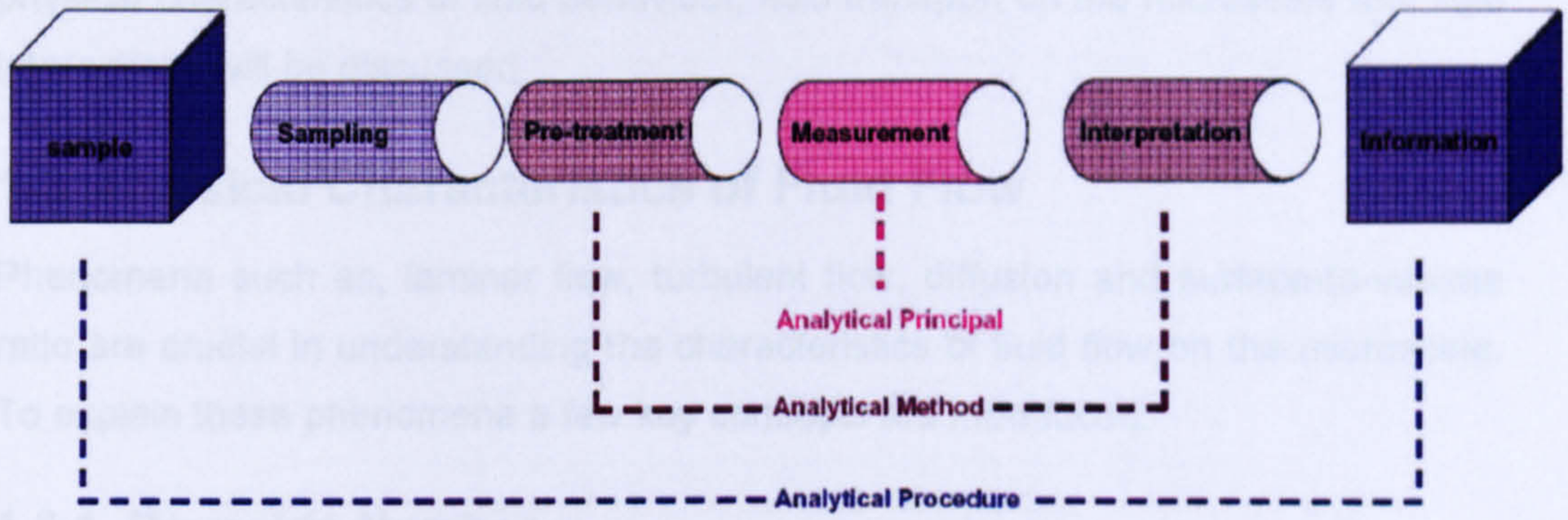


Figure 1.3 Schematic of the individual components of a generic analytical procedure

In 1990 the concept of a "micro total analysis system (μTAS) "was proposed by Manz et al. [12]. A μTAS defines an integrated miniaturised chemical analysis system that includes sample preparation, separation and detection on a monolithic device. By definition a μTAS periodically transforms chemical information into electronic information [13]. The continuous monitoring of chemical parameters is of high importance in many fields including the chemical industry and the environmental and medical sciences. In most situations, the chemical compound of interest is usually accompanied by interfering species which makes selective monitoring difficult. This problem is negated when using a μTAS since sample pre-treatment serves to eliminate interfering chemical signals. Even though initial reasons for miniaturisation were to enhance analytical performance rather than reduce instrument size, the advantages of reduced sample consumption were recognized immediately. Sample volumes were reduced from milliliters to hundreds of nanoliters and reaction times to a few seconds. Consequently working on the microscale enabled the probing of ultra-fast chemical reactions with minimal sample consumption. Such benefits have been used in countless applications such as process and quality control [14], bio-sensing and bio-medical analysis [15, 16], and

medical and pharmaceutical applications [17]. It should also be mentioned that the types of samples used in these microdevices include small ions and molecules [18, 19], single and double stranded DNA [20-24] amino acids [25, 26], peptides [27-29], proteins [4, 30] and enzymes [31-34].

Another major advantage of working with miniaturised analytical systems lies in the superior control of physical processes. Significantly fluid flow characteristics, mass and heat transfer are dependant on scale. Consequently in the following section the physical characteristics of fluid behaviour, fluid transport on the microscale and fluid interactions will be discussed.

1.3 Physical Characteristics of Fluid Flow

Phenomena such as, laminar flow, turbulent flow, diffusion and surface-to-volume ratio are crucial in understanding the characteristics of fluid flow on the microscale. To explain these phenomena a few key concepts are introduced.

1.3.1 Reynolds Number

In 1883 Osborne Reynolds discovered two general modes of fluid behaviour; laminar and turbulent flow [35]. The classic experiment in which Reynolds demonstrated these two modes involved containing water in glass tubes of various diameters and lengths. These were fitted with "bell-mouth" entrances, and were immersed horizontally in a tank of clear water having glass sides. The water in the tank was allowed to come perfectly to rest. Subsequently a valve (B in Figure 1.4 a) was opened, allowing water to flow slowly through the tube. A small amount of water, coloured with an aniline dye, was then introduced into the mouthpiece through a fine tube supplied from a vessel (A in Figure 1.4 a). At first this coloured water was drawn out into a single tubular stream, extending through the whole length of the tube. This appeared motionless unless a light motion of oscillation was given to the water in the supply tank. Under these conditions the stream line swayed gently from side to side, but did not lose its definition. As valve B was opened further, the velocity through the tube increased, and the tubular stream was progressively drawn, still retaining its definition, until at a certain critical velocity eddies began to form intermittently near the outlet end of the tube. The formation of these eddies was accompanied by the almost instantaneous diffusion of the coloured band. As the velocity was still further increased, the point of eddy initiation advanced towards the mouthpiece. The reduced tendency for eddy formation near

the inlet was due to the stabilizing influence of the convergent mouthpiece. Finally, when B was fully open the whole flow became unsteady and turbulent.

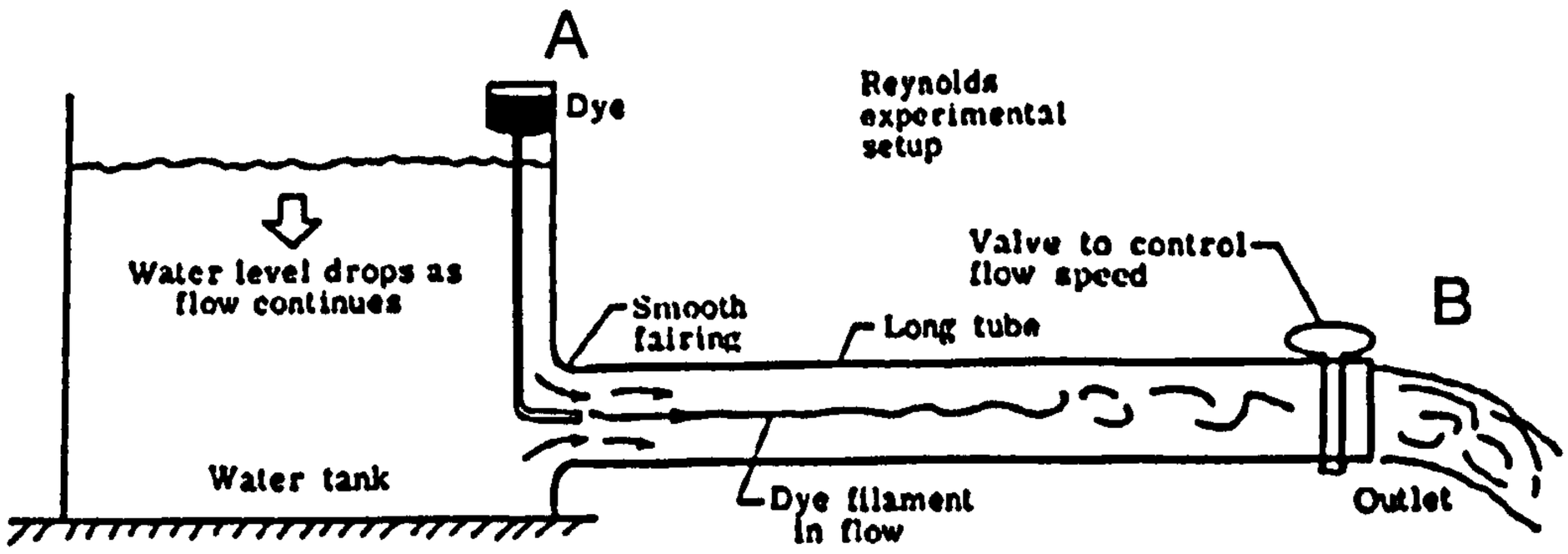


Figure 1.4 **The principle of Osborne Reynolds' experiment (a) laminar flow and (b) turbulent flow [35].**

Reynolds demonstrated that in flows within straight pipes with parallel walls turbulence does not appear if the product of the mean velocity, the diameter and the mass density of the fluid divided by the absolute viscosity coefficient is less than a specific number. This ratio became known as the Reynolds number and can be approximated to

$$Re = \frac{\rho v D_h}{\mu} \qquad (1.1)$$

Here ρ is the fluid density [kg/m^{-3}], v is the characteristic velocity of the fluid [m/s], μ is the fluid viscosity [kg/m^{-1} s^{-1}] and D_h is the hydraulic diameter [m]. The physical significance of the Reynolds number is that it is a direct measure of the ratio between inertial forces and viscous forces in a particular flow. In channel flows, Reynolds numbers < 2300 indicate laminar flow while flows with Reynolds numbers > 2300 are likely to be turbulent. For microfluidic systems, such as blood capillaries, Reynolds numbers are typically around 10^2 or lower [36-38]. Thus, flow in microchannels is normally considered to be laminar [39]. A direct consequence of laminar flow is that two or more streams flowing in contact with each other will not mix except through diffusion.

1.3.2 Diffusion

Diffusion is a process in which a population of molecules or particles will move randomly according to Brownian motion. As observed by Einstein "bodies of a microscopically-visible size suspended in a liquid will perform random movements of such magnitude that they can be easily observed in a microscope" [40]. Diffusional motion can be expressed by the Einstein-Smoluchowski equation as follows

$$d = \sqrt{2Dt} \qquad (1.2)$$

Here *d* is the distance a particle moves in a time *t* between molecular collisions, and *D* is the diffusion coefficient [m^2/s] of the particle. The diffusion time varies with the distance squared and therefore diffusion can become very important on the microscale. This can be seen using the example of haemoglobin in aqueous solution. Haemoglobin has a diffusion coefficient of 7 X 10^{-7} cm^2/s, and thus takes 10^6 seconds to diffuse 1cm in water, but only 1 second to diffuse 10μm. This great reduction in diffusion time on the microscale is ideal for accelerating diffusion-controlled bio-chemical reactions. Numerous research groups have investigated the role and importance of diffusion on microscale processes such as separation [41], and molecule transport and mixing [42-46]. While the Reynolds number and the process of diffusion describe important features of fluid flow in microfluidic environments, the surface-to-volume ratio describes the interaction of fluid with the microchannel.

1.3.3 Surface-to-Volume Ratio

As described in Section 1.2 downscaling enables the improved control and manipulation of fluid flow. Unfortunately, increased surface-to-volume ratios are also associated with miniaturisation. When scaling down a reaction from a macroscale tube to a microchannel environment, the reaction mix is subject to at least one order of magnitude increase in the surface-to-volume ratio. For example a Petri dish with a diameter of 35 mm and a volume of 2.5 ml has a surface to volume ratio of 4.2 cm^{-1}, whilst a microchannel 50 µm wide, 50 µm deep and 30 mm long has a surface to volume ratio of 800 cm^{-1}. During the transferral of a process from a macroscale to microscale environment, an increase in surface-to-volume ratio in excess of two orders of magnitude is not uncommon. It is evident that the surface plays a dominant role in defining physical and chemical processes on the microscale. A large surface-to-volume ratio is often beneficial (e.g. in enabling efficient reactions in microchannels due to the rapid removal of excess heat). Conversely, a large surface-to-volume ratio may be disadvantageous (e.g. in facilitating unacceptable levels of analyte adsorption on channel walls). This adsorption effect can, depending on the application, either be beneficial or unfavourable. Applications which gain from enhanced surface – molecule interaction are protein immobilizations [47, 48], cell culture growth [49-52], heterogeneous catalysis reactions [53-55] and trapping of proteins [56, 57]. Other systems suffer from the increased surface – molecule interactions. Depending on the material and the conditions of the surface (such as charge, hydrophilicity, hydrophobicity and polarity) many reactions and processes may be hindered. The situation can be particularly complicated in a multicomponent reaction when the concentrations of several components need to be maintained precisely throughout the reaction. For example the Polymerase Chain Reaction (PCR) is a reaction which suffers strongly when the polymerase catalyst adsorbs and interacts with the surface. The interaction of PCR components with channel walls will be discussed in detail in Chapter 5 while the reaction principles and the importance of the PCR components will be presented in Section 1.5. In the following section a literature review of numerous existing and revolutionary applications of microfluidics in the chemical and biological sciences will be presented.

1.4 Literature Review

The fundamental goal of the studies described within this thesis was to enable successful and efficient biochemical reaction within a continuous flow microfluidic device. Hence, this literature review will focus on biochemical applications such as the separation of DNA, cell analysis, amplification of DNA, clinical diagnostics, immunoassays and other selected applications such as chemical synthesis. This section will provide an overview of applications within these areas. However, the amplification of DNA will be discussed in Section 1.5 in detail. Initial biochemical reactions on the macroscale were investigated over a century ago when for example Harrison *et al.* [58] cultured nerve cells for the first time in 1907. The first immunoassay was described by Berson and Yalow [59] in 1959, whilst the first experiments sequencing DNA were presented in the late 1970s by Sanger *et al.* [60]. Since these studies, technologies and methods for biochemical reactions have continued to evolve with new applications and improved analytical platforms. Much of this evolution has incorporated advantages directly facilitated by microfluidics.

1.4.1 Molecular Separations

The separation and quantitation of DNA is of importance in the clinical diagnosis of various states of diseases. The traditional way of separating DNA involves the use of gel electrophoresis in a slab format. Different sized strands of DNA in a sponge-like matrix are separated by applying an electric voltage across the separation matrix. Beyond the issues of high sample consumption and long analysis times, the tedious and long preparation steps within this method make it unattractive for efficient DNA analysis. A viable alternative, capillary electrophoresis (CE), which offered decreased sample consumption, decreased separation times and increased resolution, was demonstrated in the 1980's [61-64]. Transferring this method to a microfluidic format offered further advantages. For example in 1995 Woolley *et al.* [65] presented ultra-high-speed DNA sequencing using a CE chip. A microfluidic glass sandwich structure contained a separation channel of 3.5 cm length, 50 µm width and 8 µm depth which was filled with a polyacrylamide matrix. DNA sequencing separations up to 433 bases were performed in 10 minutes with an accuracy of 97%. In comparison, DNA sequencing of 500 bases using slab-gel electrophoresis resulted in a separation time of 8-10 hours and sequencing using capillary electrophoresis resulted in separation times between 1 and 2 hours. In 1996 Jacobson *et al.* [66] presented an integrated glass microdevice for performing an enzymatic restriction reaction with DNA and subsequent electrophoretic sizing of

the products. After a digestion period in the 0.7 nl reaction chamber, the fragments were injected onto a 67 mm long, 60 µm wide and 12 µm deep, capillary electrophoresis channel for sizing. The whole process was completed within 5 minutes using 30 amol of DNA and 2.8 X 10^{-3} units of enzyme per run. In the following year Effenhauser *et al.* [67] presented CE on a flexible silicone microdevice for the analysis of DNA restriction fragments and detection of single DNA molecules. Separation was performed within polydimethylsiloxane (PDMS) microchannels (with a depth of 20 µm and a width between 10-50 µm) in times between 50 - 250 s. The single molecule detection efficiency of the fluorescently labeled DNA restriction fragments was higher than 50 % i.e., the majority of molecules passing the channel cross section at the detector location were registered.

In the same year Colyer *et al.* [4] presented chip-based CE of human serum proteins. Processes such as post-separation, labelling of the proteins and subsequent laser-induced fluorescence detection were facilitated on the chip. A mixture of four human serum proteins was resolved in less than 60 s which compared favorably with conventional CE with a separation time of 8 minutes. Another important contribution in this area was reported by Schmalzing *et al.* [68], who demonstrated an electrophoretic separation of PCR samples on a fused silica device in less than 2 minutes. The separation device consisted of a microfabricated channel with a 45 µm X 100 µm cross section and 26 mm length, filled with a replaceable polyacrylamide matrix. This approach showed a 10 – to -100 fold improvement in speed when compared to capillary or slab gel systems. Most approaches to chip-based CE involve the application of high voltage on both ends of a separation channel to generate a large electric field to separate DNA fragments. The required electric field is typically between 300 and 800 V/cm, which demands an applied voltage of one to several kilovolts. Lin [69] presented a design of low voltage-driven CE in order to overcome this problem. A PMMA substrate with a separation channel of 50 mm length, 80 µm width and 20 µm depth was partitioned into many smaller separation zones as shown in Figure 1.5. The separation of a DNA sample, consisting of six fragments of 50, 150, 300, 500, 750 and 1000 bp was performed by applying an electric field of 300 V/cm. Electrode pairs were used for each zone and the DNA fragments were driven from one separation zone to the next. Switching the electrode pairs on and off in series generated the necessary electric field strength in the separation zones and allowed continuous separation of

the DNA fragments. This 'moving electric field' method was used to reduce the applied voltage to one-fifth of the value required in normal set-ups.

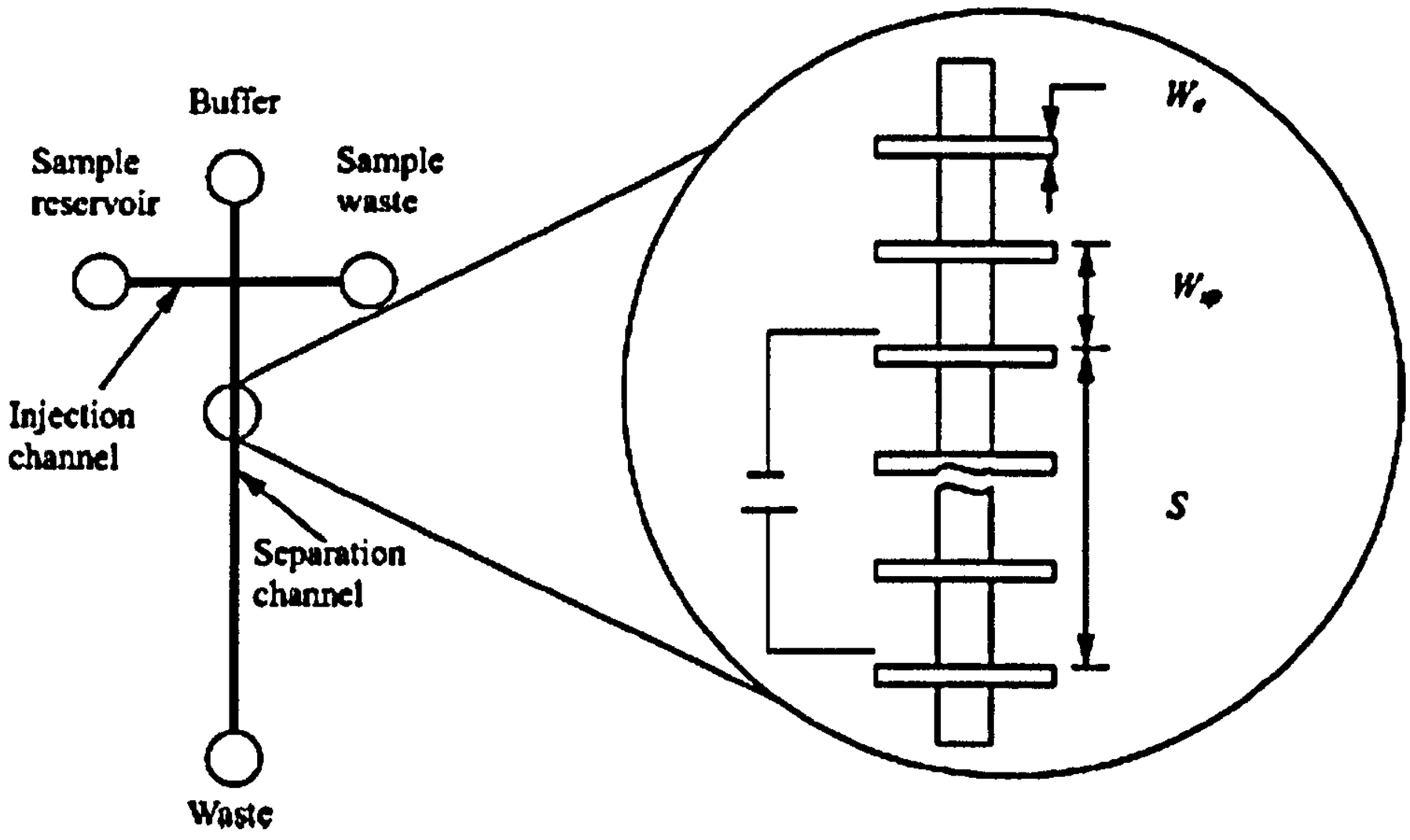


Figure 1.5 **Schematic layout of the subdivision of the separation channel [69].**

Impressive work was subsequently presented by Vrouwe *et al.* [70], with the direct measurement of lithium in whole blood using microchip CE with integrated conductivity detection. A Borofloat glass separation channel (2 cm long, 56 µm wide and 8 µm deep) was filled with a 30 µl blood sample. The detection electrodes consisted of a layer of thin-film platinum, which was in direct contact with the electrolyte inside the channel. Separation of lithium was performed within 60 - 120 s by applying a voltage of 1 kV. A lithium concentration of 2.7 mmol/l could be extracted from the electropherogram. In 2006 Goedecke *et al.* [71] presented an implementation of a genotyping assay in a microdevice format. Figure 1.6 shows the microfluidic assembly which contains a 16-lane micromachined device as the active separation element. This microdevice system replaced a standard capillary array electrophoresis (CAE) instrument and provided much higher data quality and data stability. Good reproducibility of data on the microfluidic device was due to the compact nature of the separation device combined with better heat sinking and mechanical stability. This application shows the potential of microfluidic devices in rapid genotyping and forensics.

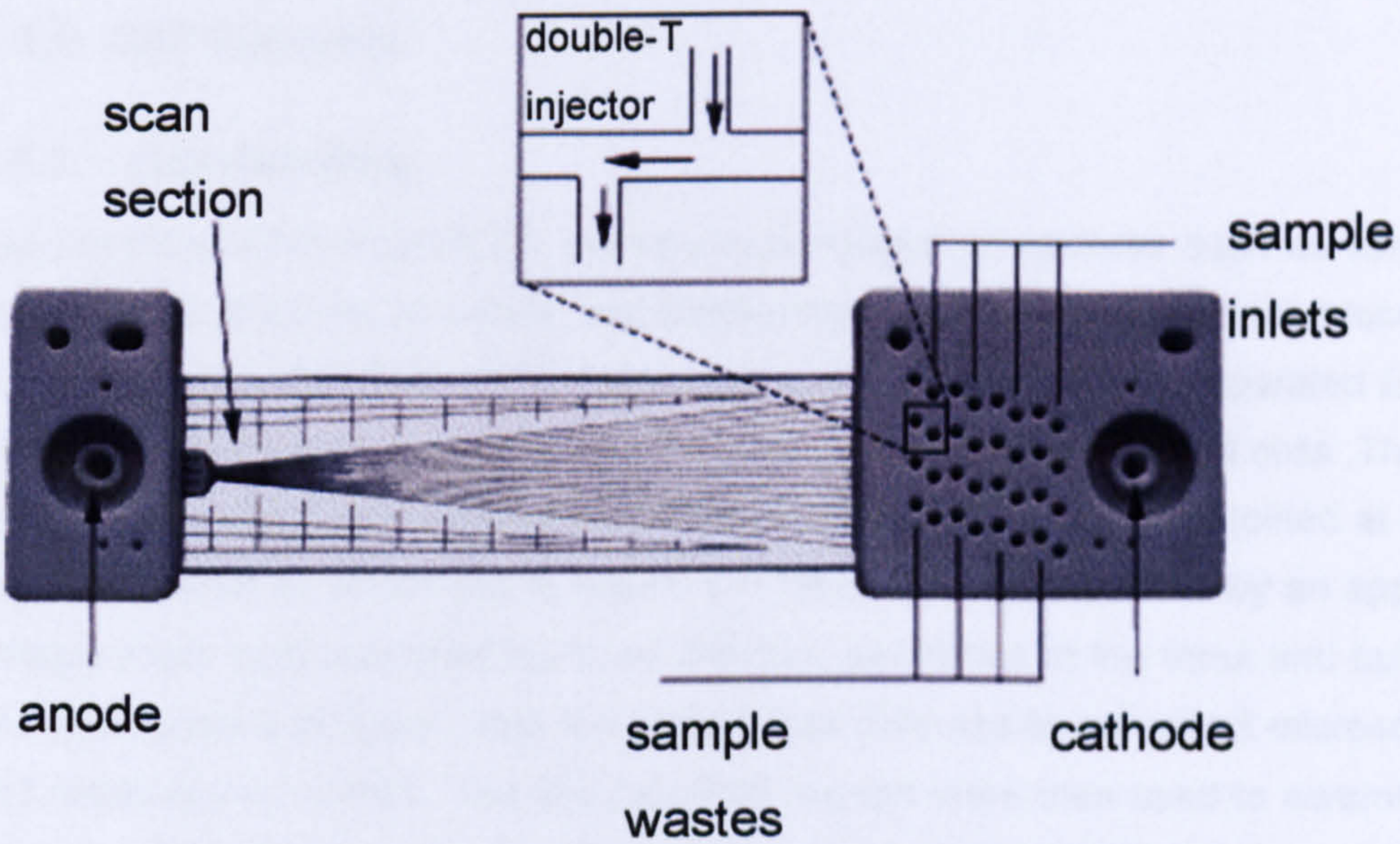


Figure 1.6 **The microfluidic assembly has a bonded two-layer glass body and two interface boards. Both boards, anode and cathode contain buffer solution. All 16 lanes taper off for the scanning region, where they are parallel and have a total width of 3.2 mm [71].**

The response of DNA strands to a uniform electric field is well known and fundamental to many common separation techniques. Less studied is the effect, often referred to as dielectrophoresis (DEP) [72], that utilizes dipole forces to manipulate DNA. In 2002 Asbury *et al.* [73] presented trapping and thereby separation of DNA fragments by dielectrophoresis on a microfluidic device. In this study a glass cover slip with patterned gold electrodes and a PDMS layer containing the microchannel were adhered to each other, so that the electrodes were inside the channel. The PDMS channel was filled with the DNA solution and a gentle flow of 1 nl/min was generated by hydrostatic pressure. A voltage of 0.5 - 4 V was applied across the gold electrodes, resulting in an average speed of 10 μm/s for the DNA. Molecules near the walls of the channel moved more slowly than average due to the viscous drag exerted on the fluid by the channel walls. Fluorescence from trapped molecules was quantitated by placing a confocal microscope downstream of the electrode nearest the inlet. This work was focused on assessing the variation of experimental parameters to control trapping efficiency. Excellent reviews on DNA separation on the microscale have been presented by Kutter [74], Chou *et al.* [75], Heller *et al.*[76], Stone *et al.* [77], Cooper *et al.* [78], Pumera. [79], Ghosal [80] and Horsman *et al.* [81].

1.4.2 Cell Analysis

1.4.2.1 Cell Handling

Cell handling within microfluidic devices must involve procedures such as sorting, manipulation, trapping, screening and monitoring of cells. Fu *et al.* [82] introduced a disposable micro fluorescence-activated cell sorter (μ-FACS) which separated E.coli cells expressing green fluorescent proteins from non-fluorescent E.coli cells. The μ-FACS device made of a silicone elastomer contained three channels joined at a T-shaped junction as presented in Figure 1.7. Cells were manipulated by an applied voltage which was controlled by three platinum electrodes at the input and output. The fluorescence emission from the sample was collected by an optical microscope and measured by a PMT. The digitized PMT signals were then used to control the applied voltage on the cells. Compared with a conventional FACS instrument higher sensitivity, no cross-contamination and lower cost were clear advantages.

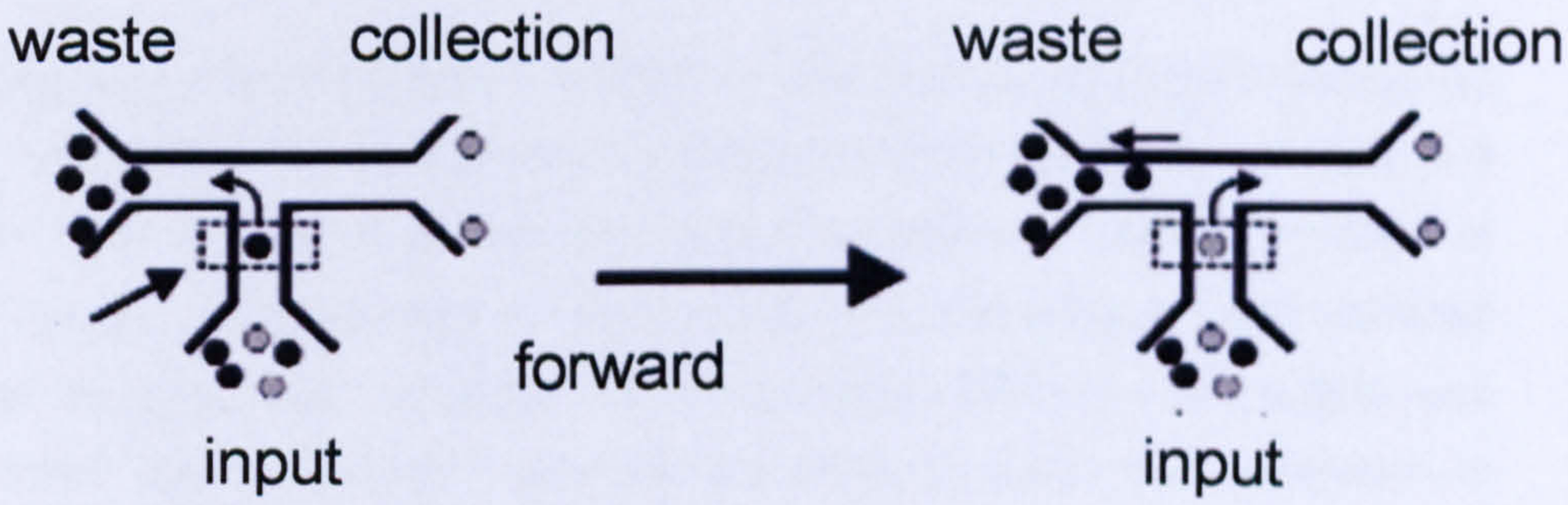


Figure 1.7 **Principle of μ-FACS. Fluid flow is switched as fluorescence is detected, so that grey beads are sent directly to the collection channel [81].**

Dittrich and Schwille [83] also demonstrated sorting of fluorescent beads in fluids with respect to their spectroscopic properties such as brightness and colour. Fluorescent beads of different colours were diluted in water and filled into a sorting channel (25 μm wide and 7.6 μm deep) in a silicone elastomer/glass chip. By application of low voltage across the channel beads could be monitored. A software interface translated the input parameters such as particle speed, brightness and colour into desired regulation parameters that in turn allowed efficient sorting. This work was aimed towards highly specific, ultra-sensitive and fast screening of large

libraries of cells. In the same year Wolff *et al.* [57] developed a μ-FACS in which fluorescent latex beads were sorted from chicken red blood cells by pressure-driven fluid flow. With a flow rate of 0.11 μL/s, 2 X 10^7 cells could be sorted within 27 minutes which resulted in the highest sample throughput on a μ-FACS to date. In the following year MacDonald *et al.* [84] demonstrated microfluidic sorting based on a 3D optical lattice, which was formed from five coherent laser beams. In this study, the trajectories of particles were dependent upon the force exerted on the particle by the optical lattice, in combination with the drag force exerted by the fluid flow. It should be noted that the strength of a particle's interaction with the lattice is determined by physical properties such as refractive index, size and shape. At a flow rate of 35 μm/s red blood cells were separated from white blood cells. Two major advantages of this method make it particularly attractive for cell sorting applications. Firstly, the interference patterns could be tailored to the particles and secondly in case of blockage during separation, the control lasers can be switched off.

More exciting work was introduced in 2006 when Kapishnikov *et al.* [85] investigated continuous separation and size sorting of particles and blood cells suspended in a microchannel flow by use of an acoustic force. Transducers, used as emitters of ultrasound waves, were mounted on both sides of a microchannel and particles were sorted as presented in Figure 1.8. A separation efficiency of 99.98% was achieved which was comparable with the efficiency of blood cell separation in commercially available centrifugation methods.

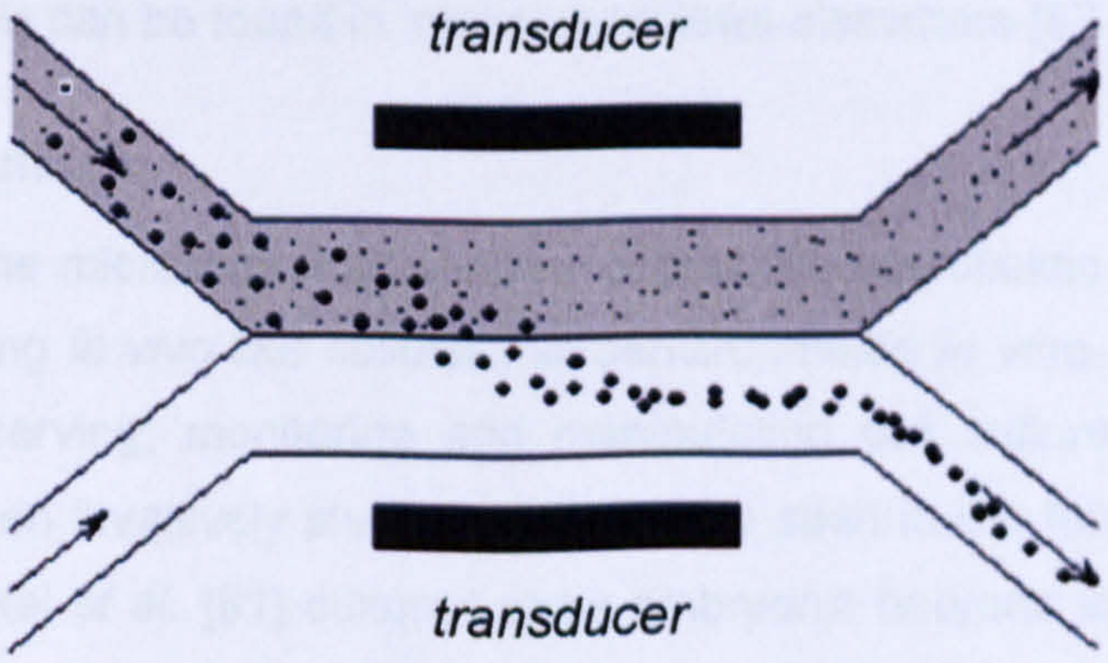


Figure 1.8 **Schematic view of a device for particle sorting with transducers as emitters of ultrasound waves.**

Another interesting approach for cell or bead sorting was introduced by Chen *et al.* [86] who introduced a high-speed micromachined thermal bubble-jet sorter with a working frequency of 50KHz or higher. This cell sorter consisted of embedded

heaters (20 μm X 20 μm in area) which required a power density of 10^9 W/m^2 to generate thermal bubbles. In this way, the movement of the cells in microchannels could be deflected as presented in Figure 1.9. Successful sorting experiments were performed by detecting scattered light from 20 μm microspheres. With a sorting rate comparable with much more complex and bulky conventional cell and bead sorting systems this sorter seems promising for the micromanipulation of a variety of biological cells.

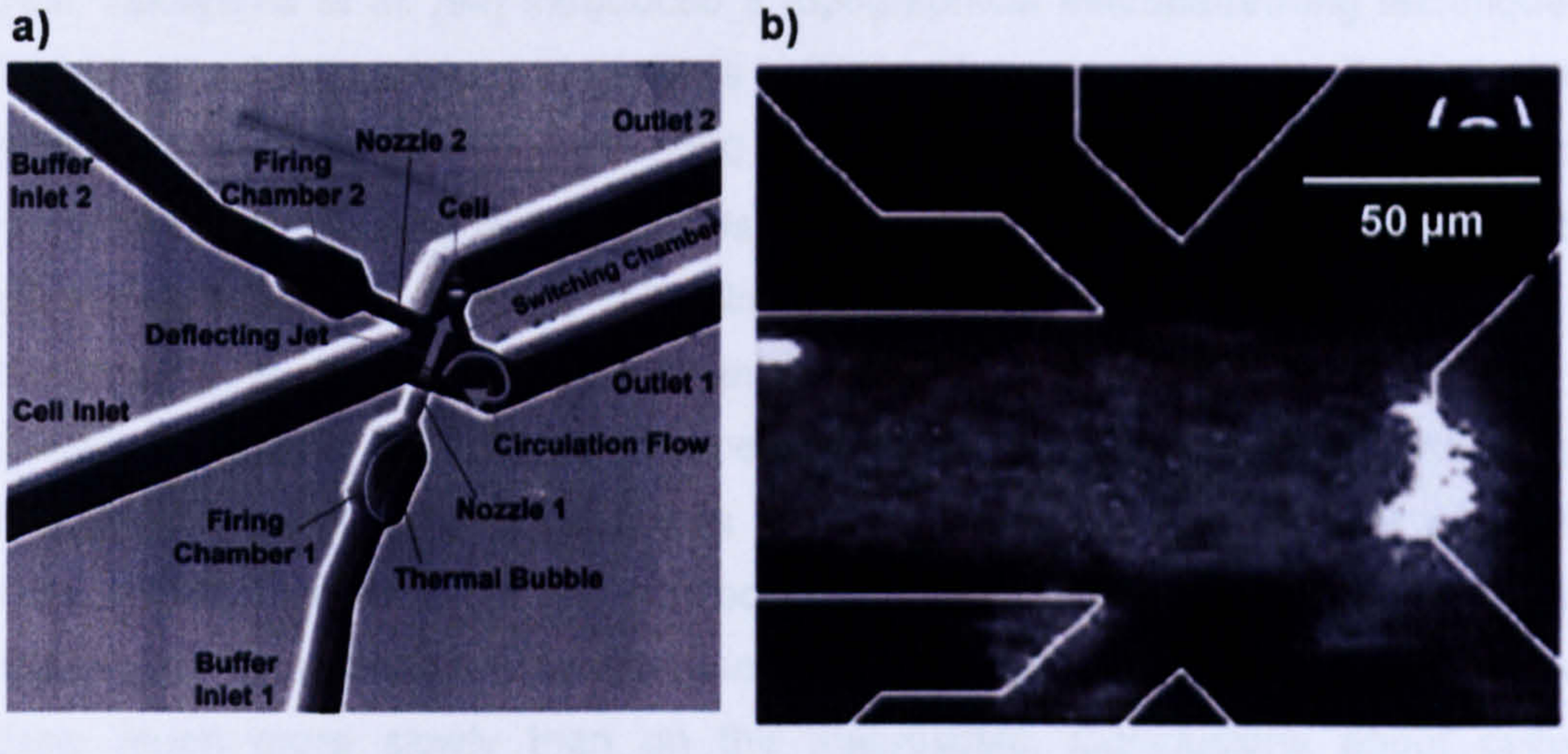


Figure 1.9 **a) A design of a high speed bubble-jet cell sorter b) A 20 μm microsphere entering the detection window and being pushed toward outlet 2 by the bubble jet on the opposite side [86].**

An assessment of processes such as manipulation, trapping, screening and monitoring of cells can be found in intensive reviews elsewhere [87-90].

1.4.2.2 Cell Culture

Cell culture on the microscale has become popular as microfluidic systems provide a route to creating *in vivo*-like cellular microenvironments *in vitro*. Processes such as growing, observing, monitoring and manipulating cell cultures in microfluidic devices have been invasively studied. This can be seen in the following examples. In 1998 Heuschkel *et al.* [91] cultured chick embryonic neurons in a photopolymer microfluidic device. Buried microchannels in a low-cost and easy to realize device made of SU-8 and Riston® provided conditions for the culturing, stimulation and recording of neural cell arrays. A couple of years later Monaghan *et al.* [92] presented work which included the culturing and detection of cells within a microfluidic device. In this work E.coli cells, which expressed green fluorescent protein, were grown on a PDMS microfluidic device with the incubation process being optically monitored. In the following year Glasgow *et al.* [93] presented the

transport and manipulation of mammalian cells on a silicon-glass microdevice. A pressure gradient of 1 Pa/mm in a microchannel (29 mm long, 250 - 400 µm wide and 160 - 200 µm deep) caused the cell media to flow at a speed of 100 nl/s. This caused the embryo cells to roll along the bottom of the channel, travelling at half of the speed of the fluid. The embryos could be held in place for several days of culturing and transported to specific locations, such as culture compartments and retrieval wells, by manipulating the pressure at the end of the channels. In the same year Takayama *et al.* [94] introduced a topographical micropatterning technique in PDMS microfluidic devices to produce patterns of mammalian cells. Topographical features with sizes between 10 – 100 µm were created by using multiple laminar streams of etching solutions. With this method controlled growth and study of the cells was facilitated. As living cells simultaneously detect multiple stimuli such as topography, surface adsorbed proteins, soluble chemicals and the presence of neighbouring cells, this laminar flow method turned out to be ideal and patterning of multiple stimuli inside a capillary was easily facilitated. In 2002 Walker *et al.* [95] cultured insect cells in PDMS microchannels and compared these results with experiments performed on the macroscale. It was found that cells on the microscale grew much more slowly than on the macroscale. Conclusions about cellular behaviour in vivo are, to date, often drawn from experiments on cells in macroscale environments but Walker *et al.* suggested that more accurate observations on cellular behaviour might be observed in microfluidic environments. In addition, Martin et al. [96] performed cell cultivation in a highly parallelized manner by high speed production of fluid segments (30 segments / second) by the use of microchip segmentor modules. These segments contained nutrient medium, cell suspension, one cell for each segment and volumes between 40 – 80 nl. The segments were incubated in a Teflon tube and rapid growth of microcultures was observed, with cell densities as high as in conventional shake flask cultures. After 24 hours of incubation at 30°C the fluorescence originating from such samples was already four times the starting value of the fluorescently labelled cells. In a tutorial review in 2004 Walker *et al.* [97] raised the question of whether microfabrication technologies were capable of replicating simple in vivo cellular microenvironments in vitro, and introduced the concept of an effective culture volume (ECV) in order to compare cell culture environments between the macro and the microscale. ECV is an indicator of a cell's ability to control its microenvironment during culture. Walker *et al.* addressed aspects of engineering a more *in vivo*-like microenvironment. In this, mechanical forces applied to the cell culture environment, transport phenomena of cells on the microscale and the influence of material interfacing with cells were discussed. It was

suggested that microfabrication technologies were indeed capable of replicating simple *in vivo* cellular microenvironments *in vitro* and this could facilitate opportunities for answering fundamental questions regarding cell structure and function. Over the years many research groups have showed significant developments in cell culturing methods using microfluidic tools [98-100]. These "cell biochips" consist of microchambers containing engineered tissue and living cell cultures interconnected by a microfluidic network, which allows the control of microfluidic flows for dynamic cultures, by continuously feeding nutrients to cultured cells and removing waste. Cell biochips have also allowed the control of physiological contact times of molecules with tissues and cells, and been used for rapid testing of sample preparations [101, 102]. Cell biochips can be thought of as existing between *in vitro* and *in vivo* testing formats. These types of systems can enhance functionality of cells by mimicking tissue architecture complexities (when compared to *in vitro* analysis), but at the same time presenting a more rapid and simple process when compared to *in vivo* testing procedures. Baudoin *et al.* [103] reviewed these trends and developments. Figure 1.10 shows an example of a liver microfluidic chip [104-106].

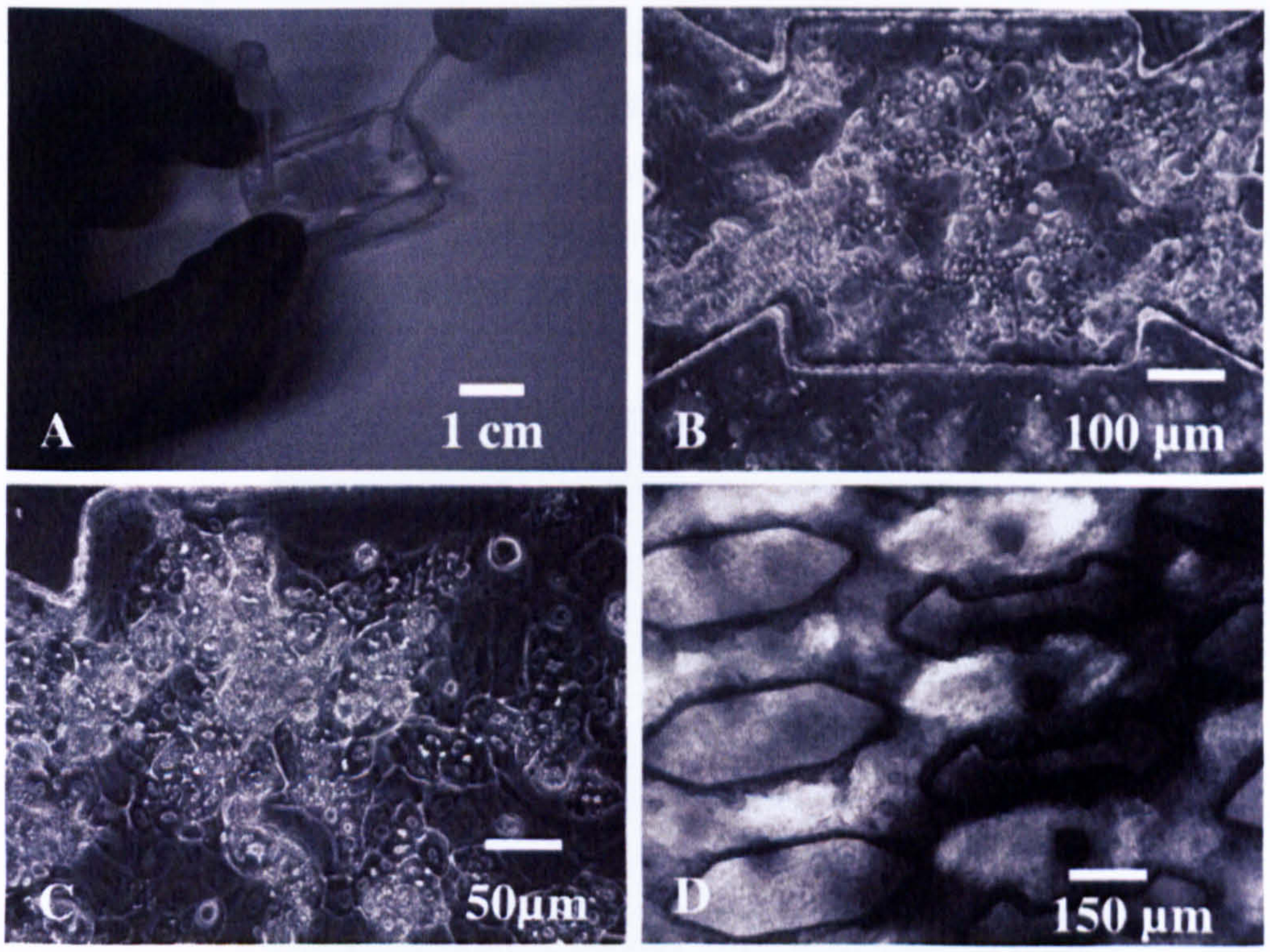


Figure 1.10 **(A) PDMS microfluidic biochip used for in vitro liver cell culturing. (B) Hepatoma-derived cell line. (C) and (D) cultivated cells in microfluidic biochip [103].**

1.4.3 Clinical Diagnostics

The early, rapid and sensitive detection of a disease state is a vital goal for clinical diagnoses. The biochemical changes in a patient's blood can signal organ damage or dysfunction prior to observable microscopic cellular damage or other symptoms. Consequently, there has been a large demand for the development of easy-to-handle, inexpensive and fully integrated clinical diagnostic devices which enable fast and reliable measurements. Clinical diagnostic applications have focused on detection of nucleotides and peptides as early indicators of diseases, detection of biological warfare agents or monitoring of regular metabolic parameters. This section will present some of the more interesting applications on the microscale such as the determination of factors for cancer, kidney, liver diseases, detection and screening of cardiovascular risk factors. For example, Tian *et al.* [107] screened common mutations in breast cancer susceptible genes using a single-strand conformation polymorphism analysis within a polymer-coated microchip. The device was filled with a sample of fluorecescently labelled DNA and buffer. Application of an electric field of 573 V/cm was used to separate different sized DNA fragments within 120 s. Du *et al.* [108] reported another microfluidic-based diagnostics device for screening cancer cells. In this approach, antibodies were bound to the surface of PDMS microchannels. Fluorescently labelled cells in buffer were flowed through the system and captured where appropriate Figure 1.11 shows cells flowing through a PDMS channel at a flow rate of 4 µl/min in (a) and 20 µl/min in (b). Successful capturing and enriching of antibody binding cancer cells was presented within this work and was considered to be a precursor approach for further cancer cell investigations.

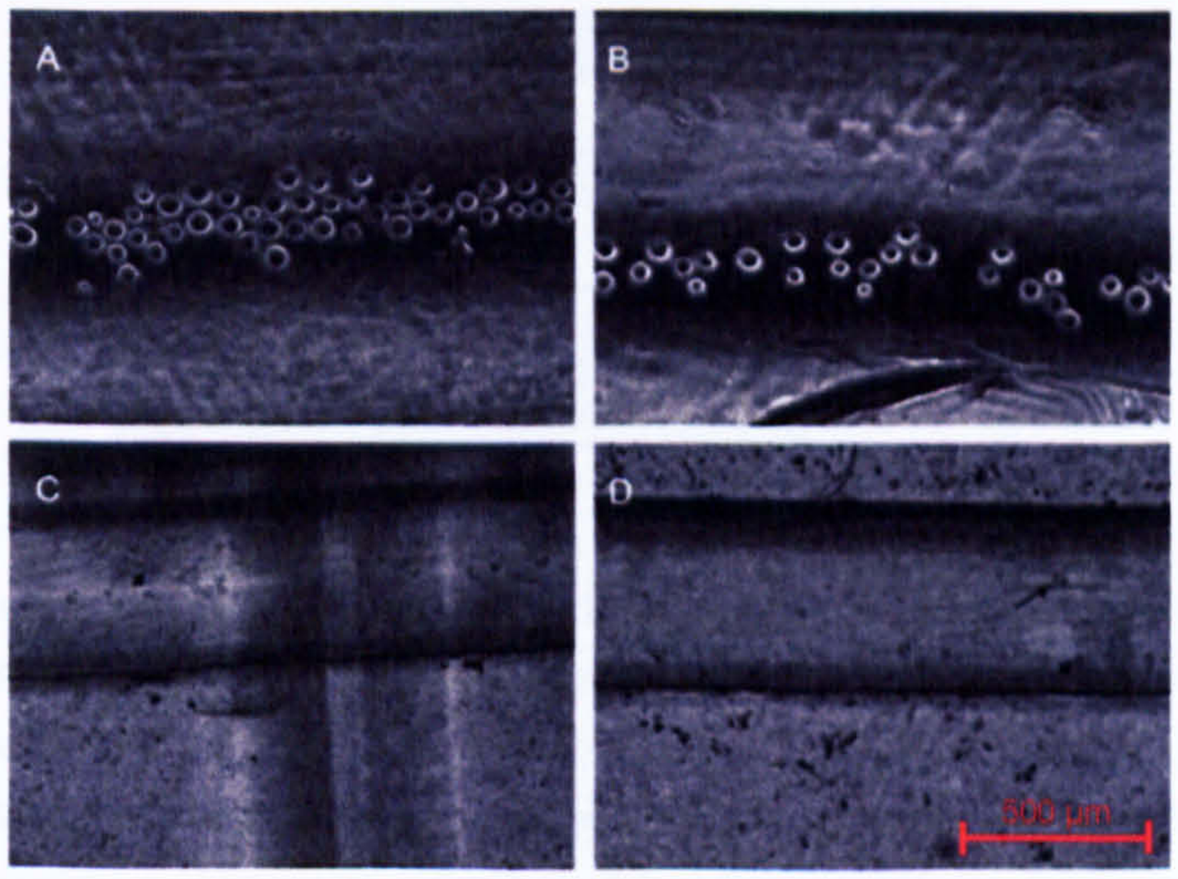


Figure 1.11 **Photomicrograph (magnification 40X) showing cancer cells flowed through PDMS channel with flow rate of 4 µl/min a) and 20 µl/min b) [108].**

Additionally, Munro *et al.* [109] have presented the analysis of urine samples containing high levels of amino acids (indicative of kidney malfunction) by performing electrophoretic separations in a microfluidic device. In this study, a glass separation channel (5.5 cm long, 50 µm wide and 10 µm deep) was filled with a filtered and diluted urine sample. An electric field of 183 V/cm was applied and nineteen standard amino acids were detected with an impressive average detection limit of 32.9 µM. Zuborova *et al.* [110] reported the determination of oxalate concentrations as an indicator of kidney diseases, from urine samples, using a PMMA electrophoresis chip. Here, the separation channel was filled with 500 nL of filtered and diluted urine and the separation of oxalate from anionic urine constituents was performed with analysis times as short as 280 s. Another application of clinical diagnostics on the microscale was the detection of cardiac risk factors. Christodoulides *et al.* [111] presented the simultaneous detection of two serum cardiac risk factors, C-reactive protein and interleukin-6. The approach is based on microbeads positioned within micromachined cavities on a silicon wafer. Specifically analyte specific antibodies were coupled to agarose microbeads. The bead-loaded chip was then packaged into a fluid flow cell, containing serum samples, that was held together by an aluminium casting (Figure 1.12). This first generation chip enabled high-throughput detection of up to 100 different antibody/antigen analytes using a single drop of sample fluid (~50 µl).

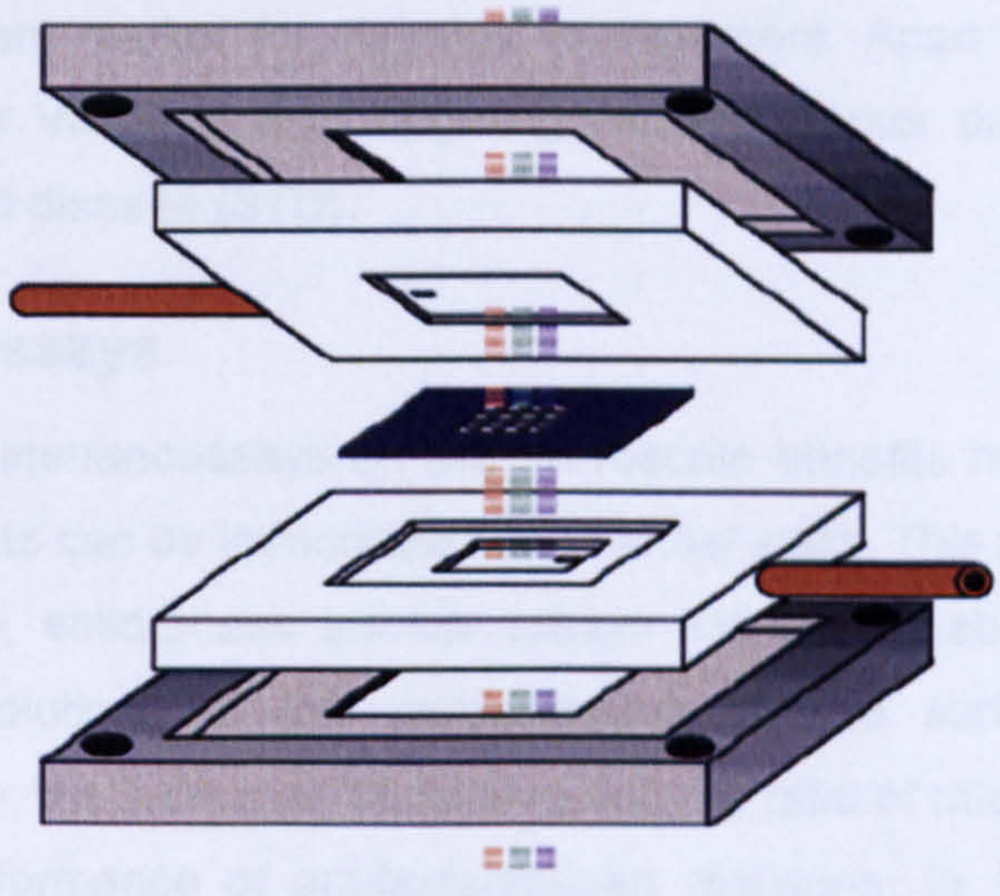


Figure 1.12 **Schematic illustration showing the bead 10 X 10 array chip which is packaged into a fluid cell. The pyramidal pits extend through the entire thickness of the wafer, thereby creating square openings (~100 µm X ~100 µm) on the remote side of the chip. These openings both provide optical access to the bead element and serve as a drain for the reaction/analysis chambers. The package assembly is suitable for both fluorometric and colorimetric analysis [111].**

Similarly Pasas *et al.* determined the concentration of a cardiovascular risk factor, homocysteine in human plasma, using chip-based capillary electrophoresis and electrochemical detection [112]. In this work, a glass separation channel was filled with a serum sample, an electric field of 360 V/cm applied, and amperometric detection with a gold / mercury amalgamated electrode performed. The separation and detection of homocysteine and related compounds was performed in 80 s with a detection limit of 500 nM for homocysteine. Extensive reviews on microfluidic technologies in clinical diagnostics are presented elsewhere [2], [113-116]. Numerous start-up companies (see Table 1 Appendix A) have taken advantage of the revolutionary improvements of clinical diagnostics on the microscale. For example Molecular Vision, an Imperial College start-up company, has combined microfluidic technology with organic light emitting diodes (OLEDs) and organic photodetectors to realise disposable diagnostic tests for point-of-care applications. Organic semiconductor-based detection components comprise an organic layer sandwiched between two electrodes and can be integrated with microfluidic systems at low cost. Molecular Vision's technology platforms are based on chemiluminescence, fluorescence or absorbance detection. Using a simple fluorescent binding assay with an AB580 dye, Human Serum Albumin (HSA) was determined at a diagnostically relevant level using OLED based excitation. Increased levels of HSA in urine (microalbuminuria) are indicative of renal disease and are an important marker for diabetes management. Apart from renal disease markers, Molecular Vision is also targeting cardiac marker panels and tests for sexually transmitted disease (STD).

1.4.4 Immunoassays

The application of immunoassays on the microscale benefits hugely from the fact that immunoreagents can be immobilized on channel walls. This results in two major advantages. Firstly, solid-phase immunoassays exhibit the ability to concentrate molecules from solutions of low concentration onto a surface for facilitated detection. Secondly, the increased surface-to-volume ratio of micron sized channels enables faster performance of antibody/antigen reactions. In 1996 Koutny *et al.* [117] presented an assay which determined cortisol in blood serum over the range of clinical interest (1-60 µg/dL) without the need for extraction or other sample preparation steps. Separation of free and bound antigen in this competitive assay was performed within 30 s by microchip-based CE. The following year Hadd *et al.* [34] presented an automated enzyme assay within a microfabricated channel network. Here, precise concentrations of substrate, enzyme and inhibitor were

mixed using electrokinetic flow and reagent dilution. The mixing process was controlled by regulating the applied potential at the end of the channels. Figure 1.13 shows the layout of the device used. Within this work an enzyme assay was performed in a 20 minute period and required only 120 pg enzyme and 7.5 ng substrate. This corresponded to a reduction of required sample of 4 orders of magnitude when compared to conventional assays.

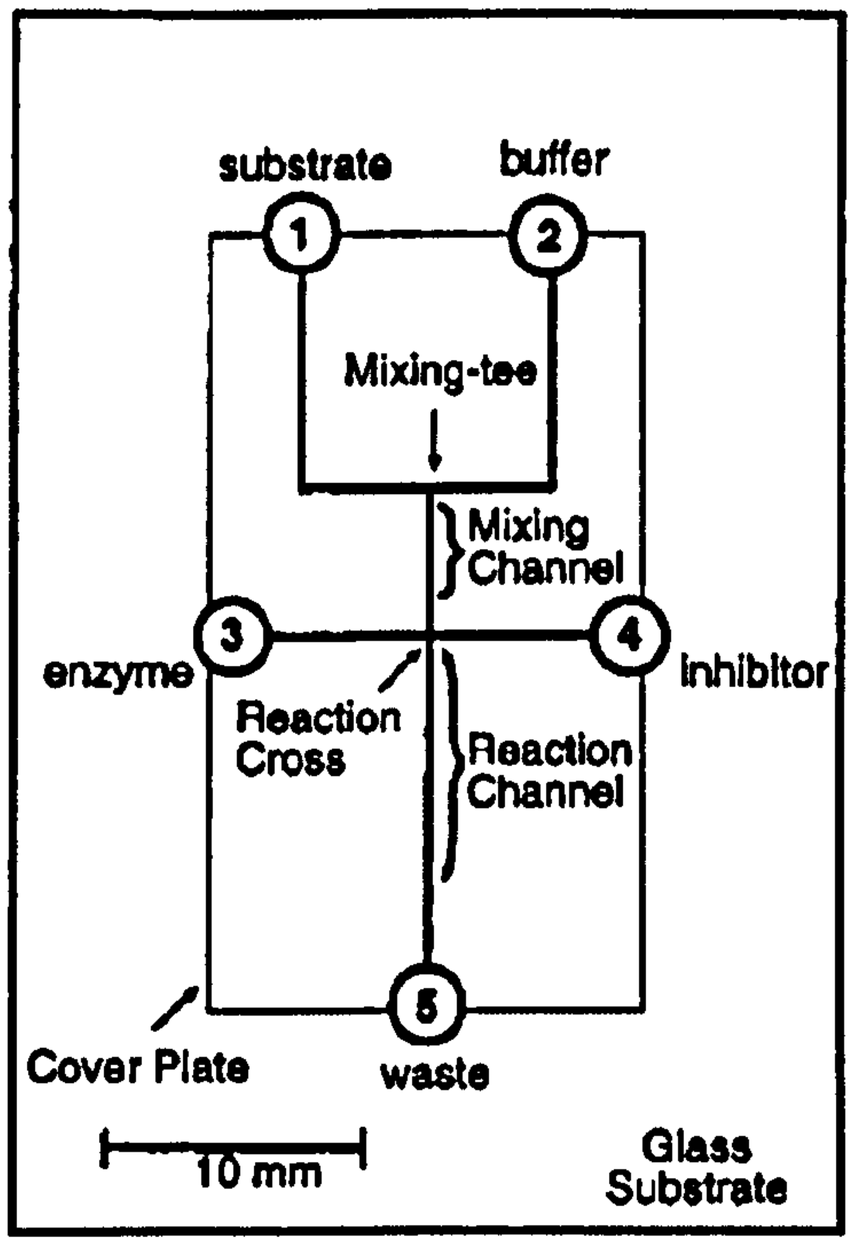


Figure 1.13 **Schematic of an enzyme analysis chip. The channels terminate at reservoirs containing the indicated solutions. The channels are 9 µm deep and 35 µm wide [34].**

In the same year a study incorporating biological material on substrates was presented by Delamarche *et al.* [118]. This relied on the patterned delivery of immunoglobulins to surfaces using microfluidic networks (µFNs). Such µFNs were used to pattern biomolecules with high resolution on a variety of substrates, such as gold, glass and polystyrene. Figure 1.14 presents a schematic of the concept. µFNs consisted of three walls moulded out of PDMS and a fourth wall formed by the Au substrate. After applying the elastomer to the substrate, the Si-SiO_2 surface was activated to achieve chemical coupling with the amino groups of the proteins. When the substrates had enough reactivity, monolayer quantities of immunoglobulin G (IgG) could be readily fixed to the surface. With this device delivery of proteins onto the Au substrate was homogenous over a few millimetres and provided practical

quantities of covalently attached material for convenient screening using enzyme-linked immunosorbent assay (ELISA) methods. Figure 1.15 shows an example of a fluorescently labeled immunoassay. This method for generating patterns of biomolecules by chemical attachment within μFNs provided several practical benefits. Firstly, the approach is compatible with many existing chemistries and substrates. Secondly, as the deposited material binds to the surface in solution the ligands are not exposed to denaturing conditions. Thirdly, the patterning is local in nature, which means that patterning only occurs in targeted areas. Finally, simultaneous reactions in adjacent flow channels are possible without cross-contamination.

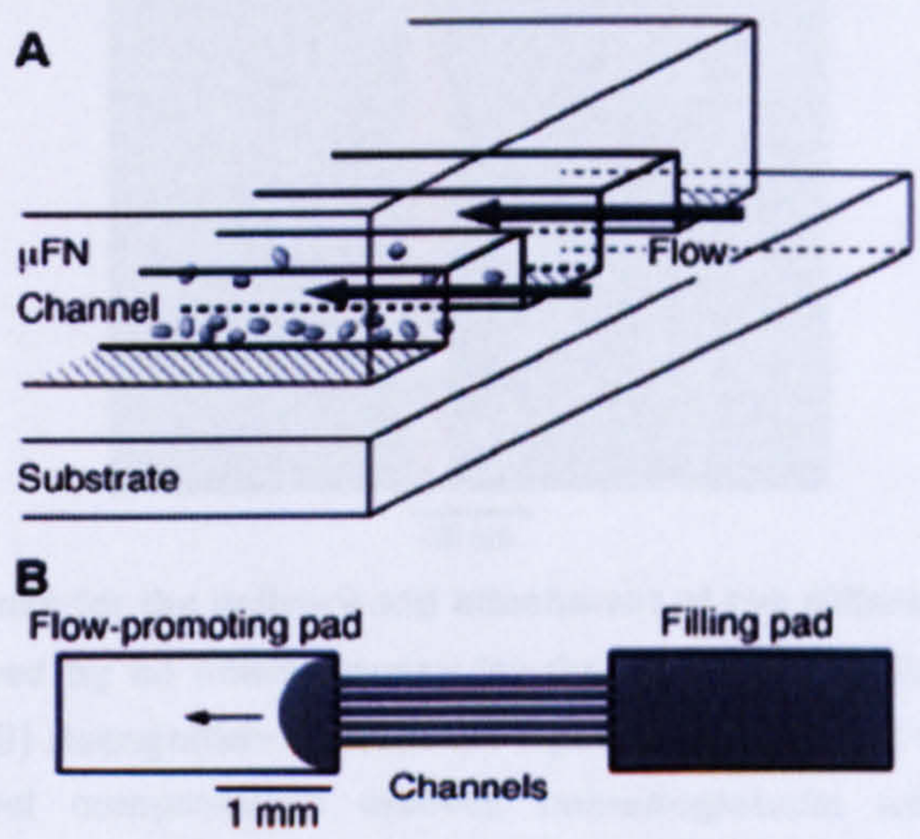


Figure 1.14 **a) Patterned elastomer that forms a microfluidic network by contact with a substrate and allows the local delivery of a solution of biomolecules to the substrate. B) flow of liquid between the filling pad and an opposite pad fills the array of microchannels that constitute the strategic part of the device [118].**

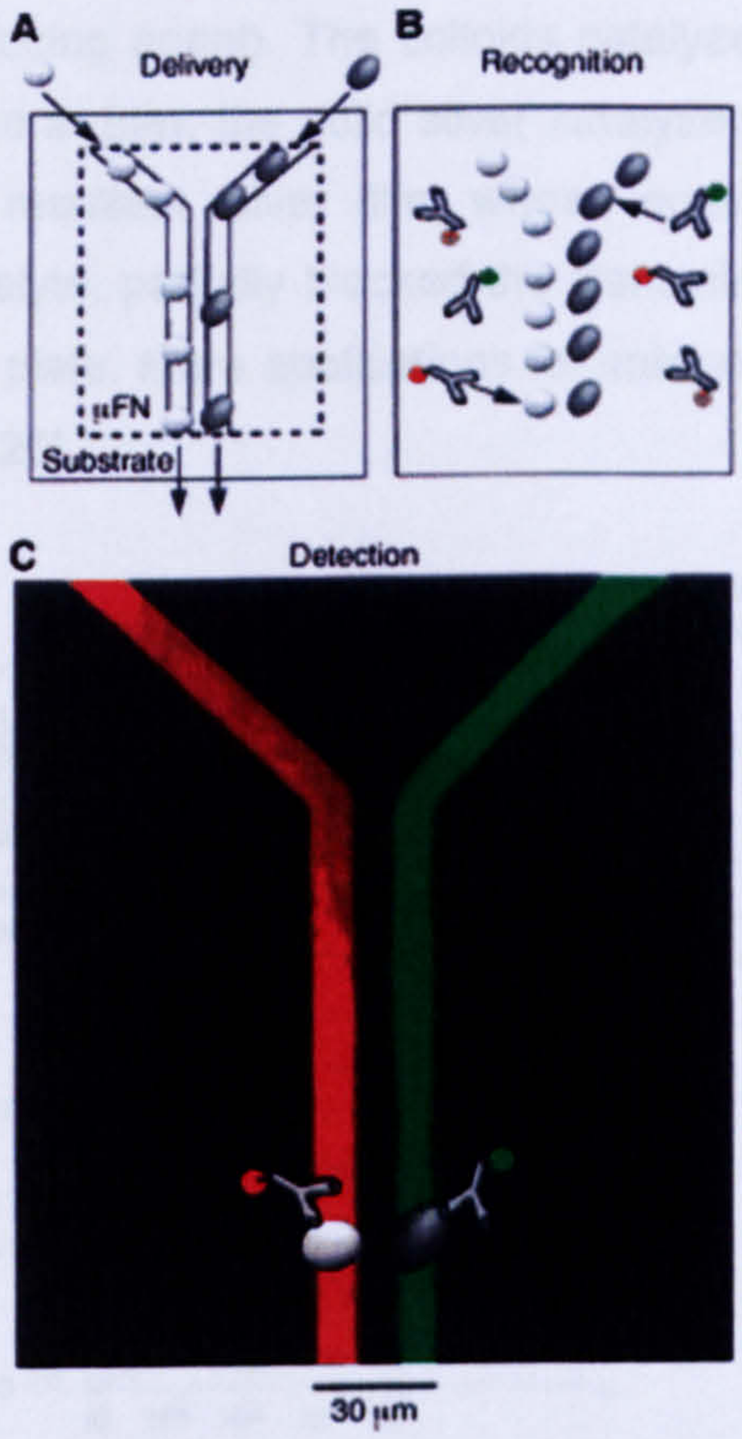


Figure 1.15 **Schemes for the delivery and attachment of two different IgGs using a µFN. A) followed by an immunoassay for the attached proteins after removal of the µFN. B) Recognition fluorescent signals when bound to each partner. C) Red channel compromises chicken Immunoglobulin and the green channel compromises mouse immunoglobulin [118].**

Subsequently, Yang *et al*. [119] presented a new class of microfluidic immunoassay based on solid supported lipid bilayers. These lipid bilayers contained dinitrophenyl (DNP)-conjugated lipids for binding with bivalent anti-DNP antibodies. In this work PDMS microchannels were coated with the lipid bilayers and filled with Alexa dye labelled anti-DNP so that the protein concentration could be determined via fluorescence. The methodology for performing heterogenous assays developed within this work not only produced rapid results but also required much less protein sample (2µl) than traditional procedures. An application which mainly focused on improving health in developing countries for the diagnosis of infectious diseases was presented by Sia *et al*. [120] who introduced a "POCKET (*PO*rtable and *C*ost-Effe*c*Tive) immunoassay". An immunoassay in a microfluidic format for quantifying anti-HIV-1 antibodies in the sera of HIV-1-infected patients was developed and is presented in Figure 1.16. Detection is based on a redox-reaction. Antibodies conjugated to 10 nm gold colloids were added to a solution of silver nitrate and

hydroquinone (as a reducing agent). The colloids catalyzed the reduction of silver ions to silver atoms; and in turn, the solid silver catalyzed the further reduction of silver ions [121]. The resultant silver film, whose opacity is a function of the concentration of the analyte, partially blocked the transmission of light through the transparent polystyrene plate. More applications for immunoassays can be found in following reviews [122-126].

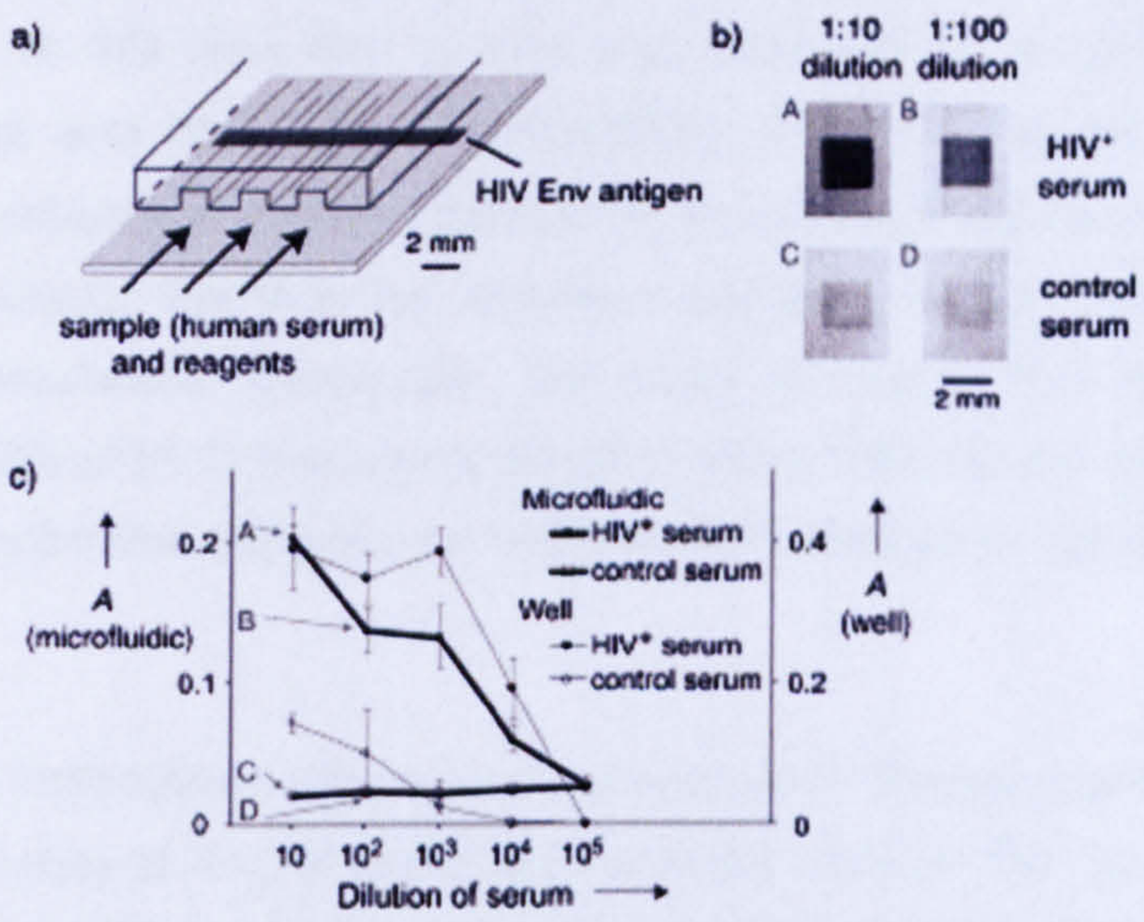


Figure 1.16 **Microfluidic device that detects ant-HIV-1 antibodies. The HIV antigen is patterned onto a polystyrene surface as a strip, and a slab of PDMS with microchannels is placed orthogonally to the stripe [120].**

1.4.5 Small Volume Detection

Numerous approaches for analyte detection in small-volume systems have been reported [127-137] on the microscale. Fluorescence-based methods are most widely used in microchip analyse, due to superior selectivity and sensitivity. Although a variety of excitation sources are available, lasers provide advantageous characteristics. These include high intensities, variable wavelengths, spatial and temporal coherence, low beam divergence and the ability to pulse the output at high frequency.

Lamp-based excitation systems represent a less expensive but more flexible alternative. Microscope-based detector set-ups using xenon or mercury lamps have been applied to a variety of different analytical problems with impressive results. Examples presented here will outline studies incorporating fluorescence detection and highlight other approaches to detection on the microscale.

In 1996 Liang *et al.* [138] presented an absorbance and fluorescence U-shaped glass detection cell for application in capillary electrophoresis and obtained a 10-fold increase in absorbance compared to a path transverse to the flow direction. Fluorescence detection limits were 20000 molecules and 3 nM concentration for fluorescein. Hodder *et al.* [139] studied mixing and reaction kinetics with fluorometric assays by combining a flow injection analysis (FIA) system with a microfabricated flow chamber. In this work one syringe was filled with an enzyme solution and another syringe was filled with a fluorescently labelled substrate solution. Both liquids were pumped into the flow chamber by generating a laminar flow. The mixing of the two solutions and thus the enzyme-substrate reaction could be observed through a fluorescence microscope. The study of mixing and reaction kinetics carried out in this μFIA format was a stepping stone towards the development of a stopped-flow cytometer designed to study reaction kinetics in cellular suspensions [139].

DNA detection methods mostly rely on fluorescence of labelled probes [140-146]. In this context Woolley *et al.* [24] presented important work in 1997 by reporting high-speed, chip-based DNA electrophoresis with online detection using a laser-excited confocal-fluorescence scanner. Figure 1.17 illustrates the set-up and Figure 1.18 presents the mask design for the microchip. The glass separation channels were filled with an 'orange' labelled DNA sample and a 'red' labelled ladder. An electric field of 200 V/cm was applied to the channels and detection could be performed during the separation. This resulted in the separation and detection of all 12 samples in less than 160 s. Liu *et al.* developed and improved this work in 2004 [147] and achieved total analysis time of less than 60 s.

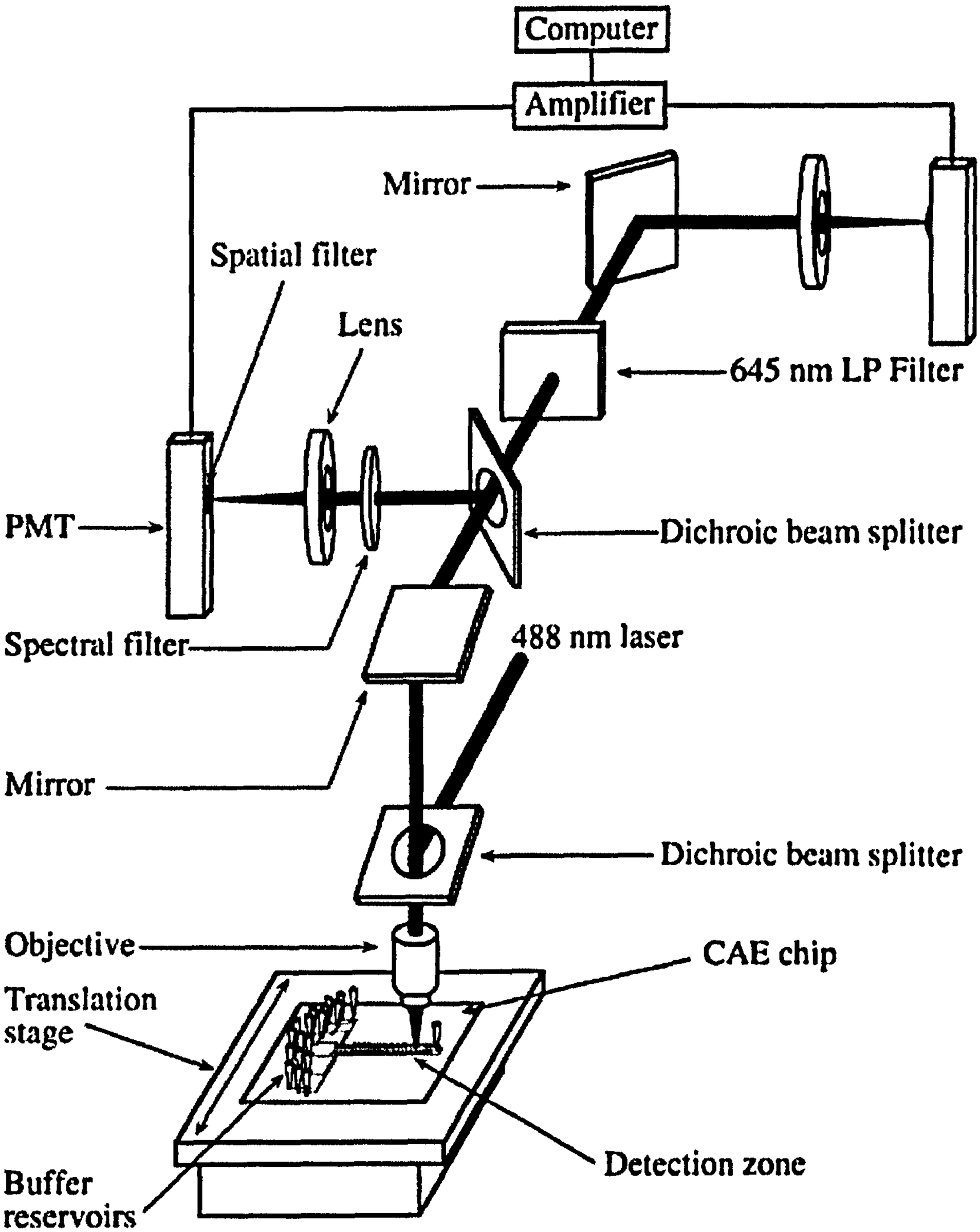


Figure 1.17 **Schematic of the laser- excited confocal-fluorescence scanner and a capillary array electrophoresis chip [24].**

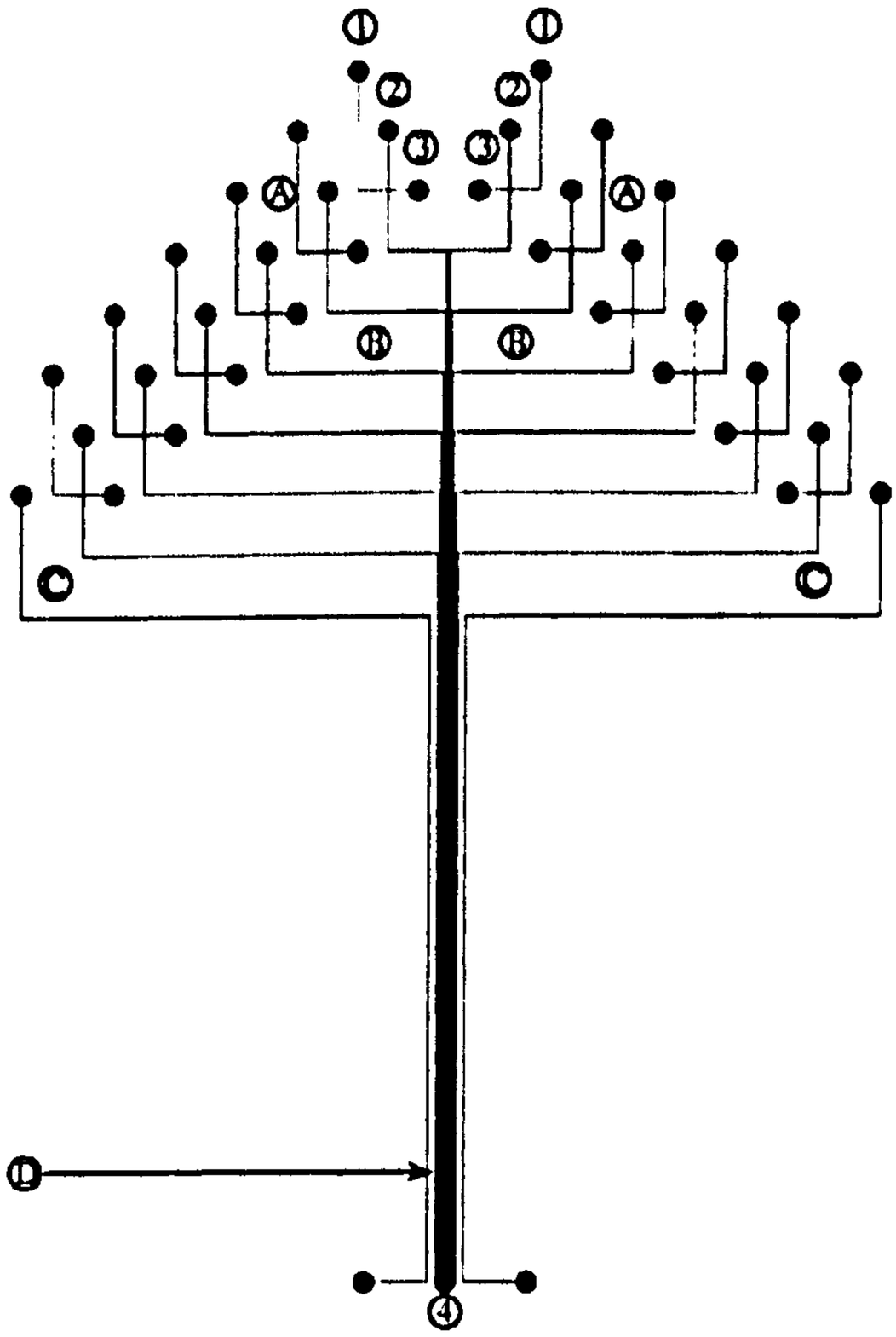


Figure 1.18 **Mask design used to photolithographically pattern the 12-channel CAE chips. A) injection channels, B) separation channels, C) optical alignment channels, D) detection region, 1) injection waste reservoirs, 2) ground reservoirs, 3) injection reservoirs, 4) high voltage anode reservoir [24].**

Numerous reviews have assessed methods for DNA detection within microfluidic devices [2],[148-150] . Other detection methods such as electrochemiluminescence, mass spectrometry, label-free detection, amperometric and acoustic-based detection have been reported as presented [151]. Hsueh *et al.* [152] microfabricated an electrochemical cell in silicon for the generation and detection of electrochemiluminescence of tris(2,2'-bipyridyl)ruthenium(II) (TBR). The cell contained a gold, thin film cathode and an indium tin oxide, thin film anode. Free TBR could be detected from 10^{-9} to 10^{-3} M with a cell volume of 85µl. In the following year Arora *et al.* [153] presented an electrochemical cell for the generation and detection of electrochemiluminescence from TBR as well but utilized a sandwich of poly(methyl methacrylate) PMMA- acetate- PMMA to define a sub-µl cell. Using this approach a concentration detection limit of 5×10^{-13}M was achieved. Xue *et al.* [154] successfully interfaced a glass device with an electrospray

ionization mass spectrometer (ESI-MS) as presented in Figure 1.18. The chip, made of glass, was designed with nine parallel channels (3.5-5 cm long, 60 µm wide and 25 µm deep). Each channel was connected to two wells, which allowed for fluid filling and sample injection into the channel. After the channels were filled with protein solutions, a high voltage for the electrospray was applied and detection could be performed on a connected triple-quadrupole mass spectrometer. Detection limits lower than 6 X 10^{-8} M were achieved using this set-up. More recent examples of integrated chip-MS systems are revised elsewhere [155-158]. Finally, electrical and electrochemical detection methods have been widely applied to microfluidic systems due to their sensitivity and ease of miniaturization and integration.

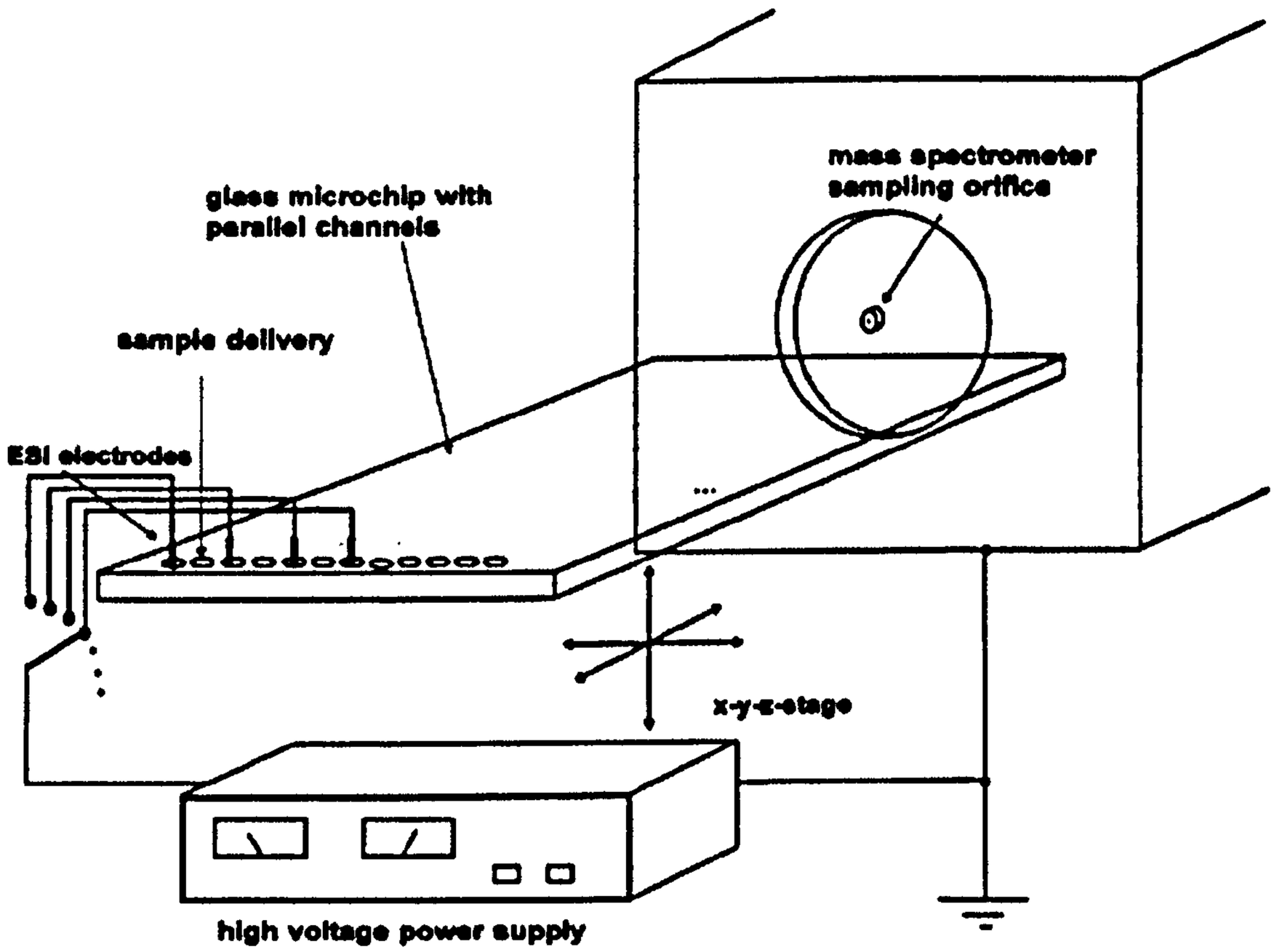


Figure 1.19 **Schematic diagram of the microchip ESI-MS interface. The voltage for ESI was sequentially applied to one well of each channel containing buffer and a platinum electrode. The second well of each channel contained sample and was connected to a syringe pump to provide a flow rate of 100-200 nl/min. The exit ports of the microchip were aligned sequentially with the orifice of the MS using a 3D stage [154].**

In the same year Figeys *et al.* [159] presented an ESI-MS with a detection limit with a sensitivity which was 4 magnitudes higher. In the last decade approaches for DNA detection have improved immensely. For example, Hou *et al.* [160] have presented

an integrated microelectronic device for amplification and label – free detection of nucleic acids (Figure 1.20). In this study the use of a microfluidic device consisting of a doped silicon substrate with a 800 nm deep sensor area and a SU-8 elastomer sample chamber was defined. Detection was based on a principle presented by Cooper *et al.* [161] who explored the capabilities of microfabricated potentiometric sensors for electrical monitoring of molecular adsorption. They demonstrated that a microfabricated field-effect sensor which is located at the terminus of a freestanding cantilever can detect surface potential changes resulting from the adsorption of charged molecules in an aqueous environment. The charge sensitive region, defined by a lightly doped silicon section, is embedded within the heavily doped silicon cantilever. Hou *et al.* applied this principle to end-point detection of PCR products. While the sample was thermocycled in the microchamber, the electronic sensor was functionalized with a polycation solution of poly-L-lysine (PLL). This positively charged sensor surface facilitated capturing of the negatively charged DNA fragments generated by the PCR. The binding of charged molecules such as PLL or DNA affected the distribution of the extrinsic mobile charge carriers and changes of capacitance in the depletion region were monitored. The absence or presence of a specific DNA sequence was determined by converting the analog surface potential output of the field-effect sensor to a simple digital true/false readout.

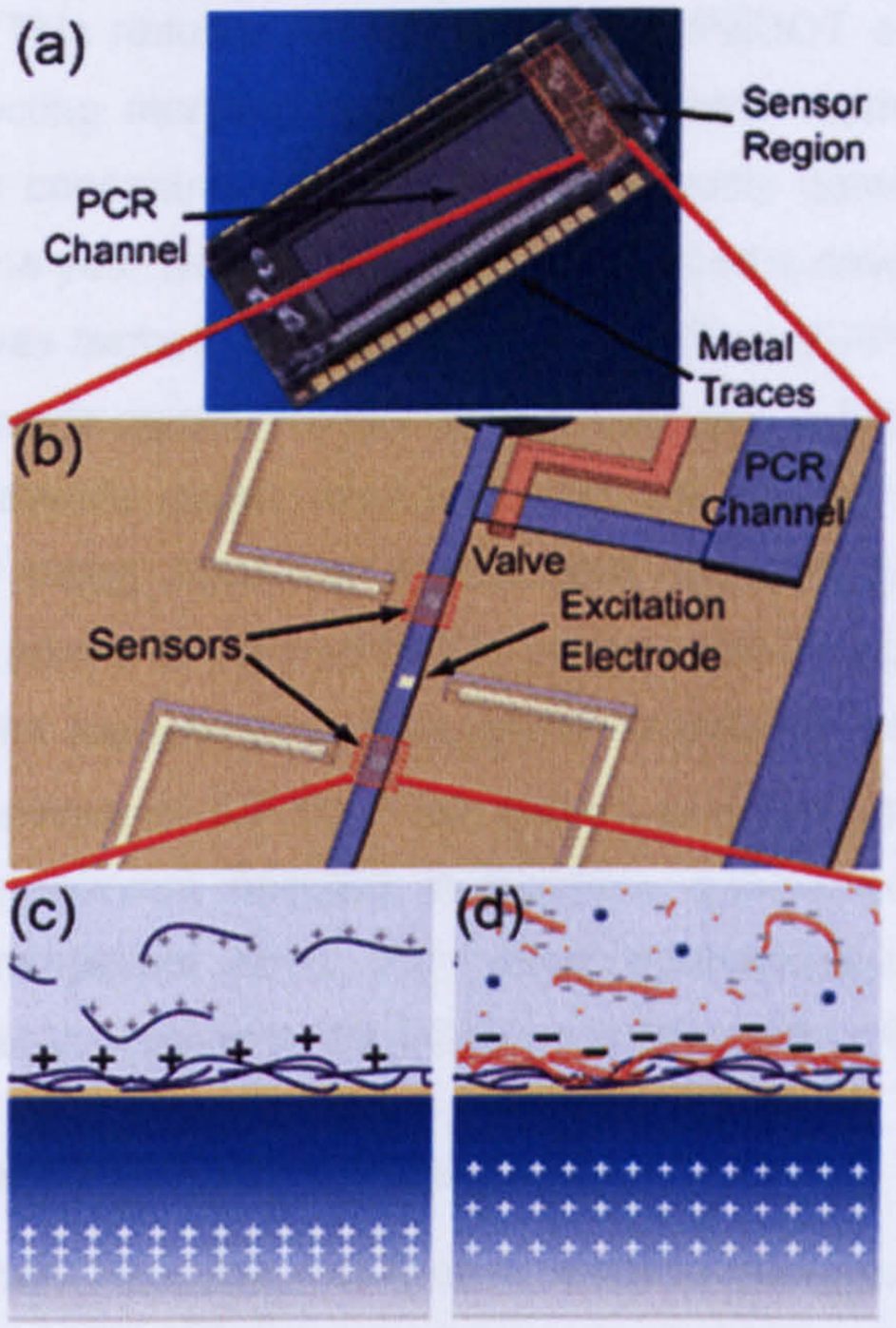


Figure 1.20 **Device layout and concept. a) Photograph of an integrated device with embedded sensors (right dotted area), PCR microfluidic channel with integrated valves (left dotted area) and metal resistive heaters and sensors (features above and below PCR channel). b) 3D rendering of device centred on sensors (top and bottom squares) and excitation metal electrode. Adjacent features include gold traces for electrical connections, inlet of sensor channel, and an integrated valve controlling the interface to the PCR channel. The gold traces are connected to the respective gold electrode and field-effect sensors by buried conductive traces in silicon (not shown). Conceptual schematic of sensor cross section illustrating the physical changes caused by binding of (c) positively charged polyelectrolyte followed by d) negatively charged product DNA in the PCR mix. The mobile positive charge carriers in the sensor redistribute depending on the polarity of surface charge, affecting the depth of the charge depletion region in the process. This subsequent change in depletion capacitance is monitored by applying an AC voltage to the metal electrode and measuring the resulting current through the doped sensor region in silicon [160].**

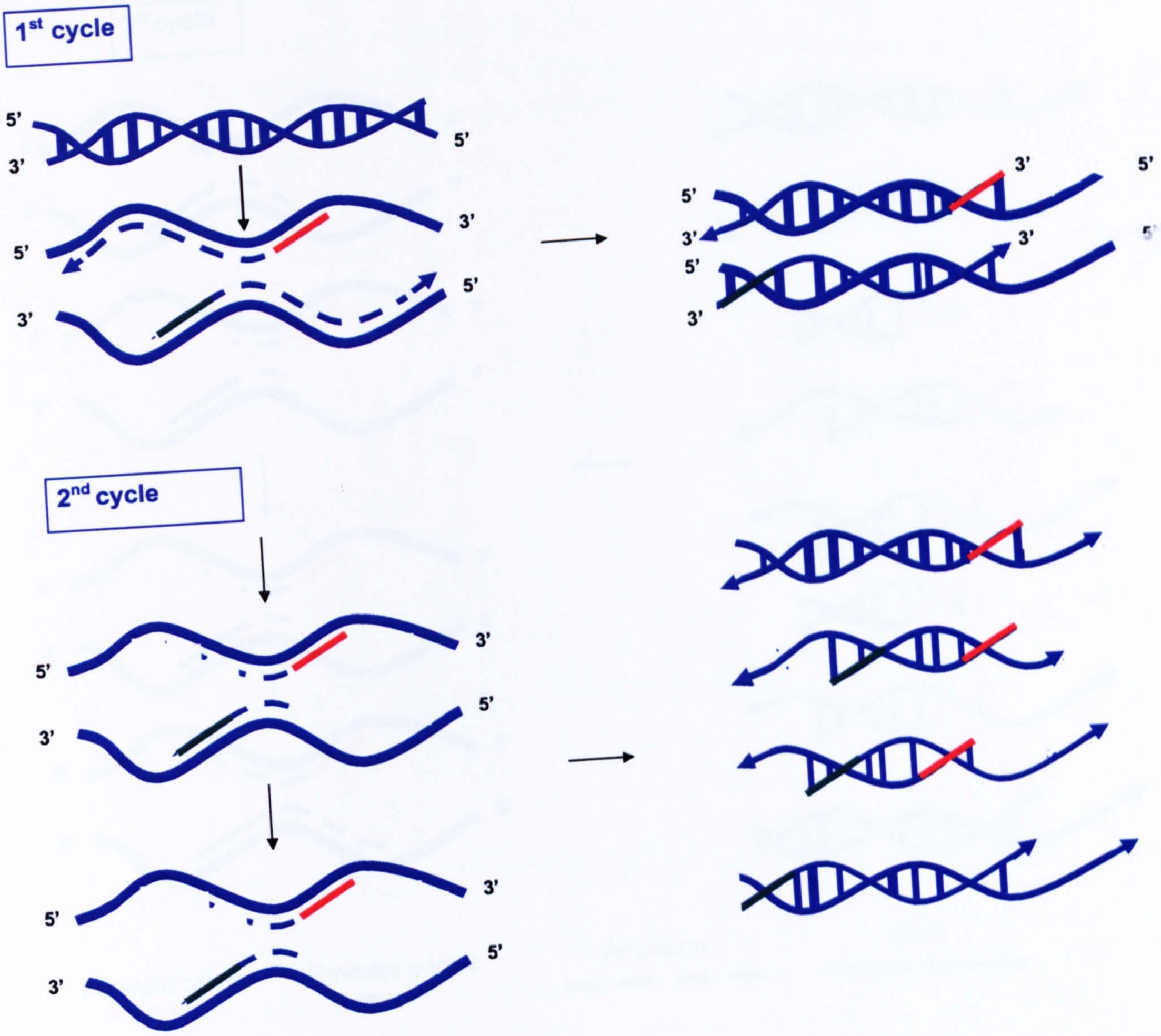
More recently Weng *et al.* [162] presented the detection of morphine by using a combination of a molecularly imprinted polymer (MIP) and electrochemical sensing techniques. In this study, a monomer (3,4-ethylenedioxythiophene) EDOT, was mixed with morphine molecules through an electropolymerization process on a

sensing electrode. This resulted in a modified MIP-PEDOT electrode which was then used for detecting morphine via an amperometric method. Using such an approach morphine concentration could be continuously detected with a LOD of 0.01 mM. In the same year Godber *et al.* [163] introduced a novel acoustic detection technology which was termed resonant acoustic profiling (RAP^{TM}). In this method, the principles of a quartz crystal microbalance are utilized. A high frequency voltage applied to a piezoelectric quartz crystal induces the crystal to oscillate with its resonant frequency being monitored in real time. Specifically, an antibody was immobilized on the sensor surface while the antigen was pumped over the sensor surface. A successful capture gave a response of 148 Hz whereas non-specific binding gave a response of 0.5 Hz. This system could be used to detect most classes of clinically relevant analytes in real-time without enzyme, fluorescent, isotopic or chemiluminescent labels. For further applications on detection on the microscale the reader is directed to the following reviews [164-166].

1.5 The Polymerase Chain Reaction

The Polymerase Chain Reaction (PCR) is an enzyme catalyzed reaction, used to amplify a specific fragment of DNA. It has profoundly transformed the practices and potential of molecular biology by vastly extending the capacity to identify and manipulate genetic material. The technique can be used to identify, disease-causing viruses and/or bacteria, the identity of a deceased person, or the identity of a suspect in a criminal investigation. PCR was conceived by Kary Mullis in 1983, and was presented for the first time in 1986 at the 51st Cold Harbour Laboratory Symposium on Quantitative Biology [167]. In 1993 Mullis was awarded the Nobel Prize for his invention. The polymerase chain reaction has been employed extensively in the medical and biological sciences and it has repeatedly resulted in complaints from the scientific community. Some argue that PCR has made DNA research "boring". Projects that formerly required some subtle deduction, clever manipulation, special insight, or good fortune are now within easy reach of anyone willing to assemble a few reagents and a thermal cycler, and follow a well-worn routine. Another complaint is a minor lament from professional molecular biologists who on seeing for the first time the simplicity of PCR openly regret that they failed to stumble on it themselves. Indeed, PCR has truly transformed molecular biology and has become an integral part of the DNA laboratory. PCR makes abundant what was once scarce- the genetic material required for experimentation. Not only is this material made abundant but it is no longer embedded in a living system. Cloning had made scarce genetic material abundant, but its obligatory use of living

organisms as the medium of reproduction was also its limitation [168]. PCR has taken a major step away from that dependency, since it has the capacity to amplify a target sequence from crude DNA preparations as well as from degraded DNA templates. The DNA in a sample does not need to be chemically pure to serve as a template. For example, in research applications (sperm lysates [169, 170]), for medical diagnostic applications (mouthwash or paraffin-embedded tissue samples [171-173]) and for forensics (individual hairs [174-176]). Consequently this step allowed flexibility of genetic intervention. The versatility of PCR has been astounding. In less than a decade PCR has become simultaneously a routine component of every molecular biology laboratory and a constantly improving tool whose growth potential has shown no signs of levelling off. In PCR strand synthesis happens exponentially by repetitive temperature cycling. Thermal cycling involves heating and cooling reagents between two or three specified temperatures. At high temperatures (between 90 and 95°C) double stranded DNA is denatured into two single strands. Primers, which are short single stranded molecules, are then annealed, to the individual strands at temperatures between 50 and 70 °C. This is followed by 'extension', at a slightly higher temperature (about 72°C), in which a complementary strand develops from each primer by the catalytic action of a DNA polymerase enzyme, in the presence of deoxynucleotide trisphosphates. Figure 1.20 shows a schematic of the first few cycles of a generic PCR. The first extension products result from DNA synthesis on the original template and do not have a distinct length as the DNA polymerase will continue to synthesize new DNA until it either stops or is interrupted by the start of the next cycle. The second cycle extension products are also of indeterminate length. The fragments of the target sequence synthesized after the third cycle are of defined length and correspond to the positions of the primers on the original template. From the fourth cycle onwards the target sequence is amplified exponentially.


1st cycle
5'
3'
5'
3'
5'
3'
5'
3'
5'
3'
2nd cycle
5'
3'
3'
5'
5'
3'
3'
5'

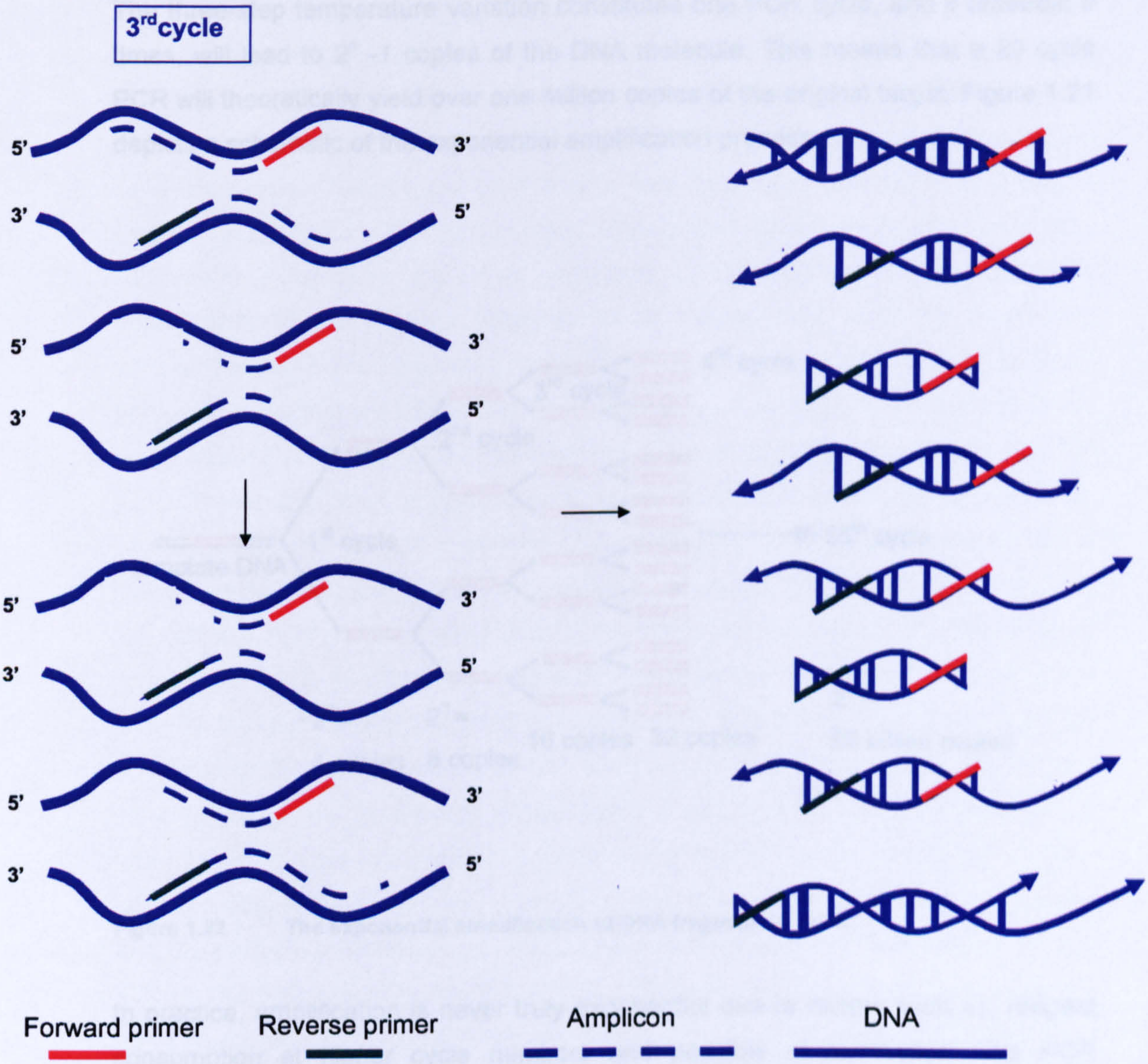


Figure 1.21 **Schematic of the PCR amplification process. During the first step of the polymerase chain reaction the double strand DNA template becomes two single strands. This step is performed between 94 °C and 96 °C to provide the energy necessary to break the hydrogen bonds between the two strands. The temperature is then lowered for the annealing step: the primers specifically bind to the DNA template. At this stage, the temperature is primer-dependant and usually varies between 50 °C and 65 °C. Finally the temperature is raised for the extension phase where the template is replicated by the polymerase enzyme. Interestingly, at the end of the 1st cycle, the product obtained is specific only at one end, as the replication lasts as long as the temperature allows it. It is only at the end of the 2nd cycle that a truly specific product is produced. Two types of replication occur at the same time: semi-specific products (e.g. from cycle 2) lead to linear replication, whereas truly specific products lead to exponential replication (see end of 3rd cycle).**

The three-step temperature variation constitutes one PCR cycle, and if repeated *n* times, will lead to $2^n - 1$ copies of the DNA molecule. This means that a 20 cycle PCR will theoretically yield over one million copies of the original target. Figure 1.21 depicts a schematic of the exponential amplification process.

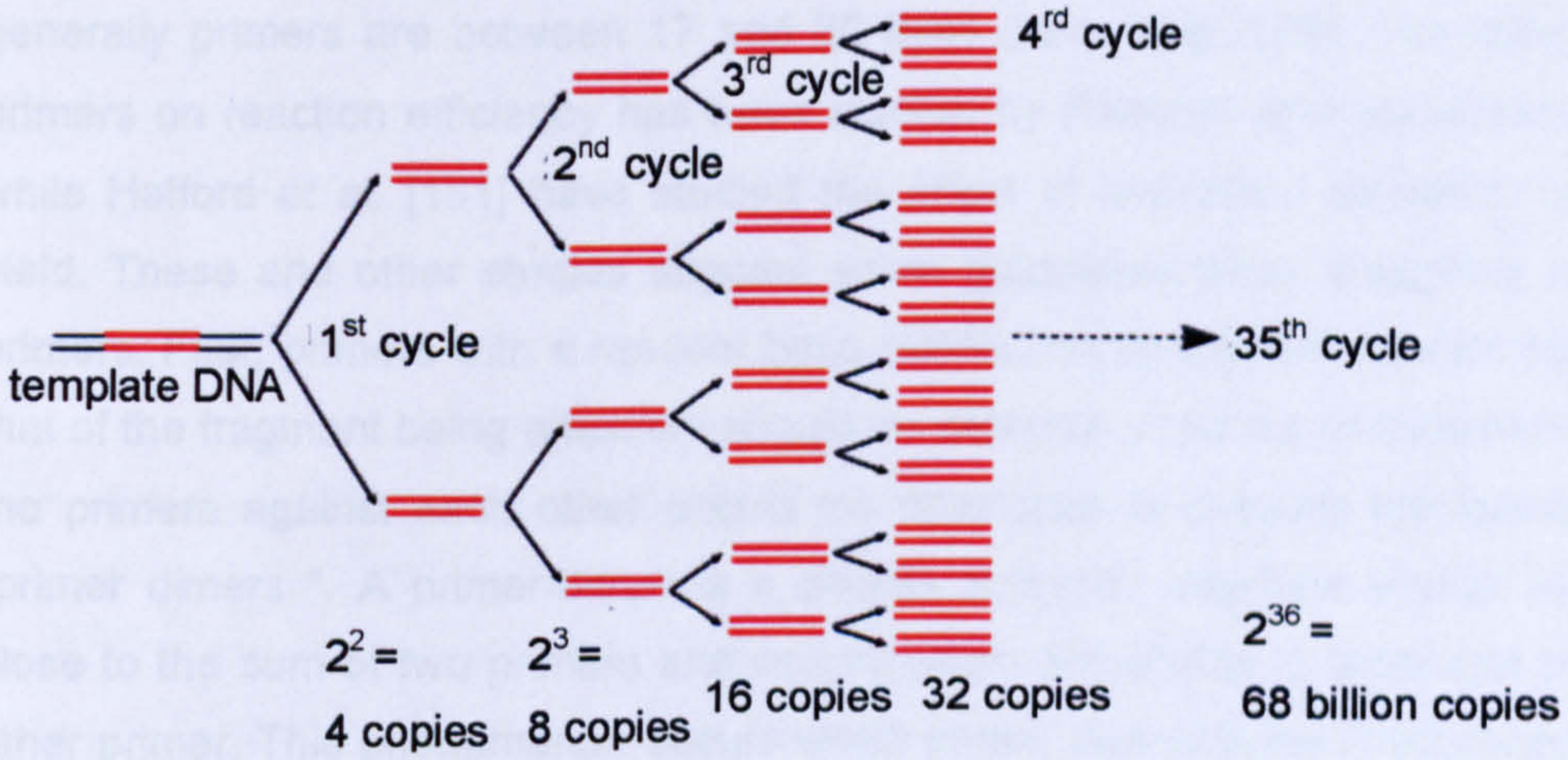


Figure 1.22 The exponential amplification of DNA fragment in PCR.

In practice, amplification is never truly exponential due to factors such as, reagent consumption at higher cycle numbers and possible contamination. The PCR reaction mixture consists of six main components whose concentrations influence the activity of other components. An important compound is the deoxyribonucleic acid (DNA) template which is the DNA sample to be amplified. DNA is constructed from four simple monomeric subunits (Adenine (A), Cytosine (C), Guanine (G) and Thymine (T)), the deoxyribonulceotides which are arranged in a precise linear sequence. These monomeric subunits or bases are classified into two types, Adenine and Guanine are five and six membered heterocyclic compounds called purines, while Cytosine and Thymine are six membered rings called pyrimidines. Two of these linear polymeric strands twist about each other to form the DNA double helix, in which each base in one strand pairs specifically with a complementary base in the opposite strand. Specifically, Adenine always pairs with Thymine and Cytosine always pairs with Guanine. It has to be mentioned that the A-

T bond consists of two hydrogen bonds whereas the C-G bond consists of three hydrogen bonds. This means that the bond between C and G is more stable than that between A and T [177]. A second component is the set of primers, which are short single stranded DNA molecules complementary to the termini of a defined DNA sequence. The specificity of the primer sequence ensures that only the targeted sequence will be amplified. Although longer primers are more specific than short ones [178], they are more expensive to synthesise and more prone to degradation. A compromise between these requirements must be found and generally primers are between 17 and 30 base pairs long [179]. The influence of primers on reaction efficiency has been studied by Resuehr and co-workers [180], while Halford *et al.* [181] have studied the effect of bi-product formation on PCR yield. These and other studies suggest some guidelines when designing a set of primers. First, primers with a random base distribution and a G-C content similar to that of the fragment being amplified should be selected. Also the complementarity of the primers against each other should be minimized to prevent the formation of "primer dimers ". A primer-dimer is a double stranded fragment whose length is close to the sum of two primers and occurs when one primer is extended over the other primer. This phenomenon occurs when primer and enzyme (Taq polymerase) concentrations are in excess. A final aspect which must be considered is the temperature required for melting and annealing primers. The melting temperature (T_m) of a chain of nucleic acids is the temperature at which 50% of the nucleotides and the perfect complement are hybridized, and the annealing temperature (T_{anneal}) defines the temperature when the primer hybridizes with the target. Annealing is a bimolecular process, but there are competing processes in which both intra-strand and inter-strand base pairs can form, ultimately leading to a stable duplex. These two temperatures should not differ by more than 5°C. Depending on the size of the primers the melting temperature and annealing temperature (in °C) can be calculated as follows:

$$T_m = (A+T)2° + (C+G)4° \qquad (\leq 20bp) \quad (1.5)$$

$$T_m = 1000\frac{\Delta H}{[B + \Delta S + R\ln(c/4)]} - 273.5 + 16.6\log(M) \qquad (20bp \leq x \leq 50bp) \quad (1.6)$$

$$T_m = 81.5 + 16.6\log(M) + 0.41[XG + XC] - 0.65F - 500/L \qquad (\geq 50bp) \quad (1.7)$$

Here T_m is the melting temperature [°C], ΔH is the sum of the nearest neighbour enthalpy changes [kcal/mol], B is a constant containing corrections for the helix shape, ΔS is the sum of the nearest neighbour entropy changes [kcal/mol], R is a gas constant [1.987Joule/ mol Kelvin], M is the molar concentration of monovalent cations, c is the oligonucleotide concentration, XC and XG are mole fractions of C and G, F is the molar concentration of formamide and L is the length of the oligonucleotide.

$$T_{anneal} = T_m^{primer} - 4°C \quad (1.8)$$

$$T_{anneal} = 0.3T_m^{primer} + 0.7T_m^{product} - 14.9 \quad (1.9)$$

The annealing temperature of the primer to the template can be calculated using either equation (8) or (9) where T_m ^{primer} is the melting temperature of the primer and T_m ^{product} is the melting temperature of the product. To ensure that primer - product annealing is favoured with respect to product-product hybridization, T_m ^{product} – T_{anneal} should be greater than 30 °C. The annealing temperature alters the specificity and the yield of the PCR reaction. If T_{anneal} is too low, the primers will not hybridize specifically and if T_{anneal} is too high, primers will fail to anneal.

Perhaps the most important component within the PCR is the enzymatic catalyst. In 1987 the Klenow fragment of E. coli DNA polymerase I was used in the first PCR performed by Kary Mullis [182]. DNA polymerase I was one of the three enzymes found in E. coli. The initial PCR method based on DNA synthesis by the Klenow enzyme at 37°C was not highly specific as mismatched primers were stable at this temperature, and thus could be extended, resulting in non-specific amplification products. Another major disadvantage associated with this enzyme was its inactivation at the high temperatures required to separate the two DNA strands at the end of each PCR cycle. Consequently, fresh enzyme had to be added during every cycle. The introduction of a thermostable DNA polymerase (Taq polymerase) isolated from Thermus Aquaticus [183] transformed PCR into a robust reaction which could be automated. With an optimum temperature between 75-80°C the use of higher temperatures for primer annealing and extension was enabled, which drastically reduced the extension of primers that were mismatched with the template, and significantly increased the specificity and the overall yield of the

reaction. Although Taq DNA polymerase has a limited ability to synthesize DNA above 90°C, the enzyme is relatively stable and is not denatured irreversibly by exposure to such high temperatures. In a PCR mix, Taq DNA polymerase retains about 50% of its initial activity after 130 minutes at 92.5°C, 40 minutes at 95 °C and 5 - 6 minutes at 97.5 °C [179]. Subsequently, the enzyme processivity (defined as the number of nucleotides added per unit time to a strand during one sequence of binding and disassociation from the primer template) and the fidelity [184] (capability of an enzyme to faithfully replicate a DNA strand without expansion, substitution or deletion in the number of base pairs) of *Taq* polymerase were enhanced [185]. While Taq polymerase amplifies up to 10kb, the Klenow fragment of E. coli DNA polymerase I only amplified up to 400 bp. It has to be noted that many more enzymes have been used in PCR. These include Thermococcus litoralis DNA polymerase [186], Pyrococcus furiosus DNA polymerase [187], Pfu [188], Klen Taq [189], Vent [186] or Tfi [190] polymerases. Other key components are the deoxynucleotide triphosphates (dNTP's). They are subunits of DNA and consist of four different molecules dATP, dCTP, dGTP and dTTP. During PCR, dNTP's are added to the extending strand according to the pairing rule mentioned above. The PCR buffer is critical in maintaining the correct pH and charge distribution. Furthermore, the concentration of magnesium ions has a profound effect on the specificity and yield of amplification [179]. For example dNTP's bind free Mg^{2+}. Consequently, if the dNTP concentration is changed significantly, a concomitant change in Mg^{2+} concentration is necessary. Moreover, magnesium ions are crucial components of a PCR as they are enzymatic co-factors [191]. Their concentration has an important influence on the shape, the charge distribution and the binding properties of the Taq polymerase. Generally, an excess of Mg^{2+} results in the accumulation of non-specific amplification products whereas insufficient Mg^{2+} will reduce reaction yield [192]. Although the effect of magnesium ions is difficult to assess, an optimal concentration has to be determined for any PCR system.

As discussed, the individual components of the PCR reaction need to be optimised. Nevertheless, nowadays protocols to optimise PCR reactions are readily available [193, 194]. PCR is conventionally performed on large thermocyclers which rely on Peltier effect thermoelectric heating. These, solid-state devices convert electrical energy into a temperature gradient. The first thermocycler was originally manufactured by Perkin-Elmer. Today numerous companies such as Applied Biosystems, Techne, Hybaid, MJ Research, and Cepheid provide commercial instruments. The basic requirements for an efficient thermocycler are: (i) fast

heating and cooling rates, (ii) accurate temperature control, (iii) programmability and (iv) high throughput operation. Although displaying reliable and efficient performances, conventional thermocyclers present some significant drawbacks. Even though, efforts have been made to render them more compact, they are still bulky and heavy, which results in low mass and heat transfer rates. It should be noted that PCR can also be performed in a isothermal manner [195-199]. The lack of thermocycling is an advantage compared to conventional PCR, however operation at relatively low temperatures (37°C) compromises reaction specificity and the need for high enzyme concentrations dramatically increases the cost of the reaction. In the current studies PCR will be performed in a microfluidic device. The following section provides an overview of existing studies of PCR on the mircoscale.

1.6 Polymerase Chain Reaction on the Microscale

Figure 1.23 shows a timeline of significant technological developments of PCR instrumentation over the last 20 years.

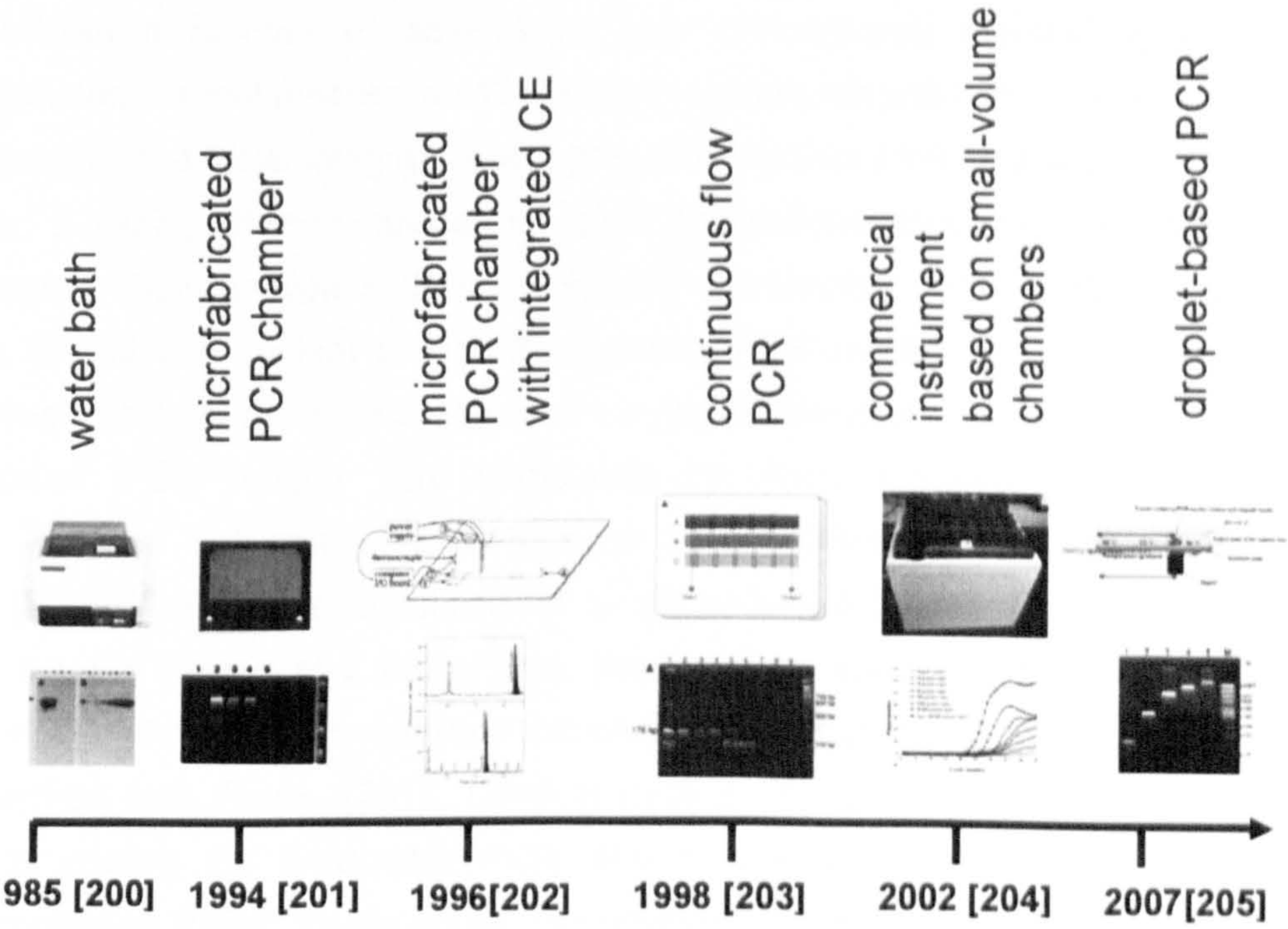


Figure 1.23 **Saiki *et al.* [200] presented first PCR by using a chamber and a water bath. Wilding *et al.* [201] performed the first PCR in a chamber. Woolley *et al.* [202] demonstrated the first chamber PCR with integrated separation and online detection. Kopp *et al* [203] presented the first continuous-flow PCR. Belanger *et al.*[204] introduced the first PCR on the fastest commercial thermal cycler. Ohashi *et al.* [205] presented droplet based- PCR.**

1.6.1 Microfluidic Thermocyclers

To achieve efficient amplification, heat must be transferred into and dissipated out of the reactor in an efficient and rapid manner. Conventional thermocyclers are disadvantageous in this respect. Almost all of them possess large thermal masses which result in slow heating and cooling rates. Moreover, temperature differentials across reaction vessels (used to contain the sample) as high as 20 °C have been reported [168]. This heterogeneity in temperature results in a loss of specificity, non-ideal strand extension and reduced annealing efficiencies. A number of approaches have been proposed to overcome the problems of cycling speed and temperature homogeneity. Rapid PCR cycling has been reported in systems using small capillary tubes as reactor vessels where low thermal capacitances allow fast thermal equilibrium. Swerdlow *et al.* [206] showed amplification of a 303 bp target at a speed of 20 s/cycle. Furthermore, Oda *et al.* [207] demonstrated infrared-mediated thermocycling at a speed of 17 s/cycle.

Subsequently, attention focused on developing microfabricated PCR devices. Such systems offered a number of advantages over conventional thermal cyclers including reduced thermal masses, small reaction volumes, ultra-fast reaction times, facile automation and facile integration with post-amplification product analysis. Not surprisingly, a variety of microdevices for such applications were demonstrated. These included chamber-type PCR chips (where a stationary PCR mixture was repeatedly heated and cooled) and continuous-flow PCR (where PCR sample is moved through spatially separated regions of varying temperature). In 1993 the first microfabricated PCR reactor was introduced by Allen Northrup (Lawrence Livermore National Laboratory) and Richard White (University of California, Berkeley) [208]. The device consisted of a silicon-based microreactor with a polysilicon thin-film heater. At a similar time, Peter Wilding and Larry Kricka at the University of Pennsylvania demonstrated microfabricated silicon chambers (5 -10 µl volume) capped with Pyrex. [201]. Thermal cycling of the PCR reagents was achieved by placing the disposable PCR chip in a small holder containing a computer-controlled Peltier heater-cooler. Amplification equivalent to conventional thermal cyclers was obtained and products were externally analyzed on an agarose gel. However a breakthrough was accomplished by introducing integrated systems. In collaboration with researchers at the Lawrence Livermore National Laboratory, Richard Mathies group at the University of California, Berkeley first presented the integration of ultra-fast PCR and DNA sizing on a single microdevice in 1996 [202]. Figure 1.24 depicts the set-up. This device enabled rapid thermal cycling with

heating rates of 10 °C/s and cooling rates of 2.5 °C/s. This is in the same range as the fastest current conventional system. Using such an approach high speed separation of amplified products was demonstrated in less than 120 s. The PCR chamber and the separation channel were directly linked through a photolithographically fabricated channel filled with a hydroxyeythlycellulose sieving matrix. Complete amplification and separation of products was achieved within 20 minutes.

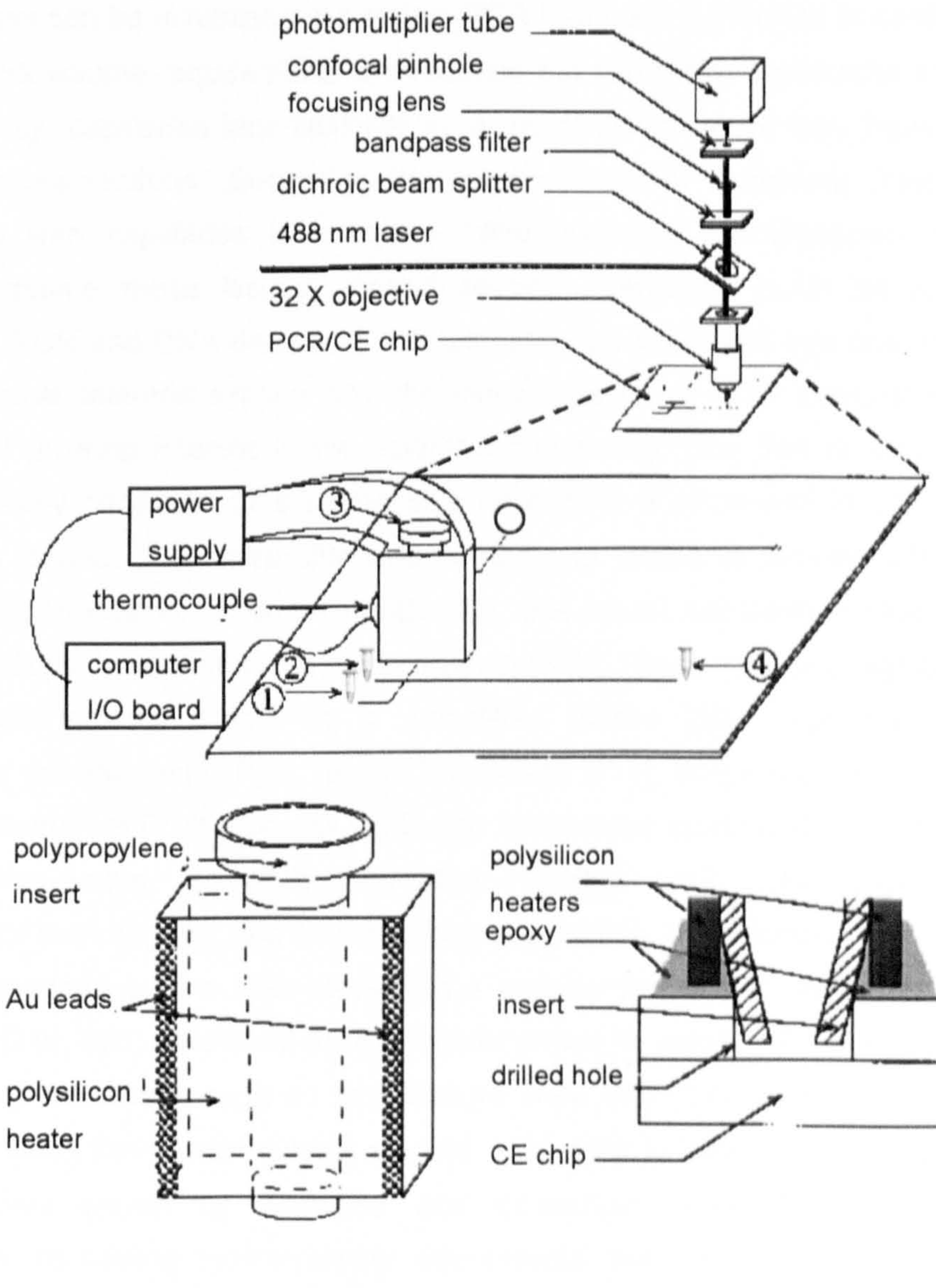


Figure 1.24 **Schematic of the integrated PCR – capillary electrophoresis microdevice. (A) Laser excitation source, detection and PCR-CE chip. (B) PCR chamber (C) Cross section of junction between PCR and CE [202].**

In 1998 Northrup and co-workers presented a Miniature Analytical Thermal Cycling Instrument (MATCI) [209] for amplification and detection of DNA. A number of other research groups have also demonstrated microfluidic devices for PCR. Even though PCR has had a tremendous impact in clinical diagnostics, medical sciences and forensics, the technique presents several problems. For example, the costs associated with each reaction are still high (primarily due to the cost of the enzyme) and PCR is also highly prone to contamination due to its efficiency and high sensitivity [210]. By employing closed miniaturized systems both these disadvantages can be minimised. As stated, PCR has been performed in capillaries where sample volume requirements are reduced but two major drawbacks are still present. Firstly, capillaries lack flexibility in terms of design since they have fixed cylindrical cross-sections. Secondly, the incorporation of additional integrated components with capillaries is complex. Lithographically manufactured micro-devices overcome these issues. Indeed several operations (such as sample preparation, PCR and DNA detection) can ultimately be integrated into one device. These attractive features explain why the miniaturization of PCR instrumentation has been of growing interest in the scientific community. The first on-chip PCR devices typically consisted of a silicon chip containing a micro-well in which the sample was loaded. The entire chip was heated and cooled to provide adequate thermocycling conditions. Since its introduction, this model has been replicated by numerous groups, sometimes with major amendments. These include integration of electrophoretic product sizing on a monolithic device [202], optimization of conditions to provide faster PCR (under 7 minutes) [211], single copy PCR [212], real-time detection of PCR products [213] and multiplexed systems [214, 215]. The use of micro-arrays [214-216] and drop-metering [217] has engendered improvements in throughput and fluid-handling capabilities. For example, Leamon *et al.* [218] introduced a *Pico Titer Plate* with a well density of 480 wells/mm^2, and Nagai *et al.* [219, 220] developed microchamber arrays for picoliter PCR. In addition thermocycling conditions, such as temperature uniformity [221] and heat transfer optimisation [222] have been closely studied. Versatility in terms of thermocycling conditions was shown by Kajiyama and co-workers when they presented microdevices containing independently addressable wells [223]. These silicon-based chips containing discrete temperature-controlled islands were developed for use in DNA microarray hybridization studies. Such an approach allowed investigation of optimal temperatures. In addition, a variety of modifications on this theme have been demonstrated, such as ligase chain reaction [224] and isothermal nucleic acid amplification [225]. Interestingly, there have been few devices based on

a well approach that differed significantly from the original design presented by Northrup. For example, Oda *et al.* [207] addressed the invasive characteristics of conventional heating elements by introducing a transparent contact-free heating technique based on infra-red-radiation as shown in Figure 1.25.

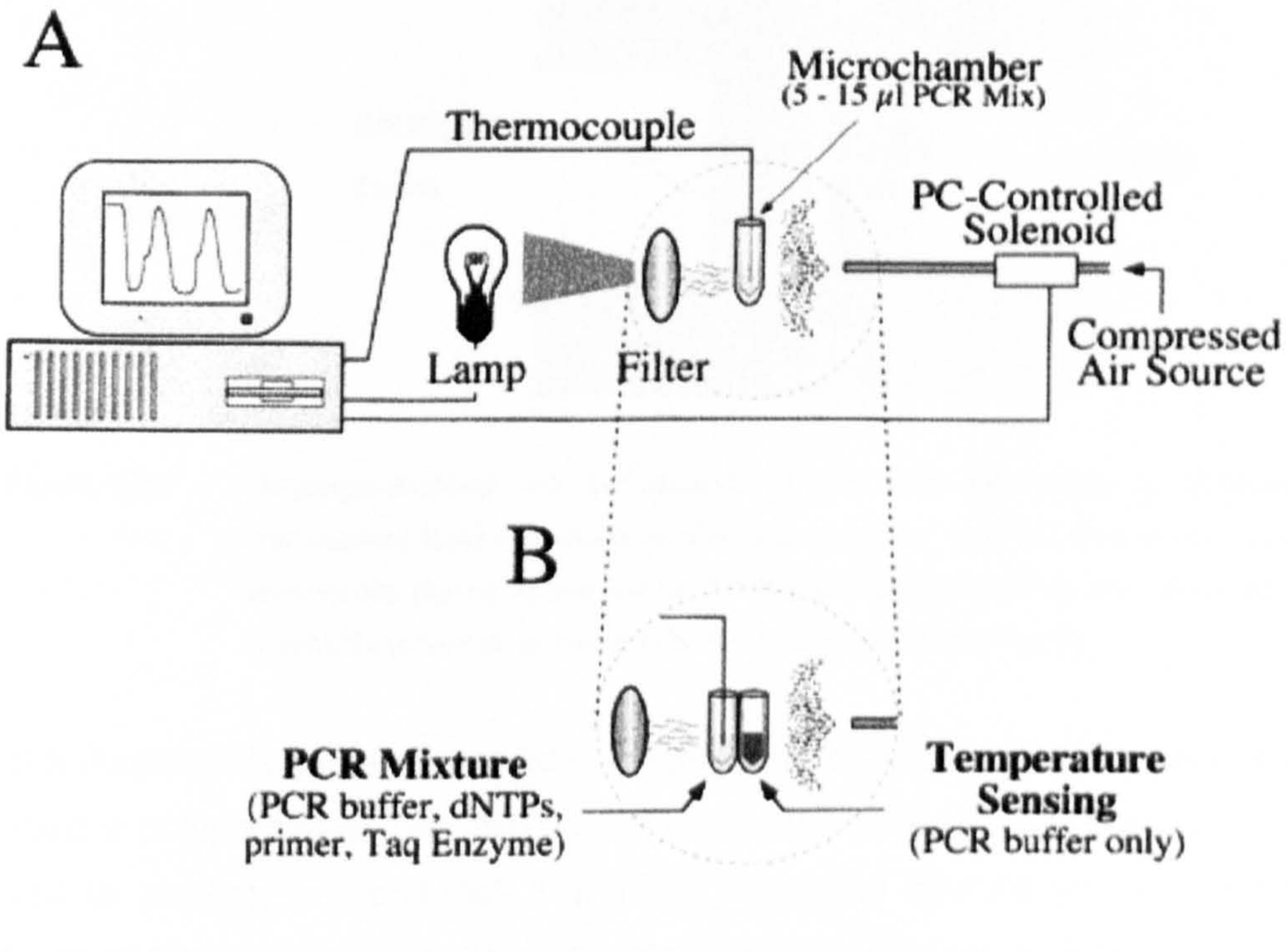


Figure 1.25 **Set-up for infrared-mediated thermocycling. (A) Single-microchamber configuration. (B) Dual-microchamber configuration where one chamber acts solely for temperature sensing while the other is used for PCR [207].**

Pal and co-workers also performed PCR using induction heating [226]. In these studies, chips were mounted onto a ferrous ring, while the inductor was made of a copper wire wound around a ferrite core. By alternating the current going through the inductor, magnetic fields were produced. Induced Eddy currents in the ferrous ring then generated localised heat without any physical contact. In 2003, Krishnan *et al.* presented an original device relying on convection to provide thermocycling conditions [227]. Two heaters sandwiched a Rayleigh-Bénard cell (Figure 1.25) and were maintained at constant temperatures, namely 97°C at the bottom and 61°C at the top. Due to the difference in temperature, a convective flow developed in the cell, with an upward flux at the centre and downward fluxes at the sides. As the sample moved up and down in the cell, thermal cycling was accomplished and DNA was successfully amplified.

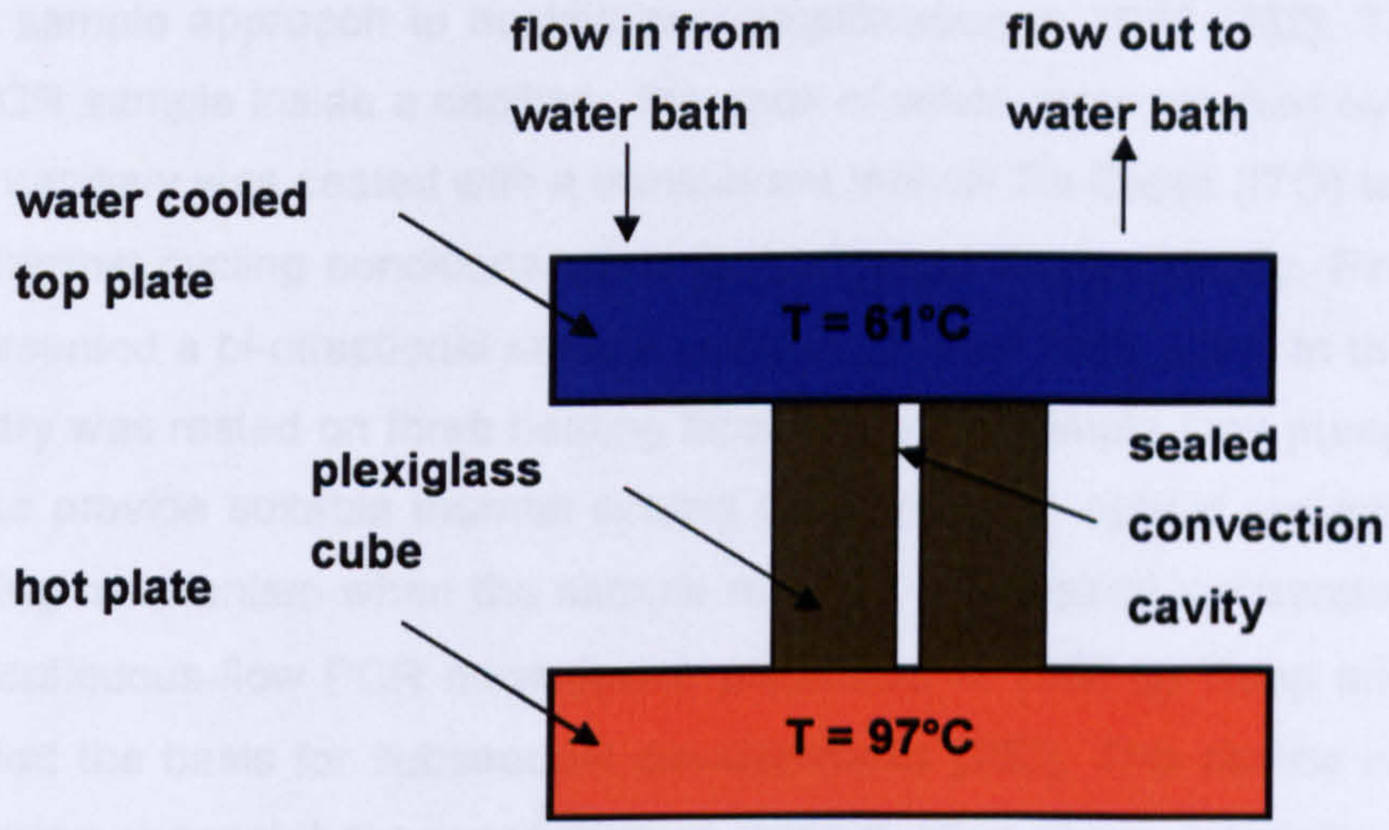


Figure 1.26 **Rayleigh-Bénard cell schematic. Due to the difference in temperature, a convective flow develops in the cell, with an upward flux in the centre and downward fluxes at the sides. As the sample moves up and down in the cell, thermal cycling is accomplished and DNA amplified [227].**

The Rayleigh-Bénard cell was later modified by Wheeler and co-workers [228] who used a polypropylene bag that was sandwiched between two boards forcing the fluid to conform to a channel. It is noted that these devices are less restricted in terms of design than capillaries, since the well geometry can be tailored to a specific application and arrays of wells are easily manufactured. The main advantage of dynamic-moving-sample approaches are the enhanced heat transport. In the case of continuous-flow systems, temperature transition times depend only on the sample pumping rate and the time the sample needs to reach temperature equilibrium. Moreover, heat inertia is reduced to a minimum because only the thermal mass of the sample needs to be considered (rather than the substrate plus sample as in the case of microwell PCR). This yields enhanced rates of heating and cooling. The first example of continuous flow-through amplification was demonstrated in 1994 by Nakano and co-workers on a capillary-based system. Their concept comprised a capillary transversing three different oil baths in a loop structure [229]. The length of capillary in each bath determined the duration of the annealing, extension and denaturation steps. The sample was continuously pumped through the capillary unidirectionally with DNA amplification occurring as the sample was moved through each temperature cycle. Based on a comparable concept, Curcio and co-workers performed high-throughput DNA analysis in a Teflon tube by separating different sample plugs with immiscible organic plugs [230]. A similar experiment was

performed in a capillary by Park *et al.* [231]. Friedman and co-workers proposed a static sample approach to nucleic acid amplification in 1998 [232]. They enclosed the PCR sample inside a capillary, the ends of which were blocked by rubber pads. Each capillary was coated with a transparent Indium Tin Oxide (ITO) layer, ensuring that thermal cycling conditions could be controlled independently. Finally Chiou *et al.* presented a bi-directional sample pumping system [233, 234]. In this device, the capillary was rested on three heating blocks and the sample then pumped back and forth to provide suitable thermal cycling conditions. An optical system stopped the pumping mechanism when the sample reached the desired temperature zone. The first continuous-flow PCR microdevice presented in 1998 by Kopp and co-workers provided the basis for subsequent developments [203]. This device consisted of a serpentine channel that passed through three heating zones maintained at constant temperature by copper blocks (Figure 1.27). Remarkably, specifically amplified products were detected in 1.5 minutes only after 20 cycles.

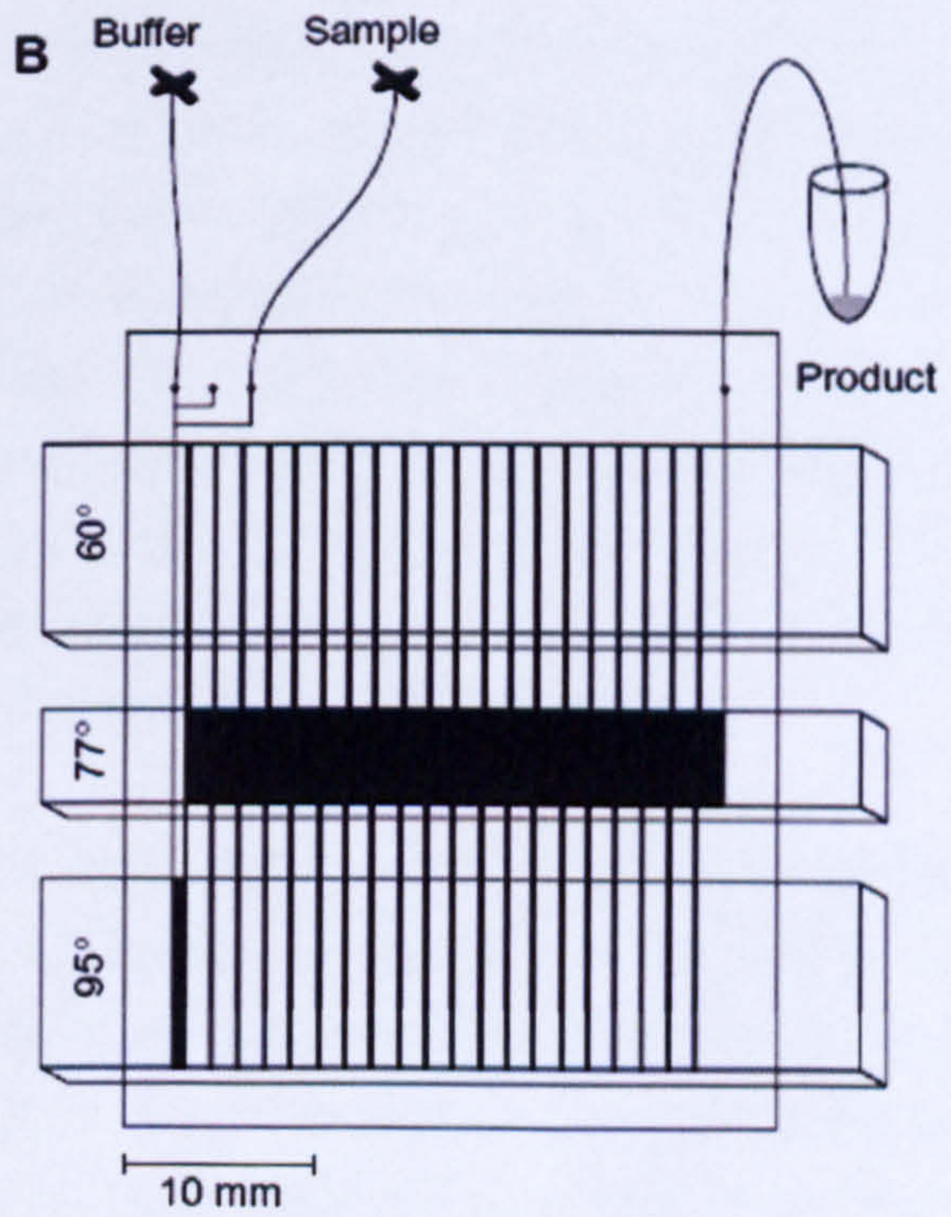


Figure 1.27 **A continuous flow PCR device with two inlets and one outlet. The sample is pumped through different temperature zones for denaturation, annealing and extension [203] .**

1.6.2 Problems with Microfluidic PCR Instrumentation

One of the main concerns when performing PCR on-chip is a loss in efficiency. Although this problem can often be traced to inhibitory materials used during micro-device fabrication e.g. residual chromium from chrome masks in glass chip fabrication [235] or thermocouples [207], the predominant problem encountered is the adsorption of PCR components onto the channel surfaces due to the increased surface-to-volume ratio. Erill and co-workers reported that the Taq polymerase enzyme [236] was most prone to adsorption. Although surface coating strategies such as silanization are possible, their effectiveness is sometimes questionable due to a lack of reproducibility [237]. Another method for preventing adsorption is to use dynamic passivation techniques. These include addition of passivating reagents directly in the PCR mixture. The most common additives are polymers such as polyethylene glycol (PEG) and polyvinlypyrolidone (PVP), or proteins such as bovine serum albumin (BSA). Lout *et al.* [238] showed that dynamic coating with PEG and PVP increased microscale PCR efficiency. Erill *et al.* [236] demonstrated that the net effect of polymerase adsorption can be counteracted by the addition of a titrated amount of competing BSA. Robinson *et al.* [239] studied the influence of the molecular weight of PVP on coating efficiency, as well as the effect of analytes in solution on BSA adsorption. Interestingly, Cui and co-workers investigated the effect of single-walled carbon nanotubes (SWCNT) on PCR yields [240]. Results showed that the addition of single walled carbon nanotubes into the reaction medium increased the amount of PCR product at concentrations below 3 μg/μL, but this effect was reversed at higher SWCNT concentrations. Finally, Yoon and co-workers examined the influence of pH on bio-molecule adsorption [241] in an electrowetting-based microdevice.

In the work presented in this thesis a number of different surface treatments and their effect on PCR efficiency are studied. A combination of silanization and dynamic passivation will be shown to generate successful results. These studies are presented in Chapter 5. The introduction of superhydrophobic materials onto microchannel surfaces is also investigated in Chapter 6. Another crucial aspect of the work described is the accurate determination and control of temperature within microchannels. When performing PCR, the ability to accurately control system temperatures is especially important since both primer annealing to single-stranded DNA and the catalytic extension of this primer to form the complementary strand only proceeds in an efficient manner within relatively narrow temperature ranges

[222]. It is therefore essential to accurately monitor temperature distributions in microfluidic channels. Accurate and spatially-resolved temperature measurements in microfluidic devices are typically achieved through the use of external or integrated thermocouples [242]. However, externally mounted thermocouples are unable to accurately monitor temperature variations within the fluidic system, and only provide an estimate of the temperature of exterior chip surfaces. Furthermore, the thermocouples used in such measurements can themselves produce inordinately large heat losses whilst offering relatively low spatial resolution. Methods for integrating thermocouple contacts within microfluidic chip-based systems to allow direct measurement of fluidic temperatures have been reported and address some of these problems but at the expense of increased fabrication complexity and limited operational lifetimes [243]. This can be seen in Figure 1.28.

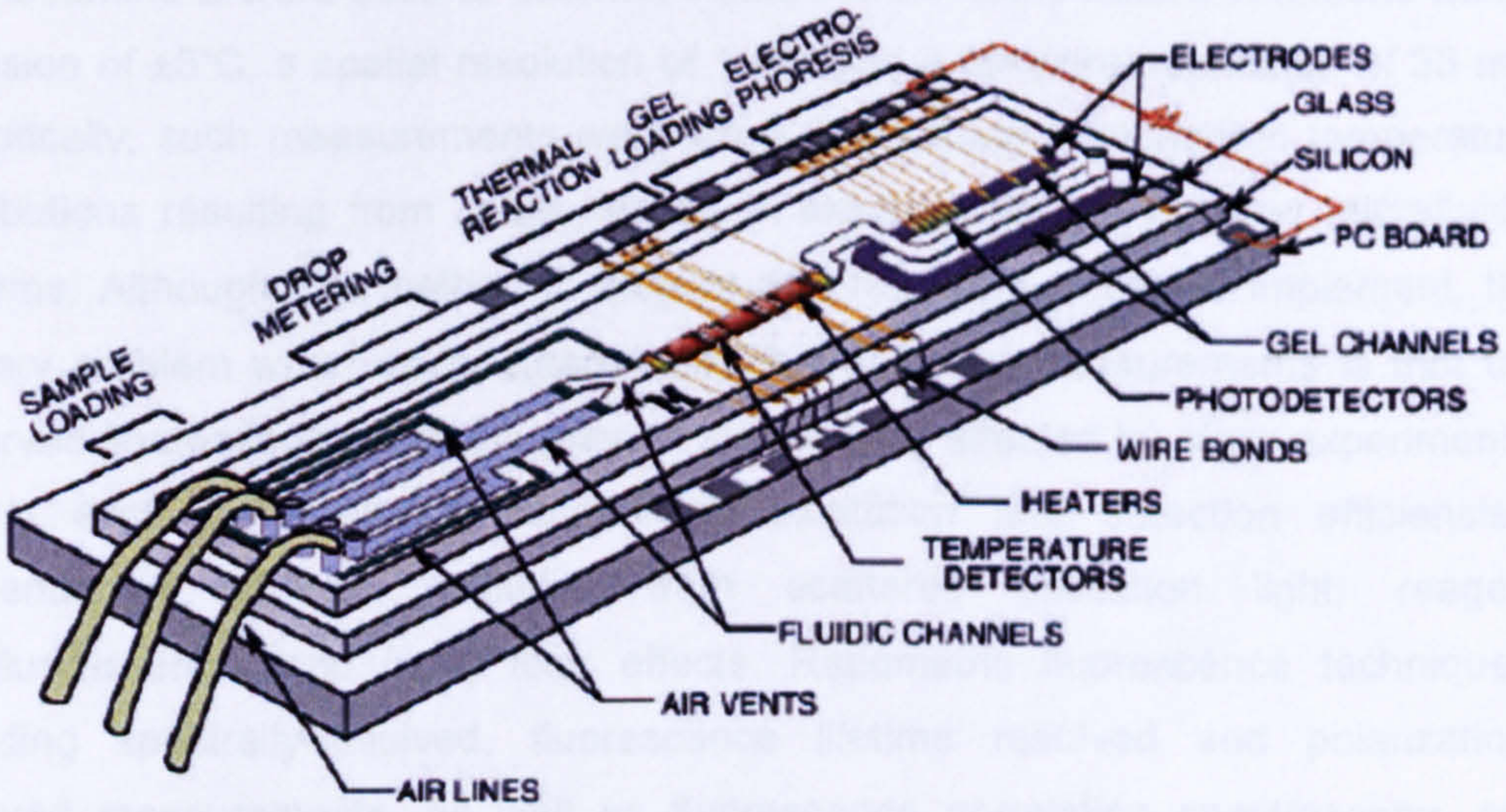


Figure 1.28 Schematic of integrated device. The only electronic component not fabricated on the silicon device is the excitation source [217].

In recent years, a number of spectroscopic techniques have been applied to temperature measurement within microfluidic environments. Such approaches are advantageous because they are non-invasive, can directly measure fluidic temperatures, and potentially offer high spatial and temporal resolution. For example, Chaudhari *et al.* reported optical measurements of temperature uniformity in a microfabricated reactor array using encapsulated liquid crystals suspended in the contained liquid medium. Thermochromic liquid crystals (TLC's) exhibit a wavelength dependent reflectivity that is strongly sensitive to temperature, within a range defined by their chemical composition. This allows local temperature

quantification to within 0.1°C through hue measurement [244]. One drawback, however, is that these crystals are comparatively large and can alter fluid flow characteristics. Morris and co-workers have utilized Raman spectroscopy to map both axial and radial temperature gradients in operating electrophoresis capillaries [245]. Intra-capillary temperature variations could be measured through the temperature-sensitive OH stretching envelope of the water Raman spectrum which is strong and free from spectral interferences. Such an approach affords a precision in temperature measurement of ±1°C and a spatial resolution of 1 to 5 μm, but is limited to single point measurements and acquisition times are lengthy [246, 247]. Steady-state fluorescence-based spatial and temporal mapping of microfluidic temperature has been demonstrated by Ross *et al*. [248]. This approach exploits the temperature dependence of the fluorescence quantum efficiency of many molecular dyes. In these reported studies, changes in the fluorescence intensity of a solution of Rhodamine B were used to determine intrachannel temperature variations with a precision of ±3°C, a spatial resolution of 1 μm and a temporal resolution of 33 ms. Specifically, such measurements were used to estimate intrachannel temperature distributions resulting from Joule heating in electrokinetically pumped microfluidic systems. Although this method is elegant and relatively simple to implement, the primary problem when using steady-state fluorescence measurements is that the observed fluorescence intensity may be significantly affected by other experimental factors such as a spatial variation of excitation and detection efficiencies, concentration artifacts, pollution from scattered excitation light, reagent autofluorescence, and inner filter effects. Ratiometric fluorescence techniques, including spectrally-resolved, fluorescence lifetime resolved and polarization-resolved measurements, as well as fluorescence correlation spectroscopy, can address these issues by providing a read-out signal that is independent of intensity, fluorophore concentration and photon path length [249]. Fluorescence lifetime sensing is most interesting for this application since the fluorescence lifetime is dependent on the non-radiative decay rate coefficient, which in turn varies with environmental parameters such as temperature, viscosity and pH [250]. The method of fluorescence lifetime imaging will be applied to temperature sensing in order to measure spatially localised temperature in microfluidic channels, and is presented in Chapter 4.

BIBL. LONDON UNIV.

1. Kamholz, A.E., *Proliferation of microfluidics in literature and intellectual property.* Lab on a chip, 2004. **4**: p. 16N-20N.
2. Abramowitz, S., *Towards inexpensive DNA diagnostics.* Trends in biotechnology, 1996. **14**(10): p. 397-401.
3. Tolfree, D.W.L., *Microfabrication using synchrotron radiation.* Reports on Progress in Physics, 1998. **61**(4): p. 313-351.
4. Colyer, C.L., Mangru, S.D., and Harrison, D.J., *Microchip-based capillary electrophoresis of human serum proteins.* Journal of Chromatography A, 1997. **781**(1-2): p. 271-276.
5. Mathies, R.A., Simpson, P.C., and Woolley, A.T. *DNA Analysis with Capillary Array Electrophoresis Microplates.* in *MicroTAS*. 1998. Banff, Canada: Springer
6. Renaud, P., Van Lintel, H., Heuschkel, M., and Guerin, L. *Photo-Polymer Microchannel Technologies and Applications.* in *MicroTAS*. 1998. Banff, Canada: Spriner.
7. Foret, F., Liu, H., Zhang, B., Felten, C., and Karger, B.L. *Microdevices for Electrospray Mass Spectrometry.* in *MicroTAS*. 1998. Banff, Canada: Springer.
8. Terry, S.C., Jerman, J.H., and Angell, J.B., *A gas chromatographic air analyzer fabricated on a silicon wafer.* I.E.E.E. Transactions on electron devices, 1979. **26**(12): p. 1880-1886.
9. Manz, A., Miyahara, Y., Miura, J., Watanabe, K., Miyagi, H., and Sato, H., *Design of an open-tubular column liquid chromatograph using silicon chip technology.* Sensor and Actuators B, 1990. **1**(1-6): p. 249-255.
10. Manz, A. and Simon, W., *Potentiometric Detector for Fast High-performance Open-tubular Column Liquid Chromatography.* Analytical Chemistry, 1987. **59**: p. 74-79.
11. Manz, A. and Simon, W., *Injectors for open-tubular column liquid chromatography with 106 theoretical plates at retention times in the minute range.* Journal of Chromatography A, 1987. **387**: p. 187-196.
12. Manz, A., Graber, N., and Widmer, H.M., *Miniaturized Total Chemical-Analysis Systems - a Novel Concept for Chemical Sensing.* Sensors and Actuators B, 1990. **1**(1-6): p. 244-248.
13. Effenhauser, C.S. and Manz, A., *Miniaturizing a Whole Analytical Laboratory Down to Chip Size.* American Laboratory, 1994. **26**(14): p. 15-&.
14. Thormann, W., Wey, A., Lurie, I.S., Gerber, H., Byland, C., Malik , N., Hochmeister, M., and Gehrig, C., *Capillary electrophoresis in clinical and forensic analysis: Recent advances and breakthrough to routine applications.* 1999. p. 3203-3236.
15. Edelstein, R.L., Tamanaha, C.R., Sheehan, P.E., Miller, M.M., Baselt, D.R., Whitman, L.J., and Colton, R.J., *The BARC biosensor applied to the detection of biological warfare agents.* Biosensors and Bioelectronics, 2000. **14**(10-11): p. 805-813.

16. Lv, Y., Zhang, Z., and Chen, F., *Chemiluminescence biosensor chip based on a microreactor using carrier air flow for determination of uric acid in human serum.* The Analyst, 2002. **127**(9): p. 1176-1179.
17. Gawron, A.J., Martin, R.S., and Lunte, S.M., *Microchip electrophoretic separation systems for biomedical and pharmaceutical analysis.* European Journal of Pharmaceutical Science, 2001. **14**(1): p. 1-12.
18. Prest, J.E., Baldock, S.J., Fielden, P.R., Goddard, N.J., and Brown, B.J.T., *Bidirectional isotachophoresis on a planar chip with integrated conductivity detection.* The Analyst, 2002. **127**: p. 1413-1419.
19. Kameoka, J., Craighead, H.G., Zhang, H., and Henion, J., *A Polymeric Microfluidic Chip for CE/MS Determination of Small Molecules.* Analytical Chemistry, 2001. **73**(9): p. 1935-1941.
20. Trau, D., Lee, T.M.H., Lao, A.I.K., Lenigk, R., Hsing, I.-M., Ip, N.Y., Carles, M.C., and Sucher, N.J., *Genotyping on a complementary metal oxide semiconductor silicon polymerase chain reaction chip with integrated DNA microarray.* Analytical Chemistry, 2002. **74**(13): p. 3168-3173.
21. Paegel, B.M., Yeung, S.H.I., and Mathies, R.A., *Microchip bioprocessor for integrated nanovolume sample purification and DNA sequencing.* Analytical Chemistry, 2002. **74**(19): p. 5092-5098.
22. Guttman, A., Ronai, Z., Barta , C., Hou, Y.-H., Sasvari-Szekely , M., Wang , X., and Briggs, S.P., *Membrane-mediated ultrafast restriction digestion and subsequent rapid gel microchip electrophoresis of DNA.* electrophoresis, 2002. **23**(10): p. 1524-1530.
23. Song, L., Fang, D., Kobos , R.K., Pace , S.J., and Chu, B., *Separation of double-stranded DNA fragments in plastic capillary electrophoresis chips by using E99P69E99 as separation medium.* Electrophoresis, 1999. **20**(14): p. 2847-2855.
24. Woolley, A.T., Sensabaugh, G.F., and Mathies, R.A., *High-speed DNA genotyping using microfabricated capillary array electrophoresis chips.* Analytical Chemistry, 1997. **69**(11): p. 2181-2186.
25. Graß, B., Hergenröder, R., Neyer, A., and Siepe, D., *Determination of selenoamino acids by coupling of isotachophoresis/capillary zone electrophoresis on a PMMA microchip.* Journal of Separation Science, 2002. **25**(3): p. 135-140.
26. Munro, N.J., Huang, Z.L., Finegold, D.N., and Landers, J.P., *Indirect fluorescence detection of amino acids on electrophoretic microchips.* Analytical Chemistry, 2000. **72**(13): p. 2765-2773.
27. Chen, H.H., *Influence of soluble polymer polyvinylpyrrolidone on separation of small peptides and amino acids by microchip-based capillary electrophoresis.* Analytical and bioanalytical chemistry, 2002. **373**(4): p. 314-317.
28. Xue, Q., Dunayevskiy, Y.M., Foret, F., and Karger, B.L., *Integrated multichannel microchip electrospray ionization mass spectrometry: analysis of peptides from on-*

chip tryptic digestion of melittin. Rapid communications in mass spectrometry, 1997. **11**: p. 1253-1256.

29. Gottschlich, N., Culbertson, C.T., McKnight, T.E., Jacobson, S.C., and Ramsey, J.M., *Integrated microchip-device for the digestion, separation and postcolumn labeling of proteins and peptides.* Journal of Chromatography B, 2000. **745**(1): p. 243-249.
30. Ekström, S., Ericsson, D., Önnerfjord, P., Bengtsson, M., Nilsson, J., Marko-Varga, G., and Laurell, T., *Signal amplification using "spot-on-a-chip" technology for the identification of proteins via MALDI-TOF MS.* Analytical Chemistry, 2001. **73**(2): p. 214-219.
31. Collins, A., Mikeladze, E., Bengtsson, M., M., K., Laurell, T., and Csöregi, E., *Interference Elimination in Glutamate Monitoring with Chip Integrated Enzyme Microreactors.* 2001. p. 425-431.
32. Kasai, S., Hirano, Y., Motochi, N., Shiku, H., Nishizawa, M., and Matsue, T., *Simultaneous detection of uric acid and glucose on a dual-enzyme chip using scanning electrochemical microscopy/scanning chemiluminescence microscopy.* Analytica Chimica Acta, 2002. **458**(2): p. 263-270.
33. Sakai-Kato, K., KAto, M., and Toyo'oka, T., *Creation of an on-chip enzyme reactor by encapsulating trypsin in sol-gel on a plastic microchip.* Analytical Chemistry, 2003. **75**(3): p. 388-393.
34. Hadd, A.G., Raymond, D.E., Halliwell, J.W., Jacobson, S.C., and Ramsey, J.M., *Microchip device for performing enzyme assays.* Analytical Chemistry, 1997. **69**(17): p. 3407-3412.
35. Tokaty, G.A., *A History and Philosophy of Fluid Mechanics* 1971, New York: Dover Publications, inc. 234.
36. Tesar, V., *"Fluid plug" microfluidic valve for low Reynolds number fluid flow selector units.* Journal of visualization, 2003. **6**(1): p. 77-85.
37. Mautner, T., *Application of the synthetic jet concept to low Reynolds number biosensor microfluidic flows for enhanced mixing: a numerical study using the lattice Boltzmann method.* Biosensors & bioelectronics, 2004. **19**(11): p. 1409-1419.
38. Sbragaglia, M. and Sugiyama, K., *Boundary induced nonlinearities at small Reynolds numbers.* Physica D: Nonlinear phenomena, 2007. **228**(2): p. 140-147.
39. White, F.M., *Fluid Mechanics*. 6th ed. 2006. 866.
40. Einstein, A., *Investigations on the theory of the brownian movement* 1926: Methuen & CO. Ltd. . 119.
41. Weigl, B.H. and Yager, P., *Microfluidics - Microfluidic diffusion-based separation and detection.* Science, 1999. **283**(5400): p. 346-347.
42. Kamholz, A.E. and Yager, P., *Theoretical analysis of molecular diffusion in pressure-driven laminar flow in microfluidic channels.* Biophysical Journal, 2001. **80**(1): p. 155-160.

43. Kamholz, A.E., Schilling, E.A., and Yager, P., *Optical measurement of transverse molecular diffusion in a microchannel.* Biophysical journal, 2001. **80**(4): p. 1967-1972.
44. Hatch, A., Kamholz, A.E., Hawkins, K.R., Munson, M.S., Schilling, E.A., Weigl, B.H., and Yager, P., *A rapid diffusion immunoassay in a T-sensor.* Nature Biotechnology, 2001. **19**(5): p. 461-465.
45. Holden, M.A., Kumar, S., Beskok, A., and Cremer, P.S., *Microfluidic diffusion diluter: bulging of PDMS microchannels under pressure-driven flow.* Journal of Micromechanics and Microengineering, 2003. **13**(3): p. 412-418.
46. Heeren, A., Luo, Y., Roth, G., Ganser, A., Brock, R., Wiesmueller, K.H., Henschel, W., and Kern, D.P., *Diffusion along microfluidic channels.* Microelectronic Engineering, 2006. **83**(4-9): p. 1669-1672.
47. Shin, D.-S., Kang, C.-K., Kim, J.-K., Chung, W.-J., Jang, K.-H., and Lee, Y.-S. *Surface modification technology for bio-mems.* in *Transducers*. 2003. Boston, MA, USA.
48. Kai, J., Sohn, Y.S., and Ahn, C.H. *Protein microarray on cyclic olefin copolymer (COC) for disposable protein lab-on-chip.* in *Micro Total Analysis Systems*. 2003. Squaw Valley, California USA.
49. Grodrian, A. and Metze, J., *Segmented flow generation by chip reactors for highly parallelized cell cultivation.* Biosensors and Bioelectronics, 2004. **19**: p. 1421-1428.
50. Tan, W. and Desai, T.A., *Layer-by-layer microfluidics for biomimetic three-dimensional structures.* Biomaterials, 2004. **25**: p. 1355-1364.
51. Schaak, B., Fouqué, B., Porte, S., Combe, S., Hennico, A., Filhol-Cochet, O., Reboud, J., Balakirev, M., and Chatelain, F. *Cell culture in microdrops, a new format for cell on chip technology.* in *Micro Total Analysis Systems*. 2003. Squaw Valley, CA, USA.
52. Tanaka, Y., Sato, K., Yamato, M., Okano, T., and Kitamori, T. *Micro liver system for bioreactor and bioconversion.* in *Micro Total Analysis Systems*. 2003. Squaw Valley, CA, USA.
53. Kobayashi, H., Mori, Y., Okamoto, K., Akiyama, R., Ueno, H., Kitamori, T., and kobayashi, S., *A microfluidic device for conducting gas-liquid-solid hydrogenation reactions.* Science, 2004. **304**: p. 1304-1308.
54. Miller, P.W., Long, N.J., de Mello, A.J., Vilar, R., Passchier, J., and Gee, A., *Rapid formation of amides via carbonylative coupling reactions using a microfluidic device.* Chemical Communications, 2006(5): p. 546-548.
55. Geyer, K., Codee, J.D.C., and Seeberger, P.H., *Microreactors as Tools for Synthetic Chemists- The Chemists' Round-Bottomed Flask of the 21st Century?* Chemistry a European Journal, 2006. **12**: p. 8434-8442.
56. Fuchs, A., Manaresi, N., Freida, D., Altomare, L., Villiers, C.L., Medoro, G., Romani, A., Chartier, I., Bory, C., Tartagni, M., Marche, P.N., Chatelain, F., and Guerrieri, R.

A microelectronic chip opens new fields in rare cell population analysis and individual cell biology. in *Micro Total Analysis Systems*. 2003. Squaw Valley, CA, USA.

57. Wolff, A.A. and Wolff, A.A., *Integrating advanced functionality in a microfabricated high-throughput fluorescent-activated cell sorter.* Lab on a chip, 2003. **3**(1): p. 22-27.
58. Harrison, R. *Observation on the living developing nerve fiber.* In *Proceedings of the Society for Experimental Biology and Medicine*. 1907. New York
59. Wu, A.H.B., *A selected history and future of immunoessay development and applications in clinical chemistry.* Clinica Chimica Acta, 2006. **369**: p. 119-124.
60. Sanger, F., Nicklen, S., and Coulson, A.R., *DNA sequencing with Chain-Terminating Inhibitors* Proceedings of the National Acadamy of Science USA, 1977. **74**(12): p. 5463-5467.
61. Kim, J.W., Park, J.H., Park, J.W., Doh, H.J., Heo, G.S., and Lee, K.J., *Quantitative analysis of serum proteins separated by capillary electrophoresis.* Clinical Chemistry, 1993. **39**(4): p. 689-692.
62. Dolnik, V., *Capillary zone electrophoresis of serum proteins: study of separation variables.* J Chromatogr A, 1995. **709**(1): p. 99-110.
63. Chen and Sternberg, *Characterization of proteins by capillary electrophoresis in fused-silica columns: Review on serum protein analysis and application to immunoassays.* Electrophoresis, 1994. **15**(1): p. 13-21.
64. Jenkins, M.A., Kulinskaya, E., Martin, H.D., and Guerin, M.D., *Evaluation of serum protein separation by capillary electrophoresis: prospective analysis of 1000 specimens.* Journal of Chromatography B: Biomedical Sciences and Applications, 1995. **672**(2): p. 241-251.
65. Woolley, A.T. and Mathies, R.A., *Ultra-high speed DNA sequencing using capillary electrophoresis chips.* Analytical Chemistry, 1995. **67**(20): p. 3676-3680.
66. Jacobson, S.C. and Ramsey, J.M., *Integrated microdevice for DNA restriction fragment analysis.* Analytical Chemistry, 1996. **68**(5): p. 720-723.
67. Effenhauser, C.S., Bruin, G.J.M., Paulus, A., and Ehrat, M., *Integrated capillary electrophoresis on flexible silicone microdevices: analysis of DNA restriction fragments and detection of single DNA molecules on microchips.* Analytical Chemistry, 1997. **69**(17): p. 3451-3457.
68. Schmalzing, D., Koutny, L., Adourian, A., Belgrader, P., Matsudaira, P., and Ehrlich, D., *DNA typing in thirty seconds with a microfabricated device.* Proceedings of the National Academy of Sciences of the United States of America, 1997. **94**: p. 10273-10278.
69. Lin, T., *Design of Low Voltage-Driven Capillary Electrophoresis Chips Using Moving Electrical Fields.* Sensors and actuators B, 2001. **80**: p. 33-40.

70. Vrouwe, E.X., R., L., and Van den Berg, A., *Direct measurement of lithium in whole blood using microchip capillary electrophoresis with integrated conductivity detection.* Electrophoresis, 2004. **25**(10-11): p. 1660-1667.
71. Goedecke, N., McKenna, B., El-Difrawy, S., Gismondi, E., Swenson, A., Carey, L., Matsudaira, P., and Ehrlich, D.J., *Microdevice DNA forensics by the simple tandem repeat method.* Journal of Chromatography A, 2006. **1111**(2): p. 206-213.
72. Pohl, H.-A., *Dielectrophoresis : the behavior of neutral matter in nonuniform electric fields.* 1978: Cambridge ; New York : Cambridge University Press.
73. Asbury, C.L., Diercks, A.H., and van den Engh, G., *Trapping of DNA by dielectrophoresis.* Electrophoresis, 2002. **23**(16): p. 2658-2666.
74. Kutter, J.P., *Current developments in electrophoretic and chromatographic separation methods on microfabricated devices.* Trends in Analytical Chemistry, 2000. **19**(6): p. 352-363.
75. Chou, C.-F., Austin, R.H., Bakajin, O., Tegenfeldt, J.O., Castelino, J.A., Chan, S.S., Cox, E.C., Craighead, H., Darnton, N., Duke, T., Han, J., and Turner, S., *Sorting biomolecules with microdevices.* Electrophoresis, 2000. **21**: p. 81-90.
76. Heller, C.C., *Principles of DNA separation with capillary electrophoresis.* Electrophoresis, 2001. **22**(4): p. 629-43.
77. Stone, H.A., Stroock, A.D., and Ajdari, A., *Engineering flows in small devices: Microfluidics toward a lab-on-a-chip.* Annual review of fluid mechanics, 2004. **36**: p. 381-411.
78. Cooper, J.W., Wang, Y.J., and Lee, C.S., *Recent advances in capillary separations for proteomics.* Electrophoresis, 2004. **25**(23-24): p. 3913-3926.
79. Pumera, M., *Analysis of explosives via microchip electrophoresis and conventional capillary electrophoresis: A review.* Electrophoresis, 2006. **27**(1): p. 244-256.
80. Ghosal, S., *Electrokinetic flow and dispersion in capillary electrophoresis.* Annual review of fluid mechanics, 2006. **38**: p. 309-338.
81. Horsman, K.M., Bienvenue, J.M., Blasier, K.R., and Landers, J.P., *Forensic DNA analysis on microfluidic devices: A review.* Journal of forensic sciences, 2007. **52**(4): p. 784-799.
82. Fu, A.Y., Spence, C., Scherer, A., Arnold, F.H., and Quake, S.R., *A microfabricated fluorescence-activated cell sorter.* Nature Biotechnology, 1999. **17**(November): p. 1109-1111.
83. Dittrich, P. and Schwille, P., *An Integrated Microfluidic System for Reaction, High-Sensitivity Detection, and Sorting of Fluorescent Cells and Particles.* Analytical chemistry, 2003. **75**(21): p. 5767-5774.
84. MacDonald, M.P., *Cell cytometry with a light touch: Sorting microscopic matter with an optical lattice.* Journal of biological regulators and homeostatic agents, 2004. **18**(2): p. 200-205.

85. Kapishnikov, S., Kantsler, V., and Steinberg, V., *Continuous particle size separation and size sorting using ultrasound in a microchannel.* Journal of Statistical Mechanics-theory and experiment 2006.

86. Chen, C.C., Wang, J.S., and Solgaard, O., *Micromachined bubble-jet cell sorter with multiple operation modes.* Sensors and Actuators B: Chemical, 2006. **117**(2): p. 523-529.

87. Reyes, D.R., Auroux, P.-A., Iossifidis, D., and Manz, A., *Micro total analysis systems. 1. Introduction, theory, and technology.* Analytical Chemistry, 2002. **74**(12): p. 2623-2636.

88. Auroux, P.-A., Reyes, D.R., Iossifidis, D., and Manz, A., *Micro Total Analysis System 2. Analytical Standard Operations and Applications.* Analytical Chemistry, 2002. **74**(12): p. 2637-2652.

89. Verpoorte, E., *Microfluidic chips for clinical and forensic analysis.* Electrophoresis, 2002. **23**: p. 677-712.

90. Vilkner, T., Janasek, D., and Manz, A., *Micro Total Analysis Systems. Recent Developments.* Analytical chemistry, 2004. **76**(12): p. 3373-3386.

91. Heuschkel, M.O., Guerin, L., Buisson, B., Bertrand, D., and Renaud, P., *Buried microchannels in photopolymer for delivering of solutions to neurons in a network.* Sensors and Actuators B: Chemical, 1998. **48**(1-3): p. 356-361.

92. Monaghan, P.B., Manz, A., and Nichols, W.W. *Microbiology on-a-chip*. in *Micro Total Analysis Systems 2000, Proceedings*. 2000. Dordrecht: Kluwer Academic Publ.

93. Glasgow, I.K., *Handling individual mammalian embryos using microfluidics.* IEEE transactions on bio-medical engineering, 2001. **48**(5): p. 570-578.

94. Takayama, S., Ostuni, E., Qian, X., McDonald, J.C., Jiang, X., LeDuc, P., Wu, M.H., Ingber, D.E., and Whitesides, G.M., *Topographical micropatterning of poly(dimethylsiloxane) using laminar flows of liquids in capillaries.* Advanced Materials, 2001. **13**(8): p. 570-+.

95. Walker, G.M., Ozers, M.S., and Beebe, D.J., *Insect Cell Culture in Microfluidic Channels.* Biomedical Microdevices, 2002. **4**(3): p. 161-166.

96. Martin, K., Henkel, T., Baier, V., Grodrian, A., Schon, T., Roth, M., Kohler, J.M., and Metze, J., *Generation of large numbers of separated microbial populations by cultivation in segmented-flow microdevices.* Lab on a Chip, 2003. **3**: p. 202-207.

97. Walker, G.M., Zeringue, H.C., and Beebe, D.J., *Microenvironment design considerations for cellular scale studies.* Lab on a chip, 2004. **4**(2): p. 91-97.

98. Kuncova-Kallio, J. and Kallio, P.J., *Lab automation in cultivation of adherent cells.* IEEE transactions on automation science and engineering, 2006. **3**(2): p. 177-186.

99. Prokop, A., Prokop, Z., Schaffer, D., Kozlov, E., Wikswo, J., Cliffel, D., and Baudenbacher, F., *NanoLiterBioReactor: Long-term mammalian cell culture at nanofabricated scale.* Biomedical Microdevices, 2004. **6**(4): p. 325-339.

100. Dusseiller, M.R., Schlaepfer, D., Koch, M., Kroschewski, R., and Textor, M., *An inverted microcontact printing method on topographically structured polystyrene chips for arrayed micro-3-D culturing of single cells.* Biomaterials, 2005. **26**(29): p. 5917-5925.

101. Vo-Dinh, T., Cullum, B.M., and Stokes, D.L., *Nanosensors and biochips: frontiers in biomolecular diagnostics.* Sensors and actuators. B, Chemical, 2001. **74**(1-3): p. 2-11.

102. Chen, H.M., Lin, M.L., and Chen, S.H., *Fabrication of piezoelectric biochips with self-assembled alkanethiol layer and hydrocoating.* Journal of the Chinese Institute of Chemical Engineers, 2003. **34**(1): p. 151-160.

103. Baudoin, R., Corlu, A., Griscom, L., Legallais, C., and Leclerc, E., *Trends in the development of microfluidic cell biochips for in vitro hepatotoxicity.* Toxicology In Vitro, 2007. **21**(4): p. 535-544.

104. Leclerc, E., Miyata, F., Furukawa, K.S., Ushida, T., Sakai, Y., and Fujii, T., *Effect on liver cells of stepwise microstructures fabricated in a photosensitive biodegradable polymer by softlithography.* Materials Science and Engineering: C, 2004. **24**(3): p. 349-354.

105. Leclerc, E., Sakai, S., and Fujii, T., *Microfluidic PDMS (Polydimethylsiloxane) Bioreactor for Large-Scale Culture of Hepatocytes.* Biotechnology progress, 2004. **20**(3): p. 750-755.

106. Leclerc, E., Corlu, A., Griscom, L., Baudoin, R., and Legallais, C., *Guidance of liver and kidney organotypic cultures inside rectangular silicone microchannels.* Biomaterials, 2006. **27**(22): p. 4109-4119.

107. Tian, H.J., Jaquins-Gerstl, A., Munro, N., Trucco, M., Brody, L.C., and Landers, J.P., *Single-strand conformation polymorphism analysis by capillary and microchip electrophoresis: A fast, simple method for detection of common mutations in BRCA1 and BRCA2.* Genomics, 2000. **63**(1): p. 25-34.

108. Du, Z., Colls, N., Cheng, K.H., Vaughn, M.W., and Gollahon, L., *Microfluidic-based diagnostics for cervical cancer cells.* Biosensors and Bioelectronics, 2006. **21**(10): p. 1991-1995.

109. Munro, N.N.J., Huang, Z.Z., Finegold, D.D.N., and Landers, J.J.P., *Indirect fluorescence detection of amino acids on electrophoretic microchips.* Analytical chemistry, 2000. **72**(13): p. 2765-73.

110. Žúborová, M., Masár, M., Kaniansky, D., Jöhnck, M., and Stanislaski, B., *Determination of oxalate in urine by zone electrophoresis on a chip with conductivity detetcion.* Electrophoresis, 2002. **23**: p. 774-781.

111. Christodoulides, N., Tran, M., Floriano, P.N., Rodriguez, H.E., Goodey, A., Ali, M., Neikirk, D., and McDevitt, J.T., *A Microchip-Based Multianalyte Assay System for the Assessment of Cardiac Risk.* Analytical chemistry, 2002. **74**(13): p. 3030-3036.

112. Pasas, S.A., Lacher, N.A., Davies, M.I., and Lunte, S.M., *Detection of homocysteine by conventional and microchip capillary electrophoresis/electrochemistry.* Electrophoresis, 2002. **23**: p. 759-766.

113. Mastrangelo, C.H., Burns, M.A., and Burke, D.T., *Microfabricated devices for genetic diagnostics.* Proceedings of the IEEE, 1998. **86**(8): p. 1769-1787.

114. Ahn, C.H., Choi, J., Beaucage, G., Nevin, J.H., lee, J.B., Puntambekar, A., and Lee, J., *Disposable Smart lab on a chip for point-of-care clinical diagnostics.* Proceedings of the IEEE, 2004. **92**(1): p. 154-173.

115. Jain, K.K., *Nanotechnology in clinical laboratory diagnostics.* Clinica chimica acta, 2005. **358**(1-2): p. 37-54.

116. Settles, G.S., *FLUID MECHANICS AND HOMELAND SECURITY.* Annual review of fluid mechanics, 2006. **38**(1): p. 87-110.

117. Koutny, L.B., Schmalzing, D., Taylor, T.A., and Fuchs, M., *Microchip electrophoretic immunoassay for serum cortisol.* Analytical Chemistry, 1996. **68**(1).

118. Delamarche, E., Bernard, A., Bietsch, A., Michel, B., and Biebuyck, H., *Patterned Delivery of Immunoglobulins to Surfaces Using Microfluidics Networks.* Science, 1997. **276**(May): p. 779-781.

119. Yang, T., Jung, S.-Y., Mao, H., and Cremer, P.S., *Fabrication of phospholipid bilayer-coated microchannels for on-chip immuoassays.* Analytical Chemistry, 2001. **73**(2): p. 165-169.

120. Sia, S.K., Linder, V., Parviz, B., Siegel, R.A., and Whitesides, G., *An integrated approach to a portable and low-cost immunoassay for resource-poor settings.* Angewandte Chemie (International ed.), 2004. **43**(4): p. 498-502.

121. Newman, G.R. and Jasani, B., *Silver development in microscopy and bioanalysis: past and present.* 1998. p. 119-125.

122. Sanders, G.H.W. and Manz, A., *Chip-based microsystems for genomic and proteomic analysis.* Trends in Analytical Chemistry, 2000. **19**(6): p. 364-378.

123. Weigl, B.H., Bardell, R.L., and Cabrera, C.R., *Lab-on-a-chip for drug development.* Advanced Drug Delivery Reviews, 2003. **55**(3): p. 349-377.

124. Erickson, D. and Li, D., *Integrated microfluidic devices.* Analytica Chimica Acta, 2004. **507**(1): p. 11-26.

125. Lim, C.T. and Zhang, Y., *Bead-based microfluidic immunoassays: The next generation.* Biosensors and Bioelectronics, 2007. **22**(7): p. 1197-1204.

126. Lion, N., Rohner, T.C., Dayon, L., Arnaud, I.L., Damoc, E., Youhnovski, N., Wu, Z.-Y., Roussel, C., Josseranc, J., Jensen, H., Rossier, J.S., Przybylski, M., and Girault, H.H., *Microsystems in proteomics.* Electrophoresis, 2003. **24**: p. 3533-3562.

127. Figeys, D. and Aebersold, R., *High sensitivity analysis of proteins and peptides by capillary electrophoresis tandem mass spectrometry: Recent developments in technology and applications.* Electrophoresis, 1998(6): p. 885-892.

128. Wang, J., *Electrochemical detection for microscale analytical systems: a review.* Talanta, 2002. **56**(2): p. 223-231.

129. Vandaveer , W.R., Pasas, S.A., Martin, R.S., and Lunte, S.M., *Recent developments in amperometric detection for microchip capillary.* Electrophoresis, 2002. **23**: p. 3667-3677.

130. Uchiyama, K., Nakajima, R., and Hobo, T., *Detection method for microchip separations.* Analytical and bioanalytical chemistry, 2004. **379**(3): p. 375-382.

131. Vandaveer, W.R., *Recent developments in electrochemical detection for microchip capillary electrophoresis.* Electrophoresis, 2004. **25**(21-22): p. 3528-3549.

132. Mogensen, K.B., *Recent developments in detection for microfluidic systems.* Electrophoresis, 2004. **25**(21-22): p. 3498-3512.

133. Dittrich, P.S. and Manz, A., *Single-molecule fluorescence detection in microfluidic channels - the Holy Grail in mu TAS?* Analytical and bioanalytical chemistry, 2005. **382**(8): p. 1771-1782.

134. Viskari, P.J., *Unconventional detection methods for microfluidic devices.* Electrophoresis, 2006. **27**(9): p. 1797-1810.

135. Gotz, S. and Karst, U., *Recent developments in optical detection methods for microchip separations.* Analytical and bioanalytical chemistry, 2007. **387**(1): p. 183-192.

136. Waggoner, P.S. and Craighead, H.G., *Micro- and nanomechanical sensors for environmental, chemical, and biological detection.* Lab on a chip, 2007. **7**(10): p. 1238-1255.

137. Yi, C., Zhang, Q., Li, C.-W., Yang, J., Zhao, J., and Yang, M., *Optical and electrochemical detection techniques for cell-based microfluidic systems.* Analytical and Bioanalytical chemistry, 2006. **384**(6): p. 1259-1268.

138. Liang, Z.H., Chiem, N., Ocvirk, G., Tang, T., Fluri, K., and Harrison, D.J., *Microfabrication of a planar absorbance and fluorescence cell for integrated capillary electrophoresis devices.* Analytical Chemistry, 1996. **68**(6): p. 1040-1046.

139. Hodder, P.S., Blankenstein, G., and Ruzicka, J., *Microfabricated flow chamber for fluorescence-based chemistries and stopped-flow injection cytometry.* The Analyst, 1997. **122**: p. 883-887.

140. Tuan, V.D., *Development of a DNA biochip: principle and applications.* Sensors and actuators. B, Chemical, 1998. **51**(1-3): p. 52-59.

141. Cheng, J., Shoffner, M.A., Hvichia, G.E., Kricka, L.J., and Wilding, P., *Chip PCR II. Investigation of different PCR amplification systems in microfabricated silicon-glass chips.* Nucleic Acids Research, 1996. **24**(2): p. 380-385.

142. Kopp, M.U., Crabtree, H.J., and Manz, A., *Developments in technology and applications of microsystems.* Current Opinion in Chemical Biology, 1997. **1**(3): p. 410-419.

143. Eggers, M., Hogan, M., Reich, R.K., Lamture, J., Ehrlich, D., Hollis, M., Kosicki, B., Powdrill, R., Beattle, K., Smith, S., Varma, R., Gangadharan, R., Mallik, A., Burke, B., and Wallace, D., *A microchip for quantitative detection of molecules utilizing luminescent and radioisotop reporter groups*. Biotechniques, 1994. **17**(3): p. 516.

144. Belgrader, P., Smith, J.K., Weedn, V.W., and Northrup, M.A., *Rapid PCR for identity testing using a battery-powered miniature thermal cycler*. Journal of Forensic Sciences, 1998. **43**(2): p. 315-319.

145. Yershov, G., Barsky, V., Belgovskiy, A., Kirillov, E., Kreindlin, E., Ivanov, I., Parinov, S., Guschin, D., Drobishev, A., Dubiley, S., and Mirzabekov, A., *DNA analysis and diagnostics on oligonucleotide microchips*. Proceedings of the National Academy of Sciences of the United States of America, 1996. **93**(10): p. 4913-4918.

146. Drobyshev, A., Mologina, N., Shik, V., Pobedimskaya, D., Yershov, G., and Mirzabekov, A., *Sequence analysis by hybridization with oligonucleotide microchip: Identification of beta-thalassemia mutations*. Gene, 1997. **188**(1): p. 45-52.

147. Liu, J.K., Pan, T., Woolley, A.T., and Lee, M.L., *Surface-modified poly(methyl methacrylate) capillary electrophoresis microchips for protein and peptide analysis*. Analytical Chemistry, 2004. **76**(23): p. 6948-6955.

148. Effenhauser, C.S., Bruin, G.J.M., and Paulus, A., *Integrated chip-based capillary electrophoresis*. Electrophoresis, 1997. **18**(12-13): p. 2203-2213.

149. Mitchelson, K.R., Cheng, J., and J., K.L., *The use of capillary electrophoresis for point-mutation screening*. Trends in Biotechnology, 1997. **15**(11): p. 448-58.

150. Jakeway, S.C., deMello, A.J., and Russell, E.L., *Miniaturized total analysis systems for biological analysis*. Fresenius' Journal of Analytical Chemistry, 2000. **366**(6-7): p. 525-539.

151. Schwarz, M.A. and Hauser, P.C., *Recent developments in detection methods for microfabricated analytical devices*. Lab on a chip, 2001. **1**(1): p. 1-6.

152. Hsueh, Y.T., Smith, R.L., and Northrup, M.A., *A microfabricated, electrochemiluminescence cell for the detection of amplified DNA*. Sensors and Actuators B, 1996. **33**(1-3): p. 110-114.

153. Arora, A., de Mello, A.J., and Manz, A., *Sub-microliter electrochemiluminescence detector - A model for small volume analysis systems*. Analytical Communications, 1997. **34**(12): p. 393-395.

154. Xue, Q., Foret, F., Dunayevskiy, Y.M., Zavracky, P.M., McGruer, N.E., and Karger, B.L., *Multichannel microchip electrospray mass spectrometry*. Analytical Chemistry, 1997. **69**(3): p. 426-430.

155. Lazar, I.M., Grym, J., and Foret, F., *Microfabricated devices: A new sample introduction approach to mass spectrometry*. Mass spectrometry reviews, 2006. **25**(4): p. 573-594.

156. Foret, F. and Kusy, P., *Microfluidics for multiplexed MS analysis*. Electrophoresis, 2006. **27**(24): p. 4877-4887.

157. Foret, F. and Kusy, P., *Microdevices in mass spectrometry.* European journal of mass spectrometry, 2007. **13**(1): p. 41-44.
158. Grym, J. and Foret, F., *Microfluidics: New method of treatment and introduction of samples for mass spectrometry.* Chemické listy, 2005. **99**(12): p. 915-921.
159. Figeys, D., Ning, Y.B., and Aebersold, R., *A microfabricated device for rapid protein identification by microelectrospray ion trap mass spectrometry.* Analytical Chemistry, 1997. **69**(16): p. 3153-3160.
160. Hou, C.S.J., Godin, M., Payer, K., Chakrabarti, R., and Manalis, S.R., *Integrated microelectronic device for label-free nucleic acid amplification and detection.* Lab on a chip, 2007. **7**(3): p. 347-354.
161. Cooper, E.B., Fritz, J., Wiegand, G., Wagner, P., and Manalis, S.R., *Robust microfabricated field-effect sensor for monitoring molecular adsorption in liquids.* Applied physics letters, 2001. **79**(23): p. 3875.
162. Weng, C.-H., Yeh, W.-M., Ho, K.-C., and Lee, G.-B., *A microfluidic system utilizing molecularly imprinted polymer films for amperometric detection of morphine.* Sensors and Actuators B: Chemical, 2007. **121**(2): p. 576-582.
163. Godber, B., Frogley, M., Rehak, M., Sleptsov, A., Thompson, K.S.J., Uludag, Y., and Cooper, M.A., *Profiling of molecular interactions in real time using acoustic detection.* Biosensors and Bioelectronics, 2007. **22**(9-10): p. 2382-2386.
164. Yeh, H.C., Chao, S.Y., Ho, Y.P., and Wang, T.H., *Single-molecule detection and probe strategies for rapid and ultrasensitive genomic detection.* Current pharmaceutical biotechnology, 2005. **6**(6): p. 453-461.
165. Dittrich, P.S. and Manz, A., *Lab-on-a-chip: microfluidics in drug discovery.* Nature reviews. Drug discovery, 2006. **5**(3): p. 210-218.
166. Pumera, M., *Microfluidics in amino acid analysis.* Electrophoresis, 2007. **28**(13): p. 2113-2124.
167. Mullis, K.B., Faloona, F., Scharf, S., Saiki, R.K., Horn, G.T., Ehrlich, A., and Arnheim, H.A. *Specific enzymatic amplification of DNA in vitro: The Polymerase Chain Reaction.* in *Cold Spring Harbour Laboratory Symposium on Quantitative Biology.* 1986.
168. Mullis, K.B., Ferre, F., and Gibbs, R.A., *The Polymerase Chain Reaction*, ed. B. Birkhauser. 1994, Boston.
169. Shah, C.P., Modi, D., Sachdeva, G., Gadkar, S., and Puri, C., *Coexistence of intracellular and membrane-bound progesterone receptors in human testis.* The Journal of clinical endocrinology & metabolism, 2005. **90**(1): p. 474-483.
170. Baxendale, R.W. and Fraser, L.R., *Mammalian sperm phosphodiesterases and their involvement in receptor-mediated cell signaling important for capacitation.* Molecular reproduction and development, 2005. **71**(4): p. 495-508.

171. Hayney, M.S., Dimanlig, P., Lipsky, J.J., and Poland, G.A., *Utility of a swish and spit technique for the collection of buccal cells for tap haplotype determination.* Mayo Clinic proceedings, 1995. **70**(10): p. 951-954.

172. Lum, A. and LeMarchand, L., *A simple mouthwash method for obtaining genomic DNA in molecular epidemiological studies.* Cancer epidemiology biomarkers & prevention, 1998. **7**(8): p. 719-724.

173. Ellis, M.A.P., Song, F., Park, E.T., Eckert, G.C., and Dean, J.A., *An evaluation of DNA yield, DNA quality and bite registration from a dental impression wafer.* The Journal of the American Dental Association, 2007. **138**(9): p. 1234-1240.

174. Reynolds, R., Sensabaugh, G.F., and Blake, E., *Analysis of genetic-makers in forensic DNA samples using the polymerase chain reaction.* Analytical chemistry, 1991. **63**(1): p. 2-15.

175. Taberlet, P. and Luikart, G., *Non-invasive genetic sampling and individual identification.* Biological journal of the Linnean Society, 1999. **68**(1-2): p. 41-55.

176. Scheppers, T.L.J., Frantz, A.C., Schaul, M., Engel, E., Breyne, P., Schley, L., and Ropert, T.J., *Estimating social group size of Eurasian badgers Meles meles by genotyping remotely plucked single hairs.* Wildlife biology, 2007. **13**(2): p. 195-207.

177. Lehninger, A.L., Nelson, D.L., and Cox, M.M., *Principles of Biochemistry*. Second Edition ed. 1993, New York Worth Publishers.

178. McPherson, M.J., Quirke, P., and Taylor, G.R., *PCR; A Practical Approach*. 1991, Oxford: Oxford University Press.

179. Ehrlich, H.A., *PCR technology; Principles and Applications for DNA Amplification*. 1989: Macmillan.

180. Resuehr, D. and Spiess, A.-N., *A real-time chain reaction-based evaluation of cDNA synthesis priming methods.* Analytical Biochemistry, 2003. **322**: p. 287-291.

181. Halford, W.P., Falco, V.C., Gebhardt, B.M., and carr, D.J.J., *The Inherent quantitative capacoty of the reverse transcritpion-polymerase chain reaction.* Analytical Biochemistry, 1999. **266**: p. 181-191.

182. Mullis, K.B. and Faloona, F., *Specific Synthesis of DNA in Vitro via a Polymerase-Catalyzed Chain Reaction* Methods in Enzymology, 1987. **155**: p. 335-350.

183. Chien, A., Edgar, D.B., and Trela, J.M., *Deoxyribonucleic acid polymerase from the extreme thermophile Thermus Aquaticus.* Journal of bacteriology, 1976. **127**(3): p. 1550-1557.

184. Tindall, K.R. and Kunkel, T.A., *Fidelity of DNA synthesis by the Thermus aquaticus DNA Polymerase.* Biochemistry, 1988. **27**: p. 6008-6013.

185. Davidson, J.F., Fox, R., Harris, D.D., Lyons-Abbott, S., and Loeb, L.A., *Insertion of the T3 DNA polymerase thioredoxin binding domain enhances the processivity and fidelity of Taq DNA polymerase.* Nucleic Acids Research, 2003. **31**(16): p. 4702-4709.

186. Mattila, P., Korpela, J., Tenkanen, T., and Pitkanen, K., *Fidelity of DNA-Synthesis by the Thermococcus-Litoralis DNA- Polymerase - an Extremely Heat-Stable Enzyme with Proofreading Activity.* Nucleic Acids Research, 1991. **19**(18): p. 4967-4973.

187. Lundberg, K.S., Short, J.M., Sorge, J.A., and Mathur, E.J., *A New Thermostable Polymerase with High Fidelity.* Faseb Journal, 1991. **5**(6): p. A1549-A1549.

188. Lundberg, K.S., Shoemaker, D.D., Adams, M.W.W., Short, J.M., Sorge, J.A., and Mathur, E.J., *High-fidelity amplification using a thermostable DNA polymerase isolated from Pyrococcus furiosus.* Gene, 1991. **108**: p. 1-6.

189. Barnes, W.M., *The fidelity of Taq polymerase catalyzing PCR is improved by an N-terminal deletion.* Gene, 1992. **112**: p. 29-35.

190. Choi, J.J., Jung, S.E., Kim, H.-K., and Kwon, S.-T., *Purification and properties of Thermus filiformis DNA polymerase expressed in Escerichia coli.* Biotechnology Applied Biochemistry, 1999. **30**: p. 19-25.

191. Al-Soud, W.A. and Radstrom, P., *Purification and Characterization of PCR-Inhibitory Components in Blood Cells.* 2001. p. 485-493.

192. Rychlik, W., *Priming efficiency in PCR.* Biotechniques, 1995. **18**(1): p. 84.

193. Markoulatos, P., Siafakas, N., and Moncany, M., *Multiplex polymerase chain reaction: a practical approach.* Journal of Clinical Laboratory Analysis, 2002. **16**: p. 47-51.

194. Henegariu, O., Heerema, N.A., Dlouhy, S.R., Vance, G.H., and Vogt, P.H., *Multiplex PCR: critical parameters and step-by-step protocol.* Bio Techniques, 1997. **23**(3): p. 504-511.

195. Guatelli, J.C., Whitfield, K.M., Kwoh, D.Y., Barringer, K.J., Richman, D.D., and Gingeras, T.R., *Isothermal, In Vitro Amplification of Nucleic Acids by a Multienzyme Reaction Modeled After Retroviral Replication.* Proc. Nat. Acad. Sci. USA, 1990. **87**(5): p. 1874-1878.

196. Fire, A. and S-Q, X., *Rolling replication of short DNA circles* Proc. Nat. Acad. Sci. USA, 1995. **92**: p. 4641-4645.

197. Notomi, T., Okayama, H., Masubuchi, H., Yonekawa, T., Watanabe, K., Amino, N., and Hase, T., *Loop-mediated isothermal amplification of DNA.* Nucleic Acids Research, 2000. **28**(12): p. e63.

198. Kornberg, A. and Baker, T., *DNA replication*, ed. second. 1992, New York: WH Freeman and Company

199. Vincent, M., Xu, Y., and Kong, H., *Helicase-dependent isothermal DNA amplification* European Molecular Biology Organization reports 2004. **5**(8): p. 795-800.

200. Saiki, R.K., Scharf, S., Faloona, F., Mullis, K.B., Horn, G.T., Erlich, H.A., and Arnheim, N., *Enzymatic Amplification of Beta-Globin Genomic Sequences and Restriction Site Analysis for Diagnosis of Sickle-Cell Anemia.* Science, 1985. **230**(4732): p. 1350-1354.

201. Wilding, P., Shoffner, M.A., and Kricka, L.J., *PCR in a silicon microstructure.* Clinical Chemistry, 1994. **40**(9): p. 1815-1818.
202. Woolley, A.T., Hadley, D., Landre, P., de Mello, A.J., Mathies, R.A., and Northrup, M.A., *Functional Integration of PCR Amplification and Capillary Electrophoresis in Microfabricated DNA Analysis device.* Analytical Chemistry, 1996. **68**: p. 4081.
203. Kopp, M.U., de Mello, A.J., and Manz, A., *Chemical amplification: Continuous-flow PCR on a chip.* Science, 1998. **280**(5366): p. 1046-1048.
204. Belanger, S.D., Boissinot, M., Menard, C., Picard, F.J., and Bergeron, M.G., *Rapid Detection of Shiga Toxin-Producing Bacteria in Feces by Multiplex PCR with Molecular Beacons on the Smart Cycler.* 2002. p. 1436-1440.
205. Ohashi, T., Kuyama, H., Hanafusa, N., and Togawa, Y., *A simple device using magnetic transportation for droplet-based PCR.* Biomedical microdevices, 2007. **9**(5): p. 695-702.
206. Swerdlow, H., Jones, B.J., and Wittwer, C.T., *Fully Automated DNA Reaction and Analysis in a Fluidic Capillary Instrument.* Analytical Chemistry, 1997. **69**: p. 848-855.
207. Oda, R.P., Strausbauch, M.A., Huhmer, A.F.R., Borson, N., Jurrens, S.R., Craighead, J., Wettstein, P.J., Eckloff, B., Kline, B., and Landers, J.P., *Infrared-Mediated Thermocycling for Ultrafast Polymerase Chain Reaction Amplification of DNA.* Analytical Chemistry, 1998. **70**: p. 4361.
208. Northrup, M.A., Ching, M.T., White, R.M., and Watson, R.T., *DNA amplification with a microfabricated reaction chamber.* Transducers '93, 1993: p. 924-926.
209. Northrup, M.A., Benett, B., Hadley, D., Landre, P., Lehew, S., Richards, J., and Stratton, P., *A miniature analytical instrument for nucleic acids based on micromachined silicon reaction chambers.* Analytical Chemistry, 1998. **70**(5): p. 918-922.
210. Corless, C.E., Guiver, M., Borrow, R., Edward-Jones, V., Kaczmarski, E.B., and Fox, A.J., *Contamination and sensitivity issues with a real-time universal 16S rRNA PCR.* Journal of Clinical Microbiology, 2000. **38**(5): p. 1747-1752.
211. Belgrader, P., Benett, W., Hadley, D., Long, G., Mariella, R.J., Milanovich, F., Nasarabadi, S., Nelson, W., Richards, J., and Stratton, P., *Infection disease: PCR detection of bacteria in seven minutes.* Science, 1999. **284**: p. 449.
212. Lagally, E.T., Medintz, I., and Mathies, R.A., *Single-molecule DNA amplification and analysis in an integrated microfluidic device.* Analytical Chemistry, 2001. **73**(3): p. 565-570.
213. Taylor, T.B., Winn-Deen, E.S., Picozza, E., Woudenberg, T., and Albin, M., *Optimization of the performance of the polymerase chain reaction in silicon-based microstructures.* Nucleic Acids Research, 1997. **25**(15): p. 3164-3168.
214. Zou, Q., Miao, Y., Chen, Y., Sridhar, U., Chong, C.S., Chai, T., Tie, Y., Teh, C.H.L., Lim, J.S., and Heng, C.K., *Micro-assembled multi-chamber thermal cycler for low-*

cost reaction chip thermal multiplexing. Sensors and Actuators A, 2002. **102**: p. 114-121.

215. Zou, Q., Sridhar, U., Chen, Y., and Singh, J., *Miniaturized independently controllable multichamber thermal cycler.* IEEE Sensors Journal, 2003. 3(6): p. 774.

216. Yu, X., Zhang, D.Y., Li, T., Hao, L., and Li, X., *3-D microarrays biochip for DNA amplification in polydimethylsiloxane (PDMS) elastomer.* Sensors and Actuators A, 2003. **108**: p. 103-107.

217. Burns, M.A., Johnson, B.N., Brahmasandra, S.N., Handique, K., Webster, J.R., Krishnan, M., Sammarco, T.S., Man, P.M., Jones, D., Heldsinger, D., Mastrangelo, C.H., and Burke, D.T., *An integrated nanoliter DNA analysis device*. Science, 1998. **282**(5388): p. 484-487.

218. Leamon, J.H., Lee, W.L., Tartaro, K.R., Lanza, J.R., Sarkis, G.J., deWinter, A.D., Berka, J., and Lohman, K.L., *A massively parallel PicoTiterPlate (TM) based platform for discrete picoliter-scale polymerase chain reactions*. Electrophoresis, 2003. **24**: p. 3769-3777.

219. Nagai, H., Murakami, Y., Morita, Y., Yokoyama, K., and Tamiya, E., *Development of a microchamber array for picoliter PCR*. Analytical Chemistry, 2001. **73**(5): p. 1043-1047.

220. Nagai, H., Murakami, Y., Yokoyama, K., and Tamiya, E., *High-throughput PCR in silicon based microchamber array*. Biosensors and Bioelectronics, 2001. **16**: p. 1015-1019.

221. Chaudhari, A.M., Woudenberg, T.M., Albin, M., and Goodson, K.E., *Transient liquid crystal thermometry of microfabricated PCR vessel arrays*. Journal of Microelectromechanical Systems, 1998. **7**(4): p. 345-355.

222. Yoon, D.S., Lee, Y.-S., Lee, Y., Cho, H.J., Sung, S.W., Oh, K.W., Cha, J., and Lim, G., *Precise temperature control and rapid thermal cycling in a micromachined DNA polymerase chain reaction*. Journal of Micromechanics & Microengineering, 2002. **12**: p. 813-823.

223. Kajiyama, T., Miyahara, Y., Kricka, L.J., Wilding, P., Graves, D.J., Surrey, S., and Fortina, P., *Genotyping on a thermal gradient DNA chip*. Genome Research, 2003: p. 467-475.

224. Cheng, J., Shoffner, M.A., Mitchelson, K.R., Kricka, L.J., and Wilding, P., *Analysis of ligase chain reaction products amplified in a silicon-glass chip using capillary electrophoresis*. Journal of Chromatography A, 1996. **732**(1): p. 151-158.

225. Gulliksen, A., Solli, L., Karlsen, F., Rogne, H., Hovig, E., Nordstrom, T., and Sirevag, R., *Real-time nucleic acid sequence-based amplification in nanoliter volumes*. Analytical Chemistry, 2004. **76**(1): p. 9-14.

226. Pal, D. and Venkataraman, V., *A portable battery-operated chip thermocycler based on induction heating*. Sensors and Actuators A, 2002. **102**: p. 151-156.

227. Krishnan, M., Ugaz, V.M., and Burns, M.A., *PCR in a Rayleigh-Benard convection cell.* Science, 2003. **298**(October): p. 793.

228. Wheeler, E.K., Benett, B., Stratton, P., Richards, J., Christian, A., Chen, A., Weisgrader, T., Ness, K., Ortega, J., and Milanovich, F. *Convectively driven polymerase chain reaction thermal cycler.* in *Micro Total Analysis Systems.* 2003. Squaw Valley, CA, USA.

229. Nakano, H., Matsuda, K., Yohda, M., Nagamune, T., Endo, I., and Yamane, T., *High-Speed Polymerase Chain-Reaction in Constant Flow.* Bioscience Biotechnology and Biochemistry, 1994. **58**(2): p. 349-352.

230. Curcio, M. and Roeraade, J., *Continuous segmented-flow polymerase chain reaction for high- throughput miniaturized DNA amplification.* Analytical Chemistry, 2003. **75**(1): p. 1-7.

231. Park, N., Kim, S., and Hahn, J.H., *Cylindrical compact thermal-cycling device for continuous-flow polymerase chain reaction.* Analytical Chemistry, 2003. **75**(21): p. 6029-6033.

232. Friedman, N.A. and Meldrum, D.R., *Capillary tube resistive thermal cycling.* Analytical Chemistry, 1998. **70**(14): p. 2997-3002.

233. Chiou, J., Matsudaira, P., Sonin, A., and Ehrlich, D., *A Closed-Cycle Capillary Polymerase Chain Reaction Machine.* Analytical Chemistry, 2001(9): p. 2018-2021.

234. Chiou, J., Matsudaira, P., Sonin, A., and Ehrlich, D.J. *Performance of a closed-cycle capillary polymerase chain reaction.* in *Micro Total Analysis System.* 2001.

235. Taylor, T.B., Harvey, S.E., Albin, M., Lebak, L., Ning, Y., Mowat, I., Schuerlein, T., and Principe, E., *Process control for optimal PCR performance in glass microstructures.* Journal of Biomedical Microdevices, 1998. **1**(1): p. 65-70.

236. Erill, I., Campoy, S., Erill, N., Barbe, J.C., and Aguilo, J., *Biochemical analysis and optimization of inhibition and adsorption phenomena in glass-silicon PCR-chips.* Sensors and Actuators B, 2003. **96**: p. 685-692.

237. Giordano, B.C., Ferrance, J., Swedberg, S., Huhmer, A.F.R., and Landers, J.P., *Polymerase chain reaction in polymeric microchips: DNA amplification in less than 240 seconds.* Analytical Biochemistry, 2001. **291**(1): p. 124-132.

238. Lou, X.J., Panaro, N.J., Wilding, P., Fortina, P., and Kricka, L.J., *Increased amplification efficiency of microchip-based PCR by dynamic surface passivation.* Biotechniques, 2004. **36**(2): p. 248-252.

239. Robinson, S. and Williams, P.A., *Inhibition of protein adsorption onto silica by polyvinylpyrrolidone.* Langmuir, 2002. **18**: p. 8743-8748.

240. Cui, D., Tian, F., Kong, Y., Titushikin, I., and Gao, H., *Effects of single-walled carbon nanotubes on the polyermase chain reaction.* Nanotechnology, 2004. **15**: p. 154-157.

241. Yoon, J.-Y. and Garrell, R.L., *Preventing biomolecular adsorption in electrowetting-based biofluidic chips.* Analytical Chemistry, 2003. **75**(19): p. 5097-5102.

242. Nishikawa, T. and Kambara, H., *Capillary Electrophoresis Temperature profile of buffer-filled electrophoresis capillaries using air convection cooling*. Electrophoresis, 1996. **17**: p. 1115-1120.

243. Burns, M.A., Johnson, B.N., Brahmasandra, S.N., Handique, K., Webster, J.R., Krishnan, M., Sammarco, T.S., Man, P.M., and Jones, D., *An Integrated Nanoliter DNA Analysis Device*. Science, 1998. **282**: p. 484-487.

244. Chaudhari, A.M., Woudenberg, T.M., Albin, M., and Goodson, K.E., *Transient Liquid Crystal Thermometry of Microfabricated PCR VEssel Arrays*. Journal of Micromechanical Systems, 1998. **7**: p. 345-355.

245. Davis, K.L., Liu, K.-L.K., Lanan, M., and Morris, M.D., *Spatially Resolved Temperature Measurements in Electrophoresis Capillaries by Raman Thermometry*. Analytical Chemistry, 1993. **65**: p. 293-298.

246. Davis, K.L., Liu, K.-L.K., Lanan, M., and M.D., M., *Spatially resolved temperature measurements in electrophoresis capillaries by Raman thermometry*. Analytical Chemistry, 1993. **65**(3): p. 293-298.

247. Liu, K.-L.K., Davis, L., and Morris, M.D., *Raman Spectroscopic Measurement of Spatial and Temporal Temperature Gradients in Operating Electrophoresis Capillaries*. Analytical Chemistry, 1994. **66**: p. 3744-3750.

248. Ross, D., Gaitan, M., and Locascio, L.E., *Temperature measurement in microfluidic systems using a temperature-dependent fluorescent dye*. Analytical Chemistry, 2001. **73**(17): p. 4117-4123.

249. Jeon, S., Turner, J., and Granick, S., *Noncontact Temperature Measurement in Microliter-Sized Volumes Using Fluorescent-Labeled DNA Oligomers*. Journal of the American Chemical Society, 2003. **125**(33): p. 9908-9909.

250. Suhling, K.K., French, P.M.W., and Phillips, D., *Time-resolved fluorescence microscopy*. Photochemical & Photobiological Sciences, 2005. **4**(1): p. 13-22.

2

Polymerase Chain Reaction on the Macroscale

Prior to performing continuous flow PCR in a microfluidic device the specific PCR components and reaction conditions were optimized in order to achieve the highest PCR yield. This chapter provides background information on the specific PCR system used in this thesis, an overview of the experimental system and the results of the optimization studies.

2.1 Bacillus Globigii - PCR System

All reactions performed involved amplifying *Bacillus globigii* which was provided in a purified and genomic form. *Bacillus globigii* is used as a biological tracer for anthrax because its size and dispersal characteristics are similar to those of anthrax [1]. The anthrax bacillus, *Bacillus anthracis*, was the first bacterium shown to be the cause of the disease. In 1877 Robert Koch grew the organism in pure culture and demonstrated its ability to form endospores (a structure which ensures the survival of a bacterium through periods of environmental stress) and produced experimental anthrax by injecting it into animals [2]. *Bacillus anthracis* approximates a large rod in shape, is 1 - 1.2 μm in width and 3 - 5 μm in length, and can be cultivated in ordinary nutrient media. Anthrax is a disease primarily affecting domesticated and wild animals, such as cattle, sheep, horses, mules and goats. Humans can become infected when brought into contact with the flesh, bones, hair and excrement of diseased animals. The natural history of *Bacillus anthracis* is obscure. In humans the most common form of the disease is cutaneous anthrax, which is usually aquired via injured skin or mucous membranes. A minor scratch or abrasion, usually on an exposed area of the face, or arms is inoculated by spores from the soil or a contaminated animal or carcass. In severe cases, where the blood stream has been invaded, the disease is frequently fatal. In addition inhalation of anthrax spores can lead to infection and disease. The possibility of creating aerosols containing anthrax spores has made *Bacillus anthracis* a chosen weapon for bioterrorism. Spores of *Bacillus anthracis* can be produced and stored in a dry form, and may remain viable for decades in storage or after release. Indeed anthrax has been used as a terrorist weapon. For example, in the United States in 2001, 22 people were infected by anthrax spores sent through the postal system [3]. Although no military use of anthrax is documented, it is suspected that several countries have stockpiled spores at various times for potential military use. Spores released by a military research facility in Sverdlovsk, USSR in 1979 led to the largest epidemic of inhalational anthrax in the twentieth century [3]. These incidents strongly corroborate the need for reliable and effective detection strategies.

The PCR system used within this project amplifies a specific (90 base pair) sequence of the anthrax gene. This is presented in Table 2.1.

90 base forward strand	
5' CTG TAT CCT AAT GGC GGC GTT GTC GAA GAT GAA GTG ACG CTT AAT CCA TTA AAA TCT TTG CTC CCT ACG GAT GCC GAA GGA GAA CAG ACG '3	
90 base reverse strand	
5' CGT CTG TTC TCC TTC GGC ATC CGT 'AGG GAG CAA AGA TTT TAA TGG ATT AAG CGT CAC TTC ATC TTC GAC AAC GCC GCC ATT AGG ATA CAG '3	
Conventional PCR	Real-time PCR
Forward primer 5' CTG TAT CCT AAT GGC GGC GTT GTC '3 Reverse primer 5' CGT CTG TTC TCC TTC GGC ATC CGT '3	Forward primer FAM – CCG CGA AGC GTC ACT TCA TCT TCG CGG – MR – HEG - CTG TAT CCT AAT GGC GGC GTT GTC Reverse primer 5' CGT CTG TTC TCC TTC GGC ATC CGT '3

Table 2.1 **Sequences of the 90 base forward (sense) and reverse (antisense) strand for both primer systems. The conventional system consists of a 24 base forward primer and a 24 base reverse primer. The real-time system differs slightly since its forward primer contains a fluorescent system which enables real-time detection.**

Amplification was performed using two primer systems; a conventional primer system where endpoint detection of the amplified product was conducted, and a real-time primer system where detection was accomplished throughout the time course of the reaction. Both primer systems and their specific sequences are presented in Table 2.1. While the conventional primer system consists of a 24 base forward and 24 base reverse primer, the real-time system differs slightly in the sequence of the forward primer. The forward primer defines a fluorescent system which enables online product detection. The mechanism for on-line detection is described in Figure 2.1. The fluorescent primer is called a Scorpion primer and was introduced by Whitcombe *et al.* [4] . A Scorpion primer consists of a specific probe sequence that is held in a hairpin loop configuration by two complementary strands which form a ladder-like structure (stem sequences) on both ends of the probe. A fluorophore (carboxyfluorescein, FAM) attached to the 5'-end is quenched by a moiety (normally methyl red, MR) which is joined to the 3'-end of the loop. Fluorescence quenching is a biomolecular process which decreases the intensity of fluorescence emission from a fluorophore. Quenching can occur via different mechanisms; here it is facilitated through fluorescent resonant energy transfer

(FRET). FRET occurs when the emission spectrum of one fluorophore (the donor) overlaps the absorption spectrum of a second fluorophore (the acceptor) and is proportional to their intermolecular separation [5]. Significantly quenching occurs only when the fluorophore and quencher are in close proximity. The hairpin loop is linked to the 5'-end of the primer via a PCR blocker which is hexethylene glycol (HEG) in most cases. A PCR blocker is a monomer which is incorporated into the oligonucleotide template and presents an impassible barrier. During PCR, these oligonucleotides no longer serve as templates for the polymerase beyond the insertion sites [4, 6]. After extension of the primer during PCR amplification, the specific probe sequence is able to bind to its complement within the same strand of DNA. This hybridization event opens the hairpin loop so that donor fluorescence is no longer quenched and an increase in signal is observed.

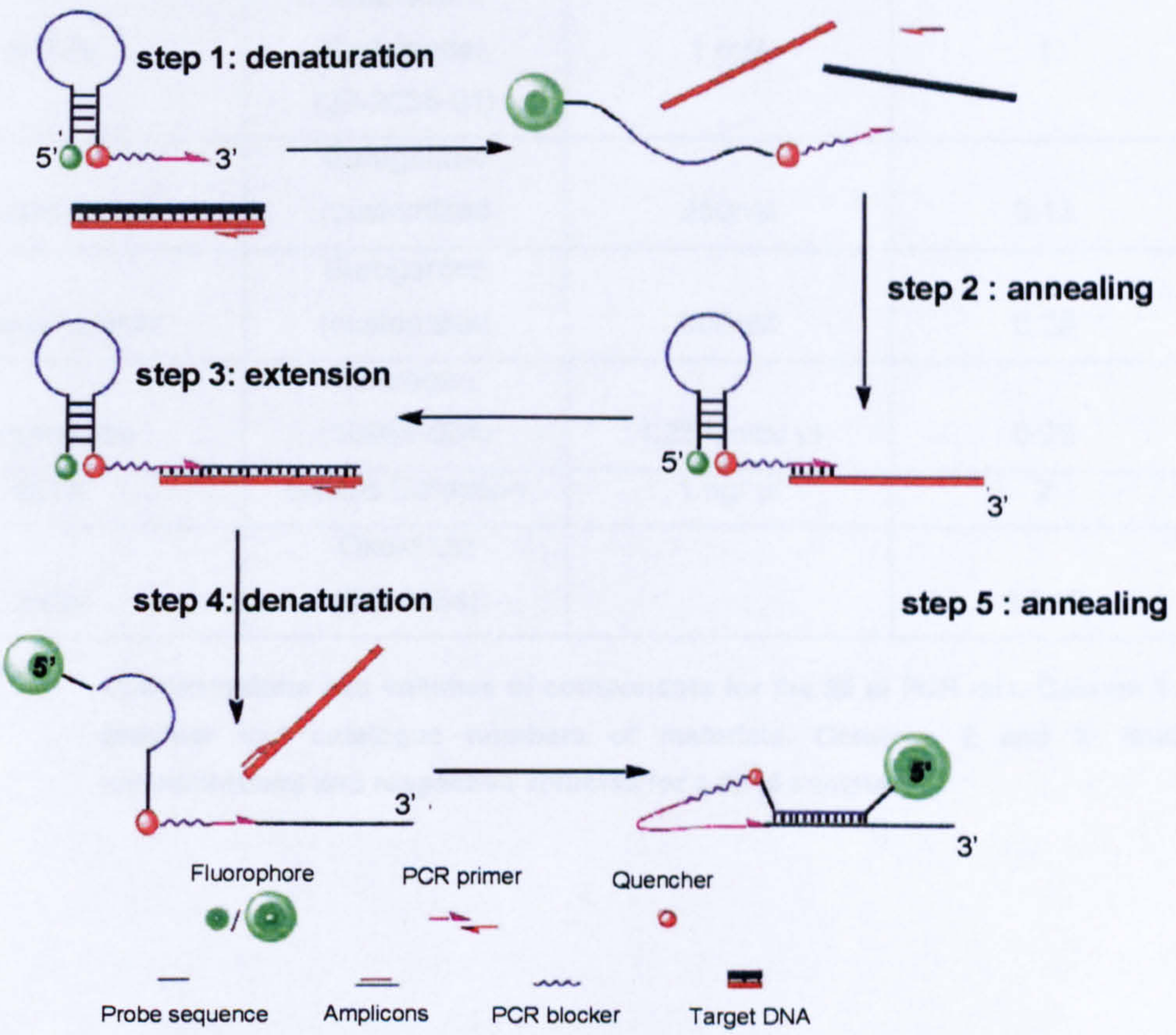


Figure 2.1 **Step 1: Target and Scorpion stem sequence are denatured. Step 2: Scorpion primer anneals to target. Step 3: Scorpion primer extends and produces double stranded DNA. Step 4: double-stranded DNA produced in step 3 is denatured. This results in a single-stranded target molecule with the Scorpion primer attached. Step 5: The mixture cools down and the Scorpion probe sequence binds to its target in an intramolecular manner.**

2.2 Experimental Methods

Volumes and concentrations of PCR components were prepared as described in Table 2.2. A total volume of 25 µl per reaction tube was used for all bulk experiments, with initial concentrations defined by the manufacturers (i.e. Invitrogen, Molecular Probes, Agilent). The prepared PCR mixture was thermally cycled according to protocols presented in Table 2.3. Analysis of both the conventional and the real-time PCR systems was accomplished using chip-based capillary gel electrophoresis.

Reactant	Provider	concentration	Volume (µl)
Tris-HCl, KCl buffer	Invitrogen (10966-034)	1X	2.5
$MgCl_2$	Invitrogen (10966-034)	5mM	2.5
dNTPs	Amersham Biosciences (27-2035-01)	1 mM	1
Forward primer	Eurogentec (customized	250nM	0.13
Reverse primer	Eurogentec (customized	500nM	0.25
Polymerase	Invitrogen (10966-034)	1.25 Units/ µl	0.25
DNA	Smiths Detection	1 ng/ µl	2
water	Oxoid Ltd (BO 0184)		16.12

Table 2.2 **Concentrations and volumes of components for the 25 µl PCR mix. Column 1: provider and catalogue numbers of materials. Columns 2 and 3: final concentrations and respective volumes for a 25 µl sample.**

Conventional System			Scorpion System		
Reaction step	Temperature (°C)	Time (seconds)	Reaction step	Temperature (°C)	Time (seconds)
Hot-start	95	30	Hot-start	95	30
Denaturation	95	5	Denaturation	95	1
Annealing/ Extension	65	10	Annealing/ Extension	65	6
Number of cycles	45		Number of cycles	45	
Total time (seconds)	705		Total time (seconds)	345	

Table 2.3 **PCR protocols for the conventional and real-time primer system. The conventional PCR is run for twice the length of the real time PCR system.**

2.2.1 Instrumentation

2.2.1.1 Thermal Cycler

A real-time thermocycler provides a fluorescence monitoring capability that permits quantitation of double stranded DNA at the end of each cycle. Four different real-time thermocyclers are commercially manufactured. These are the ABI 7700® (Applied Biosystems), the LightCycler® (Roche Molecular Diagnostics), the Smart Cycler® (Cepheid) and the Mx3000P® (Stratagene). The Smart Cycler, being the fastest thermocycler on the market, was used for all real-time PCR experiments within the current project. The instrument comprises 16 wells which can be controlled independently and thus enables simultaneous running of separate experiments. Furthermore, there are four excitation sources at wavelengths of 450-495nm, 500-550nm, 565-590nm and 630-650nm. Emission wavelengths of 510-527nm, 565-590nm, 606-650nm, 670-750nm), relate to the following reference dyes: FAM ($C_{21}H_{12}O_7$) or SYBR Green ($C_{32}H_{37}N_4S$), Cy3 ($C_{27}H_{33}N_2I$) or TET ($C_{25}H_{11}Cl_4NO_9$), Texas Red ($C_{37}H_{42}N_3S_2O_6$), and Cy5 ($C_{27}H_{33}N_4I$). This facility enables the user to measure fluorescence signals in four different channels simultaneously. Thermal cycling is performed using solid-state heaters and active (forced air) cooling. Table 2.4 provides physical performance data of the Smart Cycler and, Figure 2.2 depicts a basic schematic of the Smart Cycler indicating the relative locations and structure of the reaction and optical modules.

Heating ramp rate (max.)	10° C/sec from 95° C to 50° C
Cooling ramp rate (max.)	2.5° C/sec from 95° C to 50° C
Temperature duration accuracy	1.0 sec from programmed time
Temperature accuracy	0.5° C from 60° C to 95° C
Melt curve ramp rate	0.1° C/sec to 1° C/sec

Table 2.4 **Temperature performance data for the Smart Cycler: heating/cooling ramp rate, temperature accuracy and melt ramp rates.**

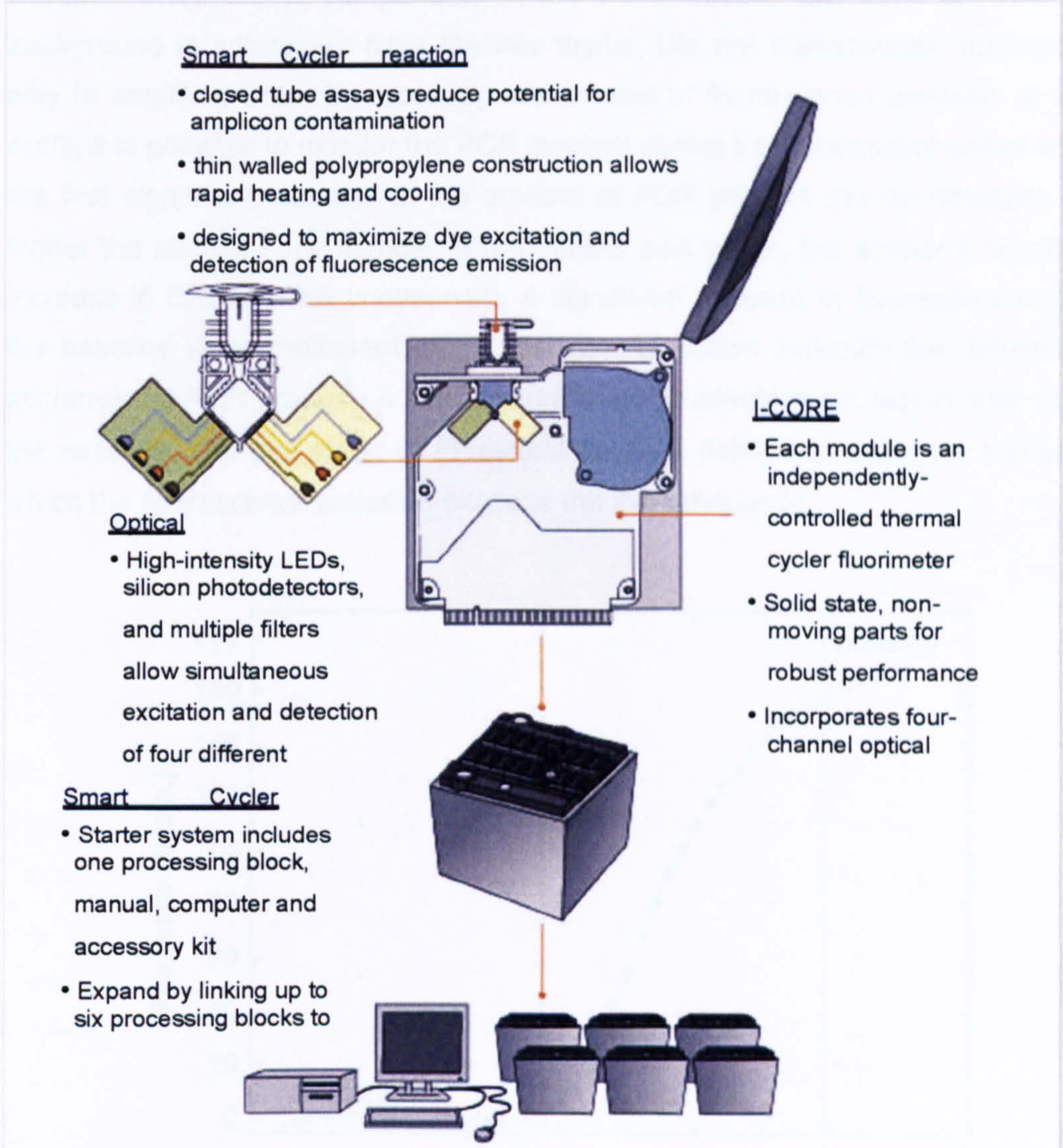


Figure 2.2 **The optical system allows the measurement of fluorescence in four channels at the same time. High intensity LEDs and optical filters are optimized for spectral separation. 16 independently programmable reaction sites can simultaneously perform 16 different cycling protocols in one system [7].**

Real time PCR offers the ability to monitor the reaction while it is taking place. A plot of fluorescence versus cycle number produces a sigmoidal shaped curve, called a growth curve. This curve can be divided into three different regions; baseline, the log-linear phase and the plateau which is presented in Figure 2.3. The base line phase of a PCR growth curve represents the background fluorescence. Background fluorescence is a property of real time PCR and can be defined as the fluorescence originating from unbound-probe, non-specific cleavage of probe or sample auto-fluorescence. The linear phase represents both background fluorescence and fluorescence corresponding to amplified DNA. The exponential growth curve plateaus when critical components of the PCR reaction are used up. After the background is subtracted from the raw signal, the net fluorescence corresponds only to amplified DNA. By recording the amount of fluorescence emission at each cycle, it is possible to monitor the PCR reaction during the exponential phase where the first significant increase in the amount of PCR product can be detected. The higher the starting copy number of the nucleic acid target, the sooner a significant increase in fluorescence is observed. A significant increase in fluorescence above the baseline value measured during the 13 - 15 cycles indicates the detection of accumulated PCR product. A fixed fluorescence threshold is set significantly above the baseline. The parameter C_t (threshold cycle) is defined as the cycle number at which the fluorescence emission exceeds the fixed threshold.

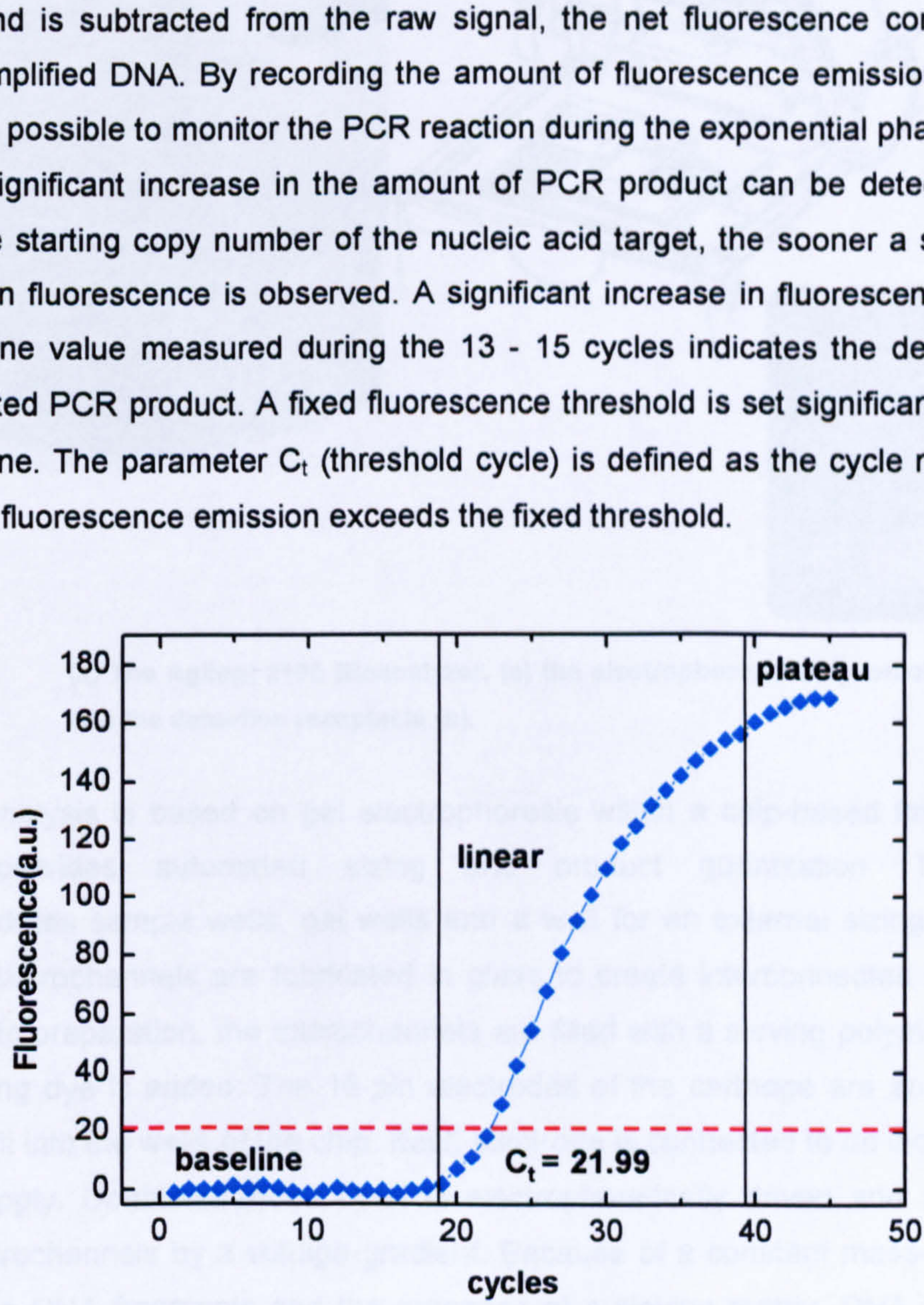


Figure 2.3 **A plot of fluorescence versus cycle number produces a sigmoidal shaped curve called the growth curve with baseline, log-linear and plateau regions.**

2.2.1.2 Chip-Based Gel-Electrophoresis Instrument

While real-time PCR could be analysed by calculation of C_t values, conventional PCR systems were analysed using endpoint analysis. This was performed on the Agilent 2100 Bioanalyzer, (a chip-based electrophoresis instrument) that allows analysis of DNA, RNA, proteins and cells. Figure 2.4 shows sample images of the instrument and the electrophoretic chip.

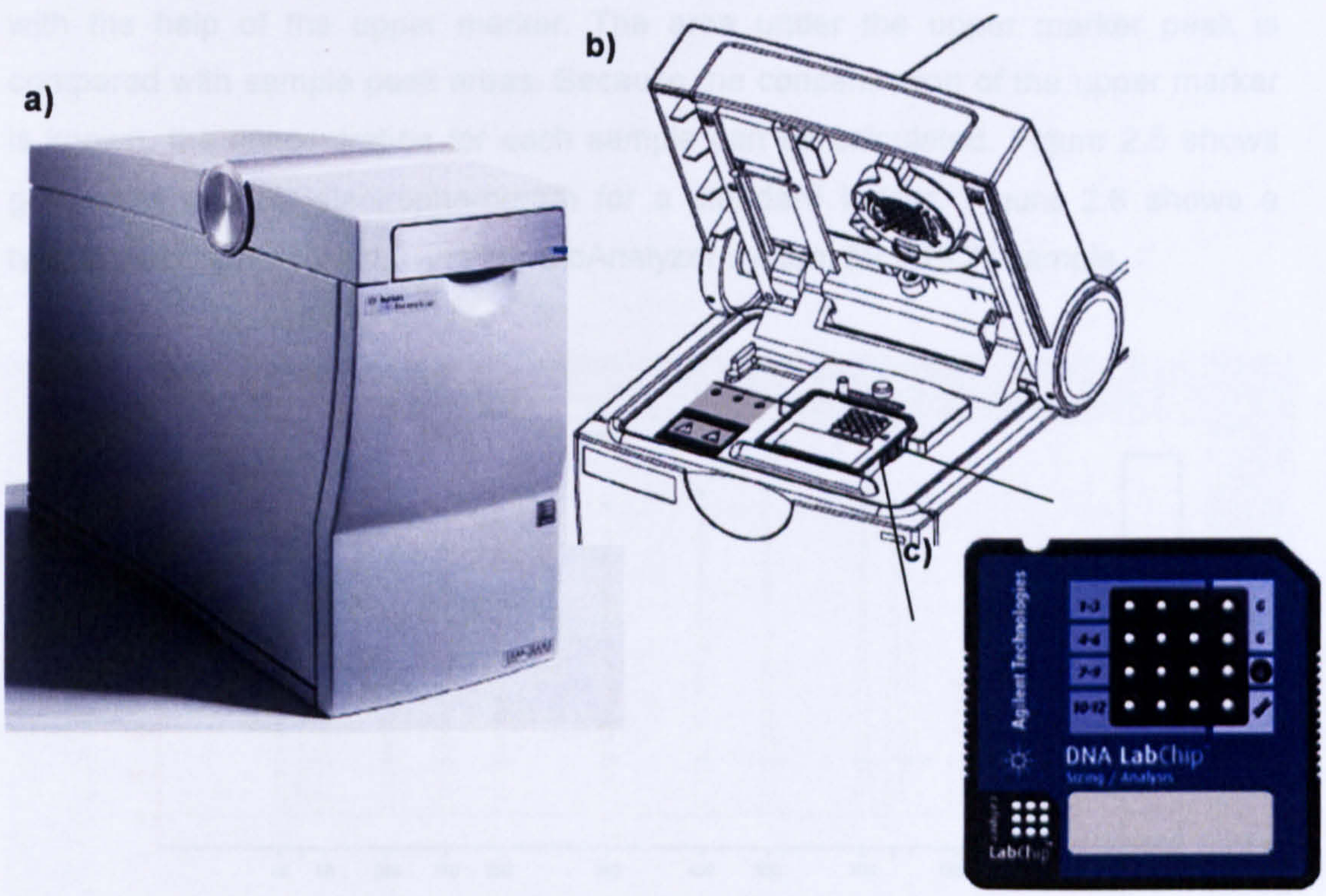
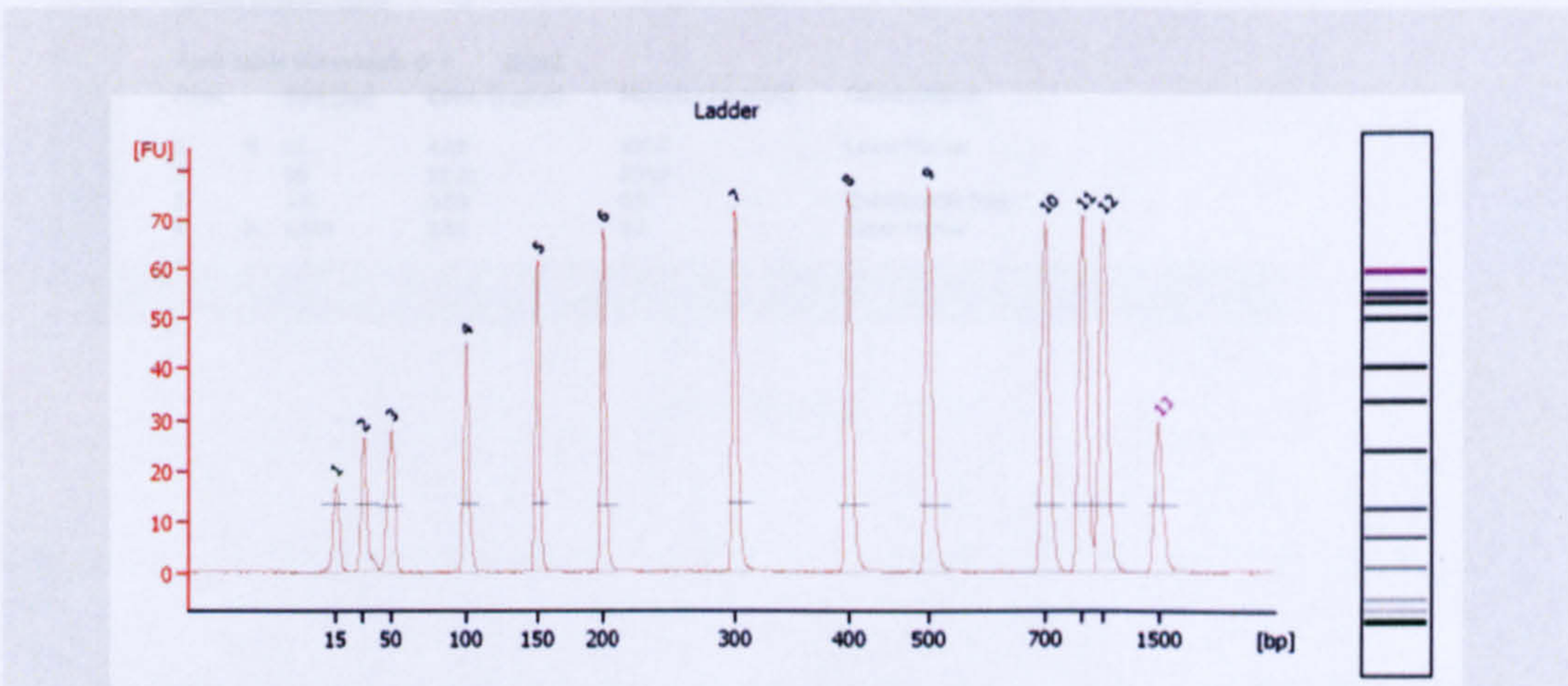


Figure 2.4 **(a) The Agilent 2100 Bioanalyzer, (c) the electrophoresis chip which is placed into the detection receptacle (b).**

Product analysis is based on gel electrophoresis within a chip-based format. The system provides automated sizing and product quantitation. The chip accommodates sample wells, gel wells and a well for an external sizing standard (ladder). Microchannels are fabricated in glass to create interconnected networks. During chip preparation, the microchannels are filled with a sieving polymer and an intercalating dye is added. The 16-pin electrodes of the cartridge are arranged so that they fit into the wells of the chip. Each electrode is connected to an independent power supply. Double-stranded DNA is electrophoretically driven and separated within microchannels by a voltage gradient. Because of a constant mass-to-charge ratio of the DNA fragments and the presence of a sieving matrix, DNA fragments are separated according to size, with smaller fragments migrating faster than larger ones. The intercalating dye SYBRGreen is used to quantify double stranded DNA

using laser-induced fluorescence. Data are translated into gel-like images and electropherograms using a DNA ladder containing components of known sizes. From the migration times measured for each fragment in the sample, the size of the target can be calculated. Two markers are run with each of the samples bracketing the overall size range. The "lower" and "upper" markers are internal standards used to align the ladder data with data from the sample wells. Quantitation is performed with the help of the upper marker. The area under the upper marker peak is compared with sample peak areas. Because the concentration of the upper marker is known, the concentration for each sample can be calculated. Figure 2.5 shows gel bands and an electropherogram for a standard ladder. Figure 2.6 shows a typical electropherogram using the BioAnalyzer system for a PCR sample.



Peak table for Ladder

Peak	Size [bp]	Conc. [ng/µl]	Molarity [nmol/l]	Observations
1	15	4.20	424.2	Lower Marker
2	25	4.00	242.4	Ladder Peak
3	50	4.00	121.2	Ladder Peak
4	100	4.00	60.6	Ladder Peak
5	150	4.00	40.4	Ladder Peak
6	200	4.00	30.3	Ladder Peak
7	300	4.00	20.2	Ladder Peak
8	400	4.00	15.2	Ladder Peak
9	500	4.00	12.1	Ladder Peak
10	700	4.00	8.7	Ladder Peak
11	850	4.00	7.1	Ladder Peak
12	1,000	4.00	6.1	Ladder Peak
13	1,500	2.10	2.1	Upper Marker

Figure 2.5 **An electropherogram for a standard DNA ladder. The concentrations and sizes of the individual base pairs are preset in the assay.**

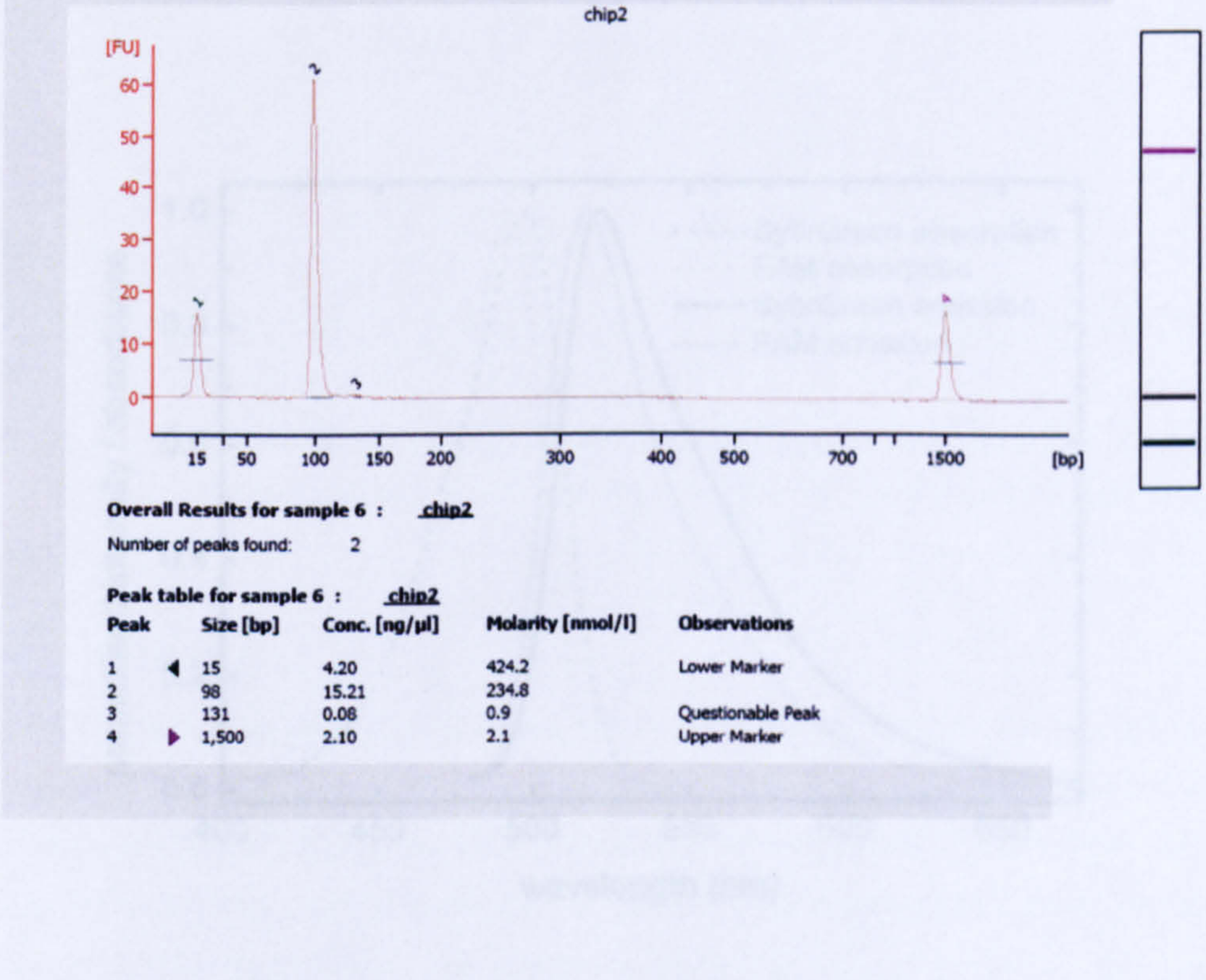


Figure 2.6 **An electropherogram of an amplified DNA sample (middle peak) bracketed by the lower marker (left peak) and the upper marker (right peak). The lower marker and upper marker are internal standards used to align the ladder data with data from the sample wells.**

For quantitative analysis of chip-based gel electrophoresis experiments concentration (ng/µl), molarity (nmol/l), sample area value, migration time (s) or product peak height of the references and samples can be compared with each other. This method of analysis works well for the conventional PCR system but problems were experienced when analyzing products from the real-time PCR system. Signal intensities of peaks originating from the real-time PCR system are approximately one order of magnitude lower than those originating from the conventional PCR system. In addition to this reduced intensity, doublets and triplets, were observed for the real-time PCR system which is down to the nature of the scorpion primers, and detection is compromised due to signal crosstalk between,

SYBR Green and FAM as both fluorescent dyes have similar absorption and emission spectra (Figure 2.7). Figure 2.8 presents electropherograms of products from both the conventional and the real-time PCR system.

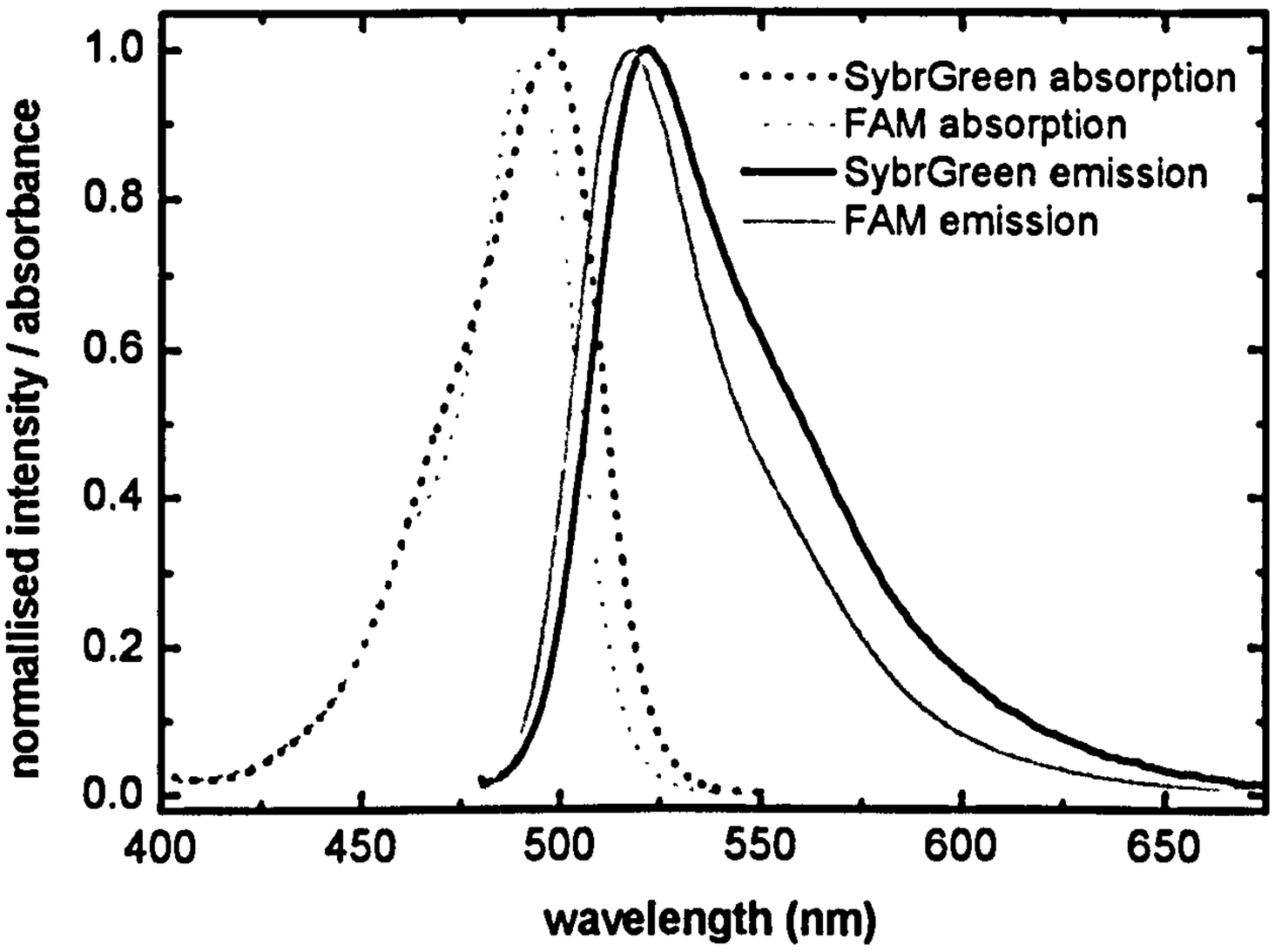


Figure 2.7 Normalised absorption and emission spectra of FAM and SYBR Green.

Fluorescence measurements were performed by comparing the emission intensity of a FAM sample, a SYBRGreen sample and a mixture of both samples. The outcome of these measurements confirmed that the signal intensity is significantly reduced when both samples are present in the same mixture.

Attempts to sequence the real-time PCR doublet and triplet products failed, since all hybridization dyes used for the sequencing had similar absorption and emission spectra to FAM. Consequently detection is compromised due to signal crosstalk between, FAM and the sequencing dyes. And for the real-time PCR system doublet or triplet product peaks are expected.

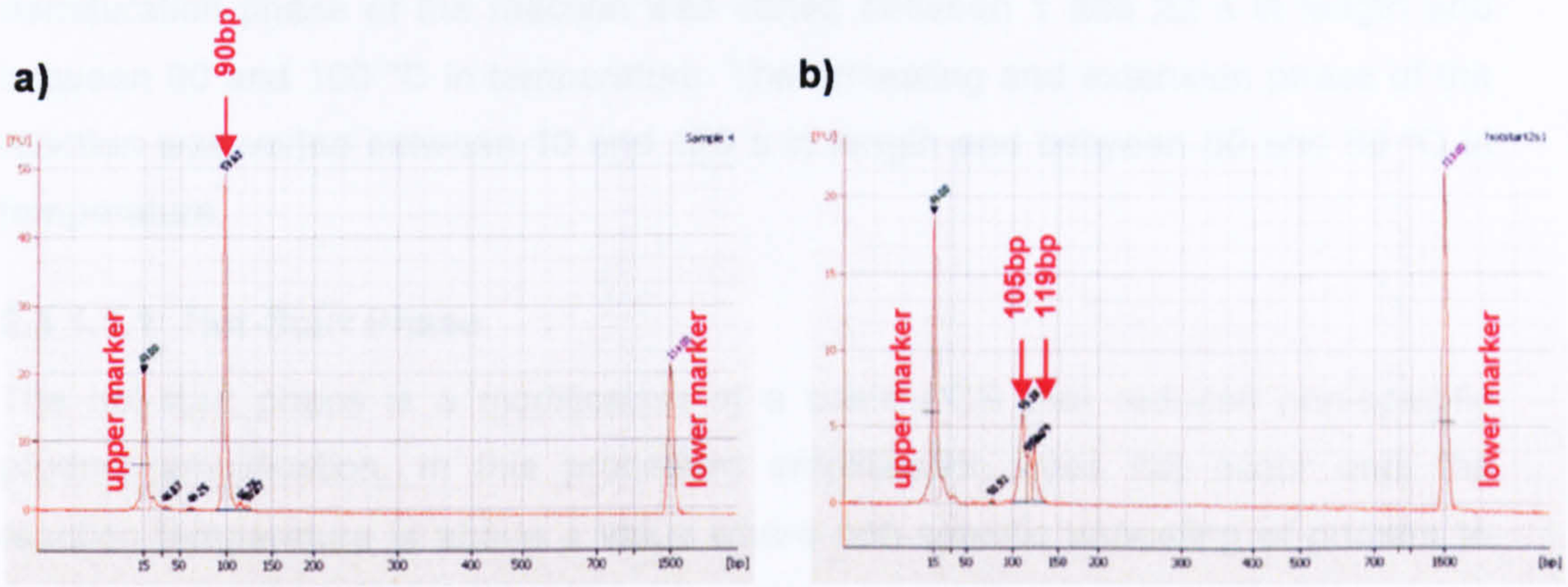


Figure 2.8 **a) Electropherogram of product amplified using a conventional PCR system.**
b) Electropherogram of products amplified using a real-time PCR sytem.

2.3 Results

Both PCR systems used in this thesis were provided by Smiths Detection Ltd. with recommended protocols listed in Tables 2.2 and 2.3. Ultimately both reaction systems would be transferred to a microfluidic format. Prior to transferal, the bulk scale PCR systems were investigated to assess their robustness towards variations in experimental parameters. The examined parameters were divided in two groups. Firstly modifications in thermocycling conditions such as temperature, temperature ramp rates, time and number of cycles were studied. Secondly variations in the relative concentrations of all PCR components and additives were investigated. The results of these studies and their implications for microfluidic PCR are now discussed.

2.3.1 Optimization of Thermal Cycling Conditions

Important parameters which will influence the design of the envisioned microfluidic device are discussed in this section. Understanding if and how times, temperatures, cycle numbers and ramp rates influence the efficiency of the *Bacillus globigii* PCR reaction will provide valuable information when designing the continuous flow PCR microdevice.

2.3.1.1 Temperature and Time

In this section the effects of time and temperature on amplification efficiency are discussed. In the current experiments the hot-start phase of the reaction was varied between 1 and 120 s in length and between 90 and 100 °C in temperature. The

denaturation phase of the reaction was varied between 1 and 22 s in length and between 90 and 100 °C in temperature. The annealing and extension phase of the reaction was varied between 10 and 120 s in length and between 50 and 80 °C in temperature.

2.3.1.1.1 Hot-Start Phase

The hot-start phase is a modification of a basic PCR that reduces non-specific product amplification. In this procedure amplification does not occur until the reaction temperature is above a value where non-specific annealing of primers to target occurs. This 'blockage' of amplification is usually accomplished using a DNA polymerase that is inactive at low temperatures. In the current experiments Platinum *Taq* DNA polymerase is used for this purpose. Here the *Taq* DNA polymerase is complexed with an antibody that inhibits its activity. Due to the specific binding of the inhibitor to the enzyme, Platinum *Taq* DNA polymerase is inactive until it is denatured. For the PCR of *Bacillus globigii* a hot-start of 30 s at 95 °C is specified by the manufacturer as listed in Table 2.3.

2.3.1.1.1.1 Conventional PCR System

Data resulting from the variation of the hot-start duration times and temperatures are presented in Figures 2.9 and 2.10 respectively. High product peak areas were observed for hot-start times between 10 and 20 s. Peak areas were then observed to decrease for times greater than 30 seconds. These data indicate that the hot-start time should be kept lower than 20 s. Studies assessing the hold temperature for the hot-start phase demonstrate highest peak areas between 95 and 96 °C. At temperatures higher than 96°C the hot-start activation is seen to be less efficient. The significant reduction in efficiency at temperatures above 100°C is most likely due to denaturation of both the enzyme and the DNA. Consequently the optimum conditions for the hot-start phase were considered to be between 95 and 96 °C for times below 20 s.

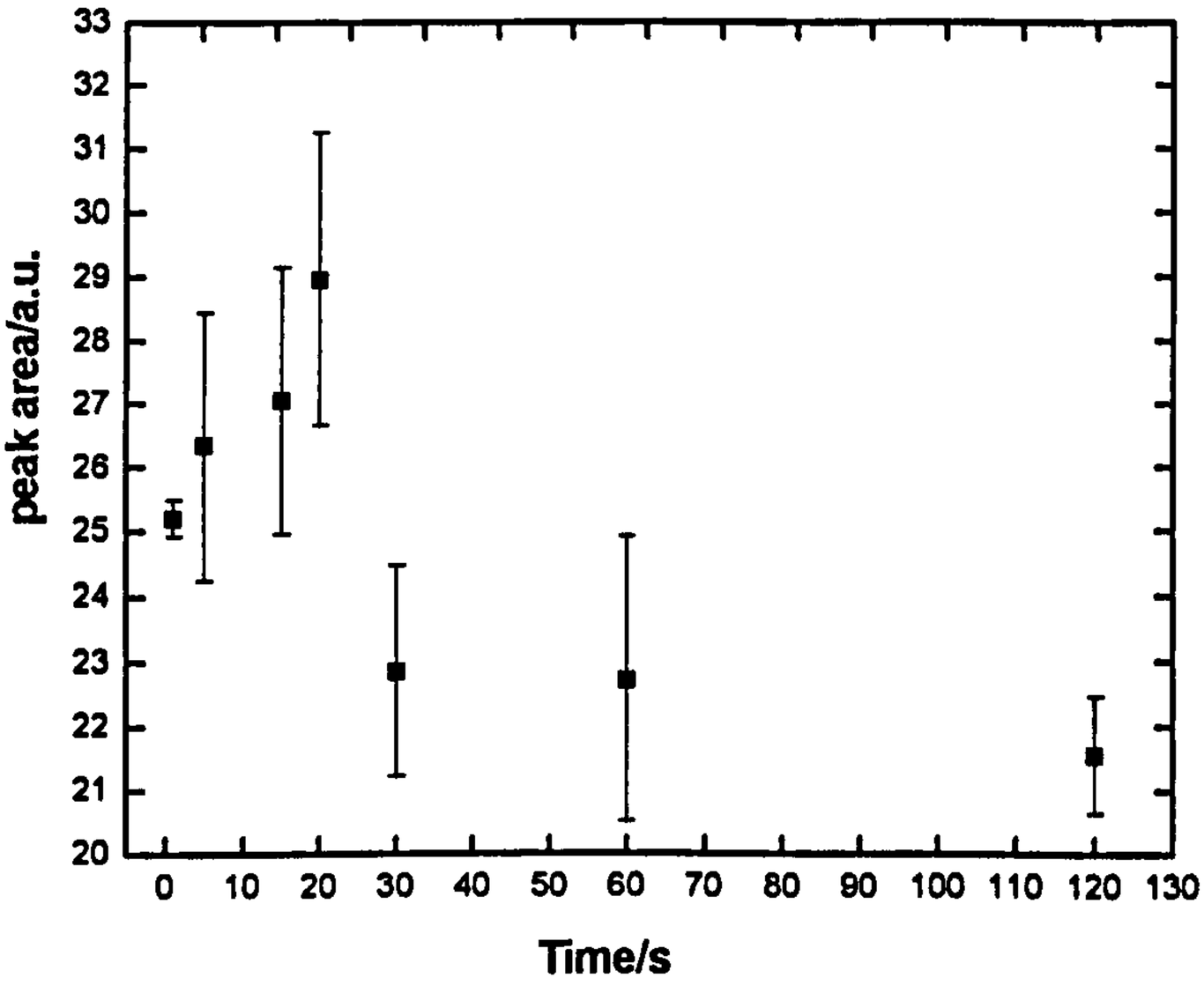


Figure 2.9 **Variation of peak area as a function of time during the hot start phase. Five replicates were used to define each data point with hot a start temperature at 95°C.**

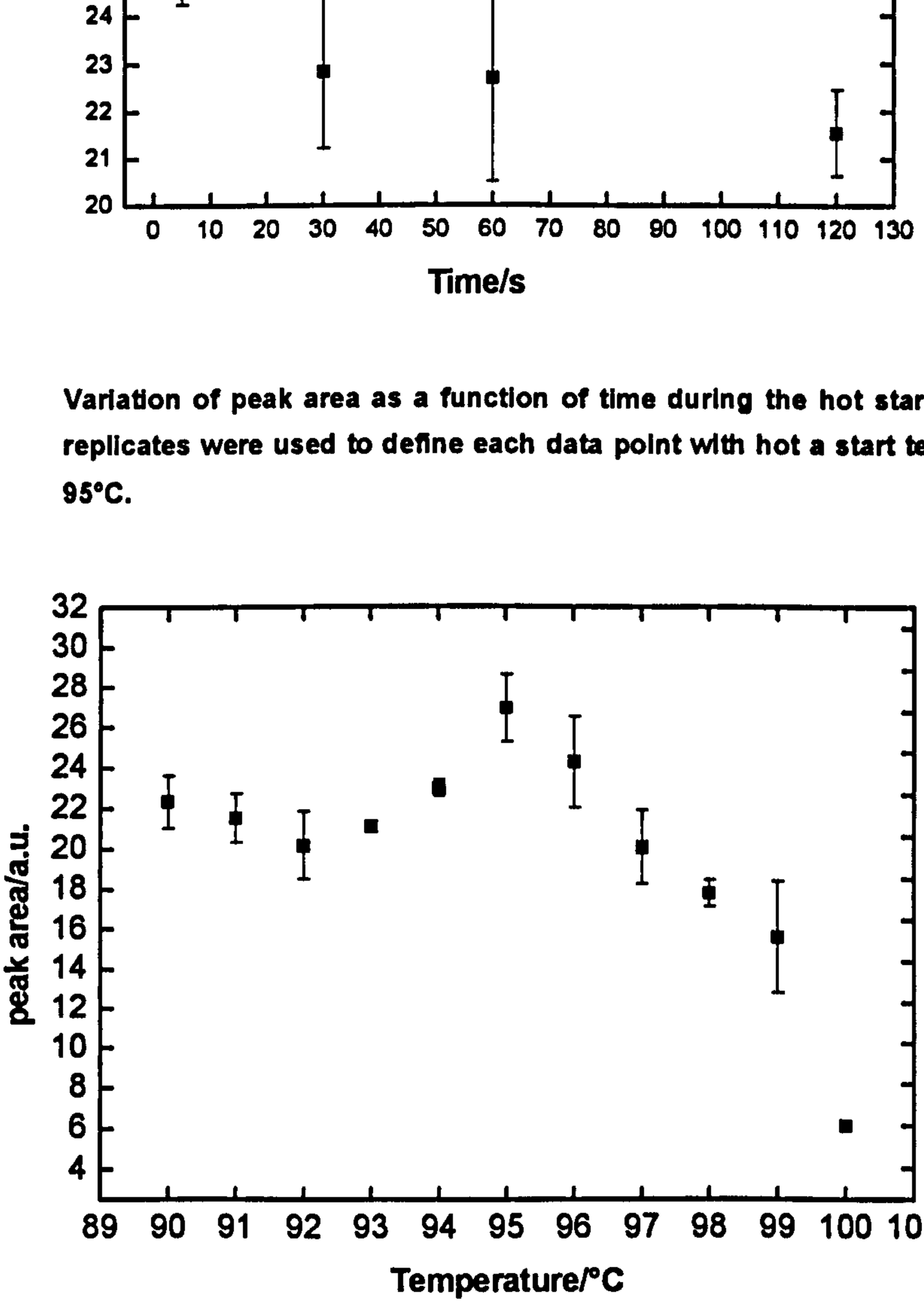


Figure 2.10 **Variation of peak area as a function of temperature during the hot start phase. Five replicates were used to define each data point with a hot start duration of 30s.**

2.3.1.1.1.2 Real-Time PCR System

Smart Cycler and BioAnalyzer results from the variation of the hot-start phase times are presented in Figures 2.11 and 2.12 respectively. Results of studies assessing the variation of efficiency with hot start phase temperatures are shown in Figures 2.13 and 2.14 respectively. While the Smart Cycler data in Figure 2.11 indicate a negligible influence of the hot-start phase times on the PCR efficiency, BioAnalyzer results in Figure 2.12 indicate higher reaction efficiencies at times below 20 seconds. Studies assessing the role of temperature in the hot-start phase (Figures 2.13 and 2.14) demonstrate highest peak areas between 92 and 96°C. At temperatures lower than 91°C and higher than 96°C the hot-start activation is less efficient (evidenced by a gradual increasing C_t value). Consequently optimum conditions for the hot - start phase involve temperatures between 92 and 96°C and a duration below 20s.

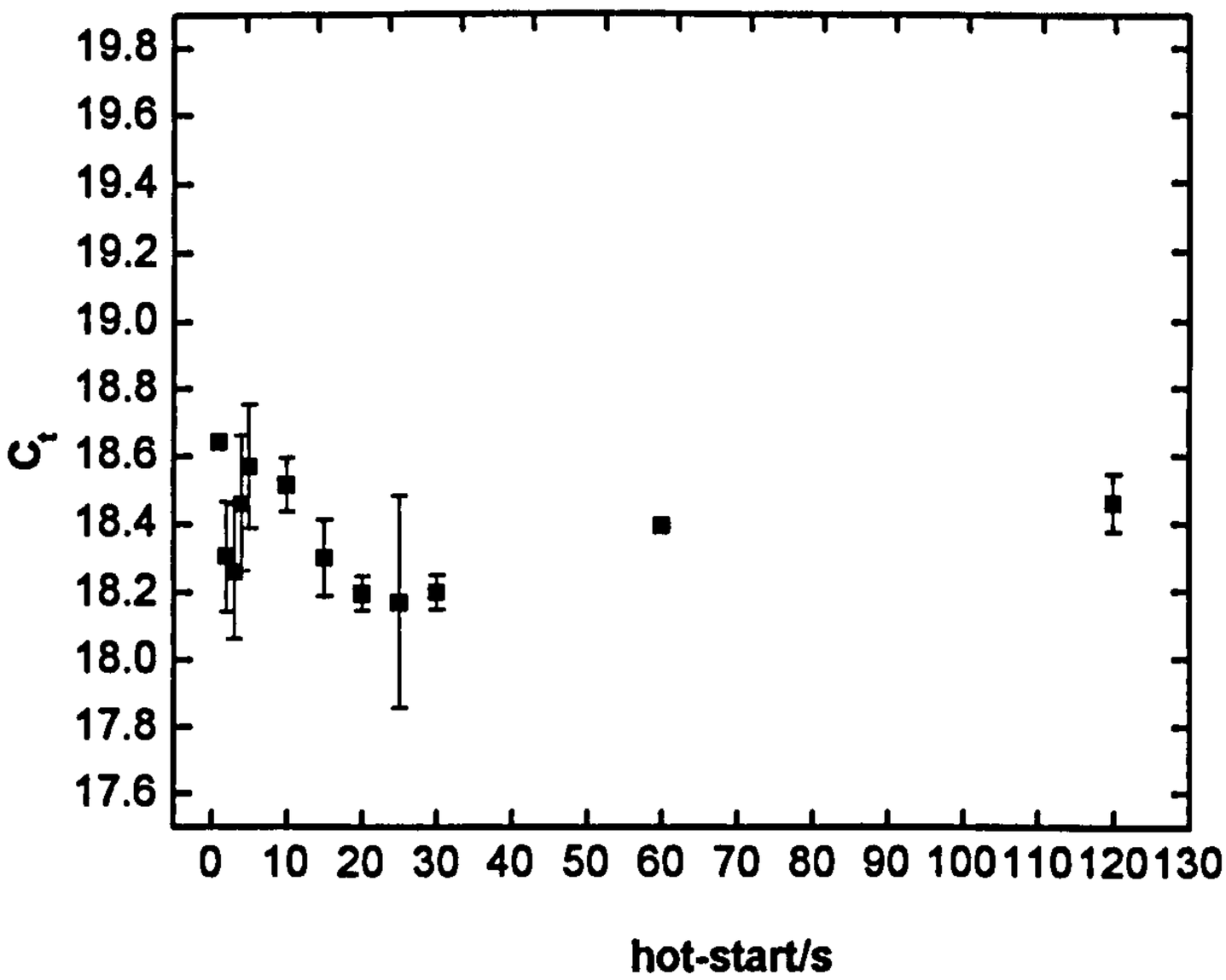


Figure 2.11 Variation of C_t value as a function of time during the hot start phase. Five replicates were used to define each data point with the hot start temperature set to 95°C.

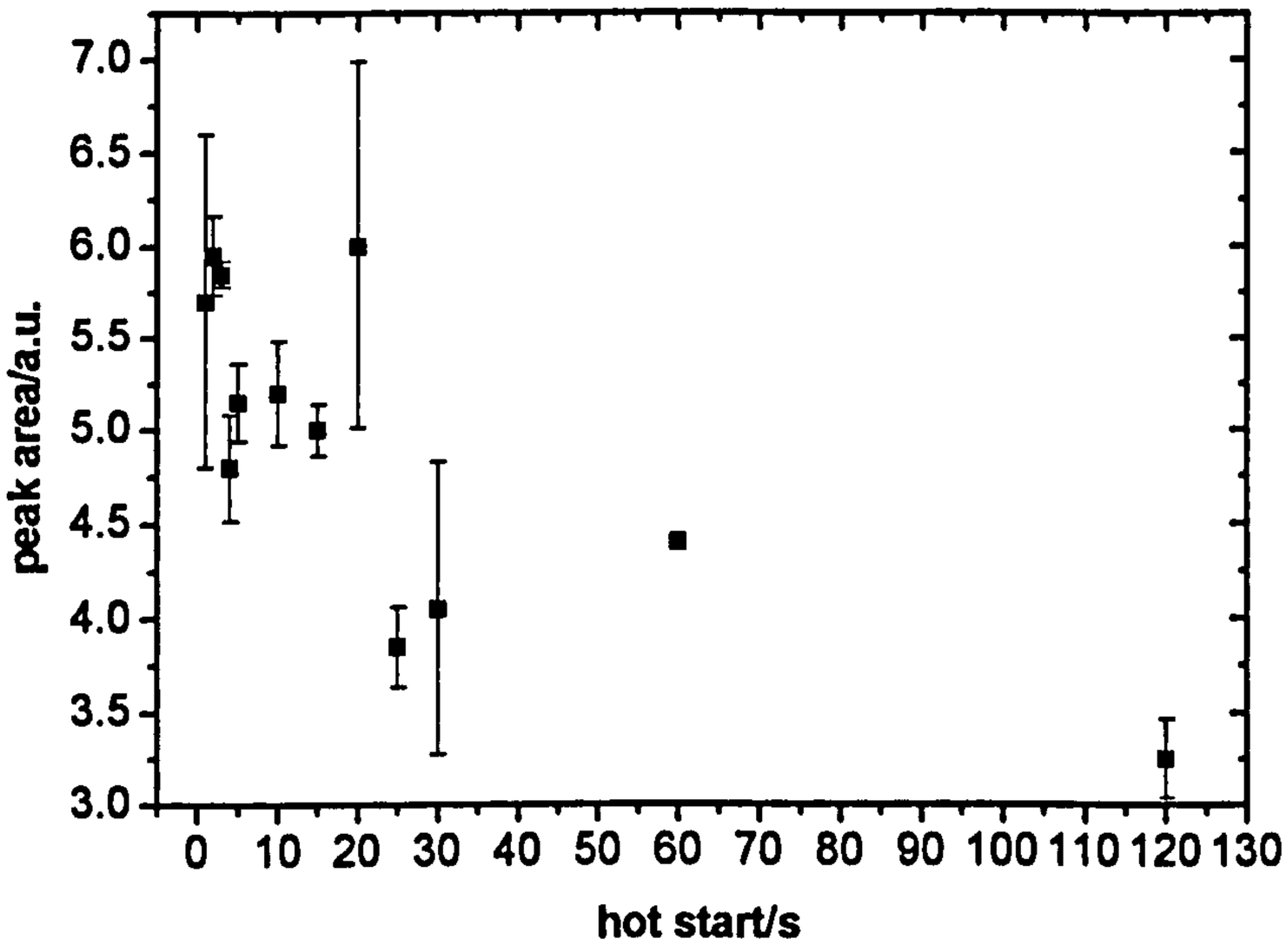


Figure 2.12 Variation of peak area as a function of time during the hot start phase. Five replicates were used to define each data point with a hot start temperature of 95°C.

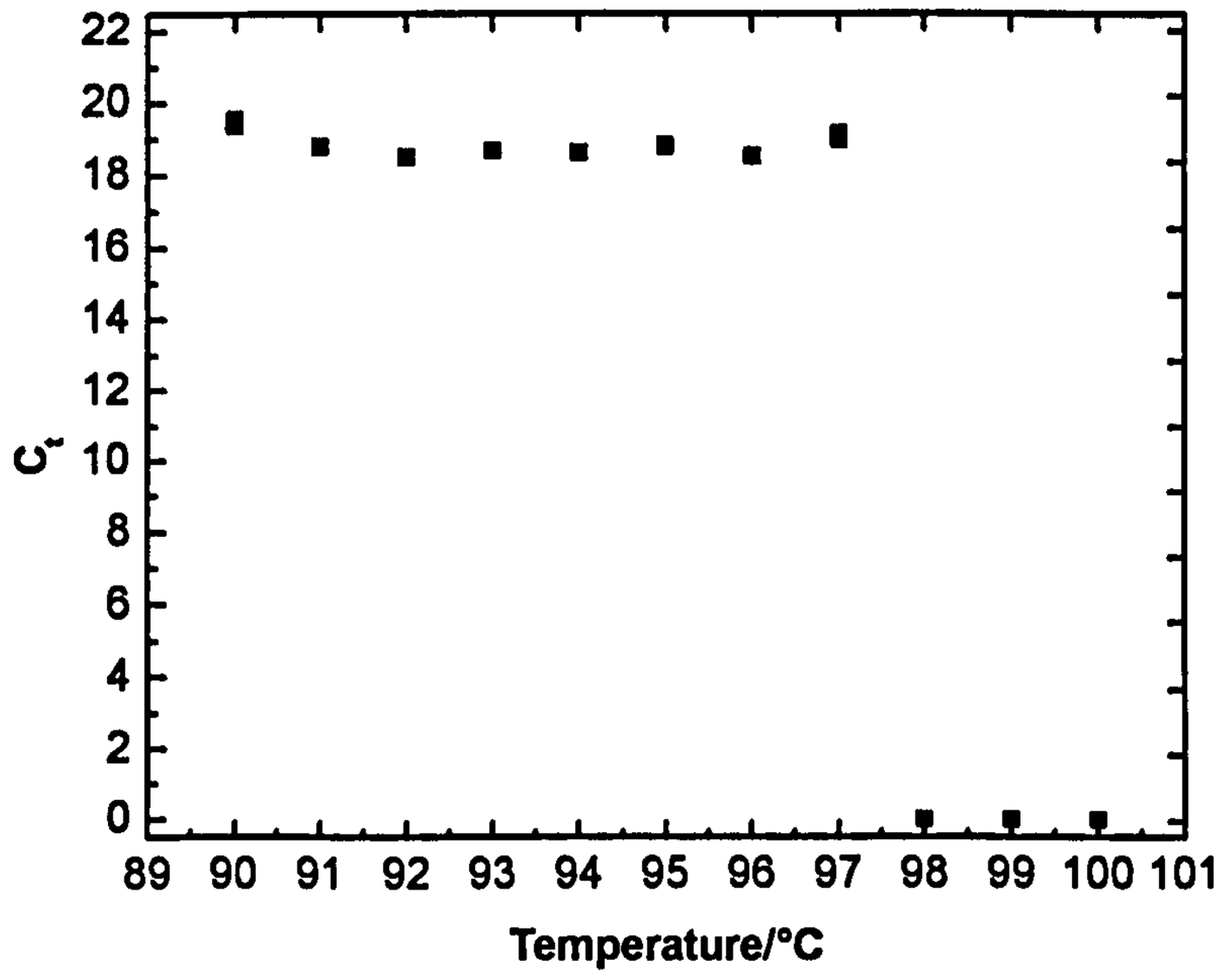


Figure 2.13 Variation of C_t value as a function of temperature during the hot start phase. Five replicates were used to define each data point with a hot start duration of 30s.

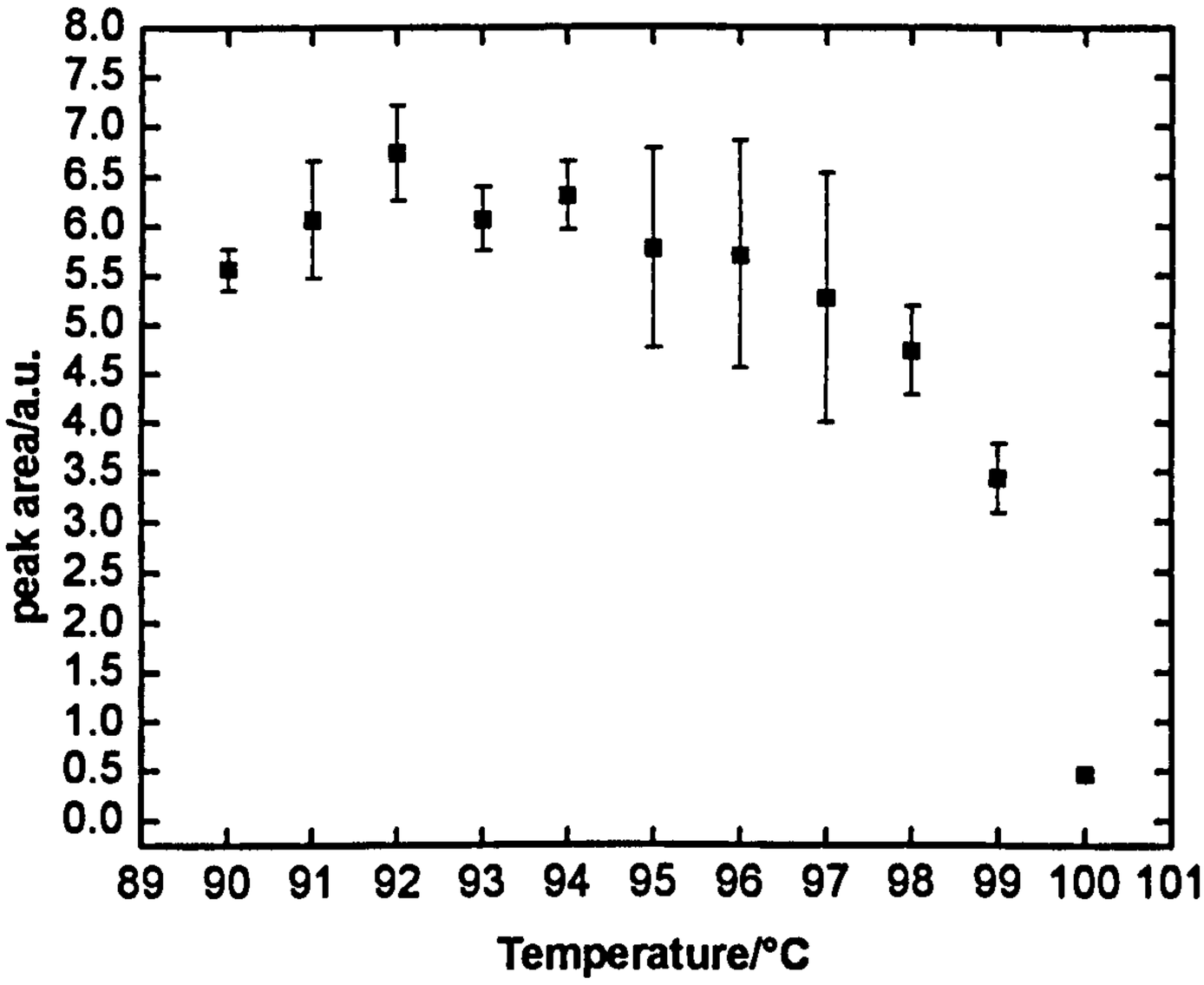


Figure 2.14 **Variation of peak area as a function of temperature during the hot start phase. Five replicates were used to define each data point with hot start times of 20s.**

In conclusion, optimum hot-start phase conditions for the conventional PCR system involve temperatures between 94 and 96°C and a duration below 20s while temperatures between 92 and 96 °C and a duration below 20s are required for the real-time PCR hot-start phase.

2.3.1.1.2 Denaturation

The denaturation step is the process in which the hydrogen bonds of the double stranded DNA are broken apart, to create two single strands. This step generally occurs at temperatures between 94 and 96°C over a period of a few seconds. For *Bacillus globigii* standard denaturation conditions are listed in Table 2.3.

2.3.1.1.2.1 Conventional PCR System

An assessment of the importance of denaturation time and temperatures was performed with results presented in Figures 2.15 and 2.16. As can be seen in Figure 2.15 highest peak areas are observed for denaturation times between 1 and 4s. As denaturation times are increased beyond 4 seconds a progressive decrease in peak height is observed which is due to the fact that most probably the DNA begins to irreversible denature. Variation of the denaturation temperature (Figure 2.16) illustrates highest peak areas in the vicinity of 92°C, with lower and higher

temperatures resulting in lower sample peak area values. Consequently optimum conditions for the denaturation phase were defined by temperatures between 90 and 94°C and durations below 4s.

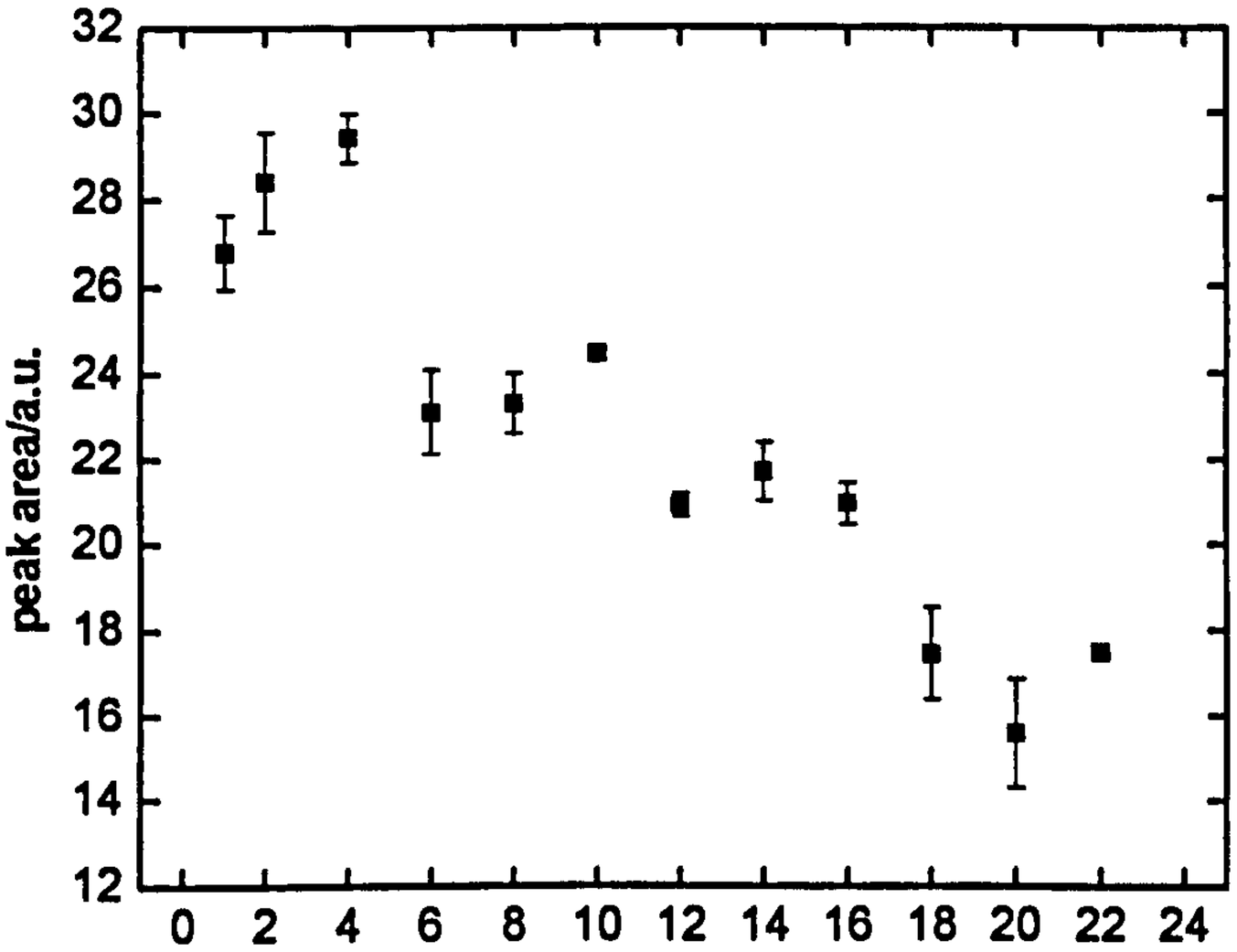


Figure 2.15 Variation of peak area as a function of time during the denaturation phase. Five replicates were used to define each data point with a denaturation temperature of 95°C.

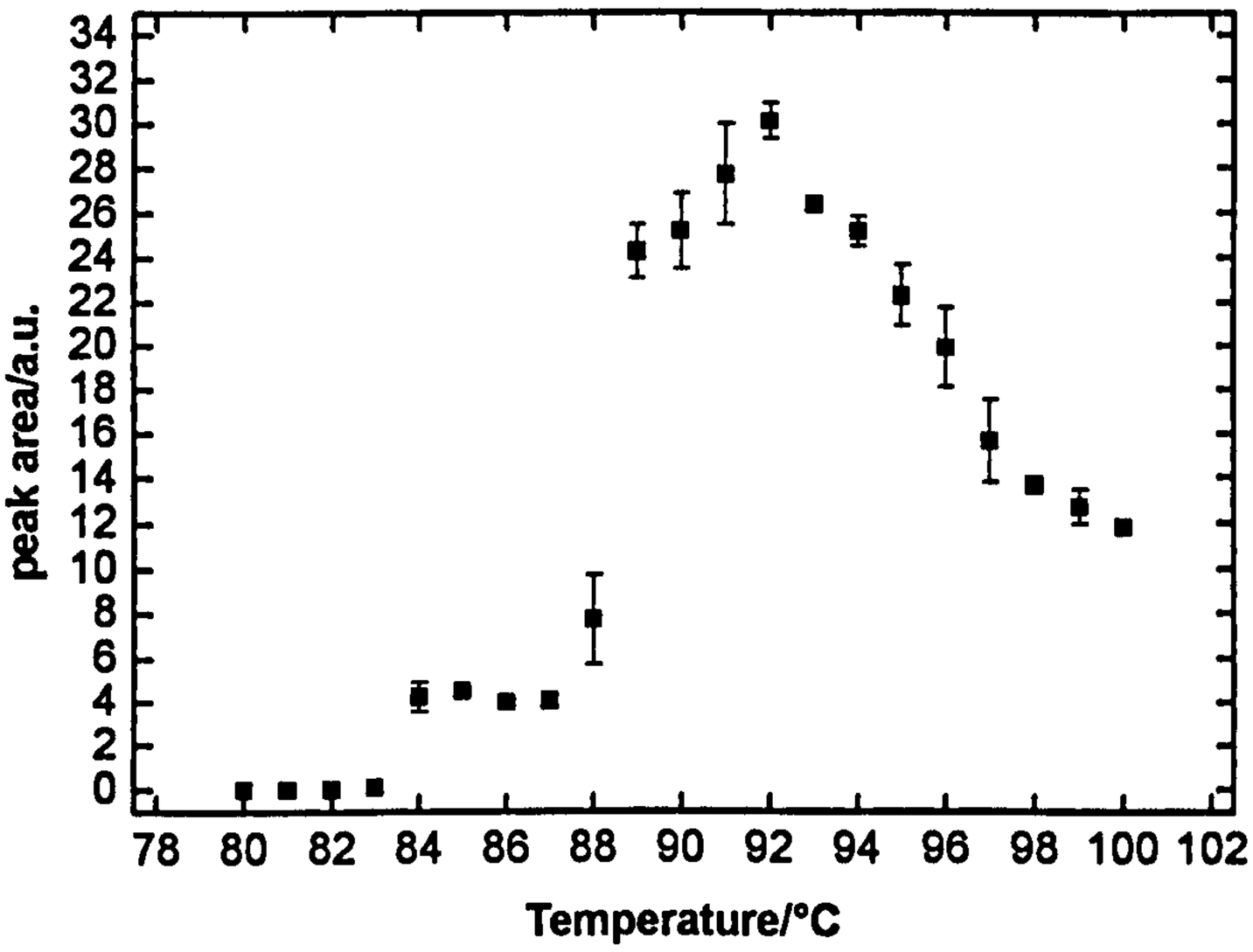


Figure 2.16 Variation of peak area as a function of temperature during the dentauration phase. Five replicates were used to define each data point with a denaturation time of 5s.

2.3.1.1.2.2 Real-Time PCR System

Smart Cycler and BioAnalyzer data summarizing the influence of denaturation phase times on efficiency are presented in Figures 2.17 and 2.18 respectively and data summarizing the influence of denaturation phase temperatures on efficiency are presented in Figures 2.19 and 2.20 respectively. Smart Cycler results in Figure 2.17 show little influence of denaturation phase times on the amplification efficiency. Figure 2.18 demonstrates highest product peak areas at a denaturation time of 2s. Peak areas were observed to decrease at longer times. These data indicate that the denaturation duration should be approximately 2s. Studies assessing the temperature for the denaturation phase demonstrate highest peak areas between 90 and 98°C. At temperatures lower than 90°C denaturation is less efficient. For denaturation temperatures lower than 86°C and higher than 98°C no denaturation is observed at all and the PCR fails. Consequently optimum conditions for the denaturation phase are defined by temperatures between 90 and 98°C and a duration of 2s.

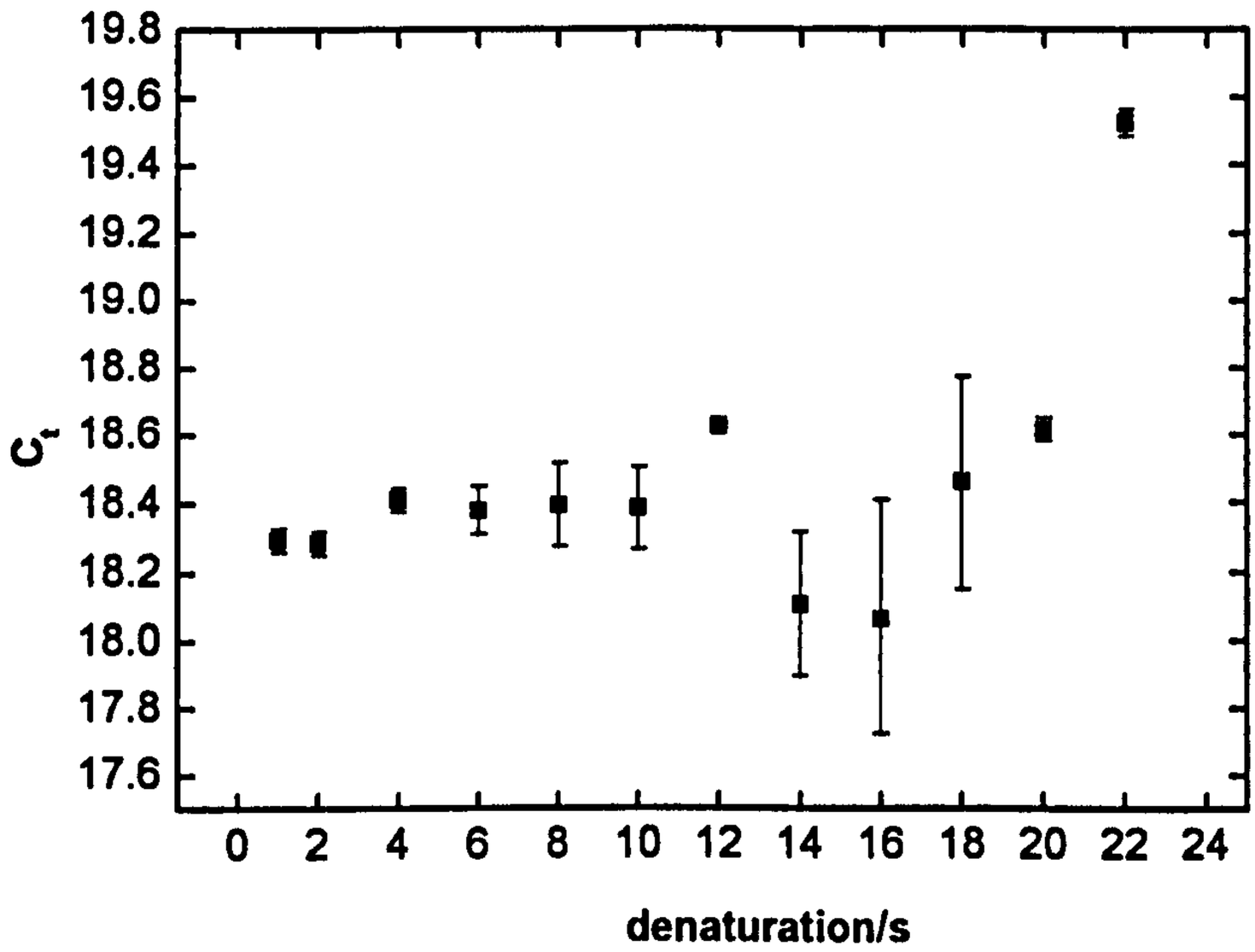


Figure 2.17 **Variation of C_t value as a function of time during the denaturation phase. Five replicates were used to define each data point with a denaturation temperature of 95°C.**

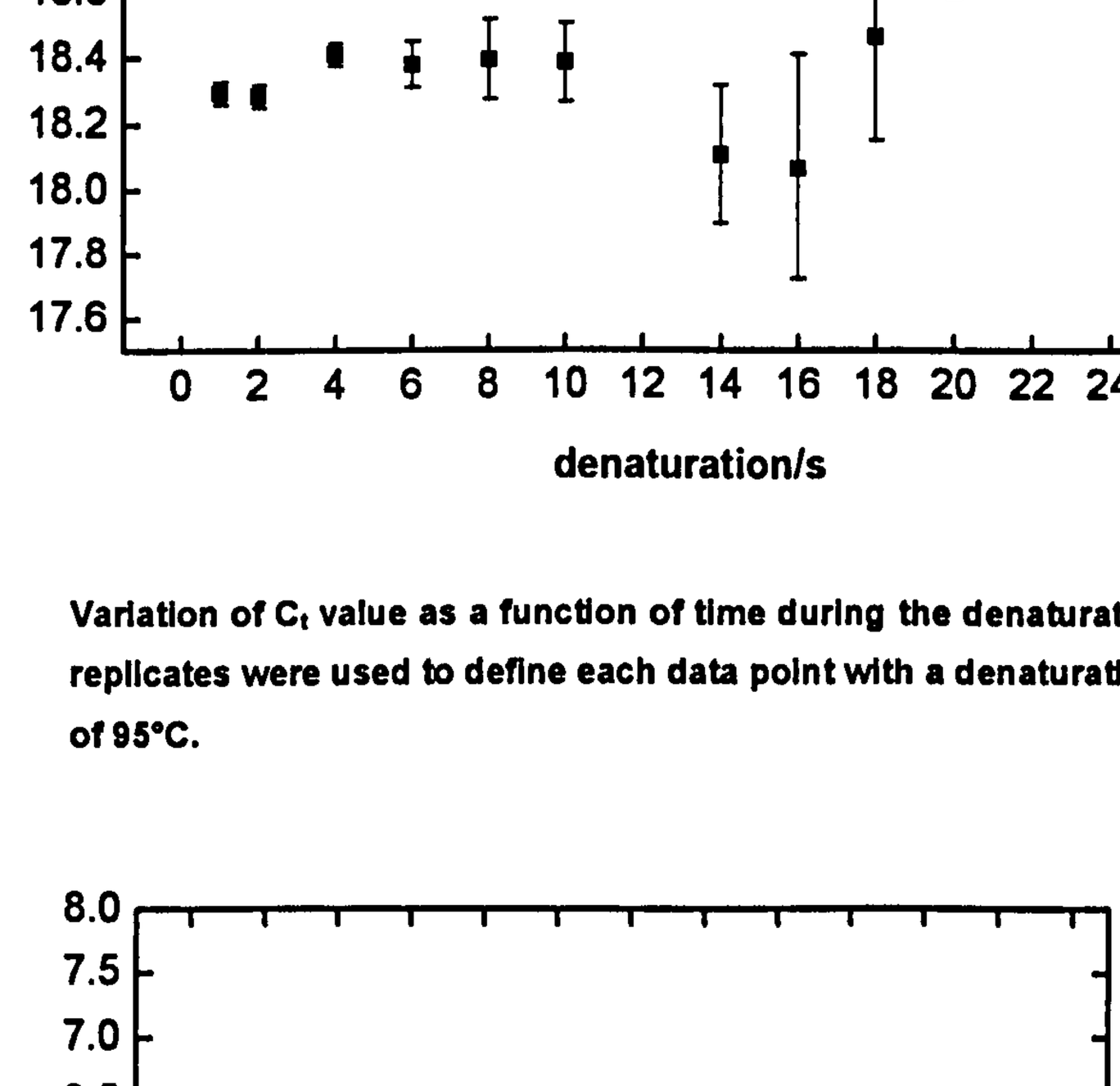


Figure 2.18 **Variation of peak area as a function of temperature during the denaturation phase. Five replicates were used to define each data point with a denaturation temperature of 95°C.**

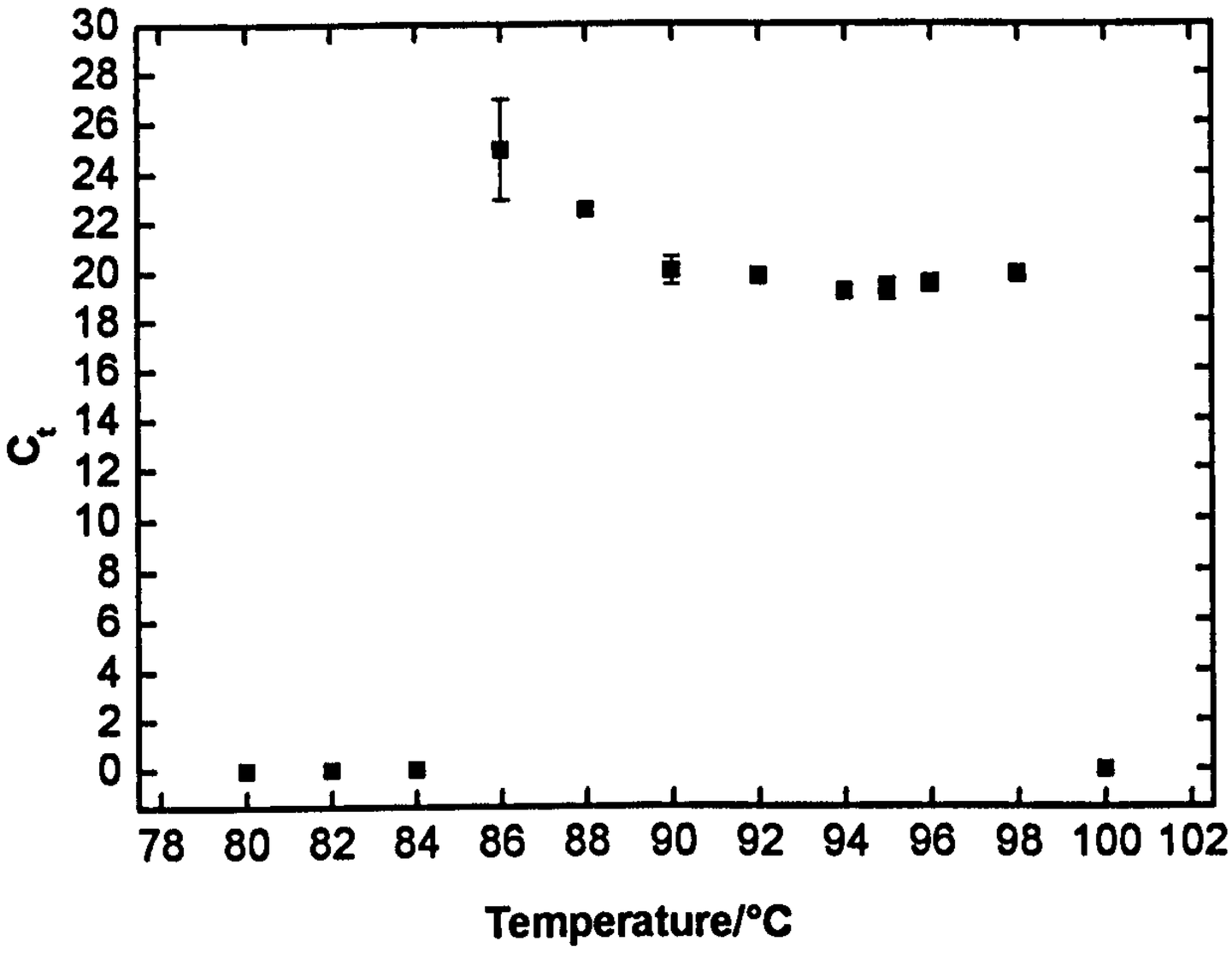


Figure 2.19 **Variation of C_t values as a function of temperature during the denaturation phase. Five replicates were used to define each data point with a denaturation time of 1s.**

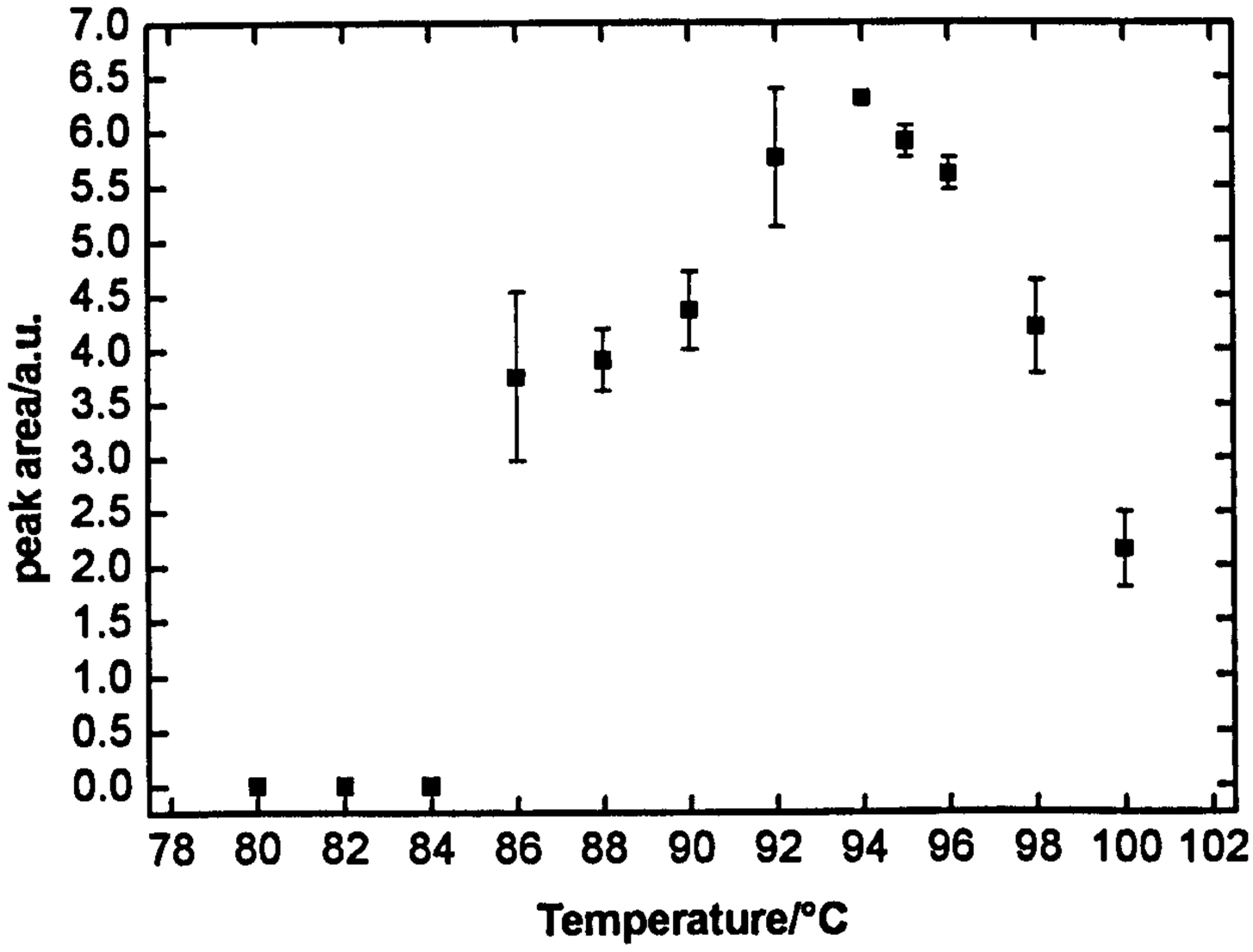


Figure 2.20 **Variation of product peak area as a function of temperature during the denaturation phase. Five replicates were used to define each data point with a denaturation time of 1s.**

Optimum denaturation phase conditions for the conventional PCR system involve temperatures between 90 and 94°C and a duration below 4s, while temperatures between 92 and 96°C and a duration below 4s are required for the real-time PCR denaturation phase.

2.3.1.1.3 Annealing and Extension

The annealing step is the process in which the primers attach to the single stranded DNA. This is followed by the extension step in which the polymerase enzyme starts copying the single stranded target DNA. For this particular system both annealing and extension occur within one step. The parameters for this step strongly depend on the nature of the primers. Their length and composition will define optimum time and temperature. General guidelines suggest temperatures between 50 - 70 °C for times up to a few minutes [8],[9],[10]. For *Bacillus globigii* annealing and extension is specified by Smiths Detection as being optimum for a temperature of 65 °C for 10 seconds and 6 seconds for the conventional and the real-time PCR system respectively.

2.3.1.1.3.1 Conventional PCR System

Data resulting from the variation of the annealing and extension phase times and temperatures are presented in Figures 2.21 and 2.22 respectively. Figure 2.21 illustrates maximum reaction efficiency for an extension time of approximately 70 seconds. Studies assessing the optimum temperature for the annealing and extension phase demonstrate good efficiency for temperatures between 50 and 70 °C. At temperatures higher than 70°C sample peak areas decrease and at temperatures higher than 76°C PCR fails. Consequently optimum conditions for the annealing and extension phase involve temperatures between 50 and 70 °C and times above 10 s.

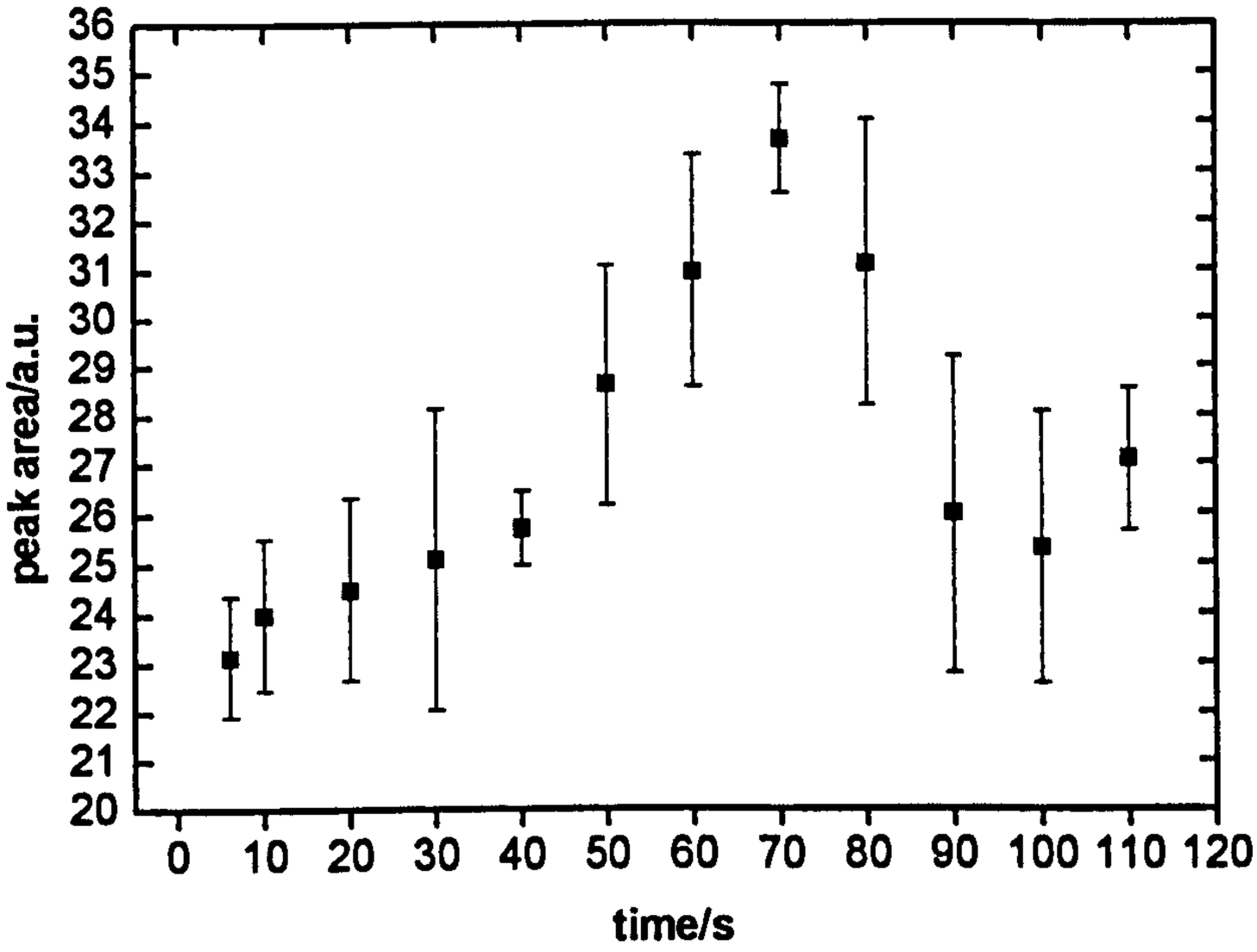


Figure 2.21 **Variation of peak area as a function of time during the annealing and extension phase. Five replicates were used to define each data point with an annealing and extension temperature of 65°C.**

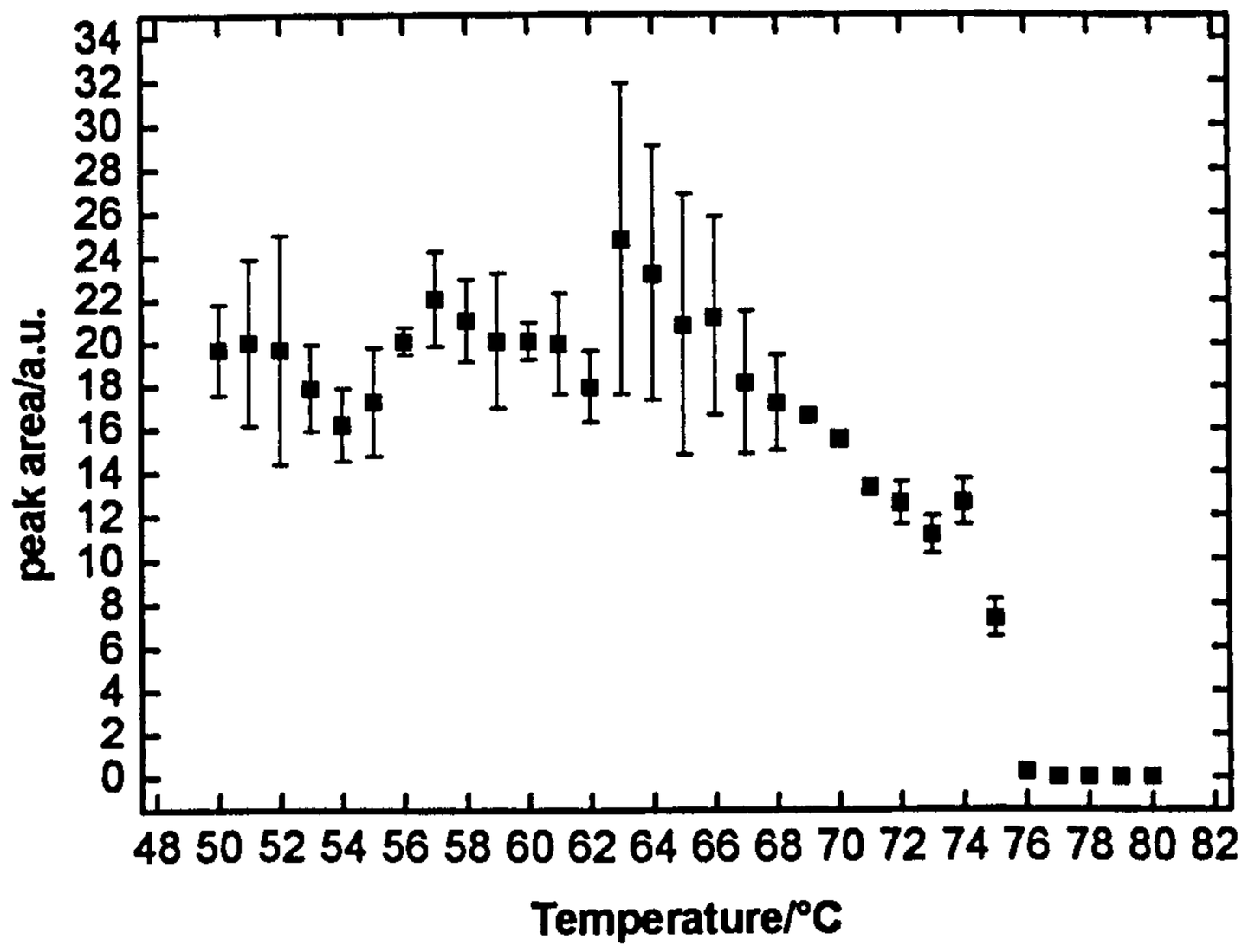


Figure 2.22 **Variation of peak area as a function of temperature during the annealing and extension phase. Five replicates were used to define each data point with an annealing and extension time of 10s.**

2.3.1.1.3.2 Real-Time PCR System

Smart Cycler and BioAnalyzer data resulting from the variation of the annealing and extension phase times are presented in Figures 2.23 and 2.24 respectively, and data resulting from the variation of the annealing and extension phase temperatures are presented in Figures 2.25 and 2.26 respectively. Poor reaction efficiencies were observed for annealing and extension times below 10 s as this is not sufficient time for the enzyme to extend the product of 90bp. Data obtained using the Smart Cycler and BioAnalyzer show some inconsistencies. Figure 2.23 indicates optimum efficiencies for a annealing and extension time of 20 seconds. However, Figure 2.24 suggests maximum product is generated for times in excess of 60 seconds. Studies assessing the influence of temperature for the annealing and extension phase on PCR efficiency demonstrate efficient amplification at temperatures between 50 and 68°C. At temperatures higher than 70°C sample peak areas decrease. Consequently optimum conditions for the annealing and extension phase were defined as being between 50 and 68°C for times in excess of 10s.

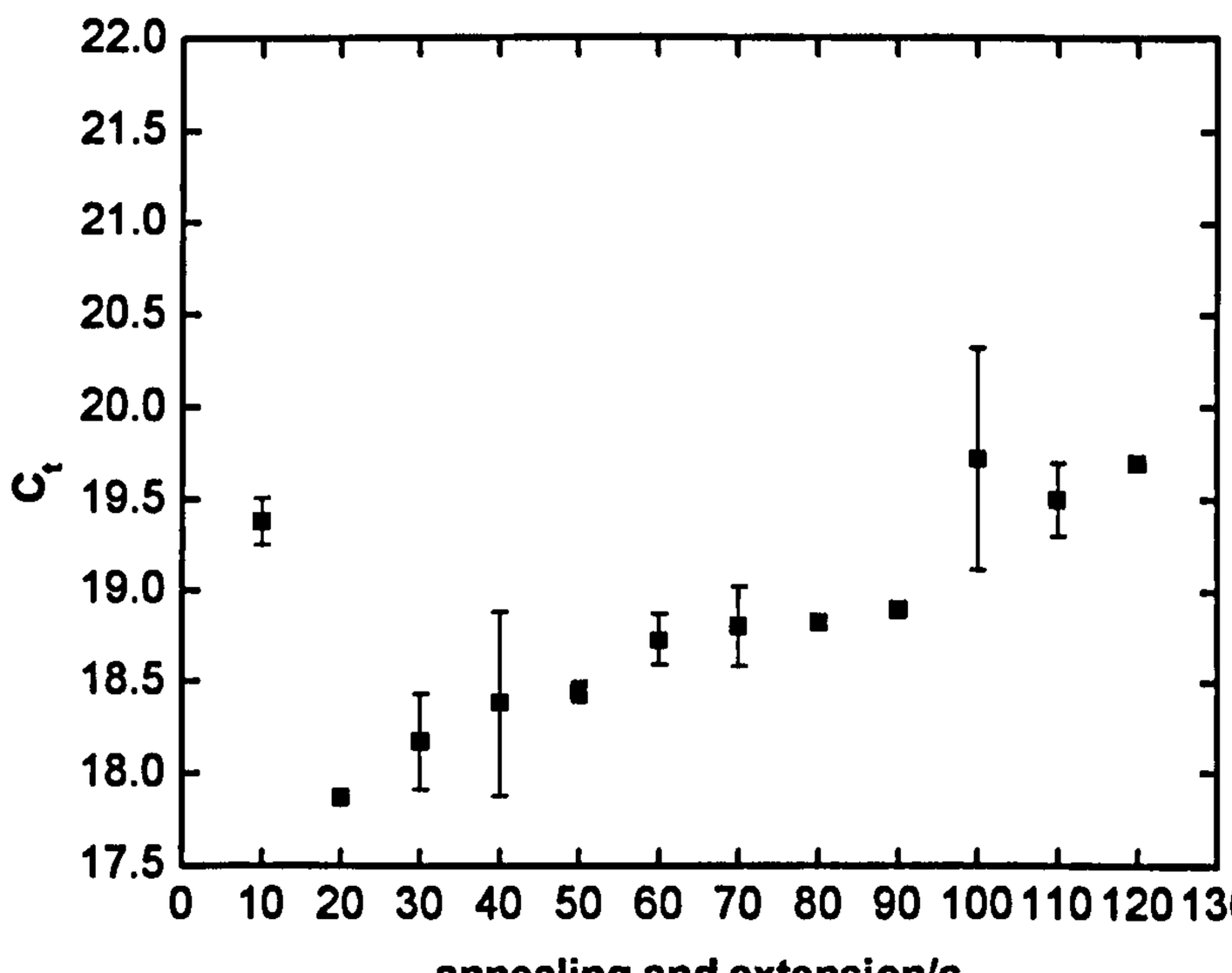


Figure 2.23 **Variation of C_t value as a function of time during the annealing and extension phase. Five replicates were used to define each data point with an annealing and extension temperature of 65°C.**

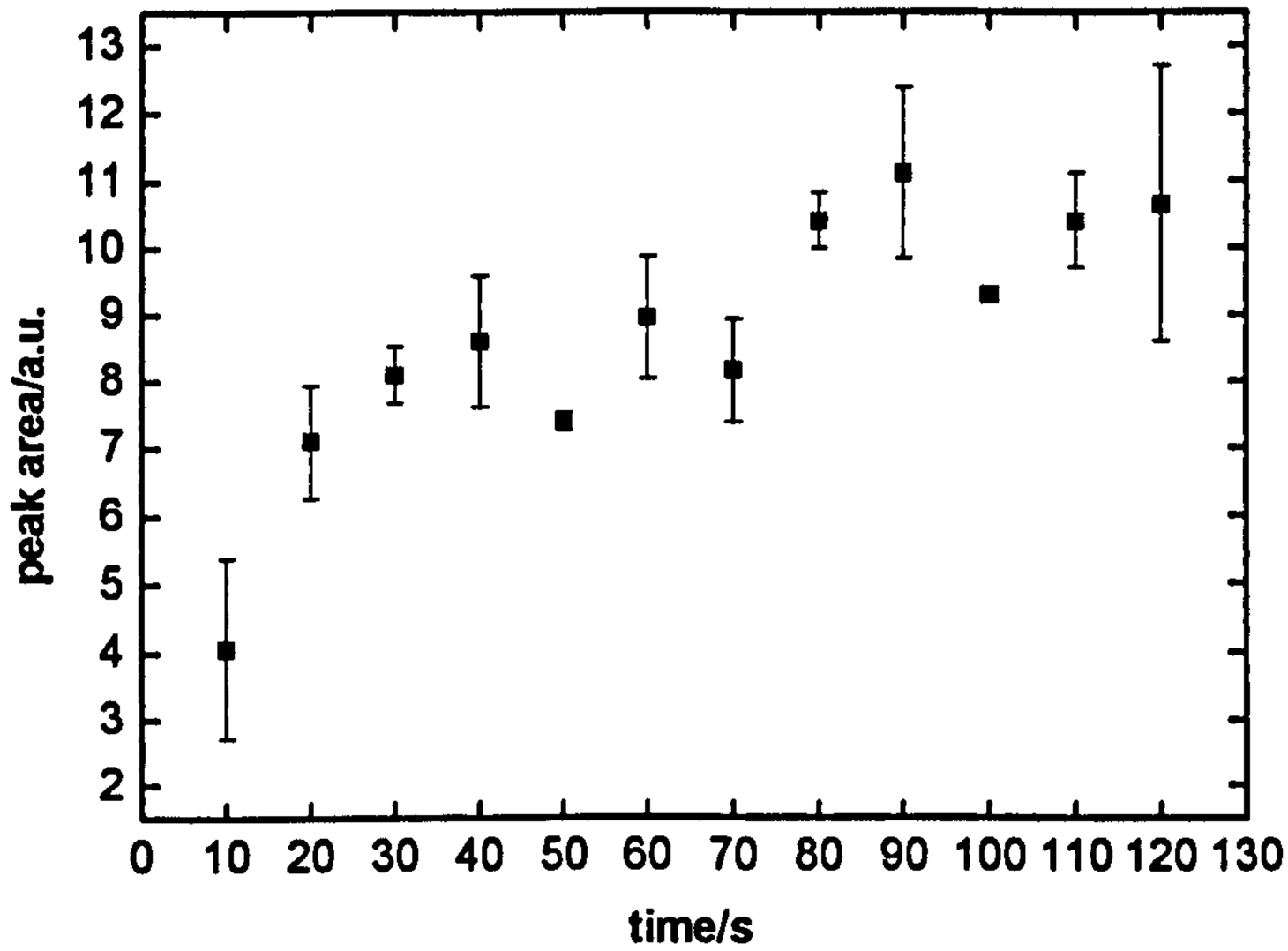


Figure 2.24 **Variation of product peak area as a function of time during the annealing and extension phase. Five replicates were used to define each data point with an annealing and extension temperature of 65°C.**

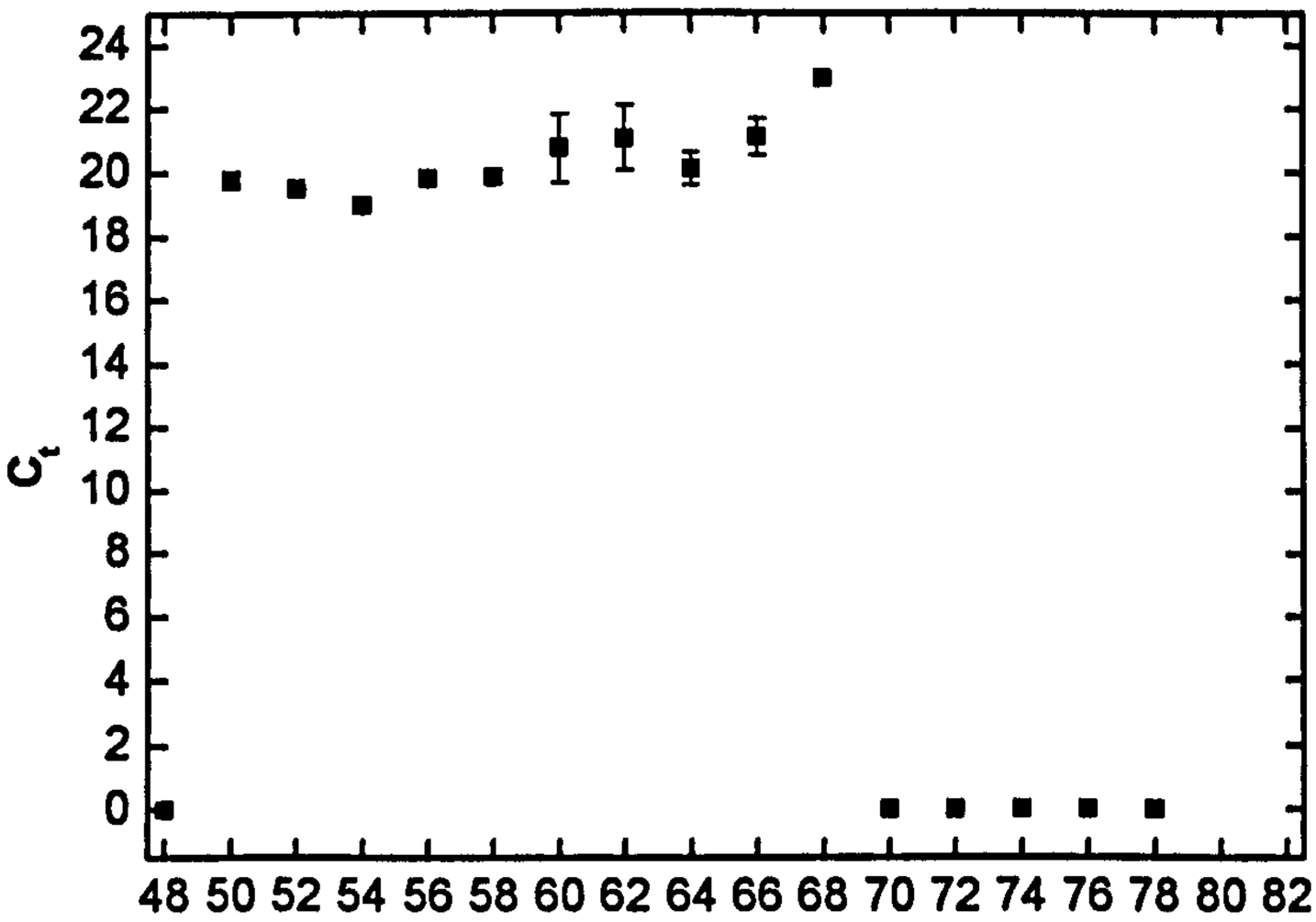


Figure 2.25 **Variation of C_t value as a function of temperature during the annealing and extension phase. Five replicates were used to define each data point with an annealing and extension time of 5s.**

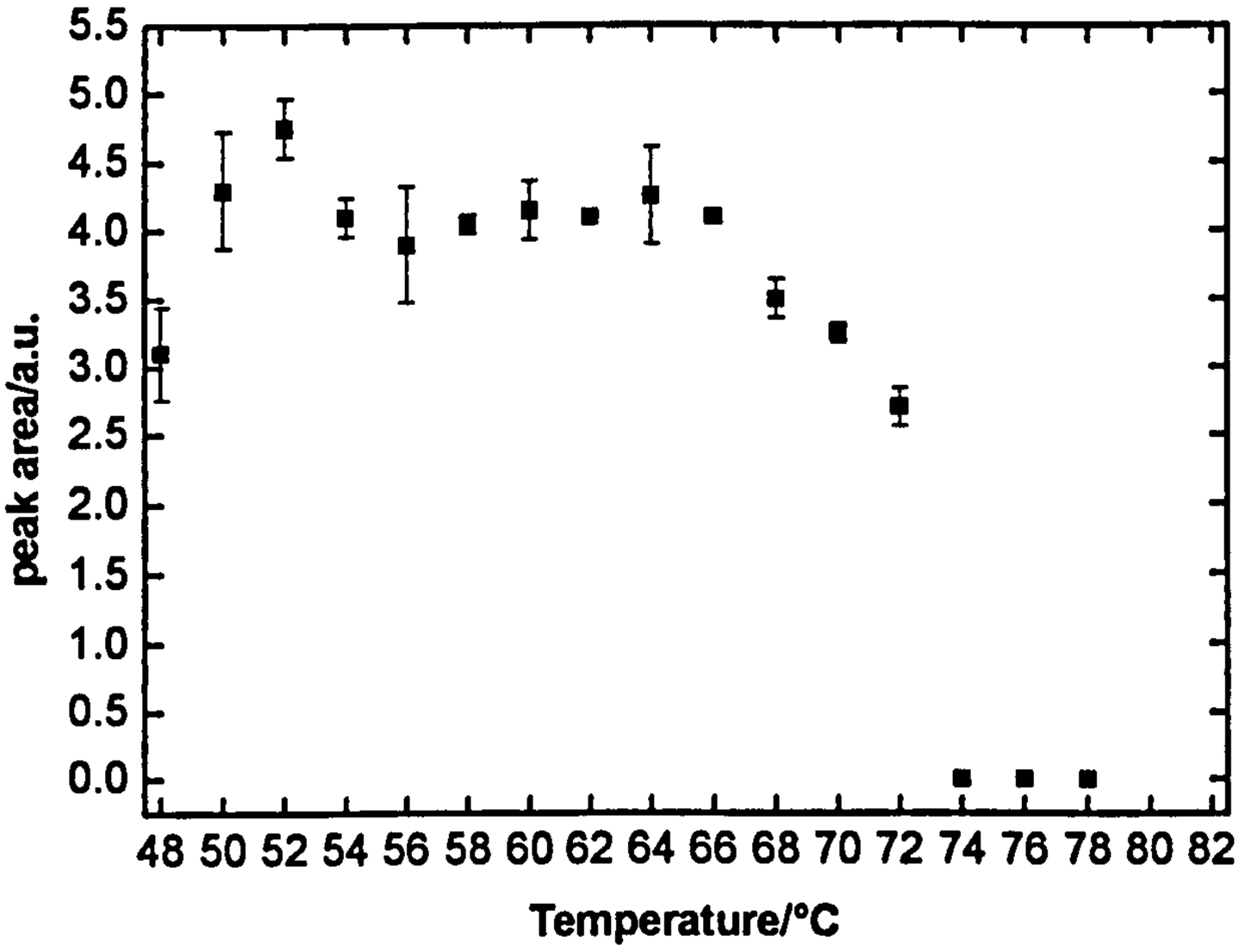


Figure 2.26 **Variation of sample peak area as a function of temperature during the annealing and extension phase. Five replicates were used to define each data point with an annealing and extension time of 5s.**

Optimum annealing and extension phase conditions for the conventional PCR system involve temperatures between 50 and 70°C and a duration above 10s, while temperatures between 50 and 68°C and a duration above 10s are required for real-time PCR annealing and extension phase optimum conditions. The outcome of the temperature and time studies (in section 2.3.1.1) is compared with previously defined protocol conditions in Tables 2.5 and 2.6. The experimental data provide close correspondence with the defined protocol. The annealing and extension temperature seems to be an exception with a wide range of 20 degrees in the experimental outcome compared with the specific value suggested by the defined protocol.

		Temperature (°C)		Time (s)	
Hot-start					
protocol	experimental	95	94-96	30	≤20
Denaturation					
protocol	experimental	95	90-94	5	1-4
Annealing/extension					
protocol	experimental	65	50-70	10	>10

Table 2.5 **Comparison of protocol and experimental PCR conditions for the conventional PCR system.**

		Temperature (°C)		Time (s)	
Hot-start					
protocol	experimental	95	92-96	30	≤20
Denaturation					
protocol	experimental	95	92-96	1	1-4
Annealing/extension					
protocol	experimental	65	50-68	6	>10

Table 2.6 **Comparison of protocol and experimental PCR conditions for the real-time PCR system.**

2.3.1.2 Assessment of Optimum Number of Cycles

In order to determine the lowest cycle number for detectable amplification and the onset of PCR saturation, a variation of cycle number between 10 and 60 cycles was performed. For the standard *Bacillus globigii* system 45 cycles for both the conventional and the real-time PCR system are specified by Smiths Detection.

2.3.1.2.1 Conventional PCR System

Data resulting from a variation in cycle number are presented in Figure 2.27. Increasing product peak areas were observed for cycle numbers between 20 and 50. Peak areas showed no further increase for cycles numbers higher than 60. These data indicate that the cycle numbers should be kept lower than 50 in all experiments (based on a fixed starting copy number).

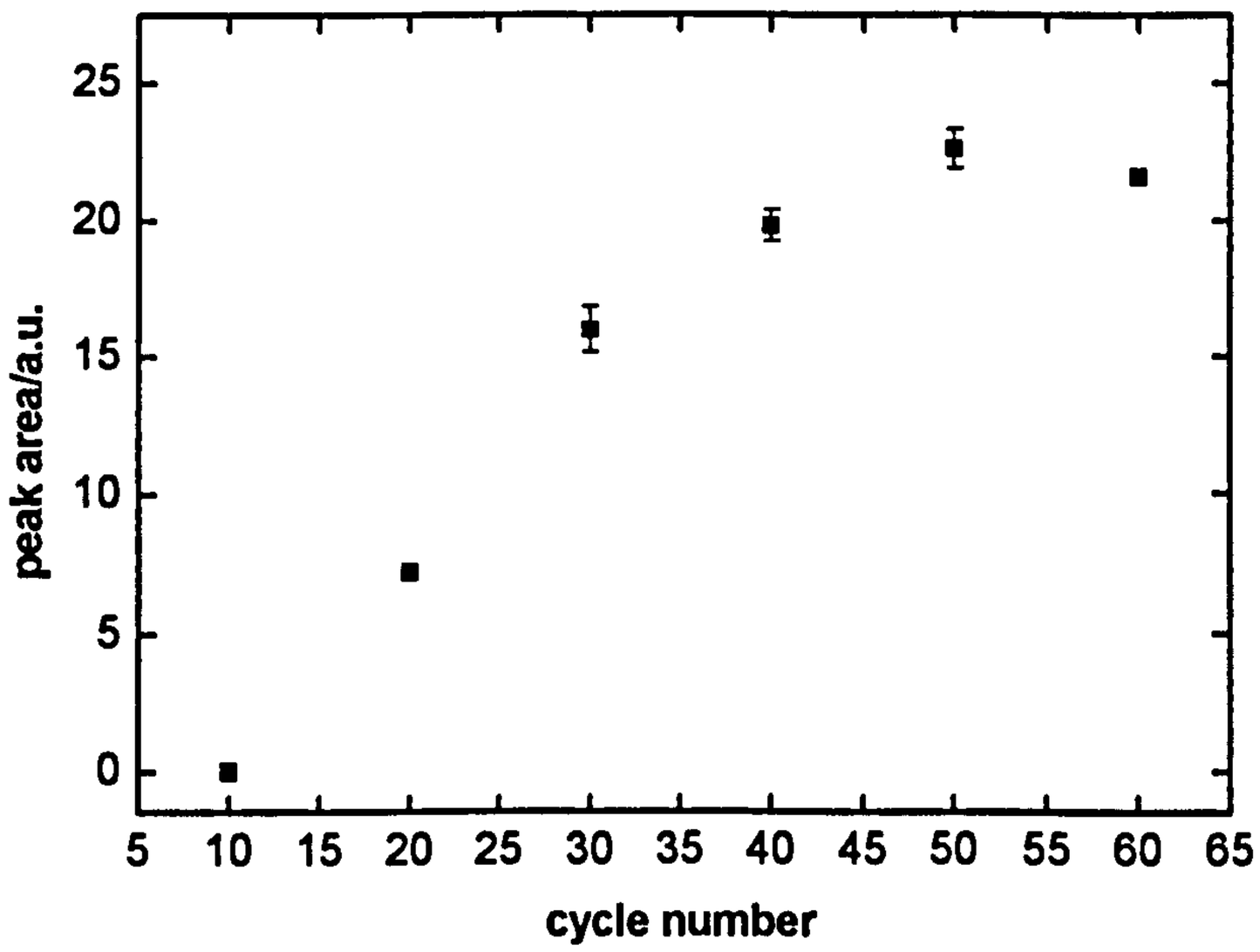


Figure 2.27 **Variation of peak area as a function of cycle number. Five replicates were used to define each data point with defined protocol conditions as presented in Table 2.5.**

2.3.1.2.2 Real-Time PCR System

Smart Cycler and BioAnalyzer results from the variation of the cycle numbers are presented in Figures 2.28 and 2.29 respectively. Studies assessing the influence of cycle number on PCR efficiency demonstrate efficient amplification for cycle numbers between 25 and 50. At cycle numbers lower than 20 and higher than 50 no C_t values are observed and PCR fails. Increasing product peak areas were observed for cycle numbers between 20 and 50 (Figure 2.29). Peak areas showed no further increase for cycle numbers higher than 55. These data indicate that the cycle numbers should be kept between 20 and 50.

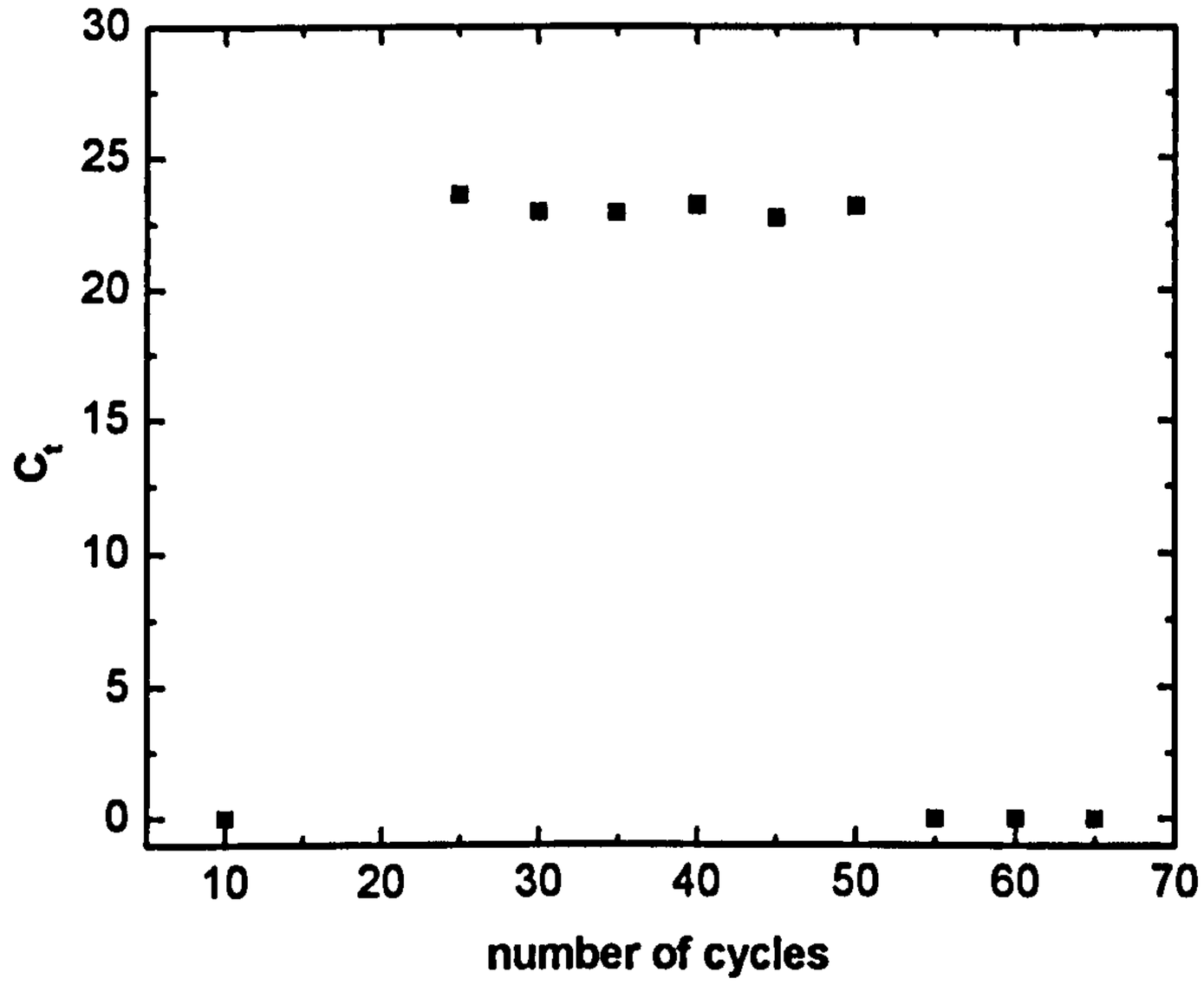


Figure 2.28 **Variation of C_t as a function of cycle number. Five replicates were used to define each data point with defined protocol conditions as presented in Table 2.6.**

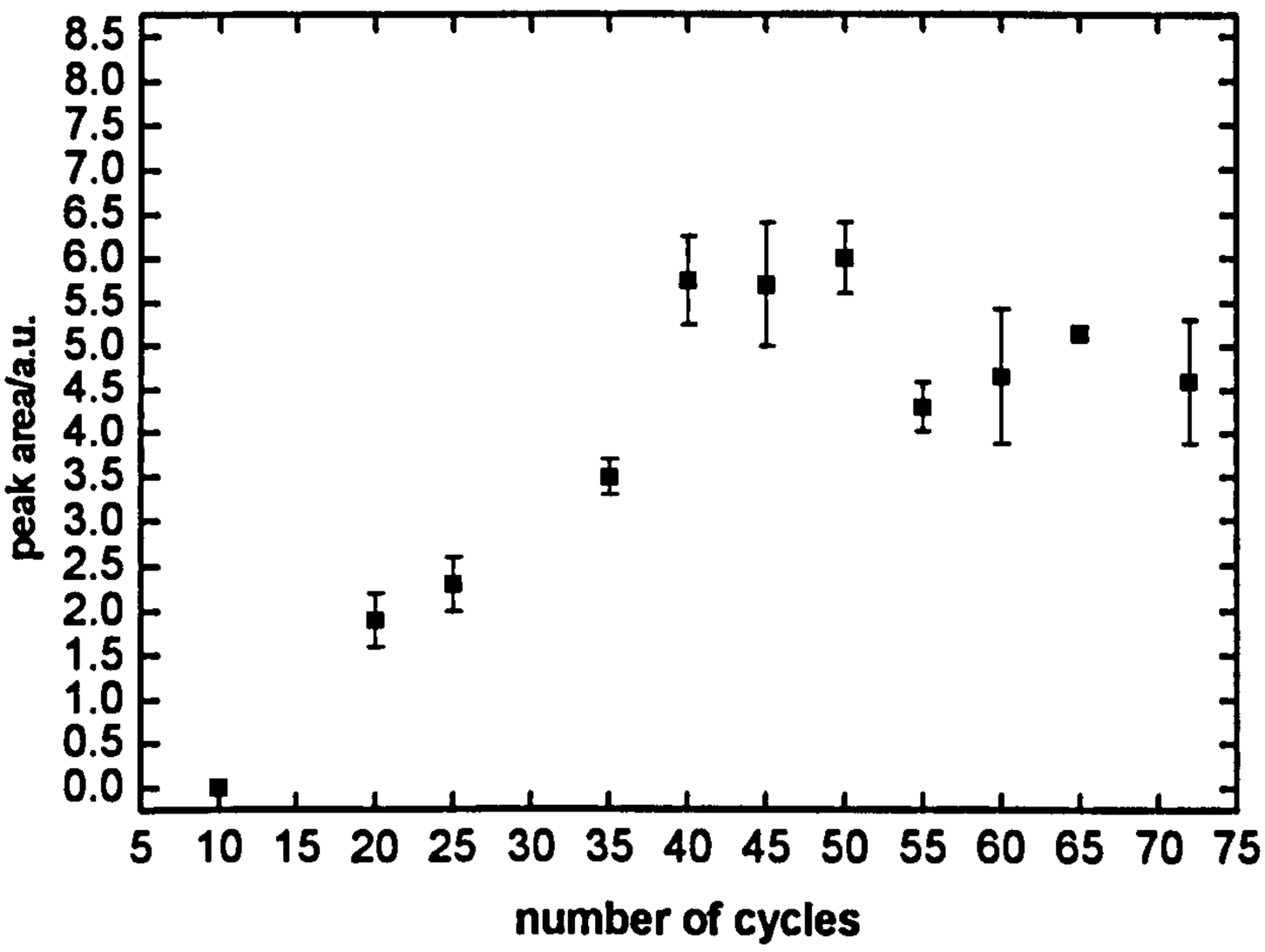


Figure 2.29 **Variation of peak area as a function of cycle number. Five replicates were used to define each data point with defined protocol conditions as presented in Table 2.6.**

Optimum cycle conditions for the conventional and real-time PCR system are between 20 and 50 cycles.

2.3.1.3 Temperature Ramp Rate Variation

All PCR reactions on the Smart Cycler were performed using cooling rates of 2.5 °C/second and heating rates at 10°C/second. To assess the influence of temperature ramp rates on PCR efficiency an additional variation study was performed. This involves cooling rates of 0.5, 1, 1.5 and 2°C/second and heating rates of 2, 4, 5, 10°C/second.

2.3.1.3.1 Conventional PCR System

Data resulting from the variation of ramp rates are presented in Figures 2.30 and show negligible influence on the PCR efficiency. Due to reduced cycling times cooling and heating rates of 2.5 °C/second and 10 °C/second were chosen for all PCR experiments described in this thesis.

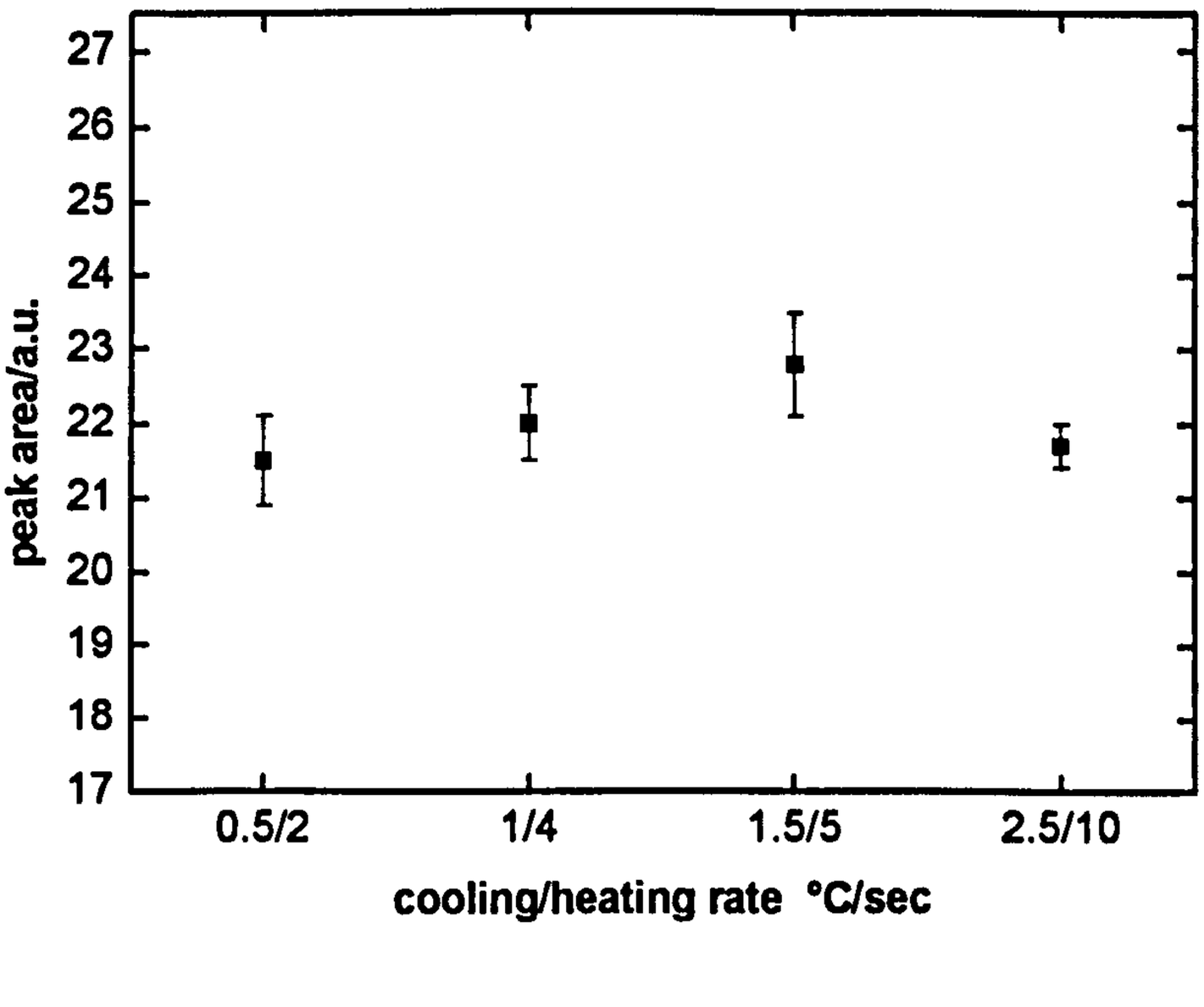


Figure 2.30 **Variation of peak areas as a function of ramp rates. Five replicates were used to define each data point with protocol conditions as presented in Table 2.5.**

2.3.1.3.2 Real-Time PCR System

Smart Cycler and BioAnalyzer data resulting from the variation of ramp rates study are presented in Figures 2.31 and 2.32 respectively. Similarly, these results show

little influence of the ramp rate on product peak area. Likewise, maximum heating and cooling rates were used for the real-time PCR system in all experiments.

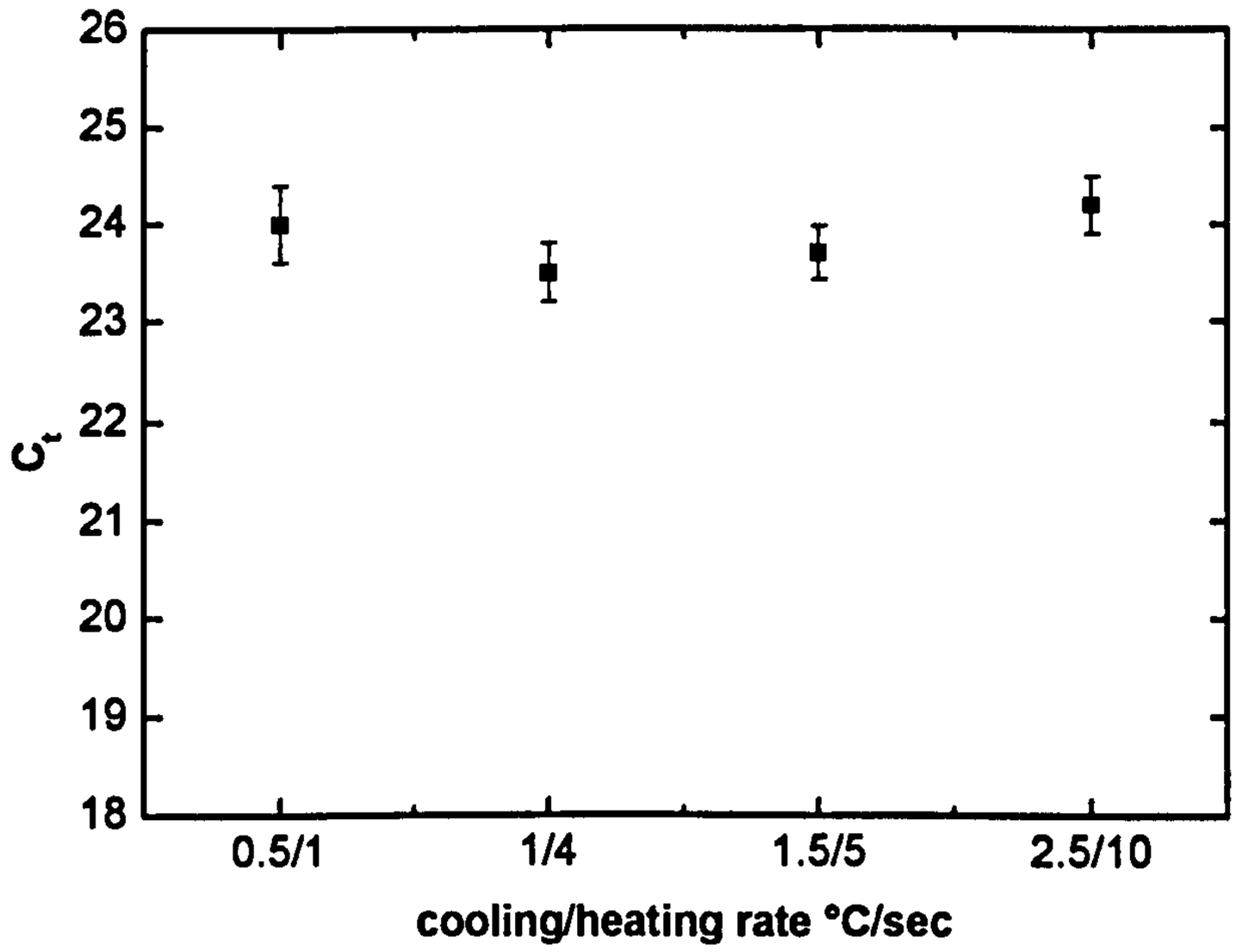


Figure 2.31 **Variation of C_t as a function of ramp rate. Five replicates were used to define each data point with defined protocol conditions as presented in Table 2.6.**

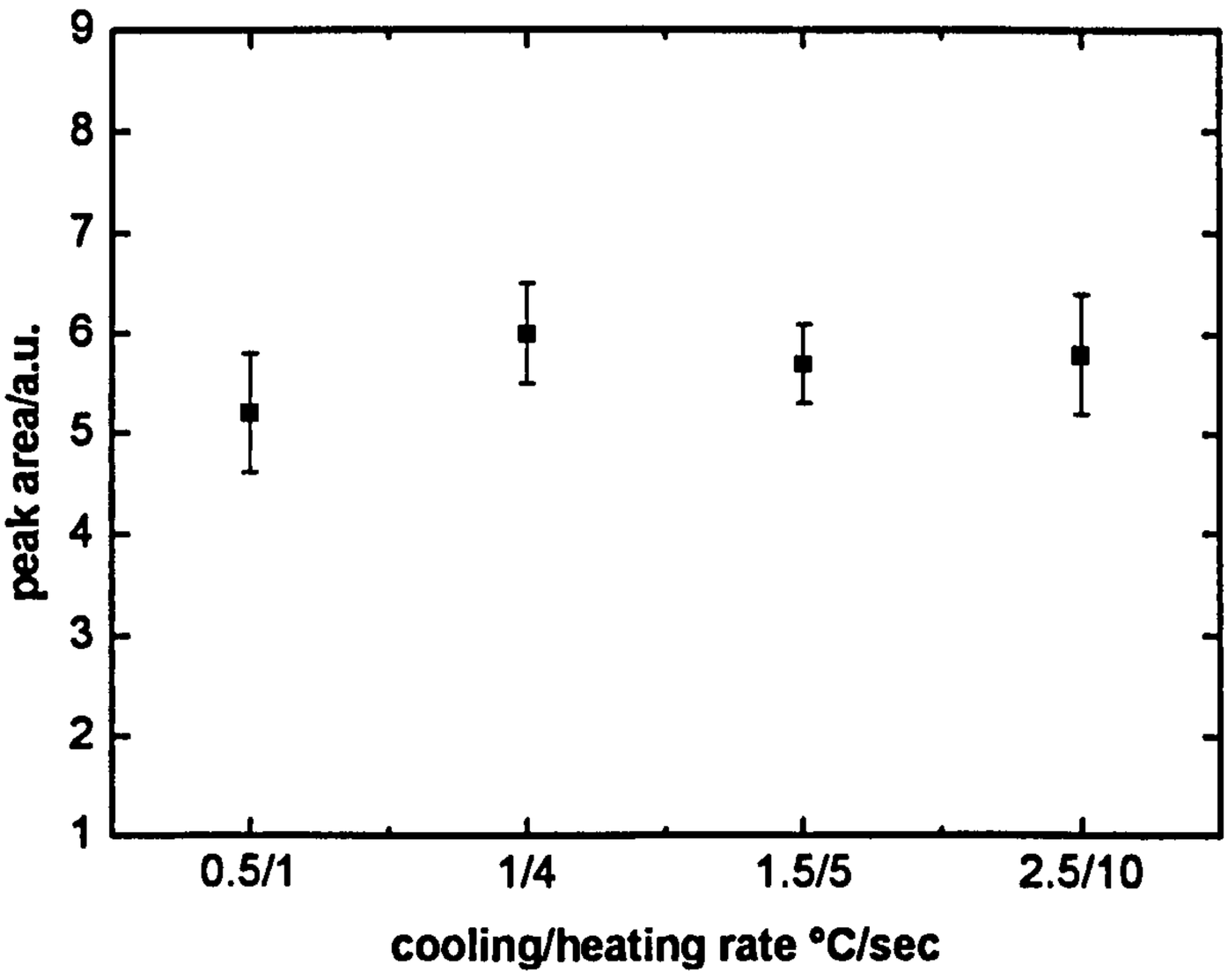


Figure 2.32 **Variation of peak areas as a function of ramp rate. Five replicates were used to define each data point with defined protocol conditions as presented in Table 2.6.**

2.3.2 Optimization of PCR Components and Additives

In this section the robustness of the *Bacillus globigii* PCR system was further tested by varying the concentrations of PCR components; specifically primer, enzyme, magnesium chloride and target concentrations. Additionally the influence of PCR additives, such as bovine serum albumin (BSA) and polyvinylpyrrolidone (PVP) was tested.

2.3.2.1 Primer Optimization

For the *Bacillus globigii* system a primer concentration of 0.5 µM for both forward and reverse primers for the conventional PCR system, and 0.25 µM for forward and 0.5 µM for reverse primer with the real-time PCR system were recommended. Primer concentration variations were performed for both primers between 0.35 and 3 µM for the conventional PCR system. For the real-time PCR system primer concentration variations were performed between 0.125 and 2 µM for the forward primer and between 0.25 µM and 4 µM for the reverse primer. Additionally a primer ratio variation for the real-time PCR system was performed. Such experiments were undertaken since the specified primer ratio for the real-time PCR system differs from the conventional PCR system. Accordingly a study of primer ratios between 0.5 and 2 was performed.

2.3.2.1.1 Conventional PCR System

Data resulting from the variation of the primer concentrations are summarized in Figure 2.33. High product peak areas were observed for primer concentrations between 0.4 and 0.7 µM. Peak areas were then observed to decrease for primer concentrations higher than 0.7 µM. These data indicate that the primer concentrations should be kept between 0.4 and 0.7 µM. The significant reduction in efficiency at primer concentrations above 0.7 µM is most likely due to the fact that the primer concentration is significantly higher than DNA concentration and therefore it is more likely that primers will anneal to each other rather than to the DNA target. This effect is seen in Figure 2.34, which presents electropherograms of PCR products when primer concentrations are 0.5 µM and 0.8 µM. It can be seen that at the higher primer concentration a significant amount of primer-dimer is formed (peak at 54 bp).

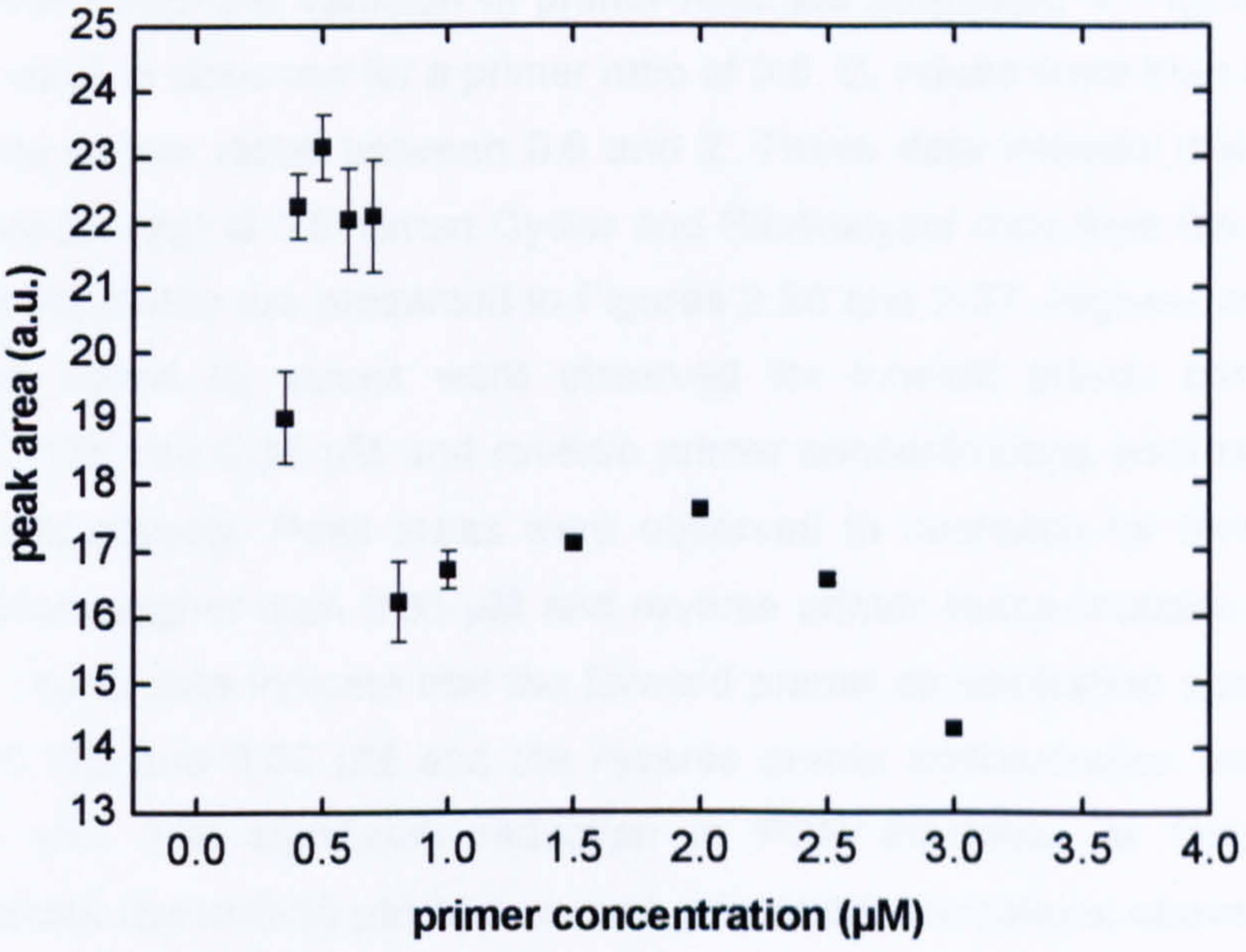


Figure 2.33 Variation of peak area as a function of primer concentration. Five replicates were used to define each data point.

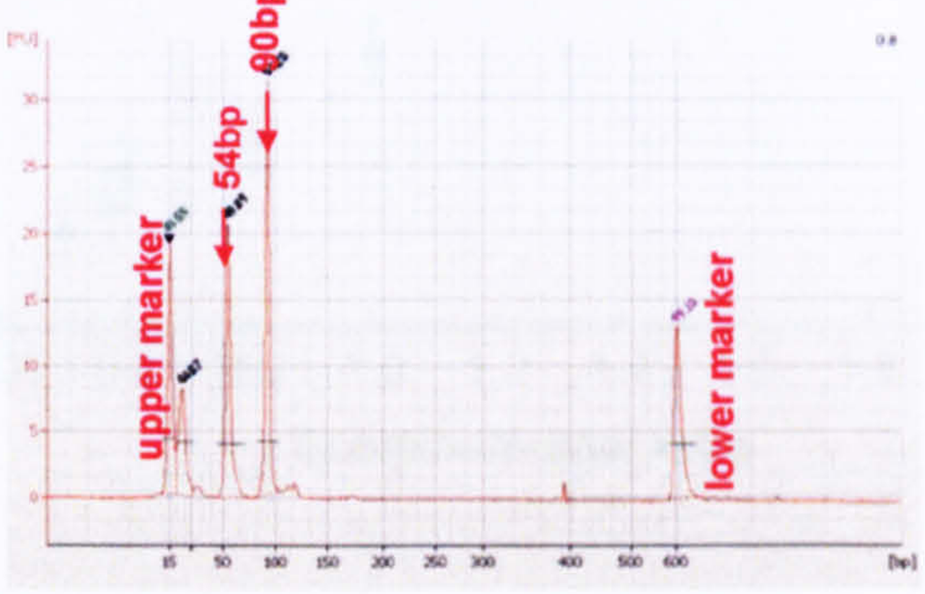


Figure 2.34 a) Electropherogram of product amplified using primer concentrations of 0.5 μM. b) Electropherogram of PCR product and bi-products using primer concentrations of 0.8 μM.

2.3.2.1.2 Real-Time PCR System

Data resulting from the variation of primer ratio are presented in Figure 2.35. The lowest C_t value is observed for a primer ratio of 0.5. C_t values were then observed to increase for primer ratios between 0.6 and 2. These data indicate that the primer ratio should be kept at 0.5. Smart Cycler and BioAnalyzer data from the variation of primer concentration are presented in Figures 2.36 and 2.37. Highest product peak areas and lowest C_t values were observed for forward primer concentrations between 0.125 and 0.35 µM and reverse primer concentrations between 0.25 and 0.75 µM respectively. Peak areas were observed to decrease for forward primer concentrations higher than 0.35 µM and reverse primer concentrations higher than 0.75 µM. These data indicate that the forward primer concentration should be kept between 0.125 and 0.35 µM and the reverse primer concentration between 0.25 and 0.75 µM. The significant reduction in PCR efficiency at forward primer concentrations above 0.35 µM and reverse primer concentrations above 0.75 µM is most likely due to a favouring of bi-product formation as explained in section 2.3.2.1.1. Consequently optimum concentrations for the forward primer are between 0.125 and 0.35 µM and between 0.25 and 0.75 µM for the reverse primer.

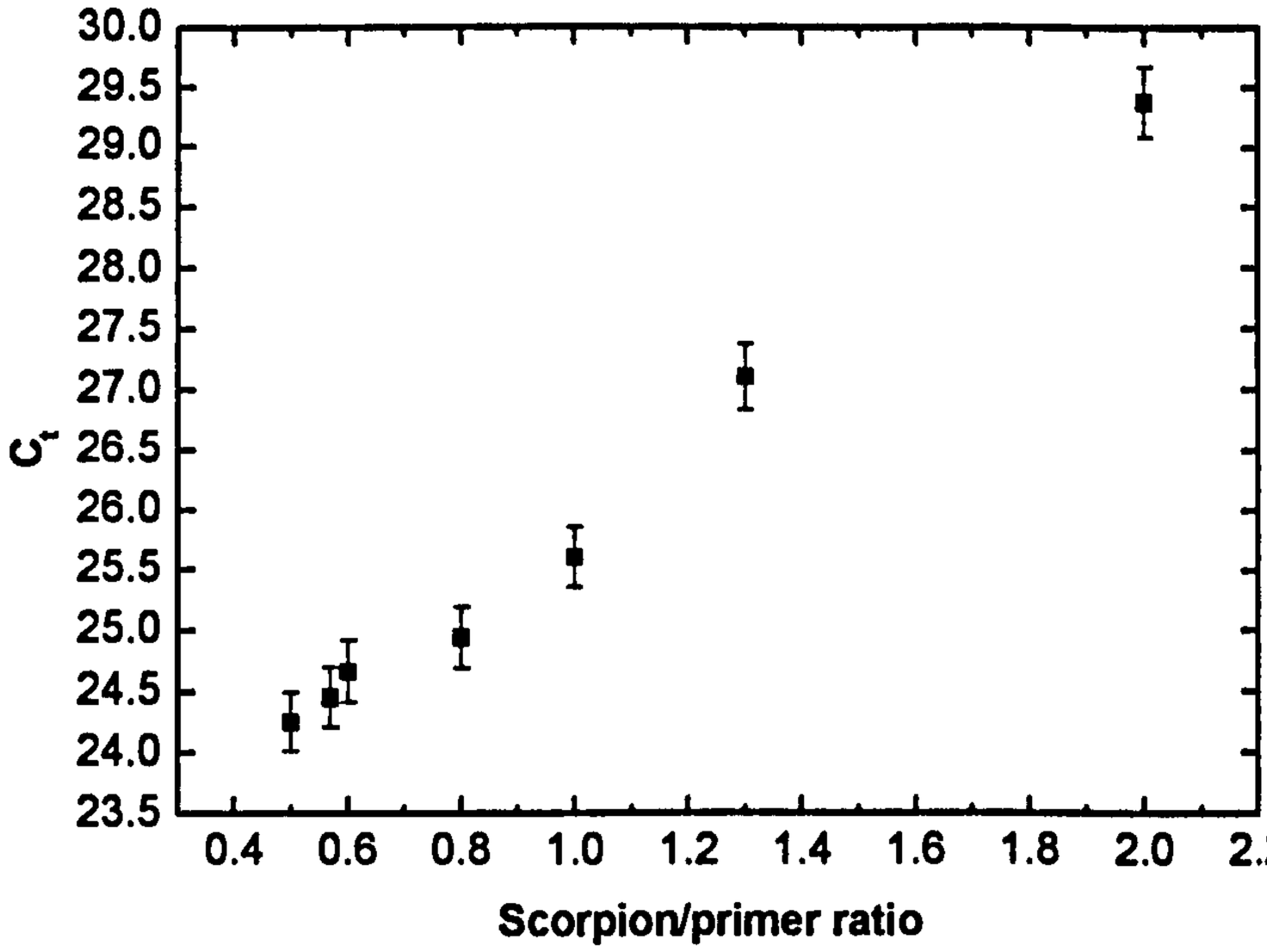


Figure 2.35 **Variation of C_t value as a function of primer ratio. Five replicates were used to define each data point.**

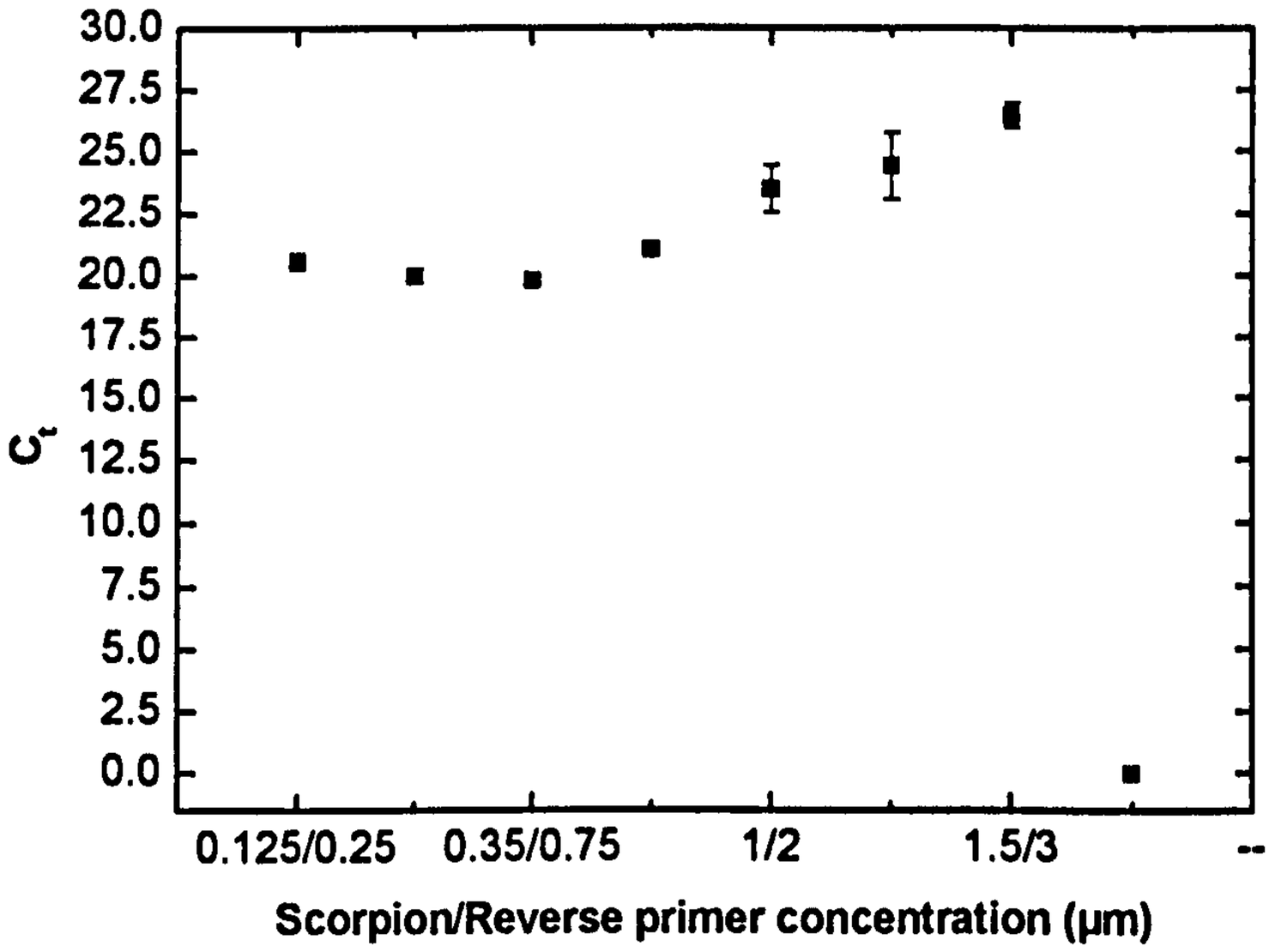


Figure 2.36 **Variation of C_t value as a function of primer concentration. Five replicates were used to define each data point.**

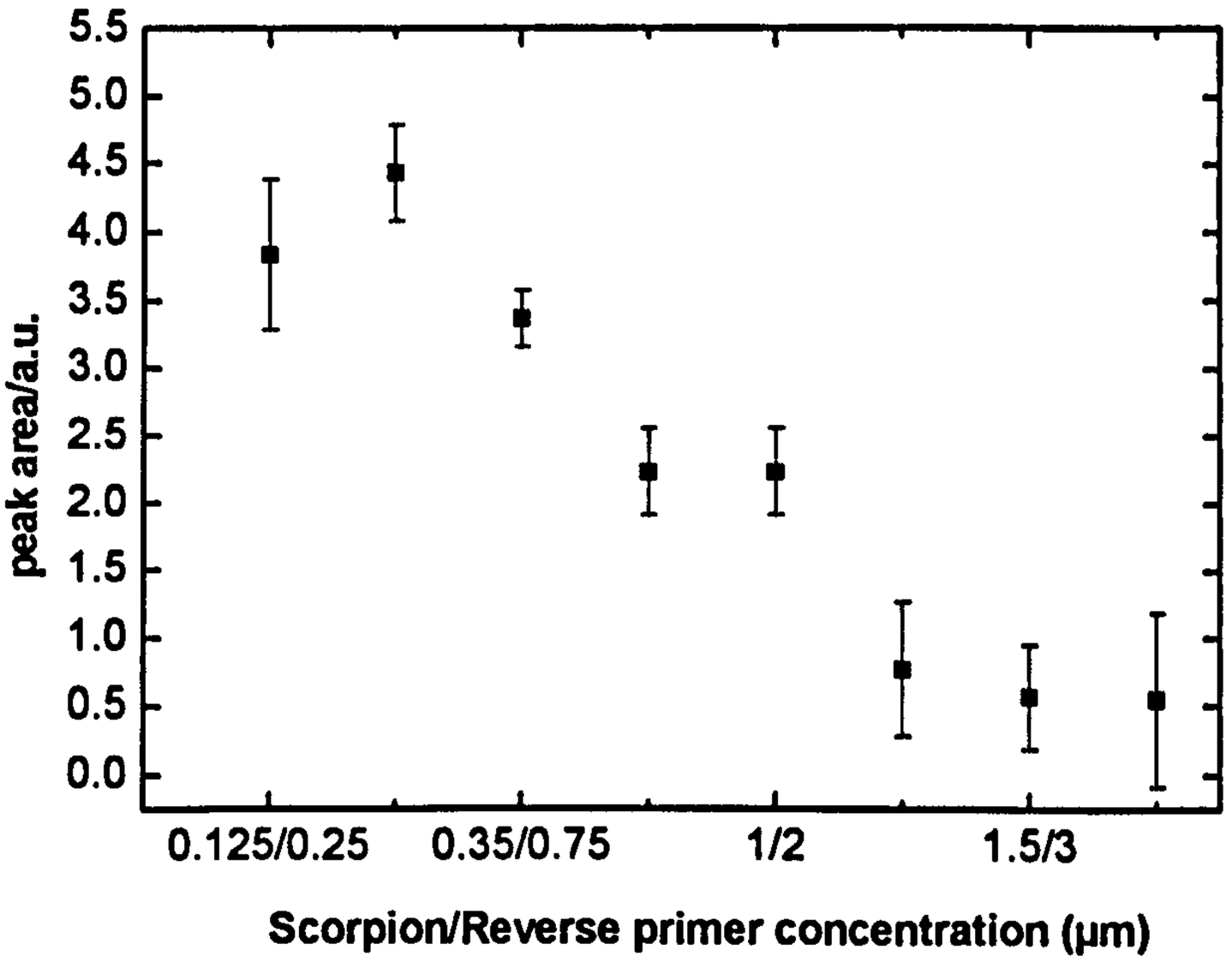


Figure 2.37 **Variation of peak areas as a function of primer concentration. Five replicates were used to define each data point.**

Optimum conventional primer concentrations for the forward as well as reverse primer are between 0.4 and 0.7 µM with an optimum primer ratio of 1. Optimum real-time primer concentrations for the forward primer are between 0.125 and 0.35 µM and between 0.25 and 0.75 µM for the reverse primer with an optimum primer ratio of 0.5.

2.3.2.2 Taq Polymerase Optimization

For the *Bacillus globigii* system the optimum *Taq polymerase* concentration specified by Smiths Detection Ltd is 0.05 Units/µl for both PCR systems. Studies were performed to assess the influence of varying the enzyme concentration between 0.1 and 1 Units/ µl for the conventional PCR system. Subsequent studies varying the enzyme concentration between 0.01 and 0.12 Units/µl for the real-time PCR system were also performed. Due to the high cost of the enzyme each set of experiments was only performed once.

2.3.2.2.1 Conventional PCR System

Data resulting from varying enzyme concentrations between 0.1 and 1 Units/µl are presented in Figure 2.38. Increasing product peak areas were observed for enzyme concentrations between 0.1 and 0.6 Units/µl. Peak areas plateaued for concentrations between 0.8 and 1 Units/µl. These data indicate that the enzyme concentration should be kept around 0.6 Units/ µl. As enzyme costs are extremely high it is desirable to keep the enzyme concentration low. Therefore studies to estimate the lowest enzyme concentration necessary for successful PCR were performed with enzyme concentrations between 0.01 and 0.12 Units/µl in Section 2.3.2.2.2.

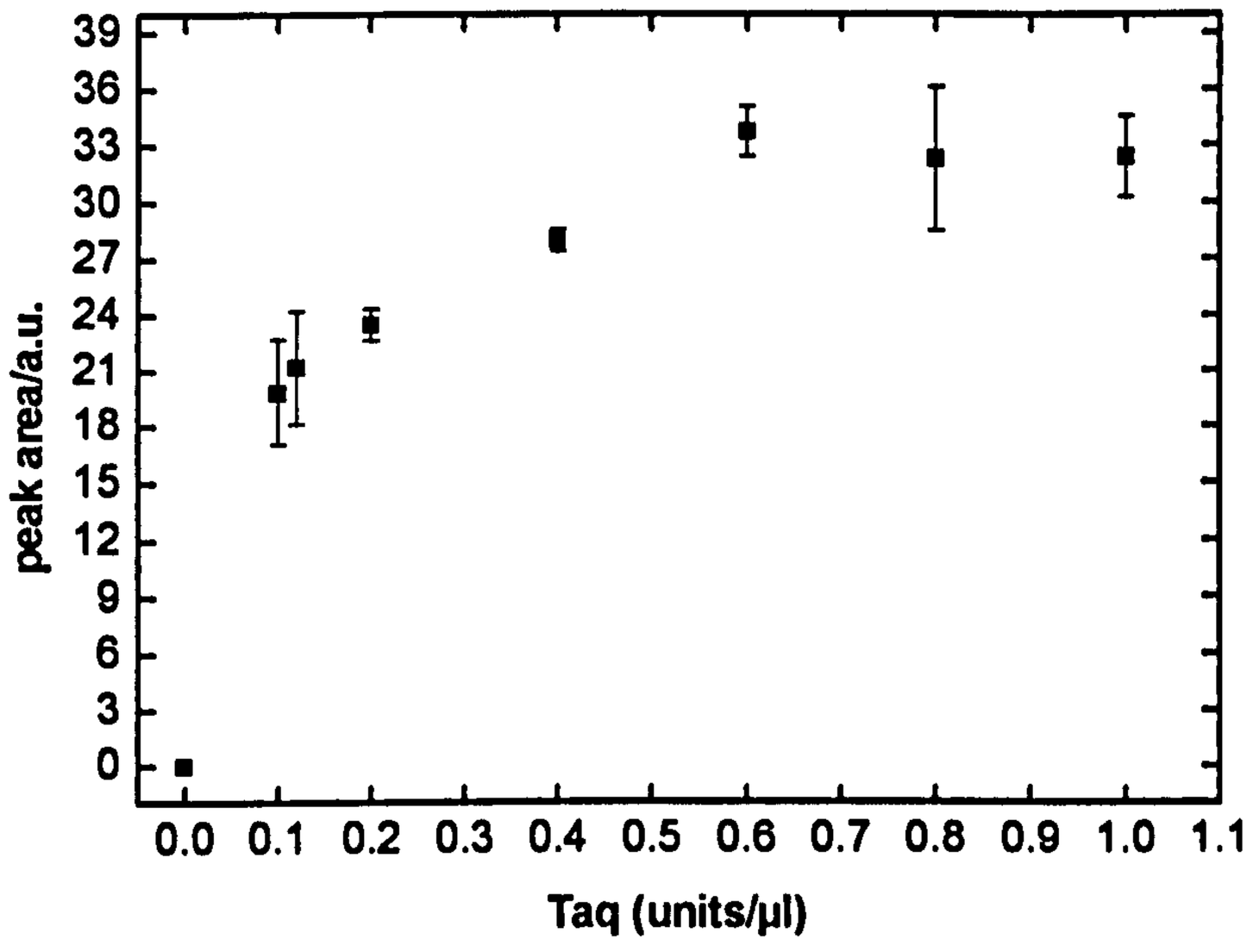


Figure 2.38 **Variation of peak area as a function of enzyme concentration. Five replicates were used to define each data point.**

2.3.2.2.2 Real-Time PCR System

Smart Cycler results for the variation of the enzyme concentration are presented in Figure 2.39. High C_t values are observed for enzyme concentrations between 0.01 and 0.4 Units/µl. C_t values were then observed to plateau for enzyme concentrations between 0.05 and 0.12 Units/µl. These data indicate that the lowest enzyme concentration for efficient PCR is approximately 0.05 Units/µl.

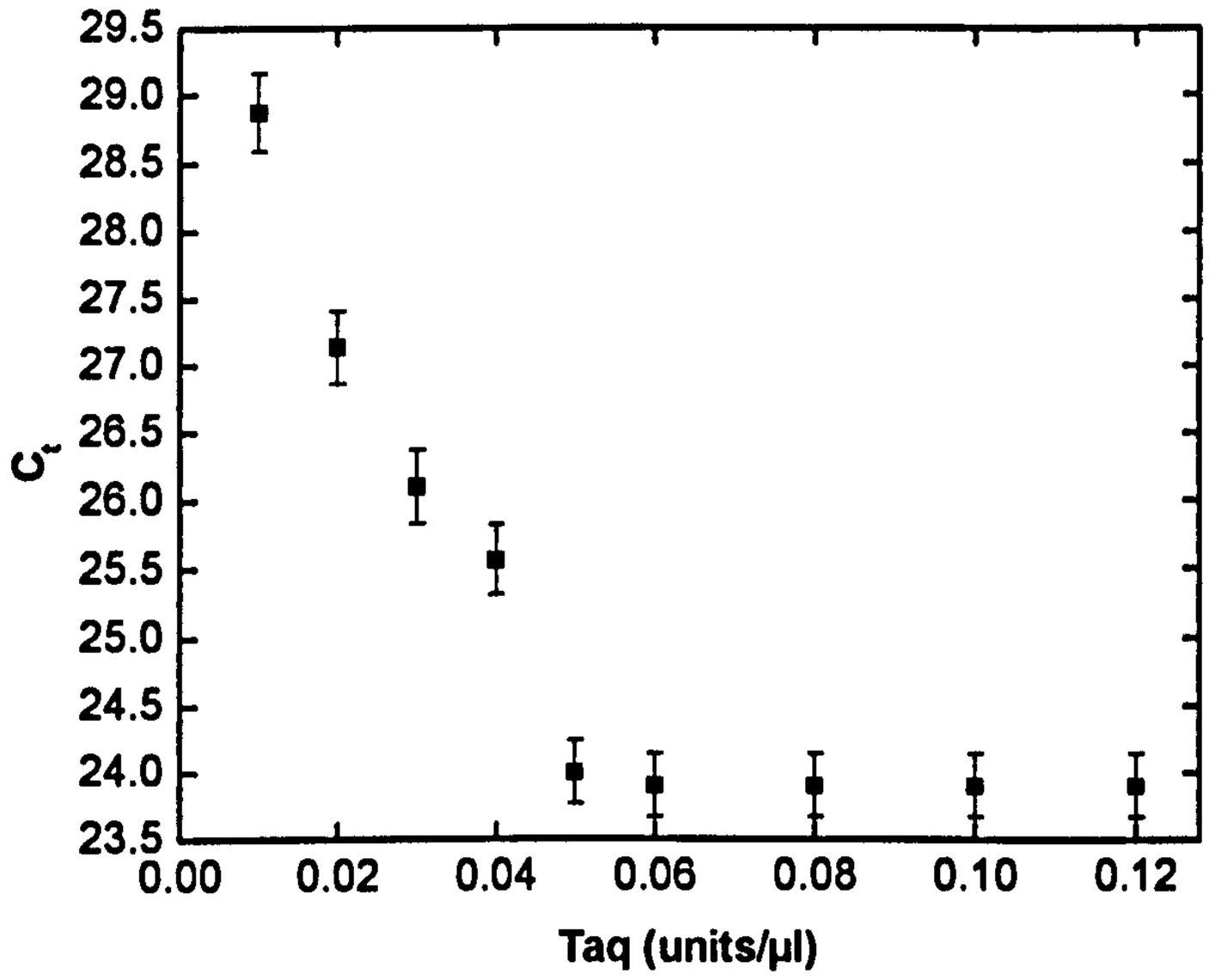


Figure 2.39 **Variation of C_t value as a function of enzyme concentration. Five replicates were used to define each data point.**

Combination of both data sets suggests that optimum enzyme concentrations are between 0.05 and 0.6 Units/µl.

2.3.2.3 Magnesium Chloride Concentration

The role of magnesium chloride in the PCR mix is crucial. As explained in Chapter 1, magnesium ions are enzymatic co-factors: their concentration has an important influence on the shape, the charge distribution and the binding properties of the Taq polymerase. For the *Bacillus globigii* system the optimum magnesium chloride concentration specified by the manufacturer is 5 mM for both PCR systems. Studies varying the magnesium chloride concentration were performed between 0 – 11 mM.

2.3.2.3.1 Conventional PCR System

Data resulting from the variation of magnesium chloride concentration are presented in Figure 2.40. High product peak areas were observed for magnesium chloride concentrations between 3 and 5 mM. For higher magnesium chloride concentrations product peak areas were then seen to gradually decrease. These data suggest that magnesium chloride concentrations should be kept between 3 and 7 mM.

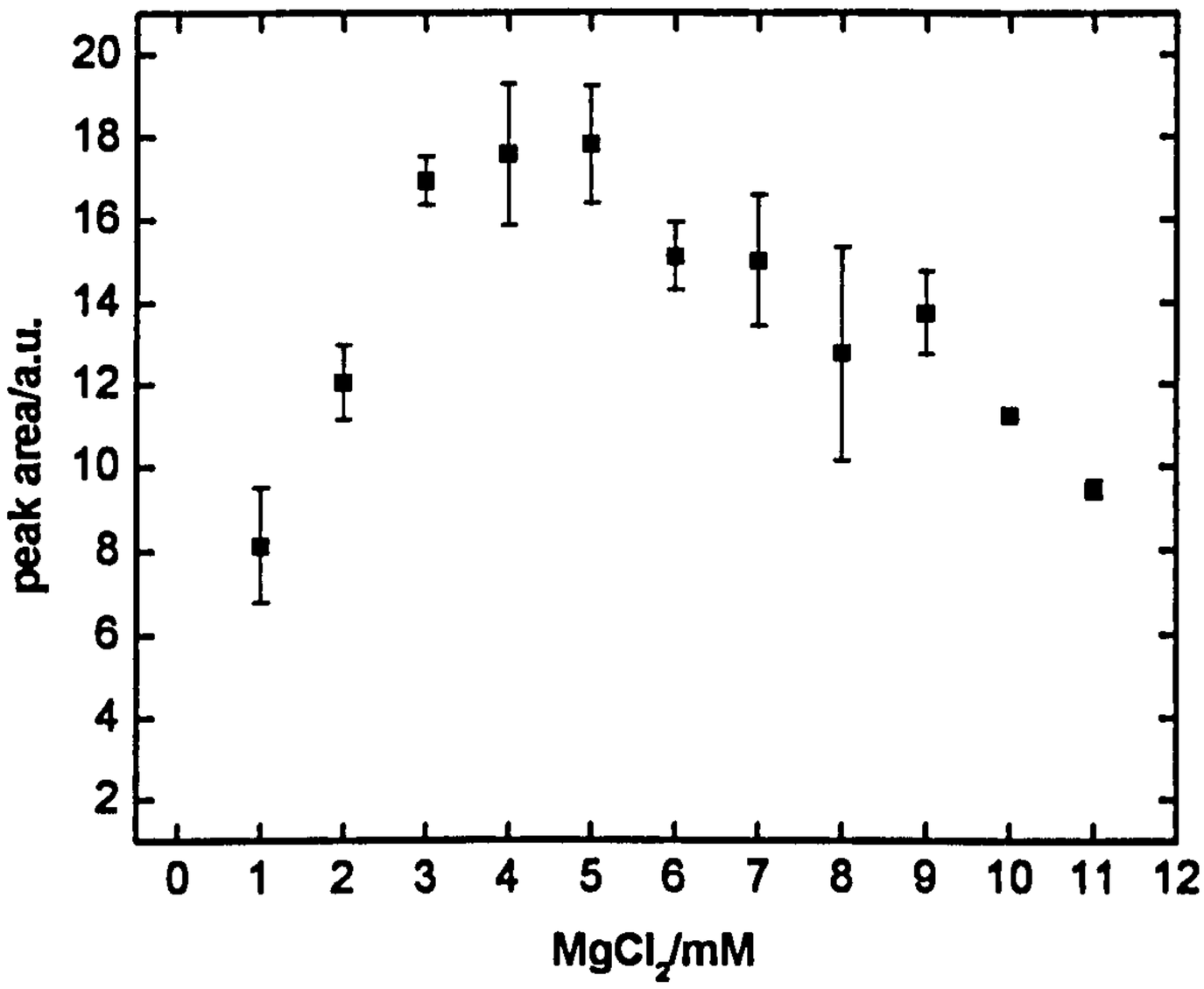


Figure 2.40 **Variation of peak area as a function of magnesium chloride concentration. Five replicates were used to define each data point.**

2.3.2.3.2 Real-Time PCR System

Smart Cycler and BioAnalyzer results for the variation of the magnesium chloride concentration are presented in Figures 2.41 and 2.42 respectively. High C_t values were observed for magnesium chloride concentrations between 2 and 3 mM. C_t values were then seen to minimize for magnesium chloride concentrations between 5 and 10 mM. These data indicate that magnesium chloride concentrations should be kept between 5 and 10 mM. Figure 2.42 demonstrates that increasing product peak areas were obtained for magnesium chloride concentrations between approximately 2 and 8 mM. Peak areas were then observed to decrease at higher magnesium chloride concentrations. These data suggest that the magnesium chloride concentration should be kept between 2 and 8 mM. The combination of both data sets suggests optimum conditions for real-time PCR are defined by magnesium chloride concentrations between 5 and 8 mM.

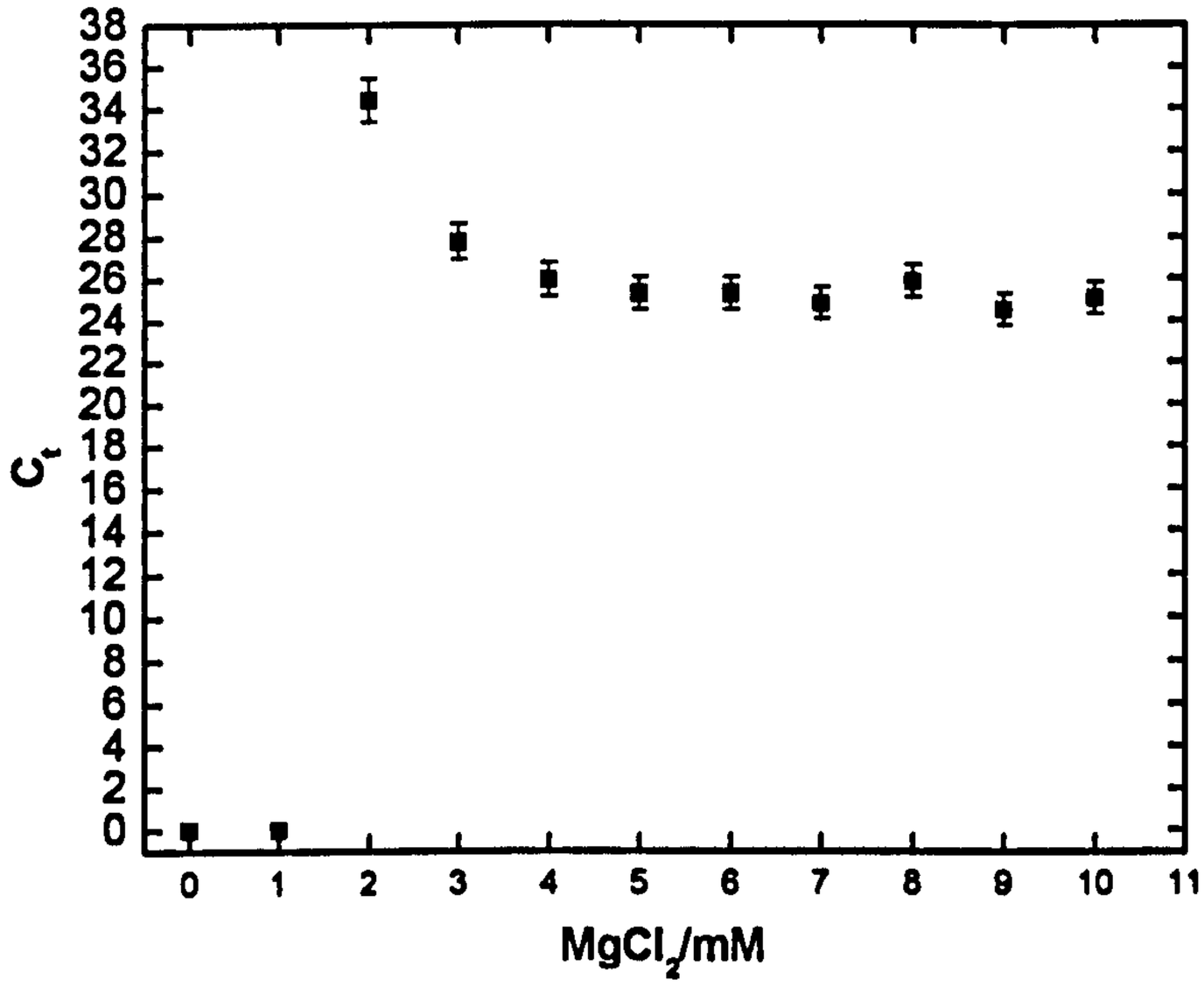


Figure 2.41 Variation of C_t value as a function of magnesium chloride concentration. Five replicates were used to define each data point.

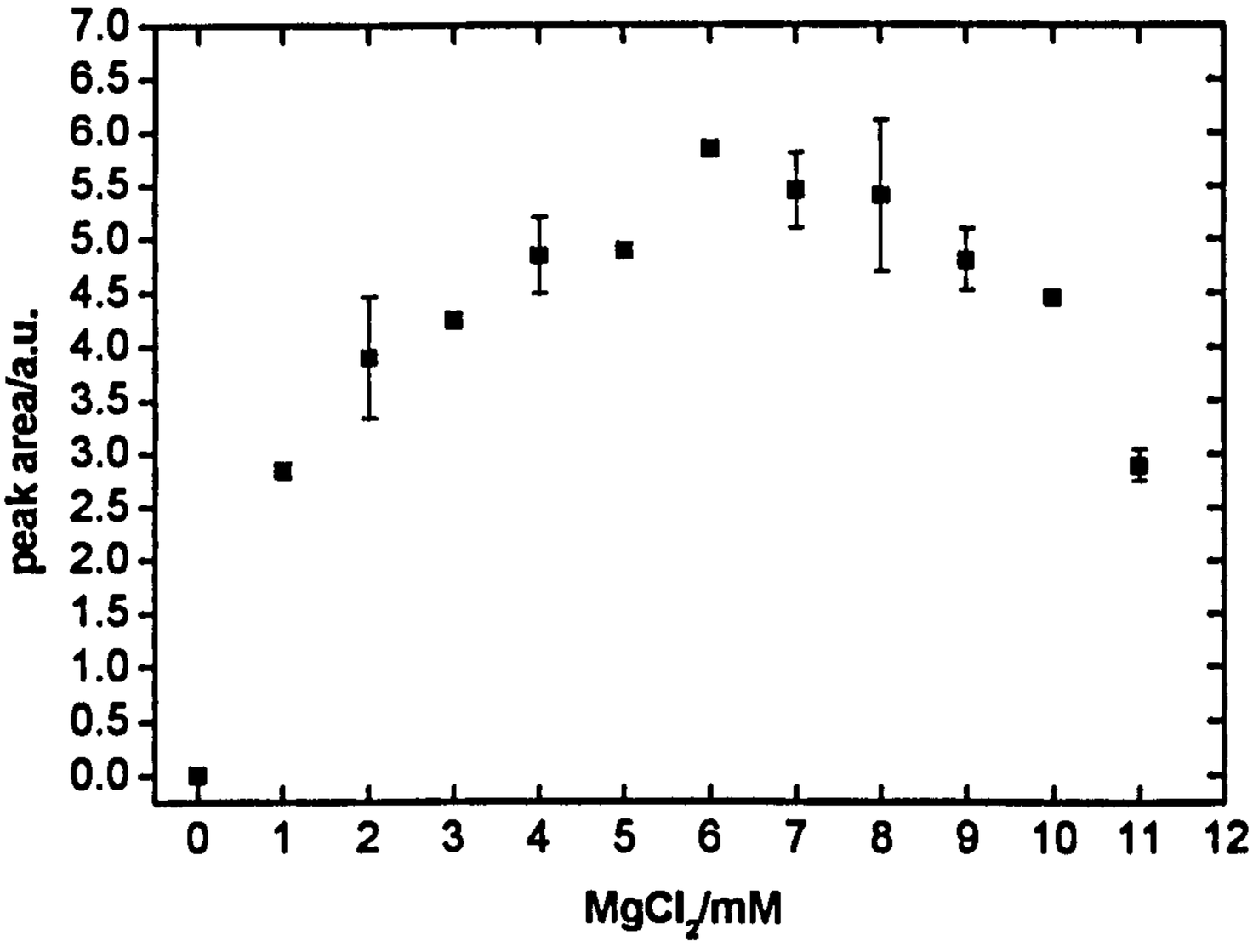


Figure 2.42 Variation of peak area as a function of magnesium chloride concentration. Five replicates were used to define each data point.

Optimum magnesium chloride concentrations for the conventional PCR system are between 3 and 7 mM. In addition, optimum magnesium chloride concentrations for the real-time PCR system are between 5 and 8mM.

2.3.2.4 Target Concentration Optimization

For the *Bacillus globigii* system a target concentration of 1 ng/µl. is recommended by the manufacturers for both PCR systems. Studies varying the target concentration were performed between 10 pg and 281 ng/µl. The upper limit is defined by the difficulty in precipitating DNA at high concentrations.

2.3.2.4.1 Real-Time PCR System

Smart Cycler results for the variation of target concentration are presented in Figure 2.43 where C_t values are plotted as a function of target concentration. Decreasing C_t values were observed with increasing target concentrations. A linear relationship between C_t value and log target concentration is observed. As the dynamic range of real-time PCR is at least six order of magnitude and within this range, the relationship between log target DNA and C_t values is expected to be linear [11]. These data indicate that target concentrations should be kept as high as possible within the range studied. Consequently an ideal target concentration would be 281 ng/µl. However, due to precipitation difficulties it was decided to keep the target concentration at the specified value of 1 ng/µl.

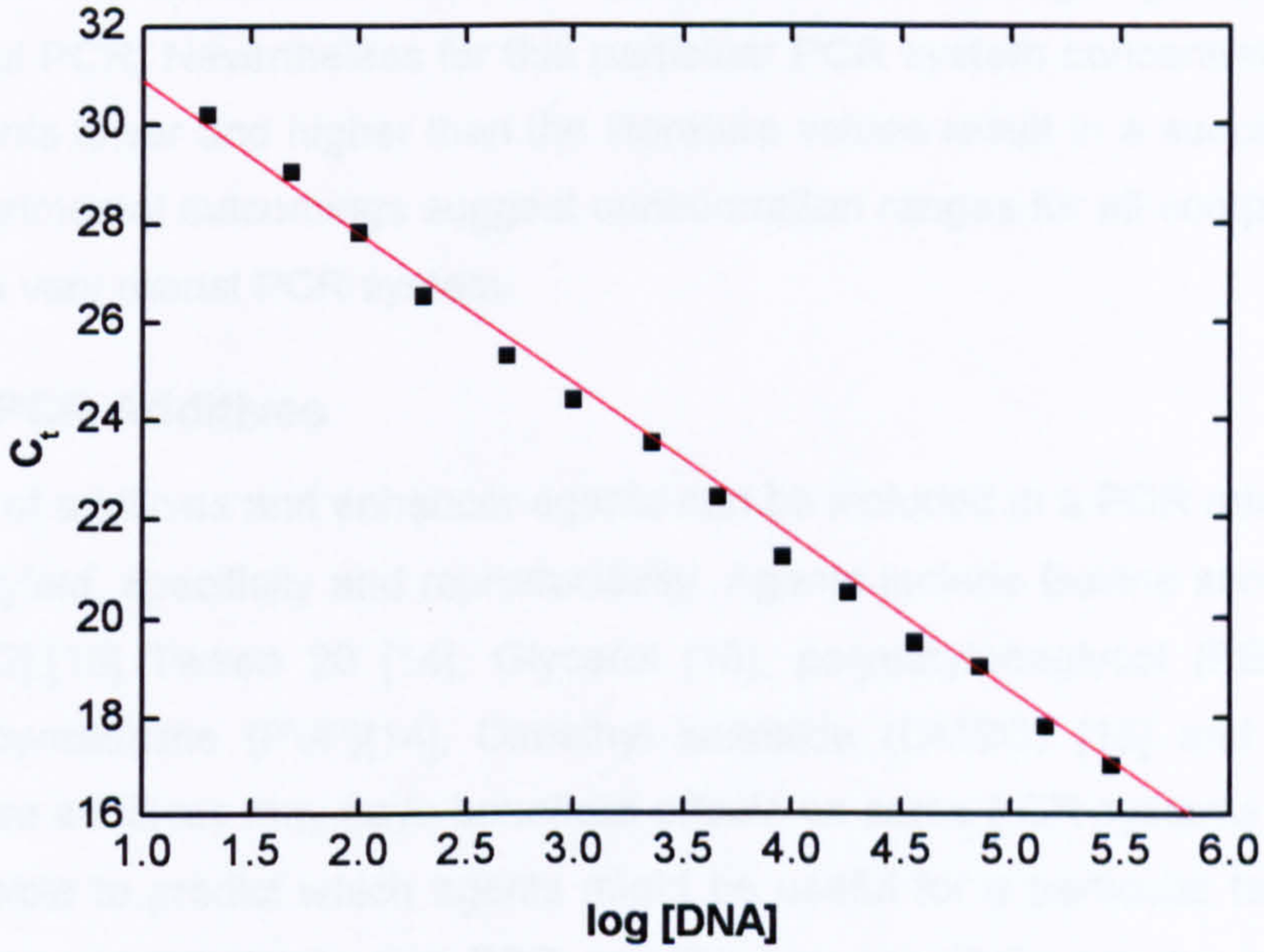


Figure 2.43 **Variation of C_t as a function of $\log_{10}$ target concentrations. Five replicates were used to define each data point.**

	Literature	Experimental
Primer concentration (μM)	0.5 μM	0.4-0.7 μM
Primer ratio	1	0.5
Taq concentration (Units/μl)	0.05Units/μl	< 0.6Units/μl
Mg_2Cl concentration (mM)	5 mM	3 – 9 mM
DNA concentration (ng/ μl)	1ng/μl	1ng/μl

Table2. 7 **Comparison of the literature and experimentally optimized PCR conditions for the conventional PCR system.**

	Literature	Experimental
Scorpion primer concentration (μM)	0.5 μM	0.25-0.75 μM
Reverse primer concentration (μM)	0.25 μM	0.125-0.35 μM
Primer ratio	0.5	0.5
Taq concentration (Units/μl)	0.05Units/μl	> 0.05Units/μl
Mg_2Cl concentration (mM)	5mM	5-9mM
DNA concentration (ng/ μl)	1ng/μl	1ng/μl

Table 2.8 **Comparison of the literature and experimentally optimized PCR conditions for the real-time PCR system.**

The experimental studies performed indicate that the literature values for all PCR component concentrations can be considered as average guidelines for a successful PCR. Nevertheless for this particular PCR system concentrations of key components lower and higher than the literature values result in a successful PCR. The experimental outcomings suggest concentration ranges for all components and indicate a very robust PCR system.

2.3.2.5 PCR Additives

A variety of additives and enhancer agents can be included in a PCR mix in order to increase yield, specificity and reproducibility. Agents include Bovine serum albumin (BSA) [12],[13] Tween 20 [14], Glycerol [15], polyethyleneglycol (PEG)[16],[17], polyvinylpyrroldilone (PVP)[14], Dimethyl sulfoxide (DMSO) [18] and formamide [19]. These additives may have beneficial effects on some PCR systems, however it is impossible to predict which agents might be useful for a particular target. There are reports which indicate that PCR amplification specificity can be improved by formamide but not DMSO [19] and reactions in which DMSO was more effective than formamide at increasing yield and specificity [20]. For the *Bacillus globigil* PCR system BSA, PVP, PEG and Tween 20 were investigated. It was found (data not shown) that only BSA and PVP resulted in an enhancement of the PCR amplification. Indeed both Tween and PEG act as effective inhibitors of this particular PCR system.

2.3.2.5.1 BSA Optimization

BSA is recognised as a PCR enhancer on the macroscale. Studies have shown that BSA competes with other proteins for surface adsorption sites [12]. Studies varying the BSA concentration between 0.2 and 3 g/l were performed for both PCR systems.

2.3.2.5.1.1 Conventional PCR System

Results from the variation of BSA concentration are presented in Figure 2.44. High product peak areas were observed for BSA concentrations between 0.2 and 0.5 g/l. Peak areas were then seen to decrease for higher BSA concentrations. These data suggest that BSA concentrations should be kept between 0.2 and 0.5 g/l.

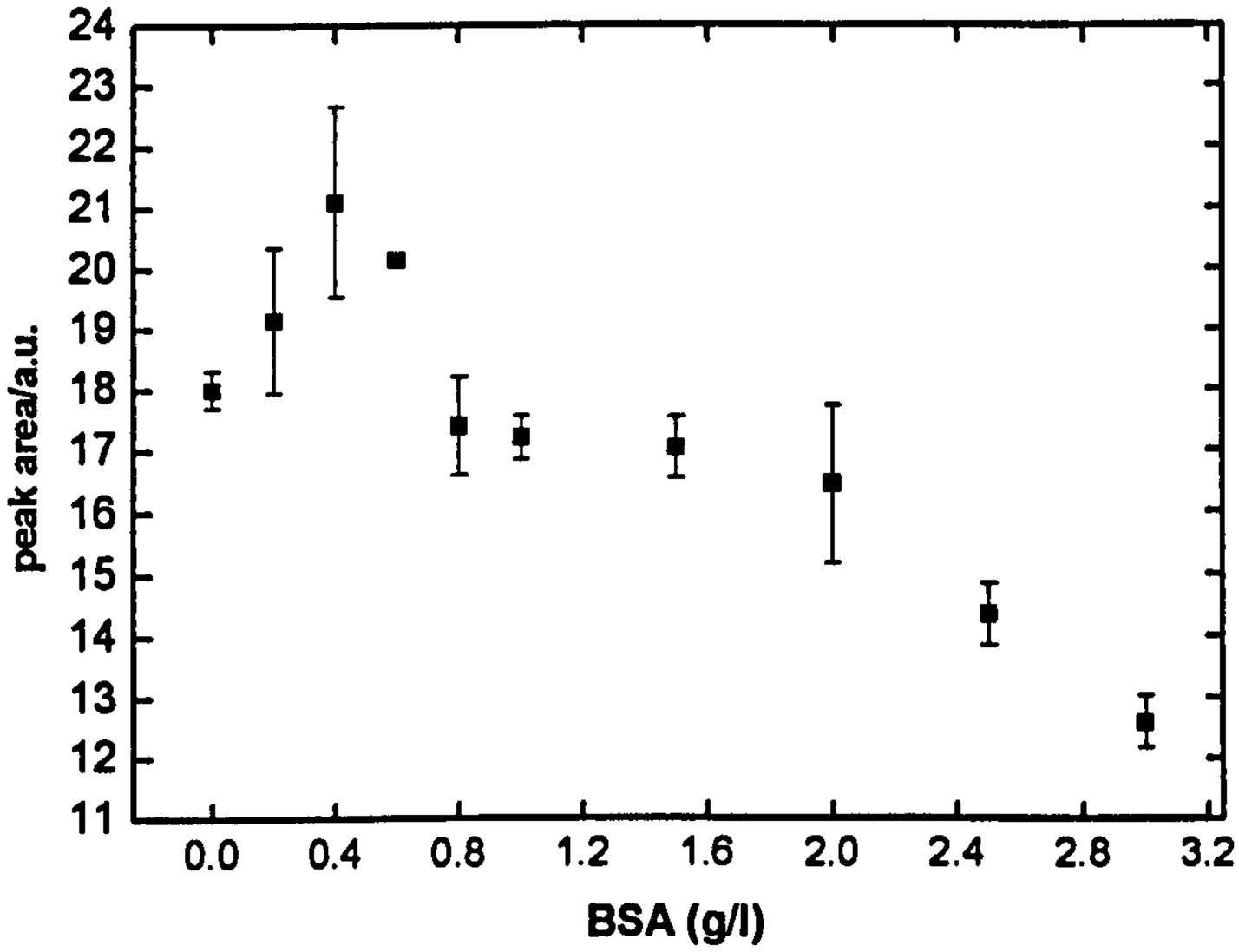


Figure 2.44 **Variation of peak area as a function of BSA concentration. Five replicates were used to define each data point.**

2.3.2.5.1.2 Real-Time PCR System

Smart Cycler and BioAnalyzer results for the variation of BSA concentrations are presented in Figure 2.45 and 2.46 respectively. While Smart Cycler data in Figure 2.45 indicate little variation in C_t value for BSA concentrations between 0 and 1.25 g/l, BioAnalyzer data in Figure 2.46 indicate high product peak areas for BSA concentrations between 0.2 and 0.6 g/l. Peak areas were then observed to decrease for BSA concentrations between 0.8 and 2.5 g/l. These data suggest that BSA concentrations should be kept between 0.2 and 0.6 g/l.

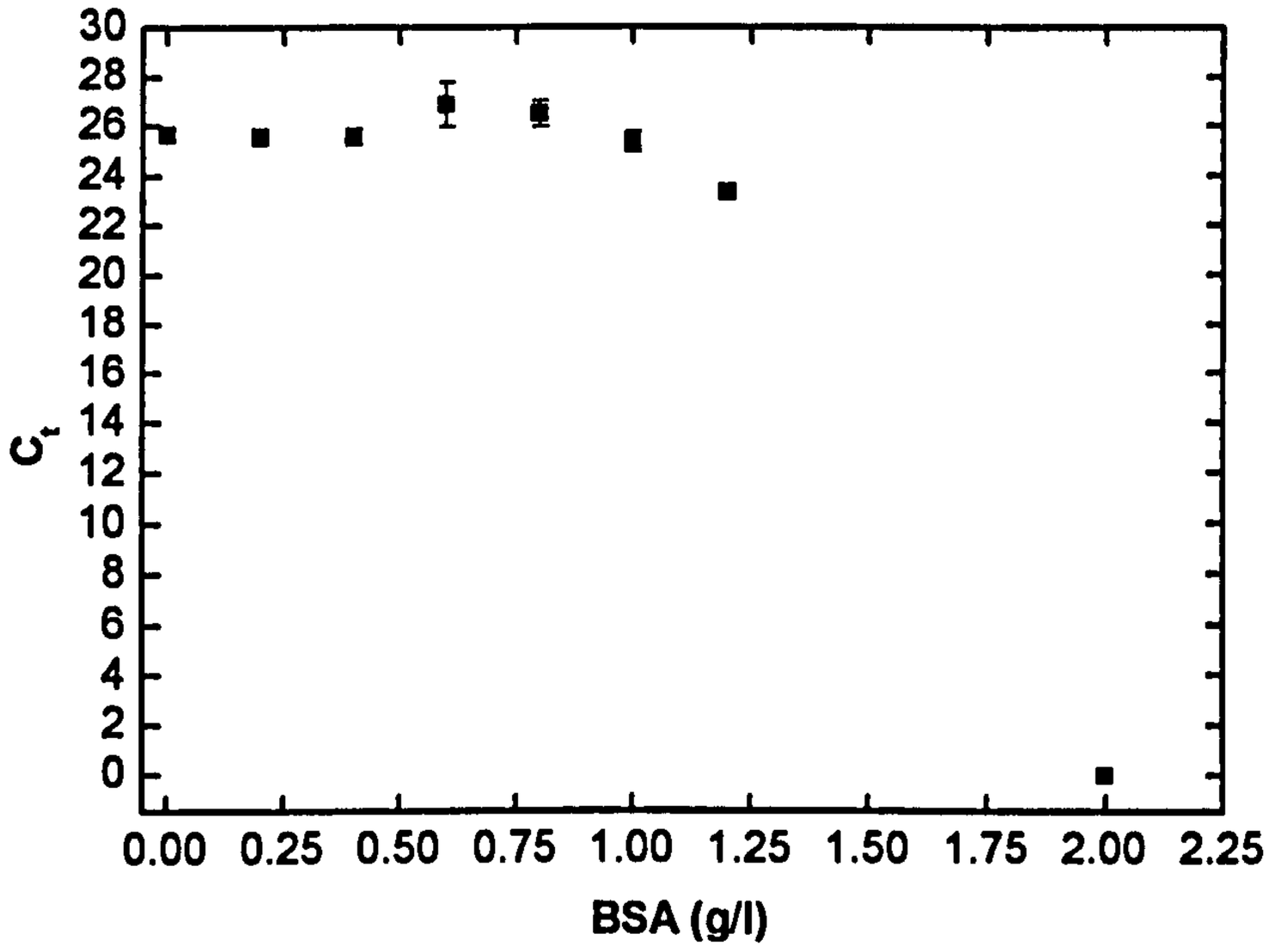


Figure 2.45 **Variation of C_t value as a function of BSA concentration. Five replicates were used to define each data point.**

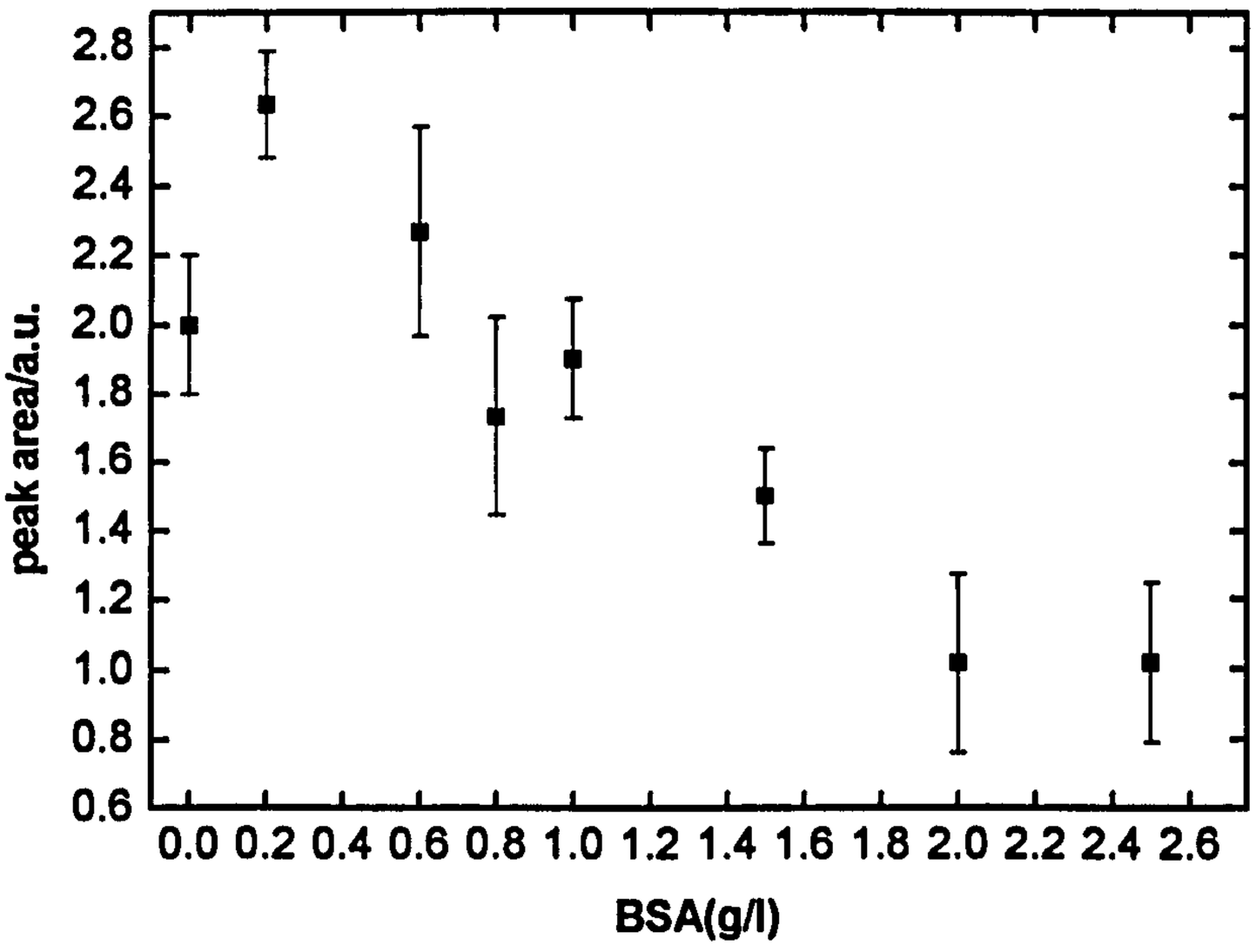


Figure 2.46 **Variation of peak area as a function of BSA concentration. Five replicates were used to define each data point.**

Optimum BSA concentrations for the conventional PCR system are between 0.2 and 0.5g/l. While optimum BSA concentrations for the real-time PCR system are between 0.2 and 0.6 g/l.

2.3.2.5.2 PVP Optimization

Depending on the PCR system PVP can reverse inhibitory effects [21]. Additionally it is known as a water-soluble polymer which has excellent wetting properties and readily forms films on surfaces. Studies varying the concentration between 1 and 16 µM were performed on both PCR systems.

2.3.2.5.2.1 Conventional PCR System

Data resulting from the variation of PVP concentration are summarized in Figure 2.47. High product peak areas were observed for PVP concentrations between 2 and 4 µM. Peak areas were then observed to decrease for PVP concentrations between 5 and 16 µM. The significant reduction in efficiency at concentrations above 5 µM is most likely to be due to inhibitory effects caused by PVP in the PCR mix such as interactions between PVP and the Taq Polymerase or a PVP-DNA complex formation which might prevent Taq Polymerase moving on to the DNA chain and therefore inhibit PCR [21, 22]. Consequently optimum conditions involve PVP concentrations between 2 and 4 µM.

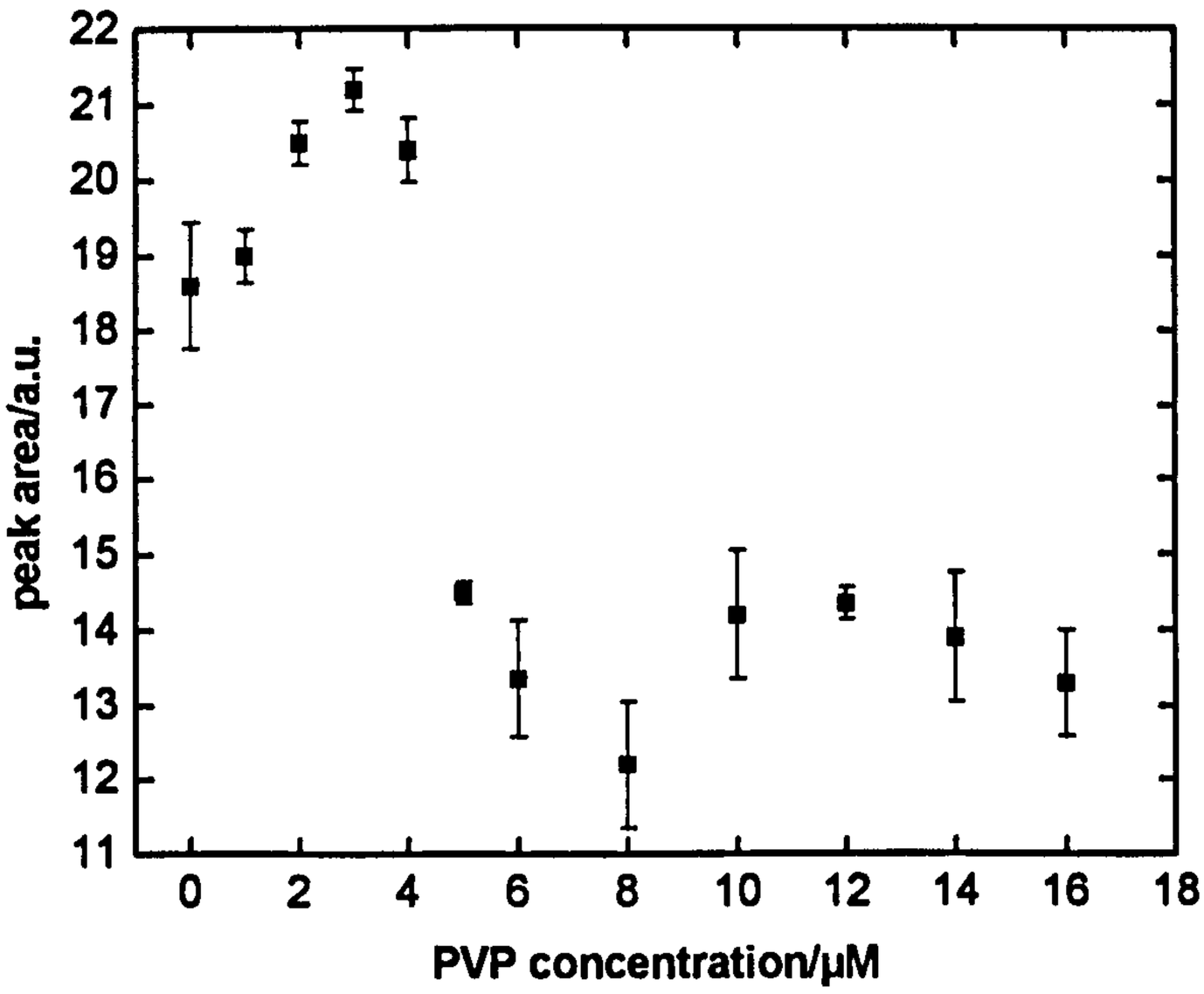


Figure 2.47 **Variation of peak area as a function of PVP concentration. Five replicates were used to define each data point.**

2.3.2.5.2.2 Real-Time PCR System

Smart Cycler and BioAnalyzer results from the variation of PVP concentrations are presented in Figures 2.48 and 2.49 respectively. While Smart Cycler results (Figure 2.48) show little dependency of C_t on PVP concentration, BioAnalyzer data in Figure 2.49 show a similar trend as seen in Figure 2.48. Highest product peak areas were observed for PVP concentrations between 1 and 4 µM. Peak areas were then seen to decrease for PVP concentrations between 5 and 15 µM. The significant reduction in efficiency at concentrations above 5 µM is most likely due to inhibitory effects caused through high concentrations of PVP in the PCR mix as mentioned in 2.3.2.2.2.1. Consequently optimum conditions involve PVP concentrations between 1 and 4 µM.

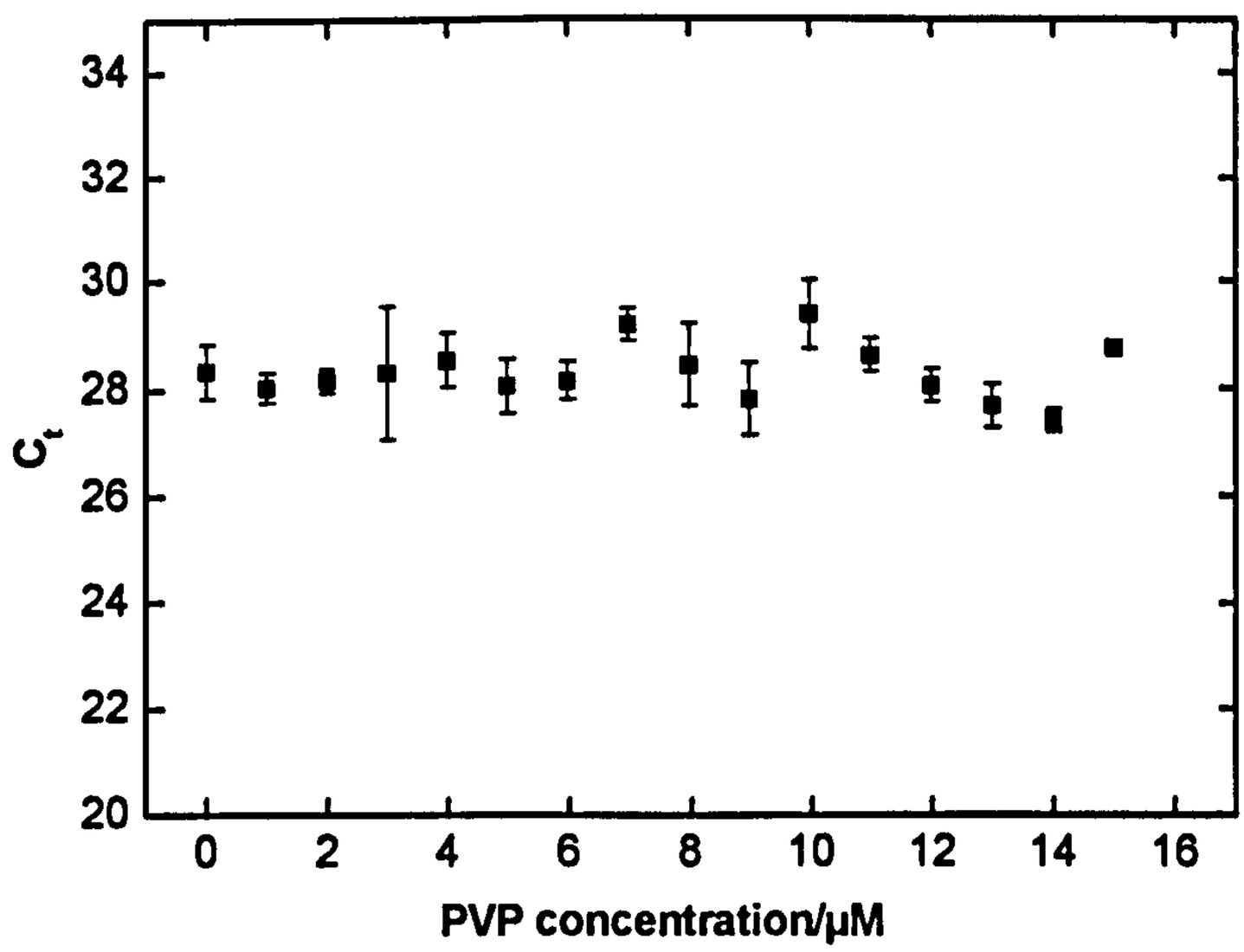


Figure 2.48 **Variation of C_t value as a function of PVP concentration. Five replicates were used to define each data point.**

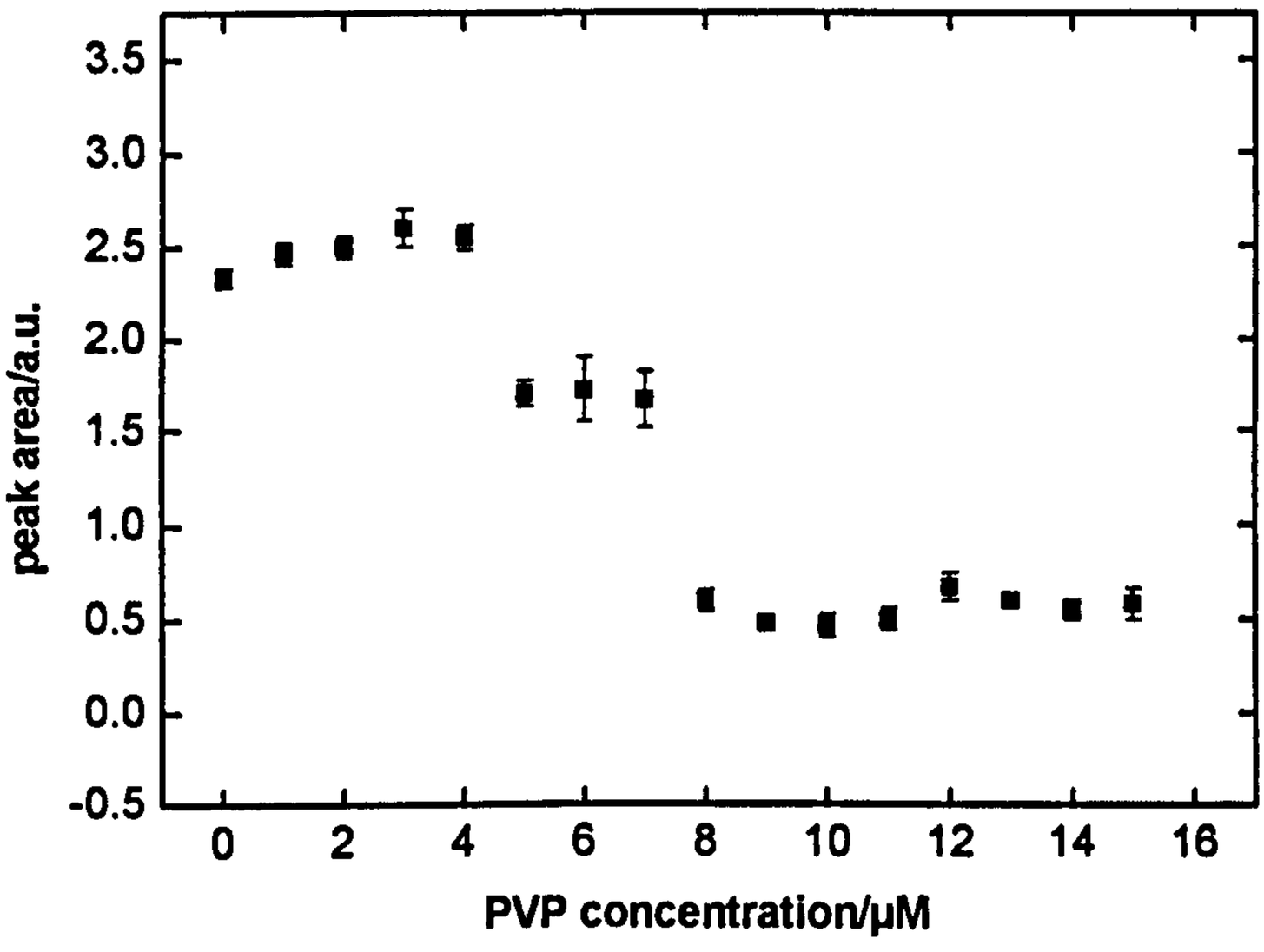


Figure 2.49 **Variation of peak area as a function of PVP concentration. Five replicates were used to define each data point.**

Optimum PVP concentrations for the conventional PCR system are between 2 and 4 μM. While optimum PVP concentrations for the real-time PCR system are between 1 and 4 μM.

2.4 Discussion

The outcome of the results presented in section 2.3.1 and 2.3.2 are summarized in Table 2.9 for the conventional PCR system and in Table 2.10 for the real-time PCR system. These results constitute the framework for the PCR conditions which will be used for micro-scale PCR. In this thesis the results from section 2.3.1 provide sufficient guidelines of the thermal cycling conditions for the PCR system of *Bacillus globigii*. The outcomes described in this section show a PCR which is robust to temperature, time, cycle number and ramp rate variation. Consequently this allows some degree of flexibility when designing the layout of the micro-scale device. Parameters such as length, depth and width of channels or individual zones, or the flow rates with which the PCR mixture is pumped through microchannels can be extensively varied. Indeed a number of different layouts are fabricated and tested and will be described subsequently.

Additionally results from section 2.3.2 provide guidelines on the concentration ranges of the PCR components for the PCR system of *Bacillus globigii*. The results here also facilitate great flexibility in terms of concentrations of PCR components. As PCR on micro-scale is likely to behave quite differently to PCR on macroscale, the results of this section enable various modifications which can be used to achieve successful PCR.

Protocol conditions	Temperature (°C)	Time (s)
Hot-start	94-96	≤25
Denaturation	90-94	1-4
Annealing/extension	50-70	>10s
Cycle numbers	20 <X>50	
PCR components	concentration	ratio
Primer	0.4-0.7 µM	1
Taq	>0.05Units/µl	
Magnesium chloride	3-9mM	
Target DNA	1ng/µl	
PCR additives	concentration	
BSA	0.2-0.5 g/l	
PVP	2-4 µM	

Table 2.9 **Summary for conventional PCR system conditions.**

Protocol conditions	Temperature (°C)	Time (s)
Hot-start	92-96	≤20
Denaturation	92-96	2
Annealing/extension	60-66	>10s
Cycle numbers	20 <X>50	
PCR components	concentration	ratio
forward primer / reverse primer	0.125-0.35 µM /0.25-0.75 µM	0.5
Taq	>0.05Units/µl	
Magnesium chloride	5-9mM	
Target DNA	1ng/µl	
PCR additives	concentration	
BSA	0.2-0.6 g/l	
PVP	1-4 µM	

Table 2.10 **Summary for real-time PCR system conditions.**

1. Todar, K. *Bacillus anthracis and anthrax*. 2005 [cited 2007 October 2007]; Available from: http://www.textbookofbacteriology.net/Anthrax.html.
2. *Anthrax*. 2005 [cited 2007 October 2007]; Available from: http://www.cdc.gov/ncidod/dbmd/diseaseinfo/anthrax_g.htm.
3. Inglesby, T.V., O'Toole, T., Henderson, D.A., Bartlett, J.G., Ascher, M.S., Eitzen, E., Friedlander, A.M., Gerberding, J., Hauer, J., Hughes, J., McDade, J., Osterholm, M.T., Parker, G., Perl, T.M., Russell, P.K., and Tonat, K., *Anthrax as a Biological Weapon, 2002: Updated Recommendations for Management*. The Journal of American Medical Association, 2002. 287(17): p. 2236-2252.
4. Whitcombe, D., Theaker, J., Guy, S.P., Brown, T., and Little, S., *Detection of PCR products using self-probing amplicons and fluorescence*. Nature Biotechnology, 1999. 17(August): p. 804-807.
5. Wu, P.G. and Brand, L., *Resonance Energy Transfer: Methods and Applications*. Analytical Biochemistry, 1994. 218(1): p. 1-13.
6. Newton, C.R., Holland, D., Heptinstall, L.E., Hodgson, I., Edge, M.D., Markham, A.F., and McLean, M.J., *The production of PCR products with 5' single-stranded tails using primers that incorporate novel phosphoramidite intermediates*. Nucleic Acids Research, 1993. 21(5): p. 1155-1162.
7. Cepheid. *Cepheid Products*. [cited 2007 October 2007]; Available from: http://www.cepheid.com/Sites/cepheid/content.cfm?id=180.
8. Ehrlich, H.A., *PCR technology; Principles and Applications for DNA Amplification*. 1989: Macmillan.
9. Mullis, K.B., Ferre, F., and Gibbs, R.A., *The Polymerase Chain Reaction*. 1994, York: Birkhaeuser. 441.
10. Quirke, P. and Taylor, G.R., *PCR - A practical Approach*. The Practical Approach Series, ed. D.a.H. Rickwood, B.D. 1991, Oxford: Oxford University Press. 280.
11. Vaerman, J.L., Saussoy, P., and Ingargiola, I., *Evaluation of real-time PCR data*. Journal of Biological Regulators and Homeostatic Agents, 2004. 18(2): p. 212-214.
12. Erill, I., Campoy, S., Erill, N., Barbe, J.C., and Aguilo, J., *Biochemical analysis and optimization of inhibition and adsorption phenomena in glass-silicon PCR-chips*. Sensors and Actuators B, 2003. 96: p. 685-692.
13. Lagally, E.T., Simpson, P.C., and Mathies, R.A., *Monolithic integrated microfluidic DNA amplification and capillary electrophoresis analysis system*. Sensors and Actuators B-Chemical, 2000. 63(3): p. 138-146.
14. Kopp, M.U., de Mello, A.J., and Manz, A., *Chemical amplification: Continuous-flow PCR on a chip*. Science, 1998. 280(5366): p. 1046-1048.
15. Woolley, A.T., Hadley, D., Landre, P., de Mello, A.J., Mathies, R.A., and Northrup, M.A., *Functional Integration of PCR Amplification and Capillary Electrophoresis in Microfabricated DNA Analysis device*. Analytical Chemistry, 1996. 68: p. 4081.

16. Giordano, B.C., Ferrance, J., Swedberg, S., Huhmer, A.F.R., and Landers, J.P., *Polymerase chain reaction in polymeric microchips: DNA amplification in less than 240 seconds.* Analytical Biochemistry, 2001. 291(1): p. 124-132.
17. Panaro, N.J., Lou, X.J., Fortina, P., Kricka, L.J., and Wilding, P., *Surface Effects on PCR Reactions in Multichip Microfluidic Platforms.* Biomedical Microdevices, 2004. 6(1): p. 75-80.
18. Frackman, S., Kobs, G., Simpson, D., and Storts, D., *Betaine and DMSO: Enhancing Agents for PCR.* Promega Notes, 1998. 65: p. 27-31.
19. Sarkar, G., Kapelner, S., and Sommer, S.S., *Formamide can dramatically improve the specificity of PCR.* Nucleic Acids Research, 1990. 18(24): p. 1.
20. Varadaraj, K. and Skinner, D.M., *Denaturants or cosolvents improve the specificity of PCR amplification of a G +C rich DNA using genetically engineered DNA polymerases* Gene 1994. 140(1): p. 1-5.
21. Koonjul, P.K., Brandt, W.F., Farrant, J.M., and Lindsey, G.G., *Inclusion of polyvinylpyrrolidone in the polymerase chain reaction reverses the inhibitory effects of polyphenolic contamination of RNA* Nucleic Acids Research, 1999(27): p. 915-916.
22. Xia, Y.M., Hua, Z.S., Srivannavit, O., Ozel, A.B., and Gulari, E., *Minimizing the surface effect of PDMS-glass microchip on polymerase chain reaction by dynamic polymer passivation.* 2007. p. 33-38.

3

Chip Fabrication

This chapter describes the methods and techniques used in the fabrication of the microfluidic systems used within this thesis. In addition an investigation of the etching process is performed. Finally the etching process is optimized and ideal microfluidic devices are presented.

Most of the methods used in the manufacture of microfluidic devices were initially developed in the 1960s, 1970s and 1980s in the silicon microprocessor industry. These are discussed in detail in a number of books, including, Fundamentals of Microfabrication [1] and the Handbook of Microlithography [2, 3]. To develop devices suitable for use in chemistry and biology, new materials and microfabrication procedures have been developed and added to the existing repertoire. Table 3.1 lists some of these new materials and the associated references that detail their micromachining. The references given in Table 3.1 represent only a small fraction of the actually published work.

material	Reference
Glass	[4-6]
Borofloat-glass	[7-9]
Fused silica	[10, 11]
Silica	[12]
Soda-lime glass	[13]
Silicon	[14, 15]
SU-8	[16-18]
Acrylic (PSA)	[19]
PDMS	[20-22]
PEEK	[23]
COC	[24]
PMMA	[24]
Polyimide	[19]
PTFE	[25]
Fluorocarbon film	[26]
PC	[27]
Diamond coated chip	[28]
Zeonor	[29, 30]

Table 3.1 Common materials used as substrates in microdevice fabrication.

For more detailed information, a study of the proceedings of international conferences such as Transducers, MEMS and μTAS is recommended. The first microfluidic systems typically used silicon [31] and glass [32] as substrate materials. While the advantages of silicon lie in its high purity and its ability for being easily structured with high precision, disadvantages associated with its use lie in its high cost, opacity to visible and ultraviolet light and poor chemical compatibility with common laboratory chemicals and solvents. In contrast, glass is cheap, transparent

to visible light, chemically and thermally resistant and relatively easy to structure. The combination of these advantages and the ease of in house fabrication make glass an ideal material for microfluidic device fabrication. However, for applications requiring the creation of thousands of devices (e.g. in medical diagnostics) alternative materials such as Polydimethylsiloxane (PDMS), Poly(methylmethacrylate) (PMMA), Polycarbonate (PC), SU-8, PEEK, PTFE, Cyclic-Olefin-Copolymer (COC) and Zeonor are required. While the fabrication of components for microanalytical systems is facile using elastomers (e.g. PDMS) rather than conventional rigid materials, the drawback in using materials like PDMS lies in poor stability to heat and chemical reagents [5]. Consequently, for the studies described in this thesis, it was decided that glass was the ideal material for making continuous flow PCR devices. In this chapter the process of glass microdevice fabrication will be introduced and briefly discussed. Problematic issues encountered within the fabrication process, and techniques used for surface analysis will be presented.

3.1 Microchip Fabrication Process

This section describes the fabrication of soda lime glass microfluidic devices. As depicted in the flow chart in Figure 3.1 the microfabrication process consists of three major steps; patterning, etching and closure of the device. Figure 3.2 provides a schematic representation of the individual fabrication steps more in detail.

Figure 3.1 **Chip fabrication consists of three main parts: patterning, etching and closure. The flow diagram presents the chronology of this process.**

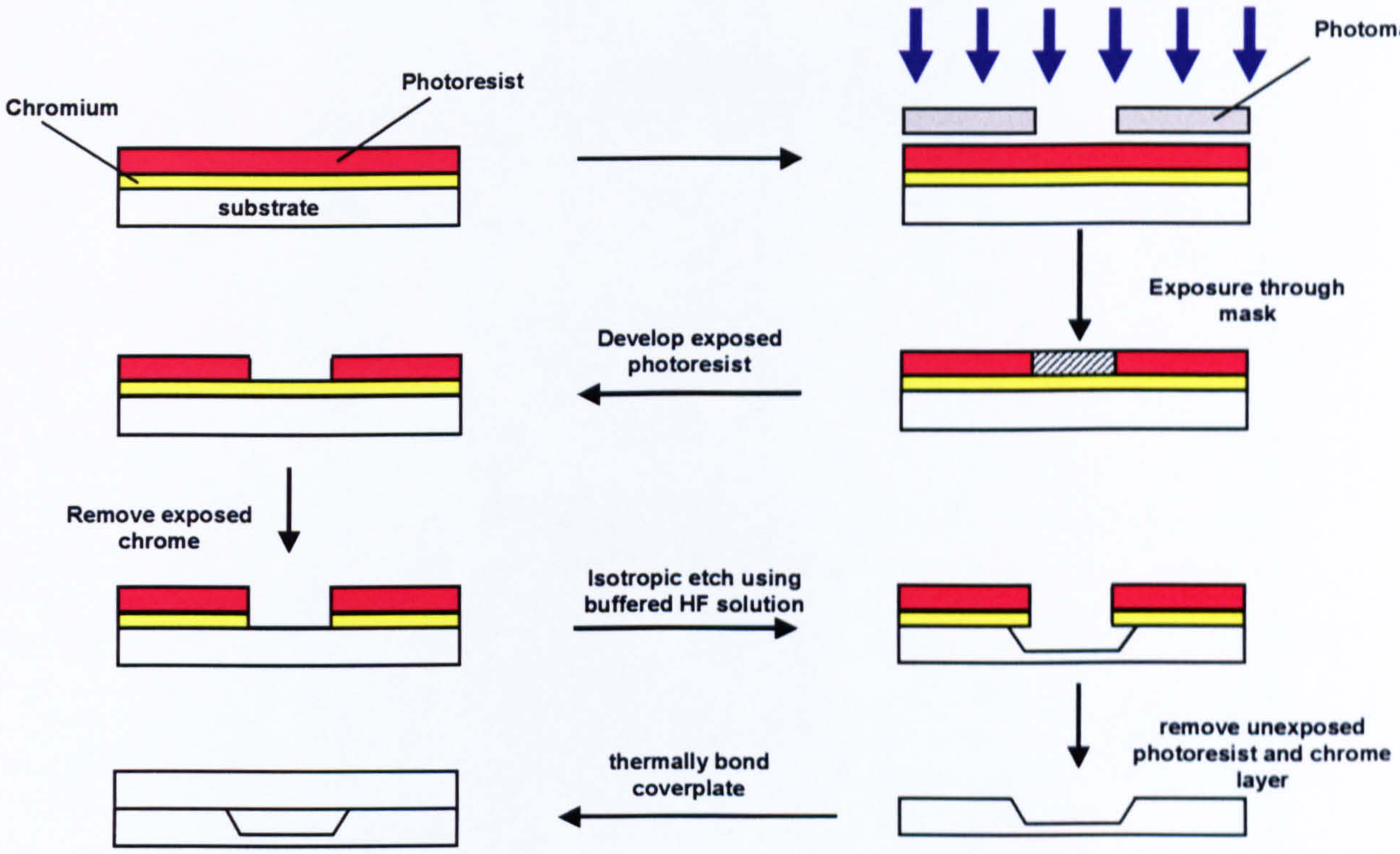


Figure 3.2 The individual steps in microchip fabrication .

It is of note to stress that the chemical, optical, thermal, mechanical and electrical properties of the substrate material are important in defining the microdevice fabrication process. While the chemical properties play a major role in the etching step, the thermal and mechanical properties are of importance during the bonding step. Optical and electrical properties play a more significant role during eventual experimentation. The chip material used in this thesis is soda lime glass (Nanofilm, Westlake Village, USA). Substrates have dimensions of 75 mm X 75 mm X 1.5 mm. Important physical properties of soda lare provided in Table 3.2.

Property	Value
Chemical composition (%)	
SiO_2	72.6
Na_2O	13.0
CaO	8.4
MgO	3.9
Fe_2O_3	0.1
Al_2O_3	1.1
K_2O	0.6
SO_3	0.3
Optical properties	
Light transmittance (%) d = 2.3 mm, λ = 400 nm	90
refractive index	1.52
Thermal properties	
Thermal conductivity	0.937 $Wm/m^2°C$
Thermal coefficient of expansion	$8.6 X 10^{-6}/°C$
Softening point	726 °C
Annealing range	546 °C
Strain point	514 °C
Mechanical Properties	
Density	$2.44g/cm^3$
Hardness (Moh's Scale)	6-7
Knoop Hardness	$585 kg/mm^2$
Modulus of Elasticity	$7200 kg/mm^2$
Modulus of Rigidity (Shear)	$3000kg/mm^2$
Electrical properties	
Dielectric constant at 20 °C	7.75

Table 3.2 Chemical and physical properties of soda lime glass. [33].

In order to enable efficient patterning and etching the soda lime glass wafers were provided by the manufacturer with a coating of 0.1 ± 0.006 µm low reflective chrome which was in turn covered with a layer of 0.53 ± 0.01 µm positive photoresist (Hoechst AZ1518, Hoechst AG, Germany). The role of these layers will be described in the following sections.

3.2 Design Patterning

The layout of a desired microchannel pattern design was created using computer aided design (CAD) software (AutoCAD 2005, Autodesk, Farnborough, Hampshire, UK) to an accuracy of 1 μm, and then transferred to a mask. A generic example of such a design is shown in Figure 3.3.

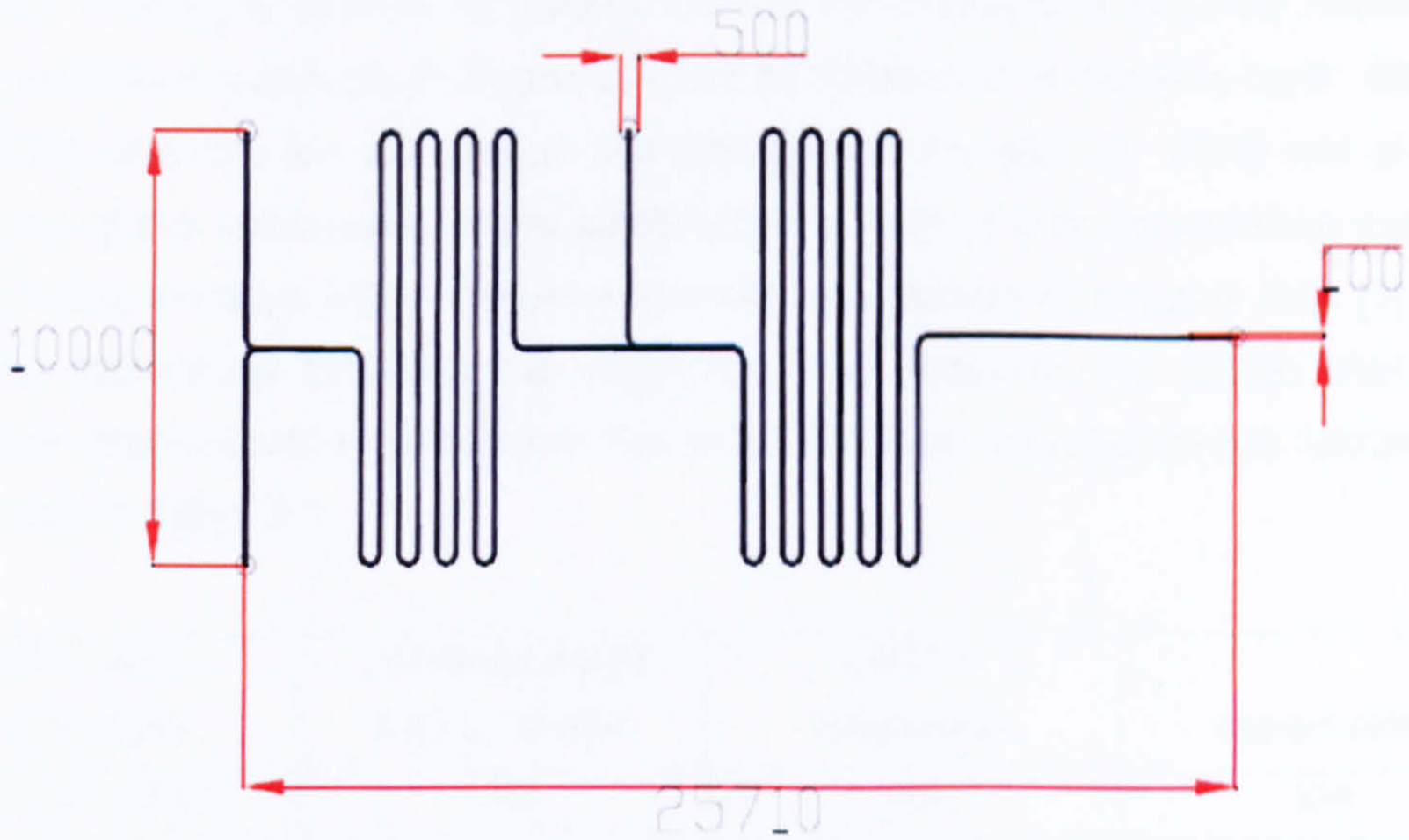


Figure 3.3 Example of an AutoCAD design with dimensions in μm [34].

The design was transferred to a mask externally. The mask is manufactured on a polyester film (J.D. Phototools, Oldham, Lancashire, England). In all cases the mask is a darkfield photomask on which the layout was printed with a resolution of 32,000 dpi. This yields an accuracy of 2.5 μm and a minimum feature size of 4 μm. In order to transfer the layout from the mask layer to the substrate, both were brought together, with the photoresist surfaces in contact. This sandwich was then introduced into a UV lamp box (UV Exposure Unit, LV 202E, RS Components, Corby, Northamptonshire, England), and exposure performed over a period of 3 - 4 minutes. During this exposure process the photoresist on the substrate is weakened by the UV radiation and then removed by soaking the substrate for 1 minute in a resist developer solution (Microposit 351, Shipley Europe Ltd., Coventry, UK 1:5 mix with water). The removal of the photoresist exposed the chrome layer which then was removed by soaking the substrate for 5 minutes in a chrome etchant solution (Chrome Etchant, Lodyne, Microchem Systems) until the underlying glass surface was exposed. The quality of the layout transferral was then inspected under an

optical microscope by assessing the channel width within the layout. It was not only necessary to ensure that channel widths across the whole device were uniform but also to make sure that no defects on the channel surfaces, caused by impurities on the mask or defects on the substrate itself were found. After successful layout transferral channels were etched into the microfluidic device.

3.3 Etching

The fabrication of the three dimensional channels is effected by a process called etching. Etching is defined as pattern transfer by chemical or physical removal of material from a substrate in a pattern which is dictated by a masking layer. Etching generally falls into two categories: wet etching and dry etching. While wet etching consists of the submersion of the substrate in a bath of a liquid chemical etchant, dry etching employs either a vapour etchant or a stream of reactive ions [1]. The etching techniques influence the roughness and shape of the etched channels. Feature characteristics for some of the most common microfabrication techniques are given in Table 3.3.

fabrication technique	cross-sectional etched shape	surface roughness	aspect ratio
Isotropic etching	oval	low	low
Anisotropic etching	rectangular	low	high
Laser ablation	square	low	high
Moulding	desired shape	low	medium
Sand blasting	rectangular	high	medium

Table 3.3 **Fabrication techniques presented with important characteristics for the etching procedure [35].**

Wet etching is the simplest technique commonly available for producing isotropic microchannels in glass. Here, glass is submersed in, for example, a buffered solution of hydrofluoric acid. The surface is then etched in an isotropic manner (Figure 3.4 a) which results in a semicircular profile. Wet etching of glass occurs in isotropic, which means that etching occurs at a uniform rate in all crystallographic directions. However, etching of silicon occurs in an anisotropic manner due to its crystal lattice orientations. Here etching happens at different rates depending on the orientation of the crystal planes of the substrate. This allows channels to be etched directly into a wafer with no lateral etching, thus generating channels with high aspect ratios. Figure 3.4 shows a schematic of isotropically and anisotropically etched channels in cross section.

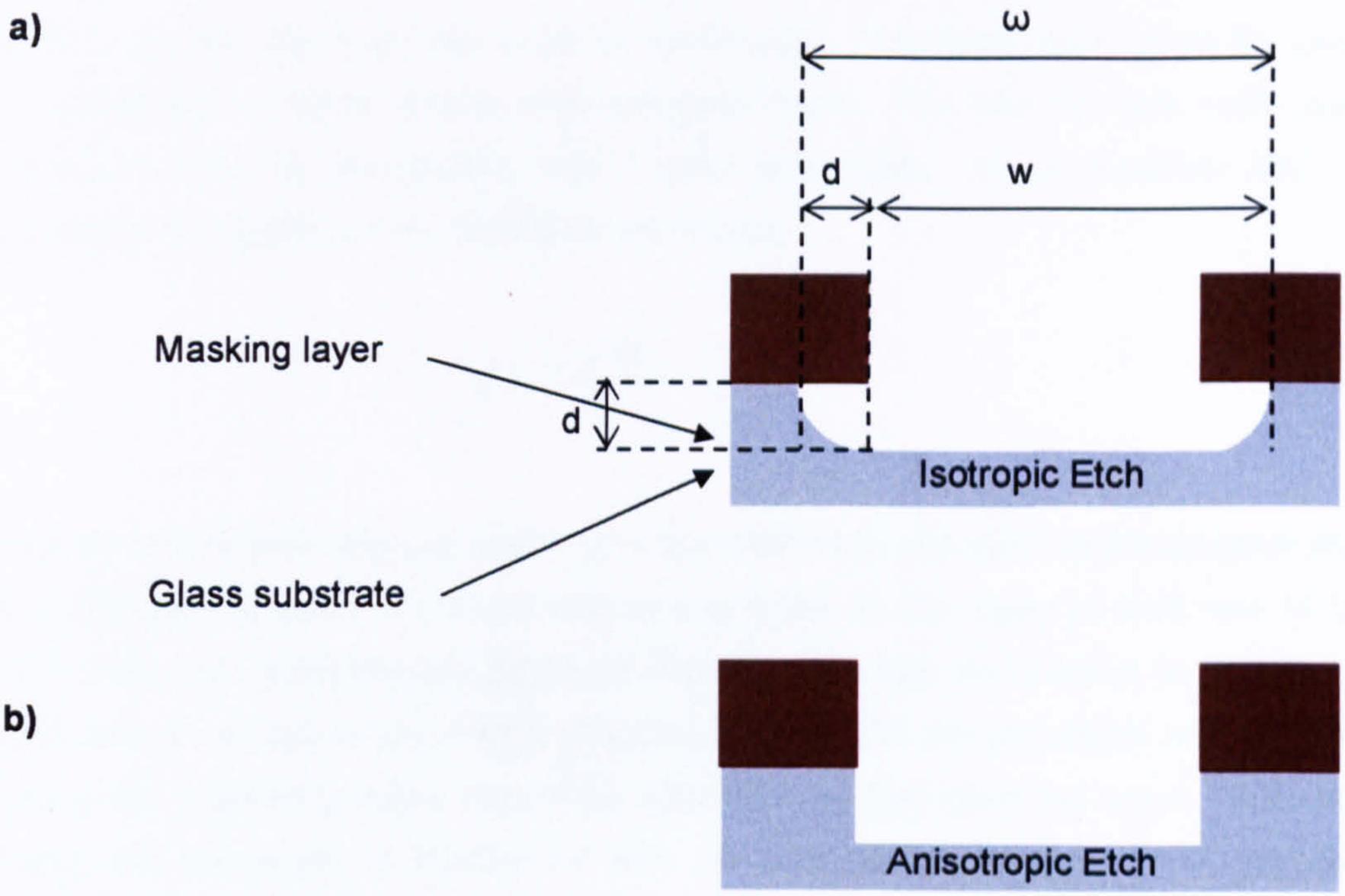


Figure 3.4 **Schematic of isotropically and anisotropically etched channels in cross section. For calculations of the etch depth of a channel, *ω* is the total channel width, *W* is the design width and *d* is the etch depth of the channel.**

Dry etching can be divided into three main techniques, sputtering, vapour phase etching and reactive ion etching (RIE) [36]. All three techniques are fundamentally similar as electric or magnetic fields are applied across a gas which results in the formation of ions, photons, electrons and highly reactive radicals. These highly reactive ions then react with the surface atoms of the substrate to initiate a bond breakage and consequently the physical removal of substrate material. Due to initial high investment costs for dry etching and a lack of established facilities, isotropic wet etching was used for the fabrication of the microfluidic devices throughout this project. Not surprisingly, difficulties were experienced during the wet etching procedure which required a deeper investigation of the solutions used.

3.3.1 Etchant Solutions

Initial etches were performed using buffered hydrofluoric acid, also known as a buffered oxide etch (BOE). Buffering is important for etching as it helps to keep the pH and ion concentrations constant, resulting in stabilized etch rates [37]. A 20 % hydrogen fluoride (HF) solution was prepared using 2 mL HF (48 %), 14 mL ammonium fluoride, 28.5 mL hydrochloric acid and 57 mL of water. Substrates were

immersed in this solution. After one hour the substrate was removed from the etch solution so that the etch rate could be estimated. This information could be used subsequently to obtain specific channel dimensions. The total channel width was measured using a microscope with a calibrated scale. As an isotropic etch is assumed, the depth can be calculated as follows

$$d = \frac{\omega - W}{2} \tag{3.1}$$

Here d is the etched channel depth, ω is the total observed width of the channel and W is the starting width of the channel on the mask. In this case an etch rate of 25 μm/hr was calculated and the substrate was put back into the solution for another 2 hours and 9 minutes to generate a channel width of 218 μm and depth of 77.75 μm. During the etching process impurities adsorbed on the channels were observed. These are presented in Figure 3.5 with no adsorption on channels in (a) and adsorption in channels in (b).

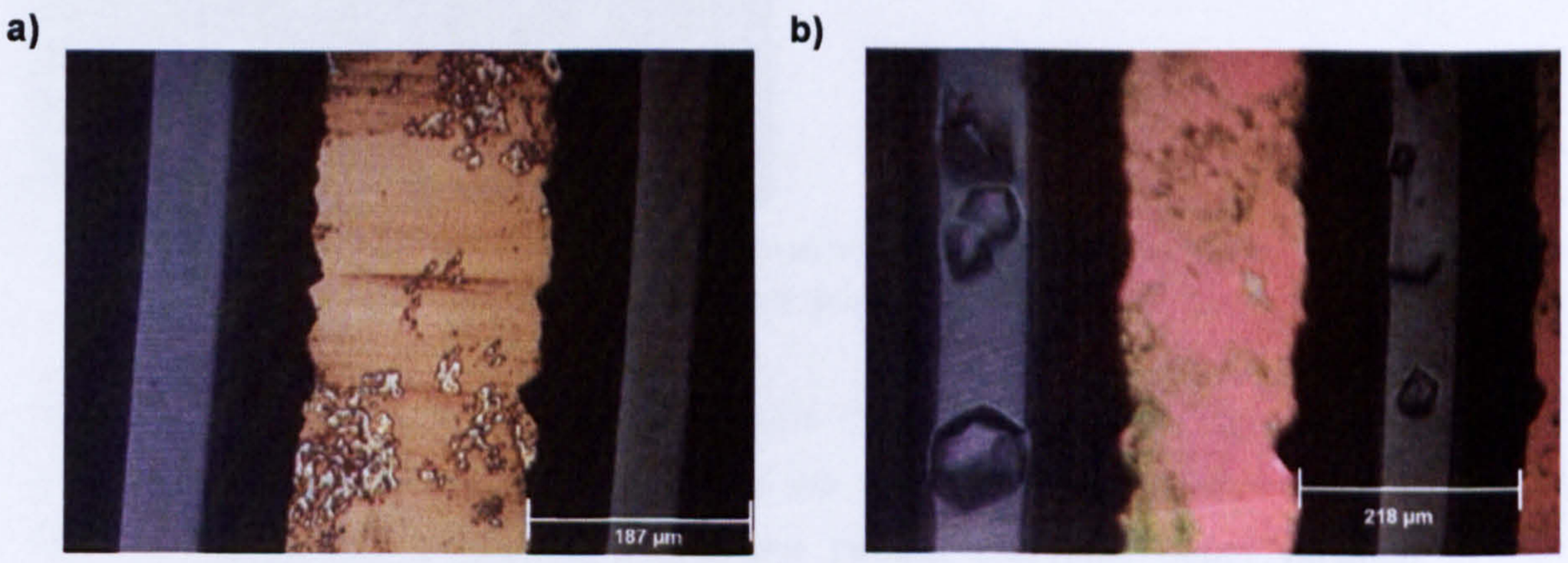


Figure 3.5 **Images of two parallel channels no impurities in (a) (187 μm wide and 62.5 μm deep) and showing impurities in (b) (218 μm wide and 77.8 μm deep).**

To assess the influence of these impurities on the channel surface uniformity depth profilometry measurements were performed. The depth profiles of the channels were measured at 2 μm intervals using a Dektak^3 surface profiler. Within this process a tip scans the channel surface allowing an assessment of roughness variations. Figure 3.6 presents the instrument, an image of the tip approaching the channels and an image of depth profiles across five parallel channels.

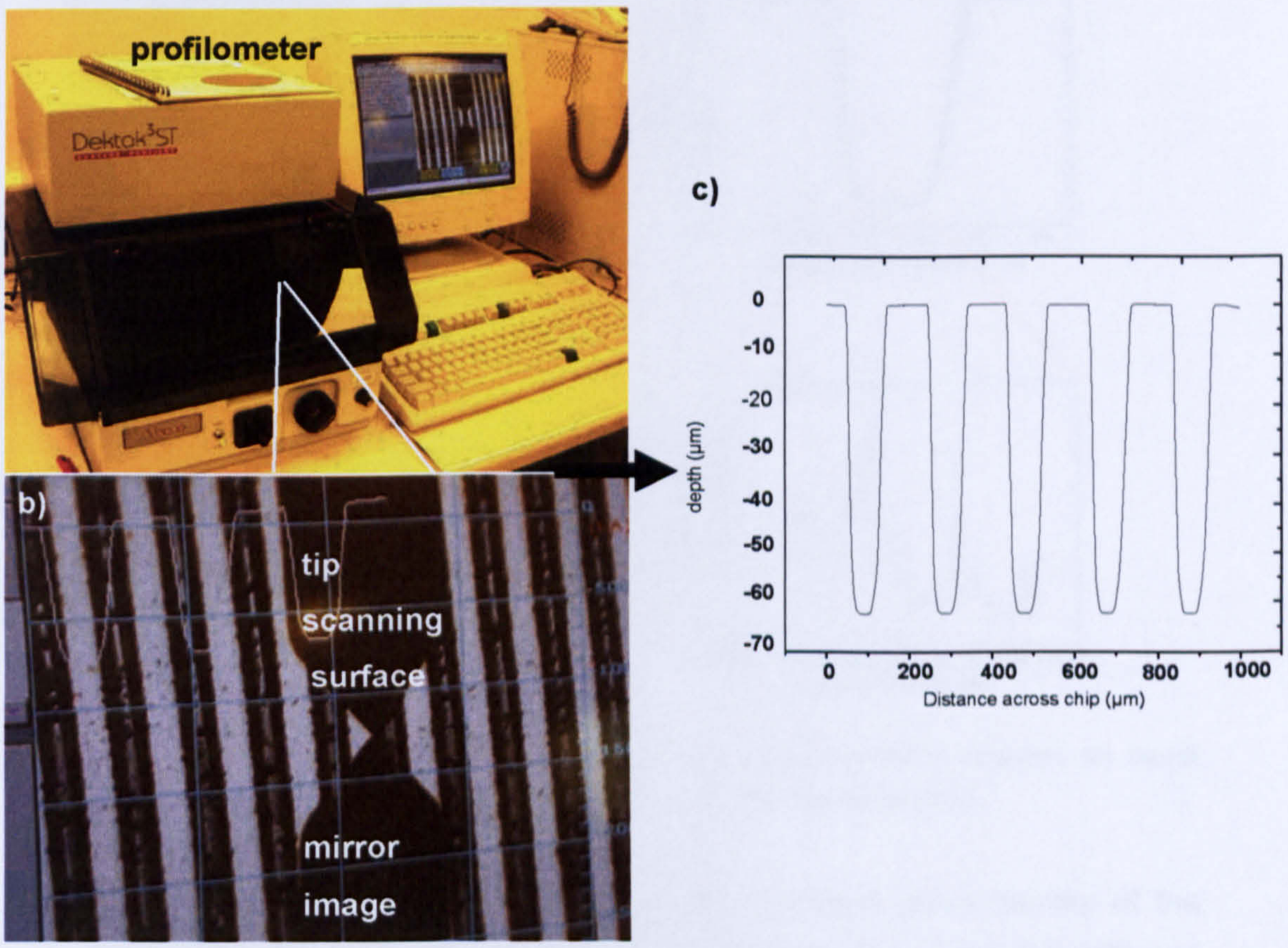


Figure 3.6 **(a) The Dektak profilometer (b) image of the scanning tip. The top tip is the tip which scans the surface, (c) A depth profile of five parallel channels.**

Figure 3.7 a) presents an example profile of a microfluidic channel. Figure 3.7 b) shows the depth variation when impurities are present on the channel surface. Figure 3.7 c) shows a depth profile of five parallel channels. Depth variation measurements on the same substrate were repeated up to ten times and resulted in a depth variation of 7 and 5 µm.

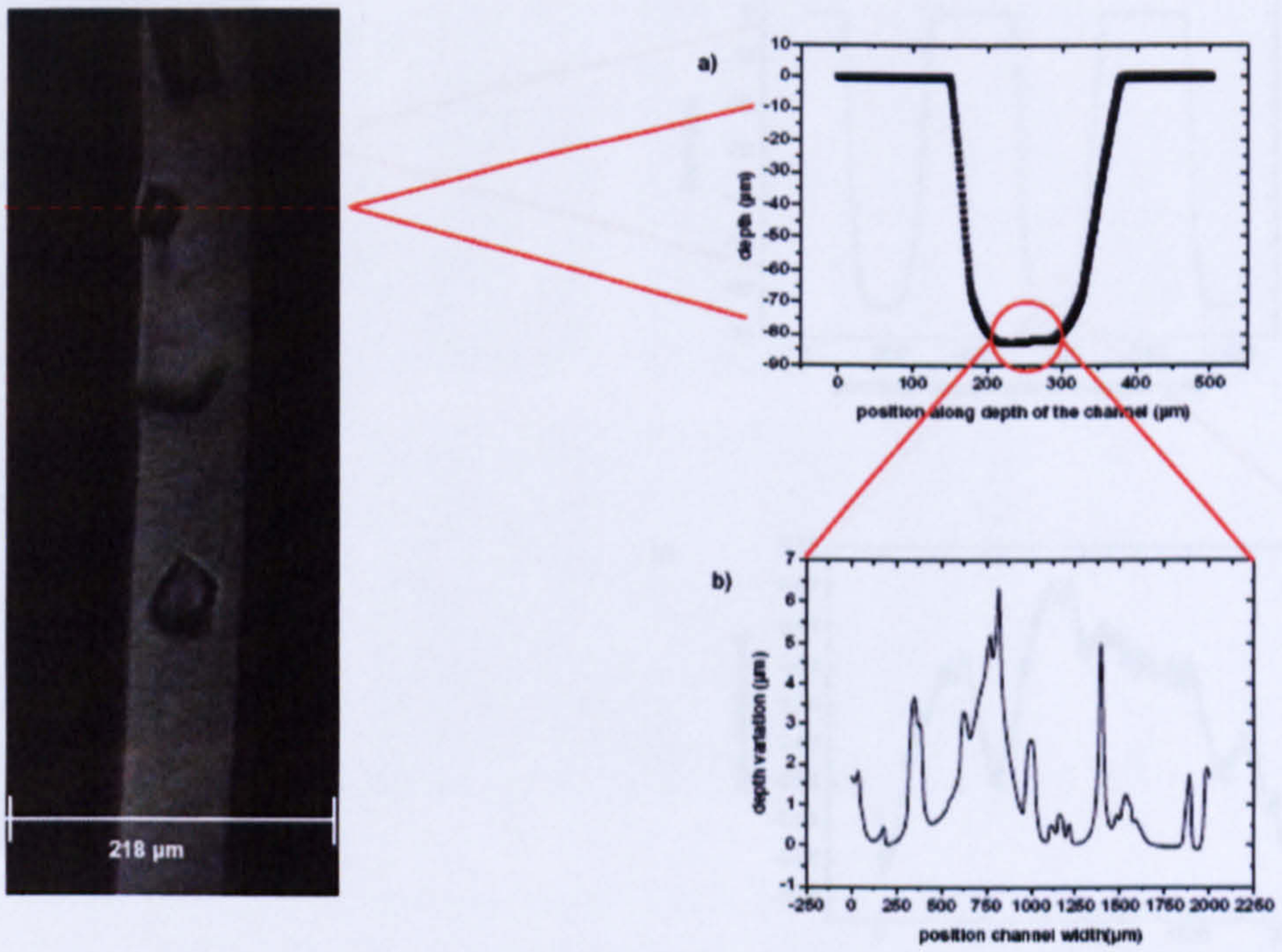


Figure 3.7 **(a) Depth variation across whole width of a microfluidic channel. (b) Depth variation when impurities are present on the channel surface.**

As etching with 20 % HF solutions resulted in significant non-uniformity of the channel surfaces, the use of more dilute etchant solutions (10, 5 and 1 % HF) was assessed. However, these etchant solutions resulted in adsorption of impurities in a similar manner and a closer look into alternative etchant solutions was necessary. A non-buffered etchant solution [38], which promised highly uniform channel surfaces was chosen for further study. This consisted of 0.75 ml HNO_3, 0.5ml HF and 180 ml water. A low etch rate of 3 µm/hr required an hourly refreshing of the etching bath but generated a depth variation of only 0.09 µm. Figure 3.5 (a) and 3.8 present images of channels etched with this etchant solution. Figure 3.5 (a) shows channels without adsorbed impurities and, Figure 3.8 indicates a depth variation of 0.09 µm. Additional profilometric measurements were performed on a microscope-based, white light interferometer (NewView200, Zygo Corp., USA) and are presented in Figures 3.9 and 3.10.

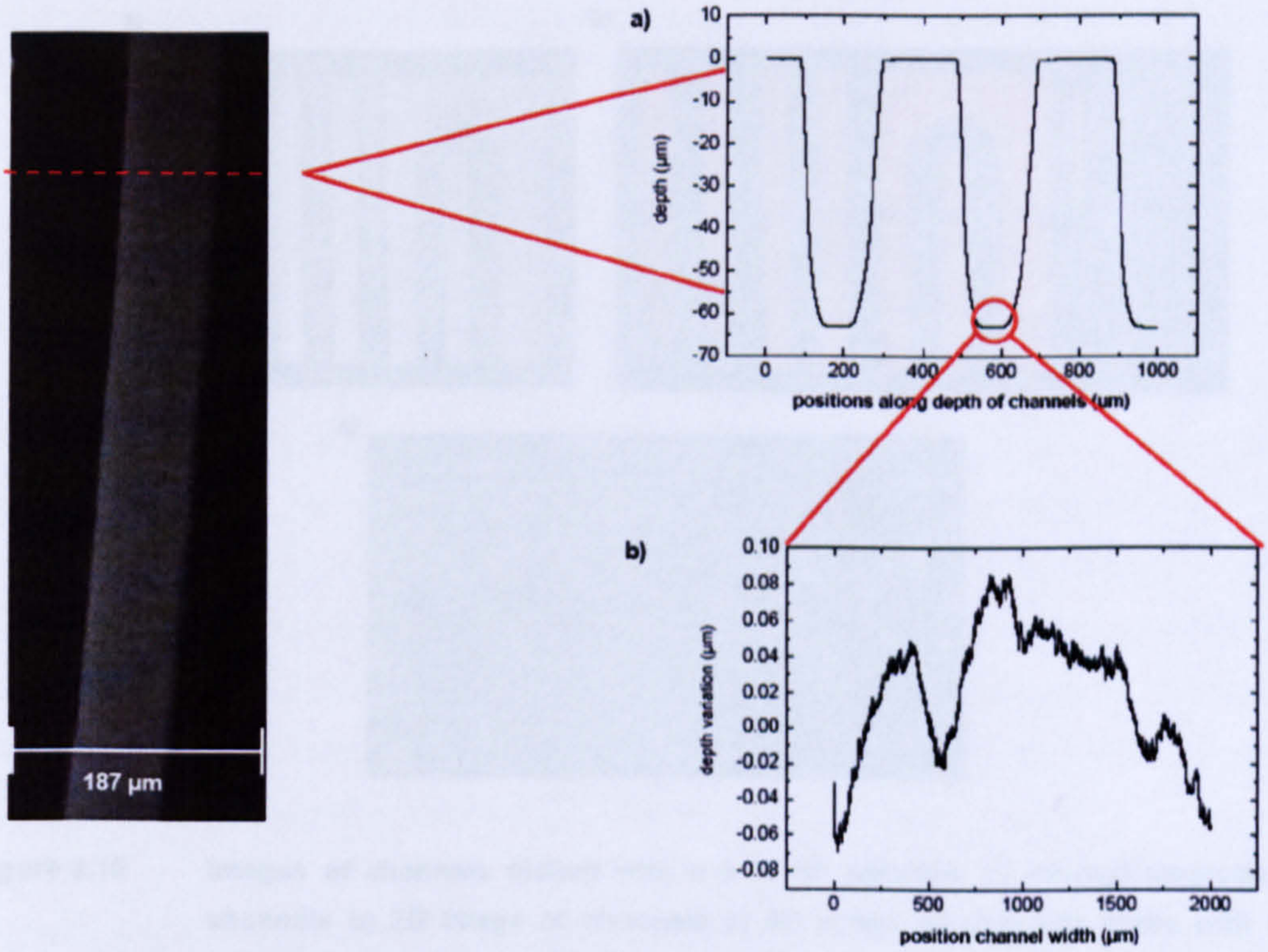


Figure 3.8 **a) Depth variation across whole width of a microfluidic channel. b) Depth variation when impurities are not present on the channel surface.**

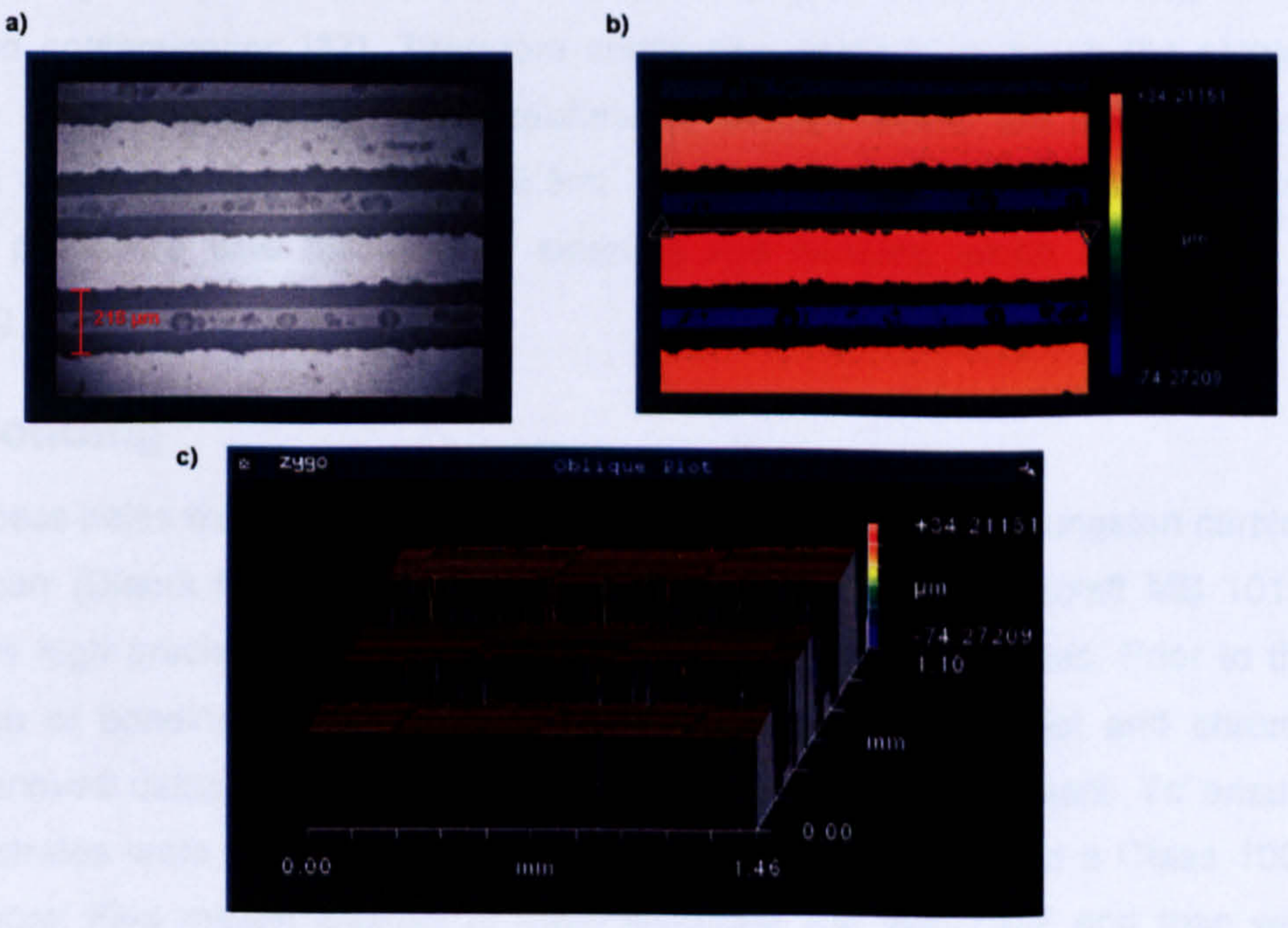


Figure 3.9 **Images of channels etched with a 20 % HF solution. a) microphotograph of channels b) 2D image of channels c) 3D image of channels made with the interferometer microscope.**

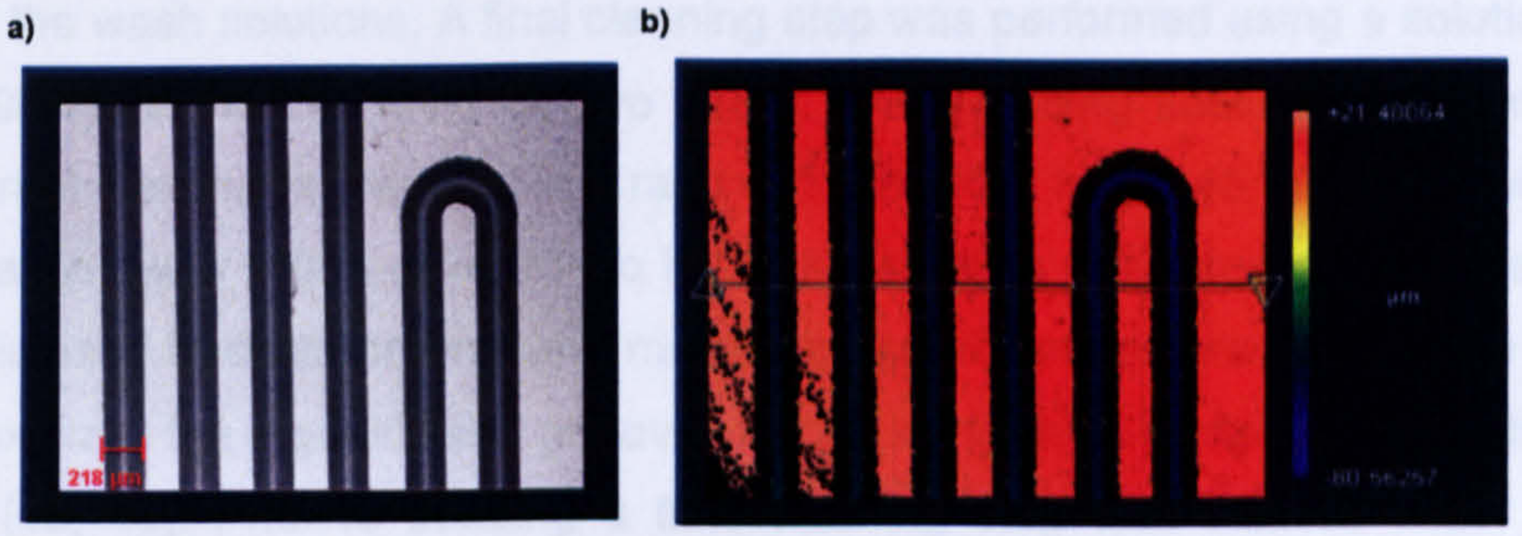


Figure 3.10 **Images of channels etched with a 5 % HF solution. a) microphotograph of channels b) 2D image of channels c) 3D image of channels made with the interferometer microscope.**

It should be noted that variations in etch rates will occur due to temperature variations [39], a loss of available reactive species [39], loss of liquid due to evaporation [40, 41], inefficient mixing of solutions [37], etch product blocking of flow [42], and contamination [37]. Therefore continuous monitoring during the etching process was necessary. For the experiments defined herein the following etch protocol was used: 0.75 ml HNO_3, 0.5ml HF and 180 ml water. The successful etching procedure was followed by cleaning and bonding which is outlined in following section.

3.4 Bonding

First access holes were drilled in the substrate. A 500 µm diameter tungsten carbide dental burr (Diama International, London, UK) fitted within a (Minicraft MB 1012) miniature high precision drill was used to mechanically drill the holes. Prior to the final step of bonding, substrates were cleaned. Excess photoresist and chrome were removed using dimethylformamide (DMF) and a chrome etchant. To ensure the substrates were kept clean, washing stages were performed in a Class 1000 clean room. Five minute washes of each substrate first with DMF and then with methanol in an ultrasound bath removed grease and contaminating organics from the surfaces. Between each washing stage the substrates were washed with deionised water and dried with filtered nitrogen to prevent cross contamination

between the wash solutions. A final cleaning step was performed using a solution of H_2SO_4 (96%) and H_2O_2 (30%) for two hours. This cleaning solution is commonly called Piranha and was prepared in a ratio of 3:1 H_2SO_4 : H_2O_2 [43, 44]. It should be noted that in lower ratios of H_2SO_4 to H_2O_2 the solution is noticeably self-heating. Piranha is used to clean organic and metallic contaminants before the furnace step since it oxidizes the organics and removes metals by forming complexes that stay in solution [45, 46]. Prior to bonding a final washing step with distilled water was performed for 10 minutes, the substrates were then dried with nitrogen, sandwiched between polished ceramic plates and placed inside a high temperature oven (Heraeus M104, Heraeus Instruments GmbH, Hanau, Germany). Metal weights were then placed on top of the ceramic plate / substrate sandwich so that a firm contact was enabled between the bonding surfaces. During the bonding process, a number of gradual heating and cooling steps were performed. These are presented in Figure 3.11 and result in the fusion of the two glass wafers.

Bonding can be achieved in a variety of ways including anodic bonding (for glass / silicon systems) [47], thermal or fusion bonding [48], HF bonding [49], and room temperature bonding with either sodium silicate [50] or UV cured epoxy [51]. Of these methods, anodic bonding and thermal bonding are most popular. Drawbacks of anodic bonding are that it requires glass substrates with high sodium borosilicate content as well as the use of a high negative potential (450 V) and a temperature of 500 °C. However, thermal bonding only requires the application of heat, so that Van der Waals repulsion forces can be overcome and silicon dioxide bonds between the two wafers can be formed. Both methods can be used to enclose microchannels but due to its simplicity the thermal bonding route was preferred in this project.

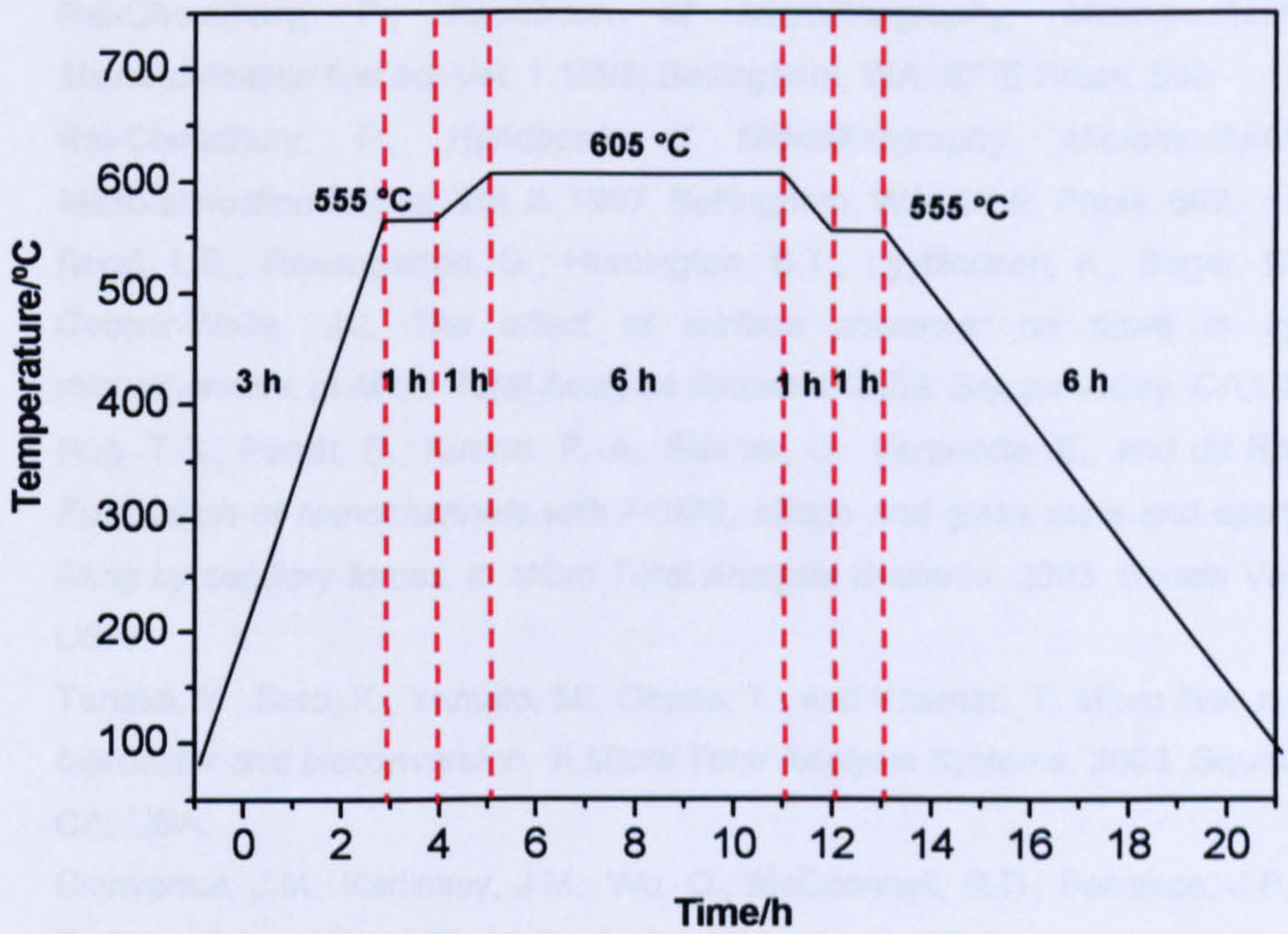


Figure 3.11 **Temperature cycle used for the thermal bonding of glass wafers in the fabrication of microfluidic devices.**

During thermal bonding the following steps occur. First glass is heated up to 555 °C, where its morphology changes from a crystalline to amorphous state. Internal stresses are prevented by holding the glass at this stage for an hour. This is followed by another heating step up to 605 °C for 6 hours. Here thermal bonding occurs, as silicone dioxide bonds between the wafers forms. The oven is then cooled down to the glass transition point to facilitate equilibration of the crystal morphology and prevent fractures caused through fast cooling. Finally the oven is cooled down to room temperature and the process of thermal bonding is finalized. Properly bonded substrates could be visually inspected. The presence of Newton's rings implied unbonded areas which necessitated in repeated bonding. Adequate bonding of the wafers typically occurred between 1 and 3 bonding cycles.

1. Madou, M.J., *Fundamentals of microfabrication: the science of miniaturization*. 2nd ed. 2002: CRC Press.
2. Rai-Choudhury, P., *Handbook of Microlithography, Micromachining and Microfabrication* first ed. Vol. 1 1997, Bellingham, WA: SPIE Press. 589.
3. Rai-Choudhury, P., *Handbook of Microlithography, Micromachining and Microfabrication* first ed. Vol. 2. 1997, Bellingham, WA: SPIE, Press. 692.
4. Rodd, L.E., Rosengarten, G., Huntington, S.T., Lyytikainen, K., Boger, D.V., and Cooper-White, J.J. *The effect of surface character on flows in cylindrical microchannels*. in *Micro Total Analysis Systems*. 2003. Squaw Valley, CA,USA.
5. Hug, T.S., Parrat, D., Kuenzi, P.-A., Staufer, U., Verpoorte, E., and de Rooij, N.F. *Fabrication of Nanochannels with PDMS, silicon and glass walls and spontaneous filling by capillary forces*. in *Micro Total Analysis Systems*. 2003. Squaw Valley, CA, USA.
6. Tanaka, Y., Sato, K., Yamato, M., Okano, T., and Kitamori, T. *Micro liver system for bioreactor and bioconversion*. in *Micro Total Analysis Systems*. 2003. Squaw Valley, CA, USA.
7. Bienvenue, J.M., Karlinsey, J.M., Wu, Q., McCconnell, R.D., Ferrance, J.P., Norris, P.M., and Landers, J.P. *Methods for high-speed, efficient purification of nucleic acids from diverse clinical and bio-hazardous samples on glass and hybrid PDMS-glass microchips*. in *Micro Total Analysis Systems*. 2003. Squaw Valley, CA, USA.
8. Ferrance, J.P., Wu, Q.J., Giordano, B.C., Hernandez, H., Kwok, Y., Snow, K., Thibodeau, S., and Landers, J.P., *Developments toward a complete micro-total analysis system for Duchenne muscular dystrophy diagnosis*. Analytica Chimica Acta, 2003. 500: p. 223-236.
9. Emmelkamp, J., da Costa, R., Andersson, H., and van den Berg, A. *Intrinsic autofluorescence of single living cells for label-free cell sorting in a microfluidic system*. in *Micro Total Analysis Systems*. 2003. Squaw Valley, CA, USA.
10. Song, S., Singh, A.K., Shepodd, T.J., and Kirby, B.J., *Microchip dialysis of proteins using in situ photopatterned nanoporous polymer membranes*. Analytical Chemistry, 2004. 76(8): p. 2367-2373.
11. Huang, L.R., Cox, E.C., Austin, R.H., and Sturm, J.C., *Tilted brownian ratchet for DNA analysis*. Analytical Chemistry, 2003. 75(24): p. 6963-6967.
12. Kirby, B.J., Wheeler, A.R., Zare, R.N., Fruetel, J.A., and Shepodd, T.J., *Programmable modification of ce;; adhesion and zeta potential in silica microchips*. Lab-on-a-chip, 2003. 3: p. 5-10.
13. Lin, C.H., Fu, L.-M., Lee, K.-H., Yang, R.-J., and Lee, G.-B. *Novel surface modification methods and surface property analysis for separation of DNA bio-molecules using capillary eletrophoresis*. in *Micro Total Analysis Systems*. 2003. Squaw Valley, CA, USA.

14. Zhao, Z., Cui, Z., Cui, D., and Xia, S., *Monolithically integrated PCR biochip for DNA amplification.* Sensors and Actuators A, 2003. 108: p. 162-167.
15. Gabig-Ciminska, M., Holmgren, A., Andresen, H., Bundvig Barken, K., Wumpelmann, M., Albers, J., Hintsche, R., Breitenstein, A., Neubauer, P., Los, M., Czyz, A., Wegrzyn, G., Silfversparre, G., Jurgen, B., Schweder, T., and Enfors, S.-O., *Electric chips for rapid detection and quantification of nucleic acids.* Biosensors and Bioelectronics, 2004. 19: p. 537-546.
16. Auroux, P.-A., Day, P.J.R., and Manz, A. *Sample-shunting based PCR microfluidic device.* in *The nanotechnology conference and trade show.* 2004. Boston, MA, USA.
17. El-Ali, J., Perch-Nielsen, I.R., Poulsen, C.R., Jensen, M., Telleman, P., and Wolff, A. *Microfabricated DNA amplification device monolithically integrated with advanced sample pre-treatment.* in *Transducers.* 2003. Boston, MA, USA.
18. Schlüter, M., Mammitzsch, S., Martens, M., Gasso, S., and Lilienhof, H.J. *Micro fluidic immunoassay chip with integrated liquid handling.* In *Micro Total Analysis Systems.* 2003. Squaw Valley, CA, USA.
19. Huang, Y., Yang, J.M., Hopkins, P.J., Kassegne, S.K., Tirado, M., Forster, A.H., and Reese, H., *Separation of simulants of biological warfare agents from blood by a miniaturized dielectrophoresis device.* Biomedical Microdevices, 2003. 5(3): p. 217-225.
20. Kanai, M., Uchida, D., Sugiura, S., Shirasaki, Y., Go, J.S., Nakanishi, H., Funatsu, T., and Shoji, S. *PDMS microfluidic devices with PTFE passivated channels.* In *Micro Total Analysis Systems.* 2003. Squaw Valley, CA, USA.
21. Marquette, C.A. and Blum, L.J., *Direct immobilization in poly(dimethylsiloxane) for DNA, protein and enzyme fluidic biochips.* Analytica Chimica Acta, 2004. 506: p. 127-132.
22. Xiao, D., Le, T.V., and Wirth, M.J., *Surface modification of the channels of poly(dimethylsiloxane) microfluidic chips with polyacrylamide for fast electriphoretic separation of proteins.* Analytical Chemistry, 2004. 76(7): p. 2055-2061.
23. Park, S.-R. and Swerdlow, H., *Concentration of DNA in a flowing stream for high-sensitivity capillary electrophoresis.* Analytical Chemistry, 2003. 75(17): p. 4467-4474.
24. Kai, J., Sohn, Y.S., and Ahn, C.H. *Protein microarray on cyclic olefin copolymer (COC) for disposable protein lab-on-chip.* in *Micro Total Analysis Systems.* 2003. Squaw Valley, California USA.
25. Kanai, M., Abe, H., Munaka, T., Fujiyama, Y., Uchida, D., Yamayoshi, A., Nakanishi, H., Murakami, A., and Shoji, S. *Integrated micro chamber for living cell analysis with negligible dead volume sample injector.* in *Transducers.* 2003. Boston, MA, USA.
26. Lee, S.-H., Lee, C.-S., Kim, B.-G., and Kim, Y.-K. *Surface characterization and a lift-off process of a fluorocarbon thin film for micro protein patterning.* in *Micro Total Analysis Systems.* 2003. Squaw Valley, CA, USA.

27. Liu, R.H., Yang, J., Lenigk, R., Bonanno, J., and Grodzinski, P., *Self-contained, fully integrated biochip for sample preparation, polymerase chain reaction amplification, and DNA microarray detection.* Analytical Chemistry, 2004. 76(7): p. 1824-1831.
28. Hanaoka, T., Takai, O., Takahashi, K., and Tsugane, S., *Chip ligating human genomic DNA serves as storage material and template for polymerase chain reaction.* Biotechnology letters, 2003. 25: p. 509-512.
29. Lai, S., Wang, S.C., Luo, J., Lee, L.M., Yang, S.-T., and Madou, M.J., *Design of a compact disk-like micrfluidic platform for enzyme-linked immunosorbent assay.* Analytical Chemistry, 2004. 76(7): p. 1832-1837.
30. Kameoka, J., Craighead, H.G., Zhang, H., and Henion, J., *A Polymeric Microfluidic Chip for CE/MS Determination of Small Molecules.* Analytical Chemistry, 2001. 73(9): p. 1935-1941.
31. Terry, S.C., Jerman, J.H., and Angell, J.B., *A gas chromatographic air analyzer fabricated on a silicon wafer.* I.E.E.E. Transactions on electron devices, 1979. 26(12): p. 1880-1886.
32. Manz, A., Harrison, D.J., Verpoorte, E.M.J., Fettinger, J.C., Paulus, A., Ludi, H., and Widmer, H.M., *Planar Chips Technology for Miniaturization and Integration of Separation Techniques into Monitoring Systems - Capillary Electrophoresis on a Chip.* Journal of Chromatography, 1992. 593(1-2): p. 253-258.
33. nanofilm. 2007 [cited; Available from: http://www.nanofilm.com/.
34. Winkle, R.F., *Novel Approaches to Online Detection in Microfluidic Reaction Systems*, in *Chemistry*. 2006, Imperial College: London. p. 219.
35. Székely, L. and Guttman, A., *New advances in microchip fabrication for electrochromatography.* 2005. p. 4590-4604.
36. Klaassen, E.H., Petersen, L., Noworoski, J.M., Logan, J., Maluf, M., Brown, J., Stormant, C., McCulley, W., and Kovacs, A., *Silicon fusion bonding and deep reactive ion etching: A new technology for microstructures.* Sensors and actuators. A, Physical, 1996. 52(1-3): p. 132-139.
37. Williams, K.R. and Muller, R.S., *Etch rates for micromachining processing.* Microelectromechanical Systems, Journal of, 1996. 5(4): p. 256-269.
38. Srinivasan, U., Houston, M.R., Howe, R.T., and Maboudian, R., *Alkyltrichlorosilane-based self-assembled monolayer films for stiction reduction in silicon micromachines.* Microelectromechanical Systems, Journal of, 1998. 7(2): p. 252-260.
39. Dickerson, R.E., Gray, H.B., and Haight Jr., G.P., *Chemical Principles*, ed. Benjamin/Cummings. 1979, Menlo Park, CA
40. Seidel, H., *Anisotropic etching of crystalline silicon in alkaline solutions. I, Orientation dependence and behavior of passivation layers.* Journal of the Electrochemical Society, 1990. 137(11): p. 3612.

41. Glembocki, O.J., *Hydration Model for the Molarity Dependence of the Etch Rate of Si in Aqueous Alkali Hydroxides*. Journal of the Electrochemical Society, 1991. 138: p. 1055.
42. Runyan, W.R. and Bean, K.E., *Semiconductor Integrated Circuit Processing Technology*. 1990: Addison-Wesley 683.
43. Yang, M.G. and Koliwad, K.M., *Auger electron spectroscopy of cleanup-related contamination on silicon surfaces*. The Journal of Electrochemical Society, 1975. 122(5): p. 675-678.
44. Pintchovski, F., Price, J.B., Tobin, P.J., Peavey, J., and Kobold, K., *Thermal characteristics of the H_2SO_4 -H_2O_2 silicon wafer cleaning solution*. The Journal of electrochemical Society 1979. 126(8): p. 1428-1430.
45. Kern, W. and Puotinen, D.A., *cleaning solutions based on hydrogen peroxide for use in silicon semiconductor technology*. RCA Review, 1970. 30(2): p. 187-206.
46. Amick, J.A., *Cleanliness and the cleaning of silicon wafers*. Solid-State Technology, 1976. 19(11): p. 47-52.
47. Obermeier, E. *Anodic bonding* in *International Symposium on Semiconductor Wafer Bonding: Science, Technology and Applications*. 1995. Pennington, N.J., USA.
48. Blom, M.T., Tas, N.R., Pandraud, G., Chmela, E., Gardeniers, J.G.E., Tijssen, R., Elwenspoek, M., and van den Berg, A., *Failure mechanisms of pressurized microchannels, model, and experiments*. Journal of Microelectromechanical Systems, 2001. 10(1): p. 158-164.
49. Nakanishi, H., Nishimoto, T., Nakamura, A., Yotsumoto, A., and Shoji, S. *Studies on SiO2-SiO2 bonding withhydrofluoric acid-room temperature and low stress bonding technique forMEMS*. in *IEEE Proceedings of the 11th Annual International Conference on MEMS* 1998. Heidelberg, Germany
50. Ito, T., Sobue, K., and Ohya, N., *Water glass bonding for micro-total analysis system*. Sensors and actuators, 2002. 81(2): p. 187.
51. Huang, Z.Z., Sanders, J.J.C., Dunsmor, C.C., Ahmadzadeh, H.H., and Landers, J.J.P., *A method for UV-bonding in the fabrication of glass electrophoretic microchips*. Electrophoresis, 2001. 22(18): p. 3924-9.

4

Fluorescence Lifetime Imaging in Microfluidic Systems

As described in Chapter 1, temperature determination and control in microfluidic devices is essential when performing successful PCR. In this chapter temperature monitoring within microfluidic systems using fluorescence lifetime Imaging is introduced. Additionally Computational Fluid Dynamics (CFD) simulations were carried out to confirm the experimental outcomes (which are presented in the Appendix). This chapter provides an overview of temperature measurement in microfluidic devices, a summary of the underlying theory of fluorescence lifetime imaging (FLIM), an overview of the instrumentation and methods used, experimental results and their outcome.

4.1 Temperature Measurements in Microfluidic Channels

As described previously all component steps (denaturation, annealing and extension) within a PCR occur at a defined temperature for a fixed period of time. For efficient amplification temperatures must be maintained within tight limits, and thus temperature control within PCR devices is essential. In the current work temperature control turns out to be difficult as PCR is performed in a continuous flow format where external heaters are set to maintain a fixed temperature at a specific location, with the PCR solution moving sequentially through these zones. The residence time of a fluid element at a particular temperature is defined by the microfluidic channel dimensions, the speed with which the solution moves through these channels and the dimensions of the heating elements.

The measurement of temperature in microfluidic channels has been performed in a variety of ways. These have been reviewed in detail by Newport *et al.* [1]. Integrated thermocouples allow the facile monitoring of average temperatures in the microchannels. Such an approach provides an indirect measurement of the temperature of a fluid within a channel but it is ill-suited to sensitive monitoring of fluidic temperature. The complexity associated with thermocouple fabrication is often vast and costly, and fabricated devices normally exhibit poor operational lifetimes. Two examples of integrated devices are shown in Figure 4.1. Figure 4.1 (a) presents an integrated microfluidic device for DNA analysis reported by Burns *et al* [2]. Here metal heaters and temperature sensors were fabricated between two barrier layers of vapour deposited plastic (p-xylylene) and platinum was placed on the surface at defined locations for use as electrophoresis electrodes. Finally, a glass substrate containing etched microfluidic channels (500 µm wide and 50 µm deep) was bonded to the silicon substrate to complete the device. As described above, the resistive metal heaters were embedded beneath a plastic coating immediately below the reaction area. One of the heaters is used as a temperature sensor because the resistance of the metal is a linear function of temperature. Even though the average temperature of the reaction chamber is controlled within 0.1 °C, measurement of temperature is indirect and the high complexity and cost of device fabrication is prohibitive for most applications.

Figure 4.1 (b) depicts an integrated device for PCR and CE by Lagally *et al.* [3]. Here an amorphous silicon layer was sputtered on a glass wafer. Next the fluidic channels and the PCR chambers were etched into the glass wafer. A resistance

temperature detector (RTD) was fabricated by coating a glass wafer with a 100 Å layer of Titanium and a 2000 Å layer of Platinum, followed by a blanket coating of a 2000 Å layer of silicon dioxide. The back side of the wafer was sputter-coated with a 100 Å layer of Titanium and a 2000 Å layer of Platinum to form an electroplating seed layer. Gold was deposited on the Ti-Pt seed layer using a gold-sulfite plating solution. The heating elements were then etched into the Ti-Pt seed layer using an ion beam etching system. Finally, a 3000 Å layer of silicon dioxide was deposited over the heaters and leads, and the channel wafer thermally bonded to the RTD/heater wafer. Although the RTD is located inside the PCR chamber and can perform direct thermal measurements, the extensive and costly fabrication steps outweigh any operational advantage.

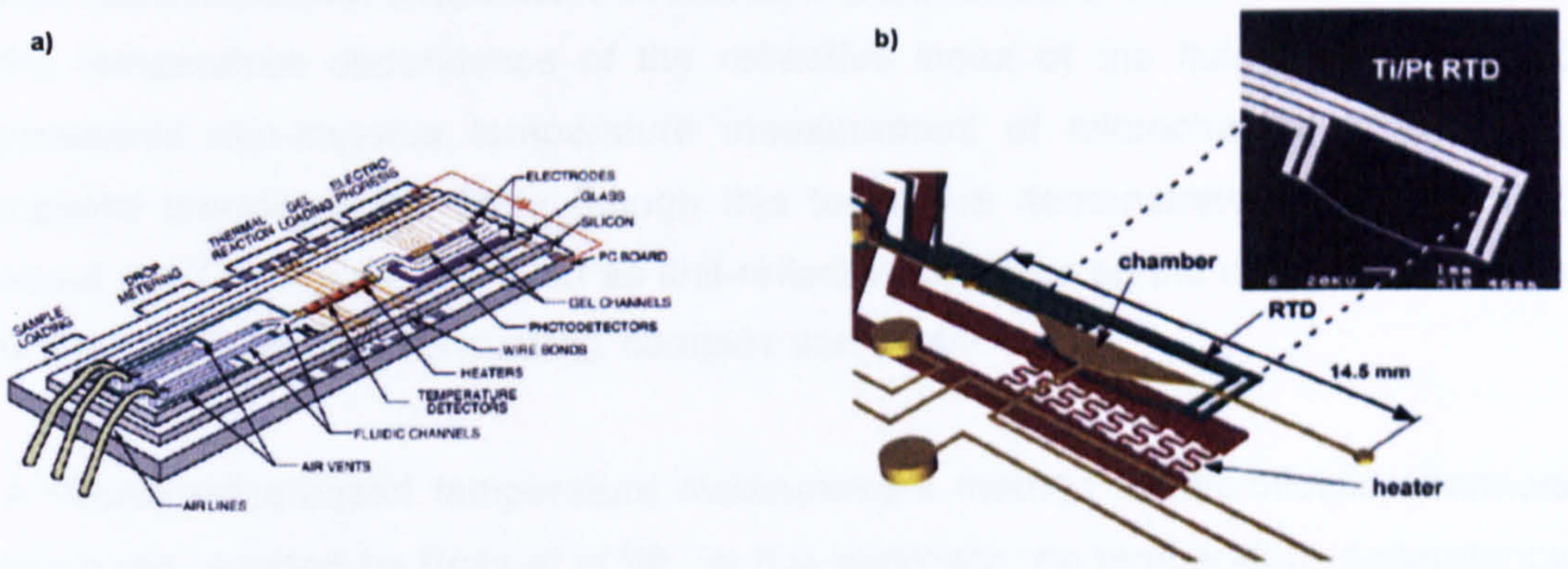


Figure 4.1 **(a) An integrated microfluidic device [2] consisting of silicon (doped with boron), silicon oxide, titanium oxide, p-xylylene and glass layers. The heater and sensor elements are embedded beneath a plastic coating immediately below the reaction area. (b) An integrated microfluidic device [3] consisting of silicon, glass, titanium, platinum and gold layers with etched heating and RTD elements.**

Spectroscopic methods have also been used to measure temperature within microfluidic environments. Such methods are advantageous as they are non-invasive and allow direct measurement of fluidic temperatures. For example, in 1998 Chaudhari *et al.* [4] measured fluid temperature in a microfluidic device using encapsulated thermochromic liquid crystals. Thermochromic liquid crystals exhibit a wavelength-dependent reflectivity that is strongly sensitive to temperature, within a range defined by their chemical composition (precision of ±0.1°). A major disadvantage with this method is the size of the liquid crystals which can influence the flow behaviour of the fluids and therefore bias temperature measurements.

Lacey *et al.* [5] have used proton nuclear magnetic resonance (NMR) spectroscopy to monitor the electrolyte temperature during CE. In this approach intra-capillary temperatures were non-invasively estimated by measuring the shift in the proton resonance frequency of the water signal. Davis *et al.* [6] have also utilized Raman spectroscopy to map both radial and axial temperature gradients in operating electrophoresis capillaries. This method is based on the temperature dependence of the water O-H stretch equilibrium between weakly bent and strongly bent hydrogen bonded species. This approach enables a temperature precision of ± 1°C and a spatial resolution of 1-5 μm, but is limited by long acquisition times. More recently Easley *et al.* [7] investigated non-contact temperature sensing with optical fibre, extrinsic Fabry-Perot interferometry (EFPI). In this approach a broadband IR source was used to monitor temperature in real time within microfluidic environments due to the temperature dependence of the refractive index of the fluid. Patil *et al.* [8] presented non-invasive temperature measurement of microchannel flows using infrared thermography. Even though this technique demonstrated a precision of about ± 1°C, preparations such as anti-reflective coatings on the microfluidic device turned out to be time consuming, complex and costly.

A fluorescence-based temperature measurement method in microfluidic channels has been reported by Ross *et al* [9] . In this approach the temperature dependence of the fluorescence quantum efficiency of the fluorone dye Rhodamine B was used to determine microfluidic temperatures with a precision of ± 3°C. Even though this method seems elegant and simple to implement, its major drawback is its dependency on experimental factors such as, variations in excitation and detection efficiencies, concentration artefacts, reagent autofluorescence and inner filter effects. These drawbacks mean that the system must be recalibrated repeatedly. Figure 4.2 presents the variation of Rhodamine B fluorescence in a carbonate buffer as a function of temperature.

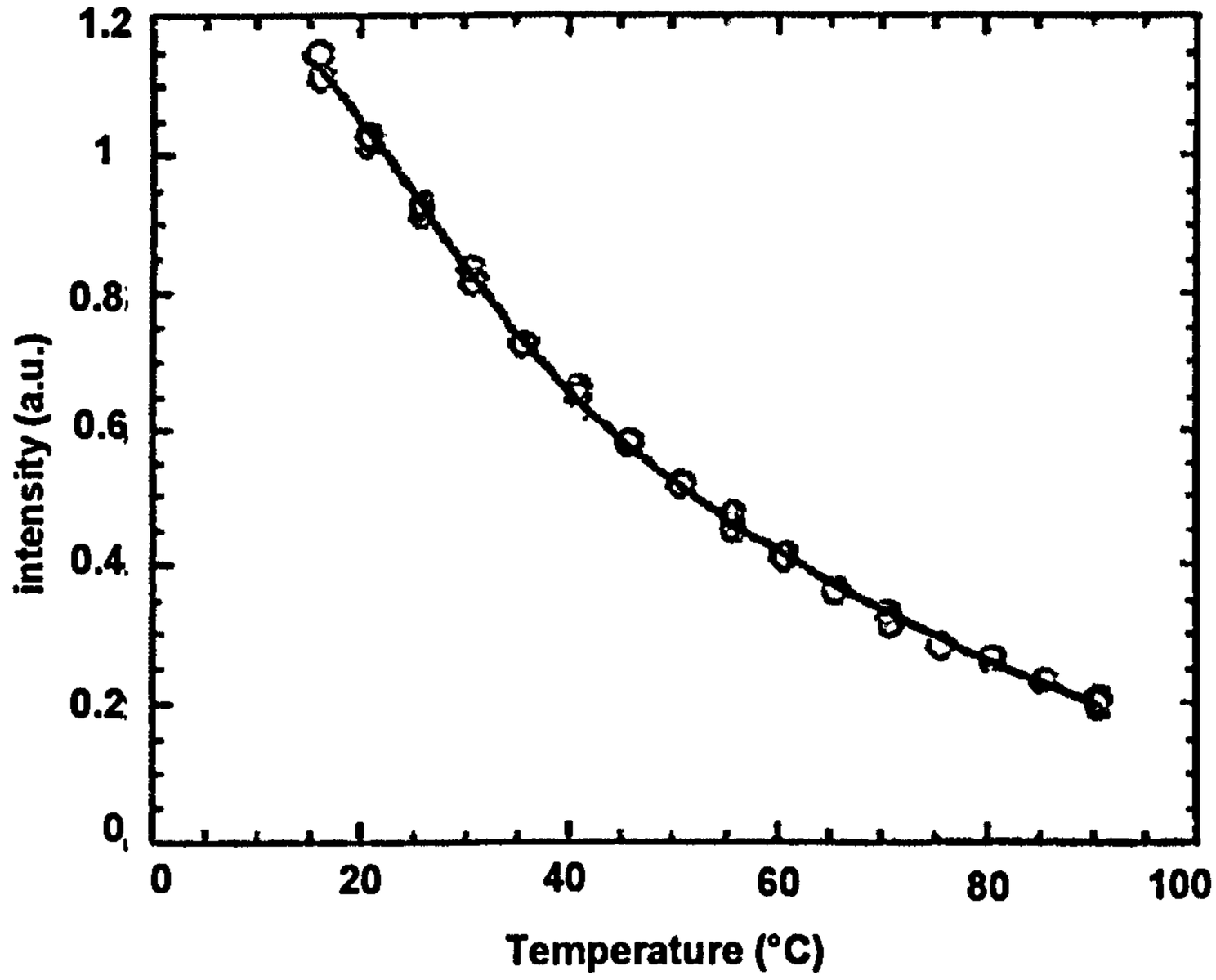


Figure 4.2 **Fluorescence intensity as a function of temperature for a 0.1mM Rhodamine B solution in carbonate buffer.**

Unfortunately appreciable amounts of Rhodamine B adsorb to channel walls. Since the temperature dependence of the fluorescence of adsorbed dye molecules does not match the dependency observed for similar molecules in bulk data must be corrected. For a dye concentration of ~ 100 µmol/l, the amount of dye adsorbed onto channel surfaces is a tiny fraction of the total fluorescence intensity. However for dye concentrations of ~ 1 µmol/l, the fluorescence intensity of the adsorbed dye molecules becomes comparable to bulk emission intensities.

Fluorescence lifetime imaging (FLIM) is a technique which addresses these issues by providing a read-out signal that is independent of excitation and detection efficiency, fluorophore concentration and photon path length. This chapter will review the basic theory of fluorescence lifetime imaging and present studies in which fluorescence lifetime imaging has been used to quantitatively image temperature distributions in three spatial dimensions within microchannel environments.

4.2 Unimolecular Photophysics

In this section the basic principles of fluorescence emission, time-resolved fluorescence instrumentation and the precise methods used for temperature monitoring are described.

4.2.1 Fluorescence

Fluorescence defines the radiative relaxation of a molecule via emission of a photon [10]. This process can be represented with the use of a Jablonski diagram (Figure 4.3) which describes the relative arrangement of both singlet and triplet energy levels of a fluorophore, along with various transitions that can occur. The ground electronic state is denoted S_0, with the first electronic excited singlet state defined as S_1 and the second electronic singlet state as S_2. Each electronic energy manifold contains vibrational energy levels that are populated according to the thermal energy of the system. A molecule is excited to a higher singlet electronic energy state when it absorbs a photon of the appropriate energy. In the condensed phase most molecules immediately undergo non-radiative relaxation back to the vibrationless level of the first excited singlet state via internal conversion and/or vibrational relaxation. Radiative decay (i.e. fluorescence) may then occur when the molecule relaxes from this excited energy state to a ground vibronic state by emitting a photon. Non-radiative decay (internal conversion or intersystem crossing) can also occur without emission of a photon but with energy dissipation through heat. Table 4.1 presents these different transitions and their typical timescales.

Transition	Name or Process	Timescale
$S_0 + h\nu \rightarrow S_n^*$	Absorption	~10^{-15} s
$S_n^* \rightarrow S_1 + \Delta$	Internal conversion and vibrational relaxation	~10^{-13} s
$S_1 \rightarrow S_0^* + h\nu$	Fluorescence	~10^{-9} s
$S_1 \rightarrow S_0^* \rightarrow S_0 + h\nu$	Internal conversion and vibrational relaxation	~10^{-9} s
$S_1 \rightarrow T^*_1 \rightarrow T_1 + \Delta$	Intersystem crossing and vibrational relaxation	~10^{-7} s
$T_1 \rightarrow S_0^* + h\nu$	Phosphorescence	>10^{-5} s
$T_1 \rightarrow S_0^* \rightarrow S_0 + \Delta$	Intersystem crossing and vibrational relaxation	>10^{-6} s

Table 4.1 **Possible photophysical processes that can occur in a unimolecular system. S is a singlet state, T is a triplet state, h is the Plank's constant, ν is the optical frequency and Δ is the energy dissipated as heat.**

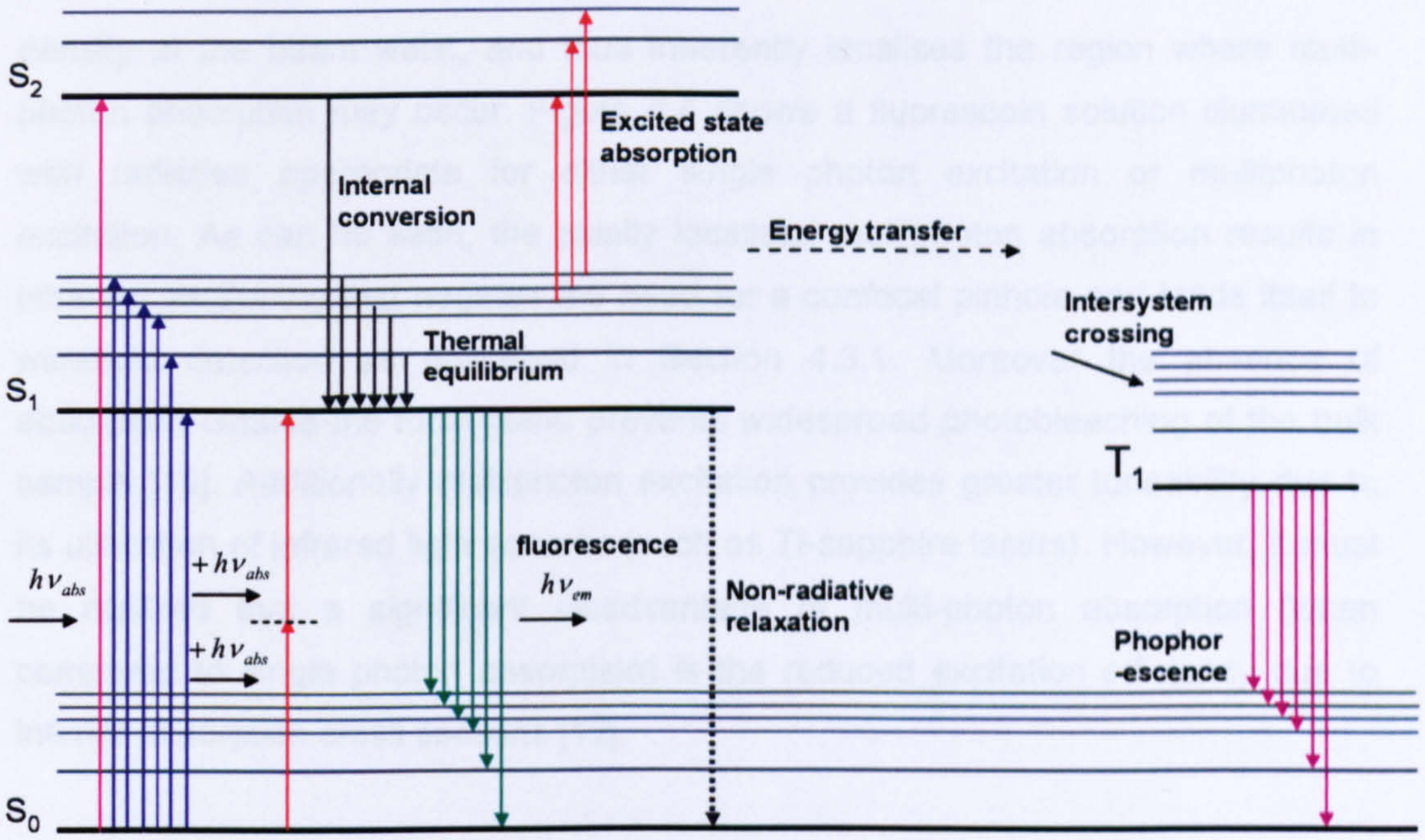


Figure 4.3 **Jablonski diagram outlining possible photophysical transitions. Blue represents single photon excitation, red represents multiphoton excitation, grey represents internal conversion, green represents radiative fluorescence emission, dotted grey represents non-radiative relaxation, brown represents phosphorescence, black represents intersystem crossing and dashed black presents energy transfer to another molecule.**

4.2.2 Single Photon and Multi Photon Excitation

Absorption of a single photon of appropriate energy will result in direct excitation of a ground state molecule to an excited state. In addition, under certain conditions, two lower energy photons (whose summed energy is equivalent to an energy level gap) may be simultaneously absorbed. This process is commonly known as 2-photon absorption [10]. The Jablonski diagram in Figure 4.3 depicts both single- and multiphoton excitation with blue and red arrows respectively. For multiphoton absorption to occur with appreciable probability, a high excitation intensity is required [10]. While single photon excitation is a linear process and proportional to the excitation intensity, two photon excitation is a non-linear process whose probability is proportional to the square of the excitation intensity [10, 11]. This property can be advantageous in optical imaging. For example, in single photon excitation, when light impinges on a sample (Figure 4.4), the amount of light absorbed is proportional to the intensity (until all molecules in the ground state are excited) and light is absorbed throughout the entire sample volume. In the case of multiphoton excitation, focusing the light source significantly increases the photon

density at the beam waist, and thus inherently localises the region where multi-photon absorption may occur. Figure 4.4 shows a fluorescein solution illuminated with radiation appropriate for either single photon excitation or multiphoton excitation. As can be seen, the axially localised multiphoton absorption results in inherent sectioning that negates the need for a confocal pinhole and lends itself to widefield detection as described in Section 4.3.1. Moreover the absence of absorption outside the focal plane prevents widespread photobleaching of the bulk sample [10]. Additionally multiphoton excitation provides greater tuneability due to its utilization of infrared light sources (such as Ti-sapphire lasers). However, it must be realized that a significant disadvantage of multi-photon absorption (when compared to single photon absorption) is the reduced excitation efficiency due to inferior absorption cross sections [12].

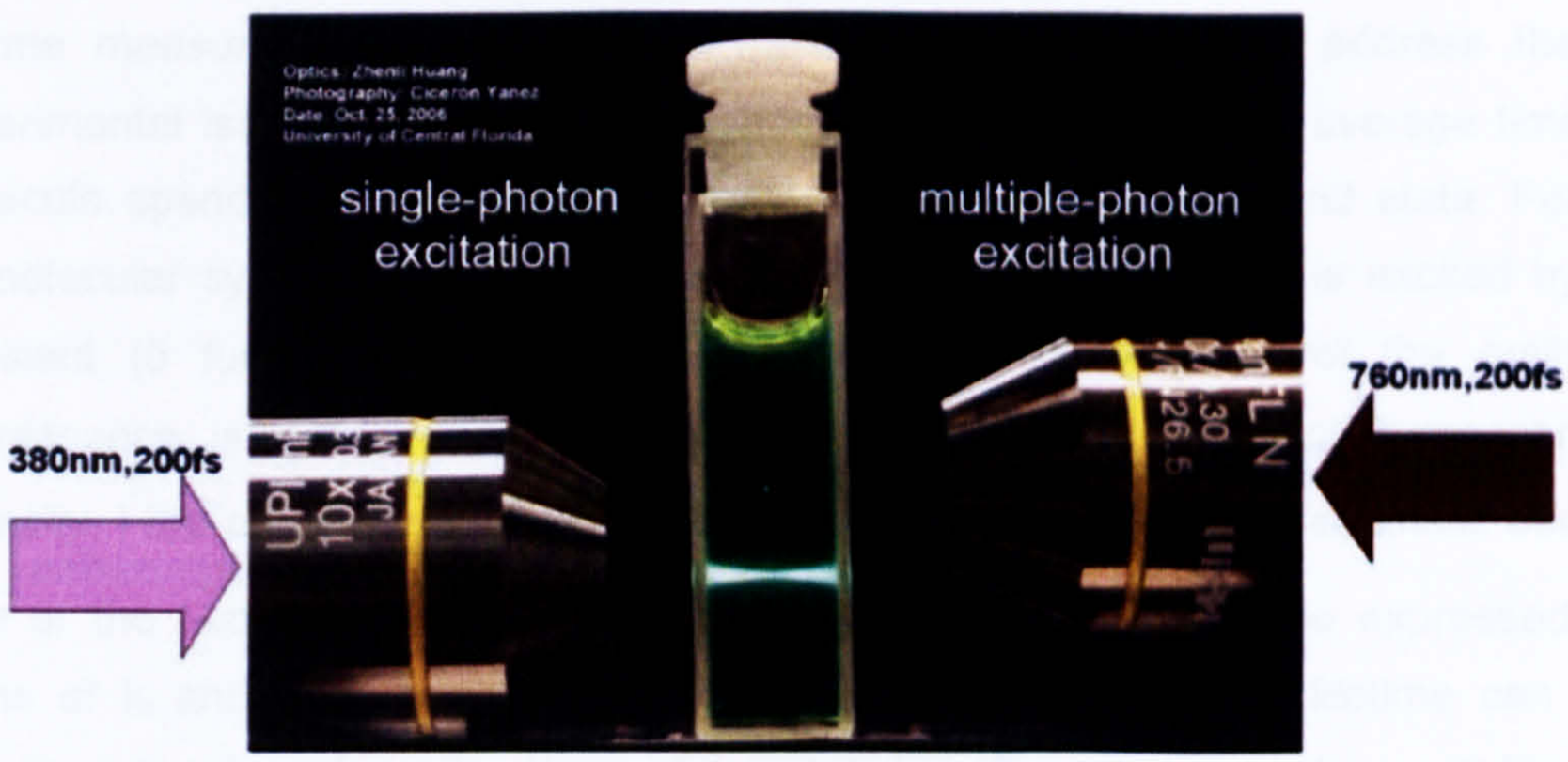


Figure 4.4 **Single photon excitation (SPE) compared with multiple photon excitation (MPE) of a fluorescein solution [13]. For SPE fluorescein is excited across the entirety of the optical path, whereas for MPE fluorescein is excited in a small volume close to the focal point of the laser beam.**

4.2.3 The Fluorescence Lifetime

Generally fluorescence experiments are based on the measurement of a time-integrated signal. In many situations this can result in quantitative information on the concentration and/or fluorescence quantum efficiency of the fluorophore if measurements are properly calibrated. The fluorescence quantum efficiency defines the ratio of the number of photons emitted to the number absorbed and is

expressed in equation 4.1 where ϕ_f is the fluorescence quantum efficiency, k_r is the radiative rate constant and k_{nr} is the non-radiative rate constant. A fluorophore will have a high fluorescence quantum efficiency when the radiative rate constant is large compared to the non-radiative rate constant. If the quantum efficiency of a fluorophore remains constant, the measured fluorescence intensity is proportional to its concentration. As both the radiative and non-radiative decay rates can be influenced by the local environment [14], a variation in intensity may be linked to a variation in the fluorescence quantum efficiency and hence environmental conditions. The dependence of the measured fluorescence intensity on the fluorescence quantum efficiency, concentration and illumination intensity make quantitative measurements very difficult, except in well calibrated and controlled systems [9]. Consequently, it is necessary to find a measurable photophysical parameter which is largely independent of experimental conditions. Fluorescence lifetime measurements are inherently ratiometric and thus can address these experimental issues [15]. The fluorescence lifetime expresses the average time a molecule spends in an excited state before returning to the ground state. For a unimolecular system in which a single population of fluorophores is excited by a transient (δ function) optical pulse, the temporal dependence of the emitted fluorescence is described by Equation 4.2. Here I_0 is the initial fluorescence intensity, I the measured intensity after a time t, and τ_f is the characteristic decay time or the fluorescence lifetime. The fluorescence lifetime can be expressed in terms of k_r and k_{nr} (Equation 4.3) Furthermore the fluorescence lifetime can be directly determined from the slope of a plot of log I(t) versus t as shown in Figure 4.5.

$$\phi_f = \frac{k_r}{k_r + k_{nr}} \tag{4.1}$$

$$I = I_0 \exp(-\frac{t}{\tau_f}) \tag{4.2}$$

$$\tau_f = \frac{1}{k_r + k_{nr}} \tag{4.3}$$

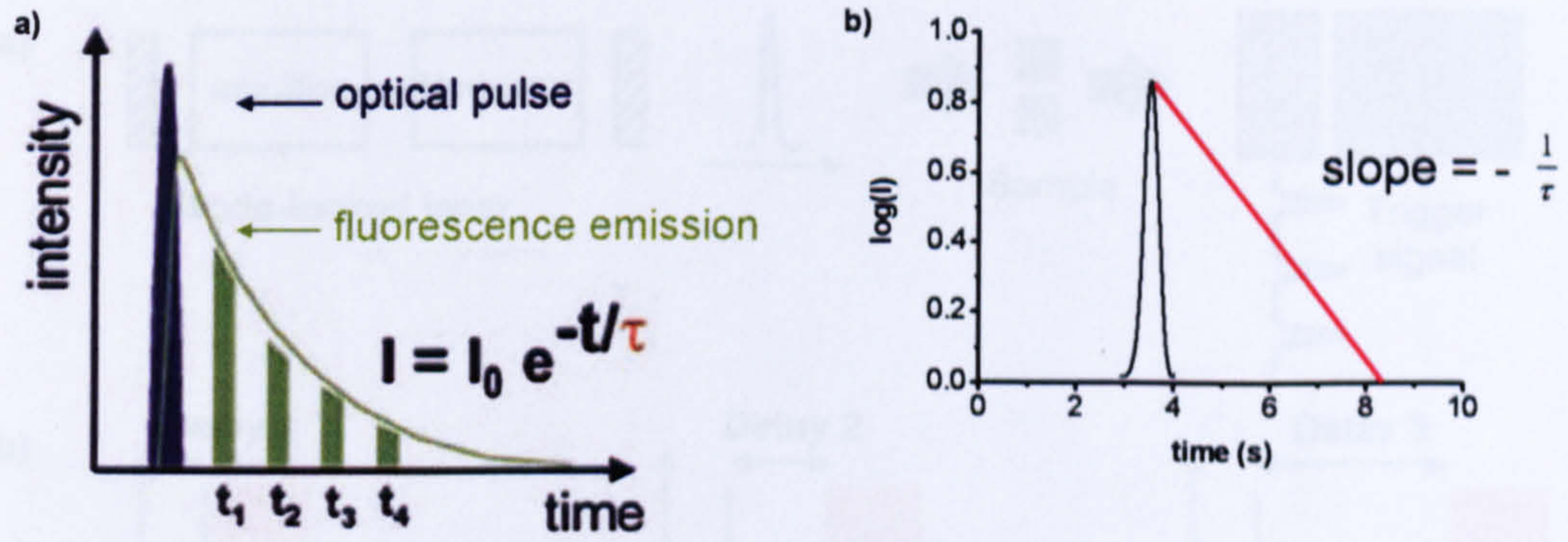


Figure 4.5 **Illustration of how the fluorescence decay is recorded on a plot with intensity (I) versus time (t) in (a) and with log intensity versus time (t) in (b). Fluorescence information is acquired at varying time points, t_n, on the fluorescence decay and fitted for fluorescence lifetimes. Here the fluorescence lifetime can be extracted from the slope of the curve.**

4.3 Methods for Measuring Fluorescence Lifetimes

Fluorescence lifetimes can be measured via a variety of techniques [10]. In this section two common approaches, time correlated single photon counting (TCSPC) and wide field techniques (time-gated or frequency domain) are described.

4.3.1 Wide-Field Techniques

Widefield FLIM techniques generally use a gated optical intensifier relayed to a CCD camera. In frequency domain techniques the intensifier gain is sinusoidally modulated and phase stepped such that a cosine function is created [16]. In time domain techniques, the intensifier is gated at varying positions after excitation to result in an exponential decay function [17].The current studies utilise a time gated approach where a sample is excited with an ultra-short pulse and the emitted decay sampled using a number of narrow time gates to build up a representation of the fluorescence decay profile (Figure 4.6). The major advantage of wide-field imaging lies in the incredibly fast, parallel acquisition of pixels and thus images [18].

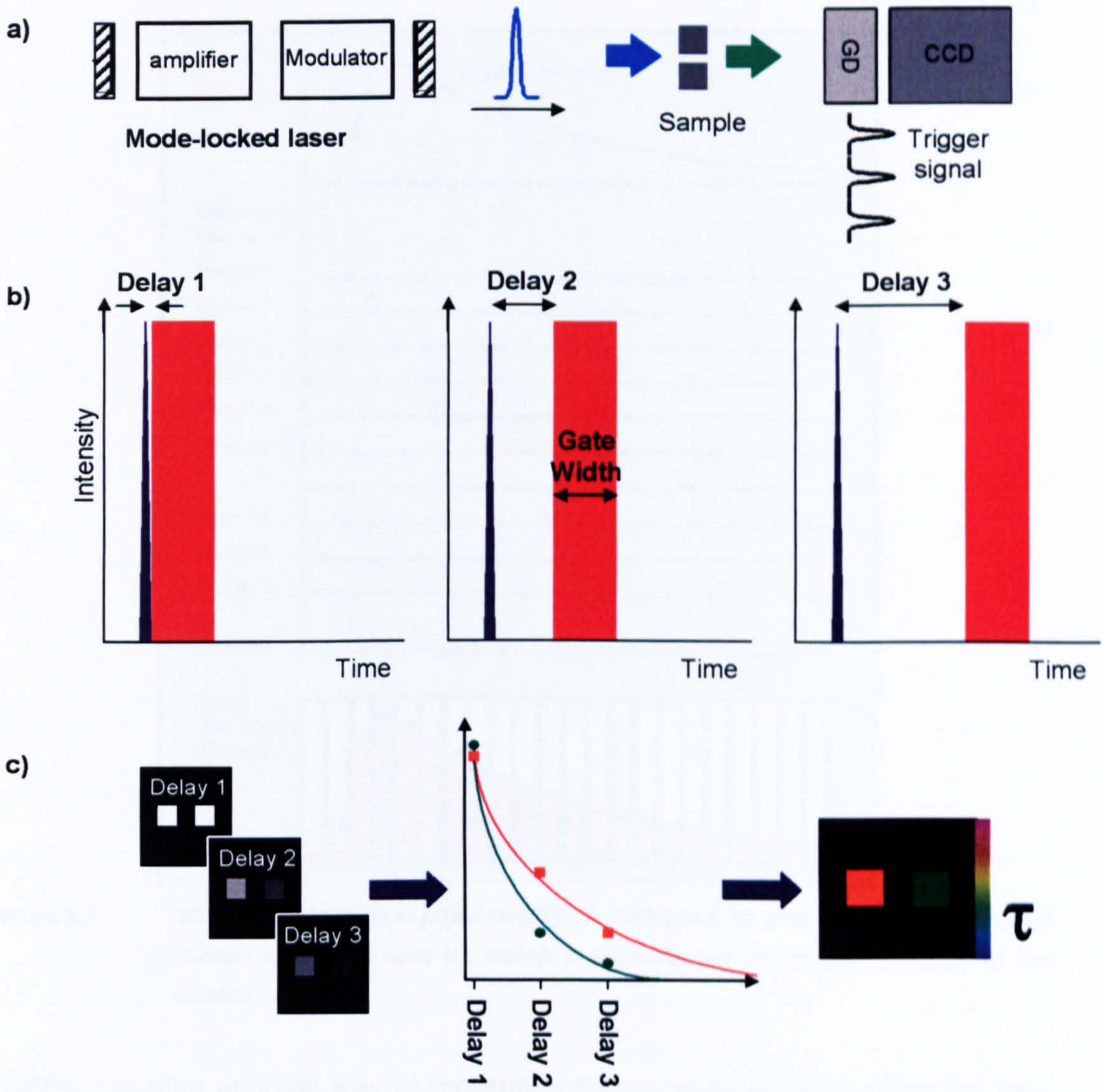


Figure 4.6 **a) Schematic of a time-gated fluorescence system with b) three different gate delay positions in respect to the excitation pulse and c) transition from gated images to FLIM images [19]. The green and red curve represent different fluorescent dyes with different fluorescence lifetime decays.**

4.3.2 Time-Correlated-Single-Photon-Counting (TCSPC)

The gold standard method for measuring fluorescence lifetimes is based on time correlated single photon counting (TCSPC) [20, 21]. In this technique the arrival time of individual fluorescence photons is measured with respect to the associated excitation pulse, producing a temporal histogram (Figure 4.7) from which the fluorescence lifetime can be deduced. This technique can be combined with scanning microscopes to produce fluorescence lifetime images [22, 23].

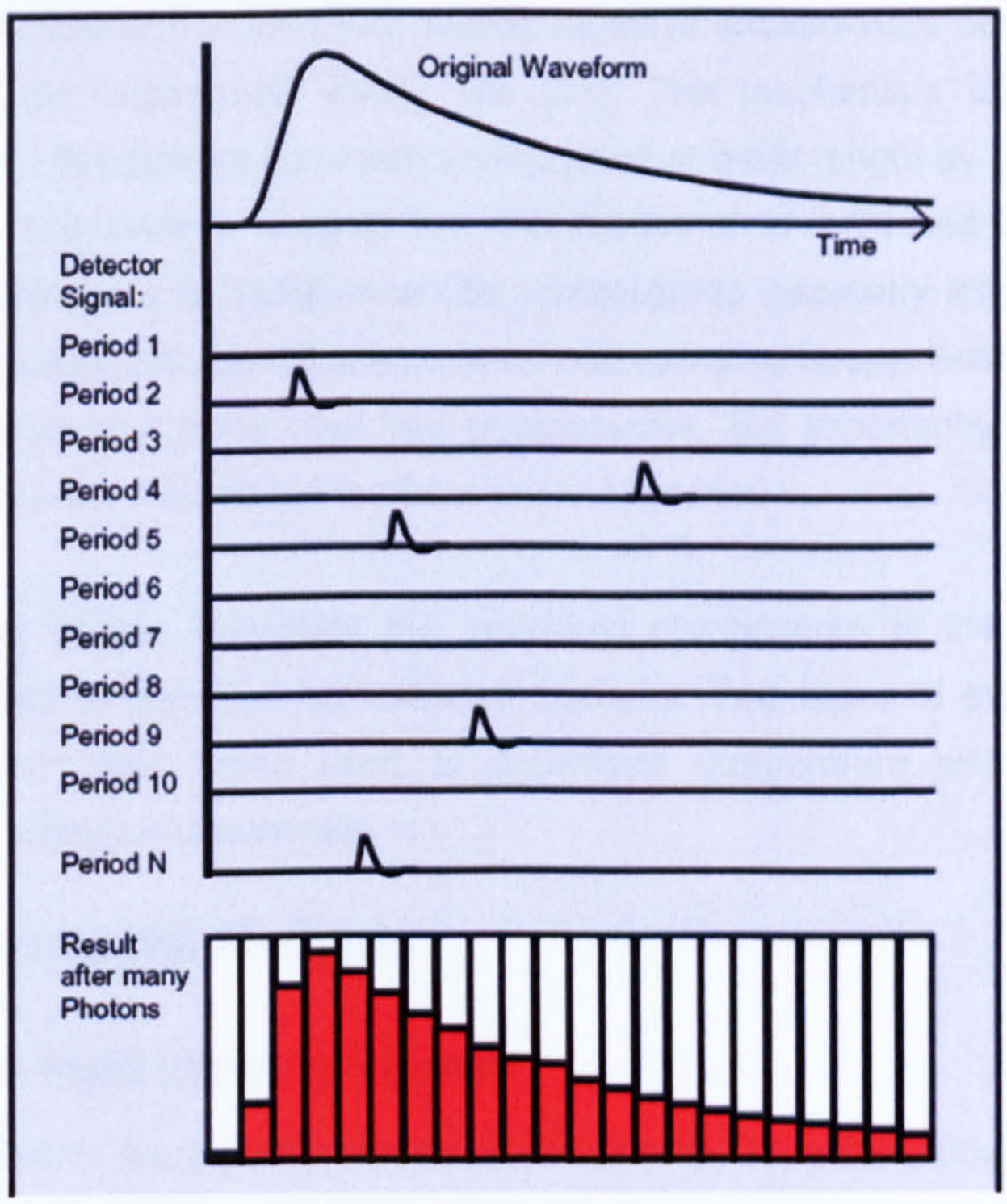


Figure 4.7 **TCSPC measurement principle[21] . A histogram of arrival times of individual photon events is built up which represents the fluorescence decay of the sample.**

TCSPC provides an ideal way of measuring fluorescence lifetimes since the time resolution is limited by the transit time spread and not by the width of the output pulse of the detector, and optimal signal to noise characteristics are achieved using a counting method. However, the counting nature of any TCSPC measurement significantly limits the detection rate. This coupled with sequential pixel acquisition may result in unacceptable acquisition speeds in imaging applications.

4.3.3 Molecular Dyes for FLIM

As previously explained fluorophores can exhibit particular dependencies which may be exploited to study environmental parameters. In the current studies the temperature dependency of the fluorescence lifetime of a Rhodamine dye [24-27], is utilized to determine the temperature of a fluid in a microfluidic channel. Extensive research on the photophysics of Rhodamine B has been performed. Indeed, its fluorescence quantum efficiency and fluorescence lifetime are well characterized

[25, 26]. Rhodamine B is known to exhibit radiative excited-state deactivation that follows a single exponential decay law [27]. The mechanism of radiationless deactivation of Rhodamine has been investigated at great length by Lopez Arbeloa *et. al* [24] . The authors suggest that the formation of a twisted intramolecular charge transfer state or variation of the amino group geometry from a planar to pyramidal structure provide a facile route for non-radiative decay. Both theories offer valid interpretations for the observed photophysics, but importantly, both models predict an increase in k_{nr} as the temperature is increased.

The following section describes the individual components of the experimental apparatus used to measure fluorescence lifetimes. Two types of experiments are presented, with both being used to determine temperature with high spatial resolution in microfluidic channels.

4.4 Experimental Methods

4.4.1 Wide-Field Imaging System

Initial experiments were performed on a multiphoton, wide-field, time-gated set up which is presented in Figure 4.8. Fluorescence is excited using 100 fs pulses (at a repetition rate of 80 MHz) from a mode-locked Ti:Sapphire laser (Mai-Tai, Spectra-Physics, Mountain View, CA), which is tuneable between 700 and 1000nm. With the laser tuned to 840 nm , the output beam is coupled to a quasi-wide-field, multibeam, multiphoton microscope (TriMScope, LaVisionBioTec GmbH, Bielefeld, Germany) that rapidly scans multiple parallel beams, generated using a cascaded beam-splitter system, over the whole field of view. Multiphoton excitation via a 10 X/ 0.25 NA air objective (Olympus) results in a femtoliter-sized excitation volume and, thus provides inherent optical sectioning. Scanning the array of excitation foci permits wide-field detection, allowing a greater fluorescence signal to be obtained per unit time when compared to conventional (single-beam scanning) multiphoton microscopes, and thus faster image acquisition. FLIM is implemented using an ultrafast, electronically shuttered, wide-field detector based on a gated optical intensifier. Fluorescence is imaged onto the photocathode of a time-gated intensifier (HRI, Kentech Instruments Ltd, Didcot, UK) and optically relayed to a CCD camera (Imager Intense, LaVision, GmbH, Gottingen, Germany). The time-gated intensifier is synchronously switched from zero to high gain for periods of a few hundred picoseconds at adjustable delay times after excitation, using a fast switching delay box (TDU, Kentech Instruments Ltd). Thus, a series of fluorescence intensity

images, averaged over many excitation pulses, is acquired which sample the fluorescence decay profiles for each pixel in the field of view. A spatial map of fluorescence lifetime is produced from a series of time-gated intensity values which are fitted to an exponential decay model on a pixel-by-pixel basis. Additionally three-dimensional measurements are performed by moving the sample axially using an automatic focus stepper (MFD, Märzhauser Wetzlar GmbH, Wetzlar-Steindorf Germany). Image acquisition is controlled by Inspector© software (LaVisionBiotec, Bielefeld, Germany), and CCD scanning and delay switching are synchronized using a trigger pulse generator (DG535, Stanford research Systems).

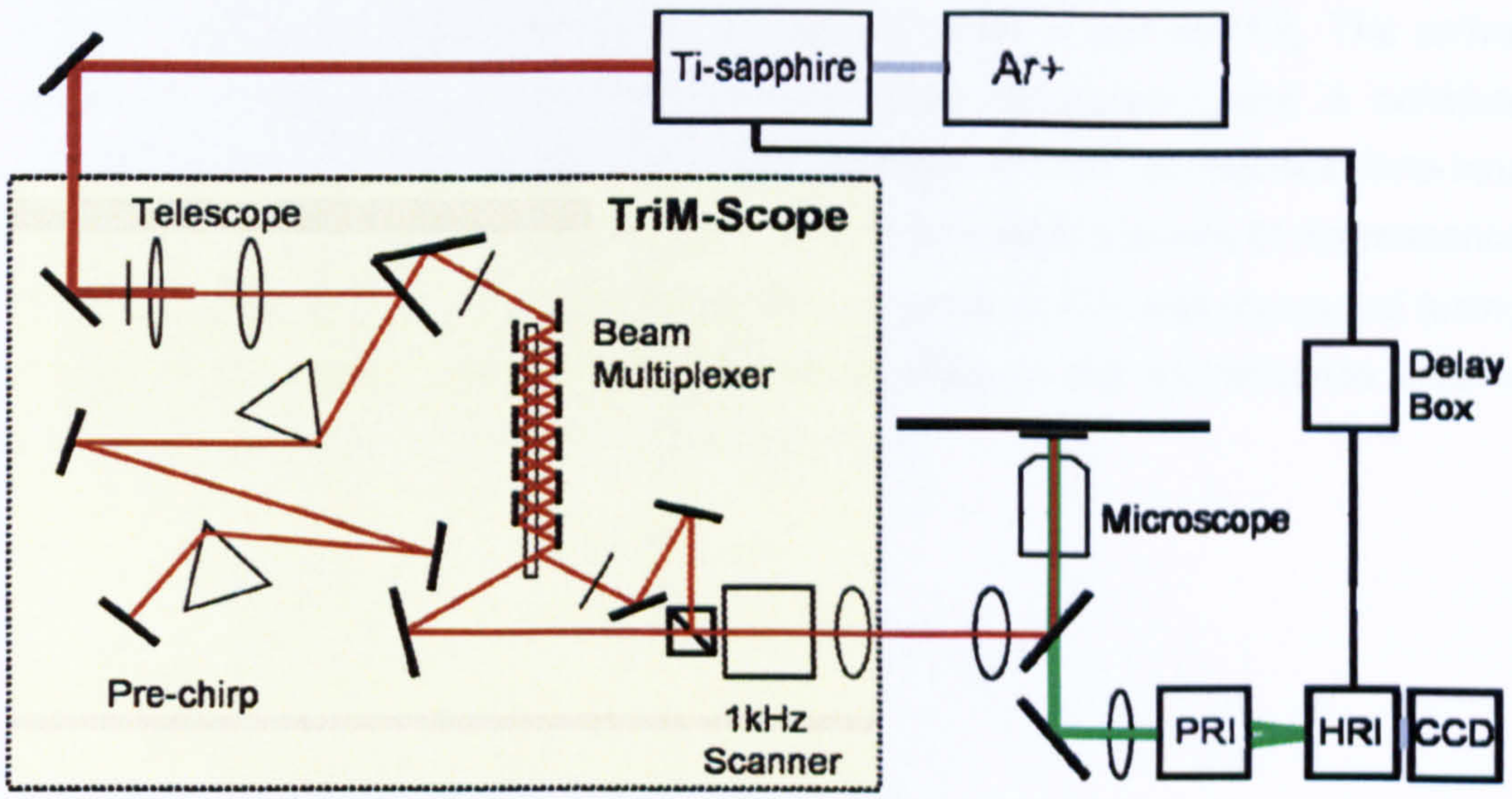


Figure 4.8 **Pulsed infrared illumination is coupled into the TriM-Scope. This illumination is focused into the sample, where two-photon absorption occurs in a thin optical section only. The fluorescence emission is then imaged onto a gated optical intensifier relayed to a CCD camera High Rate Image intensifier. Solid black lines indicate triggering connections.**

4.4.2 TCSPC - Imaging Techniques

Experiments were performed on a time-correlated single photon counting (TCSPC) enabled confocal microscope, presented in Figure 4.9. Fluorescence was excited using a Ti:Sapphire seeded supercontinuum source [28] (Mai-Tai, Spectra-Physics, Mountain View, CA). The resultant supercontinuum spans wavelengths between 435 -1150 nm at the -10dB level with approximately 70mW in the visible region at a repetition rate of 80 MHz. Using a prism-based spectrometer (see Figure 4.9) a central wavelength of 550 nm with a bandwidth of 40nm was selected and coupled to the confocal microscope and then focussed onto the sample using a 20X/ 0.5 NA

air objective (Leica). A wavelength of 550nm corresponds to the maximum absorption cross-section of Rhodamine B. The detection window was fixed to a wavelength range of 580-700nm. The confocal microscope repeatedly scans a diffraction limited spot (the excitation beam) across the sample at ~1 frame per second. The induced fluorescence is de-scanned via the scanning mirrors, spectrally separated using a dichroic mirror and imaged through a pinhole, rejecting out-of-focus and scattered light to provide an optically sectioned image. It is finally detected by a photomultiplier tube, with its x-y position and arrival time recorded by TCSPC electronics (SPC-730, Becker & Hickl GmbH). The acquisition time was fixed at 300s per image with typical detection rates of $0.5\text{-}5\times10^5$ photons per second. This is below the detection rate for the onset of pile-up [10]. The arrival times of the detected fluorescence photons were measured (using a constant fraction discriminator) and then the data digitised into 64 contiguous time-bins across the 12.5ns measurement window. Before and after a series of fluorescence lifetime measurements, an instrument response function (IRF) was measured (using a reference scatterer: 25DS00 Comar) and included in the fluorescence lifetime fitting procedure based on iterative re-convolution.

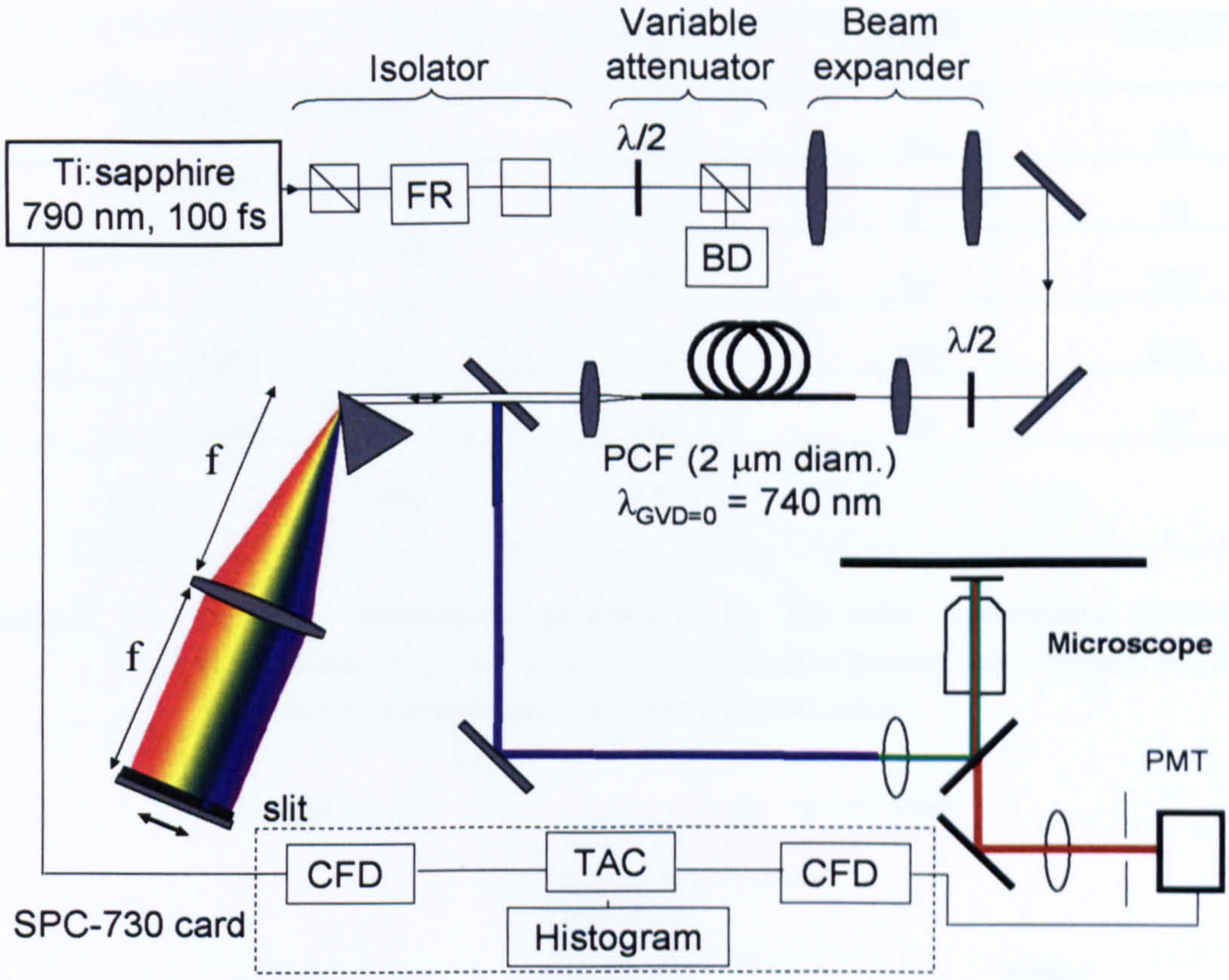


Figure 4.9 **A supercontinuum source (435-1150 nm) is coupled to a prism-based spectrometer, producing a central wavelength of 550 nm. The resulting fluorescence signal is de-scanned by the scanning mirrors, spectrally separated using a dichroic mirror, imaged through a pinhole and finally detected by a photomultiplier tube. Here back reflection to the laser is disabled by the components between laser and beam expander. The Photonic Crystal Fibre enables all wavelengths to travel at the same speed.**

4.4.3 Temperature Measurements

A calibration curve that describes the variation of τ_f as a function of temperature was generated. Temperature determination in microfluidic channels was performed using three devices. A simple microfluidic device (Chip I) was used for initial experiments. Additional experiments were performed on the microfluidic devices previously developed for CF-PCR (Chip II and III). Critical dimensions of all microfluidic devices are listed in Table 4.2 and layouts are presented in Figure 4.10.

	chip I	chip II	chip III
hot-start length (mm)	12	40	58
denaturation length (mm)	6	8	10
annealing/ extension length (mm)	20	60	160
width (μm)	130	150	218
depth (μm)	38	53	87
S/V (μm^{-1}) 0.068	0.051	0.032	

Table 4.2 **Important dimensional parameters for all three microfluidic devices investigated. Chip I was used for experiments in Section 4.4.1. Chips II and III were used for experiments described in Section 4.4.2.**

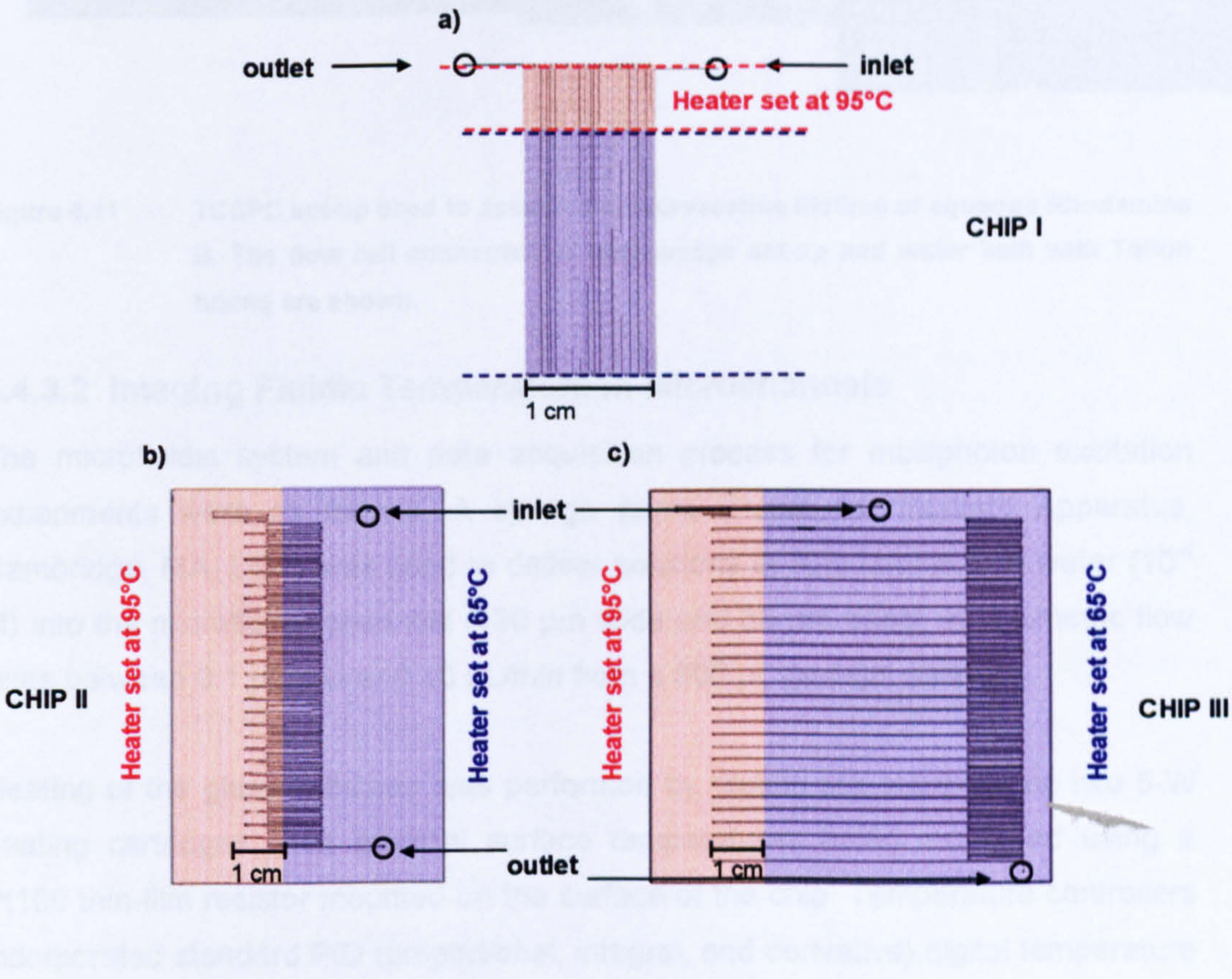


Figure 4.10 **The microfluidic devices used for temperature measurements.**

4.4.3.1 Temperature Calibration with Aqueous Rhodamine B

A water bath was connected by Teflon tubing to a heating frame which contained a flow cell. This flow cell was filled with a 10^{-4} M aqueous Rhodamine B solution and its temperature monitored directly using a thermocouple. Due to the separation

between the water bath and flow cell (approximately 2 m) a temperature difference between the water in the bath and in the flow cell was observed. Fluorescence measurements were performed at temperatures between 5 and 90 °C. Figure 4.11 presents images of the set-up and the flow cell.

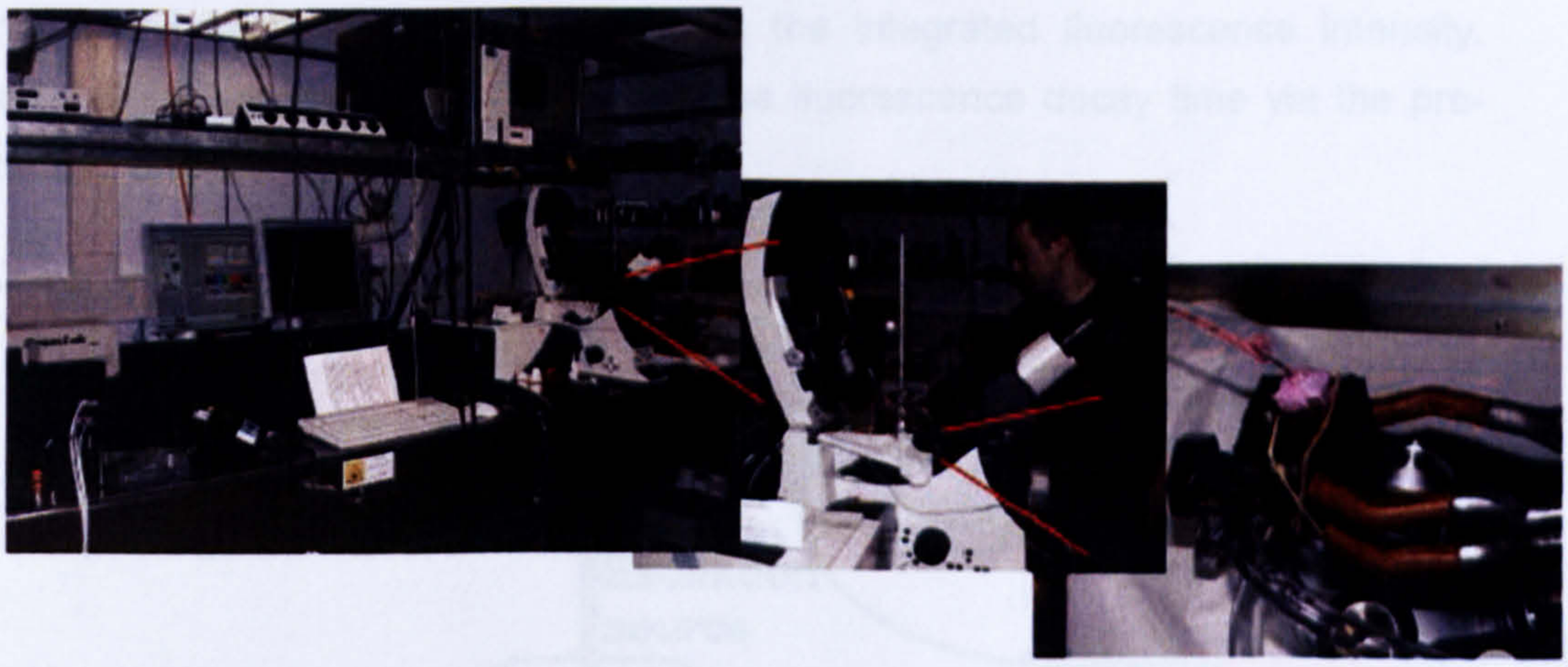


Figure 4.11 **TCSPC set-up used to assess the fluorescence lifetime of aqueous Rhodamine B. The flow cell connected to microscope set-up and water bath with Teflon tubing are shown.**

4.4.3.2 Imaging Fluidic Temperature in Microchannels

The microfluidic system and data acquisition process for multiphoton excitation experiments were as follows. A syringe pump (Pump 11, Harvard Apparatus, Cambridge, MA, USA) was used to deliver solutions of Rhodamine B in water (10^{-4} M) into the microfluidic channels (130 µm wide and 38 µm deep) at volumetric flow rates between 0.1 µL/min and 10 µL/min from a 500 µL gastight syringe.

Heating of the glass substrate was performed by resting the substrate on two 5-W heating cartridges, with external surface temperatures being monitored using a Pt100 thin-film resistor mounted on the surface of the chip. Temperature controllers incorporated standard PID (proportional, integral, and derivative) digital temperature controllers (CAL 3200, CAL Controls Ltd, Hitchin, UK), power supplies, and switch electronics for the heating cartridges. A schematic of this set-up (basic arrangement of the heater and chip) can be seen in Figure 4.12. Using this system, fluorescence lifetime imaging of fluid contained within a microchannel was performed. Initially a series of 20 time-gated intensity images per acquisition were collected. These were then fitted on a pixel-by-pixel basis to a single exponential decay model (with an

offset included to account for background light and the digital CCD offset). As mentioned previously Rhodamine B is known to exhibit a single exponential fluorescence decay [15]. Maps of both fluorescence lifetime and fluorescence intensity could be combined as a false color scale image in HSV (hue-saturation-value) format, where *hue* represents the fluorescence lifetime, *saturation* is a constant maximum, and *value* represents the integrated fluorescence intensity. Temperature can then be deduced from the fluorescence decay time via the pre-determined calibration curve.

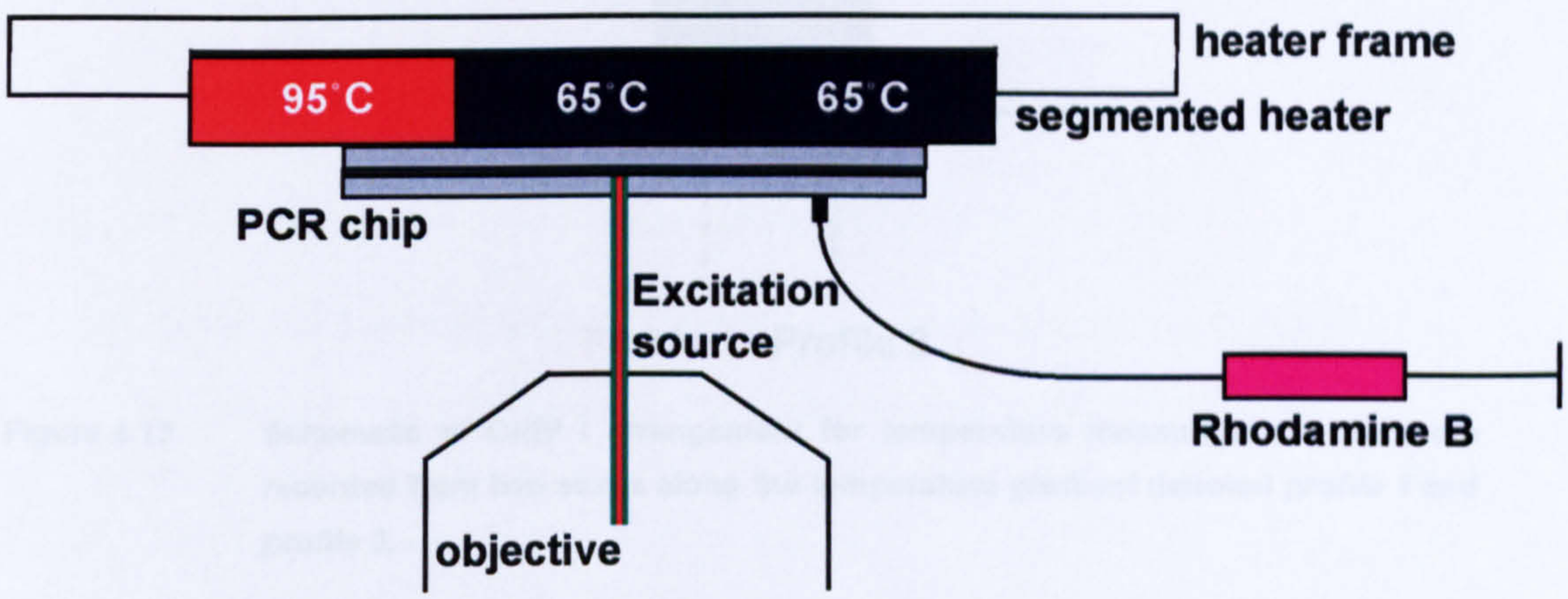


Figure 4.12 **The microfluidic chip mounted on the microchannel heater using heat-conductive paste. Rhodamine B is motivated through the microfluidic chip, while excitation and detection of fluorescence is carried out from below.**

Fluorescence lifetime data were obtained from regions of the microfluidic channel maintained at 66°C and 93°C. These values were chosen since they are typically used during thermal cycling for on-chip PCR. Acquisition times were typically 10-30 seconds per fluorescence lifetime image.

4.4.3.3 Imaging Fluidic Temperature Gradients in Microchannels

For the temperature gradient measurements the same conditions used in Section 4.4.3.2. were applied. Moreover, temperature was measured at a greater number of locations along the serpentine microchannel. Temperature gradients were created across a chip substrate (Figure 4.13) using the heating cartridges as a parallel heat source and sink.

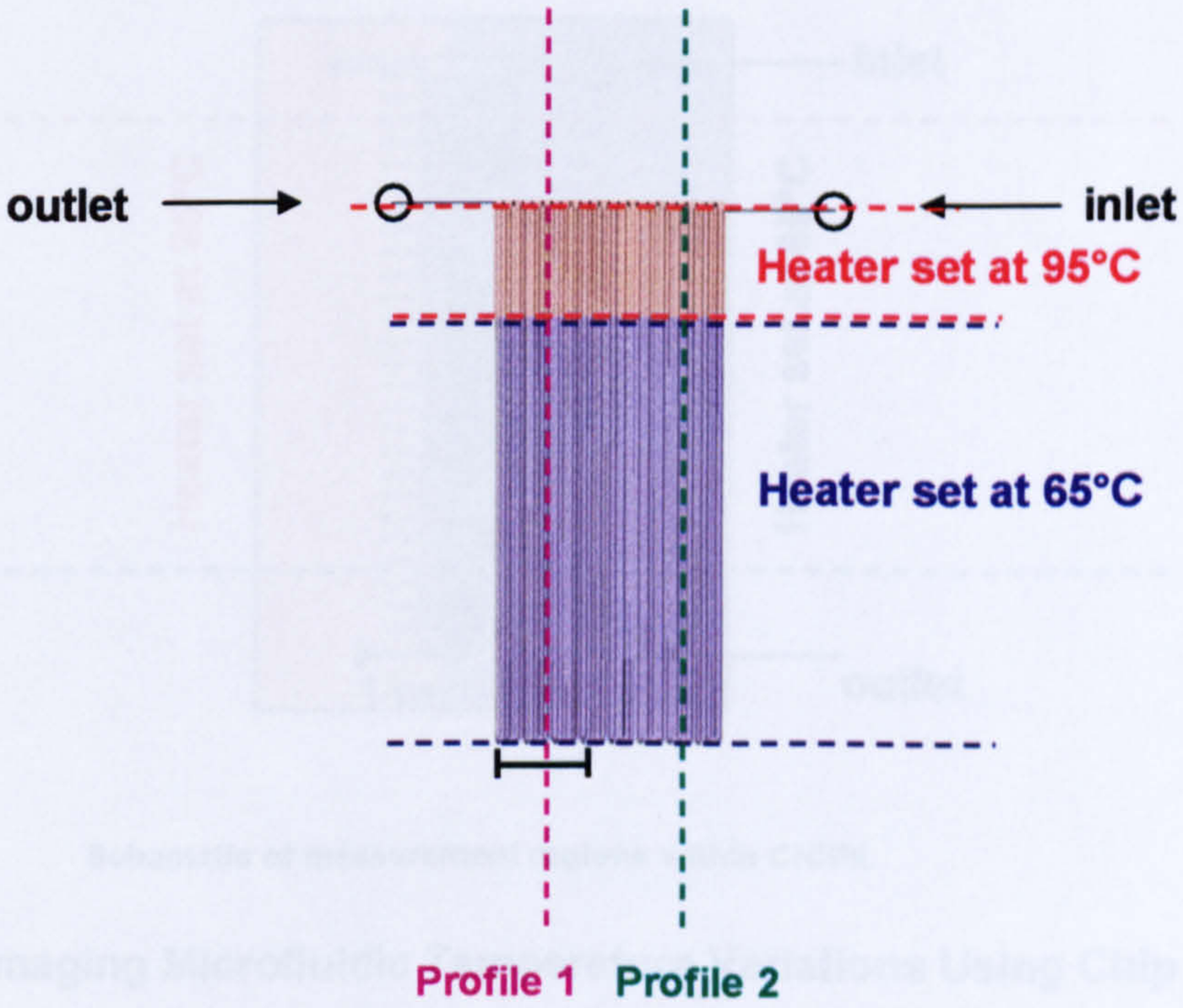


Figure 4.13 **Schematic of CHIP I arrangement for temperature measurements. Data are recorded from two scans along the temperature gradient denoted *profile 1* and *profile 2*.**

4.4.3.4 Mapping of Fluidic Temperatures in Three Dimensions

The assessment of intrachannel temperature variations in the presence of fluid flow, is crucial in understanding how efficient PCR will be. Experiments were undertaken to demonstrate how fluorescence lifetime imaging could quantitatively map fluidic temperatures in three dimensions with a spatial resolution of approximately 1µm. In these studies the microfluidic channel was contacted with a heating element placed close to the upper channel surface and measurements were performed in all three spatial dimensions.

4.4.3.5 Imaging Microfluidic Temperature Variations Using Chip II

Here initial experiments focused on measuring the temperature variation along the microfluidic channels of chip II. An aqueous Rhodamine B solution was pumped through the microfluidic device at a flow rate of 3 µl/min. The temperature gradient across the device was assessed at positions close to both the inlet and the outlet (shown in Figure 4.14). This was followed by a series of experiments in which the flow direction was switched and the volumetric flow rates varied between 1 and 10 µl/min.

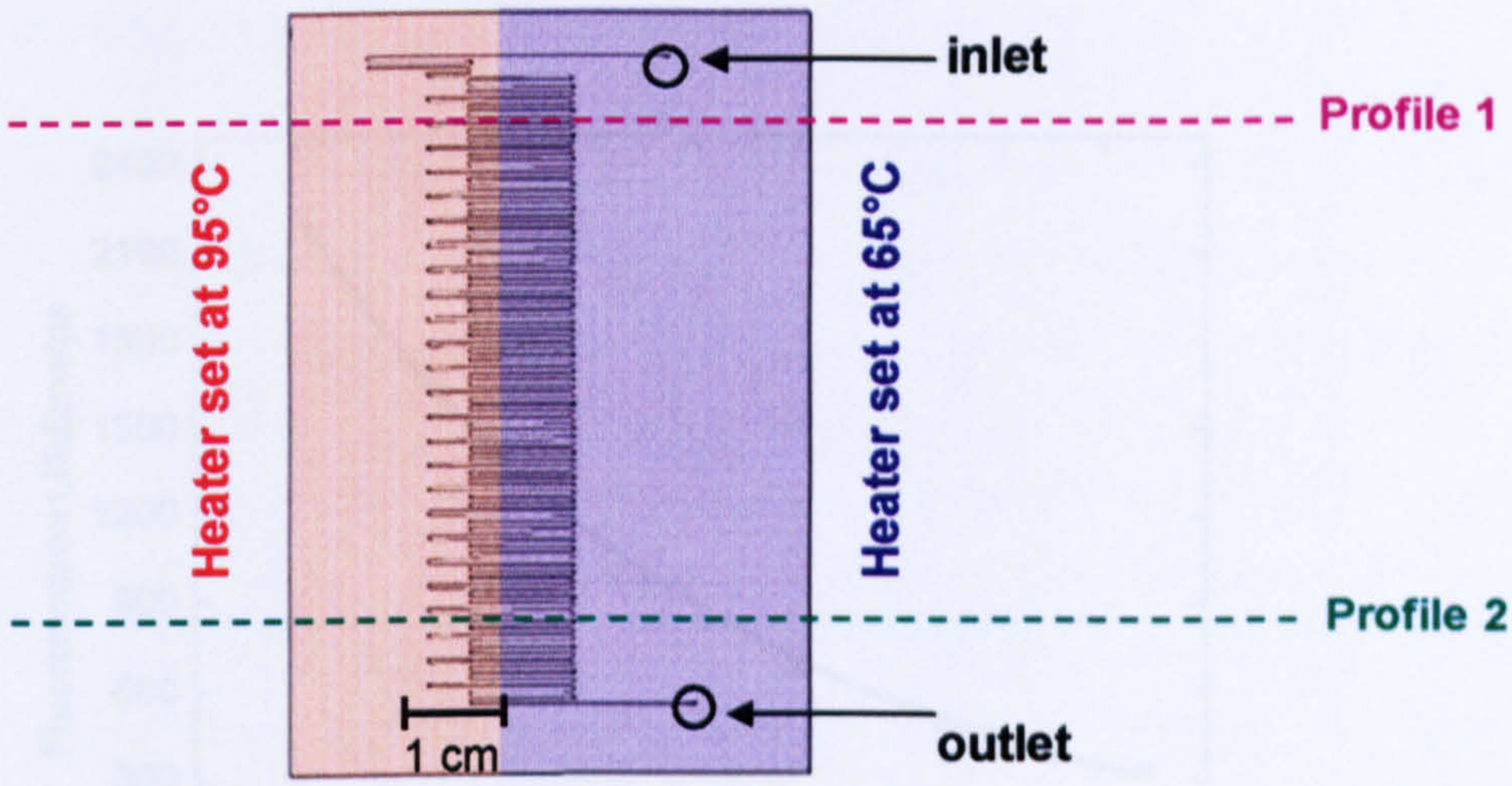


Figure 4.14 **Schematic of measurement regions within CHIPII.**

4.4.3.6 Imaging Microfluidic Temperature Variations Using Chip III

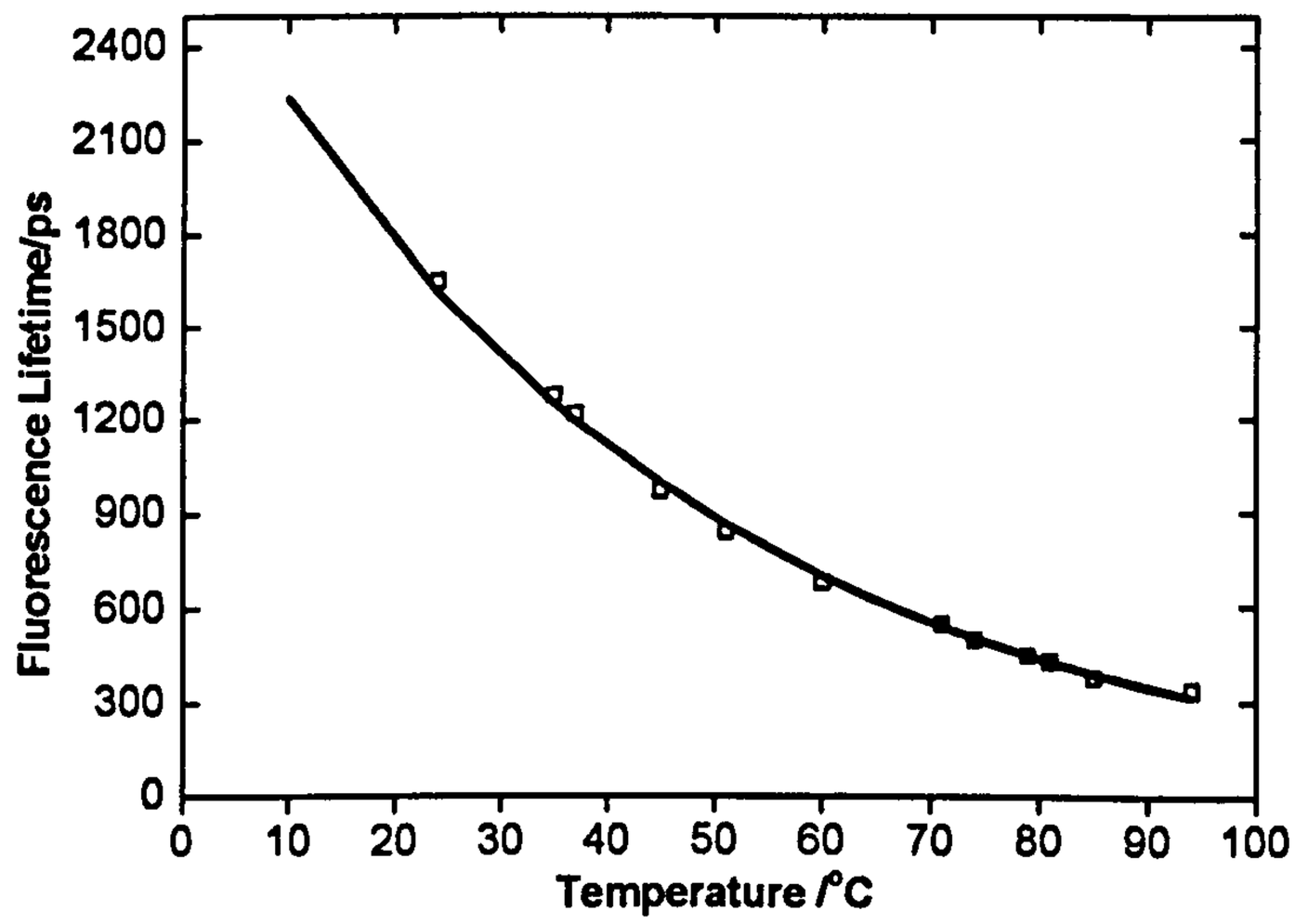
Final temperature measurements in microfluidic channels were performed by introducing a new microfluidic chip (III) (Figure 4.10 c) and performing identical experiments to those described in Section 4.4.3.5.

4.5 Results

4.5.1 System Calibration

The average fluorescence lifetimes of Rhodamine B in water were measured for a range of temperatures and are displayed in Figure 4.15. The observed fluorescence lifetime decreases as a function of temperature, due to the mechanisms explained in Section 4.3.2. A similar temperature dependency of the fluorescence lifetime of Rhodamine B has been reported previously in methanolic solutions [29]. It should also be noted that heating induced by the laser beam used for excitation is negligible for the current experiments. This is consistent with previously published findings for bulk solution measurements [30].

a)



b)

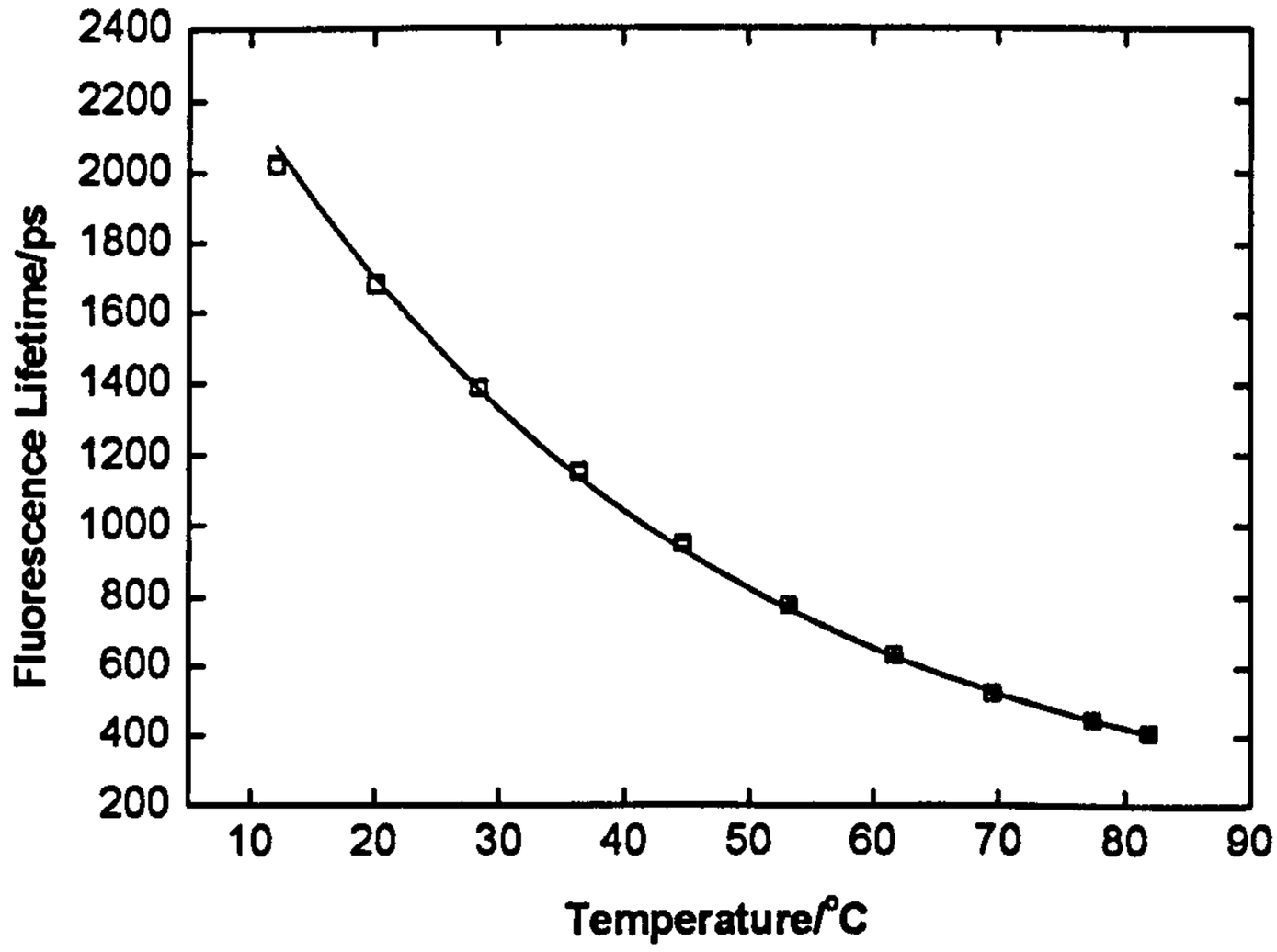


Figure 4.15 **Calibration data of 10^{-4} M Rhodamine B in water measured in flow cell. With increasing temperature a decrease in Lifetime is observed. (a) presents calibration for TCSPC set-up and (b) presents calibration for the wide-field set-up.**

4.5.2 Wide-Field Imaging Techniques

4.5.2.1 Imaging Fluidic Temperature in Microchannels

To demonstrate the robustness of the approach, fluorescence lifetime images were acquired at different spatial locations across the chip with the entire device maintained at either 66°C or 93°C. The results of these experiments are shown in Figure 4.16. At 66°C, the mean fluorescence lifetime of Rhodamine B averaged over all spatial points was 496±15 ps, whereas at 93 °C, the mean fluorescence lifetime was 277±16 ps. Using the previously measured calibration curve the apparent temperatures were calculated to be 66.5±1°C and 90±2°C, respectively. The error limits refer to the statistical error in the mean lifetime due to spatial fluctuations, and are consistent with estimated errors in the temperature measurement as discussed previously. For the 66°C region, the observed temperature of the fluid is in good agreement with the corresponding thermocouple measurement, but for the 93°C region the observed temperature is slightly lower. This is in part due to increased heat dissipation from the substrate at higher temperatures. Visual inspection of these fluorescence lifetime maps (Figure 4.16 (a) and (b)) clearly demonstrates the different Rhodamine B fluorescence lifetime within the two regions. Examination of both fluorescence lifetime and time-integrated intensity profiles across the channel width (Figure 4.16 (c)) reveal that both the fluorescence lifetime and intensity are reduced by a factor of ~2 at the higher temperature. It should also be noted that, although the fluorescence intensity falls off in regions near the channel edges (due to reduced excitation efficiency and concentration effects), the measured lifetime remains essentially constant across the entire channel width.

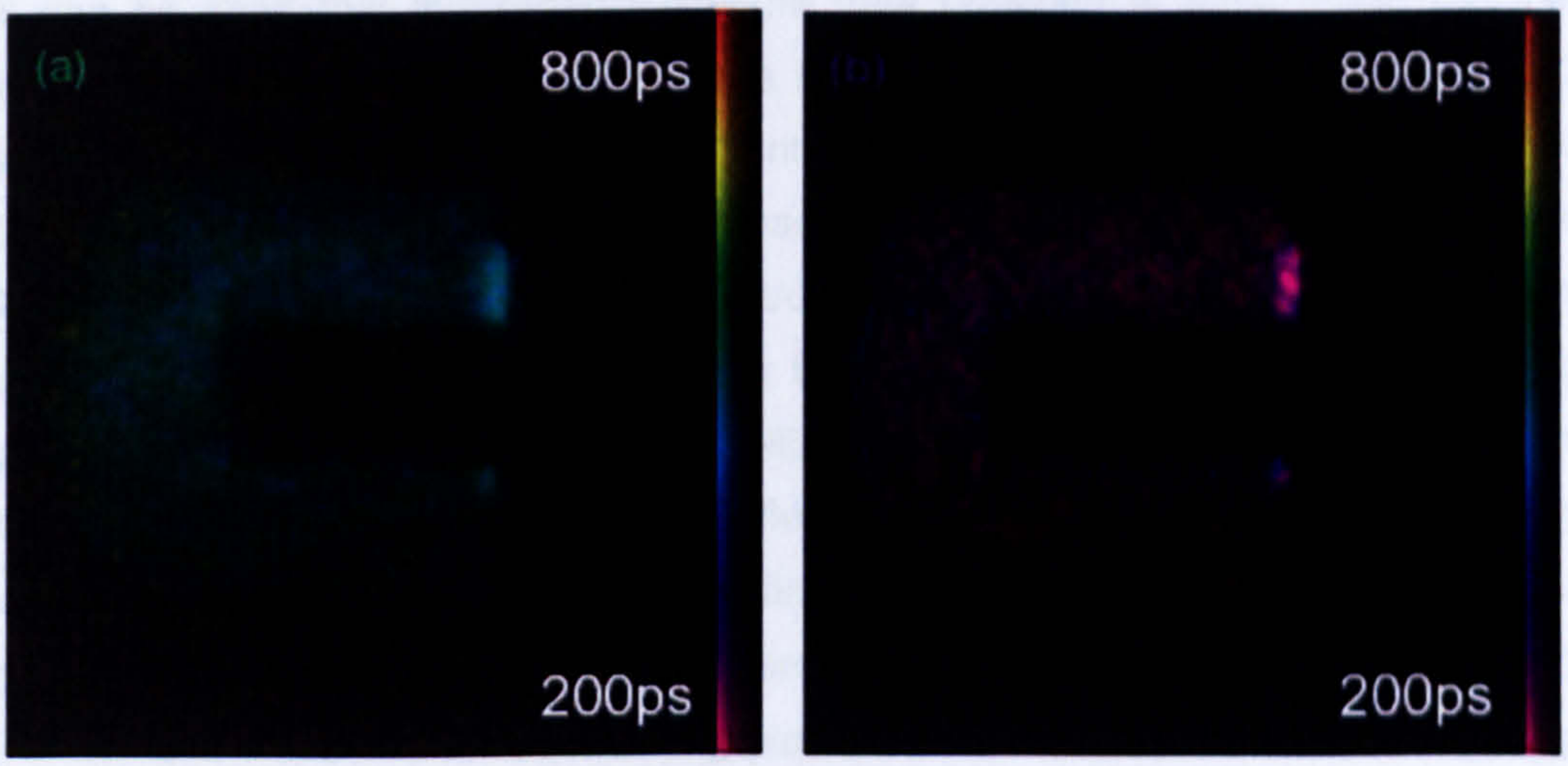


Figure 4.16 **Fluorescence lifetime imaging of a Rhodamine B solution in a microchannel. (a) fluorescence lifetime image measured at 66°C (b) fluorescence lifetime image measured at 93°C, (c) variation of fluorescence lifetimes (green and blue lines) and time-integrated intensities (green and blue dashed lines) across the microchannel width. The fluorescence lifetime is approximately constant over the width of the microchannel, whilst the fluorescence intensity shows a much less uniform behaviour.**

4.5.2.2 Imaging Microfluidic Temperature Gradients

Figure 4.13 shows a schematic of the measurement points along the temperature gradient, with Figure 4.17 showing the corresponding fluorescence lifetime variation.

It can be seen that fluorescence lifetime data obtained in each linear scan are consistent and demonstrate an increase in fluorescence lifetime from 300 to ~500 ps. Figure 4.18 illustrates the equivalent variation in the integrated fluorescence intensity. Whilst some variation is observed, consistent with the fluorescence lifetime trend, the fluctuating excitation/detection efficiency across the microchip renders the intensity data unsuitable for temperature determination, without image ratio or excitation/detection efficiency calibration. In contrast, temperature variations can be calculated directly from the fluorescence lifetime data using a single calibration curve, (Figure 4.19). Interestingly, it is observed that the optimum fluid temperatures of 65-68°C in the low temperature zone are only obtained within ~5mm of the corresponding heating block, while fluid temperatures in the high temperature zone are below the 92-95°C optimum. These variations will need to be addressed in future PCR chip designs, and are discussed later in this Chapter.

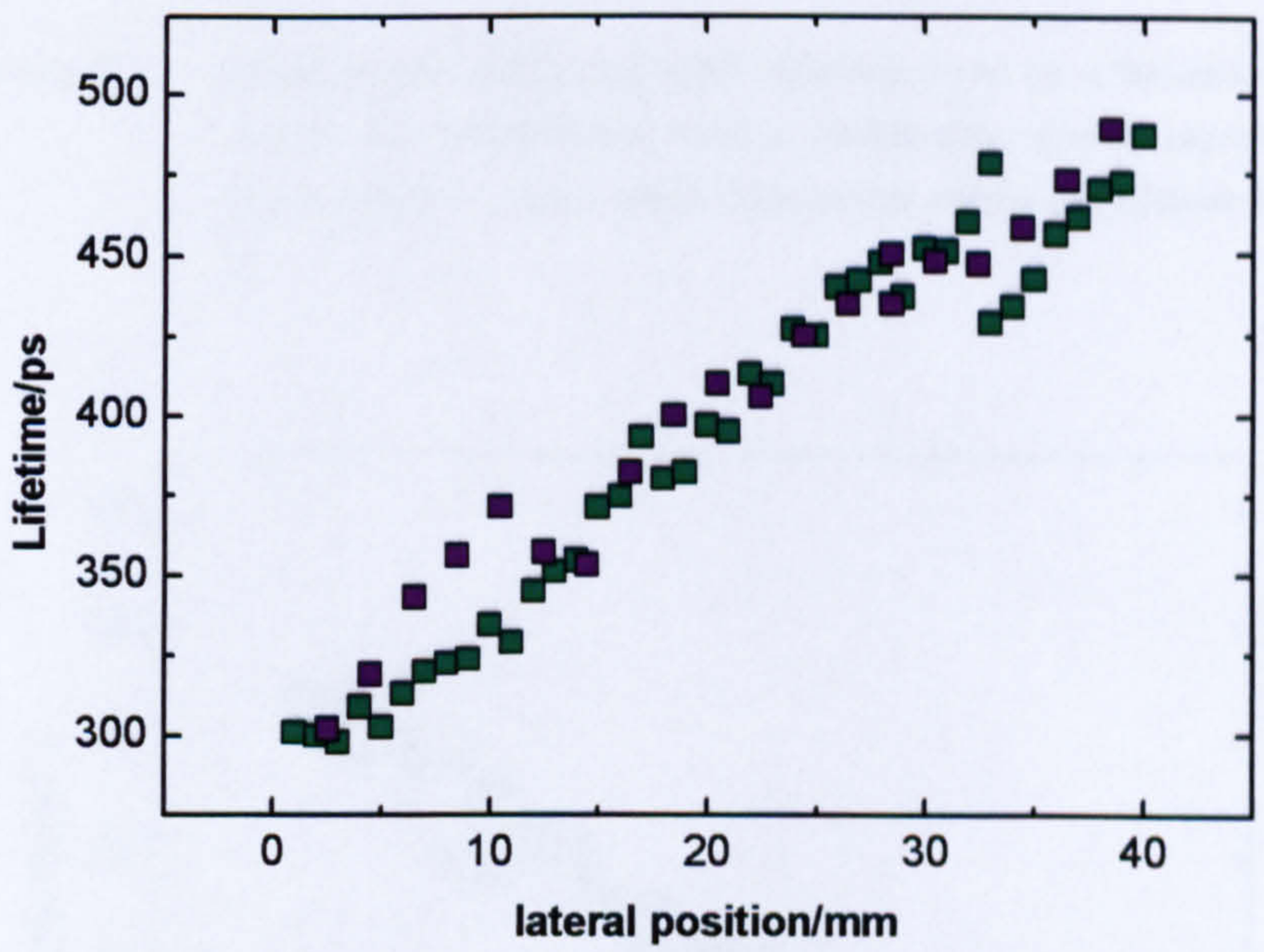


Figure 4.17 **Variation of fluorescence lifetime as a function of lateral position across the microfluidic device. Violet data points represent measurements along profile 1, while green data points represent measurements along profile 2.**

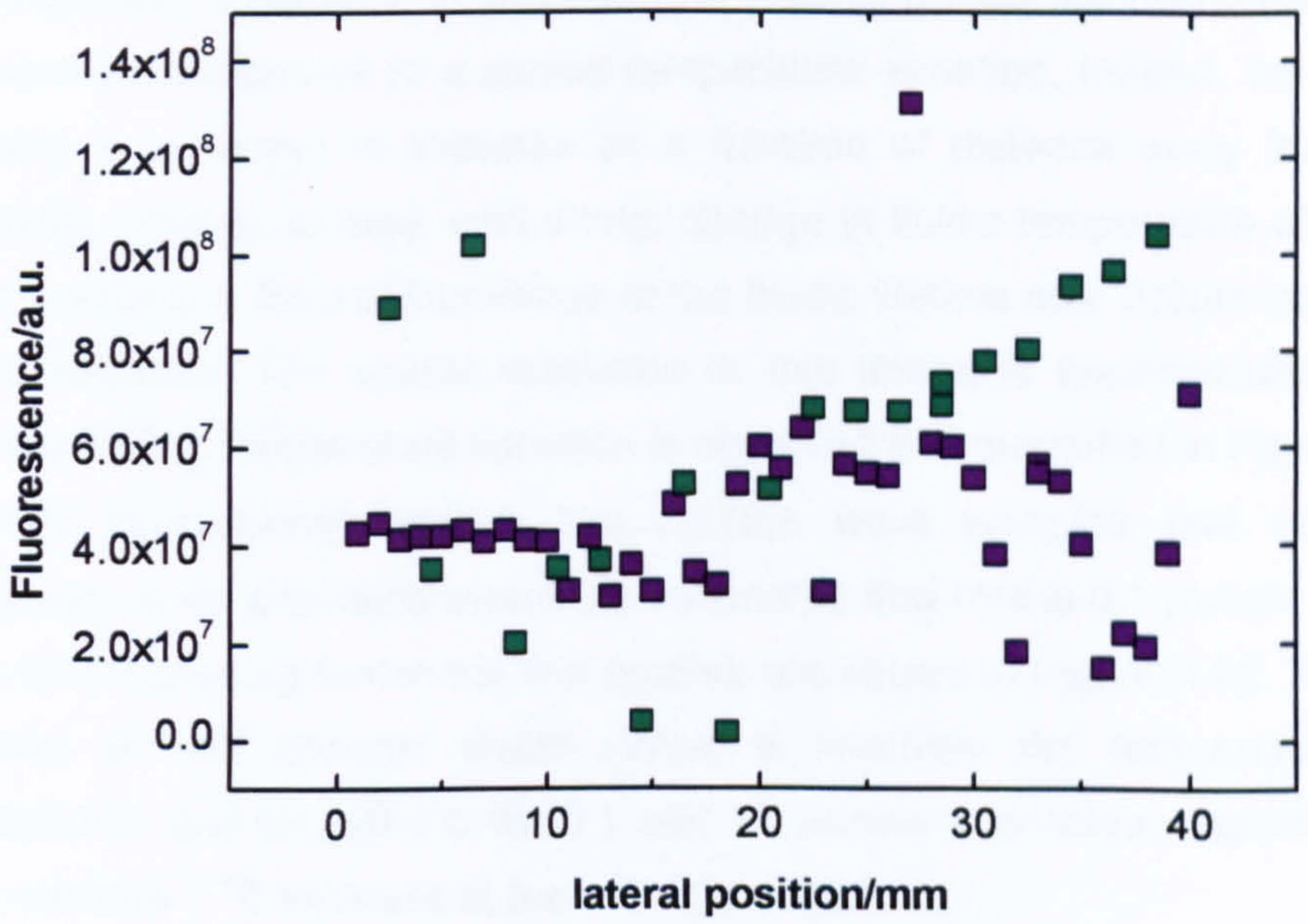


Figure 4.18 **Uncalibrated time-integrated intensity data as a function of lateral position across the microfluidic device. Violet data points represent measurements along profile 1, while green data points represent measurements along profile 2.**

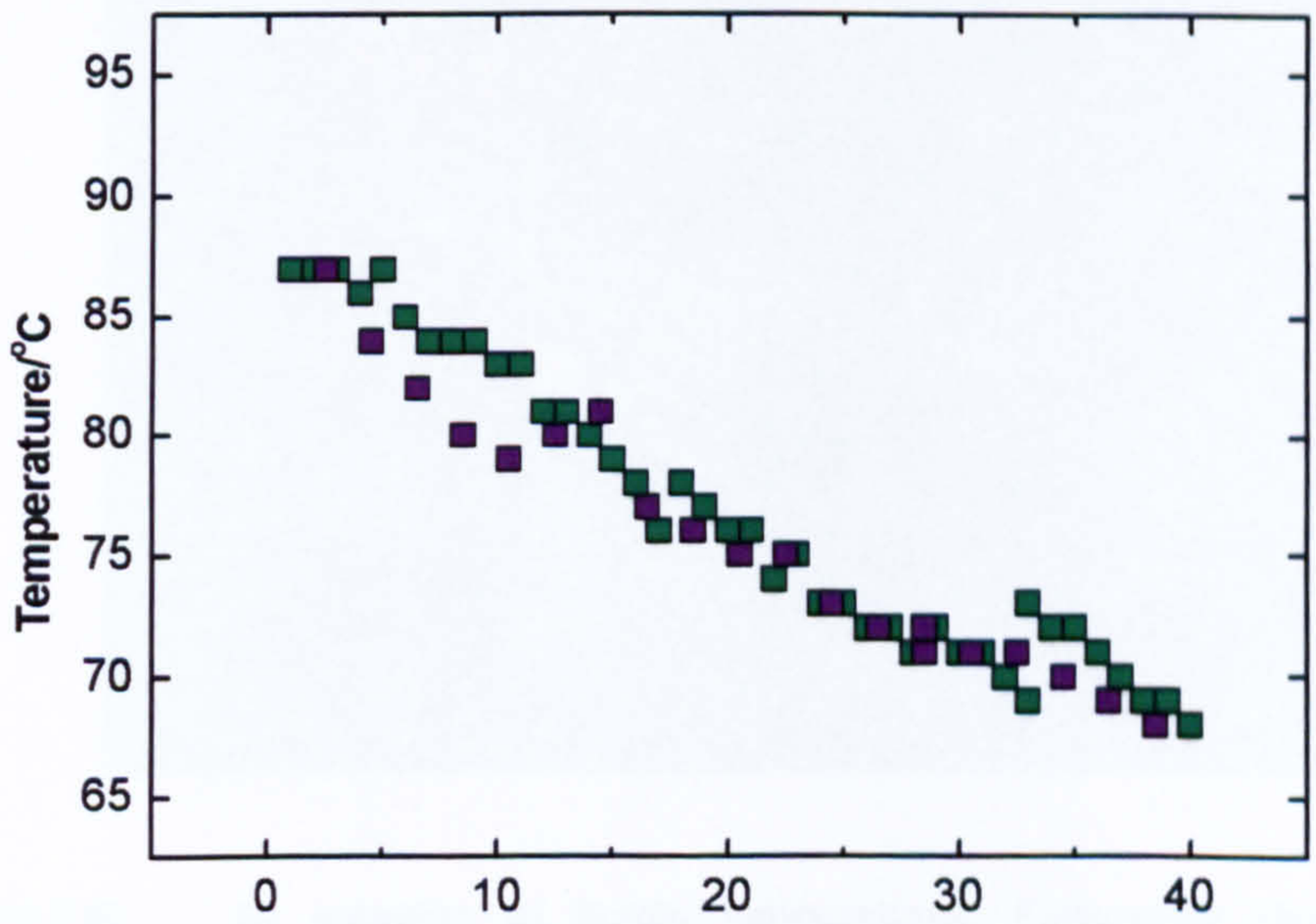


Figure 4.19 **Fluidic temperature profiles calculated using fluorescence lifetime data. Violet data points represent measurements along profile 1, while green data points represent measurements along profile 2.**

4.5.2.3 3D-Mapping of Channel Temperature

As expected, a variation in fluorescence lifetime across the microchannel (in the z direction) corresponds to a spatial temperature variation. Indeed, the fluorescence lifetime is observed to increase as a function of distance away from the upper (heated) channel surface, with a total change in fluidic temperature of ~5°C. Figure 4.20 presents a false colour image of the fluidic lifetime of a 100µm long and 38 µm deep segment. The spatial resolution in this image is approximately 1 µm. The corresponding temperature variation is observed and quantified in Figure 4.21. Here vertical fluorescence lifetime line profiles were sampled and converted into temperature for situations where the volumetric flow rate is 0.1 µL/min or 10 µL/min. The corresponding horizontal line profiles are shown in Figure 4.22. The horizontal profiles at half channel depth reveal a relatively flat temperature profile of 68.5±0.5°C and 67.5±0.5°C for 0.1 and 10 µL/min flow rates respectively, with an approximate 1 °C increase at the extreme edges.

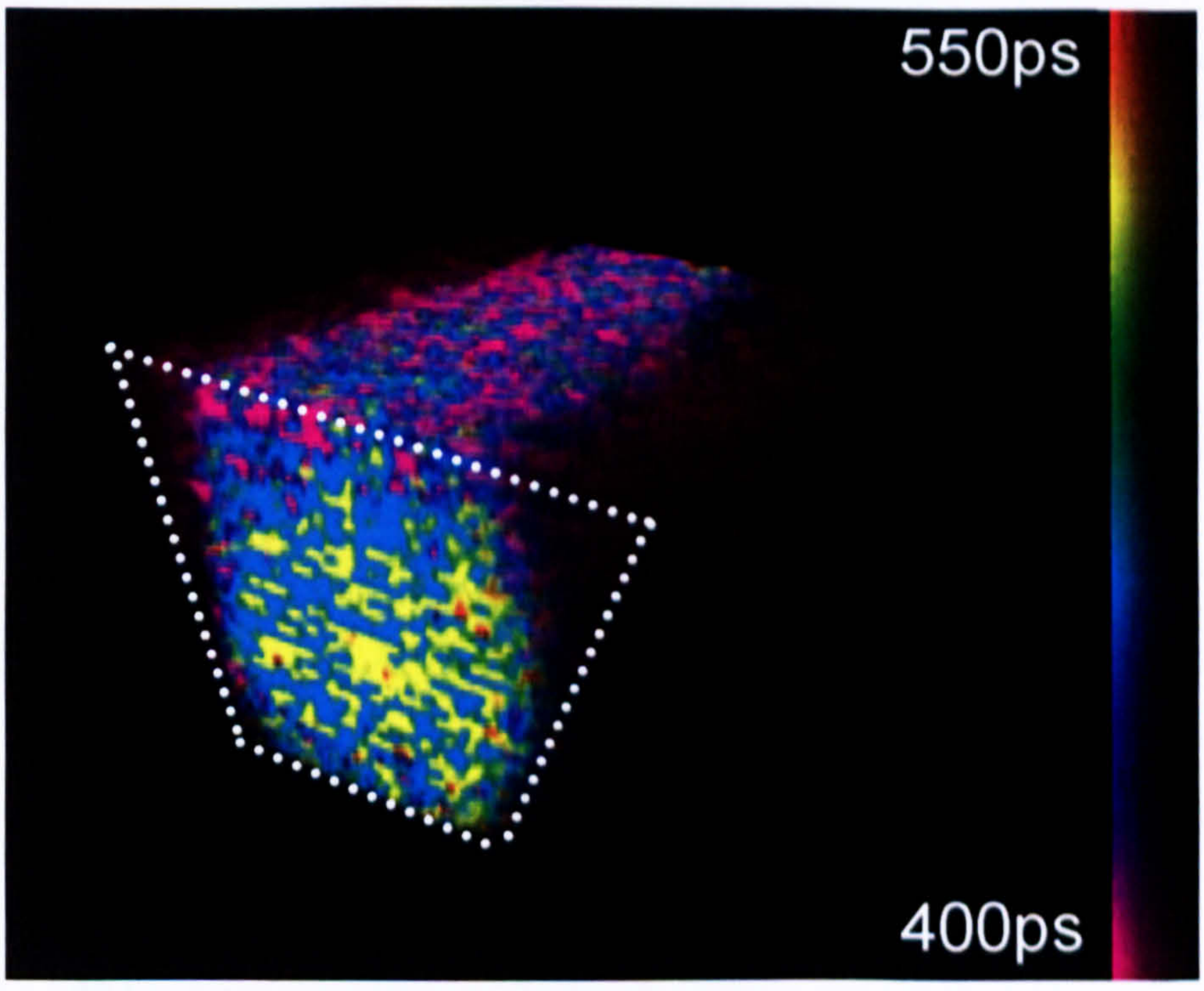


Figure 4.20 **3D mapping of fluidic temperatures. False-color rendered 3D-image of fluorescence lifetime variations of a methanolic solution of Rhodamine B within a 130x40x100 µm microchannel segment and at a flow rate of 10 µL/min. Channel boundaries are indicated with white dotted lines. The upper surface of the microchannel is held at 73°C.**

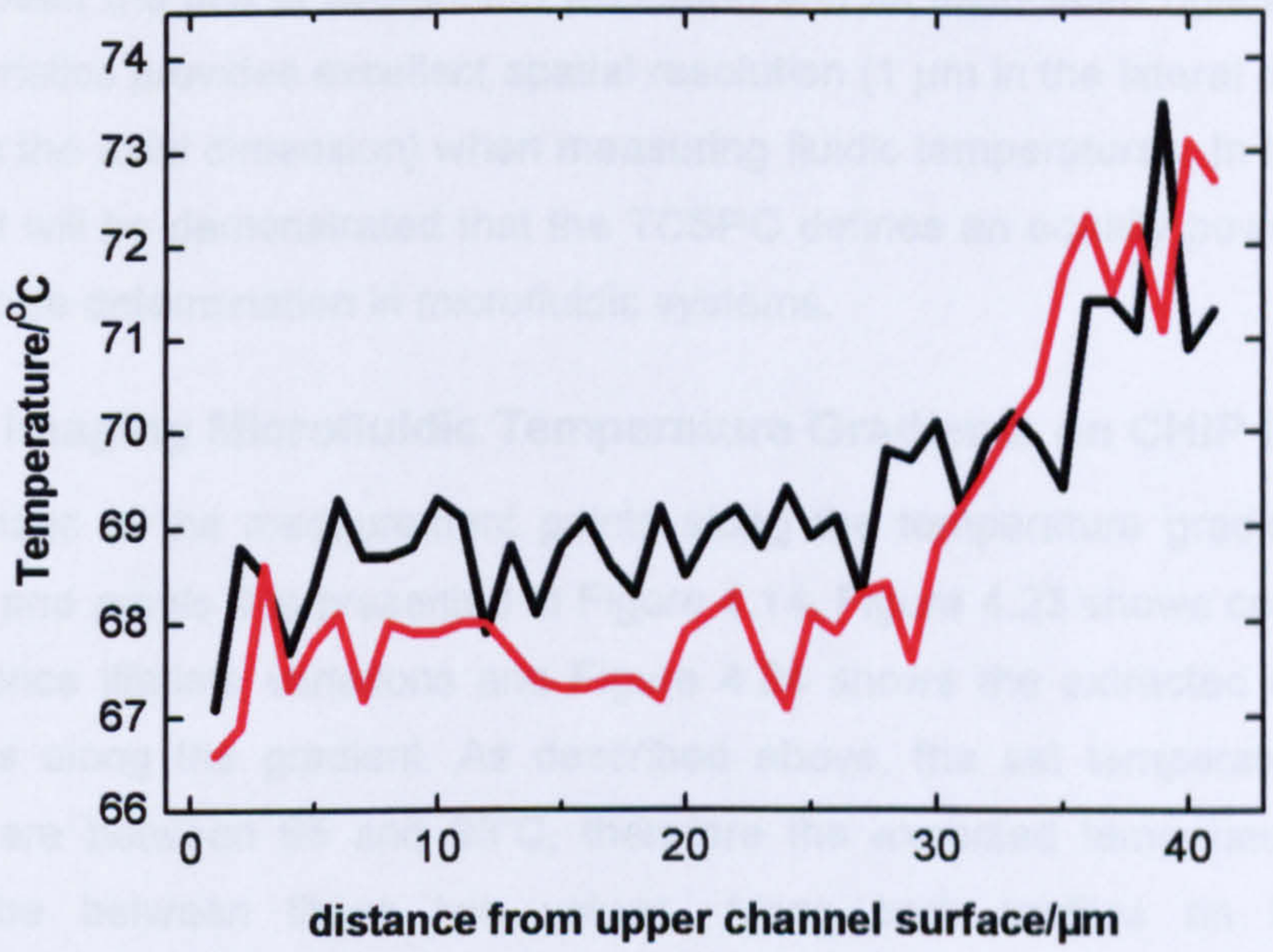


Figure 4.21 **Variation of temperature as a function of distance away from the upper microchannel surface at volumetric flow rates of 0.1 (black line) and 10 μl/min (red line).**

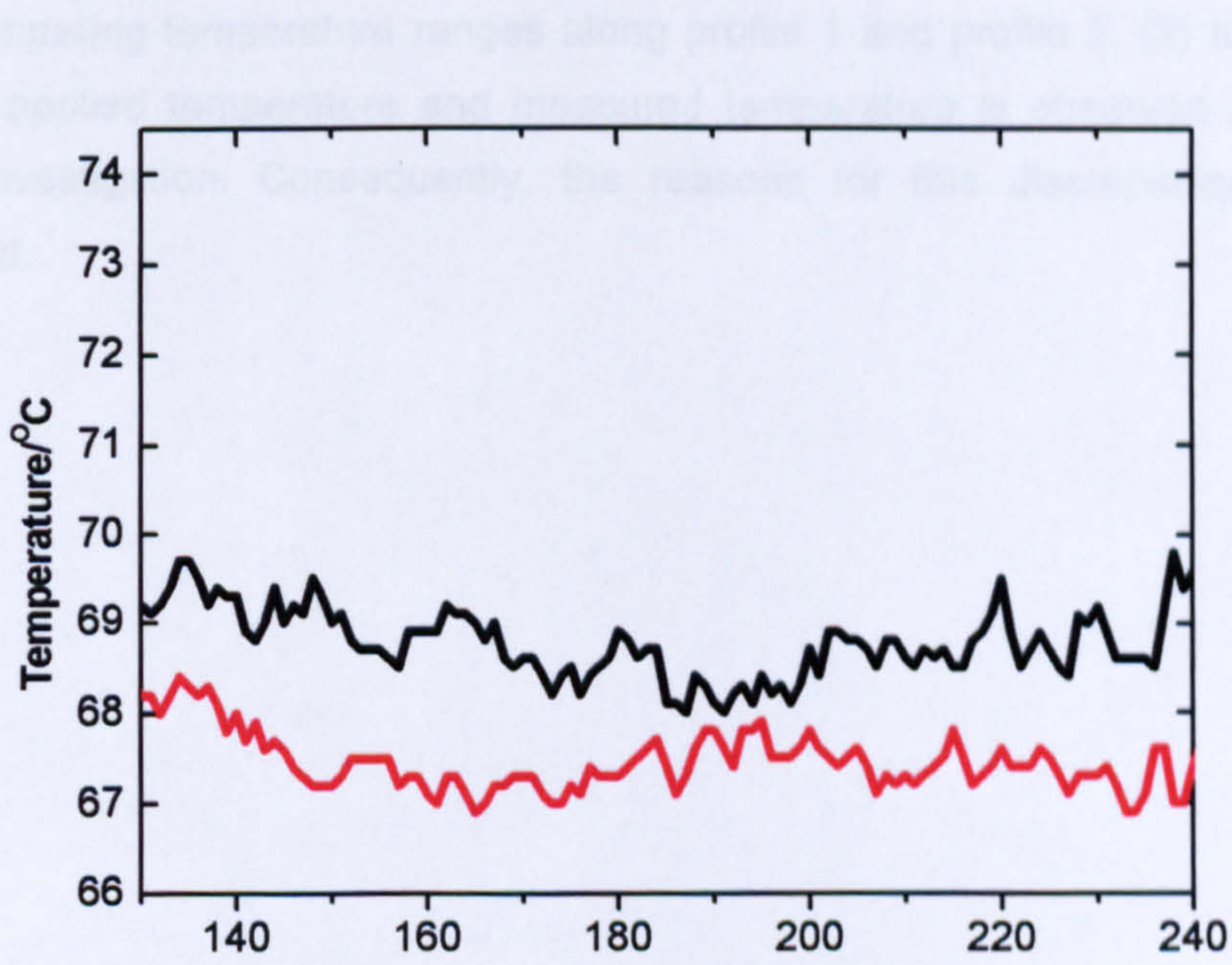


Figure 4.22 **Variation of temperature as a function of distance across the microchannel at half the channel depth and at volumetric flow rates of 0.1 (black line) and 10 (red line) μL/min.**

4.5.3 TCSPC – Techniques

As has been the use of two-photon excitation and its associated optical sectioning characteristics provides excellent spatial resolution (1 µm in the lateral direction and 10 µm in the axial dimension) when measuring fluidic temperatures. In the following section it will be demonstrated that the TCSPC defines an equally powerful tool for temperature determination in microfluidic systems.

4.5.3.1 Imaging Microfluidic Temperature Gradients on CHIP II

A schematic of the measurement points along the temperature gradient denoted *profile 1* and *profile 2* is presented in Figure 4.14. Figure 4.23 shows corresponding fluorescence lifetime variations and Figure 4.24 shows the extracted temperature variations along the gradient. As described above, the set temperatures on the heaters are between 65 and 95°C, therefore the expected temperature gradient should be between these two values. Along both profiles an increase in fluorescence lifetime and consequently a decrease in temperature was observed. However, temperatures measured along profile 1 are between 76 and 97°C and temperatures measured along profile 2 are between 71 and 91°C. These results indicate two problems: (1) a non-uniform temperature distribution was observed when comparing temperature ranges along profile 1 and profile 2, (2) a difference between applied temperature and measured temperature is observed and needs further investigation. Consequently, the reasons for this discrepancy must be elucidated.

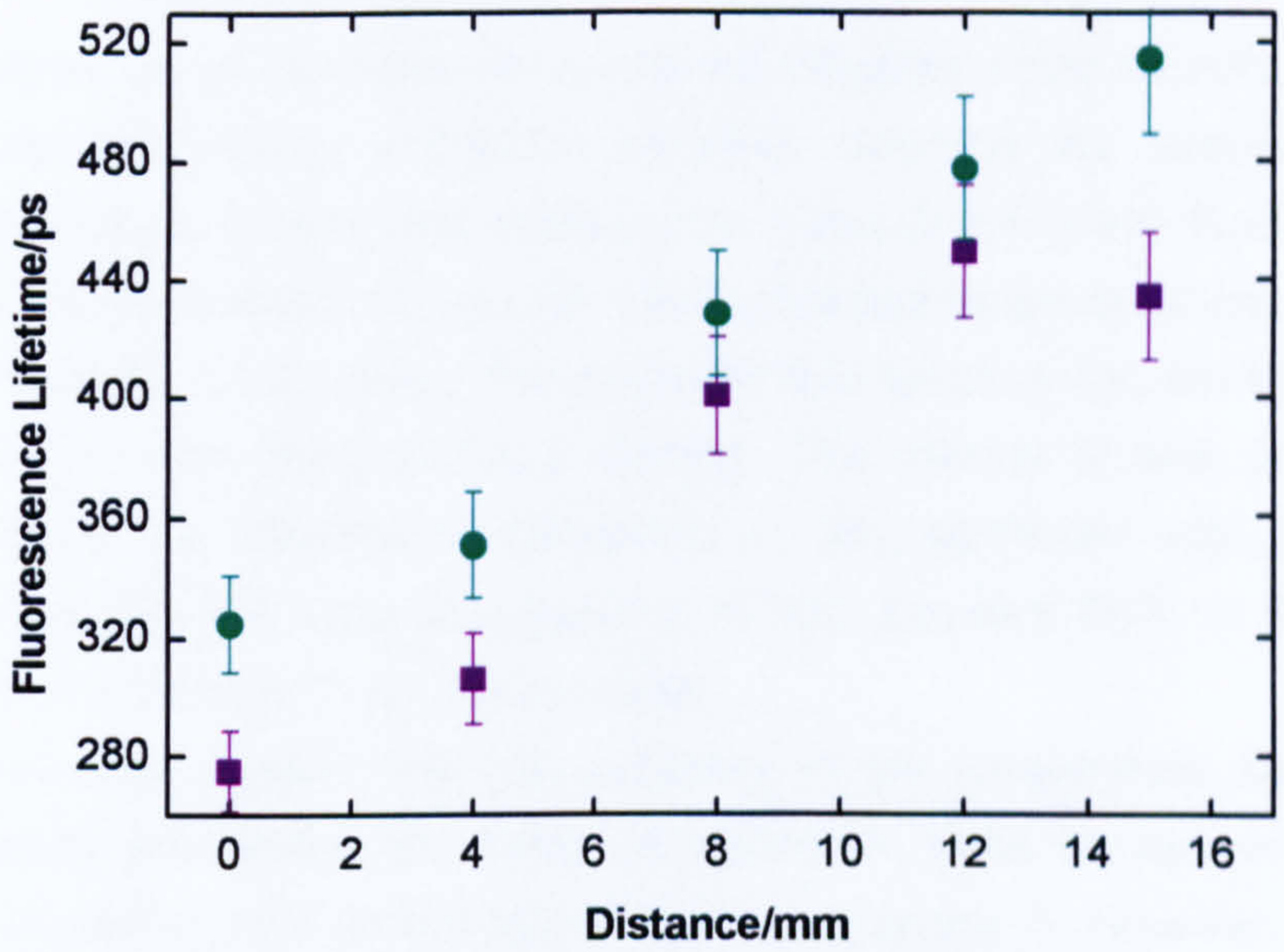


Figure 4.23 **Variation of fluorescence lifetime as a function of distance along profile 1 (violet) and profile 2 (green).**

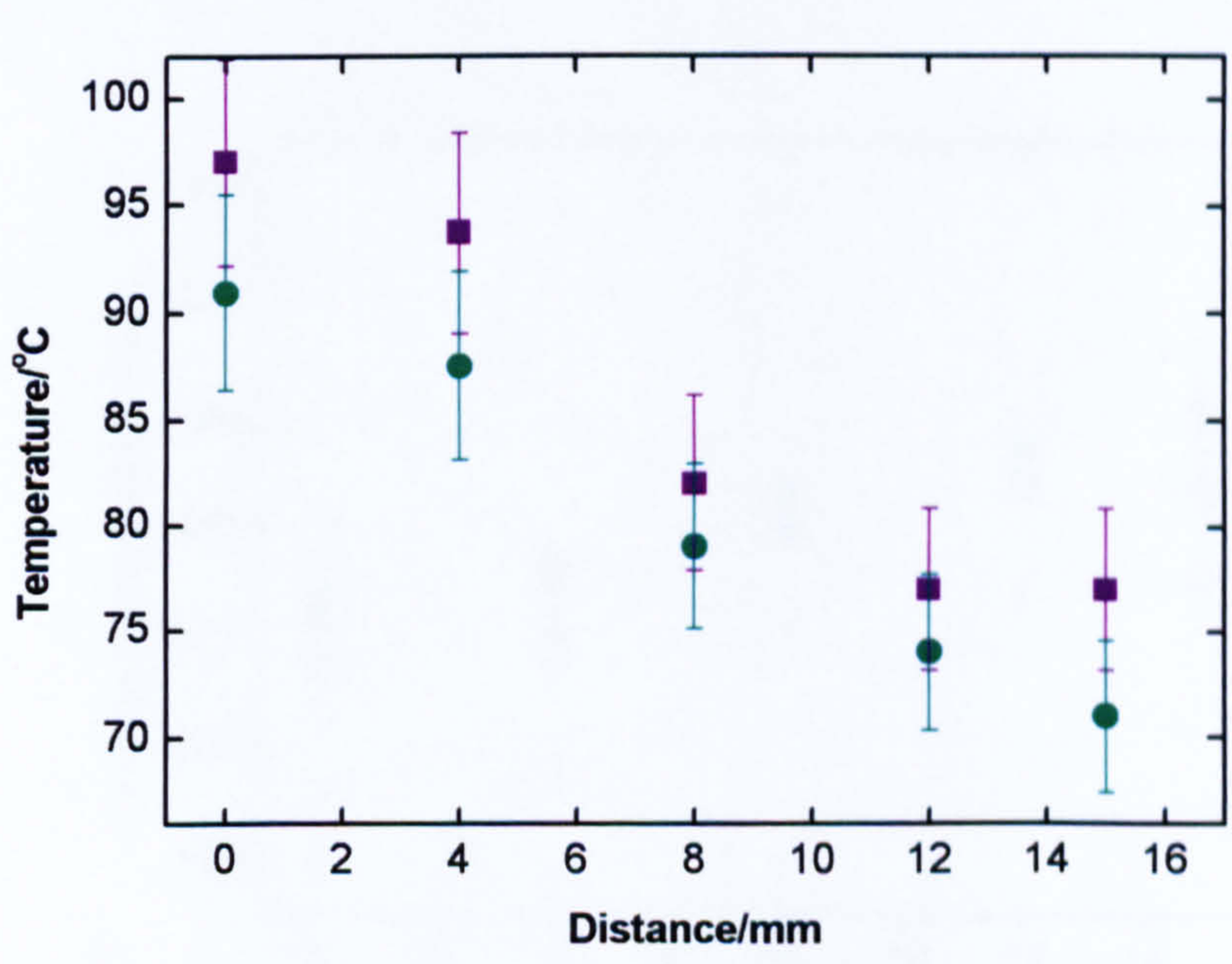


Figure 4.24 **Variation of temperature as a function of distance across the device along profile 1 (violet) and profile 2 (green).**

4.5.3.2 Imaging Microfluidic Temperature Gradients Under Reversed Flow (CHIPII)

A simple experiment used to assess the influence of the microfluidic layout on the overall temperature distribution involved reversing the direction of fluid flow. Fluorescence lifetime data along profile 1 and profile 2 with forward and reversed flow are presented in Figure 4.25, while extracted temperature data are presented in Figure 4.26. In both cases, the measured fluid temperatures are higher along profile 1 (violet) than along profile 2 (green). The change of flow direction does not influence the temperature distribution in any significant way. Additionally, it is obvious that the ideal temperatures for the two-step PCR of 65 and 95°C (as defined in Chapter 2) are not achieved.

These data suggest that non-uniformity in the temperature distribution can be primarily attributed to the heater configuration, since the temperatures measured along profile 1 are always higher than along profile 2. However, the fact that the lower set temperature of 65°C is not reached along either profile suggests some adjustment of the current heater configuration is necessary. Further experiments were performed with a recalibrated heater set-up and additional variations of volumetric flow rate between 1 and 10 µl/min on CHIP II.

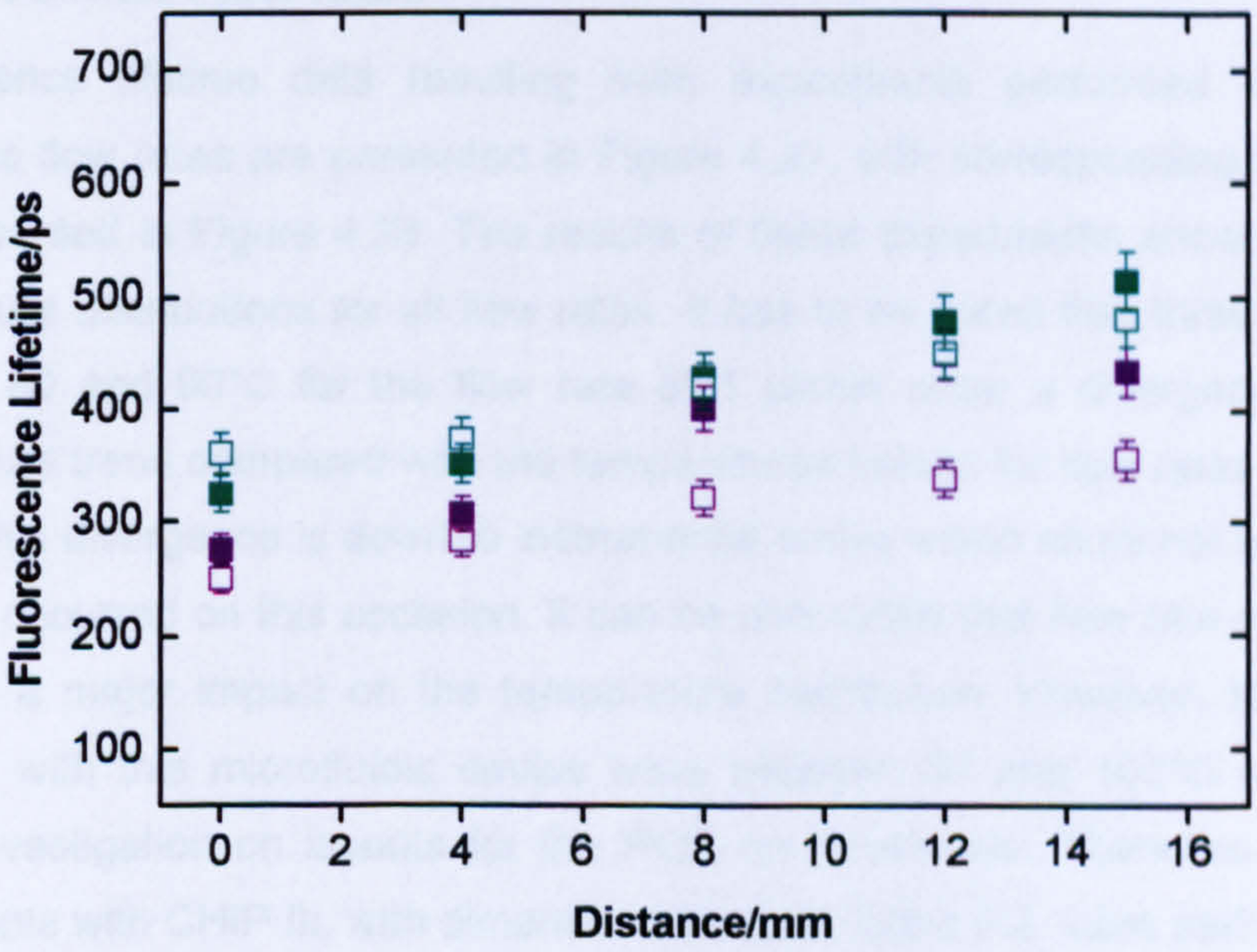


Figure 4.25 **Variation of fluorescence lifetime as a function of distance (along profile 1 (violet) and profile 2 (green)) with forward flow (filled squares) and reversed flow (empty squares).**

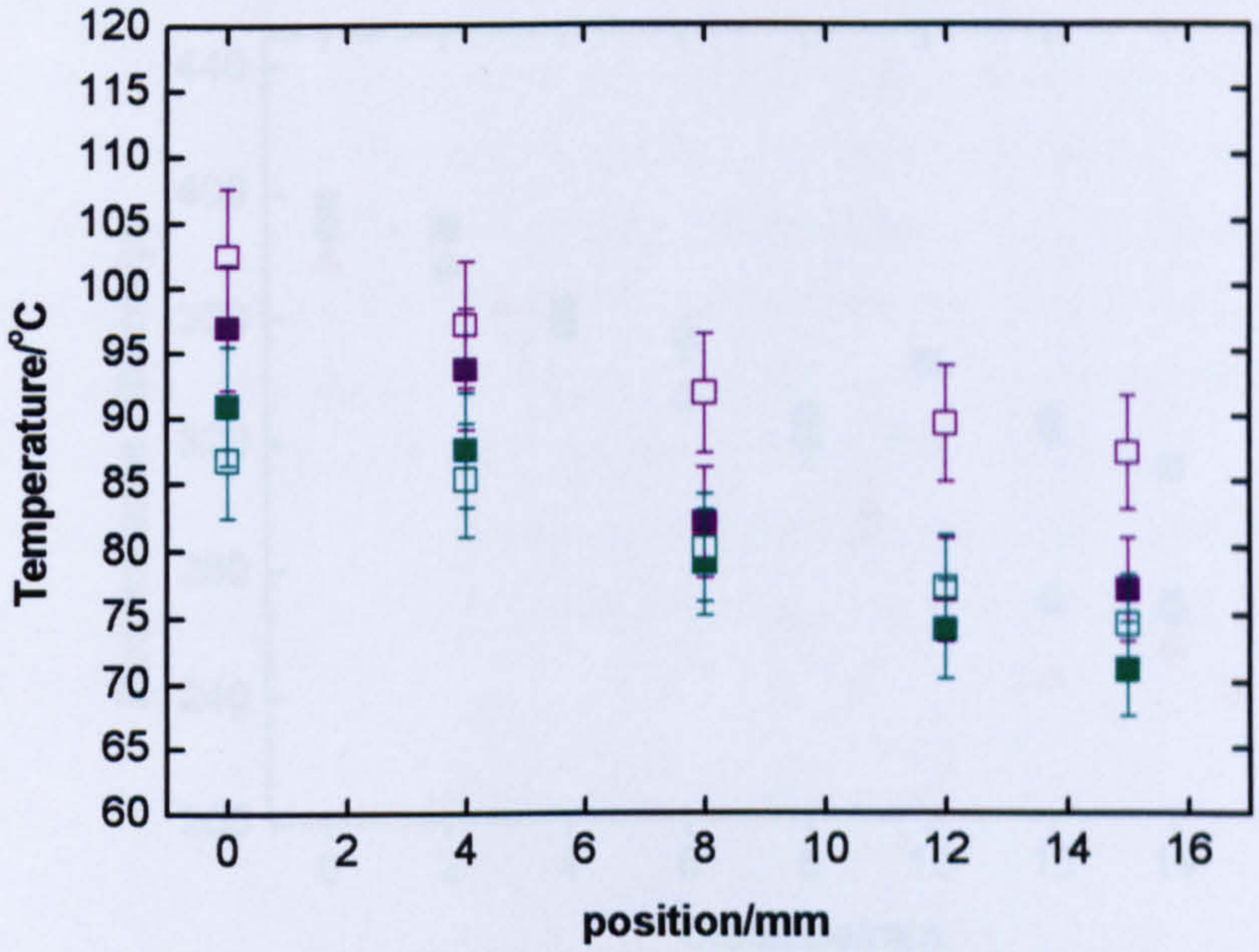


Figure 4.26 **Variation of temperature as a function of distance (along profile 1 (violet) and profile 2 (green)) with flow forward (filled squares) and reversed flow (empty squares).**

4.5.3.3 Imaging Microfluidic Temperature Gradients whilst Varying Volume Flow rates

Fluorescence lifetime data resulting from experiments performed with varying volumetric flow rates are presented in Figure 4.27, with corresponding temperature data presented in Figure 4.28. The results of these experiments show very similar temperature distributions for all flow rates. It has to be noted that three data points between 80 and 90°C for the flow rate of 1 µl/min show a divergence from the temperature trend compared with the temperatures values for flow rates of 3 and 10 µl/min. This divergence is down to instrumental errors which could not be quantified and only occurred on this occasion. It can be concluded that flow rate variations do not have a major impact on the temperature distribution. However, temperatures achieved with this microfluidic device were between 80 and 102°C and suggest further investigation on layouts for the PCR on microscale. Therefore a series of experiments with CHIP III, with dimensions listed in Table 4.2, were performed.

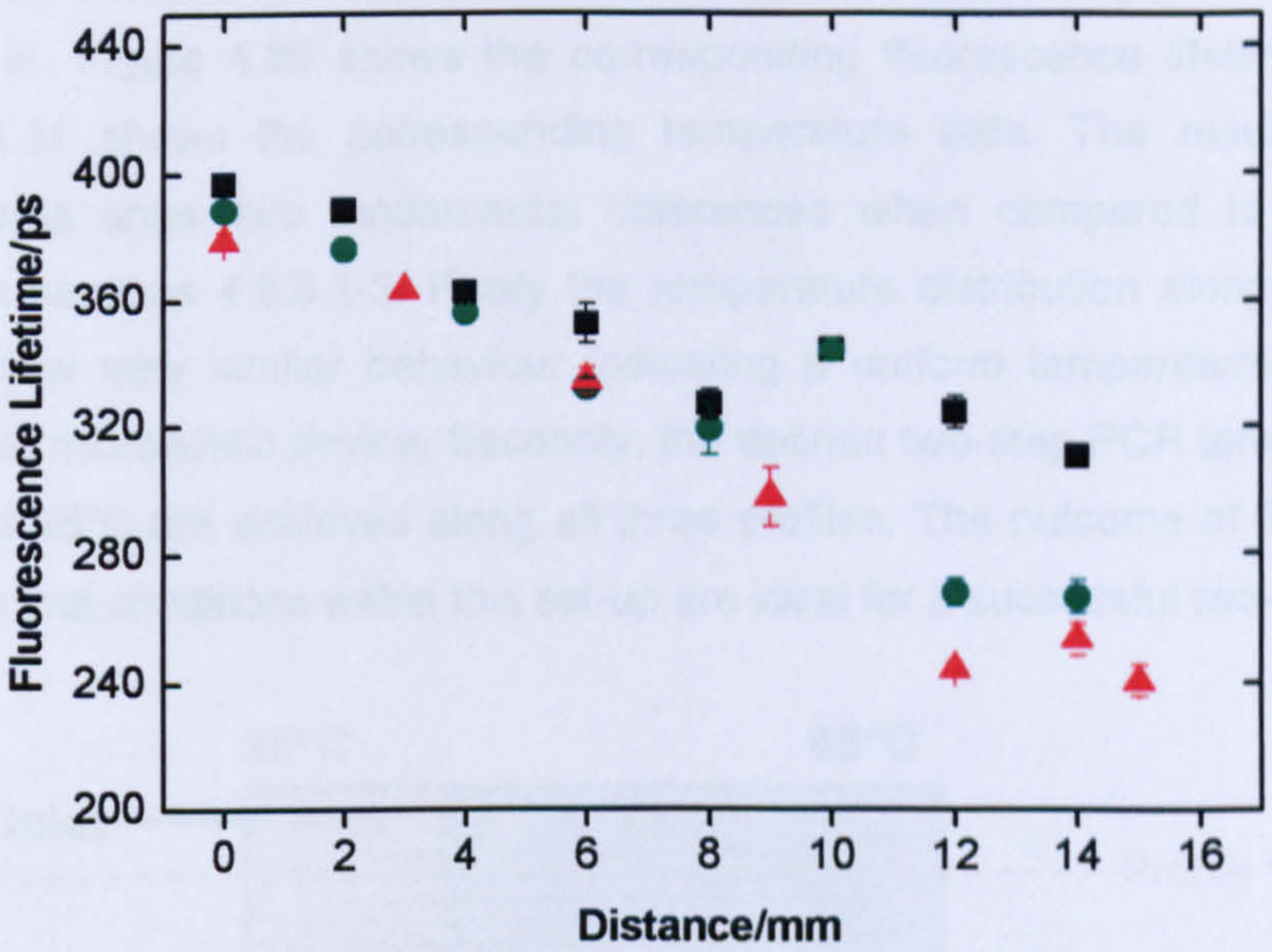


Figure 4.27 **Variation of fluorescence lifetime as a function of distance across the device with volumetric flow rates of 1 µl/min (black), 3 µl/min (green) and 10 µl/min (red).**

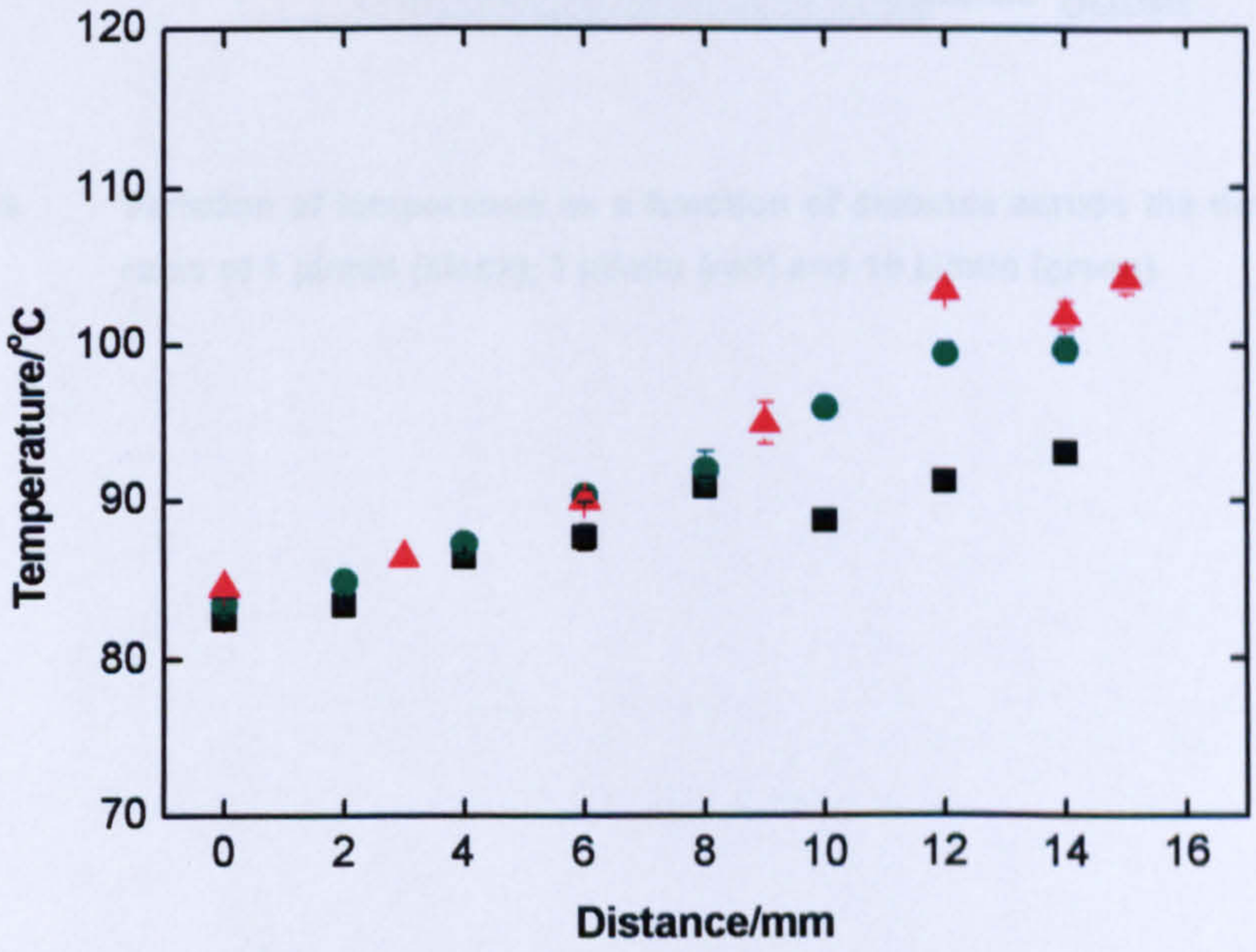


Figure 4.28 **Variation of temperature as a function of distance across the device at flow rates of 1 µl/min (black), 3 µl/min (green) and 10 µl/min (red).**

4.5.3.4 Imaging Microfluidic Temperature Gradients (CHIP III)

Figure 4.29 shows a schematic of the measurement points along profiles 1, 2 and 3 on chip III. Figure 4.30 shows the corresponding fluorescence lifetime data and Figure 4.31 shows the corresponding temperature data. The results of these experiments show two fundamental differences when compared to the results shown in sections 4.5.3.1-3. Firstly the temperature distribution along profile 1, 2 and 3 show very similar behaviour indicating a uniform temperature distribution across the microfluidic device. Secondly, the defined two-step PCR temperatures of 65°C and 95°C are achieved along all three profiles. The outcome of these results suggests that conditions within this set-up are ideal for a successful two-step PCR.

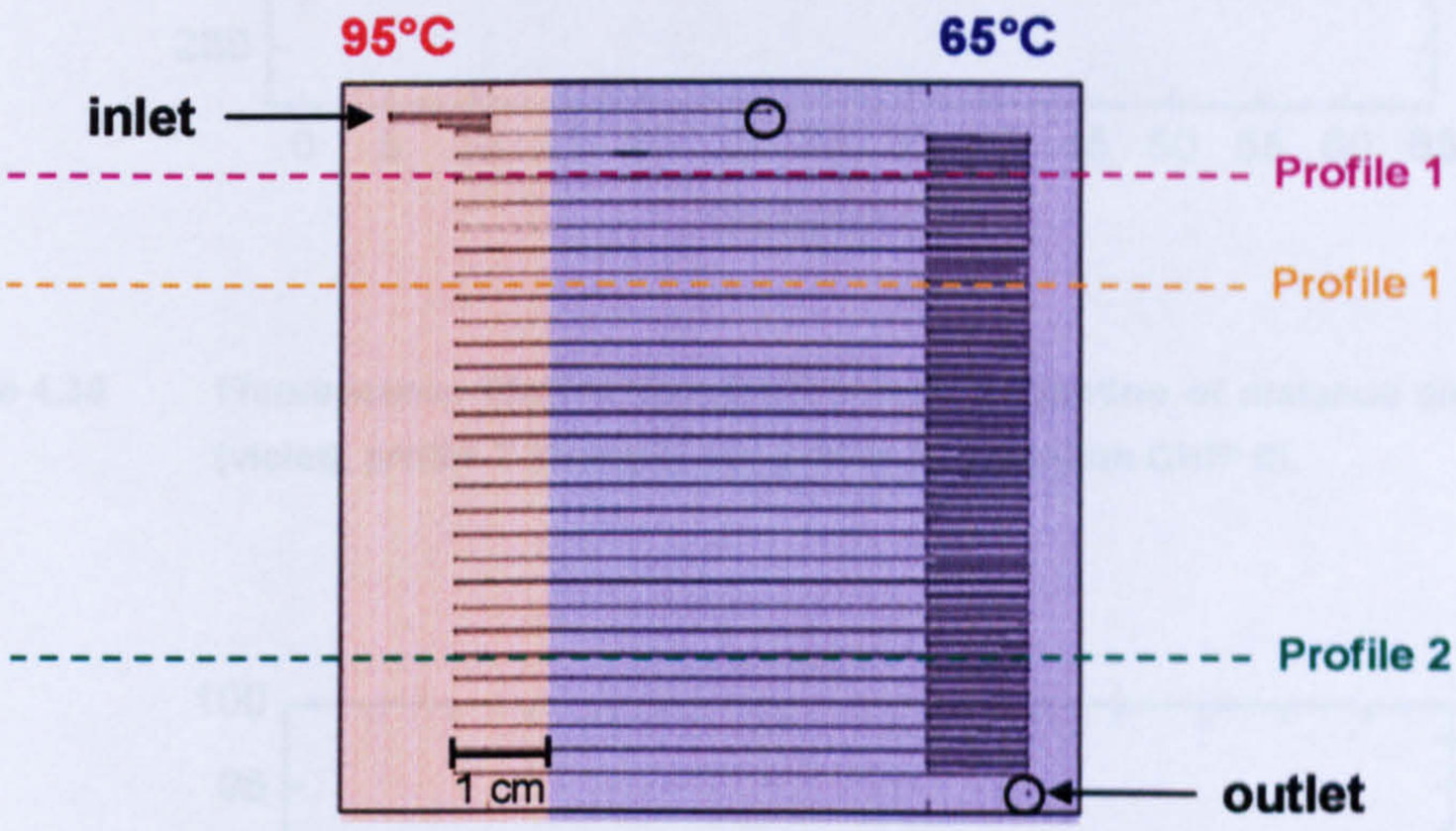


Figure 4.29 **Variation of temperature as a function of distance across the device with flow rates of 1 µl/min (black), 3 µl/min (red) and 10 µl/min (green).**

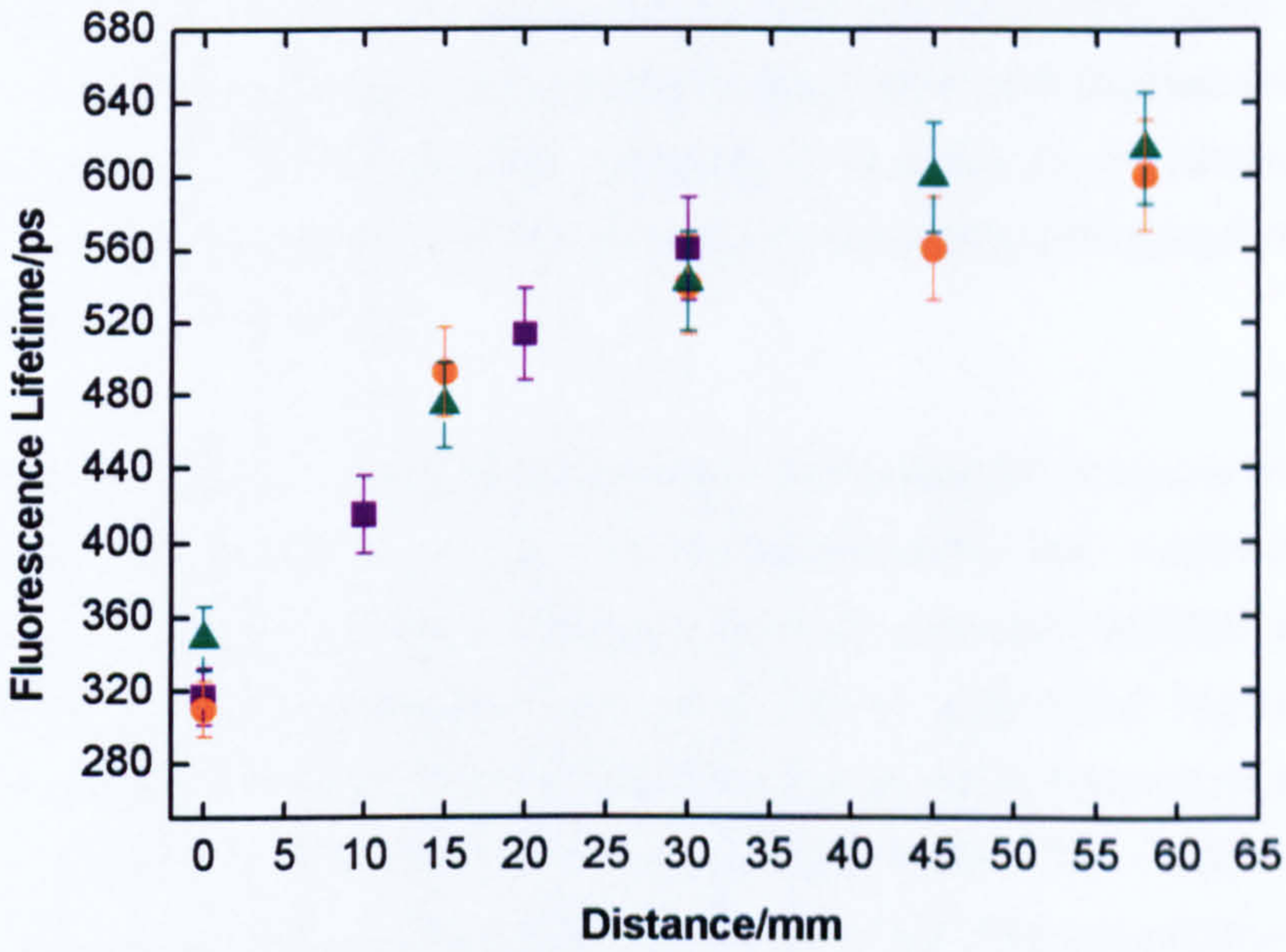


Figure 4.30 **Fluorescence lifetime determination as a function of distance along profile 1 (violet), profile 2 (orange) and profile 3 (green) on CHIP III.**

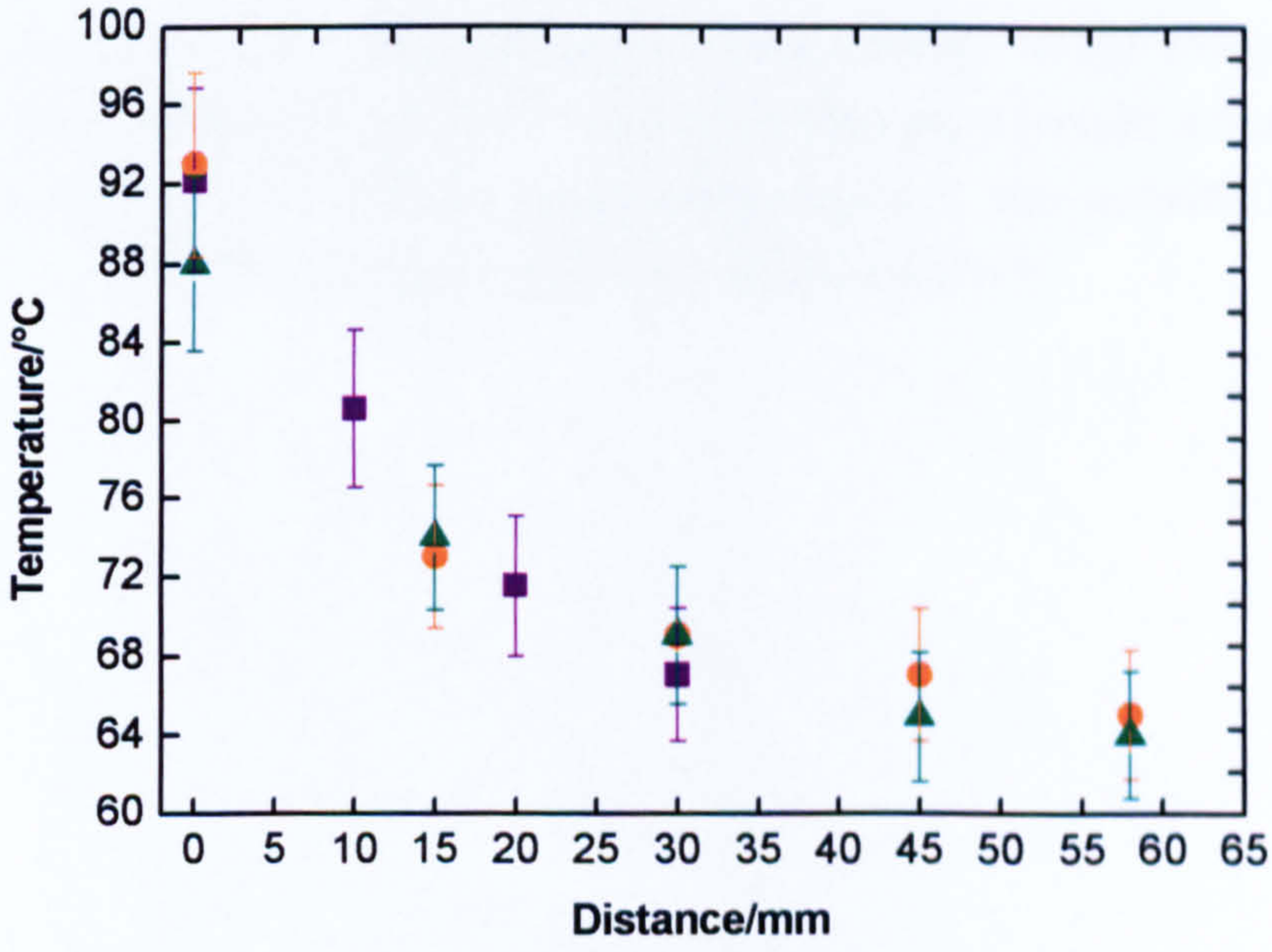


Figure 4.31 **Temperature variation as a function of distance along profile 1 (brown), profile 2 (purple) and profile 3 (green) on CHIP III.**

4.6 Discussion

The imaging of temperature in microfluidic devices has been introduced. It has been shown that FLIM overcomes many problems associated with fluorescence intensity based techniques. 3D temperature mapping is possible to an accuracy of 1°C. Specifically, FLIM has been shown successful in optimising the design of a CF-PCR chip with respect to heating.

Further improvements in the spatial resolution and statistical accuracy of quantifying temperature are possible. In the current experiments, low numerical aperture excitation was required to image through ~ 1mm of substrate material, resulting in a relatively low excitation efficiency. By using thinner substrates, higher numerical aperture excitation could be implemented, allowing a higher fluorescence signal and improved lateral and axial resolution to a sub μm scale. This could also improve acquisition rates to afford video speed FLIM and real-time temperature mapping. However, the handling of such thin devices was difficult due to their fragile nature. It was difficult to connect capillaries to such devices without blocking them. Furthermore mounting those devices onto the set-up turned out to be difficult with chip fracture occurring frequently.

Nevertheless, the direct measurement of microchannel temperatures with this approach has enabled the determination and optimization of fluidic temperatures in microchannels for the first time. Using these results it was possible to perform successful CF PCR. These results are presented in Chapter 5.

1. Newport, D., Garvey, J., Dalton, T., Egan, V., and Whelan, M., *Development of the interferometric temperature measurement procedures for microfluidic flow* Microscale thermophysical engineering, 2004. 8(2): p. 141-154.
2. Burns, M.A., Johnson, B.N., Brahmasandra, S.N., Handique, K., Webster, J.R., Krishnan, M., Sammarco, T.S., Man, P.M., Jones, D., Heldsinger, D., Mastrangelo, C.H., and Burke, D.T., *An integrated nanoliter DNA analysis device*. Science, 1998. 282(5388): p. 484-487.
3. Lagally, E.T., Emrich, C.A., and Mathies, R.A., *Fully integrated PCR-capillary electrophoresis microsystem for DNA analysis*. Lab on a chip, 2001. 1(2): p. 102-107.
4. Chaudhari, A.M., Woudenberg, T.M., Albin, M., and Goodson, K.E., *Transient liquid crystal thermometry of microfabricated PCR vessel arrays*. Journal of Microelectromechanical Systems, 1998. 7(4): p. 345-355.
5. Lacey, M.E., Webb, A.G., and Sweedler, J.V., *Monitoring Temperature Changes in Capillary Electrophoresis with Nanoliter-Volume NMR Thermometry*. Analytical chemistry, 2000. 72(20): p. 4991-4998.
6. Davis, K.L., Liu, K.-L.K., Lanan, M., and M.D., M., *Spatially resolved temperature measurements in electrophoresis capillaries by Raman thermometry*. Analytical Chemistry, 1993. 65(3): p. 293-298.
7. Easley, C.J., Legendre, L.A., Roper, M.G., Wavering, T.A., Ferrance, J., and Landers, J.P., *Extrinsic Fabry-Perot Interferometry for Noncontact Temperature Control of Nanoliter-Volume Enzymatic Reactions in Glass Microchips*. Analytical chemistry, 2005. 77(4): p. 1038-1045.
8. Patil, V.A. and Narayanan, V., *Spatially resolved temperature measurement in microchannels*. Microfluidics and Nanofluidics, 2004. 2(4): p. 291-300.
9. Ross, D., Gaitan, M., and Locascio, L.E., *Temperature Measurement in Microfluidic Systems Using a Temperature-Dependent Fluorescent Dye*. Analytical Chemistry, 2001. 73(17): p. 4117-4123.
10. Lakowicz, J.R., *Principles of Fluorescence Spectroscopy*. third ed. 2006, New York: Springer. 954.
11. Diaspro, A., Bianchini, P., Vicidomini, G., Faretta, M., Ramoino, P., and Usai, C., *Multi-photon excitation microscopy*. BioMedical Engineering OnLine, 2006. 5(1): p. 36.
12. Brakenhoff, G.J., Muller, M., and Ghauharali, R.I., *Analysis of efficiency of two-photon versus single-photon absorption for fluorescence generation in biological objects*. 1996. p. 140-144.
13. Huang, Z.-L. *One versus Two-photon Excitation*. 2007 [cited 2007 October 2007]; Available from: http://belfield.cos.ucf.edu/one%20vs%20two-photon%20excitation.html.

14. Elson, D.S., Siegel, J., Webb, S.E.D., Leveque-Fort, S., Lever, M.J., and French, P.J., *Fluorescence lifetime system for microscopy and multiwell plate imaging with a blue picosecond diode laser.* Optics letters, 2002. 27(16): p. 1409.
15. Benninger, R., Hofmann, O., McGinty, J., Requejo-Isidro, J., Munro, I., Neil, M., deMello, A.J., and French, P., *Time-resolved fluorescence imaging of solvent interactions in microfluidic devices.* Optics Express, 2005. 13(16): p. 6275.
16. Gadella, T.W.J., Jovin, T.M., and Clegg, R.M., *Fluorescence lifetime imaging microscopy (FLIM): Spatial resolution of microstructures on the nanosecond time scale.* Biophysical Chemistry, 1993. 48(2): p. 221-239.
17. Wang, X.F., Uchida, T., Coleman, D.M., and Minami, S., *A two-dimensional fluorescence lifetime imaging system using a gated image intensifier.* Applied Spectroscopy, 1991. 45(3): p. 360.
18. Suhling, K.K., French, P., and Phillips, D., *Time-resolved fluorescence microscopy.* Photochemical & Photobiological Sciences, 2005. 4(1): p. 13-22.
19. McGinty, J., *Development of wide-field fluorescence lifetime imaging for biomedical applications* in *Physics* 2006, Imperial College London. p. 277.
20. O'Connor, D.V. and Phillips, D., *Time-correlated single photon counting.* Applied Optics, 1986. 25(4): p. 460.
21. Becker, W., *Advanced Time-Correlated Single Photon Counting Techniques.* Vol. 81. 2005: Springer. 401.
22. Becker, W., Bergmann, A., Hink, M.A., König, K., and Benndorf, C.B., *Fluorescence lifetime imaging by time-correlated single-photon counting.* 2004. p. 58-66.
23. Lampert, R.A., Chewter, L.A., and Phillips, D., *Standards for nanosecond fluorescence decay time measurements.* Analytical Chemistry, 1983. 55(1): p. 68-73.
24. Lopez Arbeloa, F., Lopez Arbeloa, T., Hernandez Bartolome, P., Estevez, T., and Lopez Arbeloa, I., *TICT AND ULM Models for the radiationless deactivation of Rhodamines.* Proceedings of the Indian Academy of Sciences. Chemical sciences, 1992. 104(2): p. 165-171.
25. Lopez Arbeloa, F., Lopez Arbeloa, T., Tapia Estevez, M.J., and Lopez Arbeloa, I., *Photophysics of Rhodamines: molecular structure and solvent effects.* The Journal of physical chemistry, 1991. 95(6): p. 2203.
26. Lopez Arbeloa, T., Lopez Arbeloa, F., Bartolome, P.H., and Lopez Arbeloa, I., *On the mechanism of radiationless deactivation of Rhodamines.* Chemical Physics, 1992. 160(1): p. 123.
27. Moog, R.S., Ediger, M.D., Boxer, S.G., and Fayer, M.D., *Viscosity dependence of the rotational reorientation of rhodamine B in mono-and polyalcohols. Picosecond transient grating experiments.* The Journal of Physical Chemistry, 1982. 86(24): p. 4694.

28. Dunsby, C., Lanigan, P., McGinty, J., and Elson, D.S., *An electronically tunable ultrafast laser source applied to fluorescence imaging and fluorescence lifetime imaging microscopy.* Journal of Physics. F, Metal Physics, 2004. 37(23): p. 3296.
29. Kitamura, N., Hosoda, Y., Ueno, H., and Iwata, S., *An Application of Plastic Microchannel-Microheater Chips to a Thermal Synthetic Reaction.* Analytical Sciences, 2004. 20(5): p. 783-786.
30. Kitamura, N., Hosoda, Y., Iwasaki, C., Ueno, K., and Kim, H.-B., *Thermal phase transition of an aqueous poly(N-isopropylacrylamide) solution in a polymer microchannel-microheater chip.* Langmuir, 2003. 19: p. 8484-8489.

5

PCR on the Microscale

The studies described in Chapter 4 demonstrated that fluorescence lifetime imaging could be successfully used to monitor fluidic temperatures within microchannels to high precision. Moreover these studies allowed the modification of both the microchannel network topology and heating configuration to provide an optimal environment for thermal cycling. This chapter describes and assesses the influence of surface – molecule interactions on the PCR efficiency within microfluidic channels. Specifically, continuous flow PCR within both untreated and modified microchannels is studied and results of these studies are used to develop a standardized protocol for performing successful PCR.

5.1 Surfaces on the Microscale

Surfaces become dominating features when reactions are performed within microfluidic systems. Therefore an understanding of molecule-surface interactions is essential before transferal of PCR to the microscale. Molecules can be repelled from a surface; desorption, or attracted to a surface; adsorption. These phenomena can be explained in different ways. Electrostatic interactions dominate on the molecular scale and occur when an electric force acts on a charge q_i as a result of the presence of a second charge q_j. This can be described by Coulomb's law (equation 5.1). Here, two cases can occur. First when charges of two species are of the same polarity, repulsion is the result and second when charges of two species are opposite to each other, attraction is the result (Figure 5.1).

$$F = \frac{q_i q_j}{4\pi\varepsilon_0\varepsilon_r r_{ij}} \tag{5.1}$$

Here q_i and q_j are the magnitude of the charges, r_{ij} is their separation, ε_0 the permittivity of free space and ε_r the relative dielectric constant of the medium in which the charges are placed. This interaction between charged objects is a non-contact force which acts over some distance of separation.

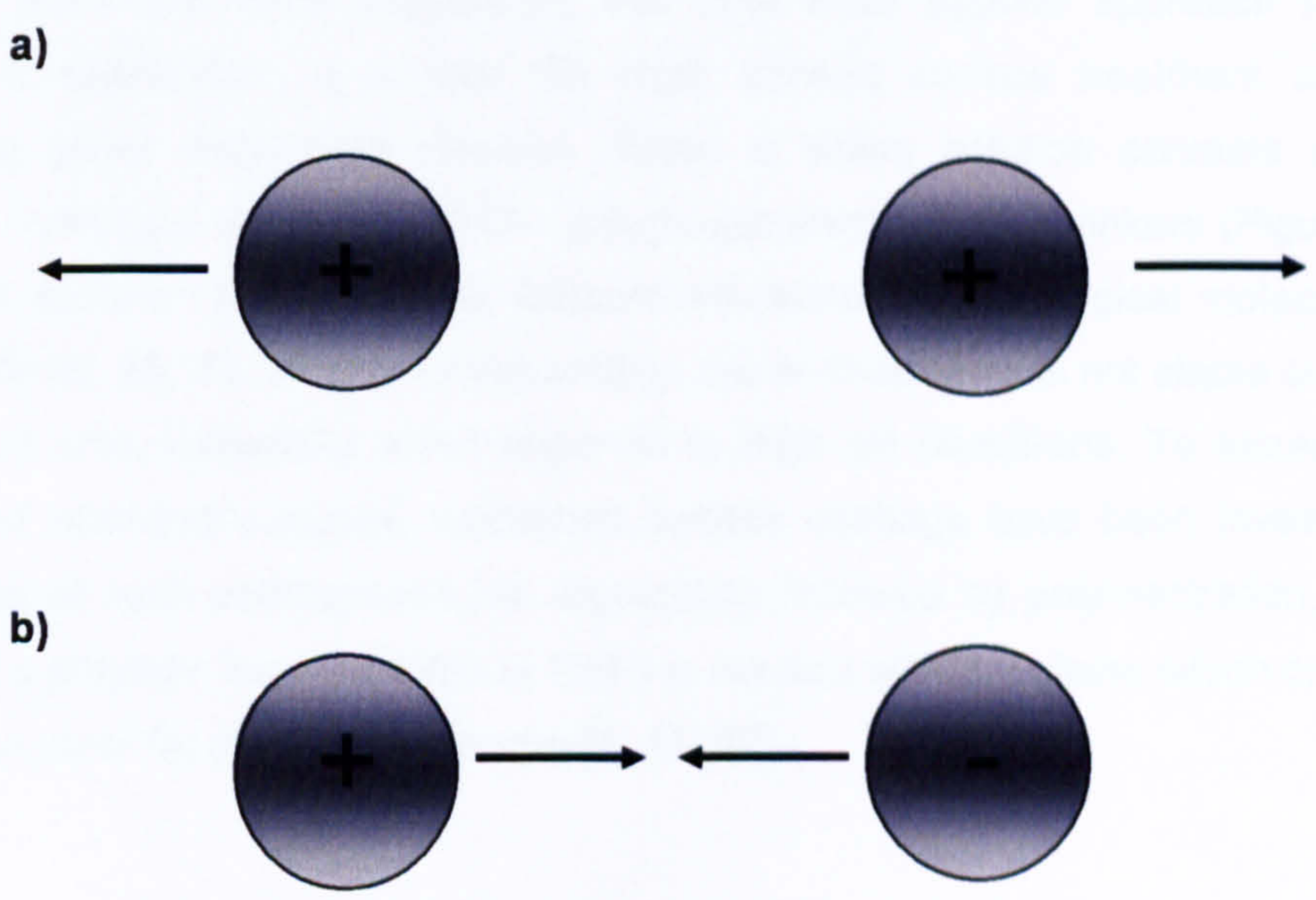


Figure 5.1 **(a) In this case charges are the same which results in repulsion. (b) In this case charges are opposite which results in attraction.**

The Van der Waals equation expresses the influence of attraction and repulsion in more detail but will not be discussed here any further [1]. However, another intermolecular influence which needs to be considered is the hydrophobic effect. The hydrophobic effect [2, 3] describes an observation that an apolar molecule tends to aggregate in the presence of water. While the majority of hydrophobic effect studies focus on protein-protein interfaces [4-7], this effect also plays a role in the application of PCR on the microscale. The nature of the interactions between PCR components and microchannels walls is still not fully understood, however, various approaches have been presented to decrease interactions between the reaction components and the channel walls by creating passive surfaces. These passive surfaces exhibit characteristics of hydrophobicity and minimal charge. Examples of these surfaces are presented here. Numerous PCR chips made out of glass, silicon-glass, borosilicate, potassium-silicate, polyimide, PDMS, PMMA and other polymeric microchips have revealed the problems of adverse surface interactions, and led to the development of passivation procedures to render the internal surfaces of microchips 'PCR friendly' [8]. Passivation procedures can be classified into two different types: static passivation where the surface is treated before performing PCR [8-16] and dynamic passivation [11-13, 17-19] where the passivating agents are introduced into the reaction mixture. Most dynamic coatings involve bovine serum albumin (BSA) [12, 13, 16, 19-26]. However polymers such as polyethylene glycol (PEG) [11, 26-31] and polyvinylpyrrolidone (PVP) [8, 11, 31-36] become more and more popular as well. The most popular approach to static coating is silanization. It is also the most generic surface treatment used for modifying glass microfluidic devices. When a silane solution contacts a glass surface, hydrolysis of surface Si-OH groups generates Si-O-Si linkers (Figure 5.2). Silanized surfaces typically show reduced interaction with biological molecules [8, 11, 13, 20-22, 28, 33, 37-39]. Unfortunately, the Si-O-Si bond is not stable over long periods of time, especially when exposed to high pH conditions. To increase the lifetime of silanized surfaces, combined surface coatings have been investigated. Examples of such coatings involve silanization followed by polymerization. In this situation a polymer (such as PEG or PVP) is reacted with the silane which creates a protection layer for the Si-O-Si groups [8, 11, 22].

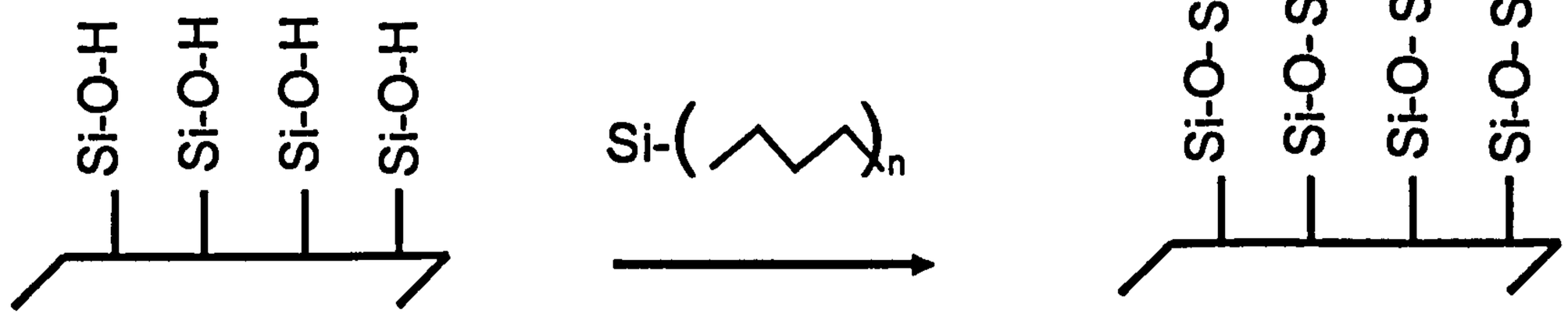


Figure 5.2 **Hydrolysis of SI-OH groups with Silane in order to create SI-O-SI groups which reduce the adsorption of components on the surface.**

An alternative method to silanization has been reported by Krishnan *et al.* [32]. In this approach a Teflon coating is applied to glass or silicon to prevent surface adsorption of PCR components. Teflon coatings of this type show high levels of biocompatibility and are commonly used for microfluidic connector parts (such as tubing) and reaction tubes (such as Eppendorf tubes) [40]. Surface coatings involving Teflon can be constructed, by merely flushing microfluidic channels with a suitable Teflon dispersion [32].

This Chapter section presents experiments which show the influence of six different surface coatings on PCR within glass microchannels. The coatings studied are silane I (dichlorodimethlysilane), combinations of silane I + PEG, BSA or PVP, Teflon and silane II (perfluorooctyltrichlorosilane).

5.1.1 Experimental Methods

5.1.1.1 Continuous-Flow PCR within Untreated Glass Microchannels

A 350µl PCR mix was prepared according to the recipe described in Table 2.2. After the mix was prepared, it was split into two parts; the reference and the sample. While the reference was kept outside the PCR chip, in a closed Eppendorf tube, the sample was pumped through the microfluidic device at room temperature and at a flow rate of 3 µl/min. After 65 minutes the sample was collected in an Eppendorf tube and both reference and sample were amplified on the Smart Cycler, according to the protocol defined in Table 2.3, and analyzed on the BioAnalyzer. Data resulting from amplification of the reference (black curve) and sample (red curve)

are presented in Figure 5.3. Whilst the expected amplification curve is observed for the reference, no amplification is observed for the sample. Figure 5.4 presents electrophoretic size analysis of both the reference and the sample product. Product formation is not observed for the sample, whilst two product peaks are observed for the reference. These results indicate that interaction between the channel walls and the PCR mix either causes a loss of a key component from the bulk PCR mix or an inhibition in the activity of the polymerase enzyme. Consequently, a series of new experiments was performed to assess the interaction between the PCR components and the channel walls in more detail.

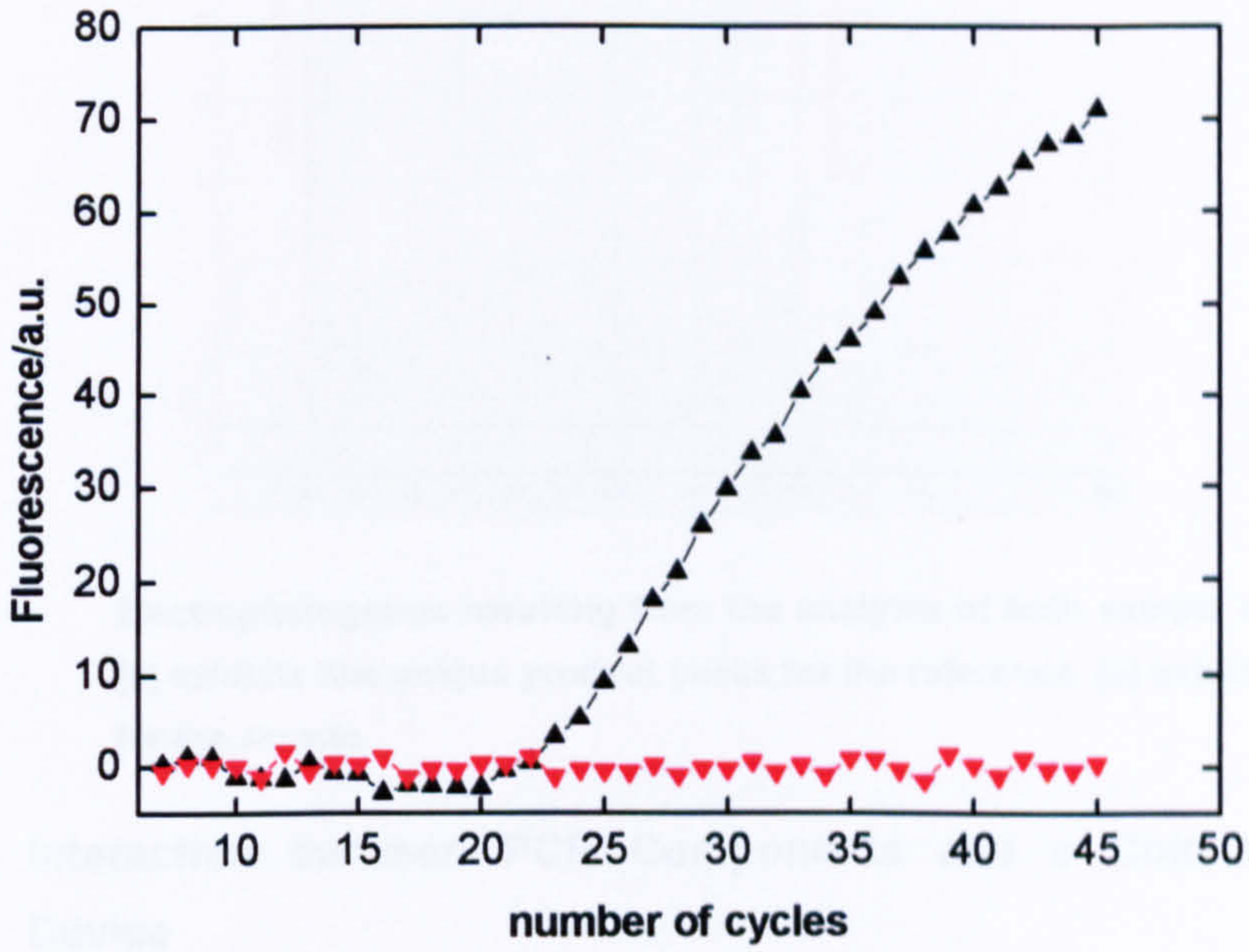


Figure 5.3 **Variation of fluorescence intensity as a function of number of cycles. Black data points represent the reference and grey data points represent the sample.**

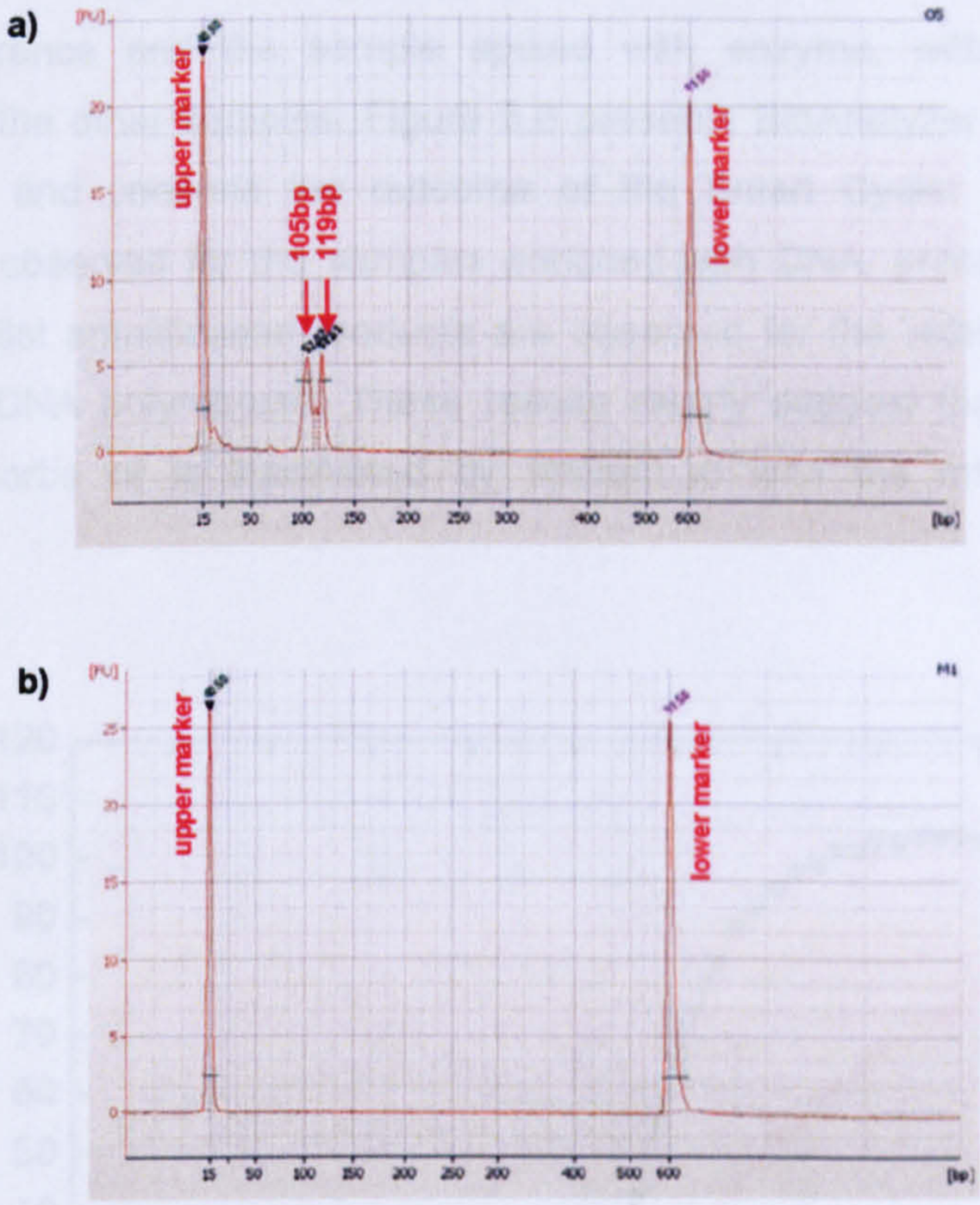


Figure 5.4 **Electropherograms resulting from the analysis of both sample and reference. (a) exhibits two unique product peaks for the reference. (b) exhibits no product for the sample.**

5.1.1.1.1 Interaction between PCR Components and a Cold Microfluidic Device

In this set of experiments a 750µl PCR mix was prepared according to the recipe described in Table 2.2. After the mix was prepared, it was split into two parts; the reference and the sample. While the reference was kept outside the PCR chip, in a closed Eppendorf tube, the sample was pumped through the microfluidic device as described previously. The collected sample was then split into four equal parts, and to each part one essential PCR component (i.e. DNA, primers, magnesium chloride or enzyme) was added in excess. All samples were then amplified using the conventional thermal cycler and products were analysed on the BioAnalyzer.

Figure 5.5 illustrates the results of this analysis. Black data points correspond to the reference, red data points correspond to sample spiked with enzyme, yellow data points correspond to the sample spiked with DNA, green data points correspond to the sample spiked with magnesium chloride and blue data points correspond to the

sample spiked with primers. Significantly, successful amplification is only observed for the reference and the sample spiked with enzyme, with no amplification observed in the other samples. Figure 5.6 presents BioAnalyzer sizing data for all experiments and confirms the outcome of the Smart Cycler data. No product formation is observed for the samples enriched with DNA, primers or magnesium chloride. Whilst amplification products are observed for the reference and sample spiked with DNA polymerase. These results clearly suggest that the polymerase enzyme adsorbs or is inactivated by interaction with the microfluidic channel surface.

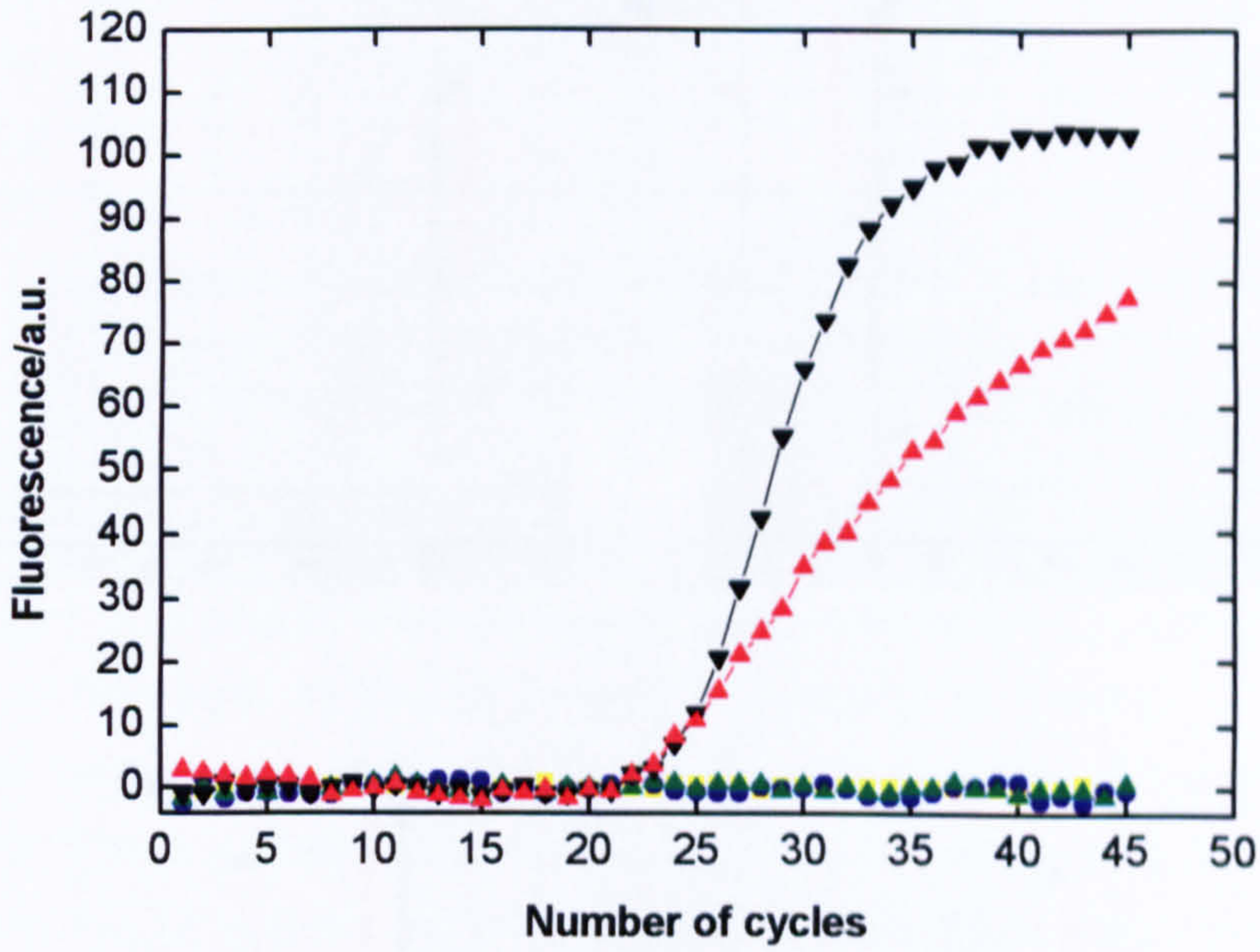


Figure 5.5 **Variation of fluorescence intensity as a function of the number of thermal cycles. Five replicates were performed to generate each curve. The black curve represents the reference, the red curve represents the sample with excess of enzyme, the yellow curve represents the sample with excess of DNA, the green curve represents the sample with excess of magnesium chloride and the blue curve represents the sample with excess of primers.**

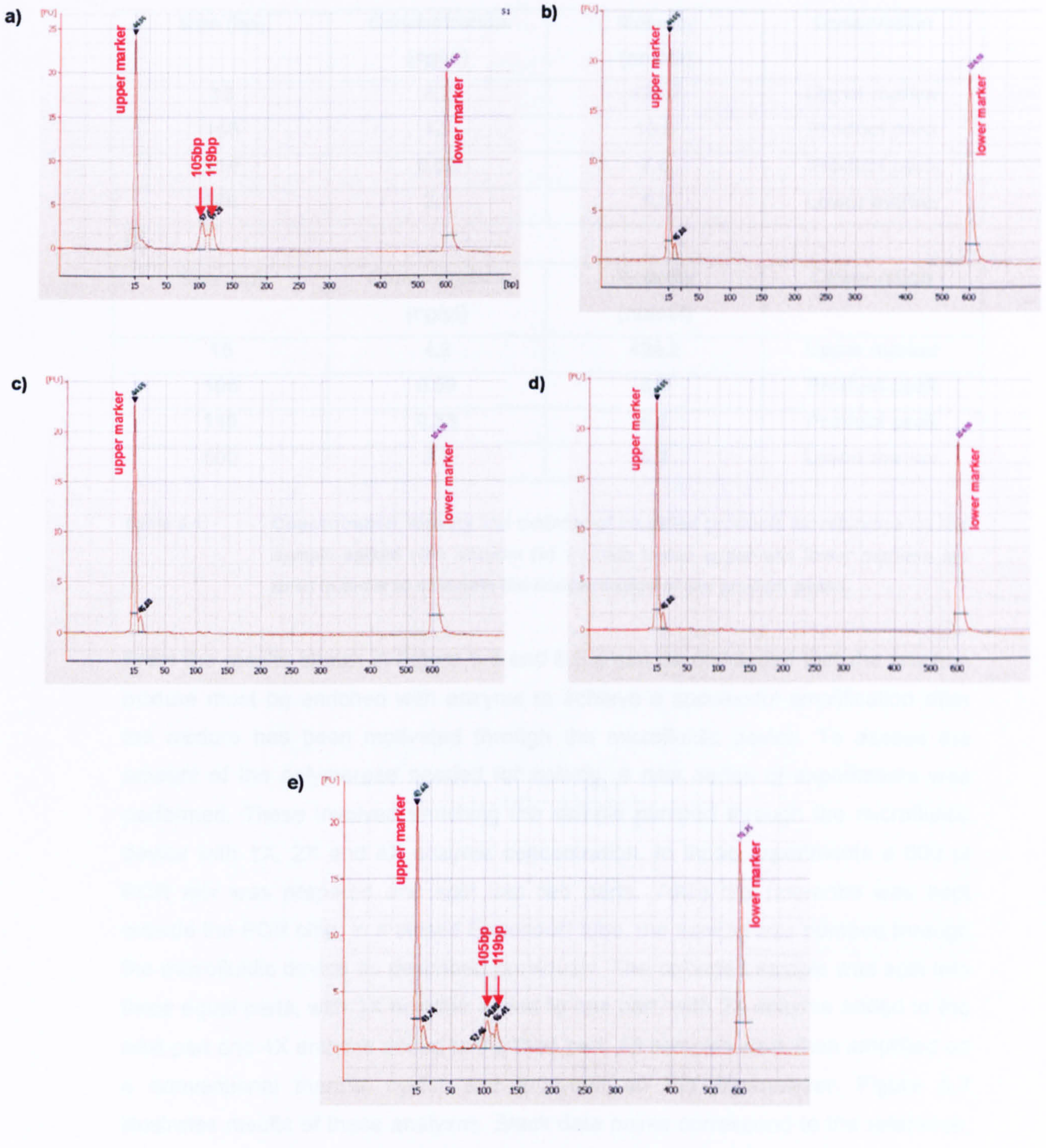


Figure 5.6 **Electropherograms resulting from the analysis of reference and samples with an excess of DNA, magnesium chloride, primers and enzyme. (a) exhibits two unique peaks for the reference sample. (b) exhibits no peaks for the sample with excess of DNA. (c) exhibits no peaks for the sample with excess of magnesium chloride. (d) exhibits no peaks for sample with excess of primers. (e) exhibits two unique peaks for the sample with excess of enzyme.**

a)

Size (bp)	Concentration (ng/µl)	Molarity (nmol/l)	Observation
15	4.2	424.2	Upper marker
105	1.3	18.9	Product peak
119	0.59	7.6	Product peak
600	2.1	5.3	Lower marker

b)

Size (bp)	Concentration (ng/µl)	Molarity (nmol/l)	Observation
15	4.2	424.2	Upper marker
105	0.59	8.6	Product peak
119	0.33	4.2	Product peak
600	2.1	5.3	Lower marker

Table 5.1 **Concentration, identity and molarity of amplified products for reference (a) and sample spiked with enzyme (b). In both tables upper and lower markers are used in order to calculate the concentration of the product peaks.**

From the results shown in Figure 5.5 and 5.6 it can be concluded that the reaction mixture must be enriched with enzyme to achieve a successful amplification after the mixture has been motivated through the microfluidic device. To assess the amount of the polymerase needed for spiking, a new series of experiments was performed. These involved enriching the sample pumped through the microfluidic device with 1X, 2X and 4X enzyme concentration. In these experiments a 600 µl PCR mix was prepared and split into two parts. While the reference was kept outside the PCR chip, in a closed Eppendorf tube, the sample was pumped through the microfluidic device as described previously. The collected sample was split into three equal parts, with 1X enzyme added to one part, with 2X enzyme added to the next part and 4X enzyme added to the third part. All samples were then amplified on a conventional thermal cycler and analysed on the BioAnalyzer. Figure 5.7 illustrates results of these analyses. Black data points correspond to the reference, yellow data points correspond to the sample with 1X enzyme, blue data points correspond to the sample with 2X enzyme and red data points correspond to the sample with 4X enzyme. Although all samples show amplification, the sample with 1X enzyme shows inconsistent behaviour with significant fluctuations in C_t. The sample containing 2X enzyme shows more consistency, however the sample containing 4X enzyme shows a close correspondence with the reference sample.

Figure 5.8 presents corresponding BioAnalyzer data for all samples. The desired products (105bp and 119bp) are observed for all samples, with highest product formation for the sample with 4X enzyme and the reference. Initial experiments described in Section 5.1.1 were performed at room temperature. However, a more realistic scenario involves reagent addition to the microfluidic device at temperatures used in a normal PCR. Accordingly, these experiments were repeated in a PCR chip containing fixed temperature zones of 95°C and 65°C.

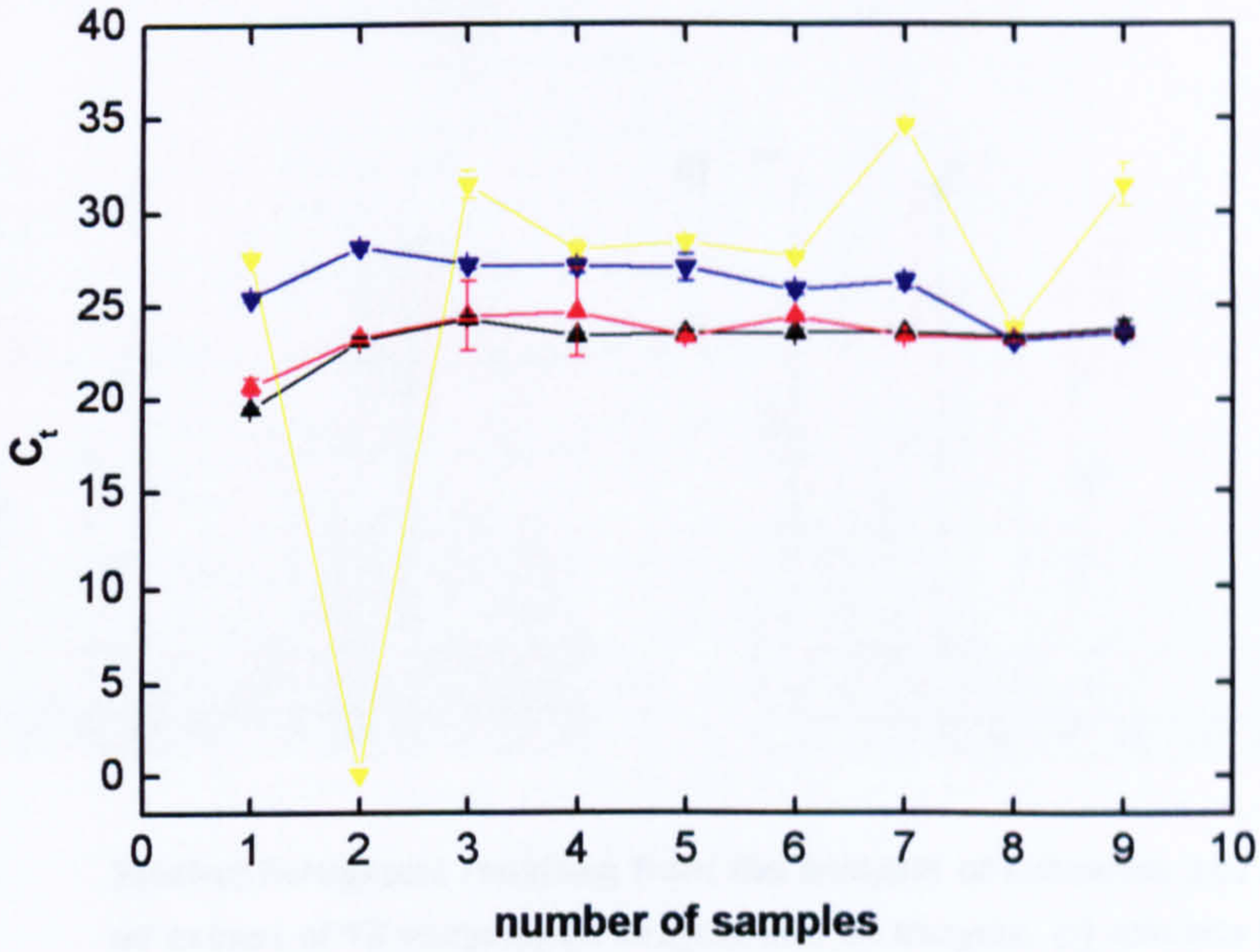


Figure 5.7 **Variation of Ct as a function of number of samples. The black curve represents the reference, the yellow curve represents sample with 1X enzyme, the blue curve represents sample with 2X enzyme and the red curve represents sample with 4X enzyme.**

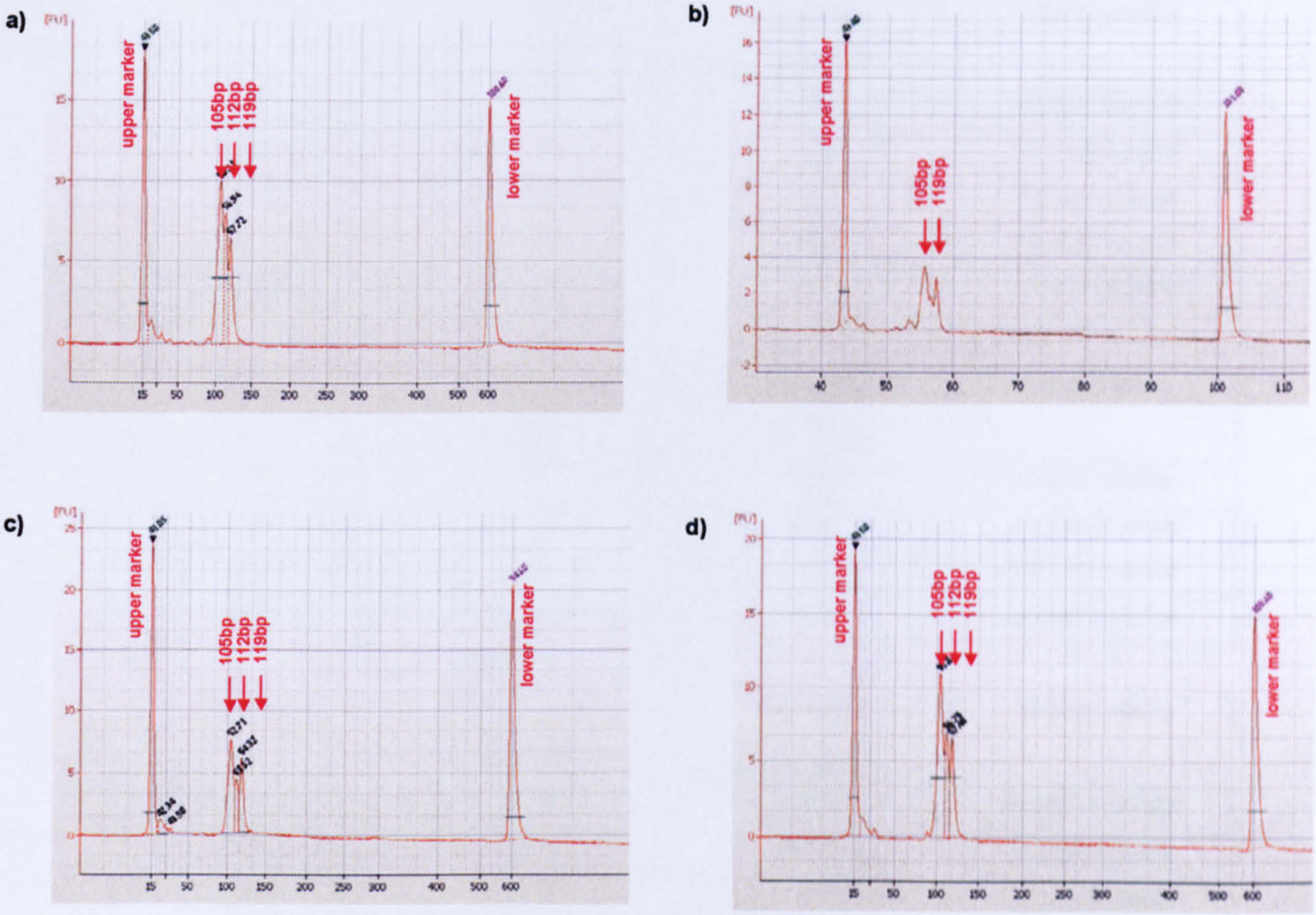


Figure 5.8 **Electropherograms resulting from the analysis of reference and samples with an excess of 1X enzyme, 2X enzyme and 3X enzyme. (a) exhibits three product peaks for the reference sample. (b) exhibits two product peaks for the sample with 1X excess of enzyme. (c) exhibits three product peaks for the sample with 2X excess of enzyme. (d) exhibits three product peaks for sample with 4X excess of enzyme.**

a)

Size (bp)	Concentration (ng/µl)	Molarity (nmol/l)	Observation
15	4.2	424.2	Upper marker
105	2.69	38.6	Product peak
113	1.27	17	Product peak
119	1.17	14.9	Product peak
600	2.1	5.3	Lower marker

b)

Size (bp)	Concentration (ng/µl)	Molarity (nmol/l)	Observation
15	4.2	424.2	Upper marker
105	1.4	20.2	Product peak
119	0.5	6.4	Product peak
600	2.1	5.3	Lower marker

c)

Size (bp)	Concentration (ng/µl)	Molarity (nmol/l)	Observation
15	4.2	424.2	Upper marker
105	1.64	23.8	Product peak
112	0.57	7.6	Product peak
119	0.85	10.9	Product peak
600	2.1	5.3	Lower marker

d)

Size (bp)	Concentration (ng/µl)	Molarity (nmol/l)	Observation
15	4.2	424.2	Upper marker
105	2.77	39.8	Product peak
113	1.22	16.4	Product peak
119	1.17	14.8	Product peak
600	2.1	5.3	Lower marker

Table 5.2 **Concentration, identity and molarity for reference and samples with 1X, 2X and 4X excess of enzyme. (a) concentration and molarity of the reference sample. (b) concentration and molarity of sample with 1X enzyme in excess. (c) concentration and molarity of sample with 2X enzyme in excess. (d) concentration and molarity of sample with 4X enzyme in excess.**

5.1.1.1.2 Assessment of Enzyme Adsorption in Hot Microfluidic Devices

In this series of experiments the same procedure as described in Section 5.1.1.1.1 was used. However the device was also heated and 4X enzyme added to the PCR mix. Figure 5.9 illustrates the results of this analysis. Black data points correspond to the reference and red data points correspond to the sample. Efficient amplification is observed for the reference, but no amplification is observed for the sample. Figure 5.10 presents BioAnalyzer data for both systems. These data suggest that the combination of a sample containing 4X enzyme and applied heat does not lead to a successful amplification. Due to the excessive cost of the polymerase enzyme, it was decided not to increase the enzyme concentration any further but rather investigate surface passivation methods. This approach was deemed experimentally superior, since passivation methods facilitating efficient microfluidic PCR would also be suitable for application in other biological systems.

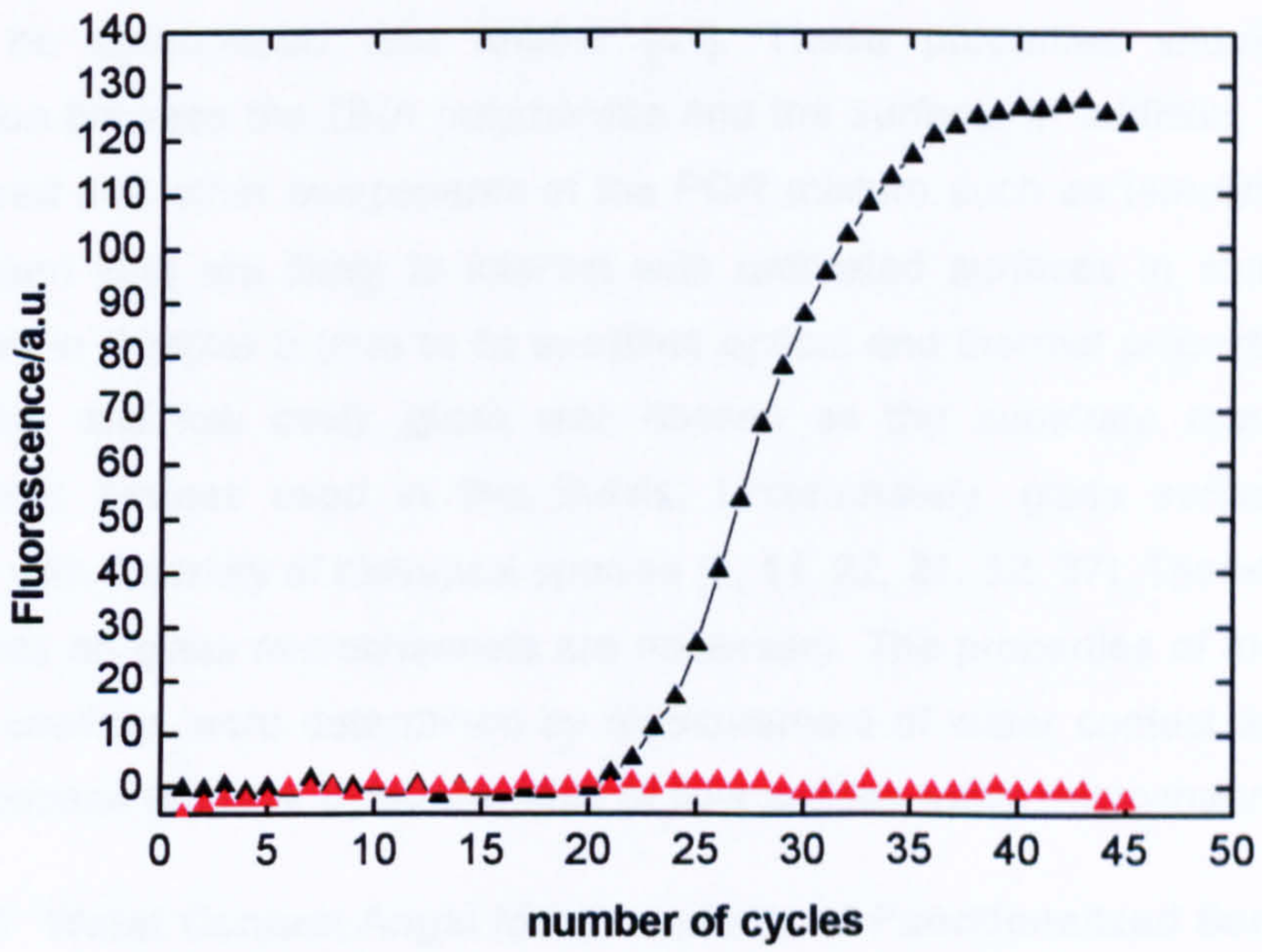


Figure 5.9 **Variation of fluorescence intensity as a function of the number of cycles. The black curve represents the reference and the red curve represents the sample.**

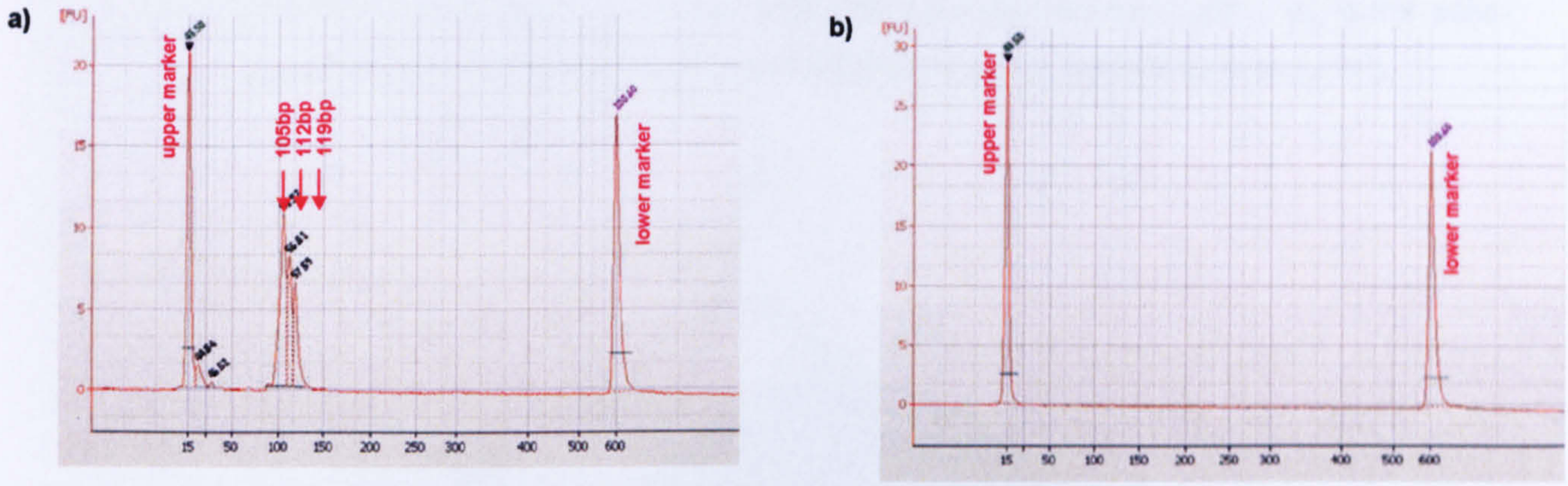


Figure 5.10 **Electropherograms resulting from the analysis of reference and the sample. (a) exhibits three unique peaks for the reference, (b) exhibits no product peaks for the sample.**

5.1.1.2 Functionalization of Microfluidic Channel Surfaces

In broad terms it was estimated that an ideal surface within a microfluidic system should be hydrophobic and neutral [41]. These properties should minimize interaction between the DNA polymerase and the surface. In addition, it had to be considered that other components of the PCR mixture such as template DNA and magnesium ions are likely to interact with untreated surfaces in some way. As described in Chapter 3 (due to its excellent optical and thermal properties, ease of structuring and low cost), glass was chosen as the substrate material for all microfluidic devices used in this thesis. Unfortunately, glass surfaces interact strongly with a variety of biological species [8, 11, 22, 31, 32, 37]. Therefore surface treatments on glass microchannels are necessary. The properties of the fabricated surface coatings were determined by measurement of water contact angles either on microscope slides or by observation of flow profiles within microchannels.

5.1.1.2.1 Water Contact Angle Measurements of Functionalized Surfaces

Contact angles of liquids on solid surfaces are widely used to assess wetting and adhesion properties. Wetting describes how a liquid deposits on a solid substrate. For example, Figure 5.11 shows a schematic of a liquid droplet at rest on a flat, solid surface. The contact angle is defined as the angle between the liquid-vapor and solid-liquid interface of a solid-liquid-vapor system [42] and is measured according to the Young equation,

$$\cos\theta = \frac{(\gamma_{SV} - \gamma_{SL})}{\gamma_{LV}} \qquad (5.2)$$

θ is the contact angle, γ_{SV} is the solid-vapor surface tension (J/m^2), γ_{SL} is the solid-liquid surface tension (J/m^2) and γ_{LV} is the liquid-vapor surface tension (J/m^2).

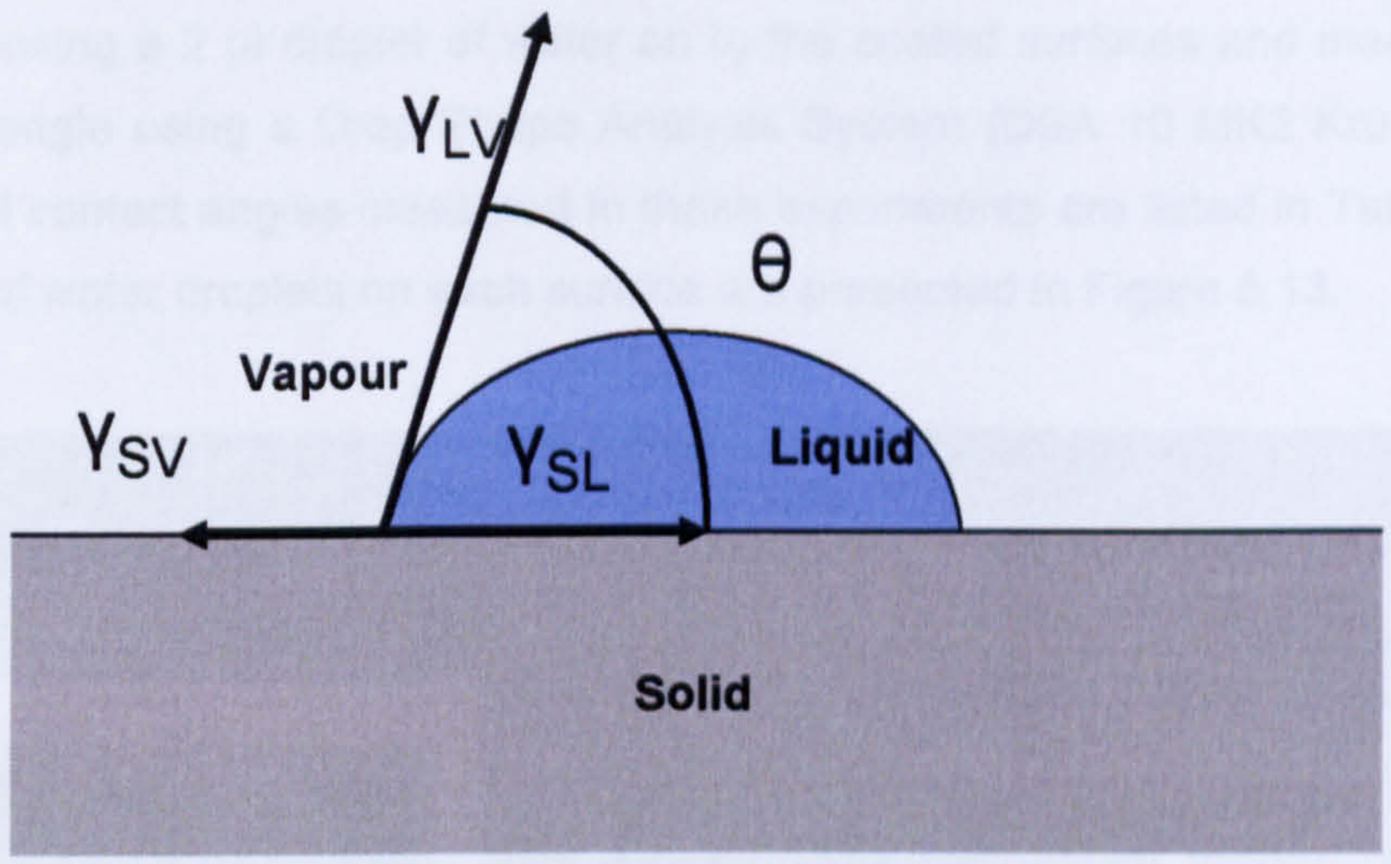


Figure 5.11 **A liquid droplet resting on a solid surface. The contact angle θ is defined as the angle between the liquid-vapor and solid-liquid interface of a solid-liquid-vapor system. γ_{SV} is the solid-vapor surface tension, γ_{SL} is the solid-liquid surface tension and γ_{LV} is liquid-vapor surface tension.**

As noted, contact angles were used to assess wetting and adhesion properties. When the contact angle of a liquid on a solid surface is smaller than 90°, the liquid can be considered to be essentially wetting. Conversely, if the contact angle is higher than 90° the liquid is considered to be non-wetting [41],[43]. Initial contact angle measurements were performed on microscope slides (BDH Ltd. Cat No. 406/0180/04) treated with six different coatings; (1) silane I (dichlorodimethylsilane), (2) silane I + PEG (600, Lancaster, Cat No 13844), (3) silane I + BSA (0.29g/l), (4) silane I + PVP (1.4 μM), (5) Teflon (0.6%) and (6) silane II (perfluoro-octyltrichlorosilane).

The coating process was generally simple to implement since it only consisted of immersing the microscope slides for 24 hours in the appropriate coating solution, followed by drying. Coating (1) was performed according to this procedure. In order to generate coatings (2), (3) and (4) glass slides were initially coated with silane and then coated with PEG (2), BSA (3) or PVP (4). Coating (5) was created by first immersing the microscope slides in a Teflon dispersion, and then baking the slides on a hot-plate at 100°C for 2 hours. Coating (6) was more difficult to generate due to the sensitivity and reactivity of the coating solution. Accordingly all steps were

performed in an inert atmosphere (glove box under an Argon atmosphere). While silane I was chosen due to its easy handling, silane II was chosen due to its high water repellent character [44]. Water contact angle measurements were performed by dispensing a 2 µl droplet of water on to the coated surfaces and measuring the contact angle using a Drop Shape Analysis System (DSA 10 MK2 Krüss) (Figure 5.12). All contact angles measured in these experiments are listed in Table 5.4 and images of water droplets on each surface are presented in Figure 5.13.

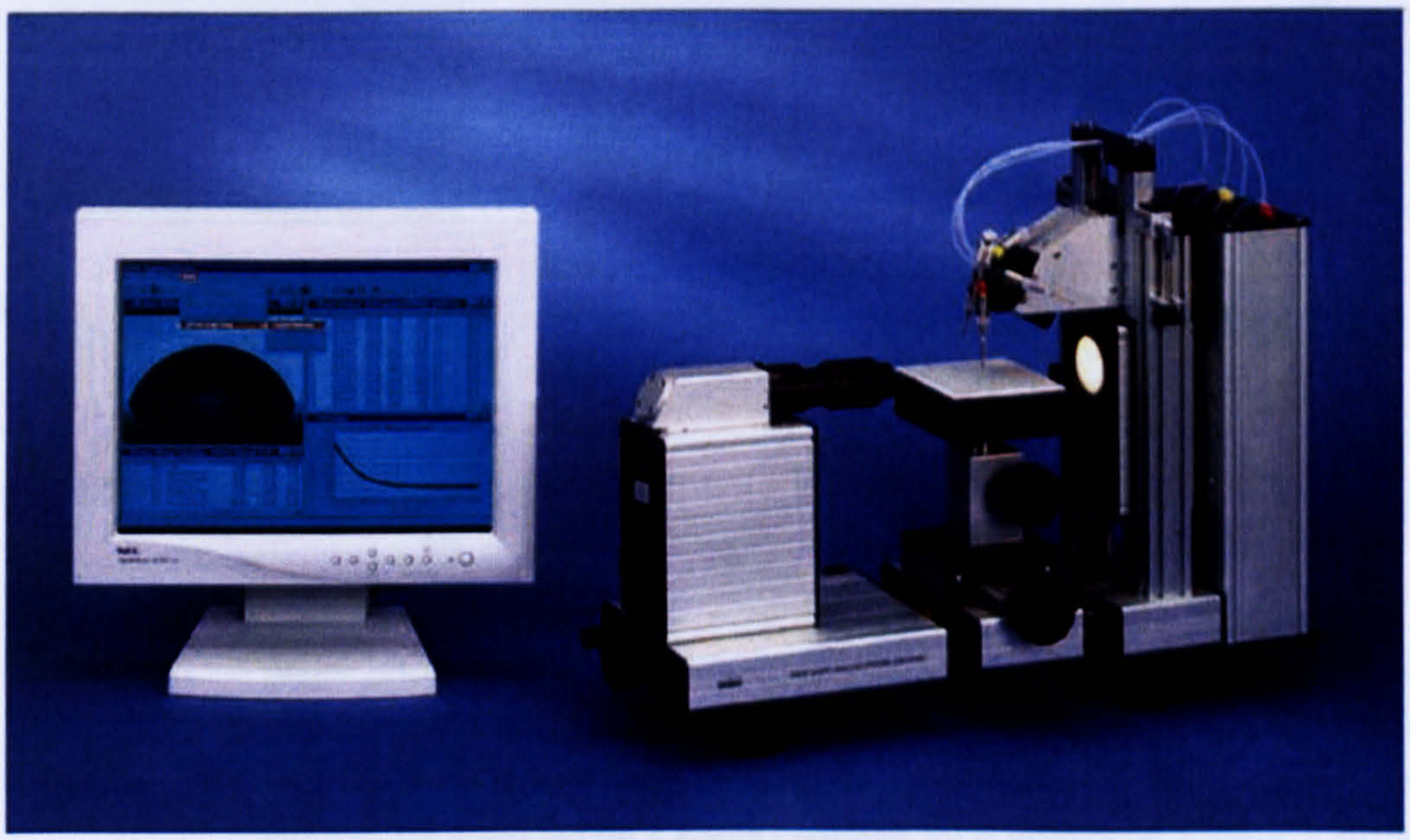


Figure 5.12 **Drop Shape Analysis (DSA 10 MK2 Krüss) for contact angle measurements. A syringe dispenses a 2µl droplet of water on a sample surface and the contact angle is measured.**

Surface coating	Contact angle
untreated glass	30.7°±1.6
silane I	100.5 °±1.2
silane II	121.3°±1.2
silane I + PEG	98.3°±1.6
silane I - BSA	89.6°±1.8
silane I - PVP	100.4°±1.6
Teflon	104.4°±1.6

Table 5.3 **Surface coatings with corresponding water contact angles which were all measure 5 times.**

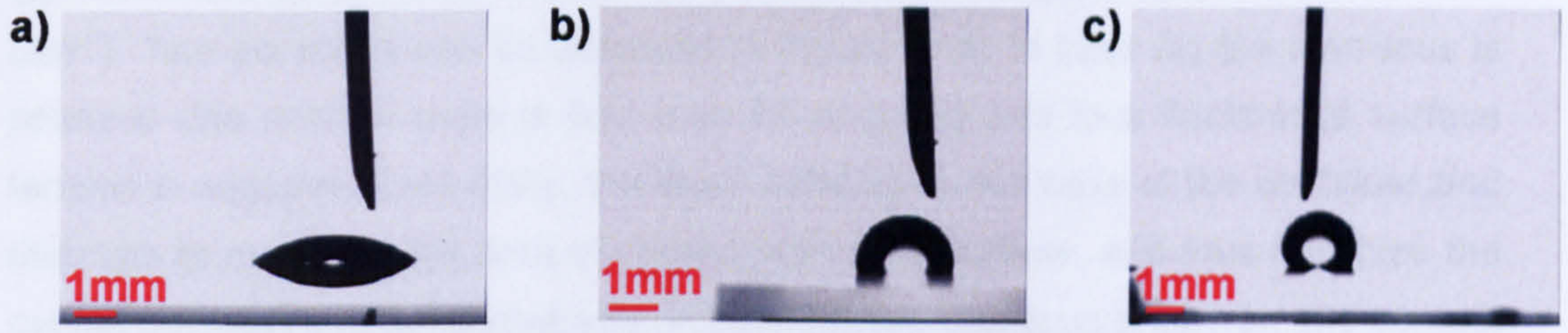


Figure 5.13 **Water droplets (2µl) on microscope slides with different surface coatings. Each droplet is ejected on a sample surface and the contact angle is measured with the Drop Shape Analysis System. (a) A droplet on an untreated glass surface. (b) A droplet on a silane I surface. (c) A droplet on a silane II surface. (d) A droplet on a silane I+PEG surface. (e) A droplet on a silane I+BSA surface. (f) A water droplet on a silane I+PVP surface and (g) A droplet on a Teflon surface.**

5.1.1.2.2 Water Flow Profile Measurements in Functionalized Channels

Wettability in channels is assessed by measuring the contact angle of the flow profile in a channel. If a gas-liquid interface comes into contact with a solid surface such as the walls of a channel the interface will curve up or down near that surface. Such a concave or convex surface shape is known as a *meniscus*. The contact angle can be determined by inspection of the meniscus in a microchannel as shown in Figure 5.14. This angle can be used to relate the liquid-solid surface tension to the liquid-vapor surface tension, i.e.

$$\gamma_{LS} = -\gamma_{LV} \cos\theta \qquad (5.2)$$

γ_{SL} is the solid-liquid surface tension (J/m^2) and γ_{LV} is the liquid-vapor surface tension (J/m^2). Two situations can be observed in Figure 5.14. In case (a) the meniscus is concave (the contact angle is less than 90 degrees) and thus liquid-solid surface tension is negative. Essentially, the liquid adheres to the walls of the container and attempts to maximize the area in contact with solid surface, and thus minimize the overall potential energy. Conversely, in case (b) the meniscus is convex (the contact angle is greater than 90 degrees) and consequently the liquid-solid surface tension will be positive. Now the liquid attempts to minimize the area in contact with solid surface and maximize the overall potential energy.

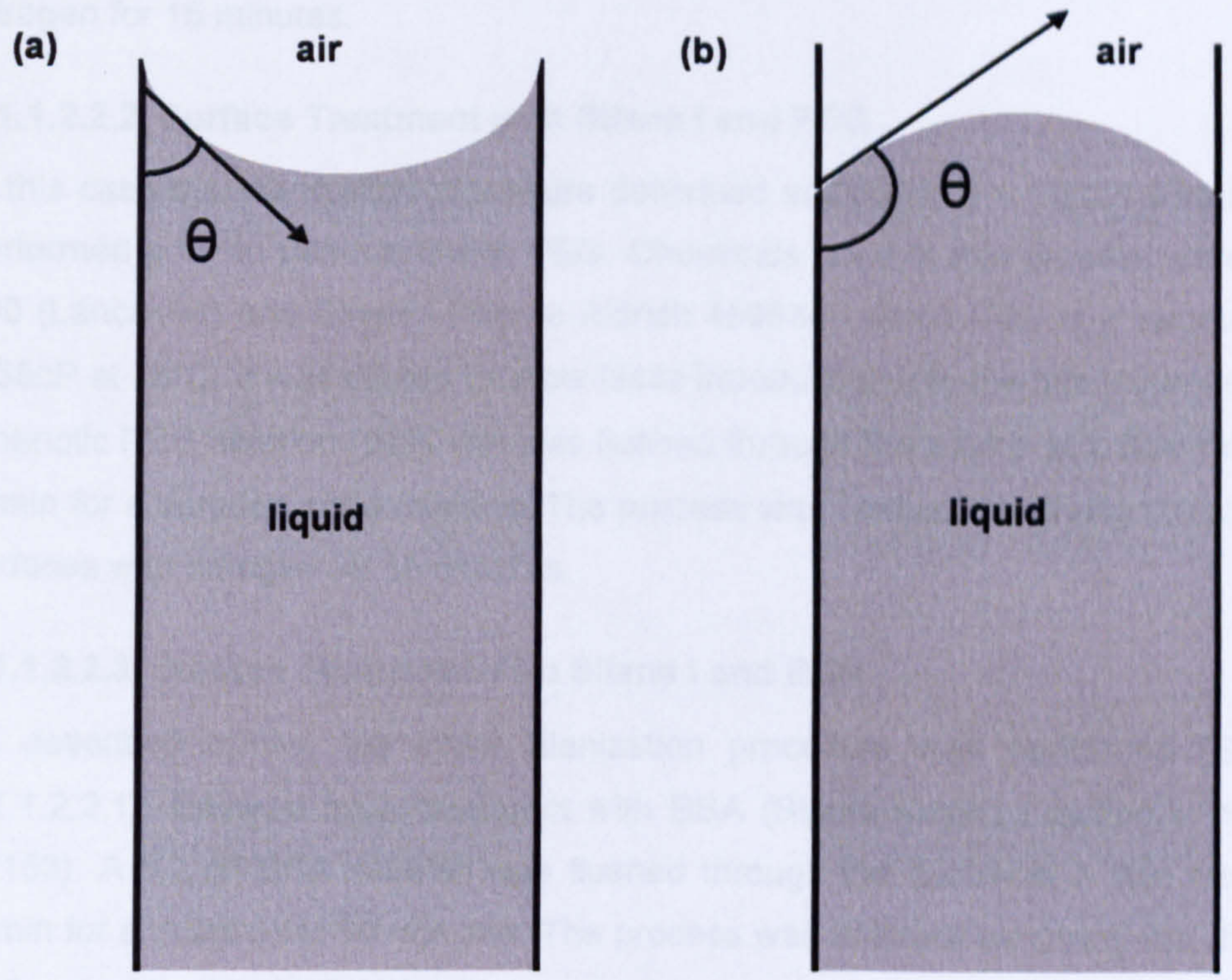


Figure 5.14 **Assessment of the contact angle θ of a liquid in a vertical tube. In case (a) the contact angle is less than 90° with the liquid adhering to the walls. In case (b) the contact angle is greater than 90° with the liquid repelled from the walls.**

In the current studies, the microfluidic channels were treated with the six different surface coatings and their wettability assessed by measuring flow profiles of water fronts.

5.1.1.2.2.1 Surface Treatment with Dichlorodimethlysilane (silane I)

All microfluidic channels were cleaned (flushed with distilled water and 0.5mM Sodium hydroxide solution) and dried in a stream of Nitrogen prior to coating.

Silanization consists of four separate steps. The following chemicals were used: dichlorodimethlysilane (Fluka 82126), heptane (Sigma-Aldrich 246654) and distilled water (Oxoid Ltd. BO 0184). First the microchannel was flushed with heptane. This was followed by the introduction of a dichlorodimethylsilane solution. A further heptane flush was performed to remove all silane residues. Finally the channel was washed with distilled water. All steps were performed in a fume hood and for a duration of 60 minutes at a flow rate of 3 µl/min. Finally channels were dried with nitrogen for 15 minutes.

5.1.1.2.2.2 Surface Treatment with Silane I and PEG

In this case the silanization procedure described in Section 5.1.1.2.2.1 was initially performed prior to treatment with PEG. Chemicals used in this process were PEG 600 (Lancaster) and Ethanol (Sigma Aldrich 459844). Since PEG is a viscous fluid (135cP at 25°C) it was diluted to allow facile introduction into the microchannels. An ethanolic PEG solution (50% v/v) was flushed through the device at a flow rate of 3 µl/min for a duration of 60 minutes. The process was finalized by drying the channel surfaces with nitrogen for 15 minutes.

5.1.1.2.2.3 Surface Treatment with Silane I and BSA

As described above, the initial silanization procedure was performed (Section 5.1.1.2.2.1), followed by a treatment with BSA (Sigma-Aldrich Fraction V powder A2153). A 0.2 g/l BSA solution was flushed through the device at a flow rate of 3 µl/min for a duration of 60 minutes. The process was finalized by drying the channel surfaces with nitrogen for 15 minutes.

5.1.1.2.2.4 Surface Treatment with Silane I and PVP

This surface treatment consisted of the initial silanization procedure described in Section 5.1.1.2.2.1 followed by a treatment with PVP. The chemical used in this process was PVP (Sigma Aldrich P856568; MW 55000). A 0.02g/l PVP solution was flushed through the device at a flow rate of 3 µl/min for a duration of 60 minutes. The process was finalized by drying the channel surfaces with nitrogen for 15 minutes.

5.1.1.2.2.5 Surface Treatment with Teflon

The Teflon coating procedure was performed in two steps according to a recipe described in [32]. A 0.6% dispersion of Teflon (DuPont Teflon PFA) was flushed through the device at a flow rate of 3 µl/min for a duration of 60 minutes. The device was then put on a hot plate at 100 °C for 2 hours to facilitate solvent evaporation from the channels.

5.1.1.2.2.6 Surface Treatment with Silane II

As mentioned previously, silane II is highly sensitive and reactive and therefore needs special precautions. The silanization procedure consisted of four separate steps, each performed in an argon filled glove box. The chemicals used in this process were perfluorooctyltrichlorosilane (Fluorochem S13125) and anhydrous hexadecane (Sigma-Aldrich H0255). Water vapour was removed from all microchannels by flushing with anhydrous hexadecane at a flow rate of 3 µl/min for a duration of 60 minutes. Channels were then flushed with perfluoro-octyltrichlorosilane at a flow rate of 3 µl/min for 60 minutes, followed by final hexadecane flushing at a flow rate of 3 µl/min for 60 minutes. All coated devices were still filled with hexadecane when the glove box was opened. The process was finalized by drying the microchannels with nitrogen for a duration of 15 minutes.

The flow profiles were measured in coated channels and can be found in literature [11, 32, 37]. The contact angle values are listed in Table 5.5.

Surface coating	Contact angle
silane I	101°±2
silane I - PEG	98°±2
silane I - BSA	88°±3
silane I - PVP	100°±2
Teflon	104°±3
silane II	122°±2

Table 5.5 **Contact angles of water flow profiles in six different coated microfluidic channels.**

5.1.2 Protein Adsorption Assessment and CF PCR Results

The six different surface coatings were tested to assess their efficiency in PCR applications. Experiments were performed in two stages. Initial experiments were

performed at room temperature as described in Section 5.1.1.1. In the case of successful amplification CF-PCR was attempted on the coated microchannels.

5.1.2.1 Protein Adsorption Assessment Studies on Coated Microchannels

Protein adsorption was assessed on microfluidic channels coated with silane I, silane I - PEG, silane I – BSA and silane I – PVP. It should be noted that for these experiments the PCR system used was varied due to availability. Whilst microchannels coated with silane I were tested with the conventional and the Scorpion primer system, microchannels coated with silane I – PEG were only tested with the conventional primer system and microchannels coated with silane I – BSA and silane I – PVP were only tested with the Scorpion primer system. Furthermore, it should be noted that the PCR mix used in all experiments contained 4X enzyme and dNTP's at ten times the normal concentration.

5.1.2.1.1 Protein Adsorption Assessment on Microchannels Coated with Silane I

The same set of experiments as described in Section 5.1.1.1 was performed. A 350µl PCR mix was prepared according to recipe described in Table 2.2. After the mix was prepared, it was split into two parts; the reference and the sample. While the reference was kept outside the PCR chip, in a closed Eppendorf tube, the sample was pumped through the microfluidic device at room temperature and at a flow rate of 3 µl/min. After 60 minutes the sample was collected in an Eppendorf tube and both reference and sample were amplified on the Smart Cycler according to the protocol defined in Table 2.3 and analyzed on the BioAnalyzer. Data resulting from amplification of reference (black curve) and sample (red curve) for room temperature experiments are presented in Figure 5.15. Whilst the expected amplification curve is observed for the reference, less efficient amplification is observed for the sample. Figure 5.16 presents electrophoretic size analysis of both sample and reference, and Table 5.6 lists concentration, identity and molarity for product peaks. Two product peaks are observed for both the reference and the sample, with lower concentration products being observed for the sample.

These experiments indicate that the interaction between the channel walls with the PCR mix still reduces the efficiency of the amplification but does allow amplification.

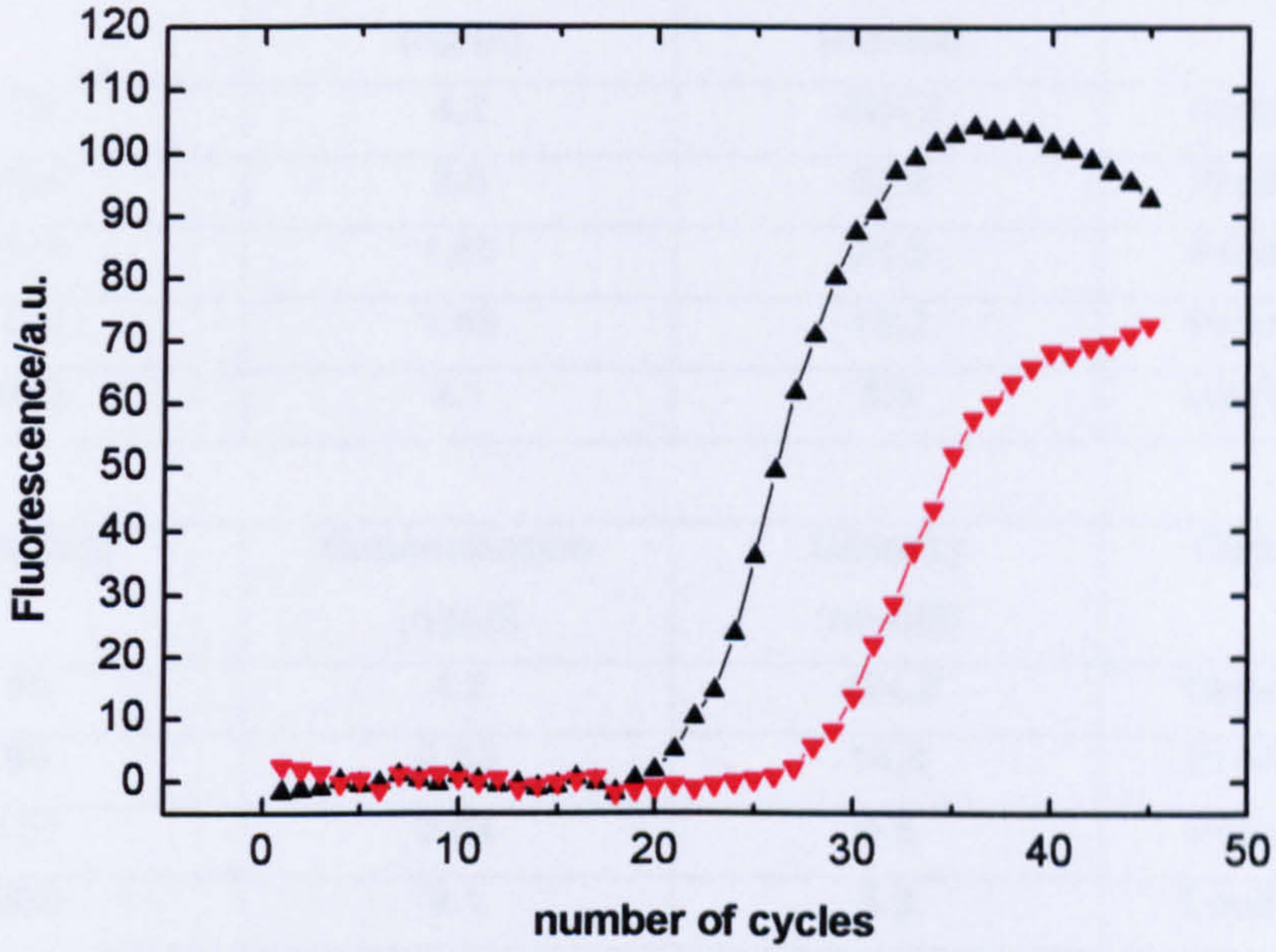


Figure 5.15 **Fluorescence intensity as a function of the number of cycles. Black curve represents the reference and red curve represents the sample. The microchannels are treated with silane I.**

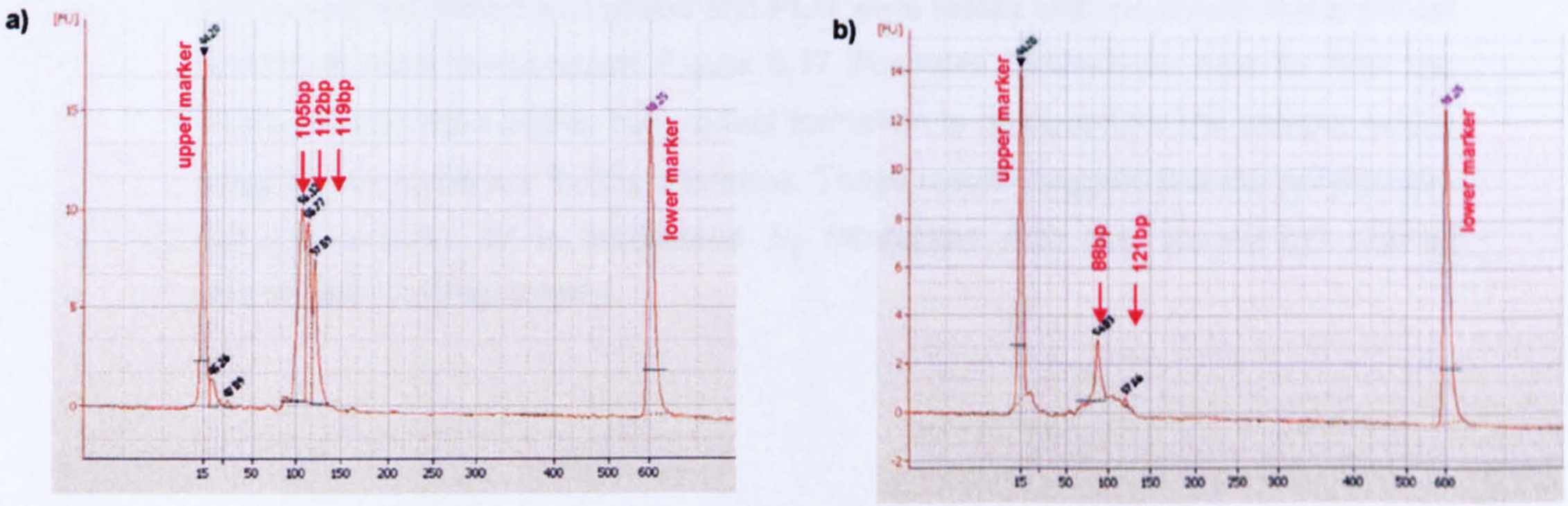


Figure 5.16 **Electropherograms resulting from the analysis of reference and sample, (a) exhibits three product peaks for reference, (b) exhibits two product peaks for the sample.**

a)

Size (bp)	Concentration (ng/µl)	Molarity (nmol/l)	Observation
15	4.2	424.2	Upper marker
105	2.6	37.2	Product peak
112	1.60	21.5	Product peak
119	1.46	18.3	Product peak
600	2.1	5.3	Lower marker

b)

Size (bp)	Concentration (ng/µl)	Molarity (nmol/l)	Observation
15	4.2	424.2	Upper marker
88	0.83	14.4	Product peak
121	0.04	0.5	Product peak
600	2.1	5.3	Lower marker

Table 5.6 **Concentration, identity and molarity of peaks for reference (a) and sample (b).**

5.1.2.1.2 Protein Adsorption Assessment on Microchannels Coated with Silane I and PEG

Microchannels coated with silane and PEG were tested with the conventional primer system at room temperature. Figure 5.17 illustrates Bioanalyzer data for both the reference and the sample. No product formation is observed for the sample, whilst amplification observed for the reference. These results suggest that the polymerase enzyme adsorbs or is inactivated by interaction with the silane-PEG coated microfluidic channel surface.

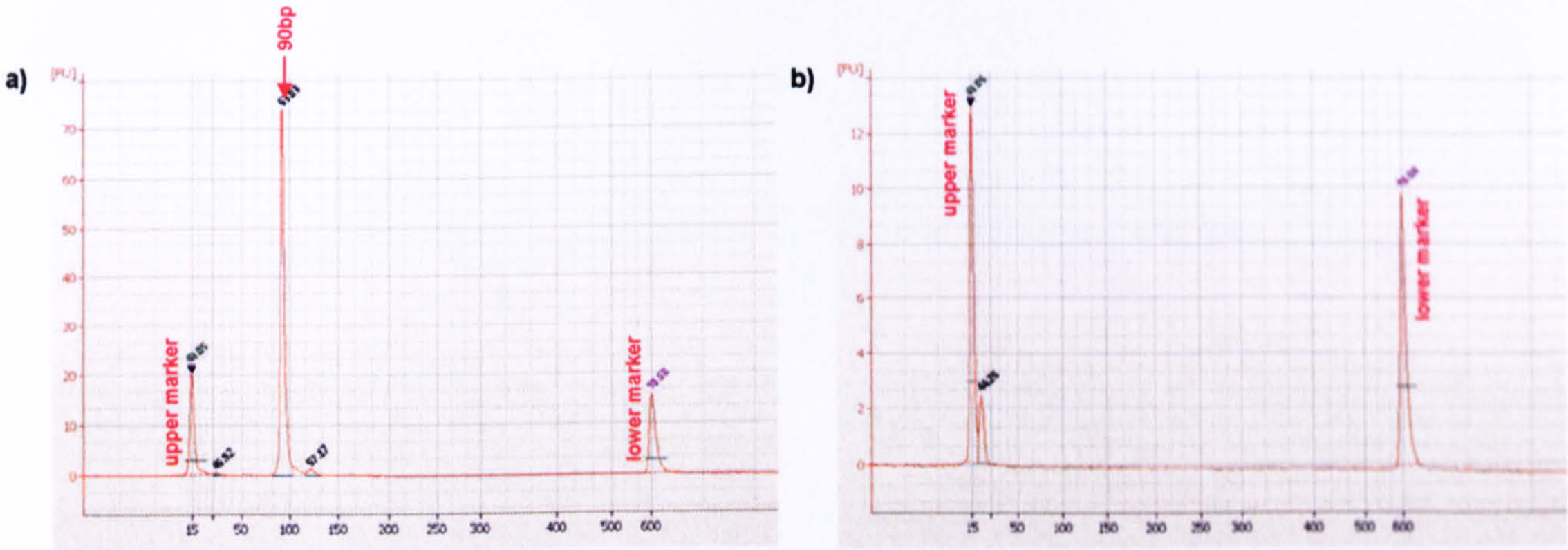


Figure 5.17 **Electropherograms resulting from the analysis of reference and sample. (a) one product peak for reference sample.(b) no product peak for the sample flushed through the microfluidic device.**

5.1.2.1.3 Protein Adsorption Assessment on Microchannels Coated with Silane I and BSA

Microchannels coated with silane and BSA were assessed for protein adsorption using the scorpion primer system. Figure 5.18 illustrates the results of these experiments. Black data points correspond to the reference and red data points correspond to the sample. Whilst the expected amplification curve is observed for the reference, less efficient amplification is observed for the sample. Figure 5.19 presents electrophoretic size analysis of both the sample and reference and Table 5.7 lists concentration, identity and molarity for product peaks. While three product peaks are observed for the reference, two product peaks are observed for the sample (see Chapter 2). Furthermore, lower concentrations of the products are observed for the sample. Two explanations can be found for this occurrence. The generated BSA coating on the microchannels may not be completely uniform and may allow for some interaction of the Taq Polymerase with the channel walls. Another explanation might be that the BSA itself reduces the PCR efficiency [45].

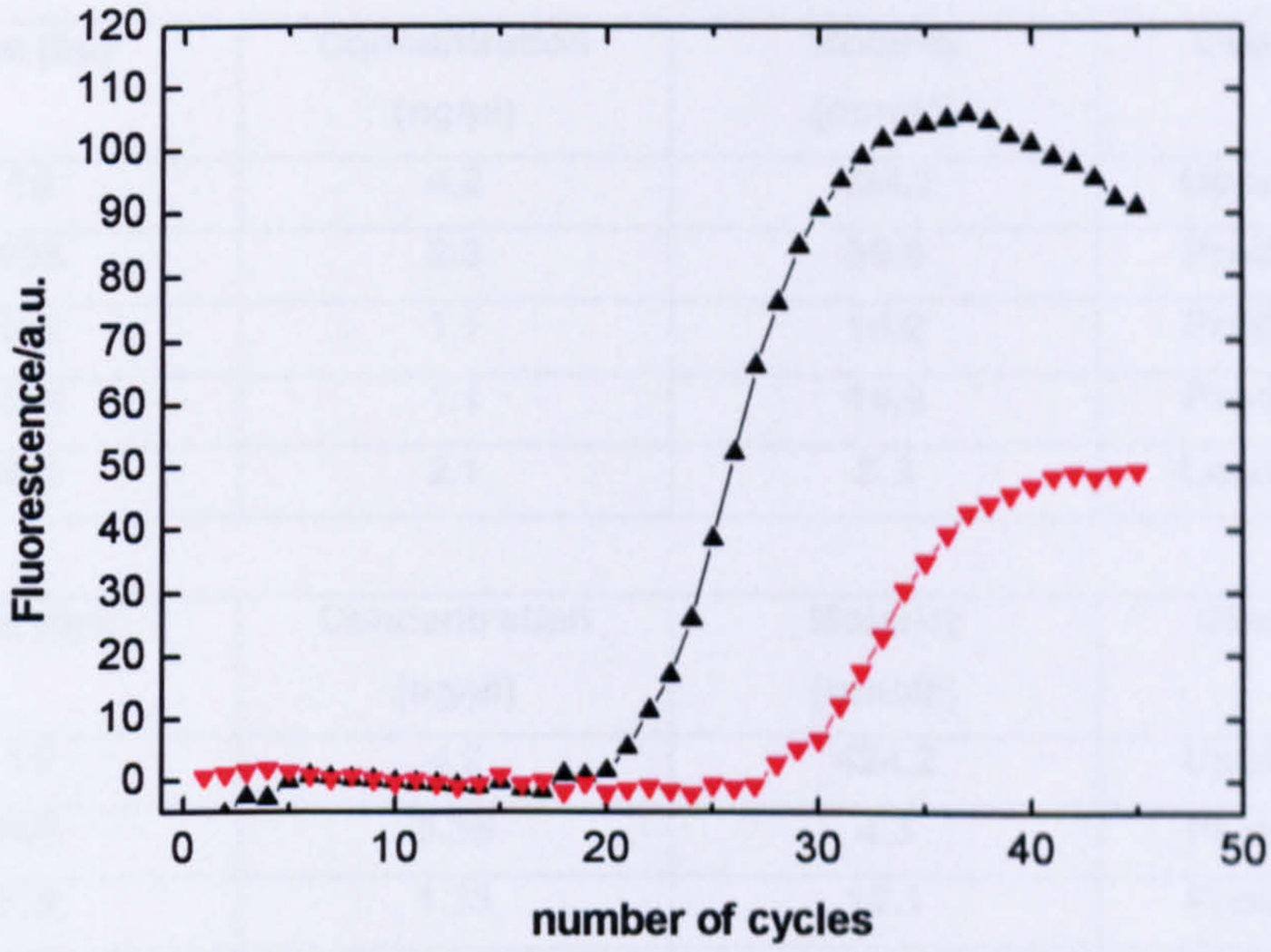


Figure 5.18 **Fluorescence intensity as a function of the number of cycles. Black curve represents the reference and red curve represents the sample flushed through the microfluidic device. Here the microchannels are treated with silane I and BSA.**

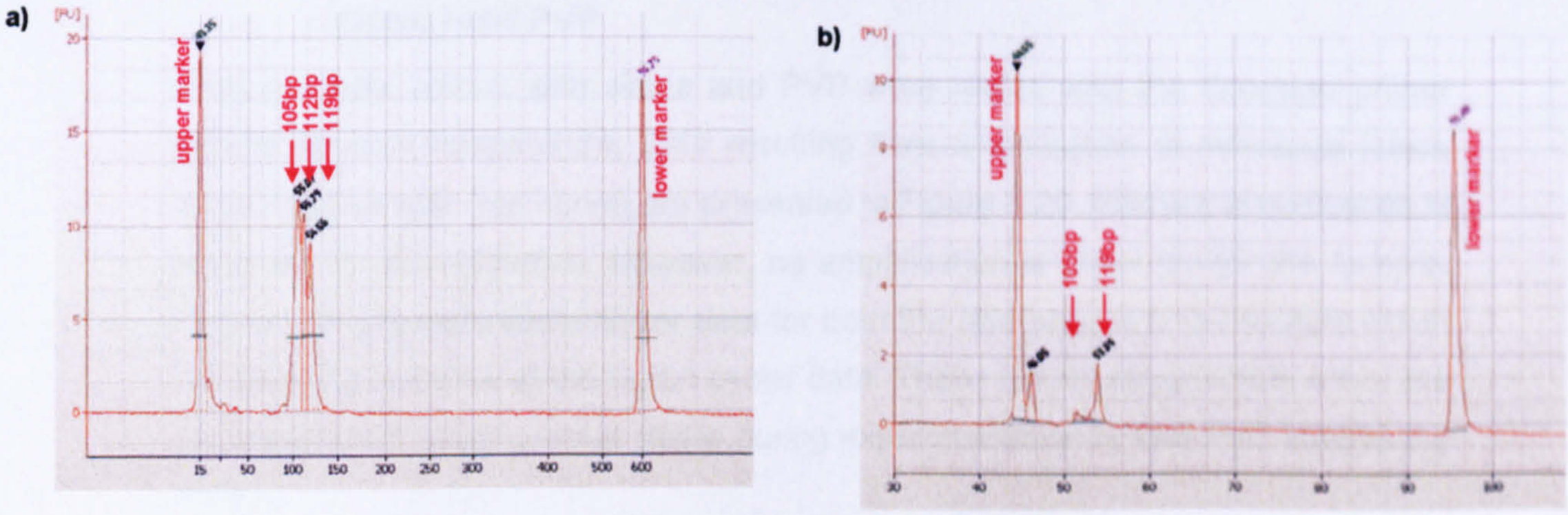


Figure 5.19 **Electropherograms resulting from the analysis of reference and sample. (a) exhibits three product peaks for the reference.(b) exhibits two product peaks for the sample flushed through the microfluidic device.**

a)

Size (bp)	Concentration (ng/µl)	Molarity (nmol/l)	Observation
15	4.2	424.2	Upper marker
105	2.3	36.5	Product peak
112	1.1	16.2	Product peak
119	1.1	14.9	Product peak
600	2.1	5.3	Lower marker

b)

Size (bp)	Concentration (ng/µl)	Molarity (nmol/l)	Observation
15	4.2	424.2	Upper marker
105	0.35	4.3	Product peak
119	1.33	12.1	Product peak
600	2.1	5.3	Lower marker

Table 5.7 **Concentration, identity and molarity of three product peaks for reference (a) and concentration and molarity of two product peaks for sample flushed through the microfluidic device (b).**

5.1.2.1.4 Protein Adsorption Assessment on Microchannels Coated with Silane I and PVP

Microchannels coated with silane and PVP were tested with the Scorpion primer system at room temperature. Data resulting from amplification of reference (black curve) and sample (red curve) are presented in Figure 5.20. Efficient amplification is observed for the reference. However, no amplification is observed for the sample. Figure 5.21 presents BioAnalyzer data for both the reference and the sample which confirms the outcome of the Smart cycler data. These results suggest that either the generated PVP coating is not stable during experimentation or that PVP inhibits the PCR.

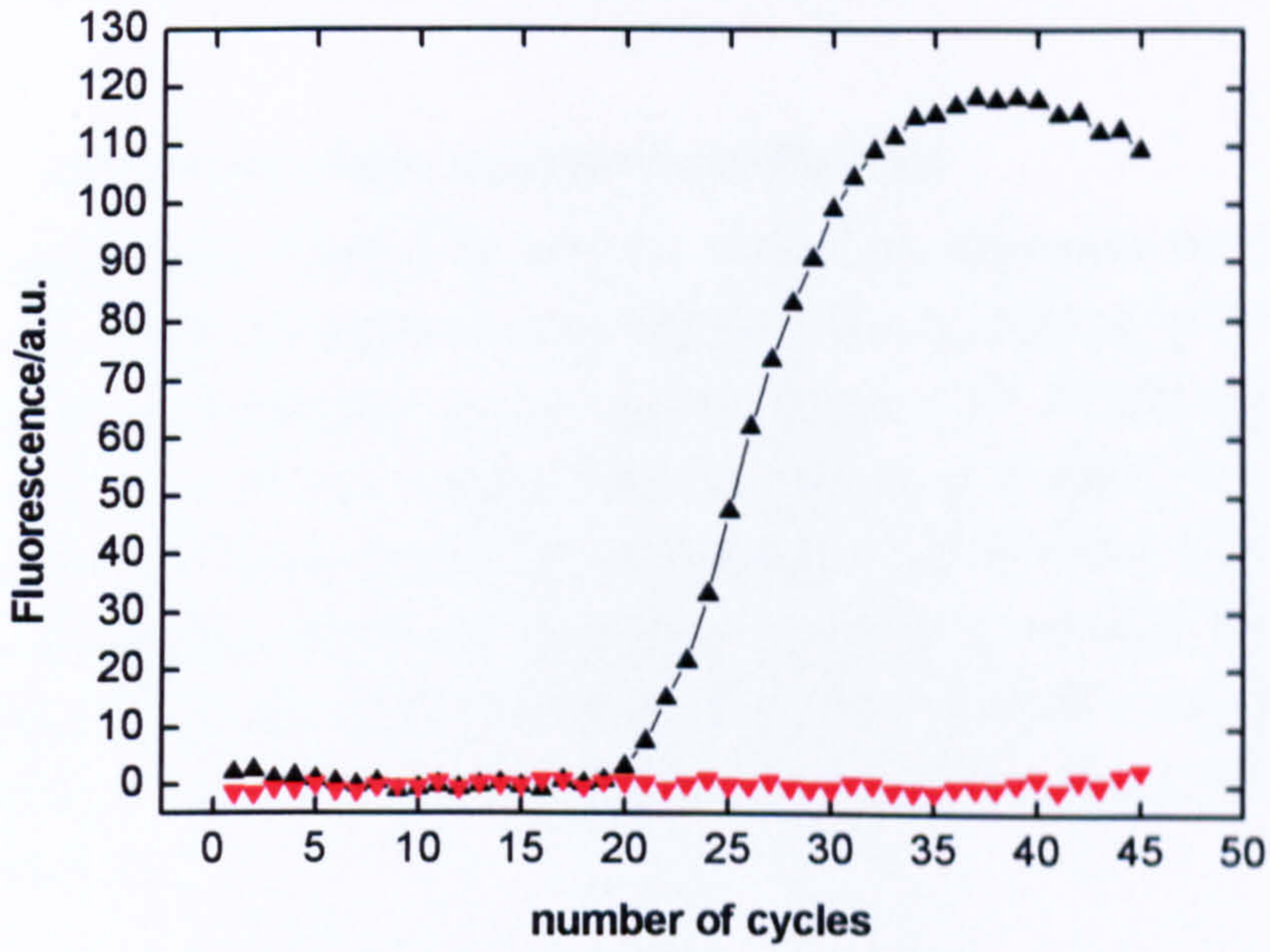


Figure 5.20 **Fluorescence intensity as a function of the number of cycles. Black curve represents the reference and red curve represents the sample flushed through the microfluidic device. Here the microchannels are treated with silane I and PVP.**

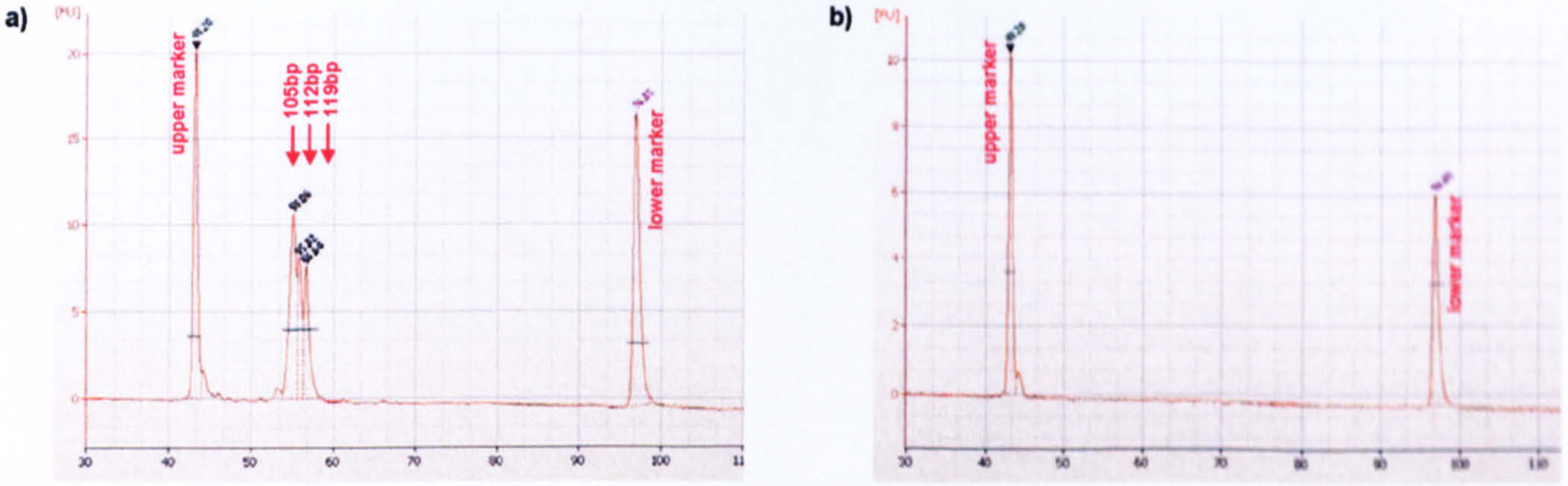


Figure 5.21 **Electropherograms resulting from the analysis of reference and the sample. (a) exhibits three product peaks for reference sample.(b) exhibits no product peak for the sample flushed through the microfluidic device.**

5.1.2.2 CF PCR on Coated Microchannels

CF PCR was performed in microfluidic channels coated with silane I, silane I – BSA, Teflon and silane II. Whilst microchannels coated with silane I and silane II could be tested with the conventional and the Scorpion primer system, microchannels coated

with silane I – BSA could only be tested with the Scorpion primer system and microchannels coated with Teflon could only be tested with the conventional primer system.

5.1.2.2.1 CF PCR on Silane I Coated Microchannels

Data resulting from CF-PCR on silane I coated microchannels are presented in Figure 5.22. Whilst the expected amplification curve is observed for the reference, no amplification is observed for the sample. Figure 5.23 presents electrophoretic size analysis of both the sample and the reference. Product formation is not observed for the sample, whilst two product peaks are observed for the reference. These experiments indicate that the silane I coating is not heat resistant, since successful PCR under similar conditions has been reported in the literature [37]. Therefore it was decided to repeat this experiment and optimize the efficiency of the coating further.

The experiment was optimized and repeated with the conventional primer system until successful amplification could be observed. Figure 5.24 presents electrophoretic size analysis of both the reference and sample. Product formation is observed in both cases. However, this experiment needed further optimization since the successful coatings could only be achieved 15 % of the time. Moreover, the yield of amplified product was low compared to the reference and significant adsorption of enzyme could be observed. Figure 5.25 presents a part of a microfluidic channel before and after CF PCR. Consequently, further surface coatings were tested.

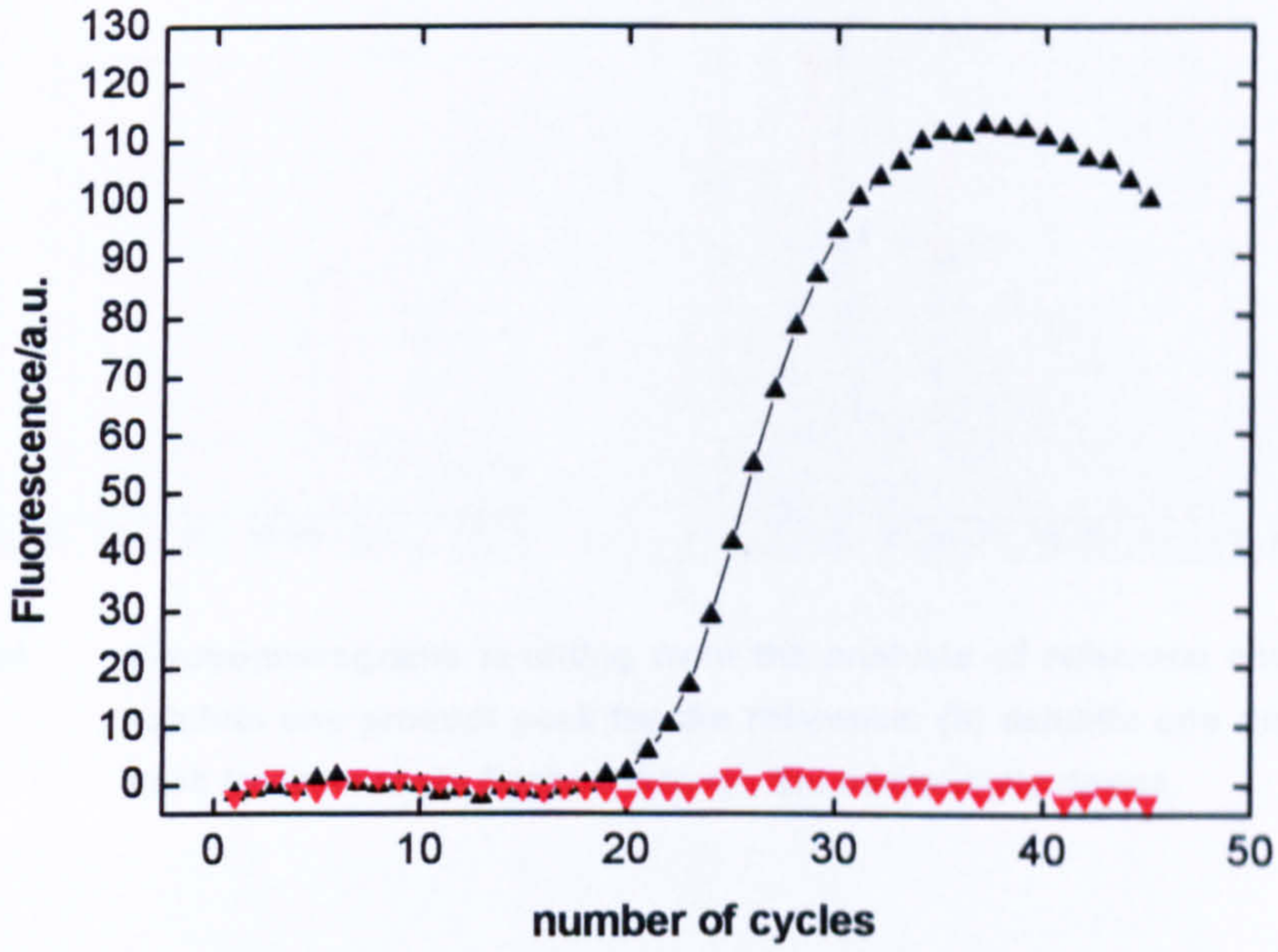


Figure 5.22 Fluorescence intensity as a function of the number of cycles. The black curve represents the reference and the red curve represents the sample flushed through the microfluidic device. Here the microchannels are treated with silane I.

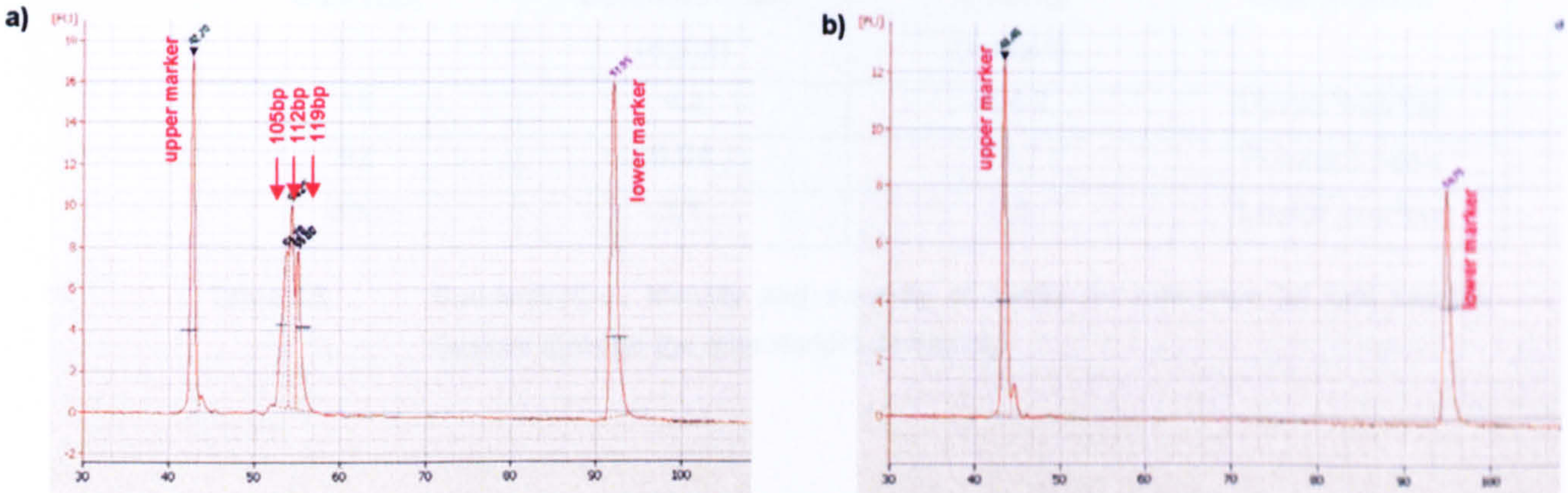


Figure 5.23 Electropherograms resulting from the analysis of reference and the sample. (a) exhibits three product peaks for reference sample, (b) exhibits no product peak for the sample flushed through the microfluidic device.

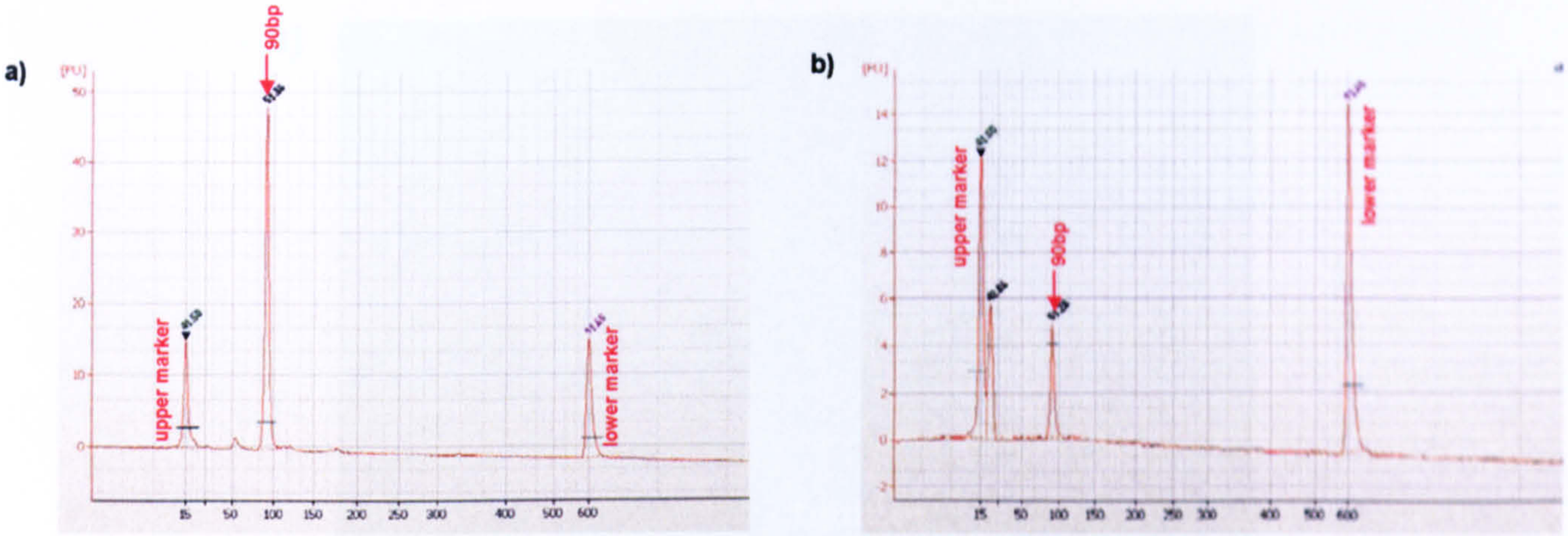


Figure 5.24 **Electropherograms resulting from the analysis of reference and sample. (a) exhibits one product peak for the reference, (b) exhibits one unique product peak for the sample flushed through the microfluidic device.**

a)

Size (bp)	Concentration (ng/µl)	Molarity (nmol/l)	Observation
15	4.2	424.2	Upper marker
92	7.76	128	Product peak
600	2.1	5.3	Lower marker

b)

Size (bp)	Concentration (ng/µl)	Molarity (nmol/l)	Observation
15	4.2	424.2	Upper marker
92	0.94	15.7	Product peak
600	2.1	5.3	Lower marker

Table 5.8 **Concentration, identity and molarity of peaks for reference (a) and sample flushed through the microfluidic device (b).**

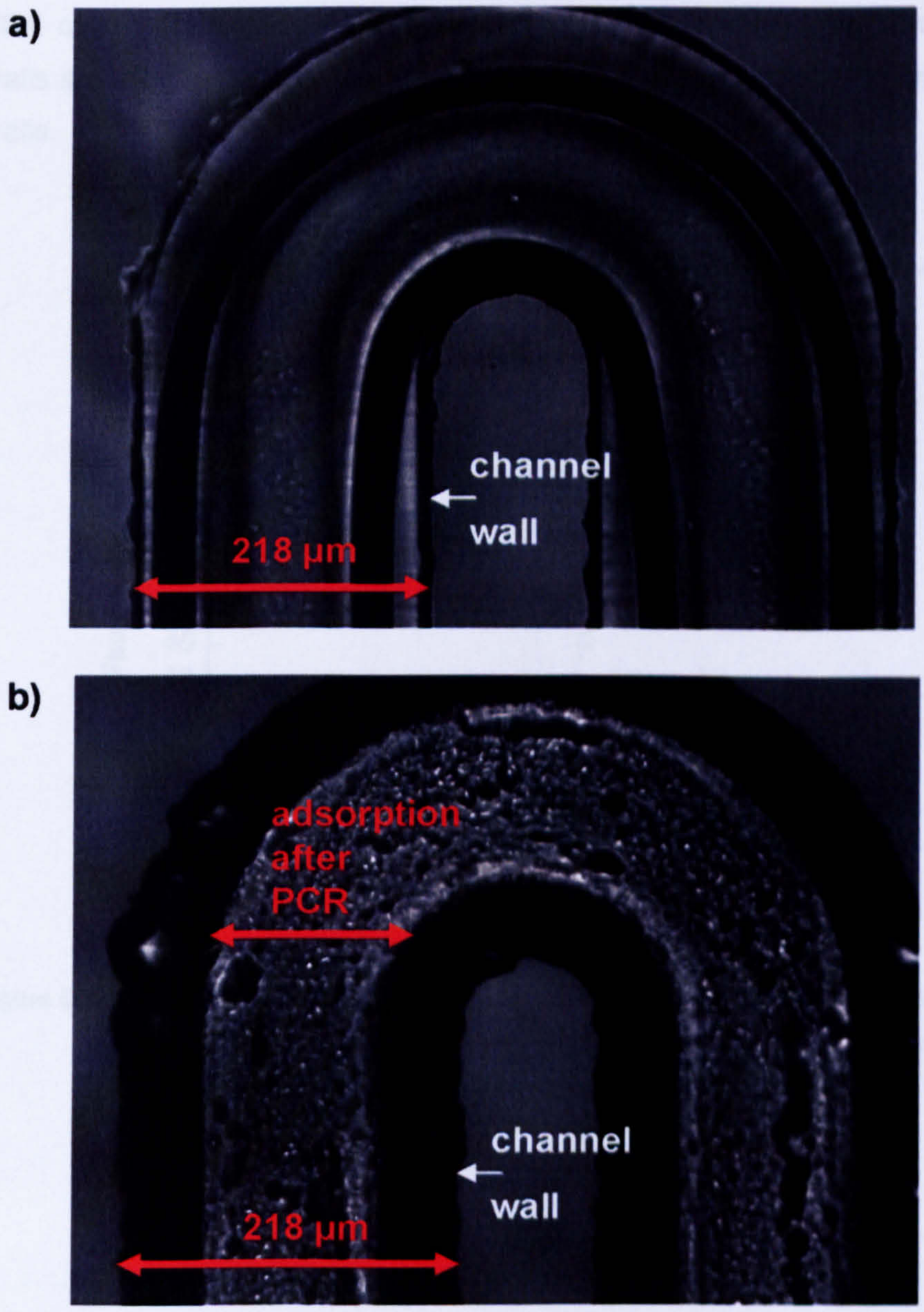


Figure 5.25 **Photograph of mirochannel coated with silane I before and after PCR. (a) shows channel with coating, (b) shows channel with adsorption after PCR.**

5.1.2.2.2 CF PCR on Silane I and BSA Coated Microchannels

As protein adsorption assessment on silane I and BSA coated microchannels resulted in amplification, it was decided to perform CF PCR using these microchannels. In this case amplification is only observed for the reference (Figure 5.26). Black data points correspond to the reference and red data points correspond to the sample. Figure 5.27 presents the corresponding BioAnalyzer data. These data suggest that the combination of a silane and BSA coated channels and applied heat does not lead to a successful amplification of target DNA. It is likely that the

BSA coating is not resistant to applied heat which means that the microchannel walls are not passivated and Taq Polymerase is likely to adsorb to the microchannel walls.

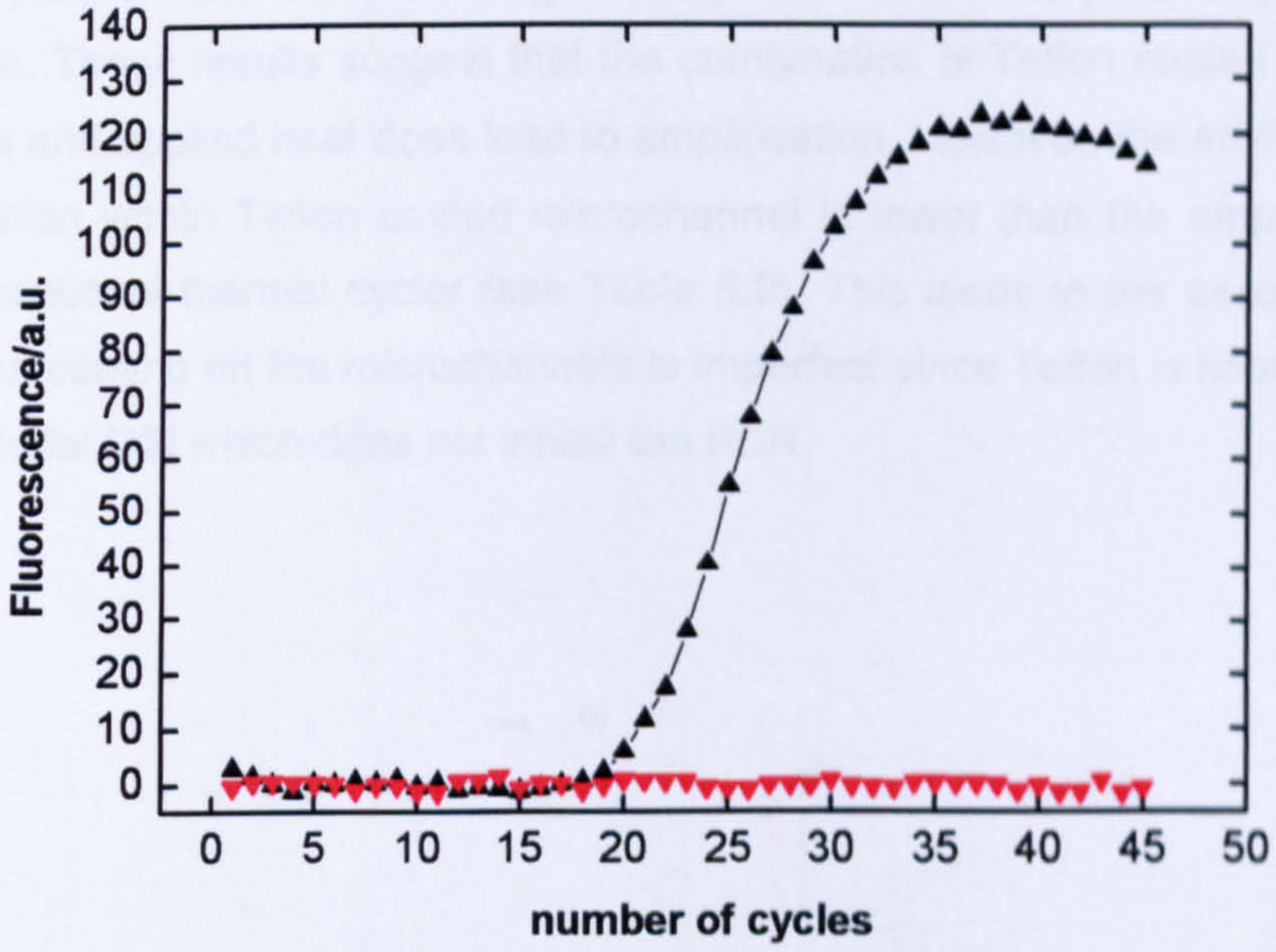


Figure 5.26 **Fluorescence intensity as a function of the number of cycles. Black curve represents the reference and red curve represents the sample flushed through the microfluidic device. Here the microchannels are treated with silane I and BSA.**

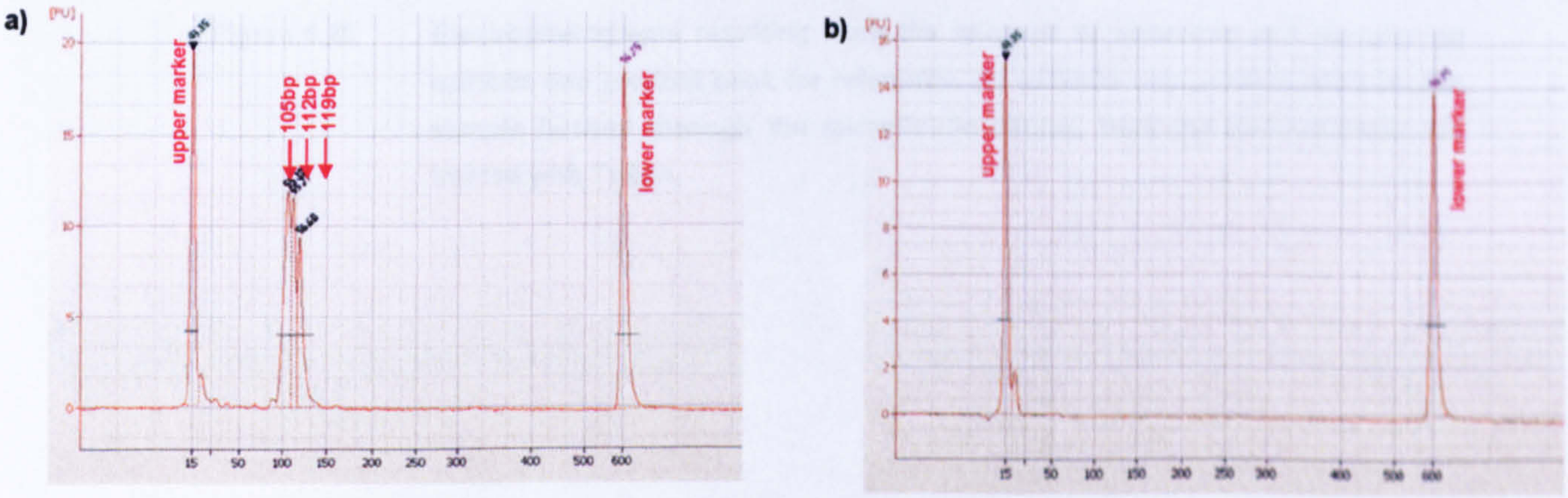


Figure 5.27 **Electropherograms resulting from the analysis of reference and sample. (a) exhibits three product peaks for the reference (b) exhibits no product peaks for the sample flushed through the microfluidic device.**

5.1.2.2.3 CF PCR on Teflon I Coated Microchannels

CF PCR with the conventional primer system was performed on microchannels coated with Teflon. BioAnalyzer data resulting from amplification of reference and sample are presented in Figure 5.28. In both cases amplification is observed but the product yield for the sample is significantly lower than the product yield for the reference. These results suggest that the combination of Teflon coated microfluidic channels and applied heat does lead to amplification. However, the efficiency of the amplification within Teflon coated microchannel is lower than the amplification on the conventional thermal cycler (see Table 5.9). This leads to the assumption that the Teflon coating on the microchannels is imperfect since Teflon is known to be an inert material [32] which does not inhibit the PCR.

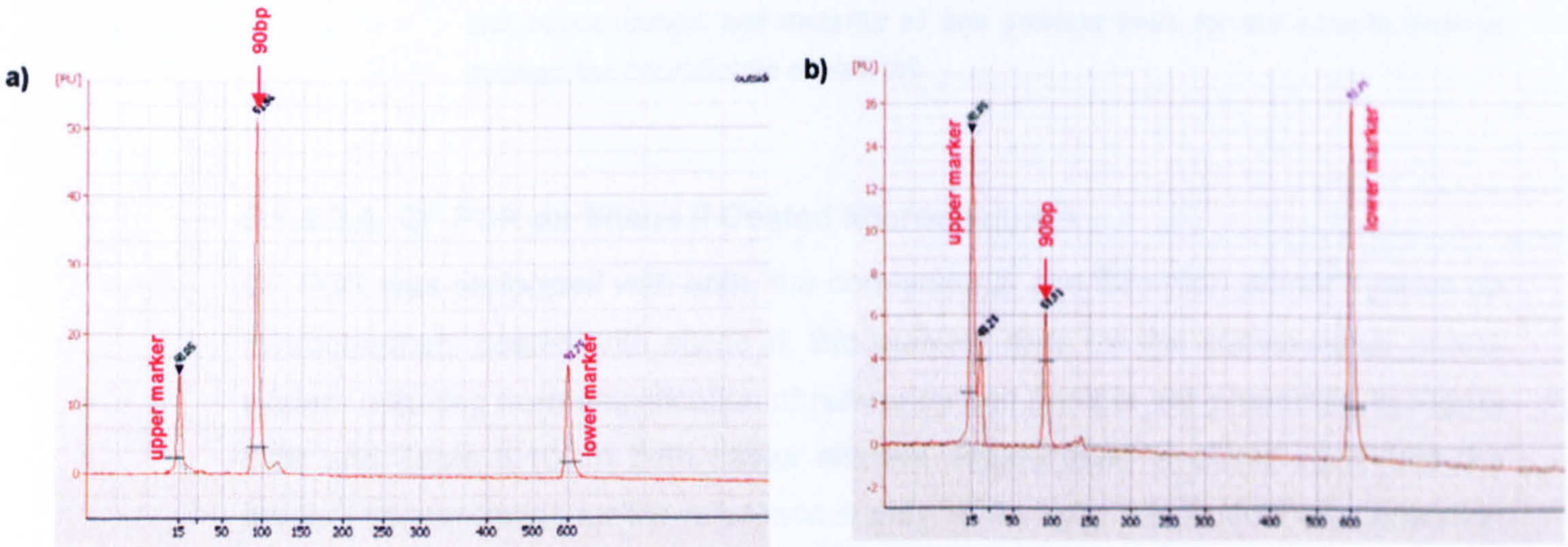


Figure 5.28 **Electropherograms resulting from the analysis of reference and sample. (a) exhibits one product peak for reference. (b) exhibits one product peak for the sample flushed through the microfluidic device. Here the microchannel are treated with Teflon.**

a)

Size (bp)	Concentration (ng/µl)	Molarity (nmol/l)	Observation
15	4.2	424.2	Upper marker
92	10.34	170.6	Product peak
600	2.1	5.3	Lower marker

b)

Size (bp)	Concentration (ng/µl)	Molarity (nmol/l)	Observation
15	4.2	424.2	Upper marker
92	1.14	18.9	Product peak
600	2.1	5.3	Lower marker

Table 5.9 **Concentration, identity and molarity of one product peak for the reference (a), and concentration and molarity of one product peak for the sample flushed through the microfluidic device (b).**

5.1.2.2.4 CF PCR on Silane II Coated Microchannels

CF PCR was performed with both, the conventional and Scorpion primer system on microchannels coated with silane II. BioAnalyzer data for the conventional primer system resulting from amplification of reference and sample are presented in Figure 5.29 and Table 5.10. In both cases efficient amplification is observed. While the product concentration for the reference is only 16.94 ng/µl the product concentration for the sample is 22.58 ng/µl. Data for the Scorpion primer system resulting from amplification of reference (black curve) and sample (red curve) are presented in Figure 5.30 and Table 5.11. Amplification is observed for both systems. While the product concentrations for the reference are 4.42 and 3.66 ng/µl, the product concentrations for the sample are 6.03 and 4.23 ng/µl, In both cases the PCR is more efficient on the microfluidic device than on the conventional thermal cycler.

Additionally, product concentrations were measured with a Nanodrop Spectrometer which confirmed the outcome of the results above. All results are listed in Table 5.12. These results suggest that no interactions between the microfluidic channel walls and the PCR mix occur. Moreover, the conditions on the microscale (i.e. fast heat transfer) afford higher amplification efficiencies when compared to the macroscale.

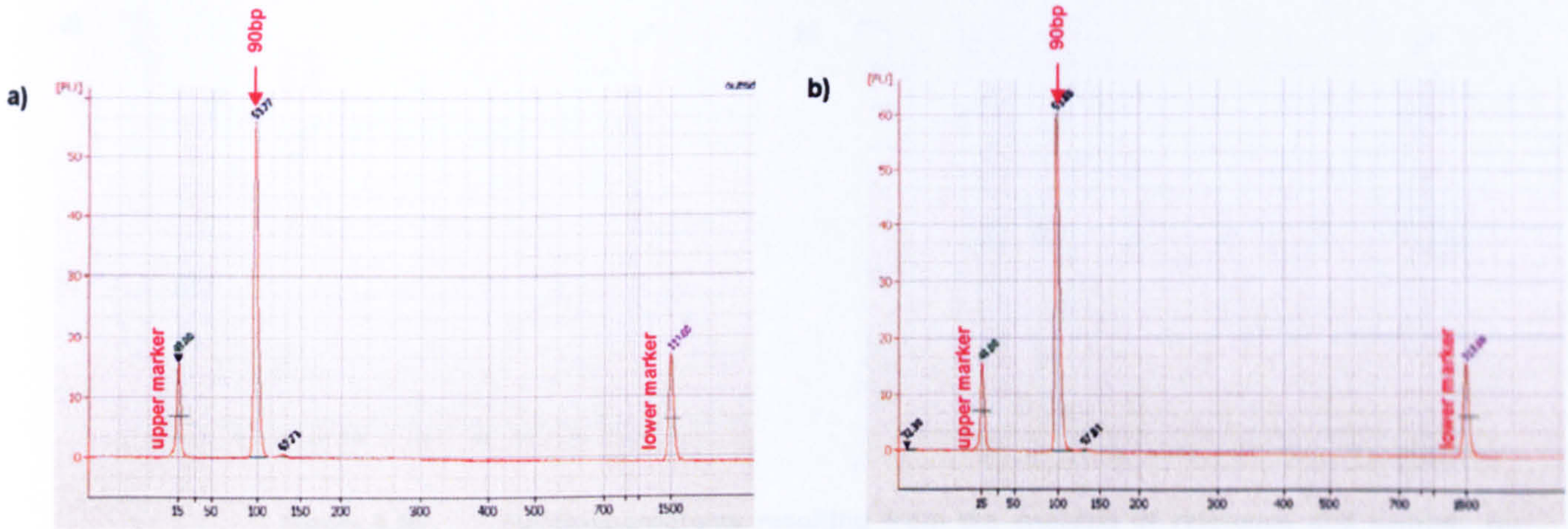


Figure 5.29 Electropherograms resulting from the analysis of reference and sample. (a) exhibits one product peak for the reference. (b) exhibits one unique sample peak for the sample flushed through the microfluidic device. Here the microchannels are treated with silane II.

a)

Size (bp)	Concentration (ng/µl)	Molarity (nmol/l)	Observation
15	4.2	424.2	Upper marker
92	16.94	262.3	Product peak
600	2.1	5.3	Lower marker

b)

Size (bp)	Concentration (ng/µl)	Molarity (nmol/l)	Observation
15	4.2	424.2	Upper marker
92	22.58	349.2	Product peak
600	2.1	5.3	Lower marker

Table 5.10 Concentration, identity and molarity of one product peak for the reference (a) and concentration, identity and molarity of one product peak for the sample (b).

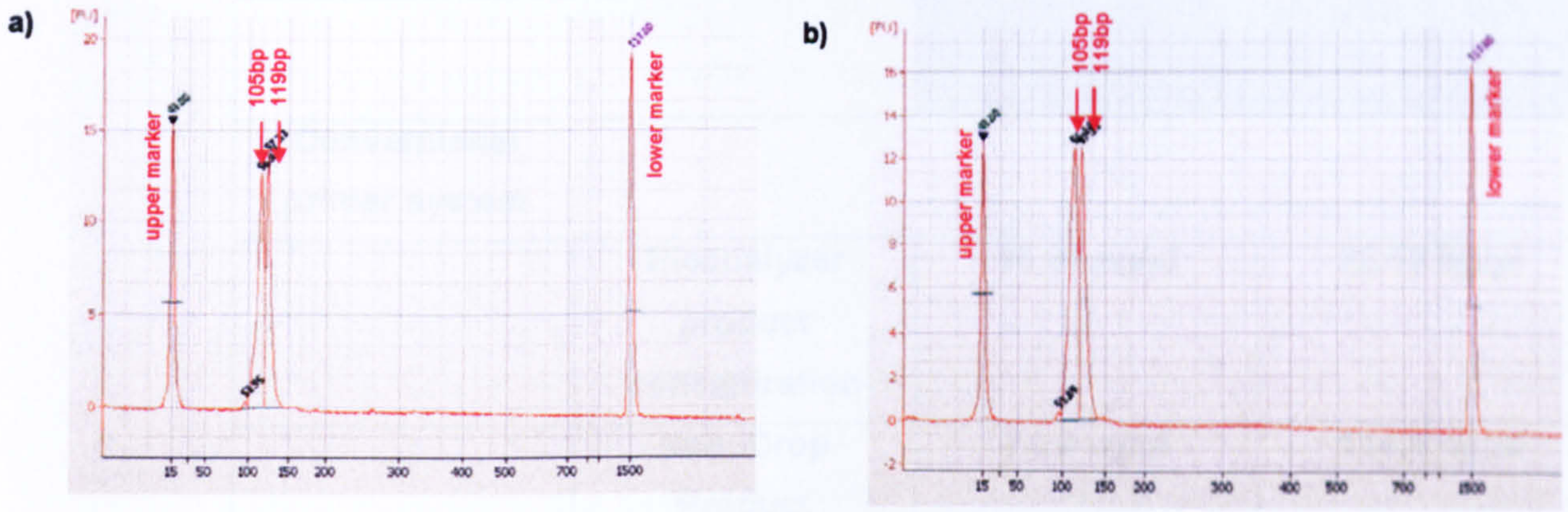


Figure 5.30 **Electropherograms resulting from the analysis of reference and sample. (a) exhibits two product peaks for reference.(b) exhibits two product peaks for the sample flushed through the microfluidic device. Here the microchannels are treated with silane II.**

a)

Size (bp)	Concentration (ng/µl)	Molarity (nmol/l)	Observation
15	4.2	424.2	Upper marker
105	4.42	57.6	Product peak
119	3.66	44.5	Product peak
600	2.1	5.3	Lower marker

b)

Size (bp)	Concentration (ng/µl)	Molarity (nmol/l)	Observation
15	4.2	424.2	Upper marker
105	6.03	79.7	Product peak
119	4.23	52.2	Product peak
600	2.1	5.3	Lower marker

Table 5.11 **Concentration, identity and molarity of two product peaks for reference (a) and concentration and molarity of two product peaks for sample flushed through the microfluidic device (b).**

		Reference PCR	Microfluidic PCR
Conventional primer system			
	Bioanalyzer product concentration	**16.94 ng/µl**	**22.58 ng/µl**
	NanoDrop Product concentration	**74.8 ng/µl**	**114.8 ng/µl**
Scorpion primer system			
	Bioanalyzer product concentration	**4.4 and 3.6 ng/µl**	**6.03 and 4.02 ng/µl**
	NanoDrop Product concentration	**64ng/µl**	**146ng/µl**

Table 5.12 PCR Results comparing reference with microfluidic samples.

5.1.3 Discussion

Coating microchannels with silane I seemed to produce partial DNA amplification. However, the efficiency and reproducibility of the PCR results are not ideal. Successful amplification with this coating has previously been reported in literature [37], but it should be noted that this was achieved using a combination of silanization and dynamic coating with PVP and Tween 20. The specific PCR system used in this project did not lead to successful amplification when Tween 20 and PVP was added to the mix.

PEG is widely used to reduce protein adsorption on microchannels [11, 31, 40, 46] and is known to form non-fouling interfaces on silicon and glass [47]. However, the results achieved here suggest that PEG coated surfaces do not allow successful amplification. Two possible explanations can be postulated. First, it is possible that this particular PCR is not compatible with PEG. Second, the generation of the PEG coating on the microchannels may not be as uniform as expected. The generation of PEG coatings in this thesis consisted of simply flushing the channels with the PEG

solution. This may not be the ideal approach. For example, Popat *et al.* [47] argues that a solvent-free vapor deposition protocol only enables uniform PEG coatings on microchannels.

The results presented in 5.1.2.1.3 show reduced PCR efficiency in silane I – BSA coated microchannels. This level of performance may be due to non-uniform BSA coating or a high BSA concentration which reduces PCR efficiency. Erill *et al.* [45] argues that the net effect of Polymerase adsorption can be counteracted by the addition of BSA and numerous studies of microscale PCR have demonstrated increased efficiency by addition of BSA [12, 13, 16, 21, 22]. However it should be noted that the ideal concentration of BSA will depend on the specific PCR systems. For the particular PCR system used in this work the optimization of BSA concentration has only been performed on the macroscale. Reduced PCR efficiency was observed for BSA concentrations higher than 0.5g/l.

The results presented in Section 5.1.2.2.2 show no amplification when using silane I – BSA coated microchannels. This is probably due to the BSA coating not being resistant to the applied temperatures.

The results presented in Section 5.1.2.1.4 show no amplification when the PCR mix is pumped through silane I – PVP coated microchannels. While numerous groups demonstrate that the addition of PVP enhances PCR efficiency [35, 36, 48, 49] by competing with proteins for surface adsorption, Xia *et al.*[50] argues that the addition of PVP will increase the efficiency of the PCR with increasing molecular weight of PVP. It can be concluded that the PVP chosen may not be the ideal for the specific PCR system.

The results presented in Section 5.1.2.2.3 show reduced amplification efficiency which is most probably down to the fact that the Teflon coating on the microchannels is not generated uniformly. Further optimizations on the coating procedure are likely to lead to an increase in PCR efficiency.

The results presented in Section 5.1.2.2.4 show higher amplification efficiencies on the silane II coated microchannels than on the conventional thermal cycler. However, further optimization of the approach is required, since the devices can only be used for up to nine repetitive runs until adsorption issues result in blockages of the channels and failure of PCR. Inspection of water flow profiles as a function of

usage shows a decrease in hydrophobicity. Cleaning with sodium hydroxide, distilled water and various acids did not unblock the microchannels.

1. Atkins, P.W., *Physical Chemistry*. 1998, Oxford: Oxford University Press. 1031.
2. Tanford, C., *The hydrophobic effect and the organization of living matter*. 1978. p. 1012-1018.
3. Hildebrand, J.H., *Is there a "hydrophobic effect"?* Proceedings of the National Academy of Sciences of the United States of America, 1979. 76(1): p. 194.
4. Avbelj, F. and Fele, L., *Role of main-chain electrostatics, hydrophobic effect and side-chain conformational entropy in determining the secondary structure of proteins*. Journal of Molecular Biology, 1998. 279(3): p. 665-684.
5. Spolar, R.S., Ha, J.H., and Record, M.T., *Hydrophobic effect in protein folding and other noncovalent processes involving proteins*. Proceedings of the National Academy of Sciences of the United States of America, 1989. 86(21): p. 8382.
6. Eriksson, A.E., Baase, W.A., Zhang, X.J., Heinz, D.W., Blaber, M., Baldwin, E.P., and Matthews, B.W., *Response of a protein structure to cavity-creating mutations and its relation to the hydrophobic effect*. Science, 1992. 255(5041): p. 178-83.
7. Tsai, C.J., Lin, S.L., Wolfson, H.J., and Nussinov, R., *Studies of protein-protein interfaces: a statistical analysis of the hydrophobic effect*. Protein Science, 1997. 6(1): p. 53-64.
8. Shoffner, M.A., Cheng, J., Hvichia, G.E., Kricka, L.J., and Wilding, P., *Chip PCR I. Surface passivation of microfabricated silicon-glass chips for PCR*. Nucleic Acids Research, 1996. 24(2): p. 375-379.
9. Woolley, A.T., Hadley, D., Landre, P., de Mello, A.J., Mathies, R.A., and Northrup, M.A., *Functional Integration of PCR Amplification and Capillary Electrophoresis in Microfabricated DNA Analysis device*. Analytical Chemistry, 1996. 68: p. 4081.
10. Anderson, R.C., Su, X., Bogdan, G.J., and Fenton, J., *A miniature integrated device for automated multistep genetic assays*. Nucleic Acids Research, 2000. 28(12): p. e60.
11. Giordano, B.C., Copeland, E.R., and Landers, J.P., *Towards dynamic coating of glass microchip chambers for amplifying DNA via the polymerase chain reaction*. Electrophoresis, 2001. 22(2): p. 334-340.
12. Khandurina, J., McKnight, T.E., Jacobson, S.C., Waters, L.C., Foote, R.S., and Ramsey, J.M., *Integrated system for rapid PCR-based DNA analysis in microfluidic devices*. Analytical Chemistry, 2000. 72(13): p. 2995-3000.
13. Lagally, E.T., Medintz, I., and Mathies, R.A., *Single-molecule DNA amplification and analysis in an integrated microfluidic device*. Analytical Chemistry, 2001. 73(3): p. 565-570.
14. Northrup, M.A., Benett, B., Hadley, D., Landre, P., Lehew, S., Richards, J., and Stratton, P., *A miniature analytical instrument for nucleic acids based on micromachined silicon reaction chambers*. Analytical Chemistry, 1998. 70(5): p. 918-922.

15. Poser, S., Schulz, T., Dillner, U., Baier, V., Kohler, J.M., Schimkat, D., Mayer, G., and Siebert, A., *Chip elements for fast thermocycling.* Sensors and Actuators a-Physical, 1997. 62(1-3): p. 672-675.

16. Taylor, T.B., Winn-Deen, E.S., Picozza, E., Woudenberg, T., and Albin, M., *Optimization of the performance of the polymerase chain reaction in silicon-based microstructures.* Nucleic Acids Research, 1997. 25(15): p. 3164-3168.

17. Giordano, B.C., Ferrance, J., Swedberg, S., Huhmer, A.F.R., and Landers, J.P., *Polymerase chain reaction in polymeric microchips: DNA amplification in less than 240 seconds.* Analytical Biochemistry, 2001. 291(1): p. 124-132.

18. Nagai, H., Murakami, Y., Morita, Y., Yokoyama, K., and Tamiya, E., *Development of a microchamber array for picoliter PCR.* Analytical Chemistry, 2001. 73(5): p. 1043-1047.

19. Trau, D., Lee, T.M.H., Lao, A.I.K., Lenigk, R., Hsing, I.-M., Ip, N.Y., Carles, M.C., and Sucher, N.J., *Genotyping on a complementary metal oxide semiconductor silicon polymerase chain reaction chip with integrated DNA microarray.* Analytical Chemistry, 2002. 74(13): p. 3168-3173.

20. Lee, T.M., Hsing, I.M., Lao, A.I., and Carles, M.C., *A miniaturized DNA amplifier: its application in traditional Chinese medicine.* Analytical Chemistry, 2000. 72(17): p. 4242-4247.

21. Lagally, E.T., Simpson, P.C., and Mathies, R.A., *Monolithic integrated microfluidic DNA amplification and capillary electrophoresis analysis system.* Sensors and Actuators B-Chemical, 2000. 63(3): p. 138-146.

22. Obeid, P.J., Christopoulos, T.K., Crabtree, H.J., and Backhouse, C.J., *Microfabricated device for DNA and RNA amplification by continuous-flow polymerase chain reaction and reverse transcription-polymerase chain reaction with cycle number selection.* Analytical Chemistry, 2003. 75(2): p. 288-295.

23. Henegariu, O., Heerema, N.A., Dlouhy, S.R., Vance, G.H., and Vogt, P.H., *Multiplex PCR: critical parameters and step-by-step protocol.* Bio Techniques, 1997. 23(3): p. 504-511.

24. Kreader, C.A., *Relief of Amplification Inhibition in PCR with Bovine Serum Albumin or T4 Gene 32 Protein.* Applied and Environmental Microbiology, 1996. 62(3): p. 1102-1106.

25. Rasmussen, S.R., Rasmussen, H.B., Larsen, M.R., Hoff-Jorgensen, R., and Cano, R.J., *combined polymerase chain reaction-hybridization microplate assay used to detect bovine leukemia virus and salmonella* molecular Pathology 1994. 40(2): p. 200-2005.

26. Schneegaß, I. and Koehler, J.M., *Flow-through polymerase chain reactions in chip thermocyclers* Molecular Biotechnology, 2001. 82: p. 101-121.

27 Drumheller, P.D. and Hubbell, J.A., *Densely crosslinked polymer networks of poly(ethylene glycol) in trimethlolpropane triaccrylate for cell-adhesion-resistant surfaces.* Journal of Biomedical Materials Reserach, 1995. 29(2): p. 207-215.

28 Popat, K.C. and Desai, T.A., *Poly(ethylene glycol) interfaces: an approach for enhanced performance of microfluidic systems.* Biosensors and Bioelectronics, 2004. 19: p. 1037-1044.

29. Popat, K.C., Johnson, R.W., and Desai, T.A., *Characterization of vapor deposited poly(ethylene glycol) films on silicon surfaces for surface modificationo of microfluidic systems* Journal of Vacuum Science & Technology B, 2003. 21(2): p. 645-654.

30. Beyer, D., Knoll, W., Ringsdorf, H., Wang, J.H., Timmons, B., and Sluka, A., *Reduced protein adsorption on plastics via direct plasma deposition of triethylene glycol monoallyl ether.* Journal of Biomedical Materials Research 1997. 36(2): p. 181-189.

31. Lou, X.J., Panaro, N.J., Wilding, P., Fortina, P., and Kricka, L.J., *Increased amplification efficiency of microchip-based PCR by dynamic surface passivation.* Biotechniques, 2004. 36(2): p. 248-252.

32. Krishnan, M., Burke, D.T., and Burns, M.A., *Polymerase Chain Reaction In High Surface-to-Volume Ratio SiO2 Microstructures.* Analytical Chemistry, 2004. 76(22): p. 6588-6593.

33. Munro, N.J., Huhmer, A.F.R., and Landers, J.P., *Robust polymeric microchannel coatings for microchip-based analysis of neat PCR products.* Analytical Chemistry, 2001. 73(8): p. 1784-1794.

34. Obeid, P.J. and Christopoulos, T.K., *Continuous-flow DNA and RNA amplification chip combined with laser-induced fluorescence detection.* Analytica Chimica Acta, 2003. 494(1-2): p. 1-9.

35. Koonjul, P.K., Brandt, W.F., Farrant, J.M., and Lindsey, G.G., *Inclusion of polyvinylpyrrolidone in the polymerase chain reaction reverses the inhibitory effects of polyphenolic contamination of RNA* Nucleic Acids Research, 1999(27): p. 915-916.

36. Horne, E.C., Kumpatla, S.P., Patterson, K.A., Gupta, M., and Thompson, A., *Improved High-throughput sunflower and cotton genomic DNA extraction and PCR fidelity.* Plant Molecular Biology Reporter, 2004. 22: p. 83a-83i.

37. Kopp, M.U., de Mello, A.J., and Manz, A., *Chemical amplification: Continuous-flow PCR on a chip.* Science, 1998. 280(5366): p. 1046-1048.

38. Clark, S.M. and Mathies, R.A., *Multiplex dsDNA fragment sizing using dimeric intercalation dyes and capillary array electrophoresis: Ionic effects on the stability and electrophoretic mobility of DNA-dye complexes.* Analytical Chemistry, 1997. 69(7): p. 1355-1363.

39. Schneegaß, I., Bräutigam, R., and Köhler, J.M., *Miniaturized flow-through PCR with different templates types in a silicon chip thermocycler.* Lab on a chip, 2001. 1(1): p. 42-49.
40. Panaro, N.J., Lou, X.J., Fortina, P., Kricka, L.J., and Wilding, P., *Surface Effects on PCR Reactions in Multichip Microfluidic Platforms.* Biomedical Microdevices, 2004. 6(1): p. 75-80.
41. Adamson, A.W. and Gast, A.P., *Physical Chemistry of Surfaces* 6th ed. 1997: Wiley-Interscience 784.
42. Decker, E.L., Frank, B., Suo, Y., and Garoff, S., *Physics of contact angle measurement.* Colloids and Surfaces A: Physicochemical and Engineering Aspects, 1999. 156(1-3): p. 177-189.
43. Bikerman, J.J., *Surface Chemistry.* 1948, New York: Academic Press 464.
44. Shibuichi, S., Yamamoto, T., Onda, T., and Tsujii, K., *Super water- and oil-repellent surfaces resulting from fractal structure.* Journal of colloid and interface science, 1998. 208(1): p. 287-294.
45. Erill, I., Campoy, S., Erill, N., Barbe, J.C., and Aguilo, J., *Biochemical analysis and optimization of inhibition and adsorption phenomena in glass-silicon PCR-chips.* Sensors and Actuators B, 2003. 96: p. 685-692.
46. Münchow, G., Dadic, D., Doffing, F., Hardt, S., and Drese, K.S., *Automated chip-based device for simple and fast nucleic acid amplification.* Expert Review of Molecular Diagnostics, 2005. 5(4): p. 613-20.
47. Popat, K.C. and Desai, T.A., *Poly(ethylene glycol) interfaces: an approach for enhanced performance of microfluidic systems.* Biosensors & bioelectronics, 2004. 19(9): p. 1037-1044.
48. Wilson, I.G., *Inhibition and facilitation of nucleic acid amplification.* Applied and environmental microbiology, 1997. 63(10): p. 3741-51.
49. Young, C.C., Burghoff, R.L., Keim, L.G., Minak-Bernero, V., Lute, J.R., and Hinton, S.M., *Polyvinylpyrrolidone-Agarose Gel Electrophoresis Purification of Polymerase Chain Reaction-Amplifiable DNA from Soils.* Applied and Environmental Microbiology, 1993. 59(6): p. 1972-1974.
50. Xia, Y.M., Hua, Z.S., Srivannavit, O., Ozel, A.B., and Gulari, E., *Minimizing the surface effect of PDMSglass microchip on polymerase chain reaction by dynamic polymer passivation.* Journal of chemical technology and biotechnology, 2007. 82(1): p. 33.

6

Development of Superhydrophobic Microfluidic Channels

In addition to the generation of hydrophobic surface coatings within microfluidic channels (presented in Chapter 5) novel superhydrophobic coating methods were applied to microfluidic channels for the first time. These novel materials were developed in collaboration with researchers at Nottingham Trent University. In this Chapter a description of the properties of superhydrophobic surfaces is presented. In addition, the methods and results of proof-of-principle experiments are described. Experiments were performed in two stages. First all coating methods were performed on bulk surfaces within a flow cell. These studies were followed by adaptation of defined protocols to microfluidic systems.

6.1 Background Theory

In simple terms a superhydrophobic surface differs from a hydrophobic surface in both its water repellent character and surface roughness. The combination of roughness and hydrophobicity critically influences the contact angles of water droplets on superhydrophobic surfaces (Figure 6.1).

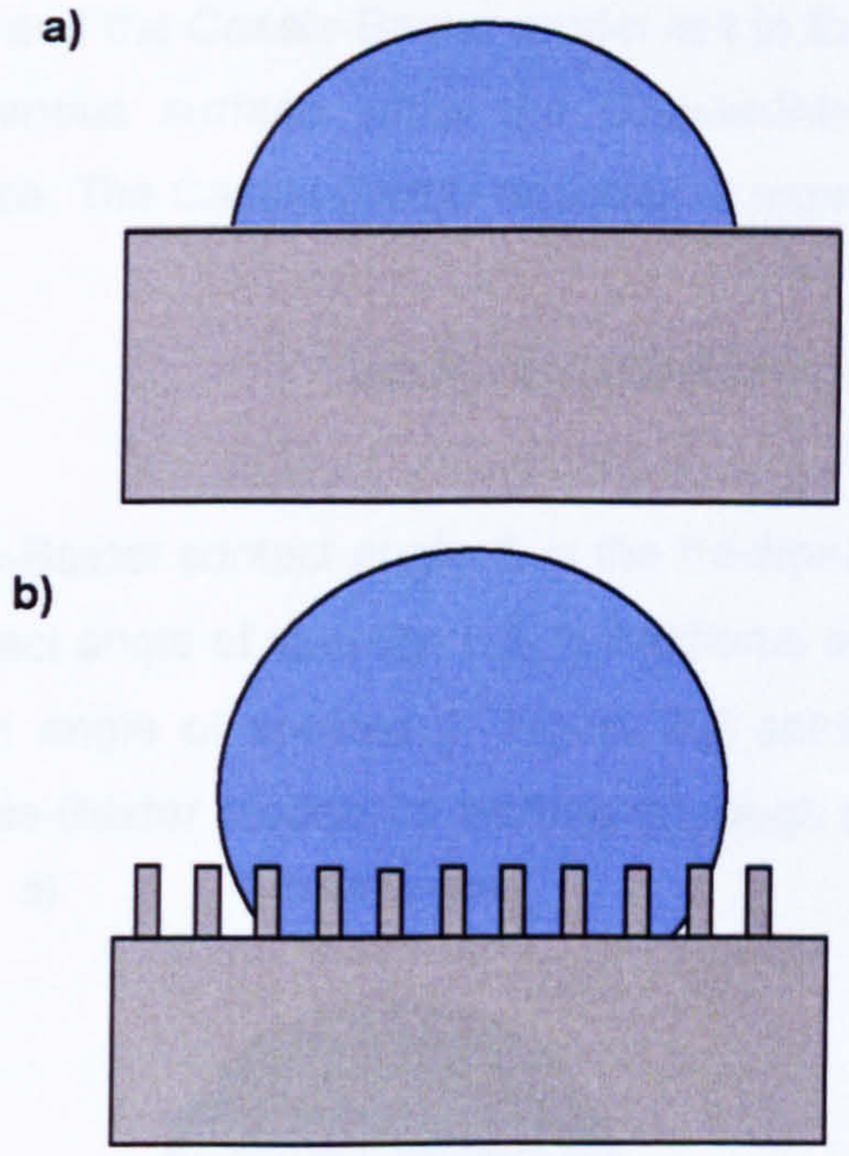


Figure 6.1 **(a) A water droplet spreads on a solid smooth surface. (b) A water droplet does not spread on a solid surface due to its roughness.**

While water contact angles on smooth homogenous surfaces are described by the Young - Laplace equation (Equation 5.2), Wenzel recognized that roughness also affects the surface wetting properties [1, 2]. This realization leads to the following equation.

$$\cos\theta_W = r\frac{\gamma_S - \gamma_{SL}}{\gamma_L} \tag{6.1}$$

$$\cos\theta_W = r\cos\theta_Y \tag{6.2}$$

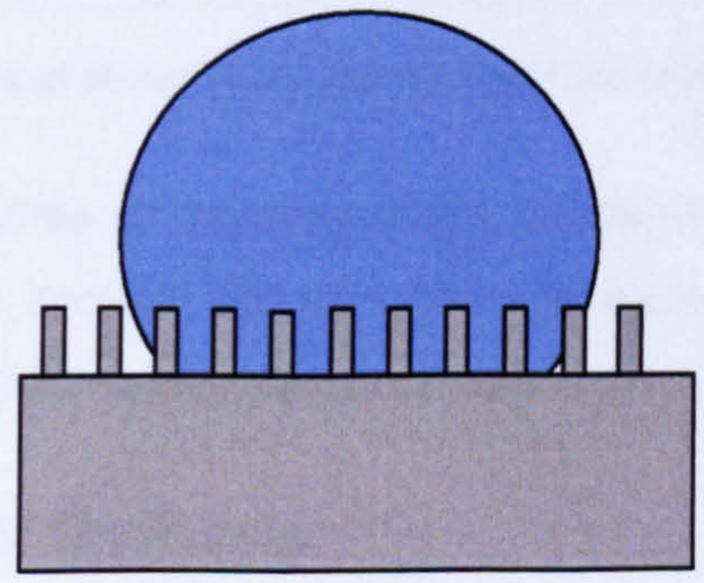
Here θ_W is the Wenzel contact angle and r is the roughness factor, which is defined as the ratio of the area of the actual surface to that of a smooth surface having the same geometric shape and dimensions, γ_S is the solid surface tension (J/m^2), γ_{SL} is the solid-liquid surface tension (J/m^2), γ_L is the liquid surface tension (J/m^2) and θ_Y is

the Young contact angle. Since r is always larger than unity, the surface roughness enhances both the hydrophilicity of a hydrophilic surface and the hydrophobicity of a hydrophobic surface. If the aspect ratio of the surface is low then liquid can follow the contours of the surface and a Wenzel model of wetting is observed. However if the aspect ratio is high then water tends to bridge between the tips of the surface structure [3] and a Cassie-Baxter model is observed (Figure 6.2). Another difference between the Wenzel and the Cassie-Baxter model lies in the fact the Wenzel model describes a homogenous surface while the Cassie-Baxter model describes a heterogeneous surface. The Cassie-Baxter equation is expressed according to.

$$\cos\theta_C = f_1 \cos\theta_1 + f_2 \cos\theta_2 \qquad (6.3)$$

Here θ_C is the Cassie-Baxter contact angle, f_1 is the fractional surface area occupied by species 1, φ_1 contact angle of species 1, f_2 is fractional surface area occupied by species 2, φ_2 contact angle of species 2. Figure 6.2 schematically illustrates the Wenzel and the Cassie-Baxter models for wetting on rough surfaces.

a) Wenzel model



b) Cassie-Baxter model

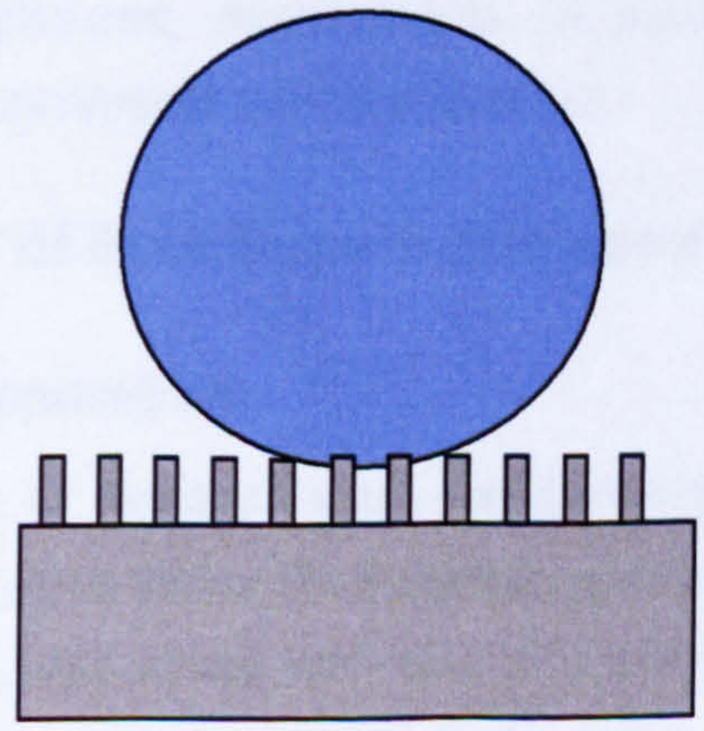


Figure 6.2 **(a) Wenzel model for a water droplet on a rough surface. (b) Cassie-Baxter model for a water droplet on a rough surface. Here water is only in contact with the tips of the surface.**

Using standard hydrophobic surface treatment methods water contact angles of 120° are readily achievable as described in Chapter 5. To create surfaces displaying higher water contact angles requires the introduction of new materials. Numerous studies on superhydrophobic materials have been performed. Table 6.1 presents a few examples reported in recent studies.

material	Contact angle	Reference
Al_2O_3	147°	[4]
TiO_2	148-156°	[5]
SiO_2 treated	114-160°	[6]
sol-gel	165°	[7]
ZnO	150°	[8]
rough PDMS	160°	[9]
polyphosphazene	159°	[10]
structured SiO_2	146-167°	[11]
CuO	150°	[12]

Table 6.1 **Examples of superhydrophobic materials found in literature.**

Additionally further studies on superhydrophobic behaviour can be found elsewhere [13-18]. The following section will describe the experimental procedures used to create surfaces displaying superhydrophobicity.

6.2 Experimental Methods

As noted experiments were performed in two stages. For each set of experiments surface coating procedures, assessments of successful surface coatings and surface adsorption experiments will be described.

6.2.1 Generation of Bulk Superhydrophobic Surfaces

6.2.1.1 Surface Preparation

Three different types of surfaces were used in these experiments. These were standard microscope glass slides (Sail Brand), copper sheets (Goodfellow, UK) and silica sol-gel coated glass slides with two different pore sizes. All three types of surface were treated in such a way that hydrocarbon (C-H) and fluorocarbon (C-F)

terminated surfaces were created. In total 8 different surfaces were created. The following section describes how these surfaces were created and treated.

6.2.1.1.1 Superhydrophobic Surfaces on Glass

Prior to chemical treatment microscope slides were sonicated in ethanol for 10 - 15 minutes. Sol-gel films were prepared as previously reported [19] by mixing methyltriethoxysilane (Alfa Aesar 98%, UK), aqueous HCl (diluted to 0.37% from Fisher 37%, UK) and a solvent (5:3:5). The mixture was stirred for 1 hr and then added to an aqueous ammonia solution (Fisher, 35%). The large grained sol-gel was prepared using ethylene glycol (Fisher, 99%) as the solvent and 0.9 M ammonia solution. The small grained material was prepared using dimethylformamide (Acros 99%, UK) as the solvent and a 3.6 M ammonia solution. A 0.4 ml aliquot of the gel solution was then cast between two glass slides using glass cover slips as a spacer. Prior to contact the top slide was made hydrophobic using a fluorocarbon coating (Grangers Wash-in solution) to facilitate removal after 6 hours without causing damage to the hardened sol-gel film. The larger grained sol-gel material was generated by the removal of an upper layer of smaller particles. Films were heated at 2°C min^{-1} to 500°C for 1 hour in a furnace and allowed to cool slowly. This heat treatment both dried the surfaces and rendered them hydrophilic, allowing further coatings to adhere. Figure 6.3 shows electron micrographs of large sol-gel particles and Figure 6.4 shows electron micrographs of small sol-gel particles.

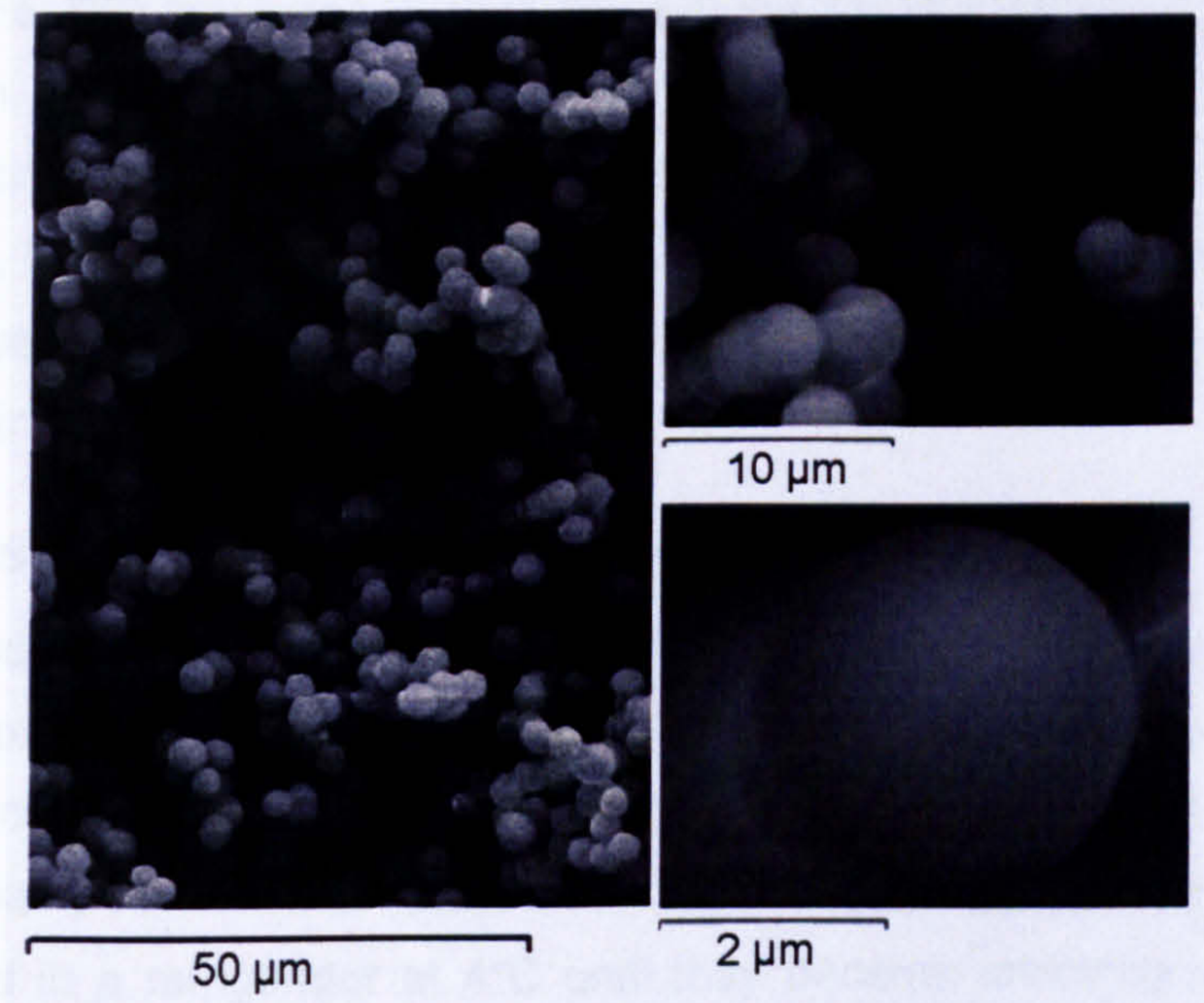


Figure 6.3 **Electron micrographs of the larger scale sol-gel material taken with a reflection electron microscope (JEOL,GSM) with an acceleration voltage of**

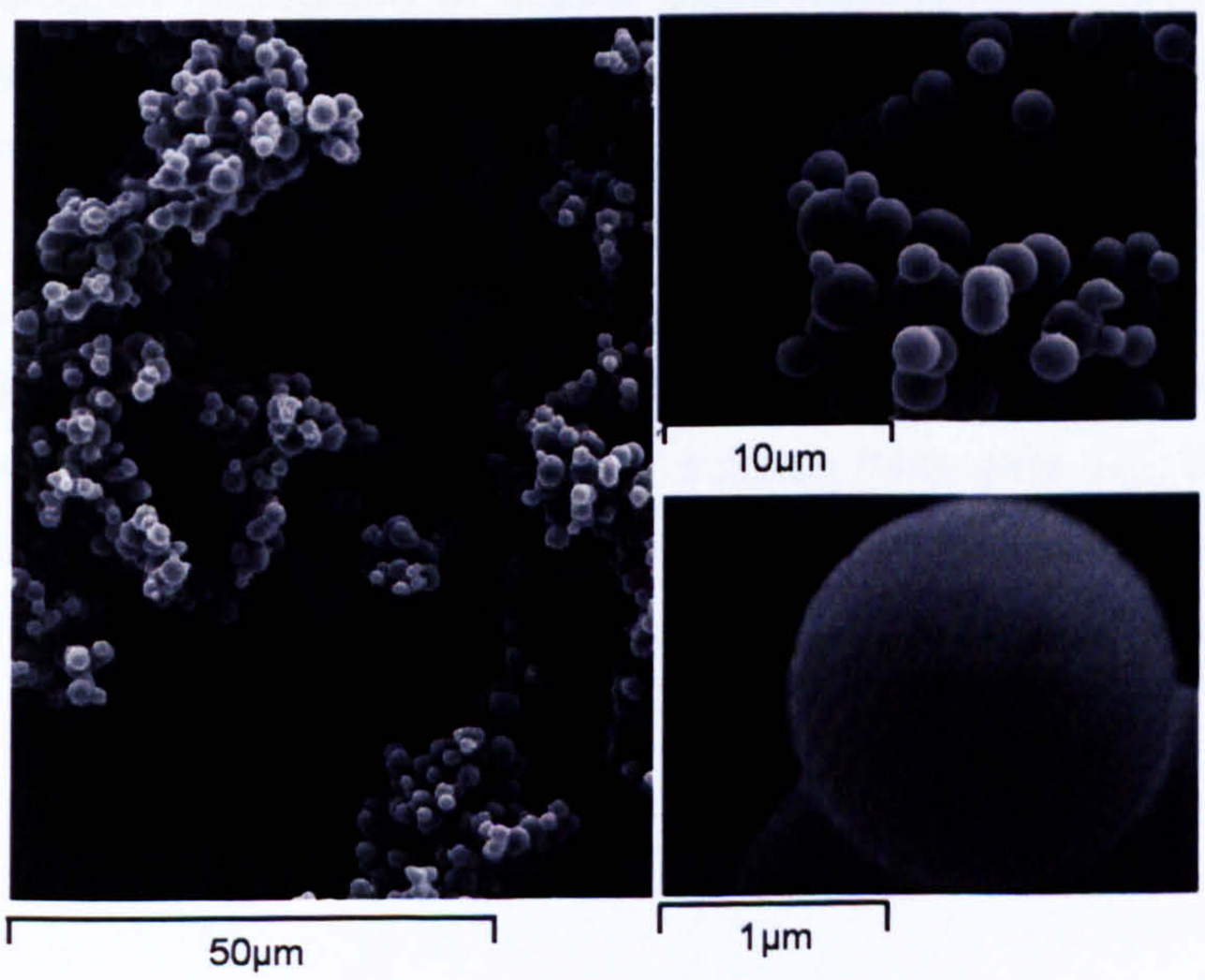


Figure 6.4 **Electron micrographs of the smaller scale sol-gel material taken with a REM (same conditions as Figure 6.3).**

Successful sample production was followed by the generation of hydrocarbon and fluorocarbon terminated surfaces. Hydrocarbon terminated surfaces were prepared

by placing samples in a glass slide holder, immersed in 2% vol. octyltriethoxysilane (ABCR 95%, DE) in toluene (Fisher, low sulphur, UK) for 24 hours. Treated samples were then rinsed in toluene and air dried before use. For the creation of fluorocarbon terminated layers, samples were placed in 'Grangers Wash-in' solution (Grangers, UK) diluted 1:9 with distilled water for 10 minutes, rinsed thoroughly with distilled water and blown dry in a stream of nitrogen before being heated to 100°C for 1 hour in a vacuum oven.

6.2.1.1.2 Superhydrophobic Surfaces on Copper

Copper oxide nano-needles were created on copper sheets according to the following procedure. Copper sheets (Goodfellow, UK) were cut to the size of standard microscope slides (76 X 26 mm) and sonicated in ethanol for 10 - 15 minutes. Samples were then placed in a 36 mM ammonia solution in a slide holder and placed in a refrigerator at 4°C until they became uniformly coated in copper hydroxide nanoneedles (Figure 6.5). The time required for this varied according to the number of samples and the volume of the solution. Surfaces were then heated in a furnace at 1°C min^{-1} from room temperature to 180°C in air and held for 3 hours, so that copper oxide was formed and the sheets turned black. Figure 6.6 shows an electron micrograph of copper oxide nanoneedles. Successful sample production was followed by generation of hydrocarbon and fluorocarbon terminated surfaces. Hydrocarbon terminated surfaces were prepared by placing samples in a glass slide holder, immersed in 2% vol. octyltriethoxysilane (ABCR 95%, DE) in toluene (Fisher, low sulphur, UK) for 24 hours. Treated samples were then rinsed in toluene and air dried before use. For the creation of fluorocarbon terminated layers, samples were placed in 'Grangers Wash-in' solution (Grangers, UK) diluted 1:9 with distilled water for 10 minutes, rinsed thoroughly with distilled water and blown dry in a stream of nitrogen before being heated to 100°C for 1 hour in a vacuum oven.

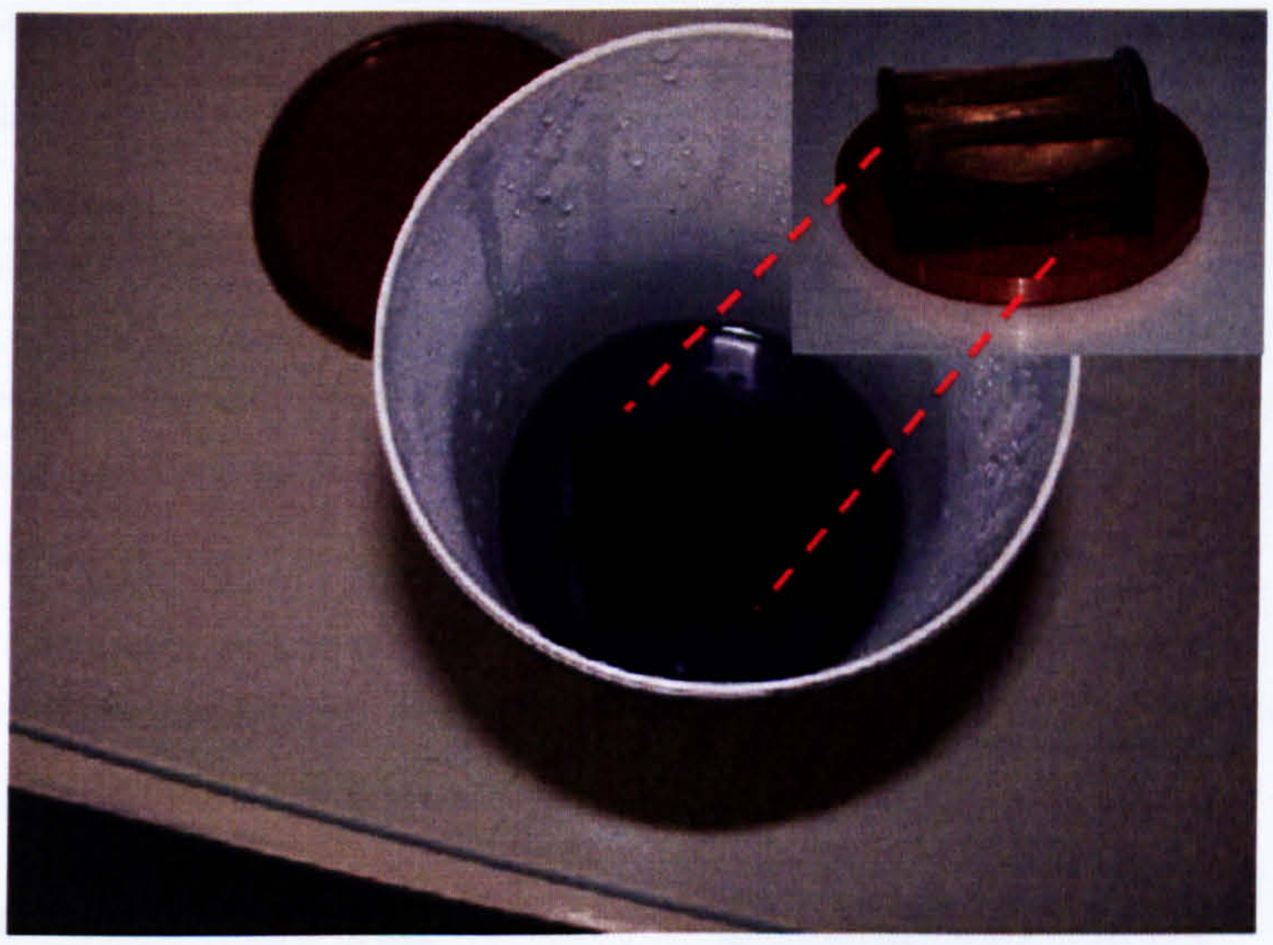


Figure 6.5 **Copper slides in slide holder soaked in 36 mM ammonia solution at 4°C.**

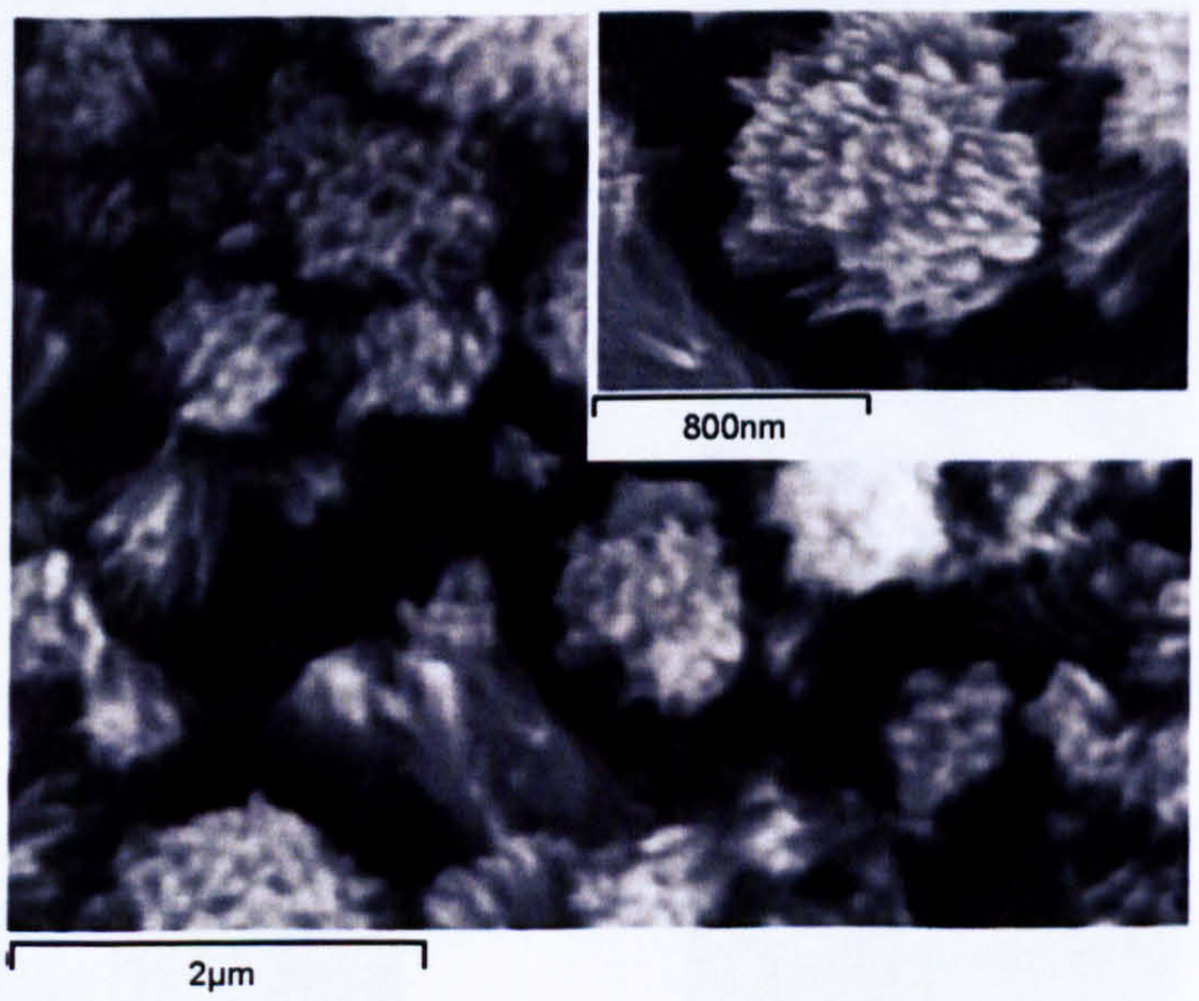


Figure 6.6 **Electron micrographs of copper oxide nano-needles taken with a REM (JEOL,GSM) with an acceleration voltage of 20kV.**

6.2.1.1.3 Assessment of Water Contact Angles on Bulk Surfaces

The assessment of successful superhydrophobic surface generation was performed by measuring contact angles of water droplets on the treated surfaces as described in Section 5.1.1.2.1. Values for water contact angles are presented in Table 6.2. Figure 6.7 presents images of water droplets on all structured surfaces.

surface	treatment	contact angle
glass	C-H	111.5°±1.5
	C-F	117.4°±1.6
Sol-Gel	C-H	145.4°±1.4
	C-F	145.5°±1.5
Cu-O	C-H	165°±1.4
	C-F	165°±1.6

Table 6.2 **Contact angles of 2 µl water droplets on structured surfaces. C-H represents the hydrocarbon terminated surfaces while C-F represents the fluorocarbon terminated surfaces.**

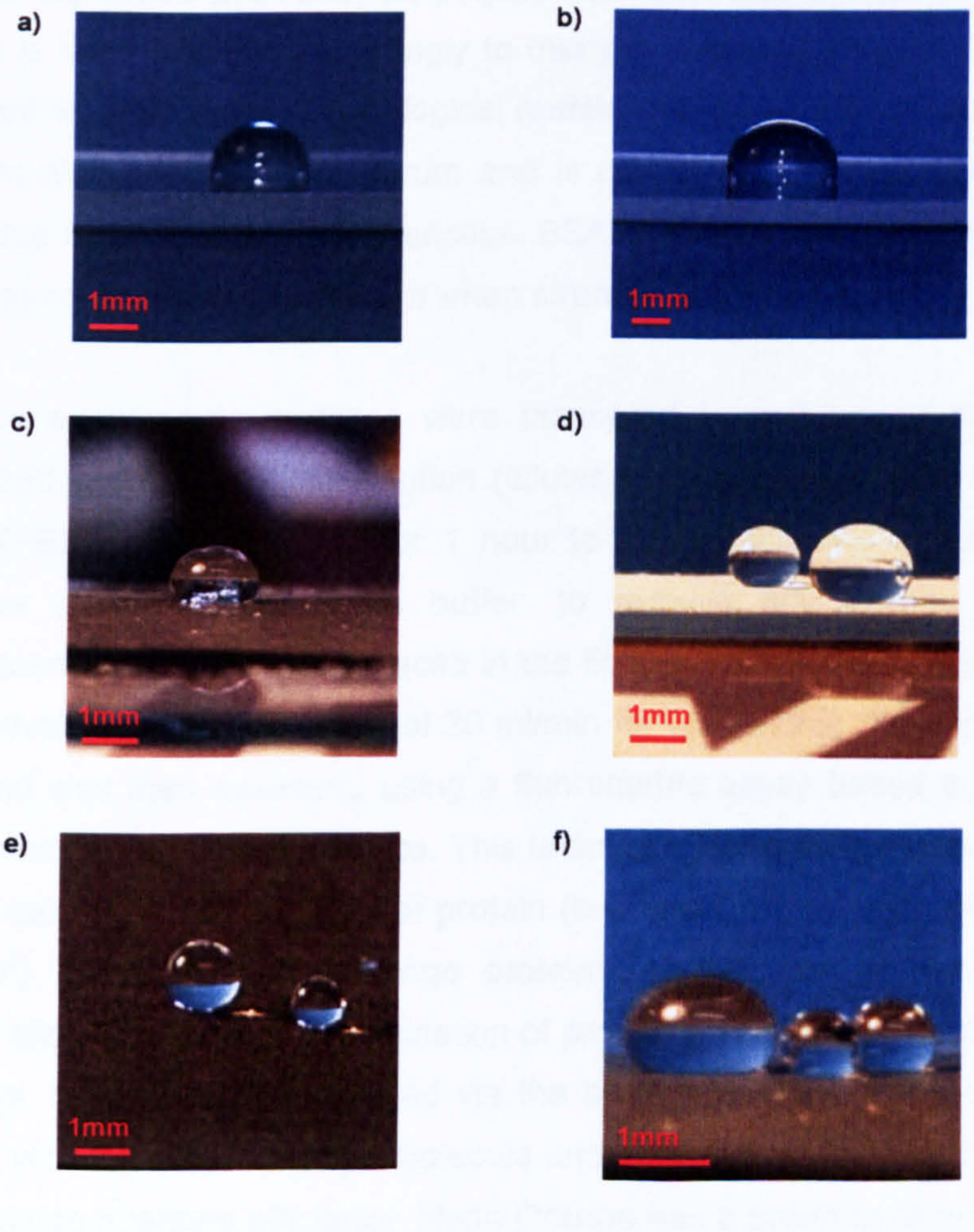


Figure 6.7 **2 µl water droplets on treated surfaces: (a) glass with a hydrocarbon terminated surface shows a contact angle of 112° (b) glass with a fluorocarbon terminated surface shows a contact angle of 117° (c) sol-gel with a hydrocarbon terminated surface shows a contact angle of 145° (d) sol-gel with a fluorocarbonated surface shows a contact angle of 145° (e) copper with hydrocarbon terminated surface shows a contact angle of 165° (f) copper with a fluorocarboanted surface shows a contact angle of 165°.**

While water droplets partially wet the treated glass surfaces, water droplets on sol-gel and copper surfaces generate spherical shapes with the highest contact angles observed on copper surfaces.

6.2.1.2 Surface Adsorption Experiments on Bulk Surfaces

As demonstrated in Chapter 5, a successful PCR within a microfluidic device was accomplished when the interaction between the DNA polymerase enzyme and the channel walls is suppressed allowing minimal adsorption or interaction of the DNA polymerase with the channel walls. Initial surface adsorption assessment studies were performed using a well studied protein, bovine serum albumin (BSA), rather than the expensive DNA enzyme polymerase. BSA was chosen as a model protein since it is known to adhere strongly to many surfaces [20-25]. Additionally, it is an important additive in various biological reactions such as PCR (see Chapter 2), it is found in high abundance in serum and is commonly used as a surface blocking agent due to its binding characteristics. BSA is approximately 15 nm in size, but is known to conformationally deform when strongly adhered [26].

In these experiments surfaces were incubated in a 2 mg/ml BSA (fraction V, lyophilized powder, Aldrich) solution (diluted in freshly prepared phosphate buffer saline (PBS tablets, GIBCO) for 1 hour to ensure maximum protein adsorption. Samples were then rinsed in buffer, to remove any loosely bound protein. Subsequently, samples were placed in the flow cell (Figure 6.8) and buffer solution flowed over them at a flow rate of 20 ml/min for 30 minutes. The amount of protein adsorbed was then assessed using a fluorometric assay based on Nano Orange, after detachment from the surface. This technique has been previously shown to be able to quantify small amounts of protein (less than a monolayer on a surface of a few cm^2) [27]. The Nano Orange protein quantification kit (Molecular Probes, N6666) allowed accurate determination of protein concentration in the range of 0.1 - 10 µg/ml. Detection was achieved via the binding of Nano Orange fluorophore to protein, with the surfactant dye molecule undergoing a dramatic enhancement in its fluorescence quantum efficiency. Nano Orange has a broad excitation peak centred at 470 nm and a broad emission peak centred at 570 nm. The working solution was prepared as per the manufacturer's instructions, using a concentrated (500X) Nano Orange protein quantitation diluent. A 22 ml Nano Orange working solution was prepared as follows: 2.1 ml of 10 X diluent solution was mixed with 18.9 ml of deionized water and 42 µl of 500 X Nano Orange reagent. Surface-bound protein was then detached from the rinsed samples following the reported method [27], by

three sequential rinse cycles of 250 µl undiluted ethanol followed by 250 µl of deionized water (six rinses in total). All wash solutions were collected, and the solvent evaporated to dryness using a speed-vacuum concentrator (Stratech Scientific, London). To each tube, 280 µl of Nano Orange working solution was added and vortex stirred for 20 minutes. The samples were heated at 96 °C for 10 minutes to ensure that all proteins were denatured. This was followed by cooling to room temperature and a final vortex to ensure homogeneity. 250 µl of each sample was pipetted into a 96-well plate (Fisher) and analyzed using a Spectra Fluor microplate reader (Tecan), with excitation/emission wavelengths set at 485/595 nm and 3-10 flashes per well with a 40 µs integration time.

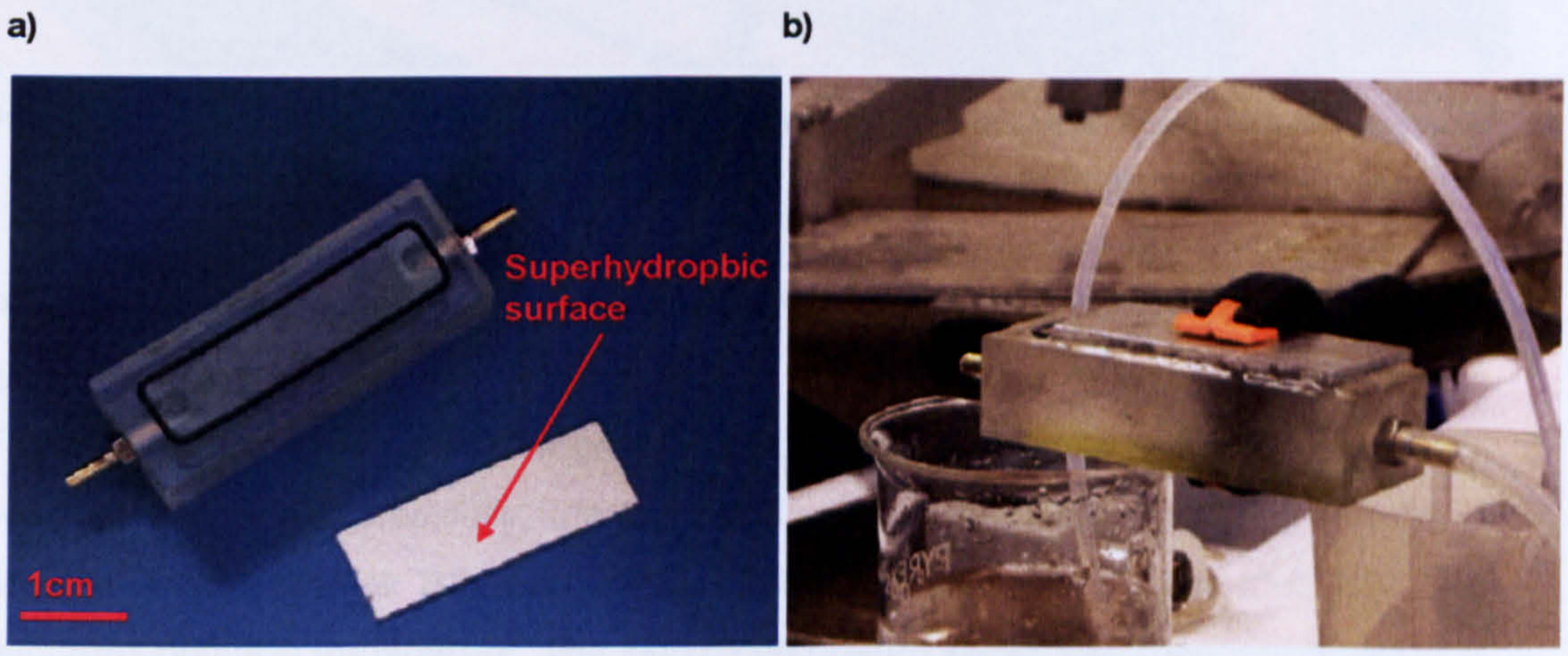


Figure 6.8 **Flow cell chamber 1500 µm wide and 500 µm deep. (a) the opened flow cell and exposed sol-gel surface, (b) the flow cell assembly during use.**

6.2.2 Generation of Superhydrophobic Surfaces in Microchannels

6.2.2.1 Surface Preparation

In this set of experiments the adsorption of PCR components on superhydrophobic microchannel surfaces was assessed for the first time. Six parallel channels, 218 µm wide and 78 µm deep, were etched into glass substrates (see Chapter 3). Superhydrophobic surfaces were created using the following procedure. First a 10 nm thick titanium layer and a 80 nm thick copper or zinc layer were sputtered onto the etched slides using an Emitech (K575X) coater with argon gas and a current of 105 mA. The set-up is presented in Figure 6.9.

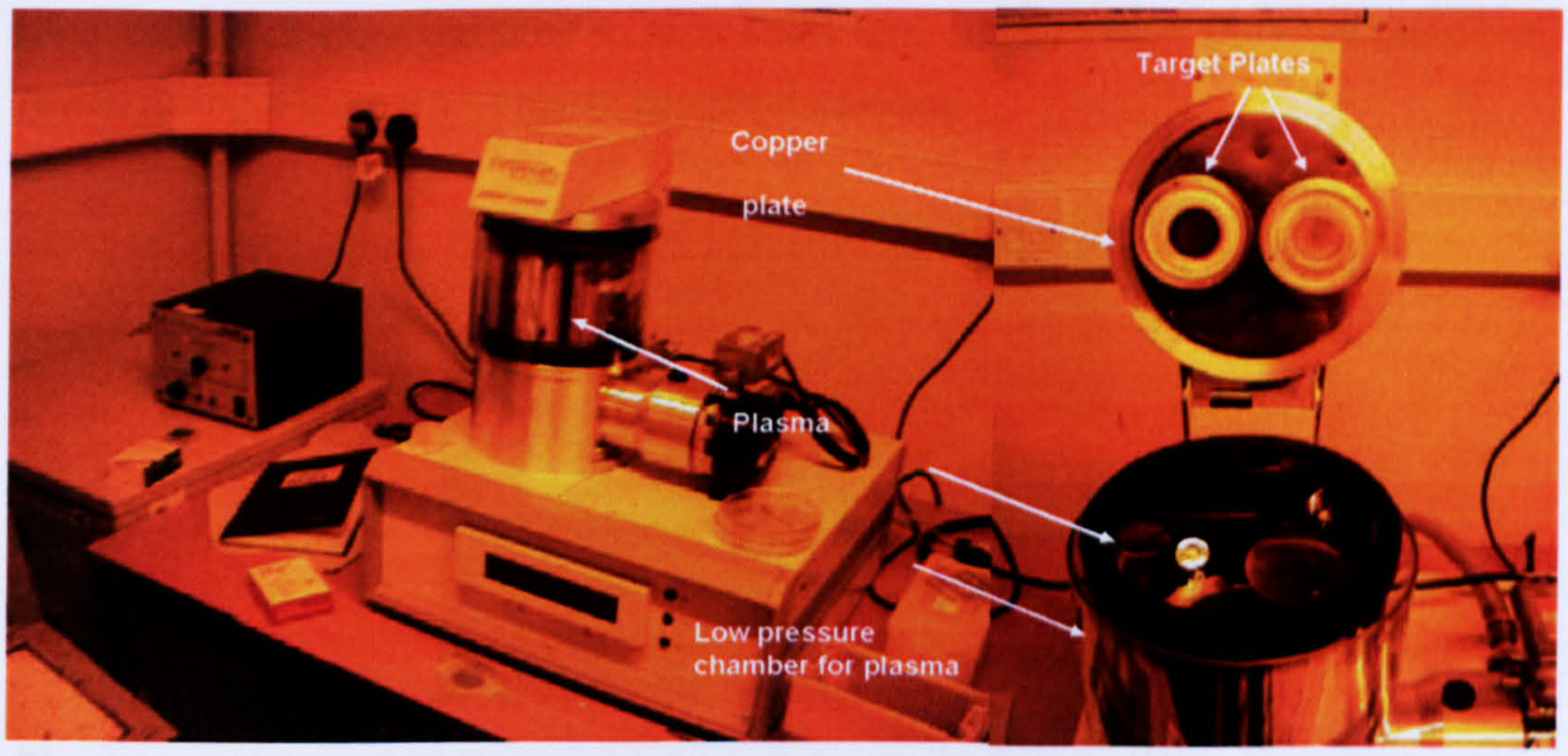


Figure 6.9 **Photograph of the sputtering system at Nottingham Trent University. Glass microscope slides are coated with both titanium and copper films.**

Prior to surface treatment the copper (or zinc) nano-needles were created. First a nanocrystalline seed layer is formed. This is then converted to a nano-needle layer. Figure 6.10 illustrates the change in substrate properties as the nanocrystalline seed layer forms. Specifically, the zinc coated glass substrate heated for about 1 hour at a temperature between 60 and 80°C, so that the surface oxidized and becomes optically transparent. The zinc oxide coated substrates then immersed in a solution containing 0.1 M zinc nitrate and 0.1 M hexamine for 4 hours at a temperature of 90 °C to allow the growth of nanoneedles on the substrate surface. This is a well documented process, and is described in detail elsewhere [28-30].

As microchannels had been etched into the glass substrates, three walls (of a complete channel) could be accessed and coated easily. Traditionally microchannels are sealed using a top glass plate and thermal bonding. As discussed in Chapter 3, both the cover plate and the microchannel substrate are normally washed in acid prior to thermal bonding. In the current studies such a wash is problematic since the acid would dissolve the oxide surface. Accordingly, it was necessary to seek an alternative bonding method. A sandwich structure was created for this purpose, incorporating a 2 μm layer of SU-8 as an adhesive. A 70% SU-8 solution in 1-methoxy-2-propanol acetate was prepared and spin-coated (for 30 seconds at 4000 rpm) onto the glass coverplate. The glass-SU-8 double layer was then brought into contact with the substrate containing the microchannels, followed by a pre-baking step at 60 °C for one hour in order to remove all solvent. This process was followed by UV exposure for 30 seconds at 40 $mJcm^{-2}$ and post-

baking on a hot-plate at 90 °C for one hour to polymerize the SU-8. Subsequently silica capillaries were attached to form inlets and outlets which were connected to Teflon tubing. Figure 6.11 depicts complete devices.

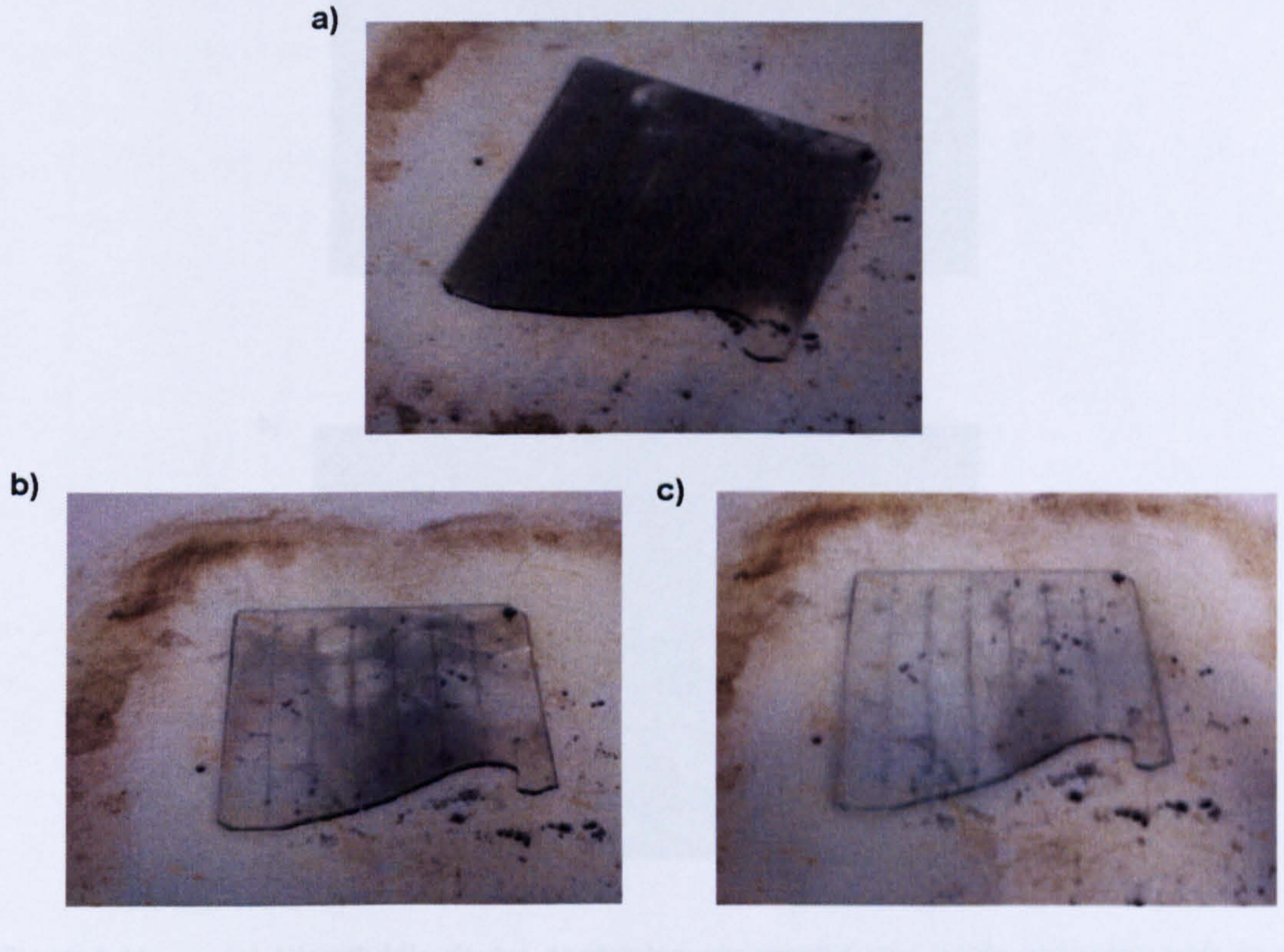
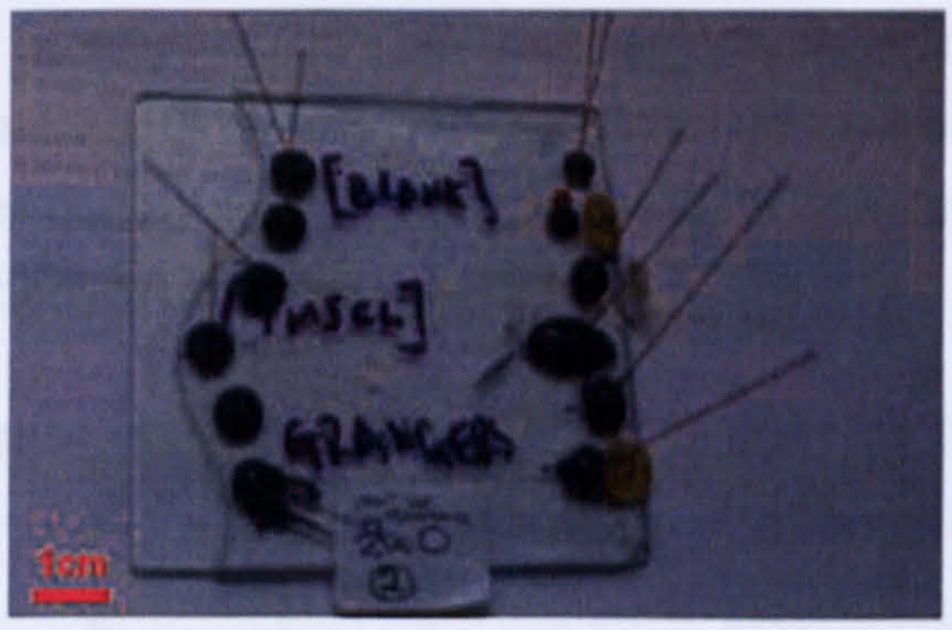


Figure 6.10 **Images of glass substrates sputtered with Zinc. (a)-(c) present different oxidization stages of Zinc with (c) being the completely oxidized state, visible when glass substrate becomes transparent.**

a)



b)



Figure 6.11 **(a) Microfluidic device containing six parallel zinc oxide channels: with two untreated channels, two hydrocarbon terminated surface channels and two fluorocarbon terminated surface channels. (b) Microfludic device containing six parallel copper oxide channels: two untreated channels, two hydrocarbon terminated surface channels and two fluorocarbon terminated surface channels.**

6.2.2.2 Assessment of Water Flow Profiles in Treated Microchannels

The assessment of wettability within microfluidic channels performed by measuring flow profiles of water as previously described in 5.1.1.2.2. Water flow profiles in ZnO and CuO coated channels presented in Figure 6.12. A strong influence on the water flow profiles in CuO channels as a function of surface coating is observed. The water flow profile in the untreated copper oxide channel exhibit a contact angle of approximately 90° and thus significant interaction of water with the channel walls. The water profile for the hydrocarbon terminated channel shows a more curved meniscus profile, with a contact angle of approximately 120°, suggesting considerably less contact with the channel walls. The water profile for the fluorocarbon terminated channel shows even less contact between water and the

channel walls. A contact angle in excess of 150° is measured. However, it should be noted that the water profiles for ZnO coated channels show little variation and an average water contact angle of 90° with significant interaction of water with the channel walls. Water in fluorocarbon terminated CuO channels shows the least interaction with the channel walls.

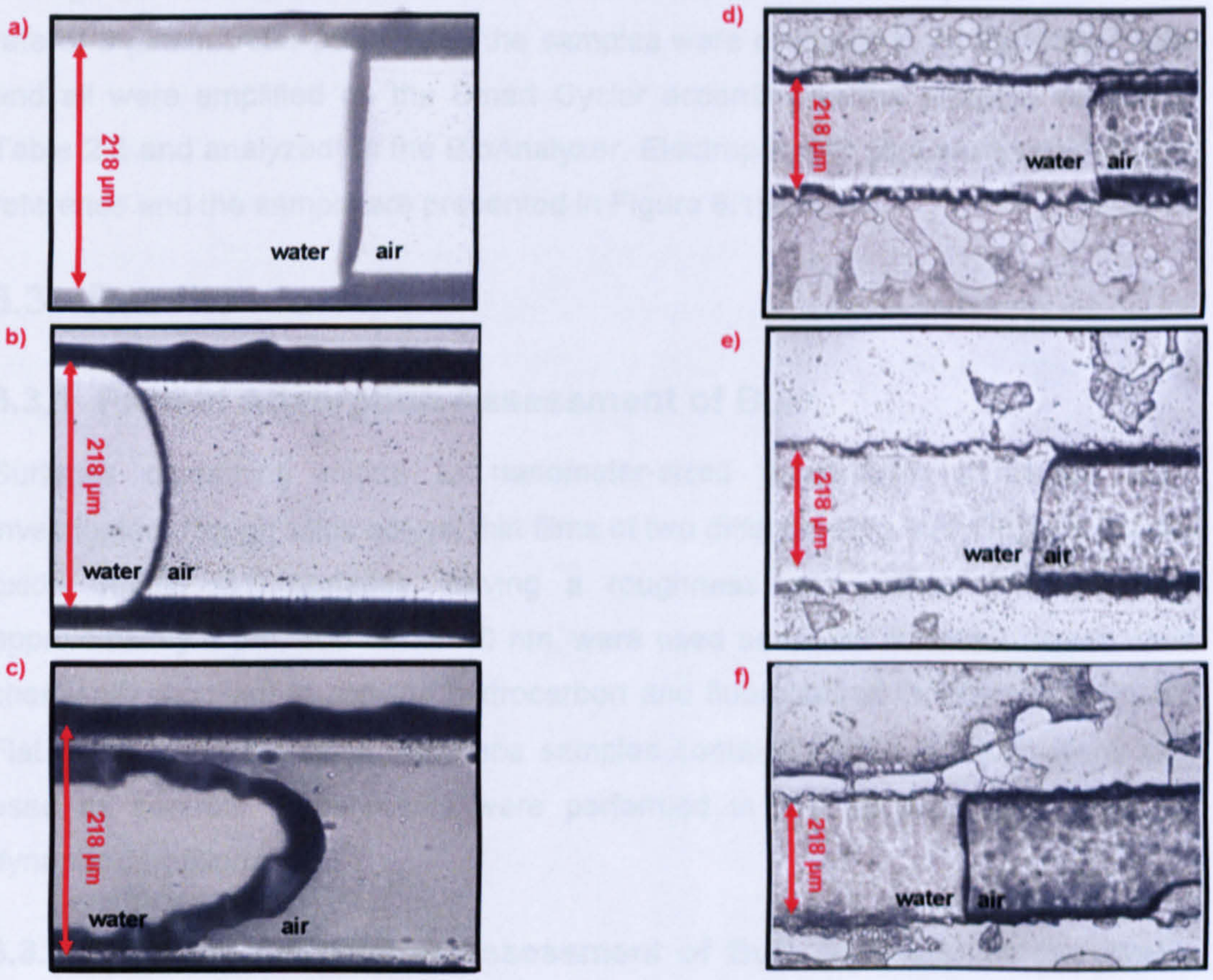


Figure 6.12 **Water flow profiles in CuO and ZnO channels. (a) presents water in an untreated CuO channel with a contact angle of 90°, (b) presents water in a hydrocarbon terminated CuO channel with a contact angle of 120°, (c) presents water in a fluorocarbon terminated CuO channel with a contact angle of 150°, (d) presents water in an untreated ZnO channel with a contact angle of 90°, (e) presents water in a hydrocarbon terminated ZnO channel with a contact angle of 90°, (f) presents water in a fluorocarbon terminated ZnO channel with contact angle of 90 °.**

6.2.2.3 Surface Adsorption Experiments in Microchannels

The broad aim of the experiments described in this chapter was to create a microfluidic device containing superhydrophobic surfaces. It was hoped that the reduced interaction between fluid and surface would improve PCR efficiency. To

assess this conjecture, the same experiments as in 5.1.1.1.1 were performed. A 550µl PCR mix was prepared according to the recipe described in Table 2.2 with 4X enzyme concentration and 100X dNTP concentration. After the mix was prepared, it was split into seven parts; the reference and six samples. While the reference was kept outside the PCR chip, in a closed Eppendorf tube, the sample was pumped through the six different coated microfluidic channels at room temperature at a flow rate of 3 µl/min. After 30 minutes the samples were collected in an Eppendorf tube and all were amplified on the Smart Cycler according to the protocol defined in Table 2.3 and analyzed on the BioAnalyzer. Electrophoretic size analysis of all, the reference and the sample are presented in Figure 6.15.

6.3 Results

6.3.1 Protein Adsorption Assessment of Bulk

Surfaces containing micro- to nanometer-sized topographic structures were investigated. Rough silica sol-gel thin films of two different pore sizes [3] and copper oxide needle [31] surfaces, having a roughness with critical dimensions of approximately 4 µm, 800 nm or 10 nm, were used as model surfaces. These were chemically modified to provide hydrocarbon and fluorocarbon terminated surfaces. Flat copper and flat silica reference samples containing both coatings were also used as controls. Experiments were performed in two stages; under static or dynamic conditions.

6.3.1.1 Protein Adsorption Assessment of Bulk Surfaces Under Static Conditions

Figure 6.13 describes the variation of protein adsorption under static conditions as a function of surface composition. In this set of experiments glass slides with hydrocarbon and fluorocarbon terminated surfaces were used as references. While in Chapter 5 it was demonstrated that the generation of hydrophobic surfaces will reduce the protein adsorption, literature [32-38] has shown that the generation of hydrophilic surface will reduce the adsorption of proteins. Figure 6.13 supports this behaviour for glass surfaces with hydrocarbon and fluorocarbon terminated surfaces. Here the amount of adsorbed protein on fluorocarbon terminated surfaces is higher than the amount of adsorbed protein on hydrocarbon surfaces.

Additionally, it can be seen that similar amounts of albumin adsorb to hydrocarbon terminated flat glass and nano-structured copper oxide surfaces, whilst sol-gel surfaces exhibit significantly higher adsorption. When, comparing the different pore

size sol-gel surfaces it is apparent that the smaller pore size sol-gel (~800 nm particle size and 4 μm pore size) exhibit less protein adsorption than the large pore size sol-gel (4 μm particle size and 20 μm pore size) material. A possible explanation for this behaviour is that the pressure in the system combined with the surfactant nature of the protein used is sufficient to significantly penetrate the structure of the larger pored material, presenting a larger available surface area for adsorption [4]. Comparison of hydrocarbon and fluorocarbon terminated rough surfaces demonstrates that the structured fluorocarbon surfaces show considerably lower protein adsorption than the equivalent hydrocarbon terminated surfaces. For fluorocarbon surfaces the increased hydrophobicity will result in a lower interfacial surface area available for protein adsorption. It can be concluded that the copper surfaces with both coatings were the most resistant to protein adhesion under static conditions allowing a coverage of only 40 $ngcm^{-2}$ in the case of fluorocarbon terminated surface and 24 $ngcm^{-2}$ in the case of hydrocarbon terminated surfaces.

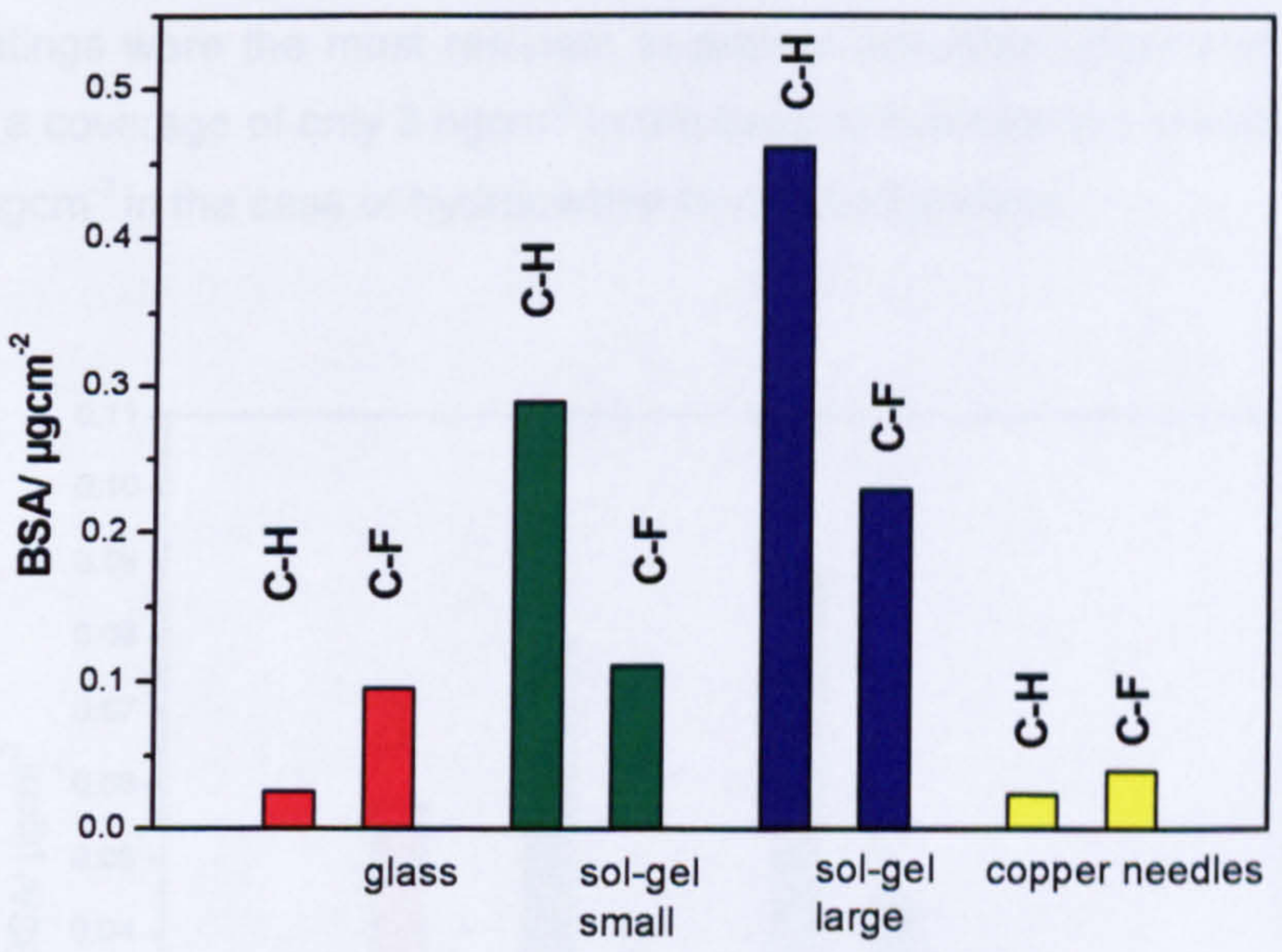


Figure 6.13 **Albumin adsorption onto micro-scale and nano-scale surfaces which are hydrocarbon or fluorocarbon terminated, under static conditions.**

6.3.1.2 Protein Adsorption Assessment of Bulk Surfaces Under Dynamic Conditions

Figure 6.14 presents an assessment of protein adsorption onto structured surfaces under dynamic conditions. It can be seen that a proportion of the adsorbed protein is removed from all surfaces under flow conditions. Considerably greater amounts of

protein, however, were lost from the superhydrophobic sol-gel surfaces than from flat surfaces (reference), with the amount remaining being lower on surfaces with successively smaller structure. This suggests that although such micro-structures are large compared to the size of protein molecules, they have a strong effect on protein retention under flow. Interfacial slip may be primarily responsible for this behaviour. Indeed Rodahl and Kasemo [39] have argued that interfacial slip may be related to the shear stress acting on a substrate surface due to a liquid. Consequently, if interfacial slip is present in the current system, high shear-fields will be created around the edges of contact areas, and induce protein desorption, leaving the centres of the contact areas unchanged. Comparison of the data from hydrocarbon and fluorocarbon terminated surfaces indicates a higher degree of desorption on fluorocarbon terminated surfaces. This effect is particularly apparent for smaller structured surfaces, where higher shear fields are expected. Fluorinated nano-structured copper oxide surfaces became almost completely clear of protein, whereas equivalent flat surfaces (reference) only lose around 10 - 20% of their protein. It can therefore be concluded that the nano-structured copper surfaces with both coatings were the most resistant to protein adhesion under static conditions, allowing a coverage of only 3 $ngcm^{-2}$ in the case of fluorocarbon terminated surface, and 12 $ngcm^{-2}$ in the case of hydrocarbon terminated surface.

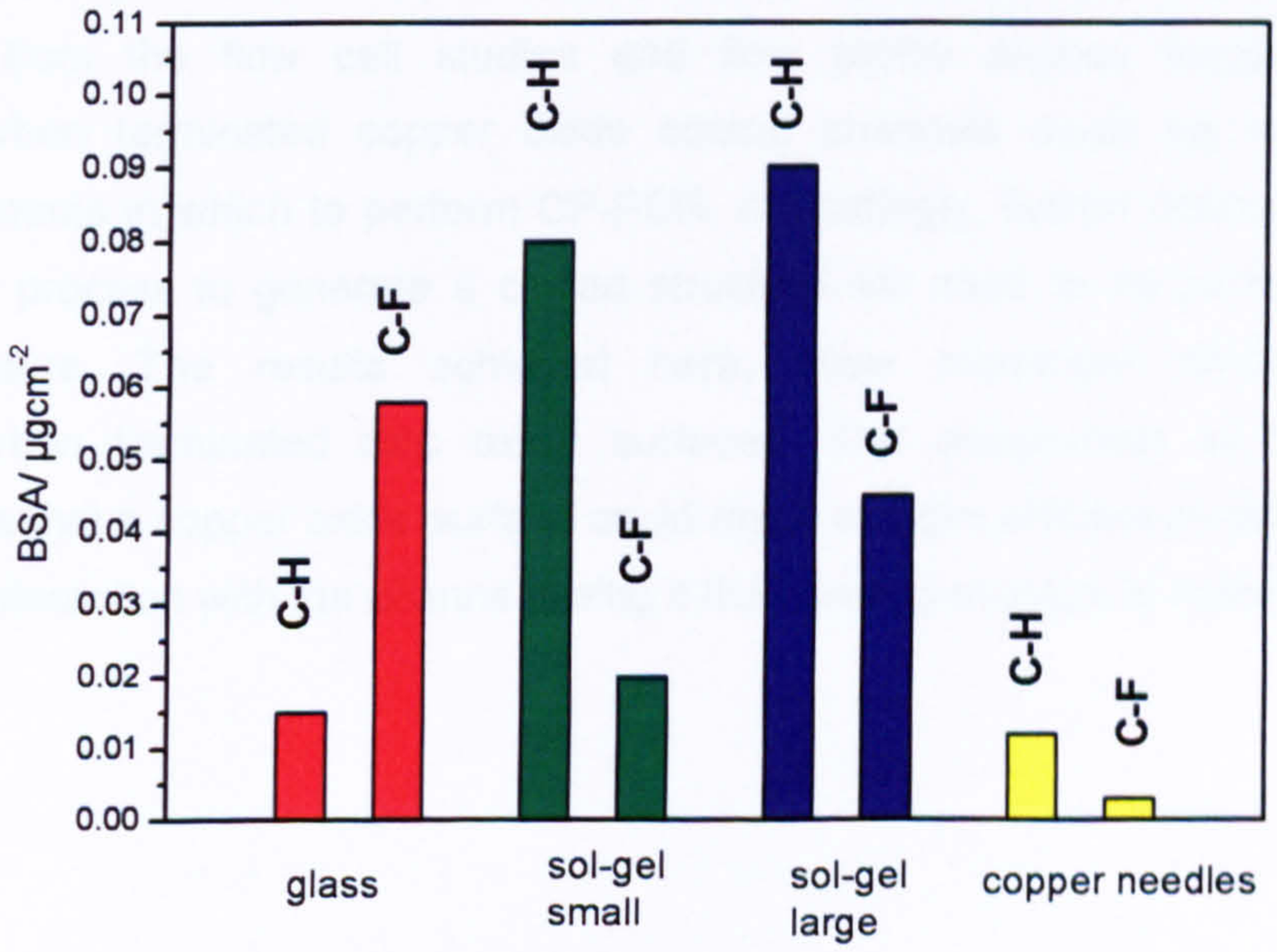


Figure 6.14 **Albumin adsorption onto micro-scale and nano-scale surfaces which are hydrocarbon or fluorocarbon terminated under dynamic conditions**

It is unclear from these measurements if the reduced protein adsorption at nano-structured surfaces is due to the reduced contact area between protein molecules and the surface due to the small size of the tips of the nano-pillars and their roughness. With the almost complete removal of protein from some of the superhydrophobic surfaces under flow conditions, the goal of creating microchannel surfaces exhibiting minimal interaction with proteins during continuous flow was achieved.

6.3.2 Protein Adsorption Assessment in Surface Treated Microchannels

Figure 6.15 presents BioAnalyzer data for the analysis of product generated by CF-PCR in an untreated glass channel, an untreated zinc oxide channel, a hydrocarbon terminated zinc oxide channel, a fluorocarbon terminated zinc oxide channel and an untreated copper oxide channel. Electrophoretic size analysis shows no amplification on the untreated copper oxide channel while all other samples show amplification. Product concentrations of 2.59, 4.85, 5.0 and 5.47 ng/µl for the reference, untreated zinc oxide, hydrocarbon terminated zinc oxide and fluorocarbon terminated zinc oxide channels respectively are obtained. Due to leakage problems with the hydrocarbon and fluorocarbon terminated copper oxide coated channels, it was not possible to generate PCR data at the current time. Therefore only untreated copper oxide channels could be tested. However, previous results from the flow cell studies and flow profile studies suggest that the fluorocarbon terminated copper oxide coated channels could be very effective environments in which to perform CF-PCR. Accordingly, further optimization of the bonding process to generate a closed structure will need to be performed in the near future. The results achieved here, show maximum amplification for fluorocarbon terminated zinc oxide surfaces. The comparison of flow profiles suggests that a copper oxide surface could result in more efficient amplification (due to less interaction with the channel walls) if the bonding process is optimized.

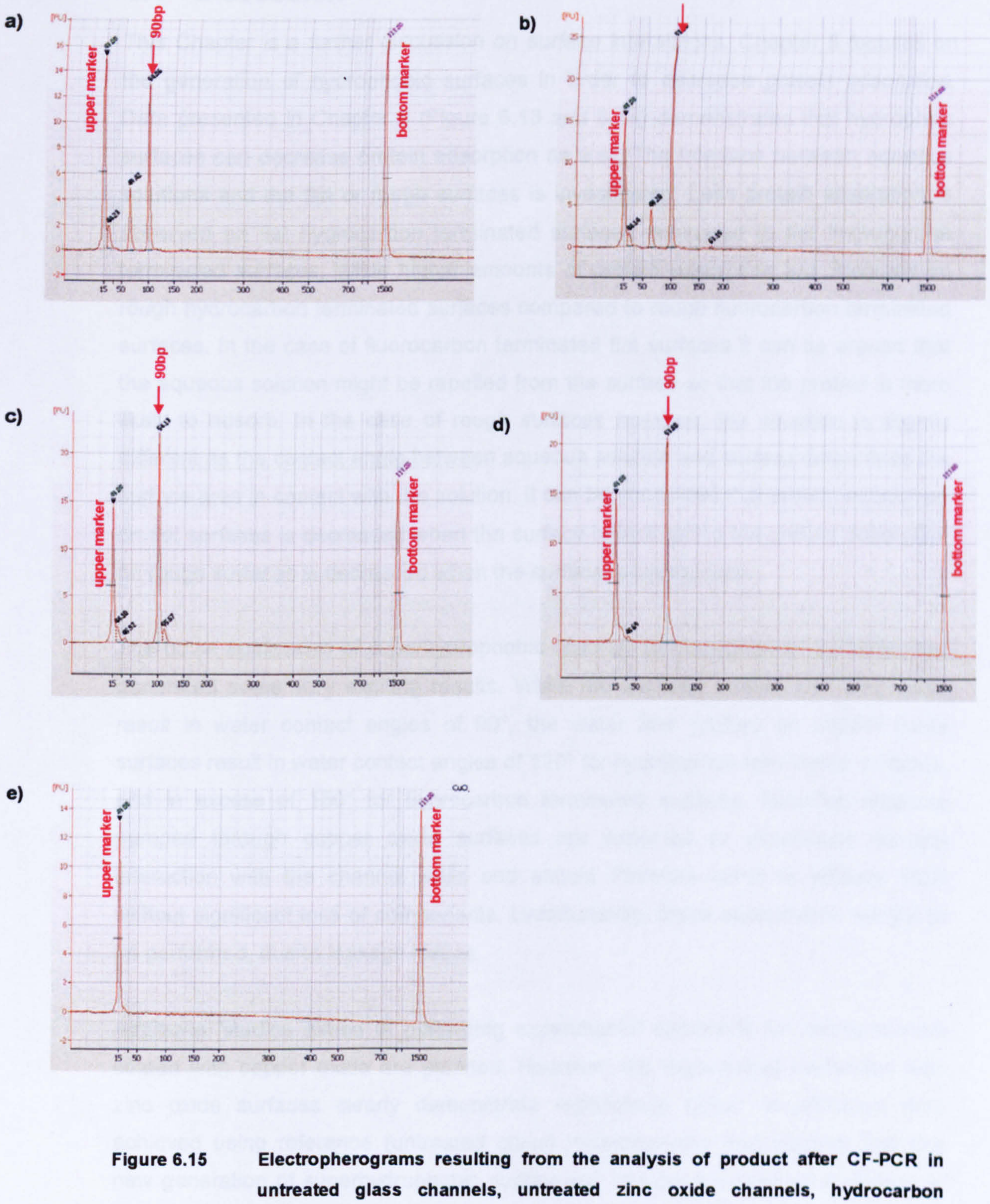


Figure 6.15 **Electropherograms resulting from the analysis of product after CF-PCR in untreated glass channels, untreated zinc oxide channels, hydrocarbon terminated zinc oxide channels, fluorocarbon terminated zinc oxide channels and untreated copper oxide channels.**

6.4 Discussion

This Chapter is a further discussion on surface interactions. Chapter 5 focuses on the generation of hydrophobic surfaces in order to decrease protein adsorption. Data presented in Chapter 6 (Figure 6.13 and 6.14) demonstrates that hydrophilic surfaces can decrease protein adsorption as well. The interface between aqueous solutions and the flat or rough surfaces is investigated. Less protein adsorption is observed on flat hydrocarbon terminated surfaces compared to flat fluorocarbon terminated surfaces. While higher amounts of protein adsorption are observed on rough hydrocarbon terminated surfaces compared to rough fluorocarbon terminated surfaces. In the case of fluorocarbon terminated flat surfaces it can be argued that the aqueous solution might be repelled from the surface so that the protein is more likely to adsorb. In the case of rough surfaces however, the situation is slightly different as the contact angle between aqueous solution and surface determines the surface area in contact with the solution. It can be concluded that protein adsorption on flat surfaces is decreased when the surface is hydrophilic but protein adsorption on rough surfaces is decreased when the surface is hydrophobic.

The novel application of superhydrophobic coatings to microchannel surfaces, has generated some very exciting results. While the surfaces coated with zinc oxide result in water contact angles of 90°, the water flow profiles on copper oxide surfaces result in water contact angles of 120° for hydrocarbon terminated surfaces, and in excess of 150° for fluorocarbon terminated surfaces. Reaction mixtures pumped through copper oxide surfaces are expected to experience minimal interaction with the channel walls and should therefore result in efficient PCR without significant loss of components. Unfortunately, these experiments are yet to be performed, due to leakage issues.

Additional studies aimed at optimizing experimental conditions for microchannels coated with copper oxide are planned. However, the experiments performed with zinc oxide surfaces clearly demonstrate significantly higher amplification than achieved using reference (untreated glass) microchannels and suggest that this new generation of superhydrophobic surface will improve the reaction efficiency of PCR on the microscale.

1. Wenzel, R.N., *Resistance of solid surfaces to wetting by water* Industrial & Engineering Chemistry Research, 1936. **28**(8): p. 988-994.
2. Cassie, A.B.D. and Baxter, S., *Wettability of porous surfaces* Transactions of the Faraday Society, 1944. **40**: p. 546-551.
3. Shirtcliffe, N.J., McHale, G., Newton, M.I., Perry, C.C., and Roach, P., *Porous materials show superhydrophobic to superhydrophilic switching.* Chemical Communications, 2005. **25**: p. 3135-3137.
4. Miwa, M., Nakajima, A., Fujishima, A., Hashimito, K., and Watanabe, T., *Effects of the surface roughness on sliding angles of water droplets on superhydrophobic surfaces.* Langmuir, 2000. **16**(13): p. 5754-5760.
5. Nakajima, A., Hashimito, K., Watanabe, T., Takai, K., Yamauchi, G., and Fujishima, A., *Transparent superhydrophobic thin films with self-cleaning properties.* Langmuir, 2000. **16**(17): p. 7044-7047.
6. Furstner, R., Barthlott, W., and Neinhuis, C., *Wetting and self-cleaning properties of artificial superhydrophobic surfaces.* Langmuir, 2005. **21**(3): p. 956-961.
7. Shang, H.M., Wang, Y., and Takahashi, K., *Nanostructured superhydrophobic surfaces.* Journal of materials science, 2005. **40**(13): p. 3587-3591.
8. Wu, X., Zheng, L., and Wu, D., *Fabrication of superhydrophobic surfaces from microstructured ZnO-based surfaces via a wet-chemical route.* Langmuir, 2005. **21**(7): p. 2665-7.
9. Jin, M.H., Feng, X.J., Xi, J.M., Zhai, J., Cho, K.W., Feng, L., and Jiang, L., *Super-hydrophobic PDMS surface with ultra-low adhesive force.* Macromolecular rapid communications, 2005. **26**(22): p. 1805-1809.
10. Allcock, H.R., Steely, L.B., and Singh, A., *Hydrophobic and superhydrophobic surfaces from polyphosphazenes.* Polymer international, 2006. **55**(6): p. 621-625.
11. Pozzato, A., Dal Zilio, S., Fois, G., Vendramin, D., Mistura, G., Belotti, M., Chen, Y., and Natali, M., *Superhydrophobic surfaces fabricated by nanoimprint lithography.* Microelectronic Engineering, 2006. **83**(4-9): p. 884-888.
12. Wu, X.F. and Shi, G.Q., *Production and characterization of stable superhydrophobic surfaces based on copper hydroxide nanoneedles mimicking the legs of water striders.* The journal of physical chemistry. B, Condensed matter, materials, surfaces, interfaces & biophysical, 2006. **110**(23): p. 11247-11252.
13. Pilotek, S. and Schmidt, H., *Wettability of microstructured hydrophobic sol-gel coatings.* Journal of sol-gel science and technology, 2003. **26**(1-3): p. 789-792.
14. Marmur, A., *The lotus effect: Superhydrophobicity and metastability.* Langmuir, 2004. **20**(9): p. 3517-3519.
15. Patankar, N.A., *Mimicking the lotus effect: Influence of double roughness structures and slender pillars.* Langmuir, 2004. **20**(19): p. 8209-8213.
16. Gao, L.C. and McCarthy, T.J., *How Wenzel and Cassie were wrong.* Langmuir, 2007. **23**(7): p. 3762-3765.

17. Lafuma, A. and Quere, D., *Superhydrophobic states.* Nature Materials, 2003. **2**(7): p. 457-460.
18. Callies, M. and Quere, D., *On water repellency.* Soft Matter, 2005. **1**(1): p. 55.
19. Shirtcliffe, N.J., McHale, G., Newton, M.I., and Perry, C.C., *Intrinsically superhydrophobic organosilica sol-gel foams* Langmuir, 2003. **19**: p. 5626-5631.
20. Anzai, J., Guo, B., and Osa, T., *Quartz-crystal microbalance and cyclic voltammetric studies of the adsorption behaviour of serum albumin on self-assembled thiol monolayers possessing different hydrophobicity and polarity.* Bioelectrochemistry and Bioenergetics, 1996. **40**(1): p. 35-40.
21. Nasir, A. and McGuire, J., *Sequential and competitive adsorption of bovine serum albumin and beta-lactoglobulin, and their resistance to exchange with alpha-lactalbumin and beta-casein.* Food hydrocolloids, 1998. **12**(1): p. 95-103.
22. Su, T.J., Lu, J.R., and Thomas, R.K., *Effect of pH on the adsorption of bovine serum albumin at the silica water interface studied by neutron reflection.* The journal of physical chemistry. B, Materials, surfaces, interfaces & biophysical, 1999. **103**(18): p. 3727-3736.
23. do Serro, A., Fernandes.A.C., and Saramago, B.D.V., *Bovine serum albumin adsorption on titania surfaces and its relation to wettability aspects.* Journal of biomedical materials research, 1999. **46**(3): p. 376-381.
24. Lu, J.R., Su, T.J., and Penfold, J., *Adsorption of serum albumins at the air/water interface.* Langmuir, 1999. **15**(20): p. 6975-6983.
25. Roach, P., Farrar, D., and Perry, C.C., *Interpretation of Protein Adsorption: Surface-Induced Conformational Changes.* Journal of American Chemical Society, 2005. **127**(22): p. 8168-8173.
26. Roach, P., Farrar, D., and Perry, C.C., *Surface tailoring for controlled protein adsorption: Effect of topography at the nanometer scale and chemistry.* Journal of American Chemical Society, 2006. **128**(12): p. 3939-3945.
27. Roach, P., Shirtcliffe, N.J., Farrar, D., and Perry, C.C., *Quantification of Surface-Bound Proteins by Fluorometric Assay: Comparison with Quartz Crystal Microbalance and Amido Black Assay.* The journal of physical chemistry. B, Condensed matter, materials, surfaces, interfaces & biophysical, 2006. **110**(41): p. 20572-20579.
28. Sun, X.H., Lam, S., Sham, T.K., Heigl, F., Jurgensen, A., and Wong, N.B., *Synthesis and synchrotron light-induced luminescence of ZnO nanostructures: Nanowires, nanoneedles, nanoflowers, and tubular whiskers.* The journal of physical chemistry. B, Condensed matter, materials, surfaces, interfaces & biophysical, 2005. **109**(8): p. 3120-3125.
29. Zhang, J., Yang, Y.D., Xu, B.L., Jiang, F.H., and Li, J.P., *Shape-controlled synthesis of ZnO nano- and micro-structures.* Journal of Crystal Growth, 2005. **280**(3-4): p. 509-515.

30. Sounart, T.L., Liu, J., Voigt, J.A., Hsu, J.P., Spoerke, E.D., Tian, Z., and Jiang, J.B., *Sequential nucleation and growth of complex nanostructured films.* Advanced functional materials, 2006. **16**(3): p. 335-344.
31. Wen, X., Zhang, W., and Yang, S., *Synthesis of Cu(OH)2 and CuO nanoribbon arrays on a copper surface* Langmuir, 2003. **19**: p. 5898-5903.
32. Grinnell, F., Feld, M.K., *Fibronectin Adsorption on Hydrophilic and Hydrophobic Surfaces Detected by Antibody Binding and Analyzed during Cell Adhesion in Serum-containing Medium*, The Journal of Biological Chemistry, 1982. **257**: p. 4888-4893.
33. Nicholls, A., Sharp, K.A., Honig, B., *Protein Folding and Association: Insights From the Interfacial and Thermodynamic Properties of Hydrocarbons*, Proteins: Structure, Function and Bioinformatics, 19991. **11**: p. 218-296.
34. Lenk, T.J., Horbett, T.A., Ratner, B.D., *Infrared Spectroscopic Studies of Time-Dependent Changes in Fibronigen Adsorbed to Polyurethanes*, Langmuir, 1991. **7**: p. 1755-1764.
35. Kasemo, B., *Biological Surface Science.* Current Opinion in Solid State & Materials Science, 1998. **3**: p. 451-459
36. Sigal, G.B., Mrksich, M., Whitesides, G.M., *Effect of Surface Wettability on the Adsorption of Proteins and Detergents.* Journal of American Chemical Society, 1998. **120**: p. 3464-3473.
37. Puleo, D.A., Nanci, A., *Understanding and Controlling the Bone-Implant Interface.* Biomaterials, 1999. **20**: p. 2311-2321.
38. Ta, T.C., McDermott, M.T., *Mapping Interfacial Chemistry Induced Variations in Protein Adsorption with Scanning Force Microscopy.* Analytical Chemistry, 2000. **72**: p. 2627-2634.
39. Rodahl, M. and Kasemo, B., *On the measurement of thin liquid overlayers with the quartz-crystal microbalance.* Sensors and Actuators A: Physical, 1996. **54**(1-3): p. 448-456.

7

Discussion

This chapter presents a discussion on the outcomes in all chapters and an outlook for future development of CF-PCR on the microscale. The ultimate goal of the studies presented in this thesis was to perform CF-PCR in a glass microfluidic device. This was established by first studying the robustness of the reaction on the macroscale (Chapter 2). Chapter 3 described studies optimizing the fabrication of microfluidic devices. These investigations were supplemented by the direct determination of fluidic temperatures in microchannels (Chapter 4) and the optimisation of surface chemistries in Chapter 5. Finally, Chapter 6 introduced the use of superhydrophobic coatings on microchannel surfaces to increase PCR efficiency.

The results presented in Chapter 2 constitute an operational framework for PCR of *Bacillus globigii* on the macroscale and were used to infer conditions that would allow efficient PCR on the microscale. Results from Section 2.3.2 provided important guidelines for Taq Polymerase concentrations. As the loss of Taq Polymerase on microchannel walls is a major problem when performing CF-PCR, it was necessary to increase the Taq Polymerase concentration within the PCR mix. The studies performed in Section 2.3.2.2 enabled determination of the upper limit of Taq Polymerase concentration which resulted in inhibition of PCR. With this knowledge it was possible increase the Taq Polymerase concentration and perform efficient CF-PCR. No other major variations of reagent concentrations had to be performed for an efficient CF-PCR.

Methods and techniques for the fabrication of glass microfluidic systems were presented in Chapter 3. During the etching with a buffered oxide etch (BOE) significant non-uniformity of the channel surfaces due to adsorption of impurities was observed. Impurity adsorption was observed after only one hour of etching. Use of a non-buffered etchant solution was therefore used to allow the fabrication of uniform channel surfaces. However, an hourly refreshment of this solution was required to ensure uniform etch rates over the time course of the process.

In Chapter 4 direct determination of fluidic temperatures in microfluidic channels was presented for the first time. The use of Fluorescence Lifetime Imaging enable precise temperature assessment to an accuracy of less than 1°C. To ensure CF-PCR operates in an efficient manner it is important that the PCR reaction mixture experiences specific temperatures for defined time periods. Experiments utilising FLIM enabled measurement of temperature in a variety of microchannels and allowed investigation of three-dimensional temperature distributions. Using this novel method it was possible to determine the ideal device geometry and ideal experimental conditions (i.e. applied temperature and applied volumetric flow rate) for efficient CF-PCR.

In Chapter 5 adsorption issues encountered on glass microchannel walls when performing CF-PCR were investigated. Numerous surface coatings are applied to the glass channels with the aim of surface passivation. While surface coatings with PEG, BSA or PVP did not lead to successful CF-PCR, microfluidic devices coated with silane I, Teflon and silane II resulted in successful amplification of *Bacillus globigii.* The contact angles of water profiles measured in microchannels coated

with PEG, BSA and PVP were estimated to be 98°±2, 88 °±3 and 100°±2 respectively, while the contact angles of water profiles measured in microchannels coated with silane I, Teflon and silane II are 101°±2,104°±2 and 122°±2 respectively. Not only were the contact angles of water profiles measured in PEG, BSA or PVP coated channels smaller than for microchannels coated with silane I, Teflon and silane II, the PEG, BSA and PVP coatings were not stable at elevated temperatures. Accordingly, a passivated surface (for these coatings) could not be generated during CF-PCR and loss of Taq Polymerase on the microchannel walls led to failure of the reaction.

Amplification achieved using silane I coated microfluidic devices is less efficient than amplification performed on the conventional thermal cycler. Contact angles of flow profiles measured in silane I coated microchannels are 101°±2. This suggests that contact between the reaction mixture and the channel walls is reduced to some extent, but such contact was observed in flow profile measurements. Additionally successful coatings were only achieved 15% of the time. Considering the water contact angles achieved with silane I coated microchannels it was concluded that performing CF-PCR in an efficient manner without significant loss of Taq Polymerase would be unlikely.

Similar observations were made for CF-PCR on Teflon coated microchannels. The amplification efficiency using Teflon coated microchannels was lower than the amplification efficiency on a conventional thermal cycler. The water contact angles measured in a Teflon coated microchannel were approximately 104°±2 and suggest significant interaction of the PCR reaction mixture with the microchannel walls. This results in a loss of Taq Polymerase and reduced amplification. This coating needs further optimization in order to increase the amplification efficiency. However, the low contact angles measured in these coated channels indicate that some loss of Taq Polymerase will still occur.

CF-PCR performed on microchannels coated with silane II show higher amplification efficiencies than amplification performed on a conventional thermal cycler. Contact angles of water flow profiles measured in silane II coated microchannels are 122°±2 and result in reduced contact between the PCR mix and the channel walls. The loss of Taq Polymerase on the channel walls is certainly minimized, and combined with the high surface area-to-volume ratios highly efficient PCR is achievable. Even though efficient CF-PCR could be performed using this

approach, a significant drawback is the coating lifetime. A microfluidic device coated with silane II could only be used in nine repetitive runs, until complete blockage of the channels occurs. Although this is an impressive achievement, it is not clear if further optimization of the coating structure could result in an extended lifetime.

An alternative approach to this challenge was presented in Chapter 6. The introduction of superhydrophobic surface coatings was presented for the first time. By definition water contact angles measured on superhydrophobic materials are higher than 150°. With the introduction of these materials it was hoped to minimize the contact between the PCR mix and the channel walls. Ultimately, this minimized contact between the PCR mix and the channel walls would increase the longevity of these microfluidic devices. The superhydrophobic materials applied to microchannels were based on zinc oxide and copper oxide. Both materials were treated so that hydrocarbon and fluorocarbon terminated surface were generated. Water contact angles were measured to be 120° and 150° for copper oxide hydrocarbon terminated and fluorocarbon terminated surfaces respectively. Water contact angles of 90° for zinc oxide hydrocarbon terminated and fluorocarbon terminated surfaces were also demonstrated. Microfluidic channels coated with fluorocarbon terminated copper oxide showed a higher water contact angle than for silane II coatings. Therefore it was hoped that performing CF-PCR within microfluidic channels coated with fluorocarbon terminated copper oxide would improve the results achieved in Section 5.1.2.2.4. However, due to leakage issues of these superhydrophobic microfluidic devices PCR could not be performed. Future work will focus on optimizing the fabrication and testing of these devices.

8

Appendix

This chapter contains a comprehensive and up to date snapshot of microfluidic companies operating in the chemical and biological sciences (A) and a brief overview on computational fluid dynamics (CFD) simulations (B) which have been performed in order to confirm experimental outcomes in Chapter 4.

8.1 Chapter 1: Appendix A

Here companies producing and commercializing miniaturized analytical devices are listed [1].

ABTECH Scientific Inc.	Miniaturized sensor devices	www.abtechsci.com
Advalytix AG	Surface acoustics wave nanopumps/chips	www.advalytix.com
Advion Biosciences	Array of nanoelectrospray nozzles	www.advion.com
Affymetrix, Inc	High density chip arrays	www.affymetrix.com
Agave Biosystems	Microfluidic flow cytometry	www.agavebio.com
Agilent Technologies	HPLC chips and microfluidics bionanalyzer	www.agilent.com
Ambion	Tissue microarrays	www.ambion.com
Amic AB	Microstructured plastic devices for microfluidics	www.4castchip.se
Amnis Corporation	High-throughput flow cytometry	www.amnis.com
Apibio	Biochips with oligonucleotide & and polypeptide probes	www.apibio.com
Applied Biophysics	Disposable electrode arrays	www.biophysics.com
Applied Biosystems	Microfluidic device for gene expression arrays	www.appliedbiosystems.com
Aurora Biosciences	Microsolenoid and piezoelectric dispensing in 3456 well plates	www.auroradiscovery.com
Ayanda Biosystems	Multielectrode array biochips for electrophysiology	www.ayanda-biosys.com

BD Biosciences	Tissue microarrays	www.bdbiosciences.com
Beckman Coulter	Liquid Handling	www.beckmancoulter.com
Bartels Mikrotechnik	Microvalves, micropumps, CE chips	www.bartels-mikrotechnik.com
Bioacore International	Sensor chip products with novel chemistries	www.biacore.com
Biocept Laboratories	Microfluidic chips for cell enrichment and extraction	www.biocept.com
BioDot	Nano-picoliter dispensing	www.biodot.com
Biofluidix	24 channel reusable print head for array printing	www.biofluidix.com
BioForce Nanosciences	Nanoarray molecular printing system	www.bioforcenano.com
Biolog	Phenotype Microarrays	www.biolog.com
Bio Logix LLC	Microfluidic devices and biosensors	www.biologix-usa.com
BioMicro Systems Inc.	Microfluidic microarray sample processing	www.biomicro.com
Bio-Rad Laboratories	Microfluidic RNA analysis	www.bio-rad.com
Bio Trove	Microfluidic lead discovery platform	www.biotrove.com
Boehringer Ingelheim micro Parts GmbH	Microfluidics for diagnostics	www.boehringer-ingelheim.de/microparts
Caliper Life Sciences	LabChip system for DNA and protein analysis	www.caliperls.com
Cascade Microtech	Microfluidic systems, microports	www.cascademicrotech.com
Cellectricon A B	Microsystems for cell based screening	www.cellectricon.com
Cellix	Microfluidic systems for drug discovery	www.cellix1ltd.com
Cybio AG	Nanodispensing technology	www.cybio-ag.com
Cellular Process Chemistry, Inc	Micro reactors	www.cpc-net.com

Cepheid	Microfluidic amplification cartridge	www.cepheid.com
Ciphergen	SELDI protein chips	www.ciphergen.com
Clondiag Chip Technologies	Point-of-care diagnostic system	www.clondiag.com
Clontech Technologies	Microarrays	www.clontech.com
Combimatrix	Customized microarray platform	www.combimatrix.com
Concept to Volume	Micro gas chromatograph	www.c2v.nl
Dantec Dynamics	Flowmap microfluidics	www.dantecdynamics.com
Decision Biomarkers	Biochip based assay system	www.decisionbiomarkers.com
Deerac Fluidics	Submicroliter dispensing	www.deerac.com
Dionex	Capillary and nano-LC	www.dionex.com
Directif Diagnostic Solutions	LOC system for DNA/RNA analysis	www.directif.de
EDC Biosystems	Non-contact dispensing	www.edcbiosystems.com
Ehrfeld Mikrotechnik	Modular micro-reaction syste,	www.ehrfeld.com
Eksigent Technologies, LLC	Micro-LC	www.eksigent.com
Epigem Limited	Polymeric Microfluidic devices	www.epigem.co.uk
Evotec Technologies	Nanoliter liquid handling	www.evotec-technologies.com
Exiqon	RNA microarrays	www.exiqon.com
Fluidigm	Microfluidic crystallography	www.fluidigm.com
Friz Biochem	Biochips for medical	www.frizbiochem.de

	diagnostics	
GE Healthcare	Code Link, Microarray Platform	www.amershambiosciences.com
Genetix	Microdispensing, tools for microarrays	www.genetix.com
Genomic solutions	Tools for liquid handling, micorarrays	www.genomicssolutions.com
Genoptics	Surface Plasmon resonance imaging, sensor chips	www.genoptics-spr.com
GeSIM	Miniaturized fluidic components, microdispensing, flow through systems	www.gesim.com
Gyros	Lab-CD	www.gyros.com
Hamilton	Liquid Handling workstation	www.hamiltoncompany.com
Handy Lab	Microfludics for Miniaturized assays	www.handylab.com
Helicos Biosciences	Single molecule nucleotide detection on microfluidic platform	www.helicosbio.com
Honeywell International	Microfluidic flow cytometry	www.honeywell.com
Hypromatrix	Antibody arrays	www.hypomatrix.com
Ibidi	Microfluidic Biodiagnostics	www.ibidi.com
Illumina	Fiber-optic array matrix for expression analysis	www.illumina.com
Innovadyne Technologies	Nanodispensing	www.innovadyne.com
Iris Biotechnologies	DNA microarrays, Piezo Arrayer, miro pump system	www.irisbiotech.com
Labcyte Inc	Nano/picoliter dispensing via acoustic ejection	www.labcyte.com
454 Life Sciences	Ultra-High throughput DNA sequencing	www.454.com
Lioni X	CE chips, micromixers, conductivity sensors, microreactors	www.lionix.nl
Meso Scale Discovery	Multi-array and multi spot plates	www.meso-scale.com
Metrigenix	Microarray devices for	www.metrigenix.com

	bioanalysis	
Mezzo Technologies	LIGA for microfluidics, LOC	www.mezzosystems.com
Micralyne	Microfluidic chips, microlens arrays	www.micralyne.com
Microchip Biotechnologies, Inc	Microfluidic sample preparation	www.microchipbiotech.com
Microdrop technologies GmbH	Nanodispensing of liquids	www.microdrop.de
Micro Fluidic Systems	Microfluidic bionanalytical instruments	www.microfluidicsystems.com
Microfluidic ChipShop GmbH	Microfluidic platform with micromixer array	www.microfluidicchipshop.de
Micronit Microfluidics bv	Capillary/chip electrophoresis, microchemical reactor chips	www.micronit.com
Microsaic Systems	Integrated mass spectrometer chip	www.microsaic.com
Microtec	Microfluidic chip system for biotechnology applications	www.microtec-d.com
Micro-Tech Scientific	Nano-HPLC system	www.microlc.com
Miraibio	Bead array system for clinical diagnostics	www.miraibio.com
Mobidiag	Lab-on-a-chip system for DNA based diagnostics	www.mobidiag.com
Molecular Devices	Liquid Handling, electrophysiology	www.moleculardevices.com
Molecular Vision	Low-cost diagnostic devices	www.molecularvision.co.uk
Nanion	Microfluidic perfusion system for electrophysiology	www.nanion.de
Nanogen	NanoChip, Molecular Biology Workstation	www.nanogen.com
Nanostream	Micro multichannel LC system	www.nanostream.com
Nicoform	Electroformed mold inserts for nanofluidics	www.nicoform.com
Oxford Gene Technology	Oligonucleotide arrays	www.ogt.co.uk
Pamgene	Porous flow through arrays	www.pamgene.com
Panomics	Protein and DNA	www.panomics.com

	microarrays	
Perkin Elmer	Protein microarray systems, reagent and micro dispensers	www.perkinelmer.com
Plexigen	3D biological microarray	www.plexigen.com
Pria Diagnostics	Miniaturized point-of use diagnostics platform	www.priadi.com
Protagen AG	Protein biochips	www.protagen.de
Qiagen	Microarray products and analysis	www.qiagen.com
Randox Laboratories	Biochips for diagnostic applications	www.randox.com
Scienion	Tools for microarraying and dispensing	www.scienion.com
Sensirion AG	Miniaturized flow sensors	www.sensirion.com
Seyonic SA	Nanodispensing with integrated flow sensor chip	www.seyonic.com
Sequenom	Miniaturized chip-based disposables, nanodispensing system	www.sequenom.com
Shimadzu Corporation	Protein array analysis	www.shimadzu-biotech.net
Silicon Valley Scientific, Inc	Modular Microfluidic Technologies	www.svsci.com
Sionex	Ion mobility sensor chips	www.sionex.com
SLS Micro Technology	Miniaturized gas chromatograph	www.sls-micro-technology.de
Syrris	Microfluidic flow reactor	www.syrris.com
Tecan	Microfluidics platform for measuring drug-drug interactions	www.tecan.com
Telechem International	Microarray instruments and substrates	www.arrayit.com
Thales Nanotechnology	Microfluidic reactors for combinatorial chemistry	www.thalesnano.com
Thermo Electron	Nanotitration, tools for array fabrication	www.thermo.com
thinXXS	Microfluidic construction kit, micropumps	www.thinxxs.com
Tomtec	Liquid transfers via non-contact dispensing and pin tools	www.tomtec.com
Velocity 11	Nanoliter dispensing	www.velocity11.com

Vysis	and handling system GenoSensor, Microarray Platform	www.vysis.com
Zeptosens	Sensichip/protein microarray	www.zeptosens.com
Zyomyx, Inc	Biochips for protein profiling	www.zyomyx.com

8.2 Chapter 4: AppendixB

This Section gives a brief overview of CFD simulation methods which were used in order to compare with the experimental outcomes in Chapter 4.

8.2.1 Modelling

8.2.1.1 Background

The objective of the modelling studies was to simulate fluid flow in a microchannel and calculate the temperature distribution. A Computational Fluid Dynamics (CFD) software package is used for this purpose. The CFD software allows analysis of fluid flow, heat transfer, mass transfer and associated phenomena such as chemical reactions. Primarily based on solving the governing Navier-Stokes equations for momentum, energy or mass transport, the effectiveness of the technique completely depends on the physics of the problem [2]. Navier-Stokes equations, such as equation 8.1, are the fundamental partial differential equations describing fluid flow.

$$u_t + (u\nabla)u = \nu\nabla^2 u - \nabla p + f \qquad (8.1)$$

u and p are unknown velocity and pressure vectors, f is the externally applied force (for example gravity), ν is the viscosity, ∇ is the gradient operator, and ∇^2 is the Laplacian operator. The methods for solving such equations will not be discussed in detail, but an overview of the simulation process which consists of three steps (pre-processing, solving and post-processing) will be described in following section briefly.

8.2.1.1.1 Pre-Processing

The pre-processor is a console which facilitates the description of the flow or transport problem in detail allowing the user to specify the necessary inputs these include the definition of the geometry of the region of interest, generation of a sub-division of this domain into a number of smaller, non-overlapping sub-domains (commonly called a grid or a mesh),definition of the fluid properties and the selection of physical or chemical phenomena to be modelled, and finally the specification of appropriate boundary conditions.

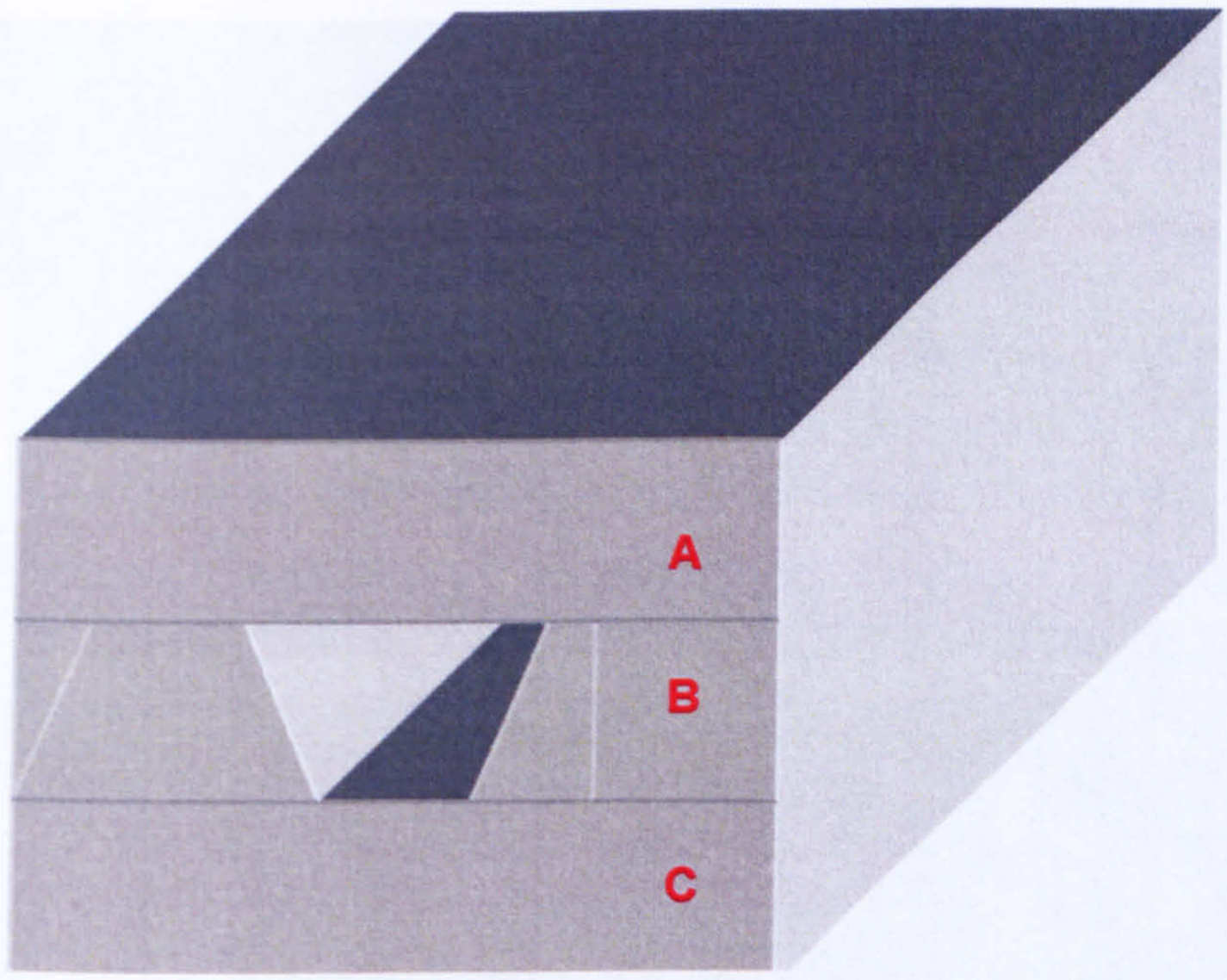
8.2.1.1.2 Solving

After describing the flow problem in detail the solver console solves the problem based on the input parameters. The solver program approximates the governing equations for the flow domain and approximates them to algebraic equations. It then uses iterations to solve these equations for each of the variables such as velocity, temperature, pressure, shear stress etc, at each point in the domain. Once iterations converge, all data generated for each of the variables is then stored in a file.

8.2.1.1.3 Post-Processing

The post processor is used for analysing the solution. This includes versatile data visualisation tools such as, domain geometry and grid display, vector plots, line and shaded contour plots, 2D and 3D surface plots, particle tracking, view manipulation, animation for dynamic result display and colour postscript output. Examples of the graphical capabilities of CFD codes can be seen in Figure 8.1 which presents a mesh grid and Figure 8.2 which presents a vector plot for velocity.

a)



b)

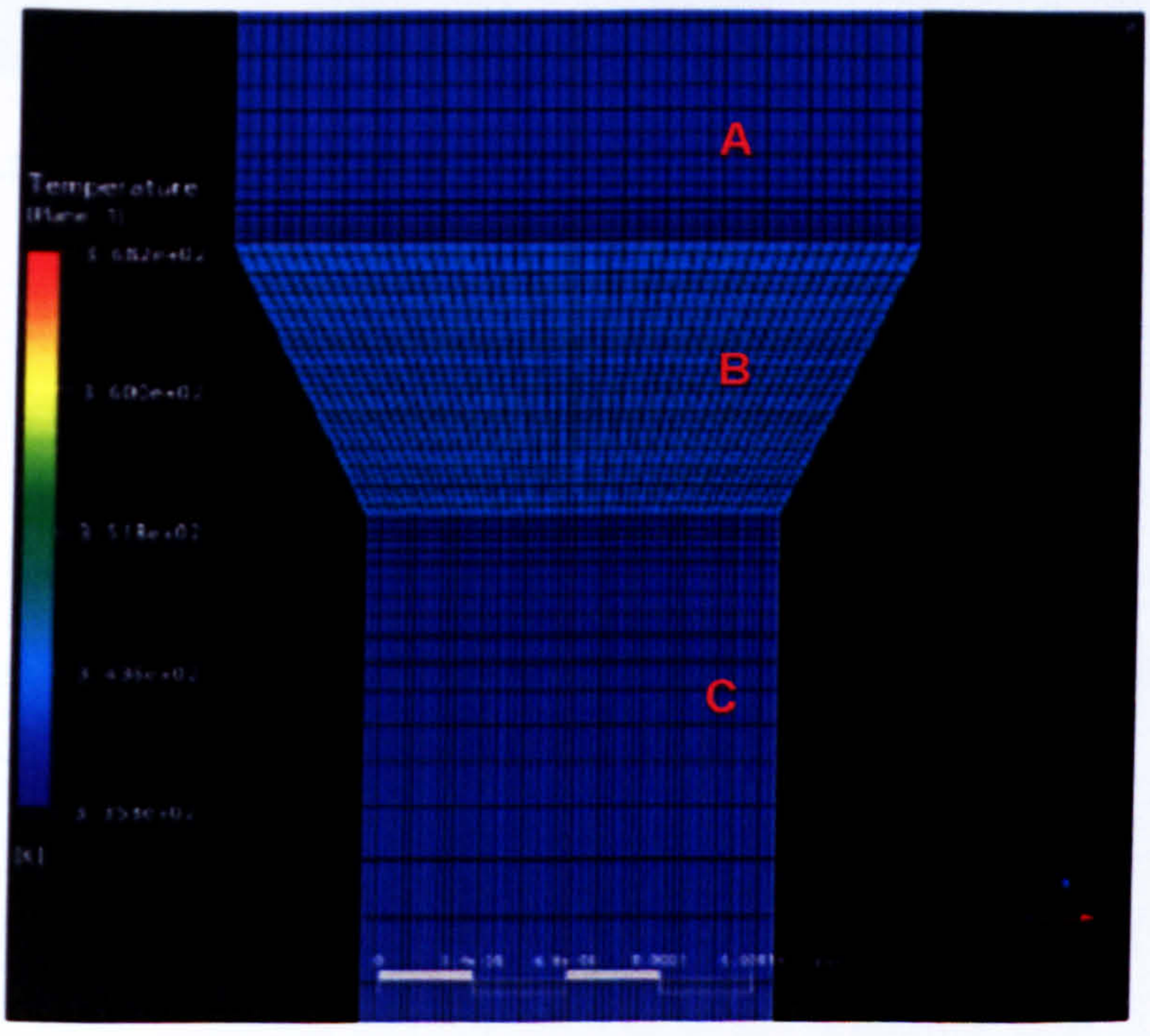


Figure 8.1 a) 3-D schematic of a trapezoidal microfluidic channel. b) mesh plot of cover glass, microfluidic channel and bottom glass. In this particular application a semi-circular microchannel was modelled (image not shown).

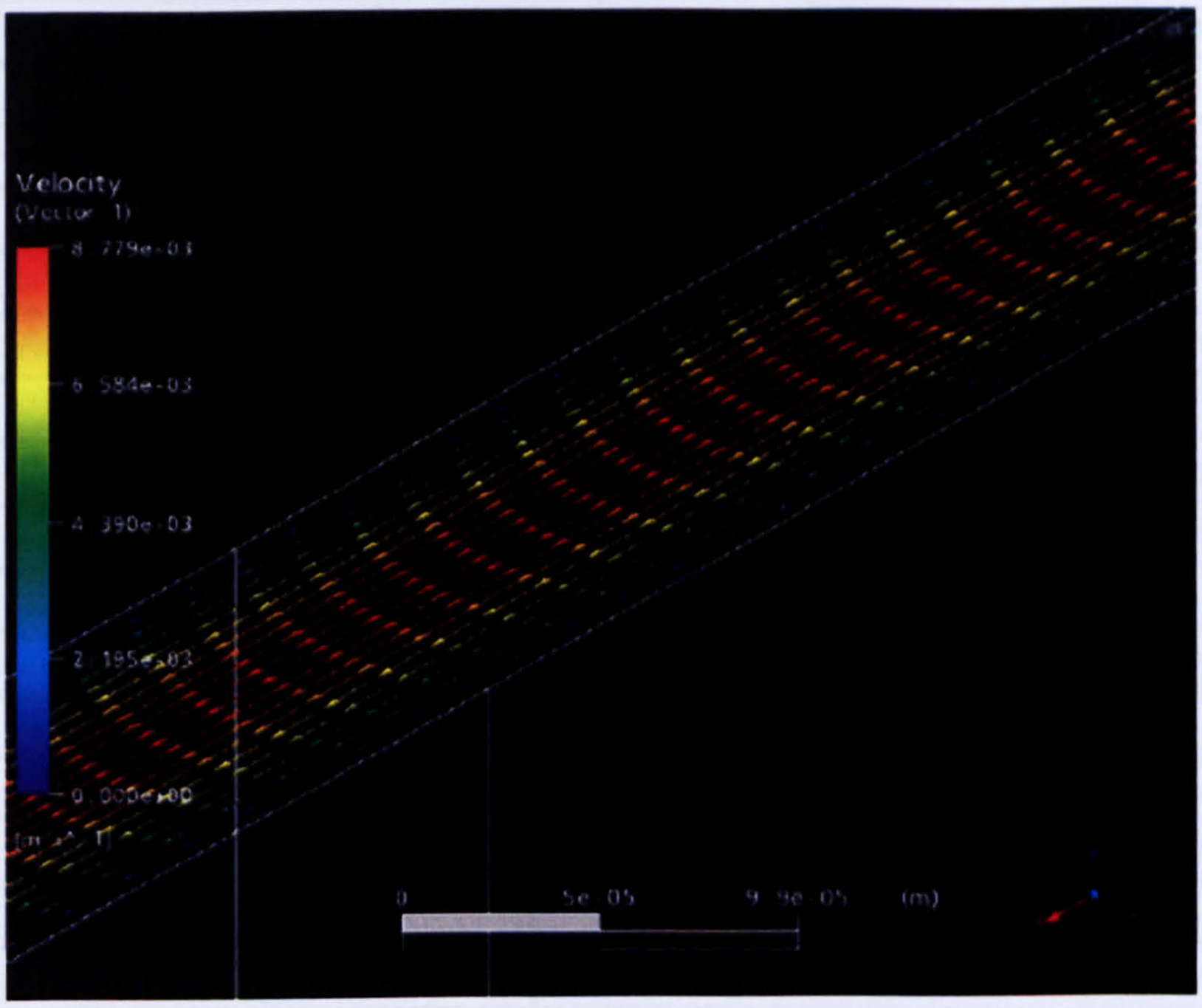


Figure 8.2 **Velocity plot of fluid in microfluidic channel. The two outer lines represent the channel walls of a microfludic channel, while the arrows represent the flow of a fluid in the microchannel. The colour of the arrows represents the speed with which the fluid moves through the channels with higher velocities in the centre of the channel and slower velocities at the edges of the channel.**

8.2.1.2 Process of Modeling

After defining the microfluidic channel dimensions and all physical parameters within the set-up (Table 8.2), the modelling can be initiated.

	air	water	glass
Viscosity(Ns/m^2)	$1.81*10^{-5}$	10^3	
Conductivity(W/m/K)	0.0257	0.6	1.1
C_p(J/Kg/K)	1006	4.18	0.88
Density(kg/m^3)	1.21	1	
Accleration due to grav(m/s^2)	9.81	n.a.	n.a.
Wall temp, T_o(°C)	93	n.a.	n.a.
Outside temp, T_{inf} (°C)	20	n.a.	n.a.
Temp diff, ΔT (°C)	73	n.a.	n.a.
Film temp, T_f	56.5	n.a.	n.a.
Thermal expansion coeff, Beta(1/°C)	0.017699115	n.a.	n.a.
Geometry dia, D (m)	$2.00* 10^{-3}$	n.a.	n.a.
		n.a.	n.a.
Pr	$7.10*10^{-1}$	n.a.	n.a.
Gr	451.6567853	n.a.	n.a.
		n.a.	n.a.
Nu	2.191783029	n.a.	n.a.
		n.a.	n.a.
heat transfer coefficient ($W/m^2/K$)	28.16441192	n.a.	n.a.

Table8.2 **Fluid, air and glass parameters and boundary conditions of inlet, pressure and wall.**

8.2.1.3 Results

Simulation data for fluidic temperature determination in chip III with flow rates between 1, 3 and 10 µl/min are presented in Figure 8.3 while corresponding FLIM experimental data are presented in Figure 8.4. Here black data points represent fluid flow rates of 1 µl/min, green data points represent fluid flow rates of 3 µl/min and red data points represent fluid flow rates of 10 µl/min. In both data sets the increase of fluidic temperature between 65 °C and 95 °C is observed. While the experimental data shows a temperature increase with similar behaviour for all flow rates, the simulation data only shows similar behaviour at flow rates of 1 and 3 µl/min but an aberration from this trend for fluidic flow at 10 µl/min (Figure 8.3). A much steeper slope is generated with the data points at a flow rate of 10 µl/min compared with data points at flow rates of 1 and 3 µl/min resulting in faster temperature increase. This theoretical outcome does not agree with the

experimental data but as presented in Figure 8.4 where similar behaviour between all flow rates is observed.

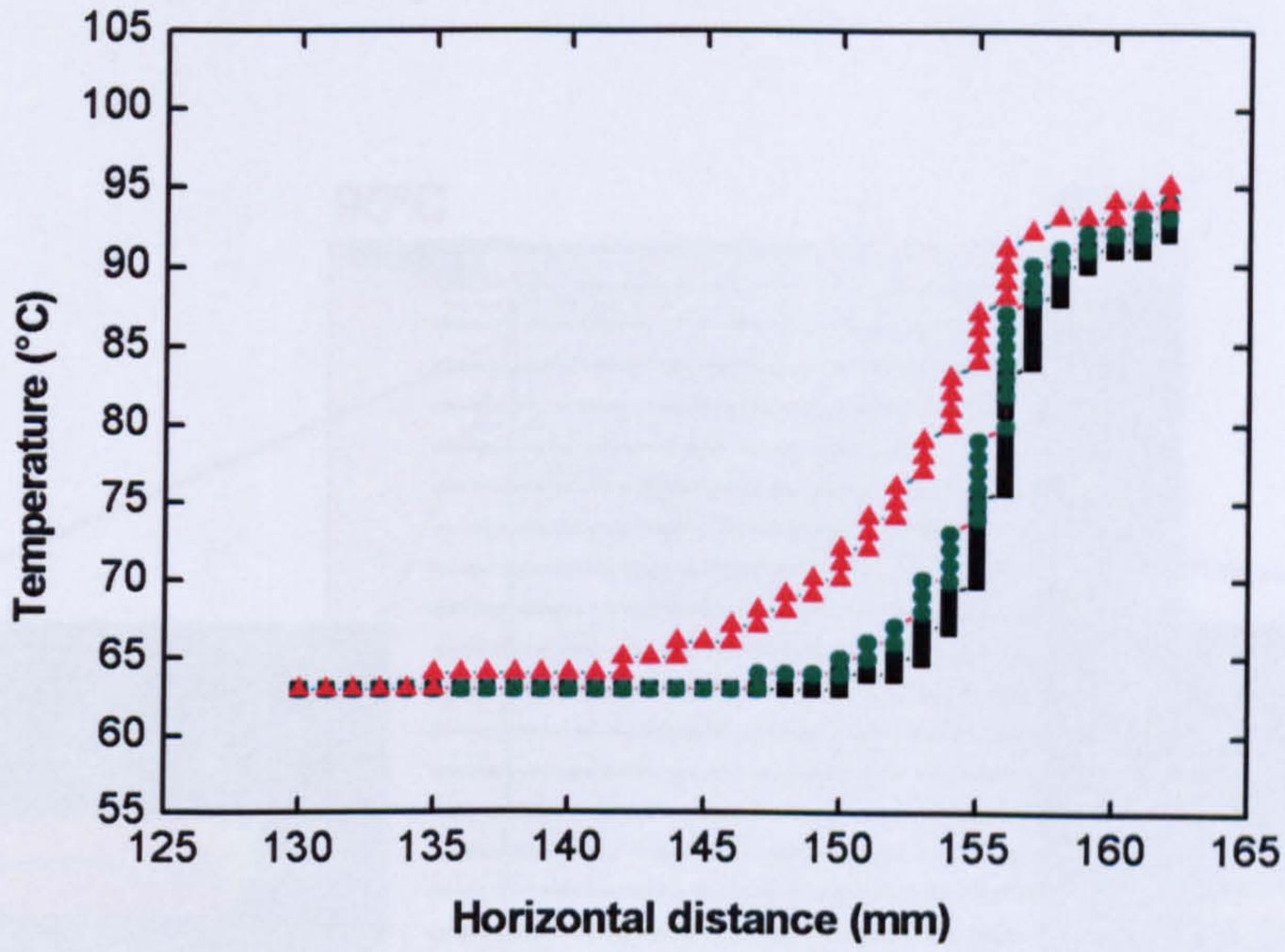


Figure 8.3 **Variation of temperature as a function of distance across the device with volumetric flow rates of 1 µl/min (black), 3 µl/min (green) and 10 µl/min (red) for simulation.**

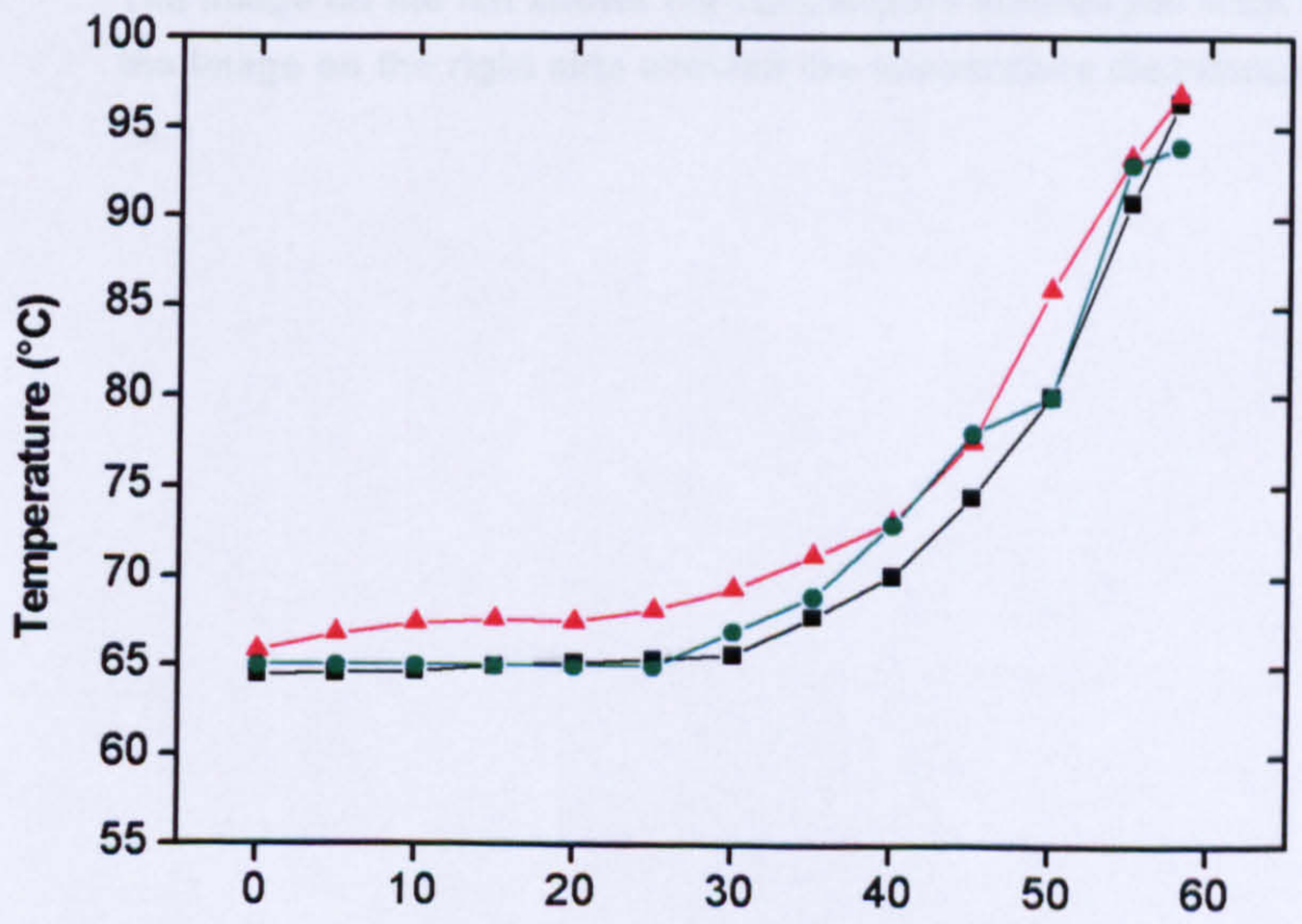


Figure 8.4 **Variation of temperature as a function of distance across the device with volumetric flow rates of 1 µl/min (black), 3 µl/min (green) and 10 µl/min (red) for fluorescence experiment.**

Due to CFD's immense graphic capabilities it was also possible to create false-colour images of the temperature distribution as presented in Figure 8.5. The transition from 95 °C to 65 °C is presented by a red arrow, and the transition from 65 °C to 95 °C is presented by a blue arrow.

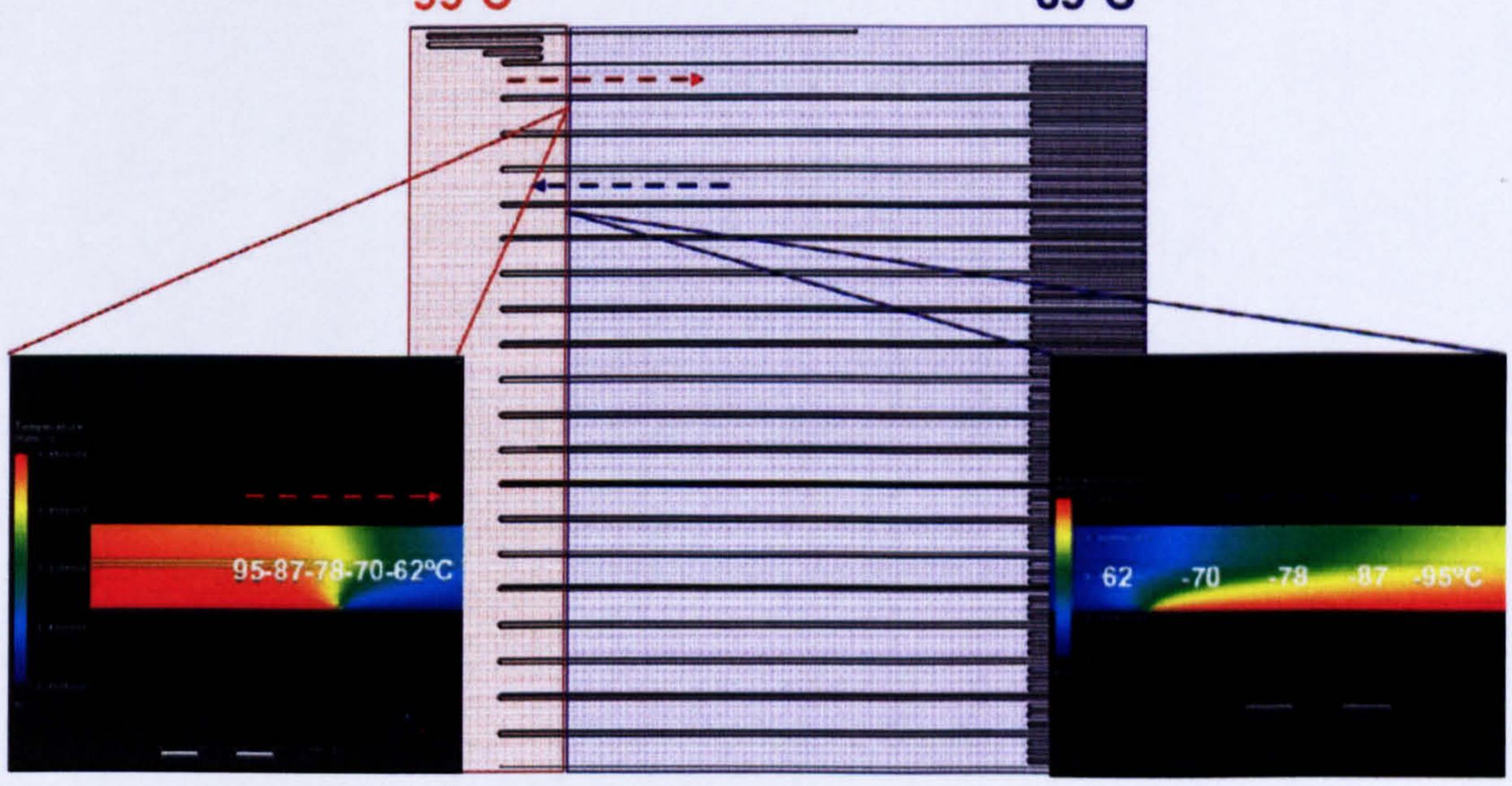


Figure 8.5 **False colour images of temperature distribution within a microfluidic channel. The image on the left shows the temperature distribution from 95 to 65 °C and the image on the right side showed the temperature distribution from 65 to 95 °C.**

1. Haber, C., *Microfluidics in commercial applications; an industry perspective.* Lab on a chip, 2006. 6: p. 1118-1121.
2. Valluri, P., *Multiphase Fluid Dynamics in Structured Packings*, in *Department of Chemical Engineering and Chemical Technology* 2004, Imperial College London. p. 280.